ICASEA 2018

CAMERON HIGHLANDS

Proceeding:

5TH INTERNATIONAL CONFERENCE ON APPLIED SCIENCES AND ENGINEERING APPLICATION (ICASEA 2018)

eISBN 978-967-15744-1-6

Co-organizer:

GLOBAL ACADEMIC EXCELLENCE

Penerbit Akademia Baru

5th International Conference On Applied Sciences and Engineering Application (ICASEA 2018)

eISBN 978-967-15744-1-6

PUBLISHED BY:
GLOBAL ACADEMIC EXCELLENCE (M) SDN BHD
(1257579-U)
KOTA BHARU MALAYSIA

CONTENT

OIL RECLAMATION OF IN-SERVICE POWER TRANSFORMER USING FULLER'S EARTH: AN EXPERIENCE 1

"DRIVE THRU" ATTENDANCE SYSTEM USING RADIO FREQUENCY IDENTIFICATION (RFID): A REVIEW 11

A REVIEW ON VARIOUS TECHNIQUES AND RECENT ADVANCES IN POLYMERIC ADDITIVES TO MITIGATE WAX PROBLEMS IN CRUDE OIL 19

SELF-CLEANING GLASS THROUGH SUPERHYDROPHILIC OF TIO_2 COATING 36

EFFECT OF VARIABLE AND LOW ORGANIC LOADING RATE ON FORMATION OF AEROBIC GRANULAR SLUDGE IN SEWAGE TREATMENT 47

LOW-COST ACTIVATED CARBON PRODUCED FROM WASTE TYRE FOR REMOVAL OF 2-CHLOROPHENOL 58

POTENTIAL OF POLYSULFONE/POLYDIMETHYL SILOXANE THIN FILM COMPOSITE (PSF-PDMS-TFC) MEMBRANE FOR CO_2/N_2 GAS SEPARATION 66

CONCEPT GENERATION OF SUGAR PALM / GLASS FIBER REINFORCE THERMOPLASTIC POLYURETHANE HYBRID COMPOSITE AUTOMOTIVE CRASH BOX 74

THE LIGNIN REDUCTION OF RICE HUSK ON ALKALINE AND DILUTE ACID PRETREATMENT (EKSPERIMENTAL AND CFD MODELING)**Error! Bookmark not defined.**

OPENFOAM IMPLEMENTATION FOR THE STUDY OF STREAMWISE VORTEX-INDUCED VIBRATION-BASED ENERGY HARVESTER FOR SENSOR NETWORKS 83

REMOVAL OF THE OLD ADHERE MORTAR FROM CRUSHED CONCRETE WASTE AGGREGATE (CCWA) WITH DIFFERENT HCL'S MOLARITY AND ITS EFFECT ON THE PROPERTIES OF THE CCWA 96

THERMOPHYSICAL AND SPECTROSCOPIC APPROACH ON MOLECULAR INTERACTIONS OF METHYL-TERT-BUTYL ETHER WITH ETHANOL AT TEMPERATURES OF 303.15 K, 308.15 K, 313.15 K, AND 318.15 K**Error! Bookmark not defined.**

PERFORMANCES OF SANDWICH MEMBRANE IN RECLAMATION OF WATER FROM FINAL DISCHARGED POME 107

FABRICATION AND PERFORMANCE OF PSf/CA BLEND ULTRAFILTRATION MEMBRANE ON EFFECT OF DIFFERENT POLYMER RATIO 115

OPTIMIZATION OF OZONATION PROCESS IMPLEMENT PERSULFATE USING AZO DYES 131

NUMERICAL STUDY FOR FLOW OVER A REALISTIC GENERIC MODEL, DRIVAER, USING URANS 144

NOISE MEASUREMENT IN ANECHOIC WIND TUNNEL OF ROD-AIRFOIL WITH LEADING EDGE SERRATIONS 157

MICROWATT ENERGY HARVESTING BY EXPLOITING FLOW-INDUCED VIBRATION 168

EFFECTS OF MICROWAVE FINISH DRYING ON THE TEXTURAL CHARACTERISTICS OF BUFFALO JERKY 179

POTENTIAL USE OF FISH COLLAGEN HYDROLYSATE AS FAT REPLACER IN BUFFALO PATTIES 187

APPLICATION OF VARIOUS MECHANICAL TREATMENTS FOR MEAT TENDERIZATION 194

REVIEW ON DIFFERENT EXTRACTION METHODS OF POLYPHENOL COMPOUNDS FROM POMEGRANATE (punica granatum) 205

ANALYSIS THE INFLUENCE OF HEART RATE AND MUSCLE ACTIVITY TOWARDS MUSCLE FATIGUE IN LAYUP WORKERS 216

OBSERVATION OF SPACE CHARGE FORMATION IN XLPE/MgO NANOCOMPOSITE 225

ACID-MODIFIED ADSORBENTS FROM SUSTAINABLE GREEN-BASED MATERIALS FOR CRUDE OIL REMOVAL 231

EXPERIMENTAL EVALUATION OF CRUDE OIL USING SAWDUST-LIGNIN SURFACTAN 241

OBSERVATION OF SPACE CHARGE FORMATION IN *XLPE/MgO NANOCOMPOSITE* ..... **Error! Bookmark not defined.**

DEVELOPMENT OF HIGH TEMPERATURE HIGH PRESSURE (HTHP) WATER BASED DRILLING MUD USING SYNTHETIC POLYMERS, AND NANOPARTICLES. 252

WATER TRANSPORT PROPERTIES OF BIO-NANOCOMPOSITES REINFORCED BY SUGAR PALM (*ARENGA PINNATA*) NANOFIBRILLATED CELLULOSE 263

EVALUATION OF EFFECTIVENESS OF NANOPARTICLES AND GEMINI SURFACTANTS ON ENHANCED OIL RECOVERY (EOR) METHOD 278

NANOCELLULOSE REINFORCED STARCH POLYMER COMPOSITES: A REVIEW OF PREPARATION, PROPERTIES AND APPLICATION 291

Proceeding: 5th International Conference on Applied Sciences and Engineering (ICASEA, 2018)
(eISBN 978-967-15744-1-6)
Capthorne Hotel, Cameron Highlands, Malaysia

OIL RECLAMATION OF IN-SERVICE POWER TRANSFORMER USING FULLER'S EARTH: AN EXPERIENCE

Sharin Ab Ghani [1]
Imran Sutan Chairul [1]
Nur Hakimah Abdul Aziz [1]
Muhammad Syahrani Johal [2]
Aminur Hazieq Zulkefli [1]

1Fakulti Kejuruteraan Elektrik, Universiti Teknikal Malaysia Melaka, Hang Tuah Jaya, Melaka.
[2]Fakulti Teknologi Kejuruteraan, Unversiti Teknikal Malaysia Melaka, Hang Tuah Jaya, Melaka

---

Abstract: *This paper described in-laboratory oil reclamation process of aged transformer oil using adsorbent; Fuller's earth. The niche of this paper is the usage of real aged transformer oil taken from an 11kV/433V in-service power transformer made by ACEC Transformer in 1986. The reclamation process is achieved by forcing a mixture of aged transformer oil and Fuller's earth through a filter paper with the aid of a vacuum pump, hence producing reclaimed transformer oil. This oil were then inserted in an amber glass bottle, blanketed with nitrogen, tightly sealed and labeled. To test the effectiveness of Fuller's earth as adsorbent, parameters of Dissolved Decay Product (DDP) were measured using UV-Visible Spectrophotometer (UV-Vis) by referring to ASTM D6802. In addition, Total Acid Number (TAN) and Breakdown Voltage (BdV) measurement were carried out complying the ASTM D974 and ASTM D1816 respectively. Results of UV-Vis indicated that Fuller's earth can adsorbed 25.24% of DDP in aged transformer oil. As the DDP decreased, TAN is 84.62% reduced while BdV increased 50%. These findings are parallel with the breakdown voltage mechanism due to acidity emergence. It is proved that Fuller's earth is effective adsorbent for oil reclamation process.*

Keywords: *Aged Mineral Oil, Reclamation, UV-Visible Spectrophotometer (UV-Vis), Total Acid Number (TAN), Breakdown Voltage (BdV).*

Introduction

Lifespan of a power transformer depends on its insulation; liquid (transformer oil) [1] and solid (cellulose-based paper/pressboard) [2]. Transformer oil such mineral oil and natural ester oil also acts as coolant for power transformer's winding due to oil ability to dissipate heat by convection [3] . Ageing of transformer oil usually cause by electrical and thermal stresses but can be speed up if humidity, high heat, oxidation and level of acidity are present in the oil [4]. Since mineral oil; a petroleum-based product is commonly used as transformer oil, ecosystem can be threatened if aged mineral oil are improperly disposed. The disposing problem can be overcome by recycling the aged mineral oil through reclamation process [5]–[7]. This process helps improving the quality of aged mineral oil by removing contaminants as well as sludge present in the aged mineral oil using various adsorbents such Fuller's earth [5], palm shell activated carbon [8] and activated bentonite [7]. Although many studies have been conducted previously, the niche of this study is a reclamation process carry out on real aged transformer oil taken from an 11kV/433V in-service power transformer made by ACEC Transformer in

1986. An almost 30 year's aged mineral oil samples. The reclamation process is conducted in laboratory using Fuller's earth as adsorbent.

Methodology

Figure 1 shows a flowchart of research methods for this study. All works were done in a laboratory. The study starts with collecting few liters of aged mineral oil samples. This oil will be used in reclamation processes. The reclamation process is based on IEEE Guide for Reclamation of Insulating Oil [5] and [8] while works of detecting Dissolved Decay Product (DDP) using UV-Visible Spectrophotometer (UV-Vis), measuring Total Acid Number (TAN) as well as determining Breakdown Voltage (BdV) are referred to standards of ASTM D6802 [9], ASTM D974 [10] and ASTM D1816 [11] respectively. Aged mineral oil samples for this research were courtesy of Tenaga Nasional Berhad (TNB) taken from an in-serviced power transformer made by ACEC. The transformer is as shown in Figure 2(a) and 2(b). The transformer's rating is 500 kVA, 11kV/433V. Mineral oil in the transformer have undergoes ageing process for nearly 30 years because it never been filtered, replaced or reclaimed since manufactured in 1986. Reclamation processes [5] used in this study is combination between contact process and filtration. Contact process is mixing an amount of adsorbent with aged mineral oil samples producing mixed oil. The mixing was done using digital hotplate magnetic stirrer as shown in Figure 3(a). The stirrer speed and temperature is maintained at 750 rpm and 60℃ for 4 hours so that the mixture can be homogenized. The mixed oil produced from contact process will be filtered through filtration process. Filtration is separating the mixed oil using filter paper to remove sludge (adsorbents and DDP formed during ageing of mineral oil) producing reclaimed oil. As the filter paper used (Whatman No 42) is a 2.5 μm in pore sizes, time taken for filtration process will take several days to complete. This delay can cause the mixed oil under filtration, exposed to moisture and oxidation. Therefore, the aid of a vacuum pump is used to speed up the process as well as preventing any moisture or oxidation. Figure 3(b) shows a filtration process. Mixed oil from contact process is poured directly to a fleaker. The oil is filtered through a filter paper initially put between the fleaker and a flask. A vacuum pump is connected to the flask using rubber hose to speed up the flow rate of the mixed oil as well removing air and moisture in the flask. With the aid of a vacuum pump, filtration can be completed within 2 hours. Figure 4 shows a UV-Vis set used to determine a relative content of DDP. Initially, a cuvette is filled with 5 ml of oil sample using a syringe. Then, the cuvette is placed into the UV-Vis set. When light radiations interact with the oil sample, the passing lights are carried to the spectrophotometer through an output fiber. The fiber is connected to a screen that displaying an absorption spectrum curve. As for analysis, the absorption spectrum of oil samples are measured over a wavelength range between 360 to 600 nm in accordance with ASTM D6802 [9]. Chemical substances such Potassium Hydroxide (KOH), Isopropyl Alcohol (IPA) and Potassium Hydrogen Phthalate (KHP) are required to determine TAN in oil samples. Procedures for this test are referred as in [12]. Firstly, 5g oil samples are weighed into a titration vessel and 20 mL IPA solvent are added. The solution is then titrated using c(KOH in IPA) = 0.1 mol/L. TAN of oil samples are displayed and recorded. Figure 5 shows a TAN test set. Initially, BdV test electrodes are cleaned using acetone and dried. Next, the gap between electrodes is set to 1mm. After that, the electrodes were immersed into a beaker of 500 ml oil samples and placed into the BdV set as shown in Figure 6. The electrodes must fully immerse into the oil and there should be no air bubbles present in the oil before BdV measurement can be done as per ASTM D1816 [11].

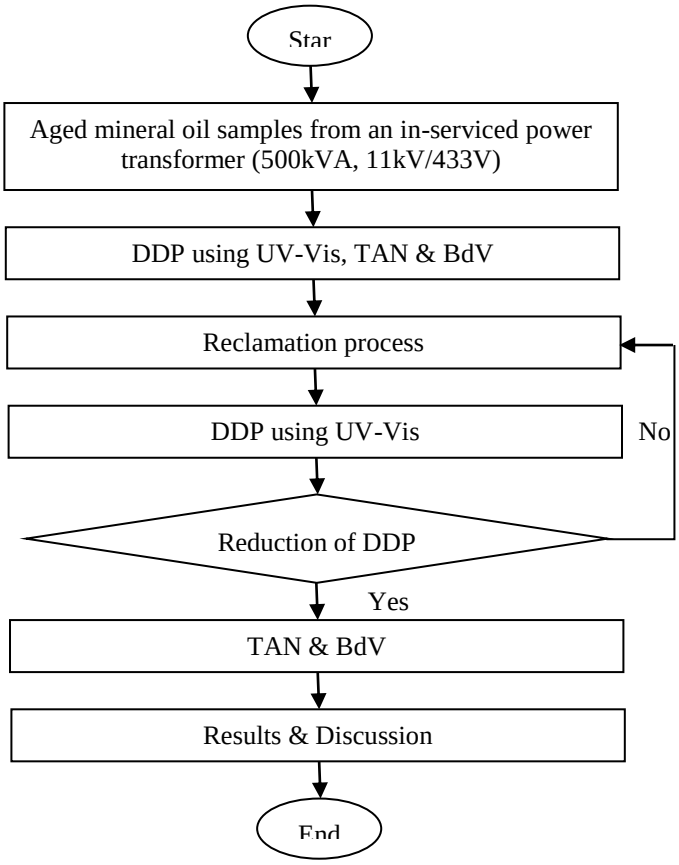

Figure 1 Flowchart of Research Methods

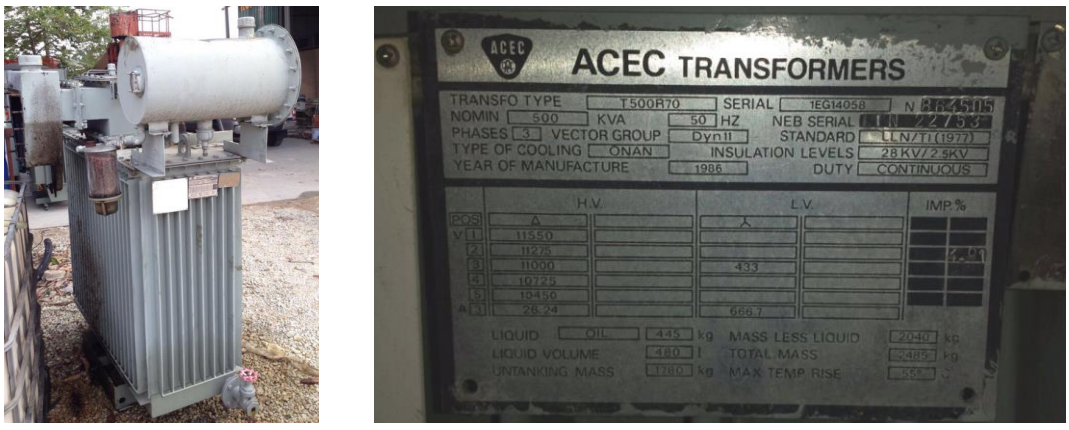

(a) (b)

Figure 2 (a) In-Serviced ACEC's Power Transformer (b) Nameplate of ACEC's Power Transformer

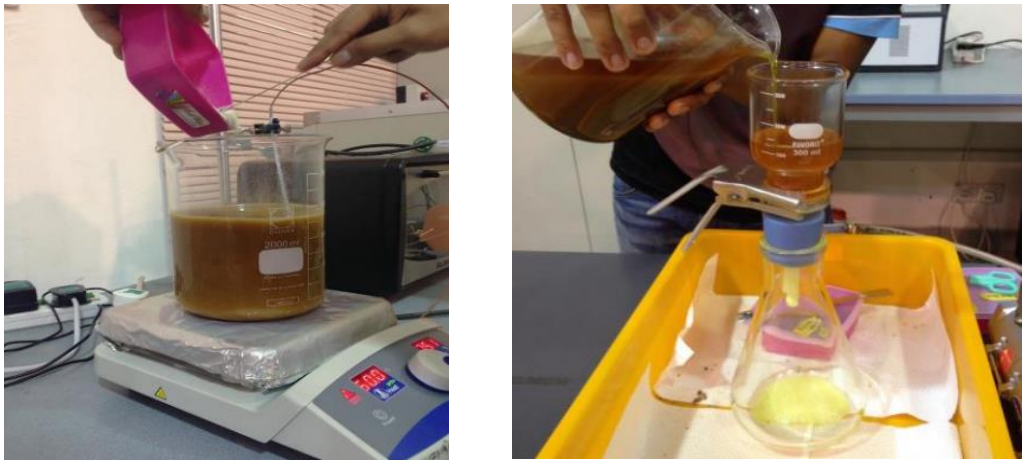

(a) (b)

Figure 3 (a) Contact Process (b) Filtration Process

Figure 4 UV-Visible Spectrophotometer (UV-Vis) Set

Figure 5 Total Acid Number (TAN) Test Set.

Figure 6 Breakdown Voltage (BdV) Set

Results and Discussion

Parameters of Dissolved Decay Product (DDP) were measured using UV-Visible Spectrophotometer (UV-Vis) by referring to ASTM D6802[9]. In addition, Total Acid Number (TAN) and Breakdown Voltage (BdV) measurements were carried out complying the ASTM D974[10] and ASTM D1816[11] respectively. All tests were carried out on aged mineral oil samples and reclaimed oil for comparison. Regarding reclamation process, there are two (2) different oil samples were prepared namely Sample 1 and Sample 2. Sample 1 is a mixture between 100g adsorbent and 1000ml aged mineral oil while Sample 2 is a mixture of 5g adsorbent with 500ml aged mineral oil. Adsorbent used for this study is Fuller's earth from Sigma-Aldrich [13]. This adsorbent is in powder forms and harmful if exposed to skin or inhale. Thus, safety gears of mask, rubber gloves and safety goggles were worn. The weights of adsorbent were measured using digital analytical balance whereas the aged mineral oil volumes were measured using beaker. The summary on quantities of adsorbent and aged mineral oil to prepare Sample 1 and 2 are shown in Table 1. The different quantities are by referring to previous research in [7] and [14].

Table 1: Quantities of Adsorbent and Aged Mineral Oil

Oil Sample	Adsorbent (g)	Aged Mineral Oil (ml)
Sample 1	100	1000
Sample 2	5	500

Sample 1 is reclaimed once to produce reclaimed oil but Sample 2 will undergoes several cycles of reclamation process. The reclaimed oil from the first cycle of Sample 2 will be reused for the second cycle of reclamation process. During new cycle, new 5g of adsorbent is used. The process is repeated 5 times. Transformer oil is exposed to oxidation process due to present of dissolved oxygen in oil. Presence of oxidation by-product as well as deterioration of transformer oil can be indicated by colour changes of oil. Figure 7(a) shows colour of aged mineral oil (AMO) while Figure 7(b) shows colour of Sample's 1 reclaimed oil (S1RO). It shows that the colour of AMO will change from dark brown to light brown due to reclamation process. Same result is achieved for Sample's 2 reclaimed oils (S2RO) as shown in Figure 8(a)-(e). The colour is lighter after each cycle of reclamation process. This decolourized of aged mineral oil from dark to lighter brown is due magnesium and calcium ion contain in Fuller's earth.

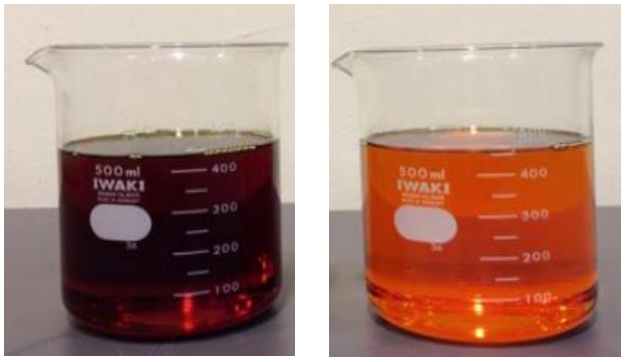

(a) *(b)*

Figure 7 (a) Colour of Aged Mineral Oil (AMO). (b) Colour of Sample 1's Reclaimed Oil (S1RO).

(a) (b) (c) (d) (e)

Figure 8 (a) Colour of Sample 2's Reclaimed Oil After 1st Reclamation. (b) Colour of Sample 2's Reclaimed Oil After 2nd Reclamation. (c) Colour of Sample 2's Reclaimed Oil After 3rd Reclamation. (d) Colour of Sample 2's Reclaimed Oil After 4th Reclamation. (e) Colour of Sample 2's Reclaimed Oil After 5th Reclamation.

The wavelength range chosen for this study is between 360 nm and 600 nm as referred to ASTM D6802[9]. The absorbance unit is a value that indicates the amount of UV-light absorb by the DDP. High value of absorbance indicates high DDP. The DDP's relative content of oil samples is determined by integrating the area under an absorbance versus wavelength curves'. Figure 9 shows curves of absorbance (range of 0-4.5a.u) with respect to wavelength (range of 360-600nm) for aged mineral oil (red line), Sample's 1 reclaimed oil (green line) and Sample's 2 reclaimed oil-after 5 cycle of reclamation process (blue line).

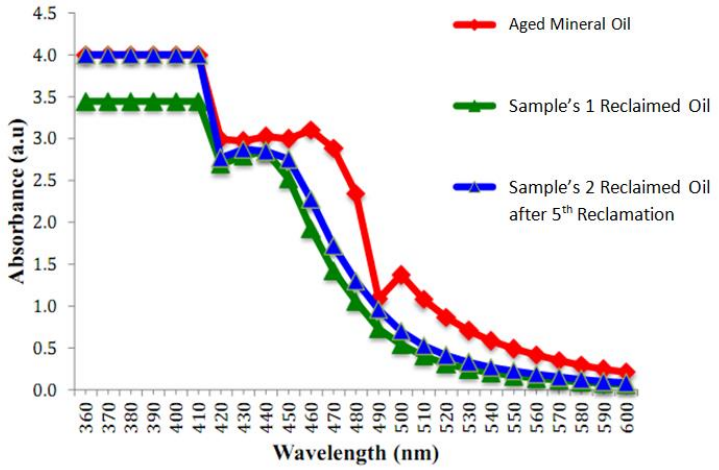

Figure 9 Curves of Absorbance (a.u) versus Wavelength (nm)

The wavelength at 420 nm is chosen as reference to analyze the reclamation process. As shown in Figure 9, at 420nm, absorbance unit of aged mineral oil, Sample's 1 reclaimed oil and Sample's 2 reclaimed oil-after 5 cycle of reclamation process is 2.9929a.u, 2.771a.u and 2.6919a.u respectively. These decrement value of absorbance unit indicate that DDP or oxidation by-products such low molecular weight acid decrease after reclamation process as found in [8]. Figure 10 shows graphs of DDP's of aged mineral oil (red), Sample's 2 reclaimed oil-after 5 cycles of reclamation process (blue) and Sample's 1 reclaimed oil (green). The DDP values are 498.34a.u, 422.8625a.u and 372.57a.u accordingly.

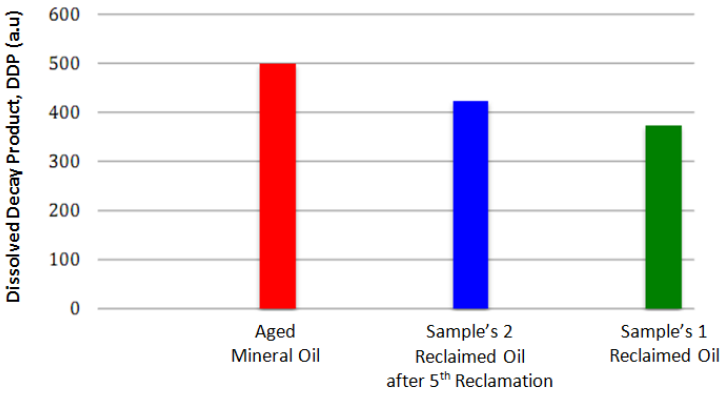

Figure 10 Dissolved Decay Product, DDP (a.u)

DDP values' signified that oil has undergone oxidation during service and by doing reclamation on the aged mineral oil such have been done on Sample 1 and Sample 2, decrement of DDP values' are shown. Yet, Sample 1 show 25.24% decrement compared to Sample 2 with only 15.15% DDP reduction. These results implying that using 100g of Fuller's earth for one cycle of reclamation (Method 1) is more effective compared to using 5g of Fuller's earth for 5 cycles of reclamation (Method 2). Additionally, the different amount of Fuller's earth used in Method 1 & 2 matching with results of reduction in DDP values of Sample 1 and Sample 2. This is because amount of adsorbent is directly proportional to the ability of adsorbents to absorb polar contaminants. Due to the effectiveness and lesser time required, Method 1 is chosen for the next two (2) study phases, Total Acid Number (TAN) and Breakdown Voltage (BdV). TAN measurements as per ASTM D974 were repeated three (3) times to find out the average value of acids in mineral oil. Figure 11 show results of average TAN for AMO and S1RO. The values are 0.13mgKOH/g and 0.02mgKOH/g respectively. As per reference, the suggested TAN limits for transformer is 0.10mgKOH/g [5]. High TAN values' proved that there is formation of acid in AMO accumulated during in-services due to oxidation process. The process can occurred between dissolved oxygen presence in oil with the mineral oil molecule or with cellulose-based insulation such as Kraft paper. Molecules of mineral oil that mainly consist of hydrogen and carbon can form carboxylic acids if interact with oxygen [1], while according to Bronsted-Lowry and Lewis Acids, the hydroxyl group (OH) in cellulose based paper can react with carboxylic acid and water to produce donating proton (H+). This donating proton (H+) can react with other molecule to form acid such as acetic and levulinic.

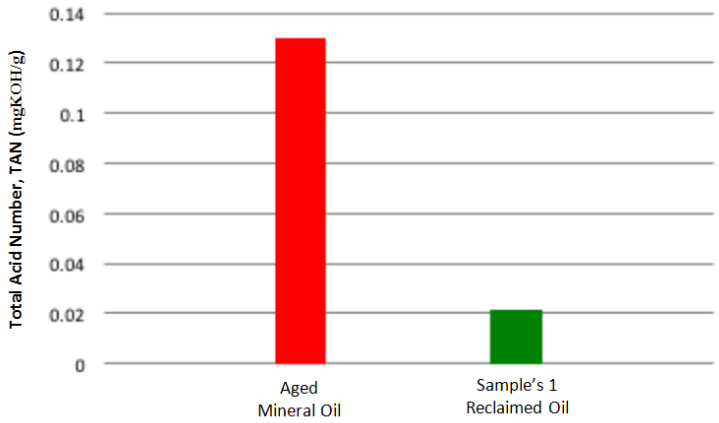

Figure 11 TAN of Aged Mineral Oil & Sample's 1 Reclaimed Oil

Subsequently, this decay product reaction will produce sludge, which can cause the dielectric strength decreases as the breakdown will occur at the sludge. Eventually, after the AMO undergone reclamation process, the S1RO average TAN values' decreased to 0.02mgKOH/g. This indicates the effectiveness of Fuller's earth as adsorbent for reclamation process thus also reducing acids in oil by 84.62%. This is due to chemical structure of Fuller's earth that containing internal and external polar active sites. It allowed the non-polar substances in the oil to flow but block or adsorb the polar contaminants dissolved in the oil. Acid is a polar molecule as they have opposing charge on their molecule [15]. 25 BdV measurements were recorded for each aged mineral oil AMO and Sample's 1 reclaimed oil S1RO. All measurements were done using Megger Oil Tester OTS60PB as per ASTM D1816. Figure 12 shows the average values for both oil samples. The values clearly indicate that the breakdown voltage for both AMO and S1RO are lower than the limit suggested by IEEE where a transformer that runs below 69kV, the BdV limit of oil insulation used should be 23 kV and above [5], Yet, BdV of S1RO is 4kV bigger than AMO's BdV or 50% improvement through reclamation process. As BdV of transformer oil is primarily depending on factors such moisture content, void or bubbles, sludge or suspended particles and acidity of oil[8], this improvement of BdV can be due to decrement of DDP, sludge and acids that have been absorbed by Fuller's earth during reclamation process. Hence, it is believed that if the reclamation process is done repeatedly for several cycles, more DDP, sludge and acids can be removed from the AMO thus increasing BdV steadily.

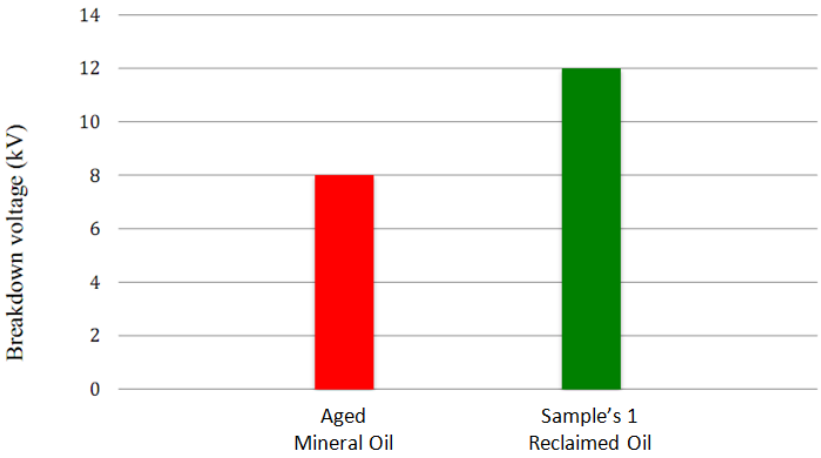

Figure 12 BdV of Aged Mineral Oil & Sample's 1 Reclaimed Oil

Conclusion

Parameter of DDP was measured using UV-Vis by referring to ASTM D6802. In addition, TAN and BdV measurements were carried out complying ASTM D974 and ASTM D1816 respectively. Through this study, it can be concluded that reclamation process using Fuller's earth can reduce 25.24% of DDP and 84.62% of acids present in aged mineral oil hence improving its' BdV by 50%. These findings are parallel with breakdown voltage mechanism due to acidity emergence. It is also proved that Fuller's earth is effective adsorbent for oil reclamation process and as Fuller's earth is harmless to environment, it can be disposed safely on landfill.

Acknowledgements

The authors gratefully acknowledge the Fakulti Kejuruteraan Elektrik, Universiti Teknikal Malaysia Melaka (UTeM) and TNB Research Sdn. Bhd. The financial support for this work is from Fundamental Research Grant Scheme, Ministry of Higher Education (FRGS/1/2017/TK04/FKE-CERIA/F00332).

References

N. Lelekakis, J. Wijaya, D. Martin, and D. Susa, "The Effect of Acid Accumulation in Power-Transformer Oil on the Aging Rate of Paper Insulation," IEEE Electrical Insulation Magazine, vol. 30, no. 3, pp. 19–26, 2014.

I. S. Chairul, S. A. Ghani, M. S. A. Khiar, Y. H. M. Thayoob, and Y. Z. Y. Ghazali, "Kraft Paper Insulation's Life Assessment and Effects of Oxygen and Moisture to Paper Insulation's Deterioration Rate," in IEEE International Conference on Power and Energy (PECon), 2012, pp. 728–731.

M. S. Naidu and V. Kamaraju, High Voltage Engineering, 2nd ed. United States of America: McGraw-Hill, 1996.

I. Liapis and M. G. Danikas, "A Study of Parameters Affecting the Ageing of Transformer Oil in Distribution Transformers," in IEEE International Conference on Dielectric Liquids, 2011, pp. 1–4.

I. S. C57.637™-2015, "IEEE Guide for the Reclamation of Insulating Oil and Criteria for Its Use," IEEE Standards Association. 2015.

J. S. N'cho, I. Fofana, A. Beroual, T. Aka-Ngnui, and J. Sabau, "Aged Oils Reclamation: Facts and Arguments Based on Laboratory Studies," IEEE Trans. Dielectr. Electr. Insul., vol. 19, no. 5, pp. 1583–1592, Oct. 2012.

A. Raymon and R. Karthik, "Reclaiming Aged Transformer Oil with Activated Bentonite and Enhancing Reclaimed and Fresh Transformer Oils with Antioxidants," IEEE Trans. Dielectr. Electr. Insul., vol. 22, no. 1, pp. 548–555, Feb. 2015.

S. A. Ghani, N. A. Muhamad, and H. Zainuddin, "Performance of Palm Shell Activated Carbon as An Alternative Adsorbent for Reclamation of Used Transformer Oil," ARPN J. Eng. Appl. Sci., vol. 10, no. 22, pp. 10752–10758, 2015.

ASTMD6802−02(2010), "Test Method for Determination of the Relative Content Of Dissolved Decay Products in Mineral Insulating Oils by Spectrophotometry." pp. 1–6, 2010.

ASTMD974-14, "Standard Test Method for Acid and Base Number by Color-Indicator Titration." pp. 1–7, 2014.

ASTMD1816-12, "Standard Test Method for Dielectric Breakdown Voltage of Insulating Liquids Using VDE Electrodes." pp. 1–5, 2012.

"Determination of The Total Acid Number in Petroleum Products," Metrohm. [Online]. Available: http://partners.metrohm.com/GetDocument?action=get_dms_document&docid=1360923. [Accessed: 05-Jan-2016].

"Product Specification Fuller's Earth," Sigma Aldrich. [Online]. Available: http://www.sigmaaldrich.com/Graphics/COfAInfo/SigmaSAPQM/SPEC/F2/F200/F200-BULK_SIGALD_. pdf. [Accessed: 07-Jan-2016].

H. M. Wilhelm, G. B. Stocco, and J. S. G. Batista, "Reclaiming of In-service Natural Ester-based Insulating Fluids," IEEE Trans. Dielectr. Electr. Insul., vol. 20, no. 1, pp. 128–134, 2013.

R. Kurtus, "Polar and Non Polar Molecules (revised 19 September 2016)." [Accessed: 07-Jan-2016].

(FRGS/1/2015/TK04/FKE/03/F00262, FRGS/1/2016/TK04/FKE-CERIA/F00309

Proceeding: 5th International Conference on Applied Sciences and Engineering (ICASEA, 2018)
(eISBN 978-967-15744-1-6)
Capthorne Hotel, Cameron Highlands, Malaysia

"DRIVE THRU" ATTENDANCE SYSTEM USING RADIO FREQUENCY IDENTIFICATION (RFID): A REVIEW

Abu Bakar Ibrahim [1]
Che Zalina Zulkifli [2]
Nurul Husna Abdul Kahar [3]

[12 3]Universiti Pendidikan Sultan Idris
Tanjung Malim Perak,
Malaysia.
bakar@fskik.upsi.edu.my
chezalina@fskik.upsi.edu.my

Abstract: *Radio Frequency Identification (RFID) play a big role in people daily lives. Various applications of RFID including transportation and logistics, manufacturing and processing, security, animal tagging, waste management, time and attendance, road toll management and etc. The aim of this research is to improve old attendance system that capable to eliminate time waste during manual collected attendance by create "Drive-Thru" attendance system. This model can be given an access badge with radio frequency identification (RFID) chip in it as its use technique of electromagnetic fields to exchange data from a tag (like a smart tag) to an object (a reader) at the post guard for the purpose of identification or tracking. Development in RFID technology widely increasing in adopting new and many features.*

Keywords: *RFID, Attendance System, Drive Thru*

Introduction

Today's, lots of colleges, schools, and universities have a problem to handle large number of students and staffs especially to get their attendances. Manually, the attendance are given whenever the lecturer comes to class and pass it around for the students to tick. This manual process shows a flaws since the students can cheat and lecturer had to enter the attendance into database for record. Zatil Singhal (2012), describes the conventional method of taking attendance by calling names or signing on paper is very time consuming and insecure, hence inefficient. Krenare R. Pireva (2013) tells that counting students' absence, teachers lose couple of minutes of their classes to fill in the attendance sheet manually by calling the students for signing the documents and the worst just come after classes where there should be spent extra time for inserting the attendance data in a computer to generate the statistics and send them per email to each student and of course to the administrator and lecturer in total. Meanwhile, the staff has to queue up for a long time to punch card and put it in the slot provided according to their name which shows that both system are slow in performance and not efficient express Mr.Tushar T. Tanpure1 et. al (2013). This would cause a big problem. In this study we implement the Radio Frequency Identification (RFID) technology as one of figures development focuses on staffs of Universiti Pendidikan Sultan Idris (UPSI) as this university have two main campus which is Kampus Sultan Azlan Shah (KSAS) and Kampus Sultan Abdul Jalil Shah (KSAJS) a niche in educational leadershipTourism in rural areas plays an important role that lead to the global change. The main purpose of this research is to develop a "drive-thru" attendance system for staff UPSI by using Radio Frequency Identification (RFID). The staffs are having difficulties to punch their card as a sign of attendances due to the long distance

between two main campuses which is 7.5km from each others as the staffs might have a lecture at one of the campus. Besides that, the flow of the traffics affect the time of the staffs to arrive punctually for the attendances due to the amount of vehicles on the road such as cars, buses and lorries' been using the same routes to their respective journey during peak hour for 8am lecture. The using of RFID in attendance system for staffs UPSI can improve the existing system that capable to eliminate time waste. This statement is supported by Fakolujo O. (2012) that RFID is an automated identification and data collection technology, that ensure more accurate and timely data entry and quickly gained more attentions due to current low cost and advances that open up more application area. On the other hands, Ankita Agrawal (2013) mentions that RFID systems have been widely used in many different application areas such as; product tracking through manufacturing and assembly, control of inventory, parking lot access and control, container tracking, ID badges and access control, equipment tracking in hospital and etc. which researcher find it is suitable to be use for taking attendances of staffs UPSI. It is one way to improve efficiency as researcher found out the parking problem on Kampus Sultan Abdul Jalil Shah (KSAJS) that is limited for the staffs. If there are any program being held on E-learning building the staffs found out the difficulties to find the parking lots and it's stressing them to punch card for the attendances. Thus, manual attendance system are very time consuming supported by Priyanka A. Sathe (2014).

Literature review

Introduction

In this section, it will focus on literature review based on the research of the current system that will be developed. The purpose of a literature review is to convey the reader about the knowledge that also establish the idea based on the topic and strengthens and weakness. Construction of development the "drive-thru" attendances system by using Radio Frequency Identification (RFID) has been made and the motive for the purpose of this study was conducted. In additional, this study also looks at the suitability of using this development as an aids among the staffs. There are several views of number of studies regarding the RFID as attendance system.

RFID technology

According to Zakiamani (2012), Radio Frequency Identification (RFID) is an automatic identification method, relying on storing and remotely retrieving data by using devices called RFID tags. It's parallel with Barid Baran Nayak (2015) research by stating that RFID is a technology which wirelessly identifies the chip or tag of interest and capture the data. The RFID idea is not new as it's began to be use for manufacturing to improve economic growth in 1800. Basically RFID use electromagnetic or electrostatic incorporate with radio frequency portion of electromagnetic spectrum to identify an object, animal or person. It can be used in many application such as in health care industry to reduce counting, looking and auditing item.

Typically, RFID system contains two main components; the reader and the tags. The tag or transponder (derive from terms transmitter and responder) normally attached to the objects to be monitored and carries information in microchip that contain radio transmitter that emits a coded identification number when carried out by the reader device. RFID technology are implement in many field such as client server based attendance system that allow the company to monitor the employees' attendance from their branch, smart card attendance system that using MyKad to record employee attendance in one shortage and fingerprint attendance system

that considered as the oldest method and most popular used for verification and identification in the field of biometric technology.

Type of RFID System

Research supported by A. A. Olanipekun (2016), tag can be passive, semi-passive or active which also can be categorized based on memory type on transmission. Figure 1 is illustration of passive RFID system. In passive RFID systems it use tags with no internal power sources and powered by electromagnetic energy transmitted from RFID reader. It's supported by Andrew W. Wgright (2012), the transmitted signal from the reader power's the tag's integrated circuit (IC) reaches a tag, and the tag reflects the signal in form of backscatter. This may affect the range are limited by the power of tags which less than 10m but they are cheaper, smaller and easier to manufacture compare active tag. Passive RFID tags can be used for application in field of file tracking, race timing, supply change management, and smart label.

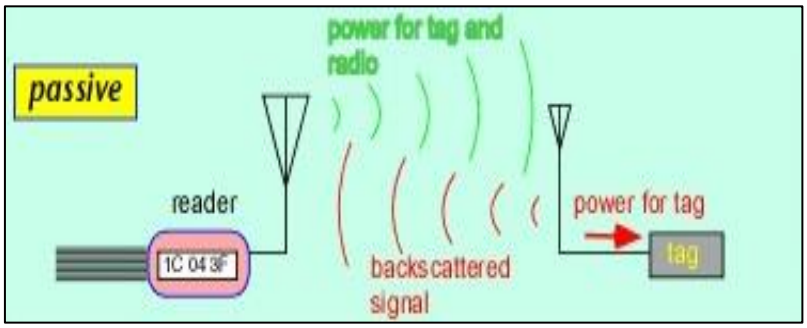

Figure 1: Passive RFID System

Semi-passive tag kind of similar to passive tag except it has additional of small power sources to power on the chip as it can captured energy from the reader to use as backscatter. According to Andrew W. Wgright (2012), the battery provided the power to transmit the signal back to the reader that increase the range. Figure 2 is illustration of semi-passive RFID system.

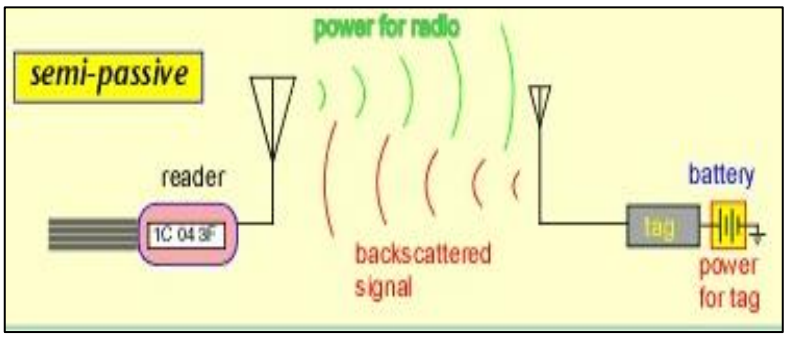

Figure 2: Semi-Passive RFID System

The active RFID system use battery-powered RFID tags that broadcast own signal to transfer information stored on the microchip. O. K. Boyinbode (2015) state that due to reliability to conduct with reader, its can transmit at a higher power level than passive allowing to be more effective in challenge environment such as water, metal and longer distance. Besides the battery ability to store up to 32,000 bytes it's also can live up to 10 years. Active tag are being used on large objects such as rail cars, big reusable container and others. Figure 3 shows the active RFID system.

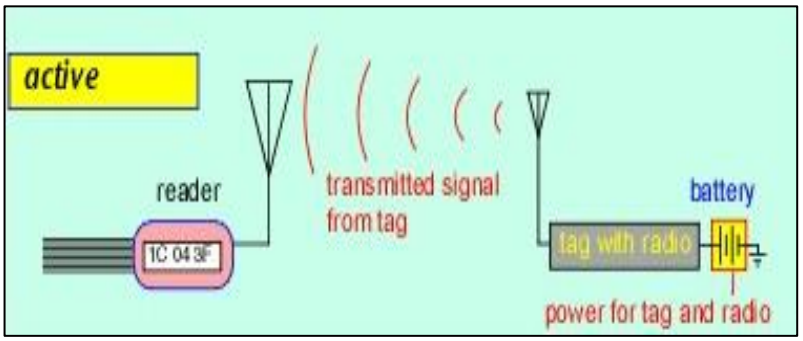

Figure 3: Active RFID System

Type of Frequency

Radio Frequency Identification (RFID) system uses radio frequency wave to detect and track the objects by using tag as the tag contain information related to the object that stored electronically. As we know, RFID system consists with tag and reader and type of RFID tag are passive, active and semi-passive. The RFID system communicate with specific frequency band when they operate that highlight the important role of radio wave in signaling between RFID. There are three types of frequency bands uses which are Low frequency, High frequency, and Ultra-High frequency. Each frequency behave differently. Figure 4 shows the different wave length of the frequency.

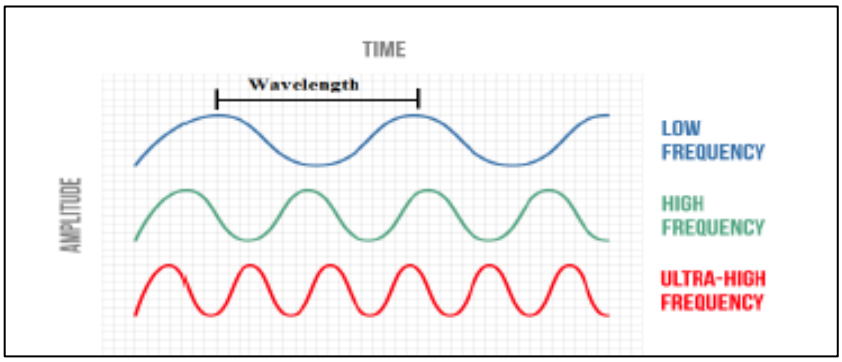

Figure 4: Different Wave Length Of The Frequency

From Figure 4 also, researcher can see the different. For Low frequency the wavelength is greater compared to the High frequency and the Ultra-High frequency, but amplitude of Ultra-High frequency is greater than the High and Low frequency.

Table 1 shows the frequency range of the difference type of frequencies with the distance travel, regulations and data speed. It reveal that Low frequency have range of 10cm but it is unregulated with 120-15KHz that have low data speed.

Table 1: Frequency Type and Specifications

Type of Frequency	Range of Frequency	regulations	Range	Data Speed	Benefits
Low Frequency (LF)	120-150KHz	Unregulated	10cm	Low	Work well round water and metal product
High Frequency (HF)	3-30 MKz	ISM band worldwide	10cm-1m	Moderate	Low cost of tag
Ultra-High Frequency (UHF)	300MKz-3GHz	Short range device	1m-100m	Moderate to High	EPC standard built around this frequency

Related Work

Through the studies, currently the existing system was not user friendly where employees record their attendance by using punch card. With a large number of workers/ employees in institutions/ university, it is difficult to manage the attendance record. Besides, everything was done manually that may cause errors and repetition work that was time consuming for a recheck. On the other hands, certain institutions still using paper-based attendance which every details such as name and matric number were written down manually on paper. It may cause loss of record and take a long time to generate the form in computer. Thus, some research have been done on the existing record to find out the method being used and problem behind the existing to develop more effective than this.

There are many types of attendance system nowadays and RFID based attendance system uses technology that eliminate the problem faced in manual attendance that may prove to be more reliable and accurate. Krenare R. Pireva, Jeton Siqeca, Shkelqim Berisha (2013) have underwent the project that track the attendance of our students in an automatic manner by using this technology in an education institution environment. The output presented in web based platform that implement using HTML, JavaScript and CSS as front-end while MySQL and PHP 5.1.x scripting language as back-end. Java is the primary way to produce code that deployed as java bytecode and MYSQL database is highly recommended database for web application which is open source. It's also supported with web server Apache and IIS to make the system more user friendly. His study demand that this helps the lectures be more concentrating of motivating the students' attendance and save their time. Author of Mr.Tushar T. Tanpure1 et. al (2013), propose research monitoring of students using RFID reader and passive where reader located in fixed area that send signal to passive RFID chip detected in range of reader. Research reviewed that every tag have own unique ID besides using Graphical User Interface (GUI) to provide efficient way review the attendance. The Graphical User Interface is created with visual basic 2010 consisting database system use to store all the student details, date and time. According to research, monitoring system can replace manual system that transform the information and convenient to be used for college/ university level.

On the other hands, Arulogun O. T. , Olatunbosun, A. , Fakolujo O. A. , and Olaniyi, O. M (2013), have developed an RFID based Attendance System that are commonly used nowadays to keep track of attendance for community organizations such as educational institutions,

business organizations etc. the program was written in Microsoft Visual C# programming language for the front end and backend of Microsoft SQL. It's supported with the advantages using passive tag with low cost and flexibility as RFID capability implementing the attendance system. Similar project was undertaken by Nurbek Saparkhojayev and Selim Guvercin (2013) to create system that makes easier to check students' attendance system implemented in Suleyman Demirel University, Kazakhtan.

Besides that, Elima Hussain, Priyanka Dugar, Vaskar Deka, Abdul Hannan (2014) propose an attendance system implement the RFID by using Open Source Software in a multi-user environment. Its use python as back up for reading tags as user can view the attendance by accessing the web portal. Its happen when Java based desktop application is being used for authenticate lecturer that then run the python code and record the tag in XML which later it is uploaded in a server for processing to interpret the data. The project occur agree that Open Source based RFID attendance system can increase the performance and efficiency make the user friendly attendance system.

According to Zatil Singhal, Rajneesh Kumar Gujral (2012), Jonathan Sidi et al. (2009) proposed a system that was capable to record student's " attendance using interactive input, generating reports, viewing students" and lecturer" profiles, and providing students timetable. The system records attendance using barcode scanner. RFID technology has a lot of advantages such as simultaneous collection of large quantities of data with high accuracy, contactless, etc. RFID technology has an increasing influence to our lives and gradually replaces barcode in supermarket and logistics management.

Comparison between Punch Card and RFID

According to Nur Halim Tunin (2016), a punched card of punch card attendance system is an old traditional system to manage the attendance of the worker by using a piece of paper that contains time of the worker/ employee enter in or exit the place by punch the exact time and date. Later, the information received from the punch card will be collected a week before the salary payment. This is because they need to calculate the exact time for each of the worker to manage give out the salary fairly. Punch card attendance system actually widely being use at office, industry section, institution, school and others because it is easily to manage the salary to be given to the worker by calculate the time on the punch card.

The difference between punch card attendance system and attendance system by using RFID is that the RFID us use tag on the worker card which can be store information easily while punch card attendance system uses paper that wasted the time where employee had to calculate the salary on it before being throw out to the dustbin. ID number is being used on the worker card in RFID system that provide employee access to enter place and manage the attendance by give permission to access through RFID scanner. The tag will be scanned immediately when worker touch the card that improve the security level.

Conclusion

In this section, various type of RFID system and frequency have been presented. Based on various example of from related work of RFID attendance system, it is efficient in alleviating the attendance system problem that arise in the institutions/ university and school due to the insufficient parking spaces that undeniable in Universiti Pendidikan Sultan Idris at both main campus.

Acknowledgment

I would like to take this opportunity to thank the Research Management & Innovation Centre (RMIC) of Sultan Idris Education University for permitting and supporting in this research (2017-0122-104-01).

References

A.A. Olanipekun, O.K. Boyinbode (2016), A RFID Based Automatic Attendance System in Educational Institution of Nigeria. International Journal of Smart Home, Vol 9(12), 1-10.

Abhijit Karle, Jyoti Borole (2016), Embedded Web Server Based Management and Monitoring for Educational Institute: A Survey. International Journal of Innovation Research in Science, Engineering and Technology, Vol 5(1), 1-6.

Arulogan O.T., Olatunbosun A., Fakolujo O.A, Olaniya O.M., (2013), RFID Based Students Attendance Management System. International Journal of Scientific & Engineering Research, Vol 4(2), 1-9.

Barid Baran Nayak (2015), RFID Based Attendance Management System using Labview. India: Department of Electronics & Communication Engineering.

Chiagozie G. O., Nwaji G. O. (2012), Radio Frequency Identification (RFID) Based Attendance System With Automatic Door Unit. Academic Research Journal, Vol 2(2), 1-16.

Farhan M. N., Nivash S., Chandran Monisha A. & Chandran Mnjusha A. (2016), Interior Tracking with Automatic Attendance and Reporting System. Indian Journal of Science and Technology, Vol 9(30), 1-5.

Harmida Binti Arobi (2011), In-Vehicle Signing System Using FRID (Master's thesis, Universiti Teknikal Malayisa Melaka, Malaysia). Retrieved from http://eprints.utem.edu.my/6359/2/In-Vehicle_Signing_System_Using_RFID_-_Full_Text.pdf

Krenare R. Pireva, Jeton Siqeca, Shkelqim Berisha (2013), RFID: Management System for Students' Attendance. 15th Workshop on International Stability, Technology, and Culture the International Federation of Automatic Control, Vol 8, 3-4.

Media Anugerah Ayu, Member IACSIT, Barroon Ismaeel Ahmad (2014), TouchIn: An NFC Supported Attendance System in a University Environment. International Journal of Information and Educational Technology, Vol 4(5), 1.

Muhammad Nurhalim Bin Mohd Tunin (2016), Intelligent Trace Attendance System (I-TAS) (Undergraduate's thesis, Universiti Teknologi Malaysia, Malaysia). Retrieved from http://portal.fke.utm.my/fkelibrary/files/muhamadnurhalimbinmohdtunin/2016/1746_MUHAMADNURHALIMBINMOHDTUNIN2016.pdf

Nor Amiyana Binti Mohd Alias (2011), Attendance and Access Control System Using RFID (Undergraduate's thesis, Universiti Teknikal Malaysia Melaka, Malaysia). Retrieved from http://eprints.utem.edu.my/3406/1/Attendance_And_Access_Control_System_Using_RFID_System_-_24_pages.pdf

Nurbek Saparkhojayev, Selim Guvercin (2012), Attendance Control System based on RFID Technology. IJCSI International Journal of Computer Science, Vol 9(1), 1-4.

Priyanka Sahare, Pranali Gaikwad, Snehal Narule, Nutan Thakre, Puja Chandekar, RTMNU Nagpur (2015), RFID Technology Based Attendance Management System. International Journal of Engineering and Computer Science, Vol 6(3), 1-6.

Rohit Chandrashekar, JayeshreeShinde, Dashrath Mane (2013), Importance and Analysis of RFID in Attendance System. International Journal of Emerging Science and Engineering, Vol 1, 1-3.

Tanpure T. & et. al (2013), Online Student Monitoring System Using Passive RFID. International Journal of Innovation Research in Computer and Communication Engineering, Vol 1(2), 1-7.

Wee Pek Ling (2012), Integrated Staff Attendance System (Undergraduate's thesis, Universiti Malaysia Pahang, Malaysia). Retrieved from http://umpir.ump.edu.my/4420/1/CD6576_WEE_PEK_LING.pdf

Zatil Singhal, Rajneesh Kumar Gujral (2012), Anytime Anywhere Remote Monitoring of Attendance System based on RFID using GSM Network. International Journal of Computer Application, Vol 39(3), 1-5.

Proceeding: 5th International Conference on Applied Sciences and Engineering (ICASEA, 2018)
(eISBN 978-967-15744-1-6)
Capthorne Hotel, Cameron Highlands, Malaysia

A REVIEW ON VARIOUS TECHNIQUES AND RECENT ADVANCES IN POLYMERIC ADDITIVES TO MITIGATE WAX PROBLEMS IN CRUDE OIL

S. M. Anisuzzaman[1,2*]
Yeow Wai Fong[2]
Merlela Madsah[2]

[1]Energy Research Unit (ERU),
[2]Chemical Engineering Programme, Faculty of Engineering,
Universiti Malaysia Sabah, 88400 Kota Kinabalu, Sabah, MALAYSIA.
[*]Correspondence author. Tel: +6088-320000 ext. 3222, Fax: +6088-320348,
E-mail address: anis_zaman@ums.edu.my; dr.anis.ums@gmail.com

Abstract: *Oil and gas industry has long recognized and is continuing to face wax deposition problems, particularly, as more unconventional crudes are being produced. As time goes by, many techniques have been developed to reduce the cost to solve this challenging issue. Polymeric additives, which falls on chemical treatment categories have been extensively used and studied to improve the flow of the crude oil along the pipeline. Nevertheless, the majority of the polymeric additives have dual functions including the use as pour point depressant. This article reviews the various techniques used to improve the flow of crude oil such as mechanical, chemical and thermal treatment, and the recent advances of using polymeric additives to mitigate the wax problems.*

Keywords: *Wax Inhibitor, Shear Rate, Viscosity, Pour Point Depressants*

Introduction

Crude oil plays an important role as the energy source for supplying energy around the world. Crude oil is a complex mixture of varying hydrocarbon chains. The mixtures of the carbon and hydrogen chains, however, also contain other elements such as sulphur, nitrogen and oxygen. These elements may react with the hydrocarbons to form other complex molecular structures. The hydrocarbons that are present in crude oil are characterized by three types: paraffins, naphthenes, and aromatics. The major percentage consists of paraffins which are important component to produce fuels such as gasoline and diesel (Leckel, 2009).

American Petroleum Institute (API) has classified crude oils into light (API > 38), medium (38 > API > 29) and heavy (29 > API) (Ahmed, 2016). The flow behavior of the heavy crude oils is the most complex because of the very high wax content (>5%) in these crude oils. Frigaard et al. (2007), reported that 20% of the world petroleum resources are made up of the waxy crude oil. In China, the production of the petroleum products is originated from the heavy or the waxy crude oil which dominates 90% of the total crude oil reserves.

Deposition of wax

Petroleum waxes are generally categorized into two kinds, paraffin wax and microcrystalline wax. *Paraffin* is *mixture of hydrocarbons* constituted of linear/normal chains, comprising mainly from *20* to 40 carbon atoms, in addition to alkanes with branched and cyclic chains

(Behbahani et al. 2015; Patel et al. 2016). Heavy straight chain paraffinic waxes are hydrocarbons that contain carbon atom ranging from C_{18} to C_{36} while, the microcrystalline waxes are consist of branched and cyclic hydrocarbons where the carbon atoms are ranging from C_{30} to C_{60}.

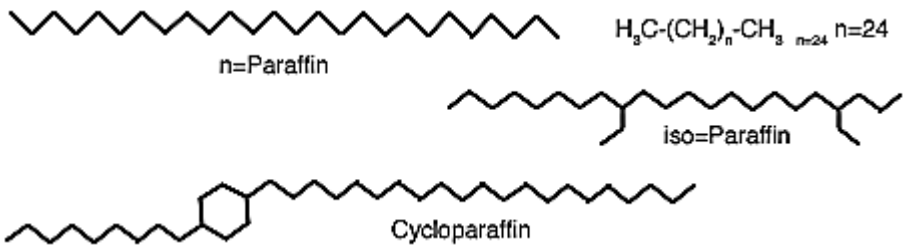

Figure 1. Molecular Structures Of Waxes (Top: Straight Chain Wax, Middle: Branched Chain Wax, Bottom: Cyclic Structured Wax)
(source: Faolain et al. 2005)

Gelling of wax within the pipelines below the wax appearance temperature (WAT) causes the fluid to act as a non-Newtonian fluid where the viscosity of the crude oil increases as the temperature reaches its pour point and will therefore inhibit the flow of crude oil (Pedersen and Ronningsen, 2003). On the other hand, when the temperature of the pipelines wall is below the WAT, the formation and deposition of a layer of paraffin molecules will be promoted. This layer can grow over time which will cause the diameter of the pipelines to decrease and therefore constricts the flow of the crude oil. This problem usually arises in the deep-sea environments as the temperature of the water in the subsea can reach as low as 5°C even in warm climate (Azevedo & Teixeira, 2003).

Wax is an aliphatic and non-polar molecule while asphaltene is an aromatic and polar molecule. Nonetheless, despite of the differences, these two oil constituents are similar in various ways where they have a high molecular weight, associate or aggregate in solutions, and have limited solubility in crude oil (Ganeeva et al. 2016). However, the deposition of the organic solid wax is a critical problem faced in the production of the crude oil. Deposition of wax is often observed in the production of the paraffinic oils, or in the offshore operations which involve low temperature environment. The causes for the solid wax to deposit and separate from the crude oil includes the heat release from the gas and the oil to the surrounding, invasion of water and vaporization of shorter chain hydrocarbons (Sanjay et al. 1995). The phenomenon where the heat is all released to the environment will decrease the system temperature below the melting point, in turn causes the wax to crystallize and deposit on the wall of the pipelines and in the reservoir.

The process of wax formation occurs when the temperature is kept below its melting point and the wax particles are being stalled due to less energy roaming around freely. Due to the restriction of the movement of the molecules, the wax molecules are coming closer to form a short-lived cluster called nuclei. The formation of nuclei indicates the onset of wax formation (Dobbs, 1999). The wax formation starts from a precipitate that act as the nuclei to allow crystallization process to begin. The crystallization process consists of two main steps: (a)

nucleation and (b) crystal growth (Myerson, 2002). Nucleation stage can be further separated into another two steps: primary nucleation and secondary nucleation. Primary nucleation comprises of spontaneous nucleation of homogeneous particles and followed by heterogeneous particles. In the next stage, secondary nucleation induces by the crystals that were formed earlier in the nucleation stage (Ozawa, 1971). Once the primary nucleation stage has completed and the temperature of the system is kept low, the growth process of the crystal will occur rapidly in the local region that has high concentration of molecules. Table 1 lists the current methods available to investigate the physical parameters of crude oil.

Table 1. Methods To Investigate The Physical Parameters Of Crude Oil

Parameter	Method
Wax deposition	Cold disk, cold finger, cold spot test
WAT or cloud point	Differential scanning calorimeter (DSC), ASTM method
Pour point	ASTM method
Flow ability	Flow loop test, viscometry, yield stress
Formation of wax	X-ray diffraction
Wax morphology	Scanning electron microscopy (SEM), cross-polarized microscopy (CPM)

A number of mechanisms have been suggested to explain the wax deposition process. Bern et al. (1980) suggested that the molecular to represent wax deposition on the wall of the pipeline. Molecular diffusion is a type of mass transfer process where molecules of a component move from a high to lower concentration region by random molecular motion. This molecular motion is affected by temperature, size of the particles and viscosity of the fluid.

The adsorption of natural oil can be classified into two elements with a focus on the asphaltene and on the wax crystals (Emiliano et al. 2014). Previous work has demonstrated that the emulsion can be stabilised by adding some fine particles such as crystals of the wax and silica where they are known as picking emulsion (Binks, 2002; Tyowua et al. 2017). The adsorption of the wax can occur very fast at the interface of the oil-water if the wax had formed co-crystals with the addition of ester or acid molecules and without the presence of a surfactant. Surfactant can, however sometimes act as inhibitors to prevent wax deposition in the crude oil and reduces the wax adsorption on the interface of crude oil. Wax adsorption becomes more stable if it is in the continuous phase of an emulsion in state oil-wax (Ma et al. 2017). Furthermore, an increase in temperature can cause the adsorption of wax on the interface of crude oil to decreases and gradually increases the solubility of wax. Figure 2 shows the wax adsorption mechanism.

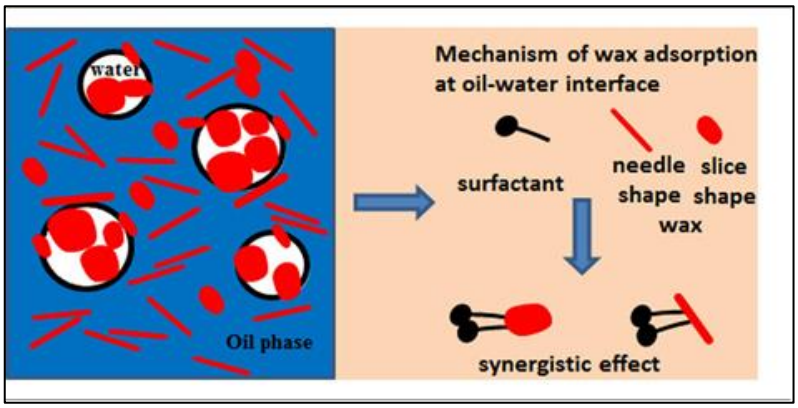

Figure 2. Adsorption With The Presence Of Surfactant
(source: Ma et al. 2017)

In the case of crude oil, the molecular motion for wax deposition is dependent on the temperature. When the temperature of the crude oil is below the cloud point, wax crystals will precipitate and come out from the crude oil. In offshore pipeline, the skin temperature at the wall of the pipeline is at the lowest as the wall is directly in contact with the seabed, while at the centre of the pipeline it has the highest temperature (Guo et al. 2014). Therefore, the gradient of the radial temperature will create a concentration gradient for the wax at the centre and at the wall of the pipeline. Thus, due to the concentration gradient, mass transfer of the wax from the centre of the pipeline towards the pipe wall is facilitated by molecular diffusion (Guo et al. 2014). Mass transfer for wax deposition can be represented by Fick's Law as:

$$\frac{dm_w}{dt_w} = \rho_w D_w A_d \frac{dC_w}{dr}$$

Where $m_w$the mass of wax is deposited, ρ_w is the density of the solid wax, D_w is the diffusion coefficient for liquid wax in crude oil, A_d is the surface area where the deposition occurs, $\frac{dC_w}{dr}$ is the radial concentration gradient and $t_w$is the time of the deposition rate.

Other than molecular diffusion, other mechanisms have been proposed to describe the wax deposition mechanism. However, some have not been accepted such as Brownian diffusion, gravity settling, and shear dispersion. This is because the proposed mechanisms do not give clear description as to how they can significantly affect on the wax deposition (Guo et al. 2014).

Remediation methods of wax deposition

Several methods to control and mitigate the wax deposition have been practised by oil production companies. The strategies for the removal of wax deposition that have been implemented are based on one or a combination of the following methods:

a. Pipeline pigging
b. Thermal insulation and pipeline heating
c. Chemical (solvent) treatment

Pipeline pigging

The term "pig" in oil and gas industry refers to a type of device that is exclusively used to clean the crude oil pipeline. Pigging has been the most common method to employ when the wax has formed on the wall inside the pipelines. Through scouring action of the device, the wax deposited inside the pipeline will be scraped and removed regularly. To ease the pigging operation, a system that has dual-flowline design that allows pigging must be constructed. When the *wax deposit* develops *excessively thick*, there *will* be *inadequate pressure* to *push* the *pig* through the line as the *wax accumulates in* front of it. Nevertheless, there is a drawback for this method. Pigging will require the system to be shut down for 1 to 3 operating days and this will incur loss of revenue. The cost in itself to perform pigging is, however costly (Wei, 2015).

Thermal insulation and pipeline heating

It is well known that wax will start to crystallize when the temperature of the crude is below its cloud point or the wax appearance temperature. Thus, having a good thermal insulator along the pipeline is important as the insulation can maintain the temperature of the system above its cloud point. Deposition of wax will occur in the storage tank when the temperature of the tank drops below the cloud point of the crude oil.

To overcome this problem, hot fluid or electric heating is used to remove wax for short flowlines and downhole. The wax will be heated at temperature above its cloud point by hot water or oil, or steam that is flowed inside the system. The wax is then removed from the wellbore so that it will not redeposited again in the system.

Chemical (solvent) treatment

Compared to the above methods, solvent treatment is often the most successful to remove wax deposition, and yet it has the highest cost. Therefore, this method is only carried out when the thermal method shows little success. Solvent treatment method works by using a suitable chemical that has the solvent to dissolve the wax deposited on the wall of the pipeline until the solvent is saturated and its capacity to dissolve further wax is stopped (Guo et al. 2014).
Rabah (2017) used toluene and methyl ethyl ketone (MEK) as the inhibitors for solvent removal method. Toluene is used to remove the wax crystals from any oil surfaces and followed by the usage of methyl ethyl ketone (MEK) to further precipitate the wax crystals. Rabah (2017) proposed that the ratio of the crude oil should be lower than the solvent ratio because increases in solvent quantity can solubilise the crystallised form of the wax. His earlier work shows that the ratio should be within 16:1 or 32:1 on a mass basis. The optimum operational conditions is with 75% MEK, a solvent to oil ration of 20:1 at -17^{o}C in 30 min with retention time of 20 min. The wax that has been consists of a smaller amount of 6% of lighter n-paraffins. Tolune could be substituted with another solvent, for example butanol or benzene and MEK with Methylcyclohexane (MCH) to obtain different set of optimum operational conditions.

Preventive technique using wax inhibitors additives

Although pigging has been the most popular method to remove wax deposits, however, its use is minimized due to its high cost. (Wei, 2015) Consequently, wax inhibitor is often employed due to lower cost. Wax inhibitor can effectively lessen the rate of wax deposition which, in turn delays the build-up of wax on solid surface (Pedersen & Ronningsen, 2003).

The effectiveness of wax inhibitors is influenced by temperature, wax concentration and shear rate of the inhibitors. In previous works, a high-pressure micro differential scanning calorimeter was used to measure the solubility curve of wax deposition under the WAT. In addition, Hosseinipour et al. (2016) have used carbon dioxide to control the initial nucleation of wax crystals. Wax inhibitors should be used for Malaysian crude oil and it is recommended that the Malaysian petroleum industry is not to use single pipeline due to the high value of WAT since the average the temperature of seabed is usually at 25^{o}C and below (Hosseinipour et al. 2016).

Wax inhibitor that exhibit characteristics as wax crystal modifiers are chemical compound that has the same chemical structure as the wax in the crude oil. Typical compounds selected as the modifiers are usually polymeric compounds consist of one or more hydrocarbon chain molecules that are similar to the wax, but with a polar portion. This type of materials will agglomerate with the wax by bonding the hydrocarbon chains of wax molecules on the crystal lattices. In addition, the inhibitor will hinder the wax crystal growth, which in turn lower the cloud point of the crude oil (Machado et al. 2001). Hoffmann and Amundsen (2010), found that the thickness of the wax could be reduced by 60% to 90% depending on the concentrations. Theyab et al. 2017 have used polymers that are classified as pour points depressants to solubilize the wax crystals in pipelines.

Previous works on flow improvers that act as pour point depressants, such as maleic anhydride and n-alkyl oleate, have demonstrated that the crude oil transportation along the pipelines could be significantly improved. (Patel et al.,2017). The free radical polymerisation was measured with the Fourier Transform Infrared Spectroscopy (FITR) and the Gel Permeation Chromatography (GPC). The results showed that the apparent viscosity, plastic viscosity and the yield value were all reduced to the appropriate values.

The behaviour of the crude oil has also been investigated in term of its rheological properties with or without the inhibitors acting as pour point depressants (PPD). The polymer that has been used is that ethylene vinyl acetate (EVA) polymer with Iranian waxy crude oil. The polymers selected based on the content of nitrogen, carbon, hydrogen, and the molecular weight of the polymer (Behbahani et al. 2015). The results indicated that the viscosity is dependent on the shear rate and the temperature of the inhibitors. The formation of the gel network increased the viscosity of the crude oil when the temperature of the wax was reduced in between 5ºC and 30ºC.

These wax inhibitors chemically modify the structure of the wax crystals and therefore reduce their growth in the pipeline. Previous studies have demonstrated that these inhibitors can only reduce the growth of the paraffin waxes but do not terminate the deposition process of wax which may lead to a continuous deposition in the pipelines (Anisuzzaman et al. 2017).

Additives that act as pour point depressant may, however, be inefficient as flow improvers. Sanjay et al. (1995) stated that the efficiencies of pour point depressant and flow improver are dependent on following factors: (a) the solubility of additive in crude oil, (b) the number of pendant alkyl side chains and the distance between these, (c) the monomer ratio in the copolymer additive must be taken into consideration, (d) the crystalline and amorphous parts of the additive, (e) the chemical and physical stabilities of the additive. Example additives are: mono- and copolymers of ethylene vinyl acetate copolymers (Machado et al. 2001), methacrylate and polyalkyl acrylates (Meyer et al. 1995) and maleic anhydride copolymers (Son et al. 1993).

Ethyl-Vinyl Acetate (EVA)

Typical materials that are usually chosen to act as crystal modifiers are polymeric compounds. Many kinds of polymers have been investigated for their effectiveness as modifiers. Ethyl-vinyl acetate (EVA) has been widely used as it has the ability to control the size of the wax crystals formed (Vieira et al. 2012). EVA is a polymer that consists of a linear chain of polyethylene fragment and vinyl acetate molecule. Figure 3 shows the chemical structure of EVA.

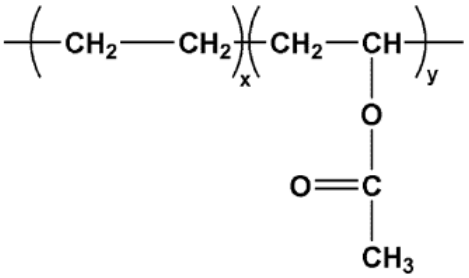

Figure 3. Chemical Structure Of Ethyl-Vinyl Acetate (EVA)
(Source: Wei, 2015)

Machado et al. (2001) have studied the effects of EVA20, EVA30, EVA40 and EVA80 on the oil viscosity and the pour point at 4°C. It was found that EVA30 and EVA40 showed a higher viscosity reduction in comparison to EVA20 and EVA80 at the optimum condition and EVA80 has the lowest efficiency. On pour point reduction property, EVA40 exhibits the higher efficiency than EVA30 as the pour point depressant for the Brazillian crude oil. Ashbaugh et al. (2005) have proposed that the efficiency of the additive to improve flowability decreases with the carbon number of the wax crystals. Jafari et al. (2013) used scanning electron microscopy (SEM) to observe the wax crystal morphology as shown in Figure 4. It was observed that EVA copolymers could greatly reduce the size of wax crystals and rearrange plate-like shape to a spherical and denser morphology.

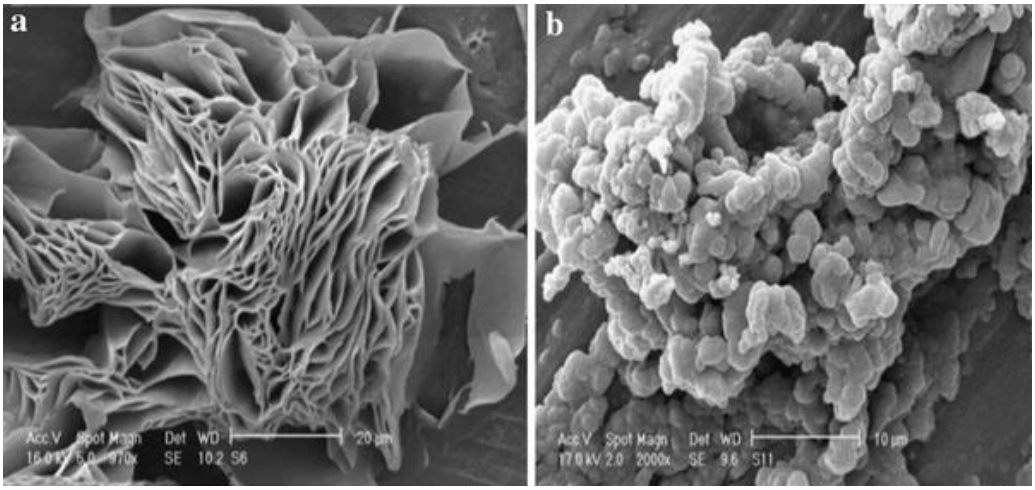

Figure 4. SEM Images Of Wax Morphologies (A) Without EVA; (B) With 100 Ppm EVA
(Source: Jafari Et Al. 2013)

Anisuzzaman et al. (2017) have evaluated the performance of EVA with methyl methacrylate (MMA) and diethanolamine (DEA) and found that EVA co-DEA reduced the pour point of the crude oil by 5°C and the paraffin inhibition efficiency at 28.4%. However, the viscosity of the crude oil did not reduce sufficiently.

Ridzuan and Al-Mahfadi (2017) evaluated the rate of wax deposition for Malaysian crude oils using cold-finger, one-factor-at-a-time (OFAT) method with EVA. They obtained 63.5% efficiency of paraffin inhibition at a stirring rate at 400 rpm and the temperature at 10°C gave. Response surface methodology (RSM) approach was applied to minimize the amount of wax deposition using central composite design (CCD) and the results of the evaluation showed that the optimum condition for the target was achieved at 400 rpm and 19°C respectively for the stirring rate and the temperature.

He et al. (2016) combined EVA with a modified montmorillonite (MMT) to create a nano-hybrid flow improver for China waxy crude oils. They showed that the hybrid pour point depressant exhibited a higher performance in reducing the viscosity by 82.1% than the 75.7% reduction with commercially developed pour point depressants. In terms of pour point, there was a reduction of 9°C at 100 ppm of depressant and the efficiency decreased as the concentration was increased beyond 100 ppm. The mechanism for the hybrid pour point depressant was not explained due to its complexity.

The performance of EVA copolymer with polymethylsilsesquioxane (PMSQ) was investigated by Yang et al. (2017) for crude oil from Qinghai oilfield in China. They showed at 50 ppm EVA with 2.5 ppm PMSQ gave the strongest effect to improve the flow of waxy crude oil by up to 45.8% and the pour point was reduced from 31°C to 18°C. Higher concentration of PMSQ did not give any further improvement towards the flow behaviour. Nevertheless, the addition of PMSQ enhances the performance of EVA.

Alkyl acrylate copolymer

A solid form of polymer acrylate polymer has also been used as a pour point depressant by Admiral et al. 2016. They found that the use of acrylate polymer could enhance the ability of a crude oil to flow in the pipeline. Alkyl acrylate that contains various sets of alkyl group with carbon number ranging from C_{14} to C_{26} is one of the most extensively explored classes for paraffin depressants. Previous studies have suggested that combining alkyl acrylate with the other co-monomers could further reduce the pour point of crude oils than using only alkyl acrylate polymer (Kazantsev et al. 2016). It has been proposed that the efficiency is influenced by the alkyl chain length and the polarity of the polymer (Erceg et al. 2008).

The viscosity of traditional acrylate polymer is usually lower when in solid form than the emulsified form. Emulsified PPD of acrylate polymer (Trade name: PD90) can be created to form droplets of PPD and it shows greater reduction of PPD than the solvent based on depressant (Trade name: PD90). This is because the kinetic energy of emulsified PD90 is higher than the pure PD90, and thus causes the molecules of wax to move freely around the molecules of crude oil and therefore inhibits the crystallization of wax (Admiral et al. 2016).

Deshmukh and Bharambe (2008) synthesized five different composite of *n*-alkyl acrylates-co-*N*-hexadecylmaleimide to investigate the rheological properties of Nada crude oil. Their result showed that the crude oil viscosity was reduced from 90.8 mPa.s to 11.27 mPa.s at 27 °C with additive used. However, the reduction was minimal at 21 °C. Indeed, there was an increased in viscosity for three types of the additives. However, the effectiveness of the additives was enhanced in reducing the pour point of the crude oil when the concentration and the alkyl chain were increased.

Litvinets et al. (2016) demonstrated the effect of polyalkyl acrylate containing ammonium on the rheological properties of two types of Siberian crude oil, coded R and W. The results showed that the viscosity of the crude oil from W and R fields was decreased by 22.4% and 87.7% respectively. They suggested that the optimum additive concentration at 0.05%. However, the additive showed little impact on pour point reduction for crude oil from W field and a small reduction of 7.5°C for crude oil from R field.

Yao et al. (2016) utilized organic nano-clay particles with polyoctadecylacrylate to serve as pour point depressant for Changqing waxy crude oil. The nanocomposite provided sites for wax nucleation where wax particles accumulated and precipitated. The pour point of the waxy crude oil was reduced by 9°C at 800 mg polyoctadecylacrylate per kg of clay. At this level, the raw waxy crude oil viscosity was decreased by 33.8%. Earlier work of Yang et al. (2015) was used differential scanning calorimetry (DSC) to show the morphology of the wax crystals changed into compact spherical template that supressed the gelation point.

Chen et al. (2017) used the castoffs from polymethyl and methacrylate to synthesise polymethacrylate for use as an additive Jinghe crude oil. They found that a pour point reduction of 7.1°C could be achieved with a viscosity reduction of 64.5% from the original viscosity. The results from the differential scanning calorimetry showed that polymethacrylate affected the crystallization of wax in crude oil, and thus inhibited the wax crystallization.

Maleic anhydrides copolymer

Al-Sabagh et al. (2009) investigated the rheological properties of Quran waxy crude oil using styrene-maleic anhydride (SMA) copolymer esters to improve the flow. Four types of SMA, labelled as PPD1, PPD2, PPD3 and PPD4, were prepared with different fatty alcohols through the esterification process as shown in Figure 5. It was found that PPD4, the longest chain of fatty acid decreased the viscosity of the Quran crude oil from 110 mPa.s to 24 mPa.s. This was due to the increased in the solubility of paraffin wax with increasing in length of the alkyl chain. This was in agreement with Xu et al. (2009)

.

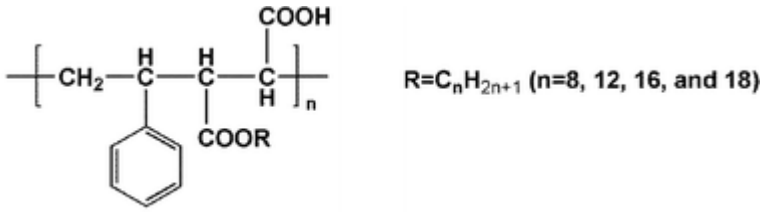

Figure 5. Chemical Structure Of Styrene Maleic Anhydride Copolymer
(Source: Al-Sabagh Et Al. 2009)

Soliman et al. (2018) studied the synthesis and the performance of maleic anhydride copolymers with alkyl linoleate or tetra-esters as flow improvers and pour point depressants on Egyptian (Alamin) waxy crude oil. Two samples of flow improver were prepared and coded as PALCOSA and PALCOTE. These synthesized flow improvers was reduced the pour point from 24°C to 6°C and 3°C respectively. Similarly, the viscosity was reduced from 376.56 mPa.s to 86.51 mPa.s and 83.50 mPa.s respectively. They discovered that the efficiency of these co-polymers was affected through their link with the asphaltenes and the paraffins which could reduce the van der Waals interaction between the molecules. The weaker interaction would eventually loss control to the energy needed to overcome the cohesiveness and adhesiveness between the oil components.

El-Ghazawy et al. (2014) evaluated a flow improver using a modified maleic anhydride-co-octadene towards the Norpetco Egyptian crude oil. Three types of samples were prepared through the esterification. At 9°C, the viscosity of the crude oil was decreased from 2940 mPa.s to 65.2 mPa.s when treated with the flow improver. The efficiency of the synthesized flow improver was affected by the carbon number in the chain, equilibrium of the hydrophobic molecule and the polar groups from the additive, the molecular weight and composition of the copolymer, ability to crystallize and the melting temperature of the additive.

Wu et al. (2012) evaluated a modified maleic anhydride and found that a greater reduction could be achieved with polymer containing aromatic rings which reduced the pour point by 19°C and a 88.4% reduction in viscosity at 26°C. Xu et al. (2015) evaluated the effect of maleic anhydride copolymer with phenyl (AMAC), octadecyl (MAC) and naphthalene (NMAC). The copolymers were ranked as AMAC > MAC > NMAC for their flowability.

Other type of additive

Other types of additives have been developed and tested. Chen et al. (2015) tested the crude oil from China oilfield with cyclohexanone pentaerythritol ketal as the flow improver and PPD. The additive was found to be suitable as flow improver which significantly reduced the flow of the crude oil by 70%, the highest among all the additives tested. However, it was not suitable as a PPD since the pour point was only slightly decreased.

A newer type of polymer, known as terpolymer, created by combining different types of polymers to produce a varieties of multicomponent polymers by varying the concentrations of the monomers. Incorporation of the hydrophobic part in the polymer could be effective in enhancing the viscosity reduction due to the intermolecular association (El-Ghazawy and Farag, 2010). Comb-shaped copolymers were synthesized to obtain poly(hexyl oleate-co-hexadecyl maleimide-co-*n*-alkyl oleate as shown in Figure 6. The poly(hexyl oleate-co-hexadecyl maleimide-co-*n*-alkyl oleate was employed to investigate its effect towards Langhnaj crude oil (Patel et al. 2017). The additives decreased the pour point by 6 ^{o}C and reduced the viscosity by 67.7%. Castro et al. (2011) have identified the key parameters to control the efficiency of the additive were the molecular weight and the composition of the monomers in the terpolymer.

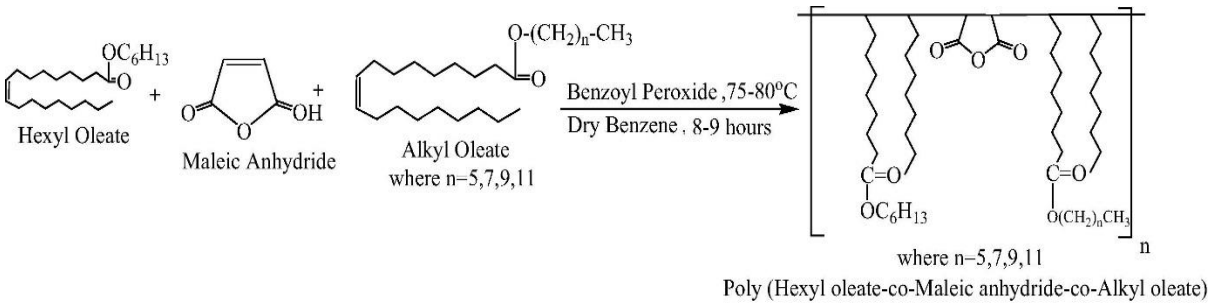

Figure 6. Synthesis Route Of Poly(Hexyl Oleate-Co-Hexadecyl Maleimide-Co-*N*-Alkyl Oleate)
(Source: Patel Et Al. 2017)

Another copolymer was synthesized by amination of terpolymer containing monomers of octadecyl acrylate, vinyl acetate and maleic anhydride (Fang et al., 2012). This type of additive depressed the Shengli crude oil pour point by 11^{o}C. It was also observed that the formation of the nucleators of the wax crystals was influenced by the presence of resin, asphaltene and additive which could enhance the flowability of the crude oil. Further work by Shang et al. (2013) used octadecyl methacrylate, maleic anhydride and styrene monomers initiated by benzoyl peroxide as shown in Figure 7. This type of paraffin inhibitor could reduced the rate of wax deposition by 50% at a molar ratio of 9:1:1.

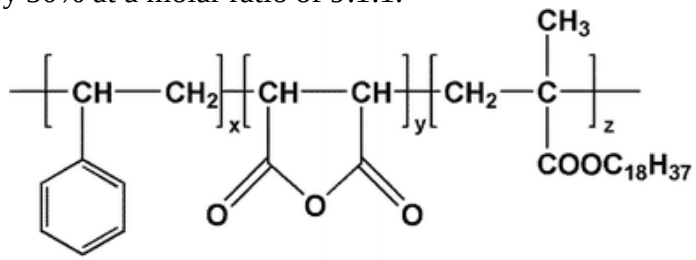

Figure 7. Chemical Structure Of Terpolymer Octadecyl Methacrylate, Maleic Anhydride And Styrene Monomers
(Source: Shang Et Al. 2013)

Chen, et al. (2011) produced polyaminoamide (PAA) through aminolysis and poly-condensation of vegetable oil as shown in Figure 8. They showed that PAA polymers were effective to inhibit wax deposition and those synthesized from canola oil and polyethylene polyamine gave the highest inhibition efficiency of 66.2%.

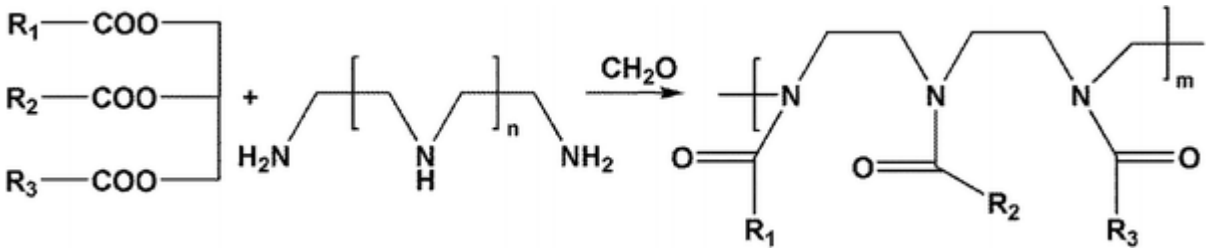

Figure 8. Synthesis Route Of Polyaminoamide (PAA)
(Source: Chen Et Al. 2011)

Elbanna et al. (2017) used octadecene copolymerized with styrene to obtain α-olefin styrene copolymers through a series of reaction of alkylation, esterification and amidation processes. This type of copolymer was capable to depress the pour point of crude oil by to 6^{o}C and to inhibit the paraffin deposition by 80%. They concluded that the best additive for crude oil was when the molecular weight of the copolymer was the highest. It was also founnd that the addition of octadecene styrene ester and amide could enhance the thermal stability and the performance of the additive. This phenomenon occurres due to the nitrogen group polarity which increases the electronegativity of the copolymer produced. Table 2 summarizes the efficiency of the various polymeric additives.

Table 2: Efficiency Of The Various Polymeric Additives

Additive	Code	Cond.	Sample oil	Pour point reduction (°C)	Viscosity reduction (%)	Ref.
EVA	EVA 20	500 ppm, 4°C	Albacora 2, Brazil	>26	N/A	Machado et al. (2001)
	EVA 30			>26	N/A	
	EVA 40			>26	N/A	
EVA-co-diethanolamine	EVA co-DEA	1 g EVA + 5 mL DEA, 4°C	Malaysian crude oil	5	7.53	Anisuzzaman et al., (2017)
EVA with modified montmorillonite	NPPD	100 ppm, 30°C	Jinqiao Pipeline Company, Xuzhao, China	9	82.1	He et al. (2016)
EVA copolymer with polymethylsilsesquioxane	EVA/PMSQ	50 ppm EVA + 2.5 ppm PMSQ, 24°C	Qinghai waxy crude oil	18	45.78	Yang et al. (2017)
n-alkyl acrylates-co-*N*-hexadecylmaleimide	A-14	1000 ppm, 24°C	Nada crude oi, Gujerat, India	27	87.88	Deshmukh and Bharambe (2008)
Polyalkyl acrylate contained ammonium	-	0.1 wt%, 15°C	Verkhne-Salatskoye	1.6	22.39	Litvinets et al. (2016)
		0.05 wt%, 15°C	Urmanskoye	7.5	87.69	
Polyoctadecylacrylate	POA/clay	800 mg/kg POA/clay, 5°C	Changqing, China	9	33.75	Yao et al. (2016)
Polymethacrylate	PMA-1	500 ppm, 50°C	Jinghe, China	5.4	49.9	Chen et al. (2017)
	PMA-2			3.2	30.7	
Polystyrene-maleic anhydride	PPD4	10000 ppm, 27°C	N/A	30	78.18	Al-Sabagh et al. (2009)
Maleic anhydride copolymers with alkyl linoleate or tetra-esters	PALCOSA	5000 ppm, 15°C	Alamin, Egypt	18	77.03	Soliman et al. (2018)
	PALCOTE	3000 ppm, 15°C		18	77.34	
Maleic anhydride-co-octadene	OM16	3000 ppm, 9°C	Norpetco, Egypt	24	97.78	El-Ghazawy, Atta, and Kabel (2014b)
	OM22			18	96.05	
Modified maleic anhydride copolymer	POM	500 ppm, 26°C	Changqing crude oil	9	N/A	Wu et al. (2012)
	POMO			12	N/A	
	POMN			13	N/A	
	POMB			19	88.4	
Cyclohexanone pentaerythritol ketal	-	500-1000 mg/L, 20°C	Jinghe, China	2.7	58.06	Chen et al. (2015)
			Xinjiang, China	2.4	42.05	

Poly(hexyl oleate-co-hexadecyl maleimide-co-*n*-alkyl oleate)	MP8	1000 ppm, 16ºC	Langhnaj, India	3	54.55	Patel et al. (2016)
	MP10			6	67.68	
	MP12			6	56.23	
α-olefin styrene	PPD1	2000 ppm, 60ºC	Western Desert, Egypt	21	N/A	Elbanna et al. (2017)

Conclusion and recommendation

We have reviewed the various techniques and the recent advances of the polymeric additives that have dual functions as flow improver and as pour point depressant in crude oil. Based on the discussions, the following conclusions can be drawn:

1. The efficiency of an additive is dependent on its ability to co-crystallize with the wax.
2. Additives that are usually formed by combining two or more monomers could achieve a higher reduction in viscosity and pour point of the crude oil than the monomer themselves.
3. A wide range of polymeric crystal modifiers have been evaluated to assess their effectiveness towards different types of crude oils. Neverthless, there is a major need in theoretical modeling to correlate the relationship between the various types of polymers to enable prediction of their efficiency to inhibit wax in the future. Furthermore, studies involved in using different solvent together with crystal modifier are needed to identify the best combination of solvent and polymers for the different type of crude oils.

Acknowledgement

The authors would like to express greatest appreciation to the Centre of Research and Innovation (PPI), Universiti Malaysia Sabah (UMS) for the support to this study (Grant No. **SBK0346-2017**).

References

Admiral, A., Abdullah, M. K., & Ariffin, A. (2016). Evaluation of emulsified acrylate polymer and its pour point depressant performance. Procedia Chemistry, 19, 319–326.

Ahmed, T. H. (2007). Equations of state and PVT analysis : applications for improved reservoir modeling (2nd ed.). Gulf Professional Publishing, Houston, Texas. 457-505

Al-Sabagh, A. M., Noor El-Din, M. R., Morsi, R. E., & Elsabee, M. Z. (2009). Styrene-maleic anhydride copolymer esters as flow improvers of waxy crude oil. Journal of Petroleum Science and Engineering, 65(3–4), 139–146.

Al-Yaari, M. (2011). Paraffin Wax Deposition: Mitigation and Removal Techniques. In SPE Saudi Arabia section Young Professionals Technical Symposium. Dhahran, Saudi Arabia, Society of Petroleum Engineers.

Anisuzzaman, S. M., Abang, S., Bono, A., Krishnaiah, D., Karali, R., & Safuan, M. K. (2017). Wax inhibitor based on ethylene vinyl acetate with methyl methacrylate and diethanolamine for crude oil pipeline. IOP Conference Series: Materials Science and Engineering, 206 **(**012074), 1-8.

Ashbaugh, H. S., Guo, X., Schwahn, D., Prud'homme, R. K., Richter, D., & Fetters, L. J. (2005). Interaction of paraffin wax gels with ethylene/vinyl acetate co-polymers. Energy & Fuels, 19(1), 138–144.

Azevedo, L. F. A., & Teixeira, A. M. (2003). A critical review of the modeling of wax deposition mechanisms. Petroleum Science and Technology, 21(3–4), 393–408.

Behbahani, T. J., Akbar, A., Beigi, M., Taheri, Z., & Ghanbari, B. (2015). Investigation of wax precipitation in crude oil : Experimental and modeling. Petroleum, 1(3), 223–230.

Bern, P. A., Withers, V. R., & Cairns, R. J. R. (1980). Wax Deposition in Crude Oil Pipelines. In European Offshore Technology Conference and Exhibition. London, United Kingdom, Society of Petroleum Engineers.

Binks B.P. 2002, Particles as surfactants—similarities and differences,Current Opinion in Colloid & Interface Science,7 (1-2), 21-41

Castro, L. V., Flores, E. A., & Vazquez, F. (2011). Terpolymers as flow improvers for Mexican crude oils. Energy & Fuels, 25(2), 539–544.

Chen, G., Li, Y., Zhao, W., Qu, K., Ning, Y., & Zhang, J. (2015). Investigation of cyclohexanone pentaerythritol ketal as a clean flow improver for crude oil. Fuel Processing Technology, 133, 64–68.

Chen, G., Tang, Y., & Zhang, J. (2011). Synthesis and application of polyaminoamide as new paraffin inhibitor from vegetable oil. Chemistry Central Journal, 5, 82.

Chen, G., Yuan, W., Zhang, F., Gu, X., Du, W., Zhang, J., Li J., Qu, C. (2017). Application of polymethacrylate from waste organic glass as a pour point depressor in heavy crude oil. Journal of Petroleum Science and Engineering, In press.

Deshmukh, S., & Bharambe, D. P. (2008). Synthesis of polymeric pour point depressants for Nada crude oil (Gujarat, India) and its impact on oil rheology. Fuel Processing Technology, 89(3), 227–233.

Dobbs, J. B. (1999). A Unique Method of Paraffin Control in Production Operations. In SPE Rocky Mountain Regional Meeting. Society of Petroleum Engineers.

El-Ghazawy, R. A., Atta, A. M., & Kabel, K. I. (2014). Modified maleic anhydride-co-octadecene copolymers as flow improver for waxy Egyptian crude oil. Journal of Petroleum Science and Engineering, 122, 411–419.

El-Ghazawy, R. A., & Farag, R. K. (2010). Synthesis and characterization of novel pour point depressants based on maleic anhydride-alkyl acrylates terpolymers. Journal of Applied Polymer Science, 115(1), 72–78.

Elbanna, S. A., Abd El Rhman, A. M. M., Al-Hussaini, A. S., & Khalil, S. A. (2017). Synthesis and characterization of polymeric additives based on α-Olefin as pour point depressant for Egyptian waxy crude oil. Petroleum Science and Technology, 35(10), 1047–1054.

Emiliano A. L., Daniel-Ricardo M. V. & Arlex C. G. (2014). Review of studies on asphaltene – wax interaction and the effect thereof on crystallization, Journal of oil, gas and alternative energy sources, 5(5), 39-53.

Erceg Kuzmić, A., Radošević, M., Bogdanić, G., Srića, V., & Vuković, R. (2008). Studies on the influence of long chain acrylic esters polymers with polar monomers as crude oil flow improver additives. Fuel, 87(13–14), 2943–2950. h

Fang, L., Zhang, X., Ma, J., & Zhang, B. (2012). Investigation into a pour point depressant for Shengli crude oil. Industrial & Engineering Chemistry Research, 51(36), 11605–11612.

Faolain, E., Hunter, M., Byrne, J., Kelehan, P., Lambkin, H., Byrne, H., et al. (2005). Raman spectroscopic evaluation of efficacy of current paraffin wax section dewaxing agents. Journal of Histochemistry and Cytochemistry, 121-129.

Frigaard, I., Vinay, G., & Wachs, A. (2007). Compressible displacement of waxy crude oils in long pipeline startup flows. Journal of Non-Newtonian Fluid Mechanics, 147(1–2), 45–64.

Ganeeva, Y. M., Yusupova, T. N., & Romanov, G. V. (2016). Waxes in asphaltenes of crude oils and wax deposits. Petroleum Science, 13(4), 737–745.

Guo, B., Song, S., Ghalambor, A., Lin, T. R., (2014). Offshore pipelines: Design,installation and maintenance (2nd edition), USA- Gulf Professional Publishing, Elsevier Inc, ISBN 978-0-12-397940-0.

He, C., Ding, Y., Chen, J., Wang, F., Gao, C., Zhang, S., & Yang, M. (2016). Influence of the nano-hybrid pour point depressant on flow properties of waxy crude oil. Fuel, 167, 40–48.

Hoffman R & Amundsen L (2010) Single-phase wax deposition experiments. Energy & Fuels, 24, 1069-1080.

Hosseinipour A, Azuraien J.J, Yusup S (2016) the effect of CO_2 on wax appearance temperature of crude oils, Procedia engineering, 148, 1022-1029

Jafari Ansaroudi, H. R., Vafaie-Sefti, M., Masoudi, S., Behbahani, T. J., & Jafari, H. (2013). Study of the Morphology of Wax Crystals in the Presence of Ethylene-co-vinyl Acetate Copolymer. Petroleum Science and Technology, 31(6), 643–651.

Kazantsev, O. A., Volkova, G. I., Prozorova, I. V., Litvinets, I. V., Orekhov, D. V., Samodurova, S. I., Kamorin D.M., Moikin A.A., Medzhibovskii, A. S. (2016). Poly(alkyl (meth)acrylate) depressants for paraffin oils. Petroleum Chemistry, 56(1), 68–72.

Leckel, D. (2009). Diesel Production from Fischer−Tropsch: The Past, the Present, and New Concepts. Energy & Fuels, 23(5), 2342–2358.

Litvinets, I. V., Prozorova, I. V., Yudina, N. V., Kazantsev, O. A., & Sivokhin, A. P. (2016). Effect of ammonium-containing polyalkyl acrylate on the rheological properties of crude oils with different ratio of resins and waxes. Journal of Petroleum Science and Engineering, 146, 96–102.

Ma, Q., Wang, W., Liu, Y., Yang, J., Shi, B., & Gong, J. (2017). Wax adsorption at paraffin oil–water interface stabilized by Span80. Colloids and Surfaces A: Physicochemical and Engineering Aspects, 518, 73–79.

Machado, A. L.C, Lucas, E. F., & González, G. (2001). Poly(ethylene-co-vinyl acetate) (EVA) as wax inhibitor of a Brazilian crude oil: oil viscosity, pour point and phase behavior of organic solutions. Journal of Petroleum Science and Engineering, 32(2–4), 159–165.

Meyer, G., Kessel, D., & Rahimian, I. (1995). The effect of pour point depressants of the polyalkylacrylate on crude oil. Erdoel Kohle Erdgas, Petrochem, 48(3), 135–137.

Myerson, A. S. (2002). Handbook of industrial crystallization. Butterworth-Heinemann. ISBN: 978-0-7506-7012-8

Ozawa, T. (1971). Kinetics of non-isothermal crystallization. Polymer, 12(3), 150–158.

Patel, M. R., Chitte, P. S., & Bharambe, D. P. (2017). Oleic acid based polymeric flow improvers for Langhnaj (North Gujarat, India) crude oil. Egyptian Journal of Petroleum, 26(4), 895–903.

Pedersen, K. S., & Ronningsen, H. P. (2003). Influence of Wax Inhibitors on Wax Appearance Temperature, Pour Point, and Viscosity of Waxy Crude Oils. Energy & Fuels, 17(2), 321–328.

Rabah, A. A. (2017). Nile Blend Crude Oil : Wax Separation Using MEK-Toluene Mixtures, University of Khartoum.

Ridzuan, N., & Al-Mahfadi, M. (2017). Evaluation on the effects of wax inhibitor and optimization of operating parameters for wax deposition in Malaysian crude oil. Petroleum Science and Technology, 35(20), 1945–1950.

Sanjay, M., Simanta, B., & Kulwant, S. (1995). Paraffin Problems in Crude Oil Production And Transportation: A Review. SPE Production & Facilities, 10(1), 50–54.

Shang, H. Y., Ying, X. H., Huang, C. F., Duan, B. H., Fan, G., Liu, P. C., & Liu, C. G. (2013). Paraffin inhibitor development and performance evaluation in Xinjiang Oilfield. Journal of China University of Petroleum, 37, 167–172.

Soliman, E. A., Elkatory, M. R., Hashem, A. I., & Ibrahim, H. S. (2018). Synthesis and performance of maleic anhydride copolymers with alkyl linoleate or tetra-esters as pour point depressants for waxy crude oil. Fuel, 211, 535–547.

Son, A. J., Graugnard, R. B., & Chai, B. J. (1993). The effect of structure on performance of maleic anhydride copolymers as flow improvers of paraffinic crude oil. In SPE International Symposium on Oilfield Chemistry. Society of Petroleum Engineers.

Theyab, M. A., & Diaz, P. (2016). Experimental Study on the effect of inhibitors on wax

deposition, Journal of Petroleum & Environmental Biotechnology, 7, 310, 1-5.

Tyowua A. T. Yiase S. G. Binks B.P (2017) Double oil-in-oil-in-oil emulsions stabilised solely by particles, Journal of Colloid and Interface Science, 488, 127-134

Vieira, L. C., Buchuid, M. B., & Lucas, E. F. (2012). Effect of pressure on the performance of poly(ethylene-vinyl acetate) as wax deposition inhibitors by calorimetric method. Journal of Applied Polymer Science, 126(1), 143–149.

Wei, B. (2015). Recent advances on mitigating wax problem using polymeric wax crystal modifier. Journal of Petroleum Exploration and Production Technology, 5(4), 391–401.

Wu, Y., Ni, G., Yang, F., Li, C., & Dong, G. (2012). Modified maleic anhydride co-polymers as pour-point depressants and their effects on waxy crude oil rheology. Energy & Fuels, 26(2), 995–1001.

Xu, J., Jiang, H., Li, T., Wei, X., Wang, T., Huang, J., Wang, W., Smith, A.L., Wang, J., Zhan, R., Xu,Y., Li Li, Prudhomme R.K., Guo, X. (2015). Effect of comb-type copolymers with various pendants on flow ability of heavy crude oil. Industrial & Engineering Chemistry Research, 54(19), 5204–5212.

Xu, J., Zhang, X., Sun, J., Li, L., & Guo, X. (2009). How comb-type poly(maleic acid alkylamide-co-α-olefin) assemble in waxy oils and improve flowing ability. Asia-Pacific Journal of Chemical Engineering, 4(5), 551–556.

Yang, F., Paso, K., Norrman, J., Li, C., Oschmann, H., & Sjöblom, J. (2015). Hydrophilic nanoparticles facilitate wax inhibition. Energy & Fuels, 29(3), 1368–1374.

Yang, F., Yao, B., Li, C., Shi, X., Sun, G., & Ma, X. (2017). Performance improvement of the ethylene-vinyl acetate copolymer (EVA) pour point depressant by small dosages of the polymethylsilsesquioxane (PMSQ) microsphere: An experimental study. Fuel, 207, 204–213.

Yao, B., Li, C., Yang, F., Sjöblom, J., Zhang, Y., Norrman, J., & Xiao, Z. (2016). Organically modified nano-clay facilitates pour point depressing activity of polyoctadecylacrylate. Fuel, 166, 96–105.

Proceeding: 5th International Conference on Applied Sciences and Engineering (ICASEA, 2018)
(eISBN 978-967-15744-1-6)
Capthorne Hotel, Cameron Highlands, Malaysia

SELF-CLEANING GLASS THROUGH SUPERHYDROPHILIC OF TIO_2 COATING

Syafiq[1]
A. K. Pandey[1*]
Vengadaesvaran B [1]
Nasrudin Abd. Rahim[1,2]

[1]UM Power Energy Dedicated Advanced Centre (UMPEDAC), University of Malaya, Level 4, JalanPantai Baharu, 59990 Kuala Lumpur, Malaysia
[2]Renewable Energy Research Group, King Abdulaziz University, Jeddah 21589, Saudi Arabia

---

Abstract: *In this study, the superhydrophilic behavior of glass substrate surfaces has been explored. The micro and nano sized titanium dioxide (TiO_2) particles have been utilized to improve the surface roughness and increase the surface energy of glass substrates. The wettability testing shows the coating surface possess water contact angle (CA) as low as 5˚ and suddenly reduce to 0˚ after 10s. The self-cleaning property on superhydrophilic coating has been investigated. Superhydrophilic coating glass clearly shows excellent dirt repellent against dilute ketchup solution due to the absence of dirt streak on the glass surface. Meanwhile, the dirt streak presents on the bare glass surface which indicating its weak self-cleaning property. The superhydrophilic coating was also found to have great anti-fog compared to the bare glass substrate. Superhydrophilic surfaces showed free tiny droplet even at 130°C of hot-boiling bath for 10 min and completely dry after 1min.*

Keywords: *Anti-Fog, Dirt-Repellent, Self-Cleaning, Superhydrophilic, Surface Roughness,*

Introduction

Self-cleaning coatings are defined into superhydrophilic coating which possess WCA close to 0° and superhydrophobic coating which have WCA higher than 150°. Self-cleaning activities on both coatings are settling down with the action of water. Superhydrophilic coating spread the water over the surfaces like a thin film later will flow dirt and other impurities away. Superhydrophobic coating slide and roll the water droplets over the surface. Metal oxides in surface coatings are widely applied in anti-reflection, self-cleaning and anti-fogging of superhydrophilic glass . Numerous research works are attempted to develop highly efficient self-cleaning glass surfaces with advanced optical qualities for solar energy applications. For example, TitanProtect® (PHOTOKAT, 2014) have developed an excellent self-cleaning-coated solar panel where the coated panels have presented a clear reduction

* Corresponding author: Email(s): adarsh.889@gmail.com,adarsh@um.edu.my
Tel: +603-22463461; Fax: +603-22463257

in reflection by 65% relative to uncoated panel. This is because the dust and dirt on coated panel were rinsed off during rainfalls. Self-cleaning superhydrophilic glass also was developed by TitanShield solar coat (Titan Shield (R), 2013) through the photocatalyst reaction and nanotechnology fabrication.

The photocatalysis and photo-induced hydrophilicity have stimulated the photocatalyst to distinguish the contaminants, however the ultraviolet rays (UV) from sunlight are insufficient for photocatalysis reaction (Zhang, Dillert, Bahnemann, & Vormoor, 2012). The TiO_2 superhydrophilic thin films is commonly employed for photocatalysis reaction but its energy band ($E_g \approx 3.2$ eV) is limited to shorter UV radiation with wavelenght lower than 387.5 nm only (Li, Li, Yang, & Ge, 2001). Besides, UV light is a small part of solar light radiation (about 5%) (Khang, Van Khanh, Anh, & Van Minh, 2011). Several research studies have suggested the doping of the titanium dioxide with metals and non-metals elements which are extended the photoresponse of TiO_2 to the visible light range and enhance the degradation rate of contaminants (W. Zhao, Ma, Chen, Zhao, & Shuai, 2004),(Sakthivel & Kisch, 2003), (Asahi, Morikawa, Ohwaki, Aoki, & Taga, 2001), (Sato, Nakamura, & Abe, 2005), (J. C. Yu et al., 2005), (Carlson, Sjong, Wan, & Londergan, 2012; J. C. Yu, Yu, Ho, Jiang, & Zhang, 2002). However, it is hard to maintain photocatalysis reaction of film for self-cleaning purposes especially at low solar light radiation, as a result the photoactive coating is being deactivated (Torgal, Labrincha, Diamanti, Yu, & Lee, 2015). Because of these limitations, we have developed self-cleaning glass through superhydrophilicity property without the UV radiation. Our superhydrophilic coating also showed great anti-fogging and anti-water streak after impacting with water spraying.

Experimental section

Materials

All the chemicals were used without any further purification. Titanium dioxide (TiO_2) powder with sizes of 100nm and purity at 99.99% and micro-powder of TiO_2 with sizes of 40µm at purity of 99% were used as inorganic nanoparticles is obtained from Sigma Aldrich, Malaysia. Polydimethylsiloxane (PDMS) with density of 5g/ml and viscosity of 100mPa at 25˚C with is employed as surface modifier purchased from ACROS organics, Malaysia. Ethanol with purity of 99.8% at molecular weight of 46.07 is used as base solution and cleaning agent for glass. Isopropyl alcohol (2-propanol) with molarity of 60.10 g/mol is used as curing agent for organic solution. Both ethanol and isopropyl alcohol were purchased from Sigma Aldrich, Malaysia.

Substrate preparation

In this study, the glass slide with dimension size of (20mm x 20mm) and glass plates (100mm x 200mm) were used as substrate. The substrates were cleaned by using ethanol in order to remove the contaminants on the glass surface. Then, the glass were rinsed using distilled water to remove the hydroxyl contaminants on the glass before drying them at room temperature

Thin film deposition

Firstly, TiO_2 nanopowders and micropowders were dissolved in ethanol with weight ratio of 1: 2:10 and were stirred vigorously above the magnetic stirrer for 30 min. The dissolved powder then was subjected to sonication in ultrasonic bath at 50˚C for another 30 min in order to disperse the nanoparticles well in the ethanol solution. Secondly, PDMS resin was dissolved in isopropyl

alcohol at weight ratio of 3:10 for 15 min to dilute the resin. The temperature was controlled at 50˚C during the stirring process. Thirdly, the 10 wt% of prepared nanoparticles and microparticles was blended together with 50 wt% of diluted PDMS resin vigorously for 30 min before subjecting to sonication at 30˚C for 15 min. A white sol-gel was formed as end product. The prepared sol-gel coating system was applied on the glass slides through dip-coating technique. Meanwhile, the sol-gel coating was applied on the glass plates through brush fabrication. Both glass samples were then left to dry for 1day before they are employed to perform all tests.

Characterizations and testing (s)

Water Contact Angle (CA) analysis

The hydrophilicity of TiO_2/PDMS coating was analyzed through water contact angle measurement. The contact angles of the droplets of distilled water were measured using Optical Contact Angle 15EC instrument where 5µL water droplet was dispensed at 2µL/s by using Automated Dispensing System on the coated glass and bare glass surface. The images of dispensed water droplets were recorded in order to measure the static contact angle.

Surface coating analysis

The surface topographical of the TiO_2/PDMS coating and bare glass were investigated through Field Emission Scanning Electron Microscope Hitachi model of SU8220 (Hitachi, Japan). Secondary Electron Detector (SED) is objected to scan the micro- and nanograph images of surface roughness of coating and nanoparticles distribution under magnification of 5µm and 500nm by using 1kV low accelerating voltage.

Anti-fog testing

The experimental for anti-fog test was prepared as followed: The bare glass and prepared coating plate were kept above boiling water bath at 130˚C for 10 min. Both glasses was placing onto the paper to investigate the formation of tiny droplets after harsh fogging. The result studies were recorded and analyzed for further analysis discussion.

Self-cleaning test

The self-cleaning performance of the highly transparent superhydrophilic surface was demonstrated with dilute kechup solution as a model for dirt contaminant. The self-cleaning process is shown in Fig. 8b. The dilute-ketchup sauce solution was prepared inside 150mL beaker. The ratio of dilute-ketchup solution to water is at 2:5. The dirt solution was pouring onto the glasses surfaces. Then, the behavior of liquid dirt onto bare glass and TiO_2/PDMS coating glass plates were observed and analyzed.

Rainfall spraying test

Rainfall spraying test has been demonstrated by using auto-sprayer bottle onto the coated glass and bare glass. Both glasses were placed against the sprayer with the horizontal distance between spray and the glass is at 10 cm. The setup was illustrated in **Fig 1**. Water was sprayed continuously on both glass surfaces for 5 min. The water streaks have been observed after harsh water spraying and were analyzed for further discussion.

Fig 1: The Experiment Setup For Rainfall Spraying

Results and discussions

Water-contact angle

The coating's wettability was directly measured through static Water contact angle (CA). The result shows the hydrophilic nature of bare glass with water CA of 30° as shown in **Fig 2**. The hydrophilicity of coating can be improved by two factors which are through surface modification and incorporating with solid nanoparticles. First, the chemical composition plays a significant role in enhancing the hydrophilicity of the surface (Feng et al., 2004; Jaleh, Parvin, Wanichapichart, Saffar, & Reyhani, 2010). Second, the hydrophilicity of coating can be improved by incorporating with micro- and nanoparticles to increases of surface roughness (Juang, Hou, Huang, Tseng, & Huang, 2016; Tsougeni, Vourdas, Tserepi, Gogolides, & Cardinaud, 2009; X. Yu, Wang, Jiang, Shi, & Zhang, 2005). The nanoparticles coating of TiO_2 shows an excellent hydrophilicity at 4.2˚ and spread the water to a thin film layer after 10 seconds. The water CA cannot be measured since the water CA approaches to 0˚.

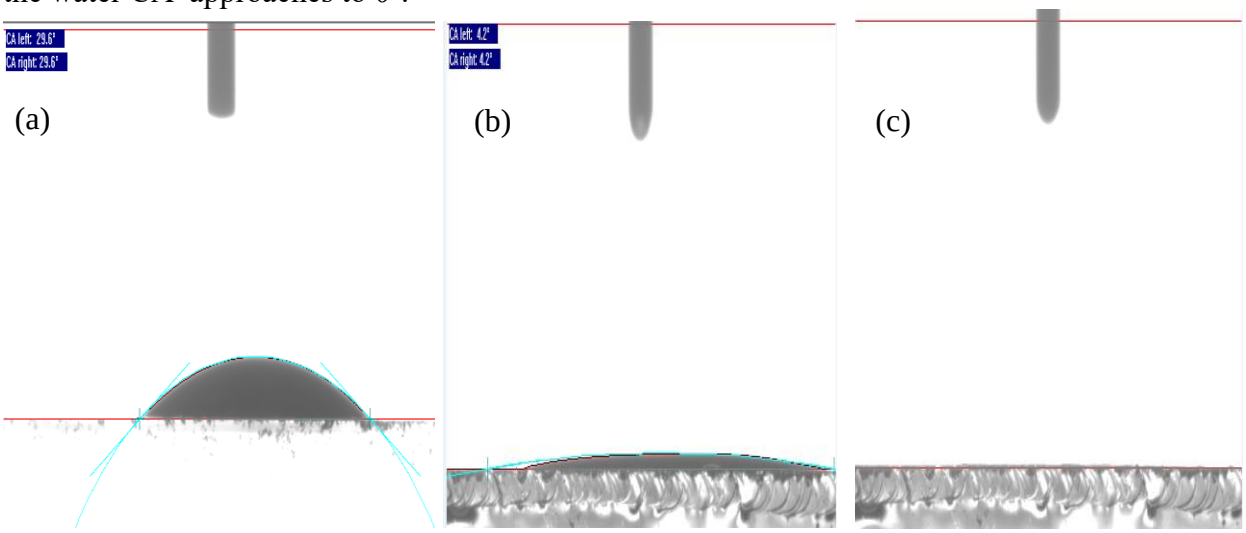

Fig 2: (A) The Water CA Of Bare Glass (B) Water CA Of Superhydrophilic Coating. (C) The Water Droplet Spreading As Thin Film Layer.

The water CA of superhydrophilic coating increases with time after placing the glass substrate inside the dark environment oven for 2 days, 4 days, and 6 days as shown in **Fig 3**. The result shows the static water CA of coating increases to 6.3° after 2 days, further increases to 8.6° after 4 days, and increases to 10.4° after 6 days. The increases in water CA is directly inferred to the tendency of TiO_2 to turn into its hydrophobicity behavior since TiO_2 films have a rapid reestablishment of hydrophobicity in dark environment. Several reports have proposed the doping of Silicon dioxide (SiO_2) into TiO_2 films to slow down the increases of water CA in dark environments (de Jesus et al., 2015; Liu, Du, & He, 2008; Tricoli, Righettoni, & Pratsinis, 2009). However, doping with inorganic nanoparticles will cause high concentration of solid nanoparticles resulting in transparency degradation of glass substrate. In this study, we have blended the organic PDMS to TiO_2 nanoparticles to provide high transparency of glass and retain high hydrophilicity of TiO_2 in dark environments. It can be observed the water CA is maintained as lower as 10.4° after 6 days which indicating that the coating have an excellent surface durability in dark environment.

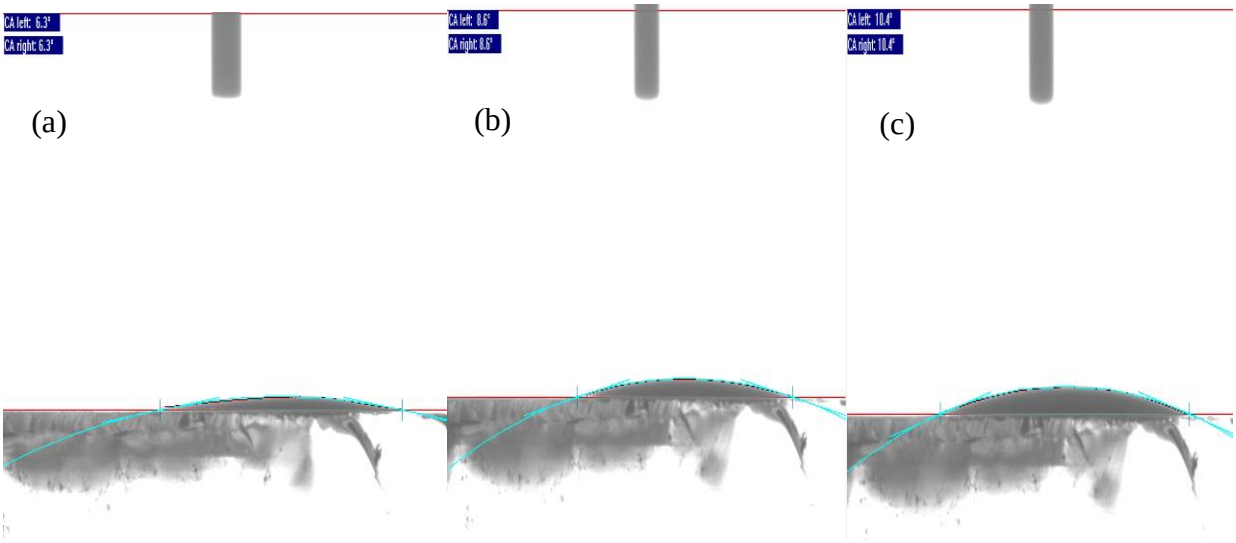

Fig 3 : The Water CA On Superhydrophilic Surface After (A) 2 Days (B) 4 Days And (C) 6 Days.

Surface morphological analysis

Wettability of surface coating is strongly dependable on surface nanostructures and roughness. High hydrophilicity and hydrophobicity coating are commonly containing numerous amounts of nanostructures and high surface roughness. **Fig 4** shows the FESEM micrograph of nano-TiO_2/PDMS coating. FESEM image have revealed that the bare glass appears smooth with free of solid structures on the surface. Most of the literatures are commonly suggested that the nanostructures on the surfaces improves the hydrophobicity of substrate [13–15,17,18], however the water CA also is being reduced for glass nanostructures especially in superhydrophilic glass as shown in Fig. 6. This decrement of water CA can be explained through the established Wenzel model. The basic assumption in Wenzel's theory is a linear relationship between apparent contact angle of the surface and the roughness factor of given surface:

$$\text{Cos } \Theta w = r \cos \Theta \quad (1)$$

where the roughness factor is the ratio of actual surface area to the apparent surface area. The rough surface presents the roughness factor, r > 1 which tuning the apparent contact angle to Θw > Θ > 90˚ for hydrophobic surface and Θw < Θ < 90˚ for hydrophilic surface. The surface roughness increases the hydrophobicity or hydrophilicity of coating which strongly dependent on the surface nature. Fig shows the surface roughness of coating film t micrograph scale at 5µm and nanograph scale at 500nm increases the surface roughness. The surface roughness consists of numerous amounts of microporous and nanopillars which have induced the water permeability on the surface, as a result increases the hydrophilicity of flat glass surface. The result study is in complete agreement with the superhydrophilic property observed in the contact angle measurement since the incorporating with nanostructures coating system reduces the water CA as explained in Wenzel model.

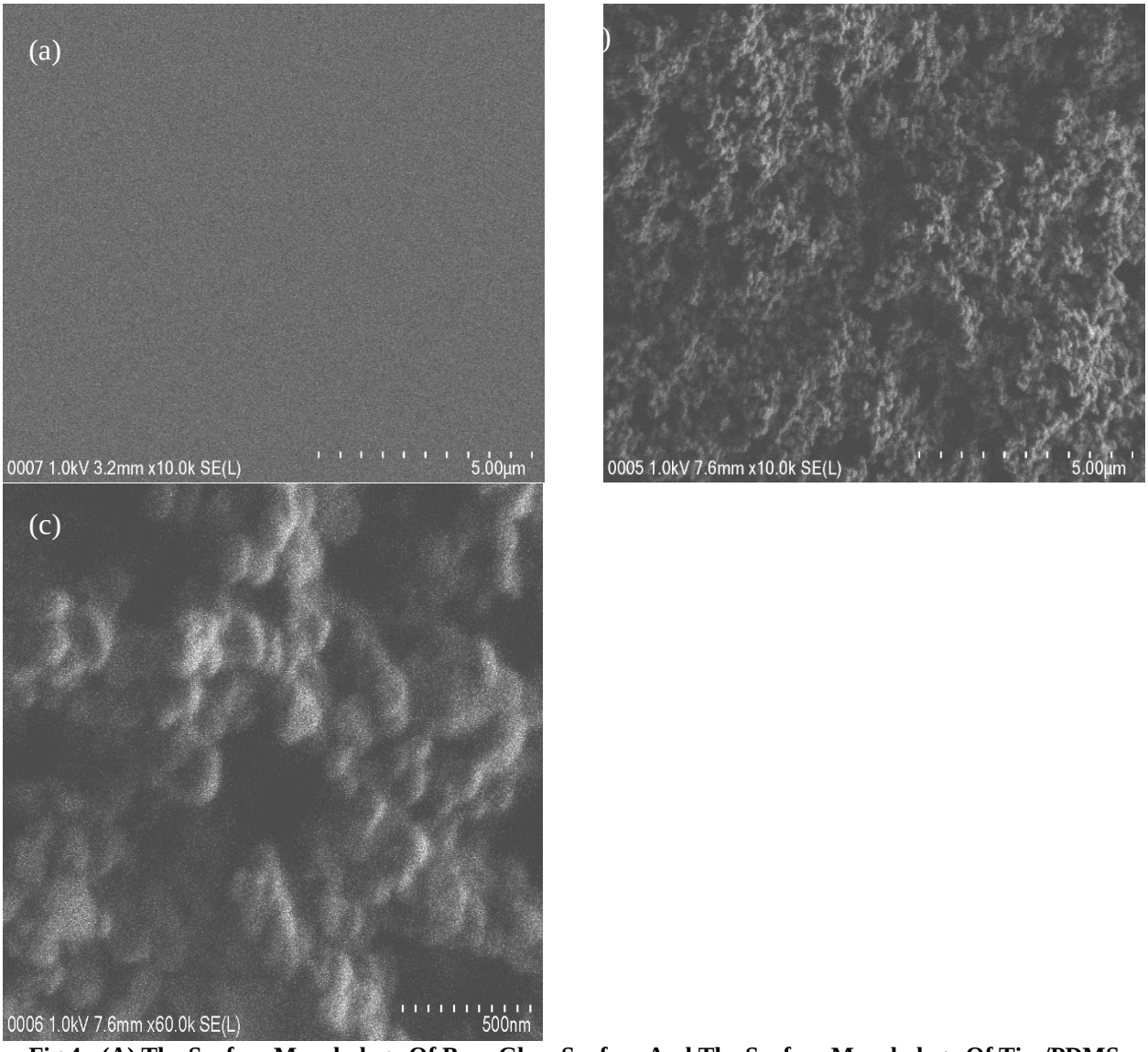

Fig 4 : (A) The Surface Morphology Of Bare Glass Surface And The Surface Morphology Of Tio_2/PDMS Coating Under Magnification Of (B) 5µm And (C) 500nm.

Anti-fog testing

In previous research studies, fog testing on the glass was conducted above the hot-boiling bath (Chen et al., 2012) (Shang & Zhou, 2016) or inside the freezer or refrigerator (Shibraen, Yagoub, Zhang, Xu, & Yang, 2016). **Fig. 5 (**a-b) shows the different formation of fog above the bare glass and coated glass surfaces after impacting to fog testing. The result shows the large tiny droplets appeared on the bare glass plate after exposed to hot vapor of hot-boiling bath for 10 min. The tiny droplets on the glass surface scatter the incident light; as a result degrade the glass transparency (Cebeci, Wu, Zhai, Cohen, & Rubner, 2006; Wu & Baghdachi, 2015; H. Zhao & Beysens, 1995). High surface energy of hydrophilic surfaces are difficult to avoid the adhered fog on the surface. Contaminants are commonly limits the traditional anti-fog coatings on hydrophilic glass. It was suggested the fogging can be prevented as if the hydrophilicity of the glass increases. The prepared superhydrophilic TiO_2 /PDMS coating glass plate shows the absence of tiny droplets on the glass surfaces due to the spreading of fog droplets on the coating glass like thin membrane. The clear image of superhydrophilic glass has indicated that its high transparency is maintained. Superhydrophilic coating glass requires 1 min only for complete drying; meanwhile the bare glass takes about 20 min for complete drying.

.

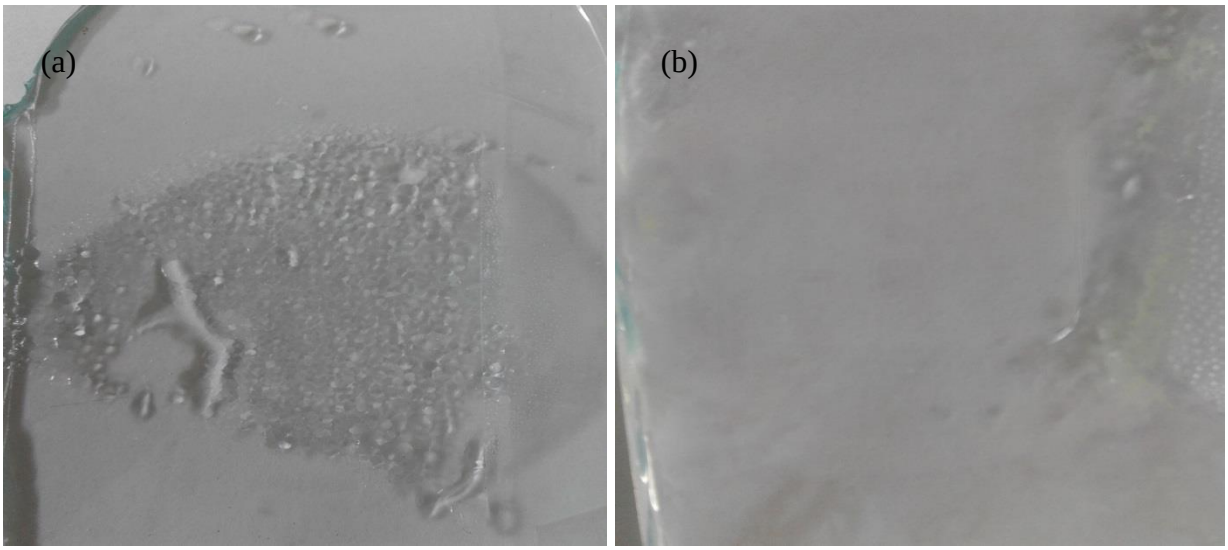

Fig 5: The Formation Of Fog On The (A) Bare Glass And (B) Coating Glass

Self-cleaning testing

Fig 6 (a) shows the formation of dirt layer on the bare glass surface. A ketchup layer with dirt-streak of contaminant was left behind the surface as the ketchup sauce solution was poured on the bare glass plate. During the sliding of ketchup solution, the dirt contaminants immediately get adhered and leaving dirt layer behind a clear surface. **Fig 6** (b) shows the free dirt layer is forming on the coating glass surface. It was observed that the superhydrophilic coating maintained its self-cleaning coating after impacting with anti-fog testing. The coating surface repels the dirt layer by spreading mechanism. The coating film's transparency slightly reduces but still maintaining a clear view. The rough and porous nanostructures generate abundant capillary percolation channels as

the ketchup solution is straining through the porous micro- and nanostructures, resulting in the superhydrophilic performance of the film against the dilute ketchup solution. The dilute ketchup solution is rapidly spreading in several hundreds of milliseconds. This observation is in completely agreed with the high surface energy of superhydrophilic coating.

Fig 6: The Formation Of Dirt Layer On (A) Bare Glass And (B) Coating Glasss

Rainfall spraying

The further superhydrophilic performance of TiO_2 coating was performed through the water-spraying with the continuous water spraying is modeled as the rainfall impact. Rainy days causes a dusty dry glass surfaces which would lower the transparency of the glass panel. In addition, acid rains will causes the corrosion process on the PV panel's frame (Ghazi & Ip, 2014). Water vapors from the rainfalls results in transmission degradation due to light scattering. Non-photocatalyst hydrophilic coating sweep the dust downward through the gravity and rain water-stream (Syafiq, Pandey, Adzman, & Rahim, 2018). In this work, we attempt to present the effect of rainfall spraying on the bare glass plate and superhydrophilic glass plate where both glass plates have been compared regarding with their optical transparency. The result study was presented in **Fig 7**. It was observed that the bare glass cannot maintain its transparent view because of the adhered water droplets and water streaks after impacting with harsh water-spraying. Differ from superhydrophilic coating glass which the glass appear clearly transparent after water-spraying because the tiny droplets do not embedding onto the surfaces. The water droplets immediately spread over the surface like a thin film as observed. The thin film layer of water possesses larger surface area compared to tiny water droplets, as a result improves the high evaporation rate of glass surface.

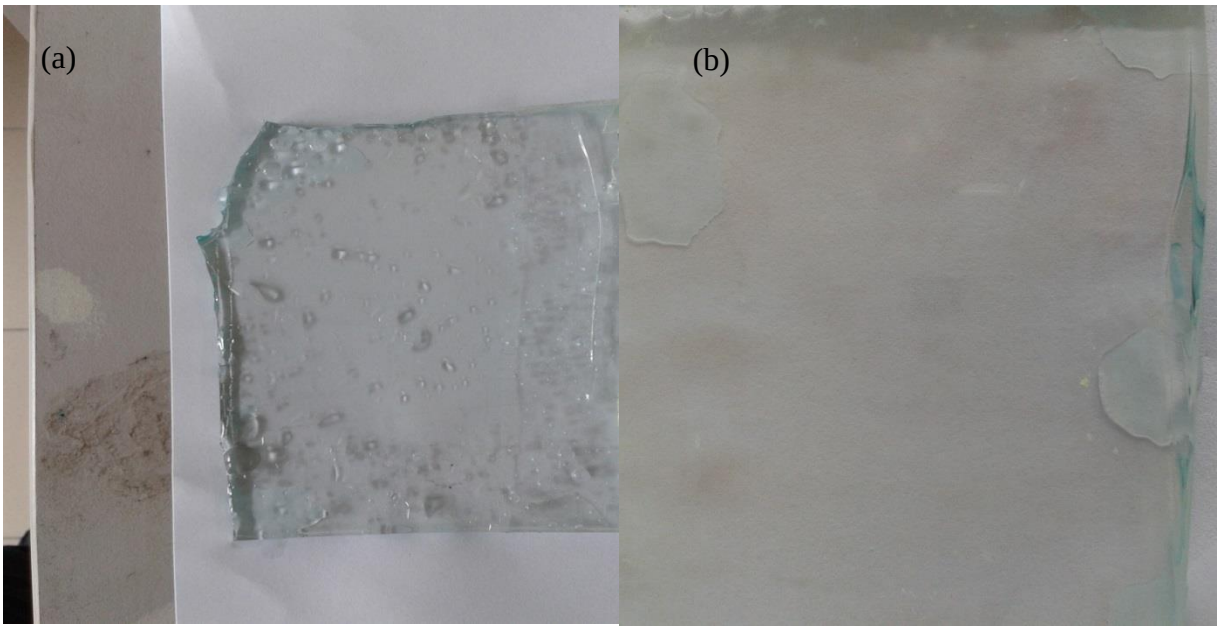

Fig 7: (A) Water Droplets And Water Streaks Appear On The Bare Glass Surfaces. (B) The Thin Film Layer Of Water Is Formed Above The Coating Glass Surface.

Conclusion

The superhydrophilic property of glass substrate was explored through the development of TiO_2/PDMS coating. The micro- and nanoparticles titanium dioxide (TiO_2) have been blended together with surface modifier PDMS to improve the surface roughness and surface hydrophilicity. The water contact angle (CA) of coating shows as low as 5˚ and suddenly reduce to 0˚ after 10s which indicating an excellent superhydrophilicity behavior. Meanwhile, the bare glass shows the water CA at 29.6°. The wettability of surface is strongly tuning the anti-fog, rainfall impact and self-cleaning property of substrate. It was clearly observed on excellent dirt-repellent against dilute ketchup solution shown by the superhydrophilic coating. The dirt solution tends to spread completely over the surface rather than emerging as droplets. The coating also is being provided with great anti-fogging surfaces since the tiny droplets spreads immediately like a thin film layer. Thin film layer of water have high evaporation rate and easy-drying as the coating completely dry after 1min.

Acknowledgement

The authors thank the technical and financial assistance of UM Power Energy Dedicated Advanced Centre (UMPEDAC) and the Higher Institution Centre of Excellence (HICoE) Program Research Grant, UMPEDAC - 2016 (MOHE HICOE - UMPEDAC).

References

Asahi, R., Morikawa, T., Ohwaki, T., Aoki, K., & Taga, Y. (2001). Visible-light photocatalysis in nitrogen-doped titanium oxides. *science, 293*(5528), 269-271.

Carlson, W. B., Sjong, A., Wan, F., & Londergan, T. (2012). Inorganic hydrophilic self-cleaning coatings: Google Patents.

Cebeci, F. Ç., Wu, Z., Zhai, L., Cohen, R. E., & Rubner, M. F. (2006). Nanoporosity-driven superhydrophilicity: a means to create multifunctional antifogging coatings. *Langmuir, 22*(6), 2856-2862.

Chen, Y., Zhang, Y., Shi, L., Li, J., Xin, Y., Yang, T., & Guo, Z. (2012). Transparent superhydrophobic/superhydrophilic coatings for self-cleaning and anti-fogging. *Applied physics letters, 101*(3), 033701.

de Jesus, M. A. M. L., da Silva Neto, J. T., Timò, G., Paiva, P. R. P., Dantas, M. S. S., & de Mello Ferreira, A. (2015). Superhydrophilic self-cleaning surfaces based on TiO 2 and TiO 2/SiO 2 composite films for photovoltaic module cover glass. *Applied Adhesion Science, 3*(1), 5.

Feng, X., Feng, L., Jin, M., Zhai, J., Jiang, L., & Zhu, D. (2004). Reversible super-hydrophobicity to super-hydrophilicity transition of aligned ZnO nanorod films. *Journal of the American Chemical Society, 126*(1), 62-63.

Ghazi, S., & Ip, K. (2014). The effect of weather conditions on the efficiency of PV panels in the southeast of UK. *Renewable Energy, 69*, 50-59.

Jaleh, B., Parvin, P., Wanichapichart, P., Saffar, A. P., & Reyhani, A. (2010). Induced super hydrophilicity due to surface modification of polypropylene membrane treated by O2 plasma. *Applied Surface Science, 257*(5), 1655-1659.

Juang, R.-S., Hou, W.-T., Huang, Y.-C., Tseng, Y.-C., & Huang, C. (2016). Surface hydrophilic modifications on polypropylene membranes by remote methane/oxygen mixture plasma discharges. *Journal of the Taiwan Institute of Chemical Engineers, 65*, 420-426.

Khang, N. C., Van Khanh, N., Anh, N. H., & Van Minh, N. (2011). The origin of visible light photocatalytic activity of N-doped and weak ferromagnetism of Fe-doped TiO2 anatase. *Advances in Natural Sciences: Nanoscience and Nanotechnology, 2*(1), 015008.

Li, X., Li, F., Yang, C., & Ge, W. (2001). Photocatalytic activity of WO x-TiO 2 under visible light irradiation. *Journal of Photochemistry and Photobiology A: Chemistry, 141*(2), 209-217.

Liu, X., Du, X., & He, J. (2008). Hierarchically Structured Porous Films of Silica Hollow Spheres via Layer-by-Layer Assembly and Their Superhydrophilic and Antifogging Properties. *ChemPhysChem, 9*(2), 305-309.

Sakthivel, S., & Kisch, H. (2003). Daylight photocatalysis by carbon-modified titanium dioxide. *Angewandte Chemie International Edition, 42*(40), 4908-4911.

Sato, S., Nakamura, R., & Abe, S. (2005). Visible-light sensitization of TiO 2 photocatalysts by wet-method N doping. *Applied Catalysis A: General, 284*(1), 131-137.

Shang, Q., & Zhou, Y. (2016). Fabrication of transparent superhydrophobic porous silica coating for self-cleaning and anti-fogging. *Ceramics International, 42*(7), 8706-8712.

Shibraen, M. H., Yagoub, H., Zhang, X., Xu, J., & Yang, S. (2016). Anti-fogging and anti-frosting behaviors of layer-by-layer assembled cellulose derivative thin film. *Applied Surface Science, 370*, 1-5.

Syafiq, A., Pandey, A., Adzman, N., & Rahim, N. A. (2018). Advances in approaches and methods for self-cleaning of solar photovoltaic panels. *Solar Energy, 162*, 597-619.

Torgal, F. P., Labrincha, J. A., Diamanti, M. V., Yu, C.-P., & Lee, H.-K. (2015). *Biotechnologies and biomimetics for civil engineering*: Springer.

Tricoli, A., Righettoni, M., & Pratsinis, S. E. (2009). Anti-fogging nanofibrous SiO2 and nanostructured SiO2− TiO2 films made by rapid flame deposition and in situ annealing. *Langmuir, 25*(21), 12578-12584.

Tsougeni, K., Vourdas, N., Tserepi, A., Gogolides, E., & Cardinaud, C. (2009). Mechanisms of oxygen plasma nanotexturing of organic polymer surfaces: from stable super hydrophilic to super hydrophobic surfaces. *Langmuir, 25*(19), 11748-11759.

Wu, L., & Baghdachi, J. (2015). *Functional Polymer Coatings: Principles, Methods, and Applications* (Vol. 12): John Wiley & Sons.

Yu, J. C., Ho, W., Yu, J., Yip, H., Wong, P. K., & Zhao, J. (2005). Efficient visible-light-induced photocatalytic disinfection on sulfur-doped nanocrystalline titania. *Environmental science & technology, 39*(4), 1175-1179.

Yu, J. C., Yu, J., Ho, W., Jiang, Z., & Zhang, L. (2002). Effects of F-doping on the photocatalytic activity and microstructures of nanocrystalline TiO2 powders. *Chemistry of Materials, 14*(9), 3808-3816.

Yu, X., Wang, Z., Jiang, Y., Shi, F., & Zhang, X. (2005). Reversible pH-Responsive Surface: From Superhydrophobicity to Superhydrophilicity. *Advanced materials, 17*(10), 1289-1293.

Zhang, L., Dillert, R., Bahnemann, D., & Vormoor, M. (2012). Photo-induced hydrophilicity and self-cleaning: models and reality. *Energy & Environmental Science, 5*(6), 7491-7507.

Zhao, H., & Beysens, D. (1995). From droplet growth to film growth on a heterogeneous surface: condensation associated with a wettability gradient. *Langmuir, 11*(2), 627-634.

Zhao, W., Ma, W., Chen, C., Zhao, J., & Shuai, Z. (2004). Efficient degradation of toxic organic pollutants with Ni2O3/TiO2-x B x under visible irradiation. *Journal of the American Chemical Society, 126*(15), 4782-4783.

Proceeding: 5th International Conference on
Applied Sciences and Engineering (ICASEA, 2018)
(eISBN 978-967-15744-1-6)
Capthorne Hotel, Cameron Highlands, Malaysia

EFFECT OF VARIABLE AND LOW ORGANIC LOADING RATE ON FORMATION OF AEROBIC GRANULAR SLUDGE IN SEWAGE TREATMENT

Nik Azimatolakma Awang [1, 2*]
Md. Ghazaly Shaaban [2]

[1]School of Civil Engineering, Engineering Campus, Universiti Sains Malaysia, 14300 Nibong Tebal, Pulau Pinang, Malaysia
[2]Department of Civil Engineering, Faculty of Engineering, University of Malaya, 50603 Kuala Lumpur, Malaysia

Abstract : *Controlling low organic loading rate (OLR) in the operational of real wastewater is challenging, and this was mainly attributed by seasonal changes. Thus, this study aimed at evaluating the correlation between variable and low OLR with formation of aerobic granular sludge (AGS) in sewage treatment. A 4.5 L column sequencing batch reactor (SBR) was operated at low superficial air velocity (SAV) of 1.33 cm/s in the development of AGS at OLR range of 0.20 to 0.48 kg CODs/m^3 d. Mature aerobic granules were attained after 55 days of formation process with an average mixed liquor suspended solids (MLSS) of 1.38 g/L, food to microorganism (F/M) ratio of 0.31 g CODs/g MLVSS d, soluble chemical oxygen demand (CODs) and suspended solids (SS) removal of 87% and 89%, respectively. Variations in OLR intrude the formation process particularly during low OLR, resulting in longer period to achieve mature AGS or full granulation of biomass in reactor.*

Keywords: *Aerobic Granular Sludge, Hydraulic Reaction Time, Organic Loading Rate, Low-Strength Wastewater*

Introduction

Granulation is an aggregation process of suspended biomass to form discrete well-defined granules without the use of carrier material. It is a self-immobilization of microbial, involving physical agitation, physicochemical and microbiological interactions of different trophic microbial groups (Lee et al., 2010; Zhu et al., 2013). The dense-spherical structure of granules led to limited diffusion gradient of dissolved oxygen inside aerobic granular sludge (AGS). As a result, aerobic, anoxic and anaerobic zones will exist simultaneously (Figure 1). Due to the different metabolic requirements, the stratification of microbial population inside aerobic granules at aerobic, anoxic and anaerobic zones existed. Hence, this will subsequently be providing simultaneous carbon, nitrogen and phosphorus removal (de Kreuk, 2006; Wagner & da Costa, 2013). AGS has a compact physical structure which favours the excellent sludge settlement and high biomass retainment to simplify the separation of mixed liquor and reduce the space demand, and the ability to withstand shock and toxic loadings (Zhu et al. 2013; de Kreuk et al. 2010)

Figure 1 shows the schematic view of the multi-layer structure of aerobic granules based on previous schematic illustration developed by de Kreuk (2006), Bassin et al. (2012) and Winkler et al. (2013). Image analysis of granule central slices via scanning electron microscopy (SEM) coupled with energy dispersive x-ray detector (EDX) by Angela et al. (2011) show that mineral cluster, mainly calcium and phosphorus are present in the core of granules. Simultaneous

nitrification and denitrification (SND) process takes place at the second and third layer, governed by ammonium-oxidising bacteria (AOB), nitrite-oxidising bacteria (NOB), glycogen-accumulating organisms (GAO) and phosphate-accumulating organisms (PAO). Cell-internally stored substrate, polyhydroxybutyrate (PHB) will be used as carbon source for growth and cell maintenance during famine (carbon source not available) period (de Kreuk, 2006).

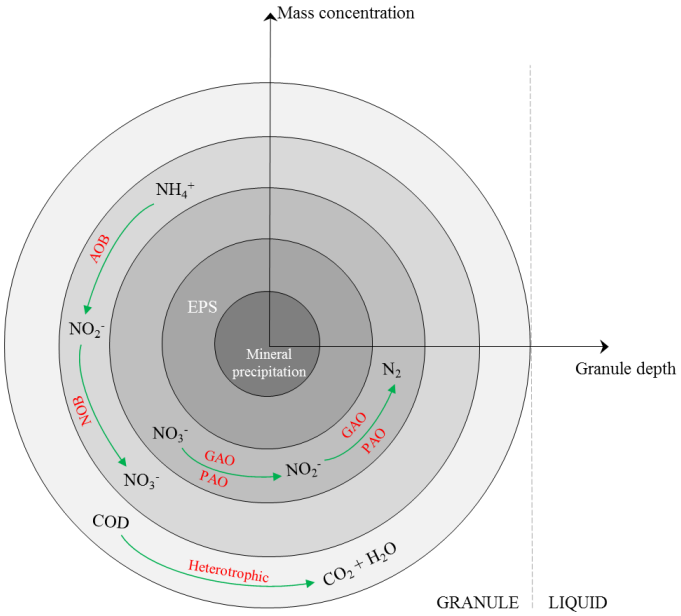

Figure 1: Schematic View Of Multi-Layer Structural Of Aerobic Granules In Biological Wastewater Treatment (Modified From De Kreuk, 2006).

As illustrated in Figure 1, the organic and inorganic substance and DO are initially transferred from liquid phase to the external surface of granule, before diffusing or being carried by an advective flow into granule interior for oxidation (Chiu et al., 2007). The oxidation or conversion process in aerobic granule is likely to be affected by external (bulk liquid to granule surface) and internal (surface to the interior of granules) mass transfer resistance (Skiadas et al., 2003). Mass transfer resistance in aerobic granules will result in a significant drop in microbial activity and growth rate, where larger aerobic granule will be affected even more severely (Li et al., 2008). The influence of mass transfer resistance also depends on other factors like granule morphology, substrate concentration (measured by organic loading rate, OLR) and diffusion, and degree of turbulence in reactor (measured by mixing intensity, aeration rate of DO or superficial air velocity, SAV) (Li et al., 2008; Skiadas et al., 2003).

Generally, in a sequencing batch reactor (SBR) system, the OLR is dependent upon substrate concentration and hydraulic retention time (HRT) (Ni et al., 2009). HRT represents the retention time of substrate at a certain period of cycle time over volume exchange ratio. A study by Muda et al. (2011) on the development of granular sludge for high strength wastewater (synthetic textile) proved that at 50% volume exchange ratio, increasing the HRT from 6 to 24 h resulted in the reduction of OLR. As the cycle time increases from 3 to 12 h, the physical properties of granular sludge in terms of MLSS, mean size and settling velocity start to decrease from 35.3 to 23.3 g/L, 843 to 385 µm and 41.3 to 21.3 m/h, respectively. Whilst, study by Wang et al. (2015) showed the deficiencies of substrate removal rate measured by chemical

oxygen demand (COD) and ammonia nitrogen from 90% and 85% to 68% and 71% with the decrease in HRT from 17 to 9 h.

Hence, it is shown here that a balance between cycle time and volume exchange ratio will ensure enough time for system to suppress the suspended growth and optimize the substrate accumulation, and enough food for microbial growth (Wang & Liu, 2008). For an AGS system that is subjected under low strength wastewater or run over a long period, decreasing the cycle time or increasing the volume exchange rate will ensure a high OLR, and hence will maintain a balance between food to microorganism ratio (F/M). In this context, the objective of the present study is to determine the dynamic granulation process of aerobic granules under variation of OLR from 0.20 to 0.48 kg CODs/m^3 d, low SAV of 1.33 cm/s, and HRT of 6 and 8 h.

Materials and Methods

Reactor setup, activated sludge and sewage collection

A lab-scale SBR with a working volume of 4.5 L and H/D ratio of 11.3 was used for aerobic granules formation process. The operating strategies for SBR comprised of two phases. During Phase 1 (HRT of 8), cycle time was 4 hour with filling, reaction, settling and discharge time fixed to 6, 195, 30 and 6 min, respectively. During Phase 2 (HRT of 6), the cycle time was changed to 3 h with filling, settling and discharge time as in Phase 1. Effluent standpipe was fixed for a volumetric exchange rate of 50%. Aeration was supplied from the bottom of SBR at an air flow rate of 4 L/min resulting in SAV of 1.33 cm/s. The SBR was operating at room temperature without pH control.

Sewage and activated sludge were collected from Pantai 1 sewage treatment plant located at Pantai Dalam at south central end of Kuala Lumpur city, Malaysia. The raw sewage and activated sludge were taken directly from primary clarifier and anoxic tank, respectively. During the start-up, 2.3 L of activated sludge after aeration for 1 day were used as seed, resulting in an initial concentrated mixed liquor suspended solids (MLSS) of 5.8 g/L. sewage was stored at 5 ºC for a maximum of 18 days. During this time, the settled suspended solids from sewage tanks were removed. Influents for the SBR were replaced for every 2 or 3 days.

Analytical methods

Parameters such as soluble COD (CODs), MLSS, mixed liquor volatile suspended solids (MLVSS), suspended solids (SS) and sludge volume index (SVI) were analysed according to APHA standard methods (2005). CODs was used instead of total COD due to a huge increment for total COD compared to CODs when the SS value increased. A high SS value contributes to an increase in the COD value, since more organic and inorganic materials are oxidized by potassium dichromate. Ammonium, nitrite and nitrate were determined by the photometric determination using Merck test kit. pH was measured just before the reaction time ended. Measurements of the parameters were carried out for two to three times per week. The morphology of aerobic granules was observed using field emission scanning electron microscope (FESEM), where sample preparation was described by Awang and Shaaban (2015). Elements compositions for aerobic granules were analysed using energy dispersive X-ray spectrometer (EDX).

Results and Discussion

Profile of biomass concentration and settling properties

Figure 2 depicted the profiles of MLSS, MLVSS, OLR and CODs influent for aerobic granules developed in SBR from the start-up until the end of the study. Within 24 hours of start-up, most of the sludge from the concentrated activated sludge was being washed out from SBR, causing a rapid decreased in the MLSS from 5.8 g/L to 1.43 g/L. An excessive elimination of poor settling activated sludge during day 1 affected the performance of SS removal but not COD removal as exhibited in Figure 3. From an observation, the proliferation of filamentous microorganisms on the reactor wall started on day 4 hindered the settling process which caused a decrease in MLVSS and increase in SS effluent. Filamentous microorganisms interfered the settling process by floating freely or protruding from small flocs. This was in conjunction with the result on SVI profile (Figure 4) that showed relatively high different concentrations in between 5 min intervals settling time during the start-up. The length of the bar with different colour (represent different settling time) could be used as an alternative to assess the current state of settling properties for aerobic granules.

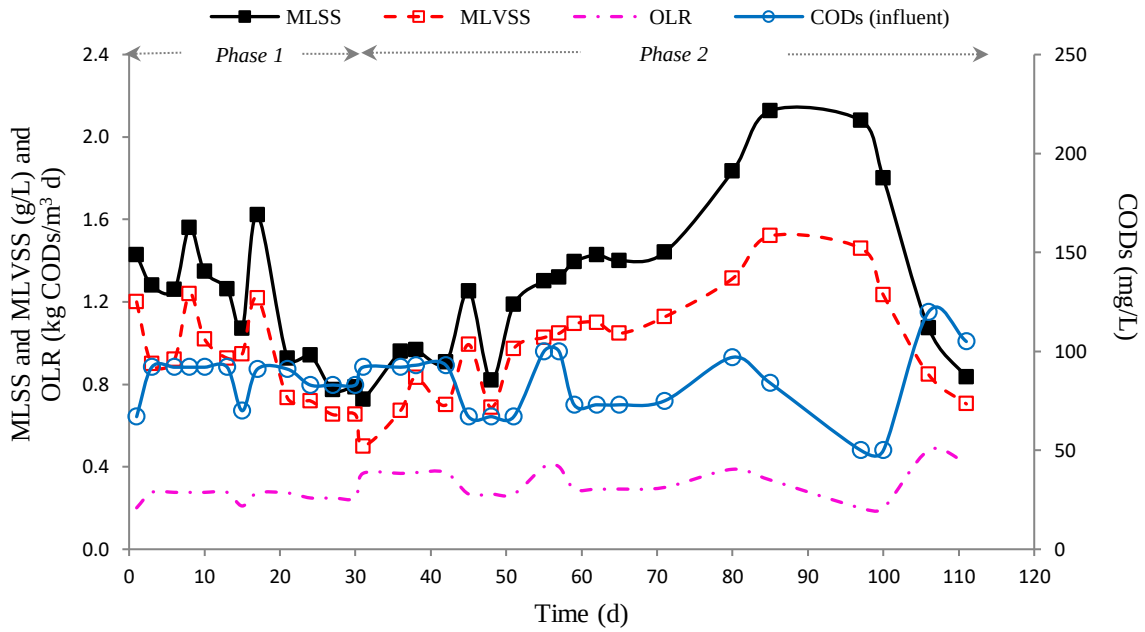

Figure 2: Profile Of Biomass Concentration, OLR And Cods Influent

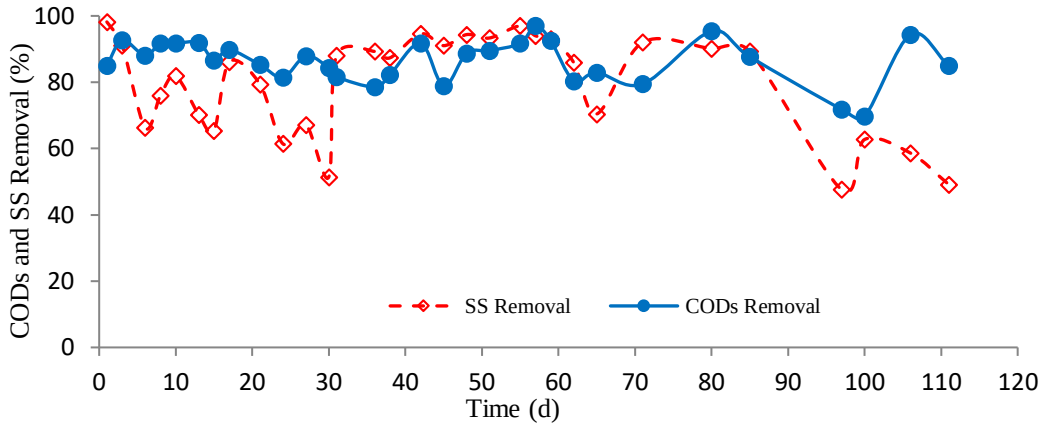

Figure 3: Removal of CODs and SS

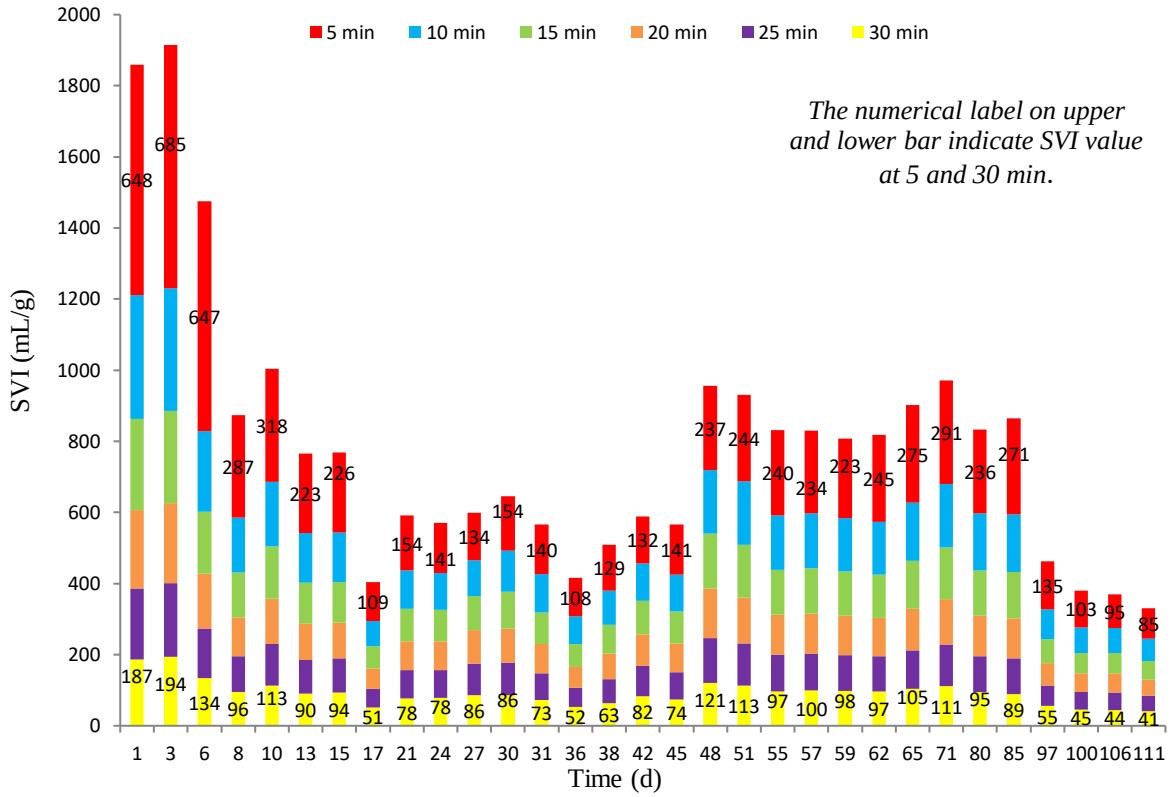

Figure 4: Profile Of SVI At 5 Min Intervals Of Settling Time

The occasional sporadic increased on day 8 and 17 for MLSS and SS removals were resulted from the reactor maintenance on the day before the analytical procedure was carried out. By removing the biofilm which had grown on the reactor wall during the reactor maintenance, aerobic granules did not have to outcompete for food with biofilm anymore. As the reactor maintenance occasion took place on day 7 and 16, more than 50% of SVI_5 decreased on the following day of analysis. However, filamentous microorganisms continued to proliferate within 4 to 5 days after the reactor maintenance occasion took places on day 7 and 16. These observations were consistent with SVI_5 result that showed sudden increases from 287 mL/g on day 8 to 318 mL/g on day 10 and 109 mL/g on day 17 to 154 mL/g on day 21.

Although MLSS and SS removal continued to decrease after 30 days of the formation process, the removal efficiency of CODs stayed high at 84%. The analysis on Food to microorganism

(F/M) ratio increased from 0.22 g COD/g MLVSS d on day 8 to 0.38 g COD/ g MLVSS d on day 30, even though OLR remained at 0.28 to 0.25 kg COD/m^3 g. Thus, this was suggested as a signal to indicate that OLR or the amount of microbial responsible for substrate degradation was not sufficient. According to Wang and Liu (2008), decreasing the cycle time or increasing the volumetric exchange rate would ensure a high OLR and keep a balance between F/M ratio for an AGS system that subjected under low strength wastewater to run over a long time. Thus, in order to increase the OLR, cycle time was adjusted from 4 hours to 3 hours (Phase 2) after the analysis on day 30 with the other operating conditions to remain unchanged.

A slight decrease in MLVSS concentration observed on day 31 was normally expected due to the adaptation process of microbial to a new selection pressure. Nevertheless, F/M ratio increased up to 0.74 g COD/g MLVSS d with the increment of OLR on day 31. The removal of CODs and SS reached above 90% in line with the increase of MLSS and MLVSS on day 42. A sudden increase in MLSS up to 1.25 g/L was observed on day 45 due to reactor maintenance on day 43. However, MLSS had slightly decreased to 0.82 g/L on day 48 due to a low OLR which was from 0.37 kg COD/m^3 d on day 42 to 0.27 kg COD/m^3 d on day 45.

At a stable condition, SBR system should be comprised of mature aerobic granules that could easily adapt and stabilize in variable substrate concentration and changes of operating conditions. As shown in Figure 2, MLSS did not substantially alter with significant changes in influent CODs between days 55 to 71. This was in conjunction with the analysis on F/M ratio that varied distinctively between 0.17 to 0.74 g CODs/g MLVSS d at an early stage of the formation process. Instead, F/M ratio was slightly varied between 0.27 to 0.39 g CODs/g MLVSS d at a stable condition. During a stable period, profile of SVI between 5 min intervals of settling time started to plateau off and distributed uniformly. Control Batch stabilized at an average MLSS of 1.38 g/L, F/M ratio of 0.31 g CODs/g MLVSS d, CODs and SS removal of 87% and 89%, respectively.

Ammonium removal efficiencies

The removal efficiencies of ammonium (NH_4^+), nitrite (NO_2^-) and nitrate (NO_3^-) from the beginning until the end of the formation period were illustrated in Figure 5. It was noted that the removal of ammonium remained high at 100% from start-up until day 97. It was suggested that a complete nitrification process took place accompanied with the CODs utilization during the reaction time. This was consistent with the result on nitrate effluent (Figure 5f) which was almost equivalent to ammonium influent from start-up until day 97. The trend in nitrate effluent (Figure 5e) results also indicated that denitrification process was likely not occurred at all. It was expected that denitrification process should occurred during the idle and settling time (anoxic conditions). This might be attributed by the insufficient of carbon source (CODs) after the reaction time took place.

It had been reported by Metcalf and Eddy (2014) that optimal nitrification process occurred at pH 7.5 to 8.0 and the culture pH below 6.8 would inhibit a nitrifying bacteria. A pH of 7.0 to 7.2 was normally used to maintain reasonable nitrification rates. In fact, a complete nitrification in turn leads to the accumulation of hydrogen ion in the reactor and decreased the pH inside the reactor. Since the pH of the raw sewage from Pantai 1 STP varied within 7.4 to 7.9, it would take sometimes for the accumulation of hydrogen ion to disturb the pH at the start of the reaction time inside the reactor. As shown in Figure 5(b), pH decreased below 6.8 between days 6 to 17 and 71 to 111. Whilst, the average pH at the end of the reaction time during a stable conditions was 7.0.

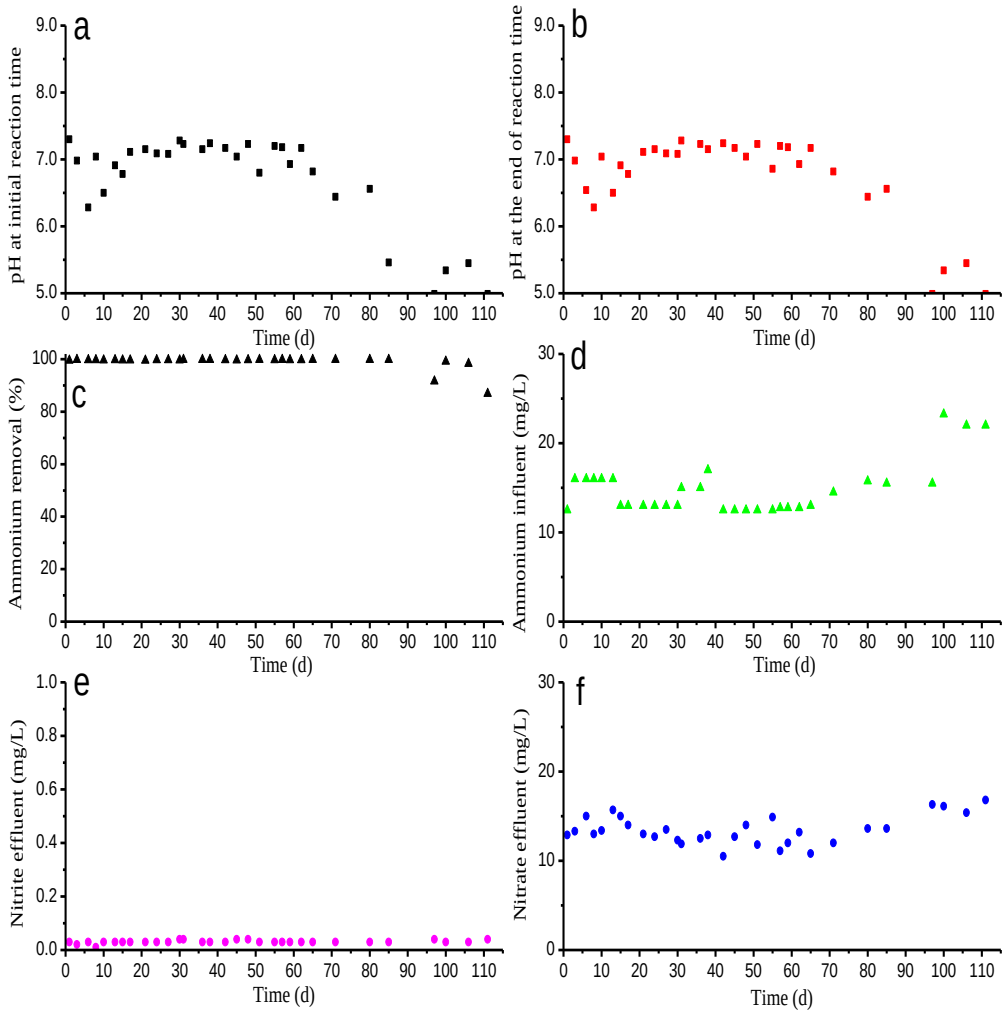

Figure 5: Profile Of Ph, Ammonium, Nitrite And Nitrate Effluent

It was anticipated that certain microbial species which were responsible for the granule formation might had decayed due to the acidic condition and the proliferation of filamentous microorganisms that took place. This was consistent with the result on SS removal and MLSS profile that significantly decreased after day 97. Alkalinity was not added to maintain acceptable pH values since pH should not be controlled during the formation process. Hence, as in between day 6 to 17, it was predicated that the performance of aerobic granule system would continue to increase if the formation period was to extend for more than 111 days.

Morphology Observation

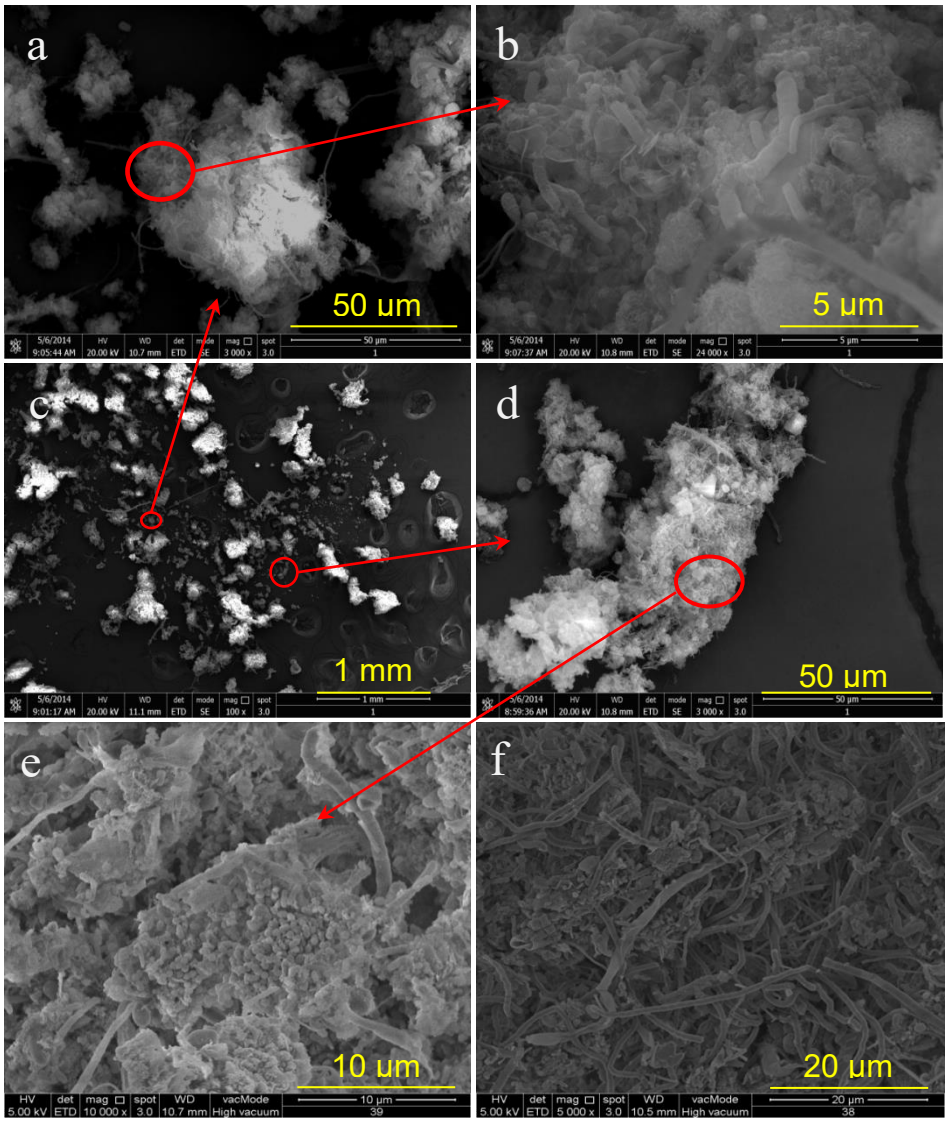

Figure 6: FESEM Images Of Mature Granules At Day 80 (A, B, C, D, E) And Activated Sludge (F).

FESEM examination was used to characterize the microstructure of aerobic granules. Figure 6 exhibited the morphology of the activated sludge and the mature aerobic granule collected on day 80, just before the performance of the aerobic granule system dropped. As showed in Figure 6(f), the activated sludge exhibited a loose-structure morphology and had a relative abundance of filamentous microorganisms. In contrast, the mature aerobic granules (Figure 6; a-e) were consisted of bacteria-dominant granules with a few filamentous microorganisms. The aerobic granules were mainly comprised of cocci-shape and bacilli-shape bacteria which were uniformly and tightly cross-linked between one another to form a compact structure. A similar result was reported by Ma et al. (2013) who found the suppression of filamentous microorganism at low OLR (0.6-1.2 kg COD/m^3 d) for the mature aerobic granules to develop in synthetic (glucose based) wastewater.

EDX analysis

EDX analysis was carried out on the surface of the aerobic granules and the activated sludge with the selected area as shown in Figure 6(b) and Figure 6(f). The localized elements spectra for the activated sludge showed that only carbon, oxygen and nitrogen were present with weight percentages of 65%, 22% and 13%, respectively. As illustrated in Figure 7, the analysis of the localized elementals spectra also clearly showed that carbon and oxygen were the major components observed on the surface of the aerobic granules. However, the EDX spectra for the activated sludge did not show any characteristic signal of magnesium, iron, calcium, sodium and titanium as present in the aerobic granules. Elemental EDX mapping image analysis by Angela et al. (2011) on the central slice mature aerobic granules depicted that carbon majorly present on the surface, whilst calcium and phosphate were formed in the core of the aerobic granules. Thus, this explained why the presence of magnesium, iron, calcium, sodium and titanium signals was lesser on the surface of the aerobic granules. EDX analysis could be a useful tool in understanding the distribution of elements if aerobic granules could be sliced. However, slicing an aerobic granule required a precise technique and equipment that could ensure the aerobic granules structure would not be disrupted during the process.

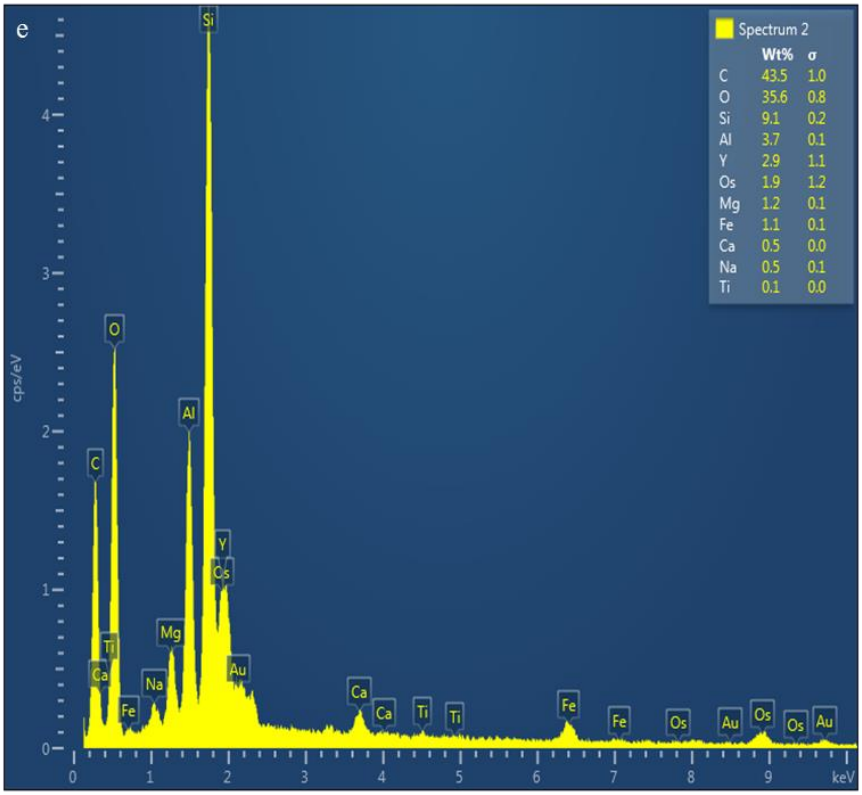

Figure 7: Localized Elementals Spectra From EDX Analysis For Figure 4.6b Surface Area

Summary

In this study, aerobic granules was successfully developed even though OLR were exceptionally low, which were in range of 0.2 to 0.48 kg COD/m^3 d. Mature aerobic granules were attained after 55 days of formation process with an average MLSS of 1.38 g/L, F/M ratio of 0.31 g CODs/g MLVSS d, CODs and SS removal of 87% and 89%, respectively. It can be conclude that aerobic granules developed under a low OLR or F/M ratio required longer period to attained maturity periods.

References

Angela, M., Béatrice, B., & Mathieu, S. (2011). Biologically induced phosphorus precipitation in aerobic granular sludge process. *Water Research*, *45*(12): 3776–3786.

APHA. (2005). Standard Methods for the Examination of Water and Wastewater, 21st ed. American Public Health Association/ American Water Works Association/ Water Environment Federation, Washington.

Awang, N.A., & Shaaban, M.G. (2015). Impact of height to diameter (H/D) ratio on aerobic granular sludge (AGS) formation in sewage treatment. *Jurnal Teknologi (Sciences & Engineering), 77:32*, 95-103.

Bassin, J. P., Kleerebezem, R., Dezotti, M., & van Loosdrecht, M.C.M. (2012). Simultaneous nitrogen and phosphate removal in aerobic granular sludge reactors operated at different temperatures. *Water Research*, *46*(12): 3805–3816.

Chiu, Z. C., Chen, M. Y., Lee, D. J., Wang, C. H., & Lai, J. Y. (2007). Oxygen diffusion and consumption in active aerobic granules of heterogeneous structure. *Applied Microbiology and Biotechnology*, *75*(3): 685–691.

de Kreuk, M.K. (2006). *Aerobic granular sludge: scaling up a new technology*. (Doctoral thesis, Technical University Delft, The Netherlands).

de Kreuk, M.K., Kishida, N., Tsuneda, S., & van Loosdrecht, M.C.M. (2010). Behaviour of polymeric substrates in an aerobic granualr sludge system. Water Res 44: 5929-5938.

Lee, D.J., Chen, Y.Y., Show, K.Y., Whiteley, C.G., & Tay, J.H. (2010). Advances in aerobic granule formation and granule stability in the course of storage and reactor operation. *Biotechnology Advances*, *28*(6): 919–934.

Li, Y., Wang, Z., & Liu, Y. (2008). Diffusion of Substrate and oxygen in aerobic granules. In Y. Liu (Ed.), *Wastewater purification: Aerobic granulation in sequencing batch reactors* (1st ed., pp. 131–147). Taylor & Franchis Group.

Ma, J., Quan, X., & Li, H. (2013). Application of high OLR-fed aerobic granules for the treatment of low-strength wastewater: Performance, granule morphology and microbial community. *Journal of Environmental Sciences*, *25*(8): 1549–1556.

Metcalf and Eddy., Tchobanoglous, G., Stensel, H.D., Tsuchihashi, R., & Burton, F., (2014). *Wastewater engineering: Treatment and Resource Recovery*, 5th ed. Boston: McGraw-Hill.

Muda, K., Aris, A., Razman, M., Ibrahim, Z., van Loosdrecht, M. C. M., Ahmad, A., & Zaini, M. (2011). The effect of hydraulic retention time on granular sludge biomass in treating textile wastewater. *Water Research*, *45*: 4711–4721

Ni, B.-J., Xie, W.-M., Liu, S.-G., Yu, H.-Q., Wang, Y.-Z., Wang, G., & Dai, X.-L. (2009). Granulation of activated sludge in a pilot-scale sequencing batch reactor for the treatment of low-strength municipal wastewater. *Water Research*, *43*(3): 751-761

Skiadas, I. V, Gavala, H. N., Schmidt, J. E., & Ahring, B. K. (2003). Anaerobic granular sludge and biofilm reactors. *Advances in Biochemical Engineering/biotechnology*, *82*: 35–67.

Wagner, J., & da Costa, R.H.R. (2013). Aerobic Granulation in a Sequencing Batch Reactor Using Real Domestic Wastewater. *Journal of Environmental Engineering, 139(11):* 1391–1396

Wang, Z.C., Gao, M.C., Ren, Y., Wang, Z., She, Z.L., Jin, C.J., Chang, Q.B., Sun, C.Q., Zhang, J., & Yang, N. (2015). Effect of hydraulic retention time on performance of an anoxic–aerobic sequencing batch reactor treating saline wastewater. *International Journal of Environmental Science and Technology*, 12(6); 2043-2054

Wang, Z., & Liu, Y. (2008). Aerobic granulation at different SBR cycle times. In Y. Liu (Ed.), *Wastewater purification: Aerobic granulation in sequencing batch reactors* (1st ed., pp. 37–50). Taylor & Franchis Group.

Winkler, M.-K. H., Kleerebezem, R., Strous, M., Chandran, K., & van Loosdrecht, M. C. M. (2013). Factors influencing the density of aerobic granular sludge. *Applied Microbiology and Biotechnology*, *97*(16): 7459–7468.

Zhu, L., Yu, Y., Dai, X., Xu, X., & Qi, H. (2013a). Optimization of selective sludge discharge mode for enhancing the stability of aerobic granular sludge process. *Chemical Engineering Journal*, *217*: 442–446.

Proceeding: 5th International Conference on Applied Sciences and Engineering (ICASEA, 2018)
(eISBN 978-967-15744-1-6)
Capthorne Hotel, Cameron Highlands, Malaysia

LOW-COST ACTIVATED CARBON PRODUCED FROM WASTE TYRE FOR REMOVAL OF 2-CHLOROPHENOL

Nurul Ainirazali[1]
Kanchana Manirajah[2]
Sheela V.Sukumaran[3]

[1,2,3]Faculty of Chemical & Natural Resources Engineering, Universiti Malaysia Pahang, Lebuhraya Tun Razak, 26300 Gambang, Kuantan, Pahang, Malaysia.

Abstract: *Waste tyre was used as a precursor for preparation of low-cost activated carbon (AC) as an adsorbent for removal of 2-chlorophenol (2-CP) from an aqueous solutions. The AC was produced by pyrolysis process. The physical and chemical properties of as-synthesized adsorbent were characterized by XRD, BET, FESEM, and FTIR. The influence of initial adsorbate concentration, pH and adsorbent dosage on the removal of 2-CP in the batch-operational mode at ambient temperature were investigated. The as-synthesized AC presence an amorphous carbon with high surface area (208 m^2/g) and average pore volume (0.5817 cm^3/g) as revealed by XRD and BET. The maximum adsorption capacity for 2-CP by activated carbon was achieved at initial concentration 10mg/L, pH 5, and adsorbent dosage 0.5g in 10 minutes. From this finding, the activated carbon produced from waste tyre can be used for effective and economic removal of chemical plant wastewater containing toxic 2-CP.*

Keywords: *Waste tire; AC; Adsorption; 2-Chlorophenol*

Introduction

Many phenolic compounds are regulated as priority pollutants for environmental control because of their high toxicity to human beings even at low concentration exposure [1]. Chlorophenols (CPs) constitute an important class of aquatic pollutants that are present in aquatic ecosystems. 2-Chlorophenol (2-CP), a low chlorine-substituted phenol and the precursor of the higher-substituted CPs, has been introduced into the environment via anthropogenic activities. Chlorophenols have been extensively used in the production of fungicides, herbicides, insecticides, pharmaceuticals, preservatives, glue, paint, fibers, leather, and as intermediates in chemical synthesis [2]. Exposure to 2-CP may cause carcinogenic and teratogenic properties in humans and the environment. Due to their toxicity and adverse effects upon human and biota, the United States Environmental Protection Agency (US EPA) has classified them as toxics or hazardous pollutants [3]. High amounts of chlorinated solvents were found to cause dizziness, reduce the ability to concentrate and remember, damage the nervous system, and produce an irregular heartbeat. Thus, it is important to eliminate these compounds before discarding the wastewater into the environment.

Techniques engaged for the removal of chlorophenols from waste water include adsorption [4], catalytic wet oxidation [5], biodegradation [6], ozonation and electrochemical degradation [7]. Among them, adsorption technology is widely considered the most applicable technique for the removal of CPs. However, an appropriate cost-effective material for CPs capture is important. The most widely used adsorbent among the various adsorbents for CPs adsorption is activated carbon because of its low cost, high surface area, and high porosity which can help

to enrich the organic substrate around the adsorbent [8]. Obtaining AC from the waste tyre is a great importance since it can lower the cost of commercial ACs, eliminate fire hazard and address pollution problems associated with the disposal process of old tires. Producing AC from waste tyre resulted in high amount of carbon and doubly effective solution for the environmental pollution where it reducing waste in a green way [9]. Activated carbon derived from waste tyre shows high adsorption performance.

The aim of the study was to evaluate the performance of activated carbon produced from waste tyre for the removal of chlorine from 2-CP. As the activated carbon was derived from waste rubber tires, the study is considered a doubly effective solution for environmental pollution. It represents sustainable way to dispose the waste tires and an economic source of carbonaceous material.

Methodology

Materials

All chemicals 2-chlorophenol (2-CP), hydrogen peroxide (H_2O_2), potassium hydroxide (KOH) and hydrochloric acid (HCl) were used analytically pure and purchased from Sigma-Aldrich. The waster rubber tyre was used as precursor in preparation of AC.

Preparation of activated carbon from waste tyre

The waste rubber tyre was cut into small pieces and washed thoroughly with distilled water, then then dried in an oven at 105°C for 2 h. The granule was heated up to 300°C in furnace for 3 h to separate the black tire crude oil, distilled diesel oil and produced oil. Then, the activations of char was take place at 500^{o}C for 5 h in 200 mlmin^{-1} of nitrogen gas. Then, the chars recovered from the pyrolysis reactor was treated with hydrogen peroxide solution. For this purpose, the product treated with H_2O_2 (6% concentration) with a ratio of 1 g/20 mL carbon/H_2O_2. The mixture (carbon and acid solution) was stirred and heated at 100^{o}C for 24 h in oven. Then, the sample washed thoroughly with deionized water and dried at 110^{o}C for 2h to form activated carbon.

Characterization of adsorbent

The characteristics of the synthesized catalysts were investigated using XRD, BET, FESEM and FTIR. The X-ray diffraction (XRD) was used to determine the crystalline structure of the AC in the range of $2\theta = 10 – 80^o$ with Cu Kα radiation ($\lambda = 1.5405$Å). The measurement of BET surface area, pore diameter and pore volume for AC were conducted using AUTOSORB-1 model AS1 MP-LP instrument at 77 K. The surface morphology of the AC was analyzed by field emission scanning electron microscope (FESEM), JEOL/JSM-7800F with accelerating voltage employed to be in the range of 5-15 kV. The IR spectra of the AC adsorbent was measured on Perkin- Elmer System 2000 spectrometer using the KBr disk method over the range of 2000–400 cm^{-1}.

Batch adsorption procedure

The equilibrium adsorption studied by using batch mode adsorption. A constant mass of adsorbent (0.1 g) was contacted with 50 mL of 2-CP solutions of 10mg/L. The bottles were sealed and placed in a shaker until equilibrium was reached. Samples were then withdrawn for every 5 minutes of reaction by syringe, filtered through 0.22m syringe filter, and diluted to the required level for analysis. Similar adsorption procedure was repeated by varying the initial pH of 2-CP solution (3, 5, 7, and 10) and adsorbent dosage (0.05g, 0.1 g, 0.3g and 0.5g). The percentage removal of CPs (R%) calculated.

Analysis of 2-Chlorophenol

Samples were analysed using a Varian Cary 1E UV/Vis spectrophotometer at their maximum wavelength of 284nm. The equilibrium amount of CPs adsorbed per unit mass of adsorbent, qe (mg/g), at different 2-CP concentrations was identified using Eq. 2.1.

$$qe = \frac{(\mathrm{Co} - \mathrm{Ce})\mathrm{V}}{W} \qquad (\mathbf{Eq\ 2.1})$$

where qe (mg/g) is the equilibrium amount of adsorbate (CPs) adsorbed per unit mass of adsorbent (AC) ; V (L) is the volume of the solution and W(g) is the mass of the adsorbent used.

The percentage removals (% R) of the adsorbates (CPs) in solution calculated using Eq. (2.2).

$$\mathrm{CPsremoval}\ (\%) = \frac{\mathrm{Co} - \mathrm{Ce}}{\mathrm{Co}} \qquad (\mathbf{Eq\ 2.2})$$

where Co and Ce are the liquid-phase concentrations at initial and equilibrium states (mg/L), respectively.

Results and Discussion

Characterization of AC

Figure 1 shows XRD pattern for the AC adsorbent produced from waste tyre. The result indicates the presence of two peaks at 2θ = 25.43 and 43.89. The peaks were appeared in the pattern due to the presence of amorphous carbon that caused by disordered stacked of carbon ring [10].

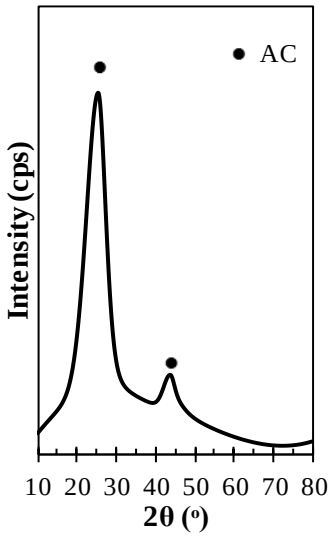

Figure 1. XRD Analysis Of AC

The isotherms produced by AC showed type IV adsoption characteristics according to IUPAC classification [4]. The hysteresis loop was determined to be type H3 due to the type of capillary condensation taking place in its mesopores. Type IV isotherm is usually attributed to monolayer-multilayer adsorption since it follows a similar part of the corresponding part of a

Type II isotherm obtained with the given adsorptive on the similar surface area as the adsorbent in a non-porous form [10]. Table 4.2 summarizes the BET surface area and pore volume and pore diameter of the researched adsorbent. According to the results, AC produced in the current research possesses high specific surface area (208 m^2/g) and average pore volume (0.5817 cm^3/g) compared the other adsorbents. However, the average pore diameter for the current researched catalyst is the highest. This indicates that the synthesis of AC using waste tyre as precursor can give high surface area which can increase the adsorption capacity.

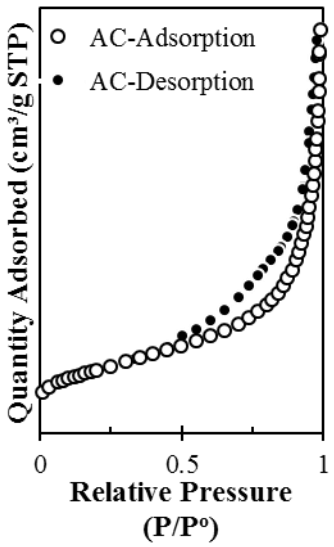

Figure 2. N_2 Adsorption-Desorption Isotherm For AC

Table 2. Comparison of properties of AC

Adsorbents	BET surface area (m^2/g)	Pore volume (cm^3/g)	Average pore diameter (Å)	Researchers
AC	62	0.9592	615	[11]
ACZnO	15	0.3041	802	[11]
$ZrSAC_4$	115	0.0800	N/A	[12]
AC	208	0.5817	126	Current Research

The morphology of the activated carbon produced from waste rubber tyre was characterized by FESEM, and shows in Figure 3. From the analysis, the morphological region of the AC is granular with particle diameter between 80-100 nm. High resolution of the image of the developed activated carbon indicates that there are different pore structures in the adsorbent. High surface area and pore structure of the AC were effective to be as an adsorbent. When the porosity increases, the surface area also increases [11].

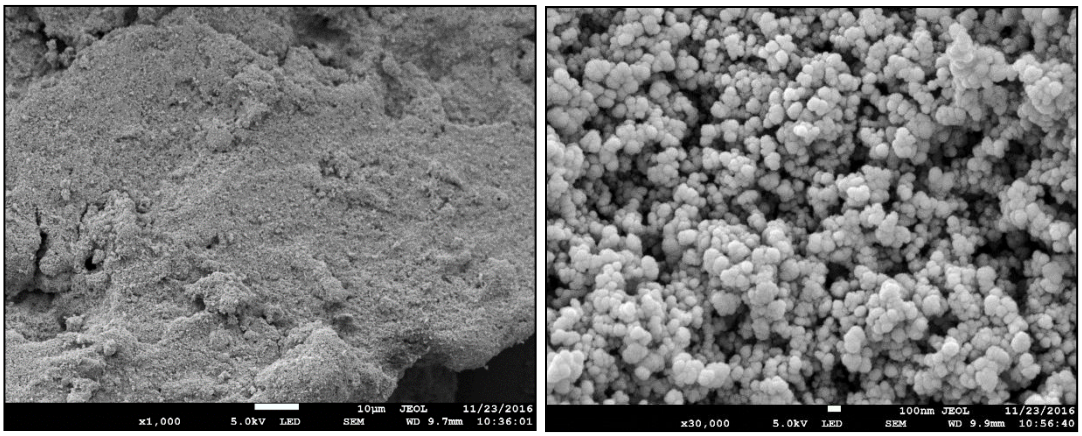

Figure 3. FESEM Images Under Magnification (A) 1000x And (B) 30000x

Figure 4 shows the FTIR spectrum for AC. The first peak at 2665 cm^{-1} indicates the strong bonded functional group of O-H and C-H stretching absorption. Next, the band centered on 1992 cm^{-1} indicates enhancement in the aromatic C=C groups (carbonization). Then the peak at 997 cm^{-1} represents C-O stretching functional group. Fingerprint region occurs towards the end. Fingerprint region is the region consists of absorptions due to all other single bonds (except H-Z), making it often a complex region that is very difficult to analyze [13, 14]

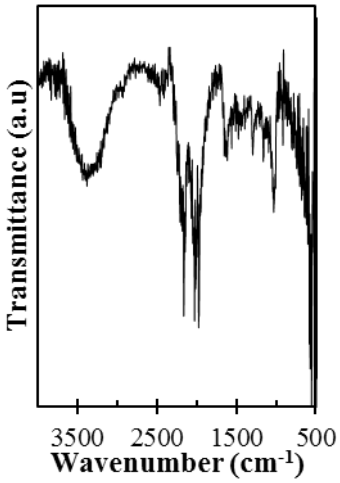

Figure 4. FTIR Spectrum Of The AC

Adsorption study on AC

Effect of initial 2-CP concentration

The effect of concentration on the adsorption capacity of chlorinated hydrocarbons by using AC at different concentrations is illustrated in Figure 5. The adsorption of chlorinated hydrocarbons rapidly increased with contact time and then proceeded at a slower rate until the equilibrium was achieved. Fixed amount of adsorbent dosage (0.1g) used in this experiment whereby concentrations of adsorbate were manipulated. The rapid adsorption was achieved at 10 ppm (mg/L). The adsorption process takes place rapidly at the initial step on the external surface of the adsorbent followed by a slower internal diffusion process [15]. The rapid adsorption at the initial step is due to the presence of a large number of vacant active sites

observed after a certain time indicated that the uptake of the solute molecules was made difficult due to the repulsive forces between the solute molecules on the surface of the AC as well as in the bulk phases. Longer contact times were required for solutions of higher initial concentrations to reach equilibrium [16].

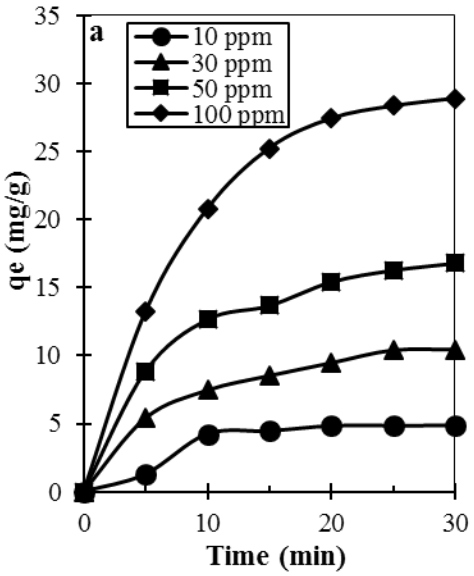

Figure 5. Effect Of Contact Time On Adsorption At Different Concentrations

Effect of pH

Figure 6 indicates the influences of pH on adsorption of 2-CP. Removal of chlorinated hydrocarbons were examined in pH range between 3 to 10. Adsorption was attributed to the acidic character of the solute molecules. In terms of pH, it signifying that endothermic nature of the process with acidic solution pH being the most favorable for the adsorption where its capacity increase at pH 5 because 2-CP is a weak acid and it associated with the electron withdrawal effect of the chlorine substitution on the aromatic ring thus reducing the overall electron density of the aromatic ring of the adsorbate [17, 18].

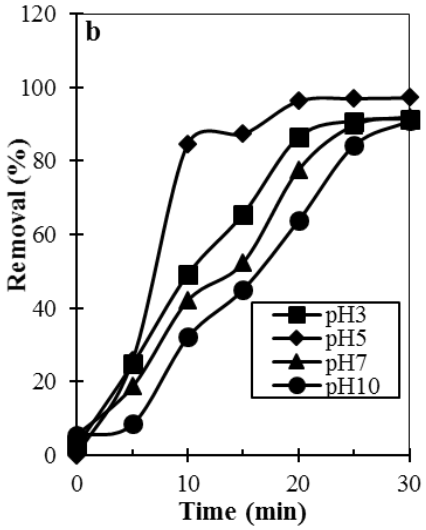

Figure 6. Effect Of Ph On Removal Efficiency Of 2-CP

Effect of adsorbent dosage

The amount of the adsorbent is considered a significant factor because it can identify the capacity of the adsorption for a given initial concentration of the adsorbate. The effect of AC dosage on the adsorption of chlorinated hydrocarbons illustrated in Figure 7. Various adsorbent dosage utilized for adsorption of 2-CP at initial concentration 10 mg/L, temperature 25 °C and shaking time 30 min. The result shows that as the adsorbent dosage increased, the percent removal of chlorinated hydrocarbons increased from 96.98% to 99.43%. As seen in figure below, increase in adsorption sites for a constant concentration relatively increase the performance on AC on adsorption of 2-CP.

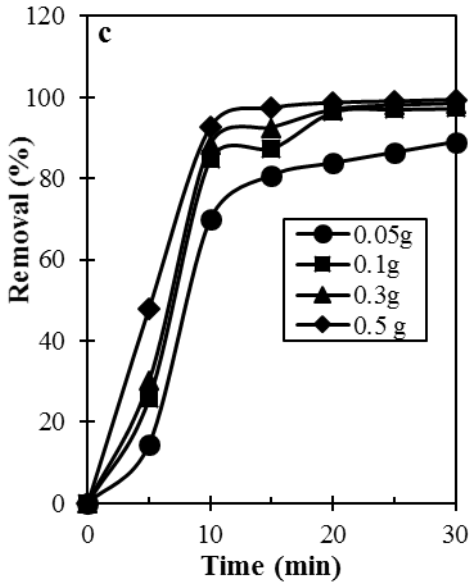

Figure 7. Effect Of Adsorbent Dosage On Removal Efficiency Of 2-CP

Conclusion

This research has notably demonstrated the effective performance of AC derived from waste rubber tyres for the removal of 2-chlorophenol. AC was characterized by the means of XRD, BET, FESEM and FTIR indicated AC have high adsorption capacity. Adsorption studies showed that rapid adsorption of chlorine from 2-CP was achieved with 0.5g of adsorbent dosage at 10 ppm and pH 5. The studies reveal that AC derived from waste rubber tyres possess high adsorption capacity hence it could be employed effectively as low-cost adsorbents for removal of chlorophenols.

Acknowledgments

The authors express their gratitude to the Universiti Malaysia Pahang for the support under the internal research grant (RDU170330).

References

Yagub M T, Sen T K, Afroze S, Ang H M (2014), Advance in Colloid and Interface Science, 209, 172-184.

Huong T H, Lee B K, Kim J (2016), Process Safety and Environmental Protection 104, 314–322.

WHO. (1989). Environmental Health Criteria 93.

Soltani T and Lee B K, (2016) Journal of Colloid and Interface Science 481 , 168-180. Chaliha S and Bhattacharyya K G, (2008) Chemical Engineering Journal 139, 575–588.

Dobaradaran S, Nodehi R N, Yaghmaeian K, Jaafari J, Niari M H, Bharti A K, Agarwal S, Gupta V K, Azari A, Shariatifar N (2018) Journal of Colloid and Interface Science, 512, 172-189.

Lim J W, Lim P E, Seng C E, Adnan R (2013) Bioresources Technology 129, 485-494.

Teng H. Journal of the Taiwan Institute of Chemical Engineers (2012), 43, 491 -492.

Al-Rahbi A S and Williams P T (2016). Waste Management. 49, 188-195.

Swat A A A, Saleh T A, Ganiyu S A, Siddiqui M N, Alhooshani K R (2017), Journal of Analytical and Applied Pyrolysis, 128 246–256.

Saleh T A, Gupta V K, Al-Saadi A A (2013) Journal of Colloid and Interface Science, 396, 264-269.

Suresh P, Vijaya J J, Kennedy L J (2014). Materials Science in Semiconductor Processing 27, 482-493.

He X, Wu Z, Sun Z, Wei X, Wu Z, Ge X,Cravotto G, Journal of Molecular Liquids 255 (2018) 160–167.

Begum S, Ahmaruzzaman Md, Materials Today: Proceedings 5 (2018) 2314–2320.

Gialamouidis D, Mitrakas M, Liakopoulou-Kyriakides M. (2010). Journal of Hazardous Materials 182 (2010) 672–680.

Sharifpour E, Khafri H Z, Ghaedi M, Asfaram A, Jannesar R. (2018). UltrasonicSonochemistry 40, 373-382.

László (2004). Colloids Surface. A: Physicochem. Eng. Asp. 230, 13–22.

Tang YB, Qiang L, Fang-yan C (2012), Chemical Engineering Journal 203, 19-24

.

Proceeding: 5th International Conference on Applied Sciences and Engineering (ICASEA, 2018)
(eISBN 978-967-15744-1-6)
Capthorne Hotel, Cameron Highlands, Malaysia

POTENTIAL OF POLYSULFONE/POLYDIMETHYL SILOXANE THIN FILM COMPOSITE (PSF-PDMS-TFC) MEMBRANE FOR CO_2/N_2 GAS SEPARATION

Sunarti Abd Rahman[1]*
Nur Atikah Che Embi[1]
Siti Noraishah Ismail[1]
Abdul Latif Ahmad[2]
Hasrinah Hasbullah[3]

[1]Faculty of Chemical & Natural Resources Engineering, Universiti Malaysia Pahang, 26300 Gambang, Pahang, Malaysia.
[2]School of Chemical Engineering, Engineering Campus, Universiti Sains Malaysia, 14300 Nibong Tebal, Pulau Pinang, Malaysia.
[3]Advanced Membrane Technology Research Centre (AMTEC), Universiti Teknologi Malaysia, 81310 Skudai, Johor Darul Ta'zim, Malaysia.

Abstract: *The capture and storage of carbon dioxide has been identified as one potential solution to greenhouse gas driven climate change. Efficient separation technologies are required for removal of carbon dioxide from flue gas streams to allow this solution to be widely implemented. This study is mainly focusing on the effect of different concentration of polydimethyl siloxane (PDMS) in dip-coating solution on the membrane's performance. The asymmetric thin flat sheet membrane was prepared by dry/ wet phase inversion process consisting 20 %w/v of polysulfone (PSf) as the support layer polymer and 80 %w/v of N-methyl-2-pyrrolidone (NMP) as the solvent. PDMS was coated on the support PSf membrane with the composition of 10, 15 and 20 wt% of PSf in n-hexane respectively. The characterization of morphology of TFC membrane will be conducted by using Scanning Electron Microscopy (SEM) and Fourier Transform Infrared (FTIR). The membrane's performance and the selectivity of CO2/N2 separation will be determined by conducting gas permeation test. The result obtained, show that membrane with highest concentration of PDMS in dip-coating solution give a highest performance in selectivity and unfortunately it contributes to lower permeability. It is vice versa from the membrane without PDMS in the top layer which gives highest value of permeability but lowest in selectivity. From the characterization and permeation test of the membrane, hereby the membrane with highest percentage of PDMS should be selected for the future development of membrane due to its highest value of selectivity which contributes to highest efficiency in separating the gas.*

Keywords: *Gas Separation, Membrane, Flat Sheet*

Introduction

Enhancements of the greenhouse effect in the worldwide have contributed to the study that can recover this problem. The most abundant greenhouse gas CO_2 has risen from preindustrial levels of 280 parts per million (ppm) to present levels of over 365 ppm [1]. Carbon dioxide, CO_2 arise from different emission sources, particularly flue gas from power stations, steel works and chemical industries. According to the study done by Mitsubishi Heavy Industries, Ltd., 98% of CO_2 emissions are derived from fossil fuel combustion, exhausted to atmosphere by flue gas stacks from furnace boilers, gas turbines and engine emission. The content of the

flue gases that released at atmospheric pressure usually containing Oxygen, Carbon Dioxide, Nitrogen, NOx, SOx and dust particulate impurities.

The separation of gas by thin barrier termed as membranes is a dynamic and rapidly growing field, and it has been proven to be technically and economically superior to other emerging technology. Materials for effective separation of gases can follow one of two overall strategies; increasing the rate of diffusion of gases through the polymeric structure and increasing the solubility of gases through the polymeric structure. Unfortunately, there is frequently a trade-off between selectivity and permeability [2]. In preparation of gas and vapour separating membranes, a polymer should have the following intrinsic properties:(1) High selectivity for the components to be separated, (2) High permeability for the permeating components and (3) High life expectance under operating condition such as good thermal, chemical and mechanical stability. In this particular study, PSf and PDMS were selected as a polymer in developing support membrane and thin film due to their great characteristic such as a tough and rigid polymer, high-temperature properties and chemically inert.

Methodology

Chemicals

PSf pellet purchased from Sigma Aldrich (M) Sdn. Bhd. PSf used is without any modification. Anhydrous NMP supplied from Sigma Aldrich (M) Sdn. Bhd was used as a solvent. Water is used as a coagulation medium. CO_2 and N_2 used in permeation test.

Membranes Preparation

With the amount of 20% PSf pellet, it was being added gradually into beaker contains 80% of NMP solvent and mixed by mechanical stirrer. The mixing step continues for at least 7 to 8 hours till homogenous and clear solution was formed. The dope solution was prepared within a range of temperature between 60^{o}C to 80^{o}C.

Dope Solution Casting Process

The dope solution was casted on a glass plate by using a glass rod. It is followed by the immersion in a water bath in accordance of dry/ wet phase inversion process. Casting process was conducted at room temperature (30^{o}C±2). The cast membrane was immersed into water to initiate delamination and slightly peel the membrane film from the glass plate. After that the membrane is transferred and immersed into the coagulation medium with water act as a coagulation medium for 1 hour and further dried in the air at room temperature.

Thin Film Composite Membrane Preparation

The dip-coating solution is prepared by mixing PDMS with n-hexane solvent with stirring. The dip-coating solution is consisting of three different percentages of PDMS which were 10%, 15% and 20% in n-hexane solvent. The prepared asymmetric PSf membranes were placed on a glass plate. The coating solution is placed on the PSf membrane by dropped the PDMS/n-hexane solution on the skin layer of the membrane. PSf membrane is allowed to dry for 5 minutes and cure process is carried out in oven at 60^{o}C for 1 hour.

Gas Permeation Test

The thin film composite of PSf/ PDMS membrane is tested on pure gas CO_2 and N_2. The pure gas will be tested at pressure in the range of 0.5 bar to 1.5 bar. The time of the first bubble formed and volume difference of the soap water by each membrane was taken.

The gas permeation rate (P) was calculated by using equation as followed:

$$P = \frac{Vl}{At\Delta p}\ (cm^3(STP)cm)/(cm^2 s.cmHg)$$

Equation 1

The permeance (P/l) was calculated using equation as followed:

$$\frac{P}{l} = \frac{V}{At\Delta p}(cm^3(STP))/(cm^2 s.Hg)$$

Equation 2

where,
V = the volume (cm^3) displaced in time $\boldsymbol{t}$ ($\boldsymbol{s}$)
A = the effective membrane area (cm^2)
Δp=The transmembrane pressure expressed in cmHg.

Meanwhile, Selectivity was calculated using this equation:

$$\alpha = P_i / P_j$$

Equation 3

P_i = Permeance of one gas component
P_j = Permeance of another gas component

Membrane Characterization (SEM and FTIR)

The prepared membrane is characterized using two methods which are by using Scanning Electron Microscopy (SEM) and Fourier Transform Infrared Radiation (FTIR). There are several parameters that will be evaluated from this study which were morphological studies and effect of concentration of polymer.

Results and Discussion

Effect of Dip Coating Percentage on the Membrane Morphology

Structure of the surface membranes produced from 0%, 10%, 15% and 20% of PDMS are illustrated in Figure 1 (a), (c), (e) and (g) respectively. As shown in the surface structure of the membrane, as the amount of percentage of PDMS increased, a fewer number of macro-voids in the membrane structure are observed. Figures 1(b) illustrate that membrane without dip coating solution figured as finger-like macro-voids. The finger-like macro-voids ends at the top surface of the skin layer, making the surface defective with pin-holes [4]. The enhancement of the PDMS illustrate in Figure 1 (d), (f) and (h) shows that the sub-layer has a nodular structure, diminishing the chance of pin-hole formation at the membrane surface.

In the sequence of Figure 1 (d), (f) and (h), a new selective layer was formed and covered the entire surface pore in order 10%, 15% and 20% of PDMS percentage respectively. The presence of 10% PDMS in the dip coating solution has no obvious effect on the cross section structure of the membranes. Proceeding in increasing the percentage of PDMS results in higher polymer concentration in the upper layer of the membrane forming films and in a denser coating layer with smaller pores in the final membranes.

Effect of Concentration of Top Layer on the FTIR Analysis

FTIR spectra of 0%, 10%, 15% and 20% of PDMS concentration are shown in Figure 2 (a), (b), (c) and (d) respectively. The spectrum indicates the functional groups that presence in the sample, which are siloxane group (Si-O) stretching vibration at 1000-1100 cm-1 and sulfone group (S=O) at 1150-1300 cm-1. The changes in the intensity of the sulfone group can be attributed to the consumption of sulfone group due to increasing siloxane group content. The characteristic IR absorption bands for PSf polymer will decrease in the sequence of 0 % > 10 % > 15 % > 20 % of the PDMS solutions. This is the consequence from the siloxane group is taking place of sulfone group in their reaction. The IR spectrum for the PSfs samples prepared with a 0% of PDMS content shows a peak at 1243.85 cm-1 indicating the sulfone groups still in the support polymer sample. For PSf samples prepared with 10, 15 and 20% PDMS content, there are no apparent peaks at 1243.85 cm-1, suggesting the sulfone group is reacted with siloxane groups. The Si-O absorption cannot be clearly detected for the polymer samples prepared at 0% PDMS content. For 10, 15 and 20% PDMS the changes in the intensity of Si-O groups were due to the addition of percentage of PDMS.

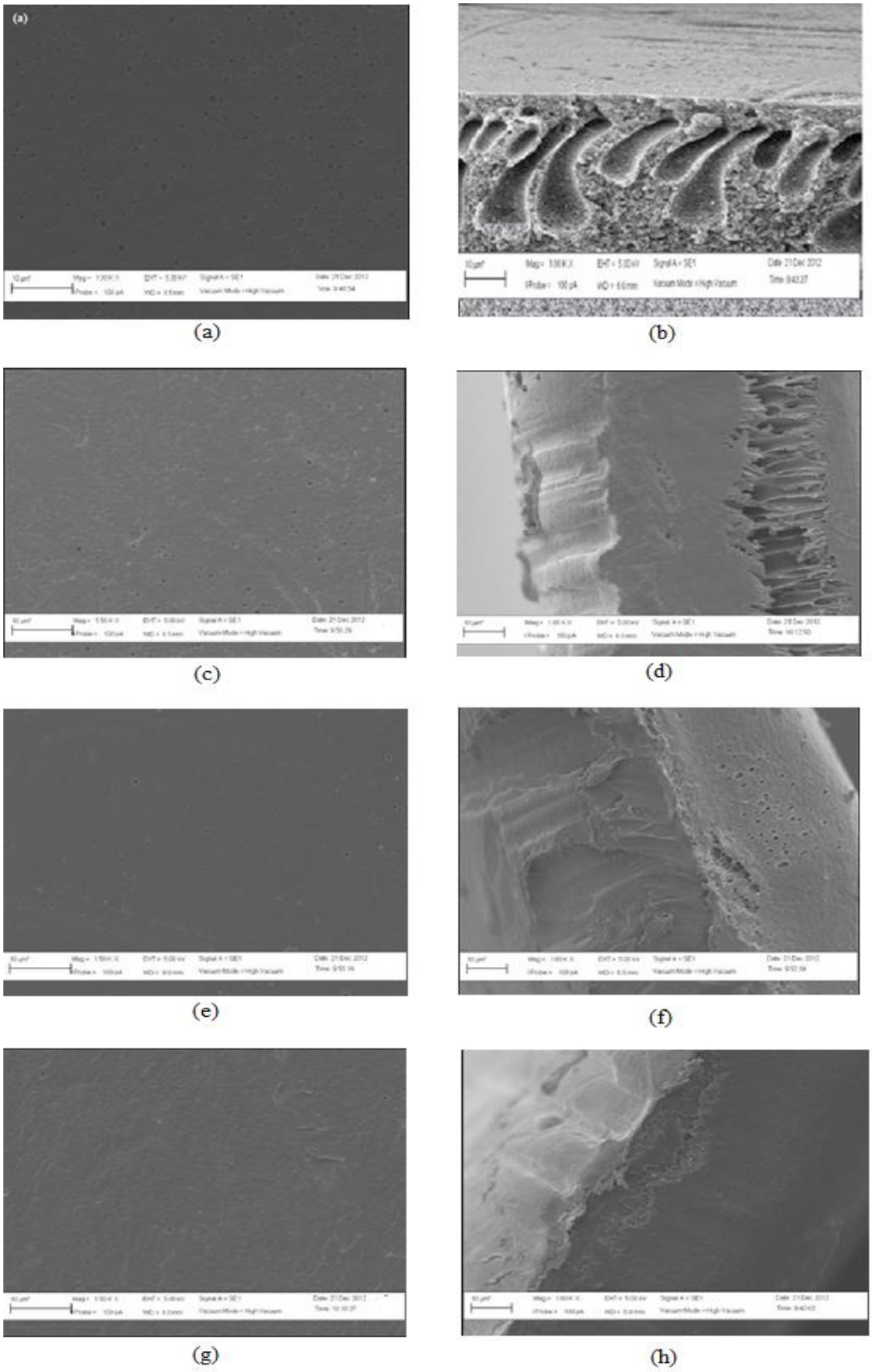

Figure 1 (a) Surface Image of PSf Membrane with 0% PDMS at Magnification 1.50 K X; (b) Cross Section Image of PSf Membrane with 0% PDMS at Magnification 1.00 K X; (c) Surface Image of PSf Membrane with 10% PDMS at Magnification 1.50 K X (d) Cross Section Image of PSf Membrane with 10% PDMS at Magnification 1.00 K X (e) Surface Image of PSf Membrane with 15% PDMS at

Magnification 1.50 K X (f) Cross Section Image of PSf Membrane with 15% PDMS at Magnification 1.00 K X (g) Surface Image of PSf Membrane with 20% PDMS at Magnification 1.50 K X (h) Cross Section Image of PSf Membrane with 20% PDMS at Magnification 1.00 K X.

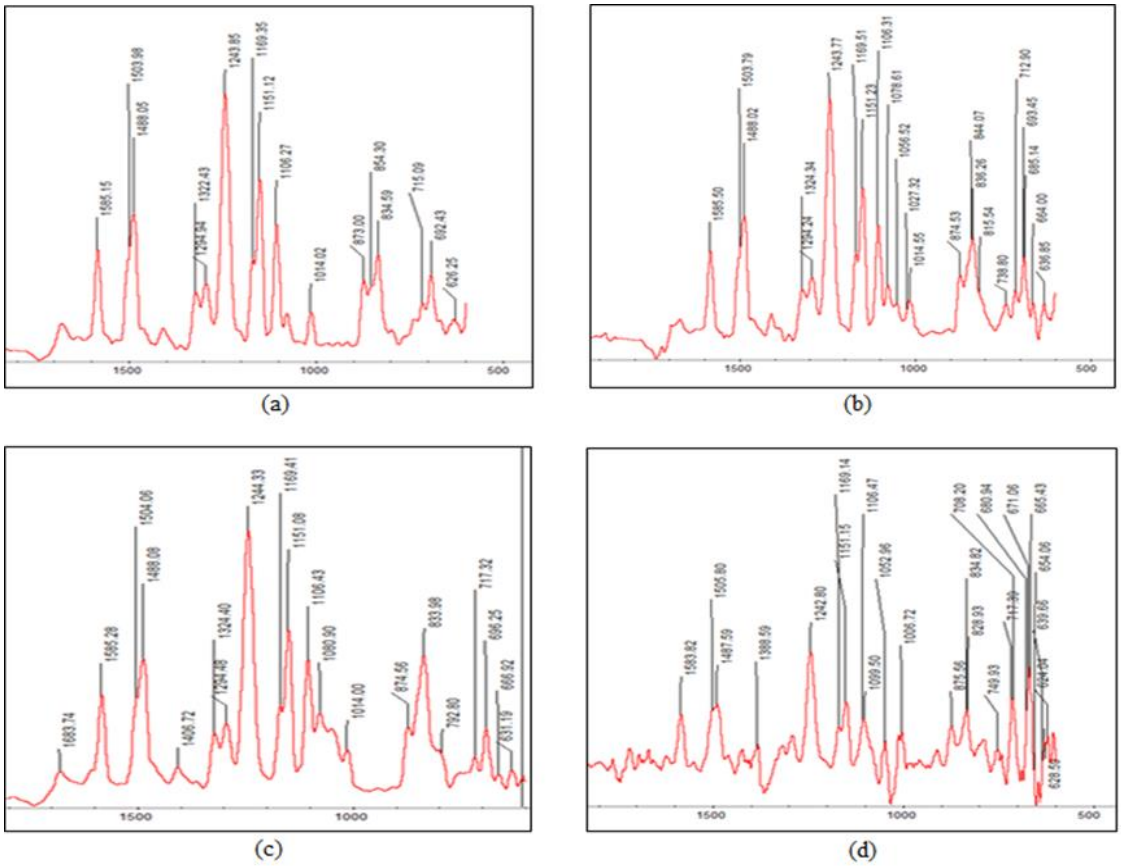

Figure 2 FTIR Absorbance Peak for (a) 0% PDMS of PSf-PDMS Membrane; (b) 10% PDMS of PSf-PDMS Membrane; (c) 15% PDMS of PSf-PDMS Membrane; (d) 20% PDMS of PSf-PDMS Membrane

Effect of Concentration of Selective Top Layer on the Membrane Performance for Gas Separation

The permeability graph trends obtained in Figure 3 and Figure 4, it is show that the permeability of CO_2 is slightly higher than permeability of N_2 due to kinetic molecular diameter for CO_2 is much smaller which is 3.3 angstroms rather than kinetic diameter of N_2 molecule approximately 3.6 angstroms. CO_2 molecule is easier to pass through the membrane due to its molecular diameter is smaller than N_2 and resulting higher permeability of CO_2 gas [5]. The changes in permeability of single pure gases with change in feed pressure. The decrease in viscosity of polymer for the dip coating solution can allow higher diffusion of gas rate in sub-layer which makes the permeability of certain gas to be higher. As a result, thin film composite membrane with a thin and porous skin layer and open cell sub-layer will result higher permeability value. Meanwhile, N_2 permeability is slightly increased as well as feed pressure is increase. Feed pressure is acting as a driving force of the N_2 molecule to pass through the membrane. Since larger driving forces were applied to N2 molecule, it will contribute to a lot of N_2 particle will pass through the polymeric membranes then resulting to high permeability value.

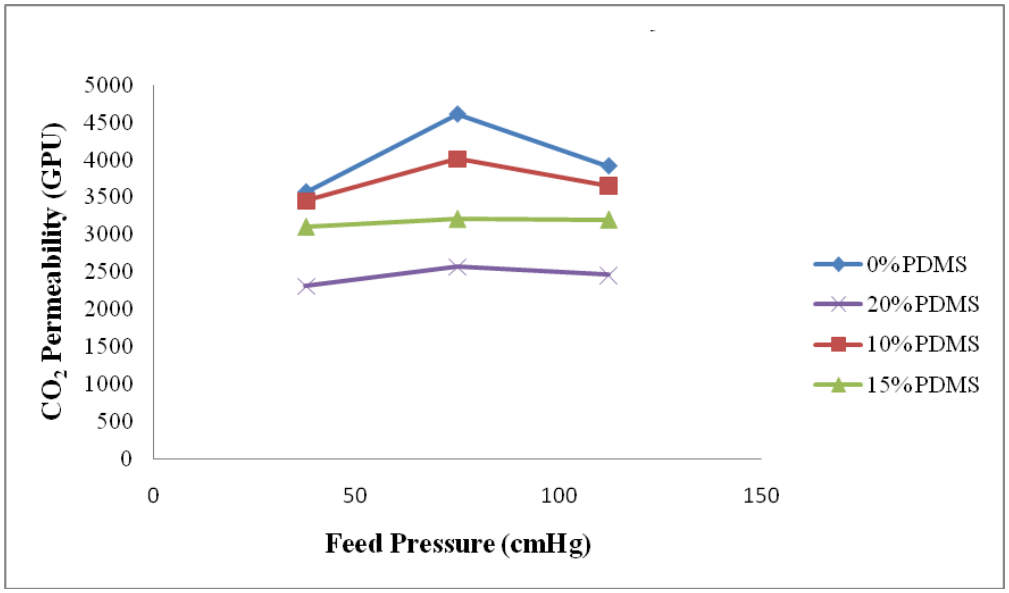

Figure 3 CO_2 Permeability versus Feed Pressure

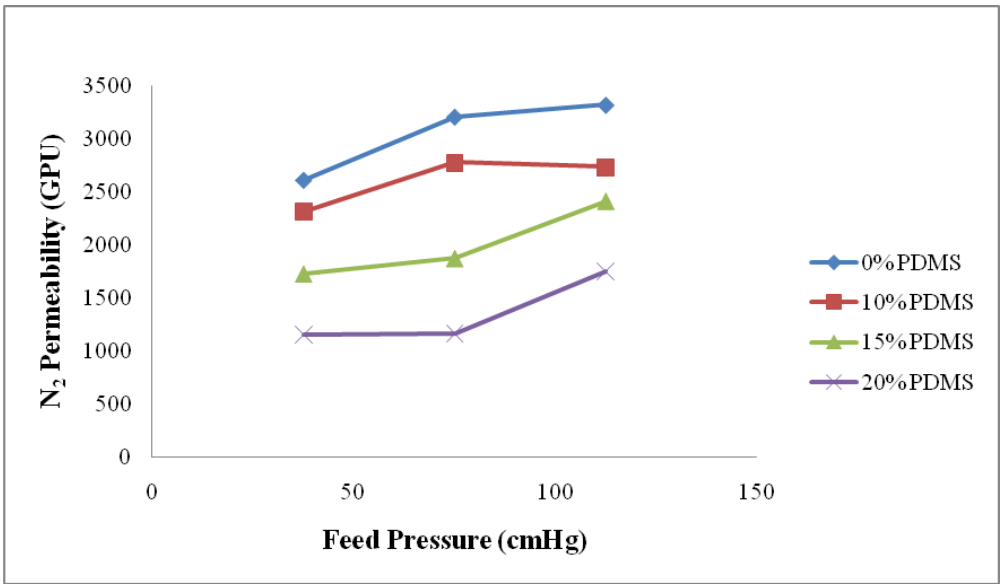

Figure 4 N_2 Permeability versus Feed Pressure

By referring to the Figure 5, the selectivity of the membrane increase with the increase of the percentage of PDMS in the order of 0 % < 10 % < 15 % < 20% of the PDMS concentration. Membrane with concentration 20% PDMS exhibit highest selectivity about 1.57 because increasing the polymer concentration, resulted a denser and thicker skin layer membrane. Furthermore, since the polymer concentration in dip coating solution is increased, it was observed that the skin layer thickness increased while both mean pore size and surface porosity decreased. The uncoated membranes seem to exhibit lowest selectivity probably due to existence of defect (pores) and the enhancement of free volume in the thin skin layers. The relationship between selectivity and the feed pressure show that with increasing the feed pressure, it is resulted lower selectivity. This is suggesting that when there was large driving force that drive the molecule to pass through the membranes, the efficiency of separating the gas is getting lower hence contribute to the bad performance.

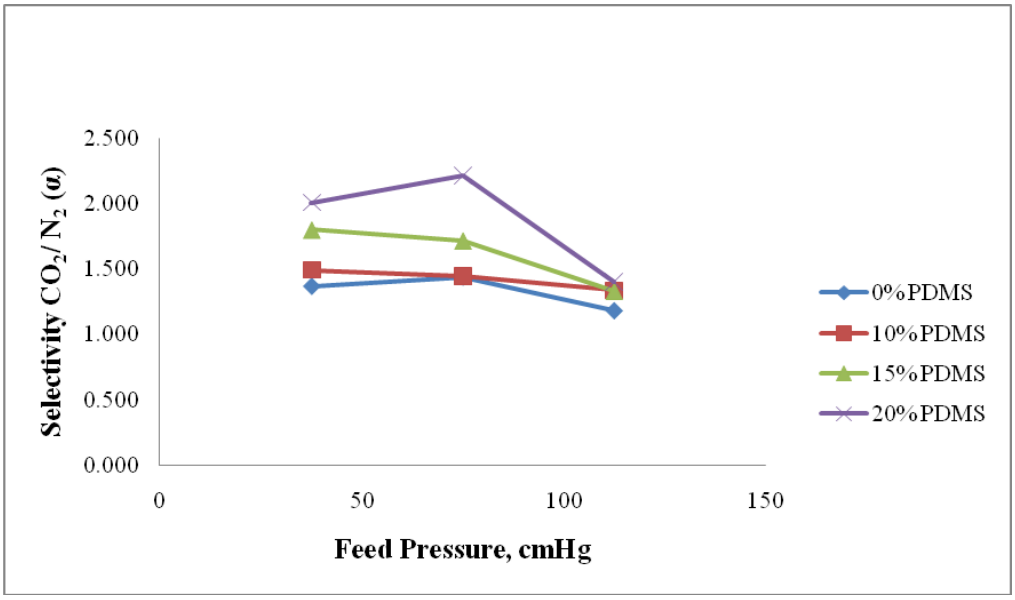

Figure 5 CO_2/ N_2 Selectivity Versus Feed Pressure

Conclusion

This study successful developed the TFC PVDF/ PEBAX membrane. More sponge-like asymmetric structures were formed across the membrane wall and the macro void formation is suppressed. This is due to the higher viscosity of the casting solution that delayed the phase inversion rate (kinetic effect) which results in a sponge-like structure.

Acknowledgments

This research is fully supported by LRGS grant (RDU150901) and 304/PJKIMIA/6050296/U124) and UMP Grant (RDU1703203). The authors fully acknowledged Ministry of Higher Education (MOHE) and Universiti Malaysia Pahang for the approved fund which makes this important research viable and effective.

References

Dantas, T. L. P., Luna, F. M. T., Jr, I. J. S., Azevedo, D. C. S., Grande, C. A., Rodrigues, A. E., 2011.*Chemical Engineering Journal* :**169** 11

Burling I R, Yokelson R J, Griffith D W T, Johnson T J, Veres P and Roberts J M 2010 Atmospheric Chemistry and Physics: **10** 1115

I. Pinnau, and Koros, W. J. 1991 *Journal of Applied Polymer Science*: 43 1491

Aroon, M. A., Ismail, A. F., Montazer-Rahmati, M. M. and Matsuura, T. 2010*Separation and Purification Technology*: **72** 194

Elashmawi I S 2011 *Materials Chemistry and Physics*: **107** 96

Proceeding: 5th International Conference on Applied Sciences and Engineering (ICASEA, 2018)
(eISBN 978-967-15744-1-6)
Capthorne Hotel, Cameron Highlands, Malaysia

CONCEPT GENERATION OF SUGAR PALM / GLASS FIBER REINFORCE THERMOPLASTIC POLYURETHANE HYBRID COMPOSITE AUTOMOTIVE CRASH BOX

N.S.B. Yusof,[1,2]
S.M. Sapuan,[3]
M.T.H. Sultan,[1,4]
M. Jawaid[1]

[1]Laboratory of Biocomposite Technology, Institute of Tropical Forestry and Forest Products (INTROP), Universiti Putra Malaysia, 43400 UPM Serdang, Selangor, Malaysia
[2]Faculty of Information Sciences and Engineering
Management Science & University, Seksyen 13, 40100 Shah Alam, Selangor, Malaysia
[3]Department of Mechanical and Manufacturing Engineering,
Universiti Putra Malaysia, 43400 UPM Serdang, Selangor, Malaysia
[4]Department of Aerospace Engineering,
Universiti Putra Malaysia, 43400 UPM Serdang, Selangor, Malaysia

---

Abstract: *This paper present a hybrid method of design technique introduced in development of conceptual design of sugar palm polymer composite Automotive Crash Box (ACB). Integration of theory of inventive problem solving (TRIZ), How-How diagram, Morphological Chart (MC) and Ishikawa method is applied in development of concept design of sugar palm polymer composite automotive crash box ACB. The important requirements of the function specification and failure mode analysis as well as geometry specification are considered. The aim of this paper is to produce a new concept design of sugar palm polymer composite ACB was determine and add into consideration of limitation from the material properties that are different with the conventional steel ACB. The selected final concept design of sugar palm polymer composite ACB has covered element of low cost, avoid complex manufacturing process to reduce the cost and efficient performance of ACB to absorb energy during collision.*

Keywords: *Conceptual Design, Automotive Crash Box, Hybrid Method*

Introduction

Concept generation is a process getting the ideas, starting with a set of customer needs and target specifications, the process concludes a selection of alternatives solutions until a final design is selected. There are multiple steps involved in the generic concept generation process, as well as various approaches. Hambali (Hambali et al. 2009) applied analytical hierarchy process to generate idea for automotive composite bumper beam. Sapuan (Sapuan 2005) using integration method of morphological chart, extension of search space, gallery method and voice of customer to generate concept design for the polymeric based composite automotive pedals. Mansor (Mansor et al. 2014) using hybrid method of TRIZ, Morphological Chart and Analytic Hierarchy Process method for concept generation on kenaf
Fiber polymer composite automotive parking brake lever. Currently, the conceptual generation method which is theory of inventive problem solving (TRIZ), How-How diagram, Morphological Chart (MC), Functional Analysis Diagram FAD and Ishikawa method selected

in this paper have not implement by any researcher to generate idea in conceptual development process.

Methodology

Method of research in this study are using Technical FAD method to understand the technical aspect of a specific portion of a total product. Ishikawa method used to minimize the possibility of failure, mechanical failure happens once some components in the system unable to perform its operation sufficiently owing to the bound condition such as assembly errors, manufacturing defect or design deficiencies (Maleque & Salit 2013). Then, Triz method provided general principal solution in conceptual idea generation, referring to the selected solution taken from TRIZ inventive principle, how-how morphology diagram method introduce to propose initial ACB conceptual design. How-how morphology is a hybrid method between how-how technique with morphological chart.

Functional Analysis Diagram (FAD)

In this study, automotive crash box (ACB) is a component that installed in a vehicle to absorb kinetic energy during low speed collision. Function analysis is a technique for analysing and developing a perform structure. Perform structure is an abstract model of the new product, while exclude the material options as well as the dimensions. It describes the function for each devices, elements and indicates the mutual relations. The underlying plan is that a perform structure is also designed up from a restricted range of elementary functions on a high level of abstraction. Functions is an abstractions of what a product ought to do. Being forced to consider the product in an abstract method stimulates creativeness, and prevents the designer from jumping to a solutions immediately on the first idea that comes to mind, which may not be the best. There are two types of FAD which is technical FAD and customer FAD.

Ishikawa Diagram

There are two major concerns within the style of automotive structures for crash energy management which is absorption of the kinetics energy of the vehicle and therefore the crash resistance or strength to sustain the crush method or maintain rider compartment integrity. As for energy absorption, two basic modes or mechanisms found in automobiles which is axial collapse and bending. Pure axial collapse will provide most effective mechanism for energy absorption to the ACB but very difficult to achieve while bending collapse will form a local hinge and the structure of ACB could failed in this mode (Bois et al. 2004). At this point, Ishikawa method selected to be applied in order to identify the cause of the failure ACB producing axial collapse mode during collision. Thus, action of prevention will be taken at the earlier production stage to avoid any repeated failure.

TRIZ method

The crash box idea is driven by the large amount of car crashes taking place at low speed impact which is velocities below 40 km/h. The aim of the conceptual design for ACB is to absorb maximum energy during collision, hence to obtain an axial collapse. According to (Liu 2008)(Tarlochan et al. 2013) (Qing-fen & Hai-dou 2009)(Zimmer & Technische 2014), beside the material properties (consider to use similar material for all conceptual design which sugar palm glass fiber reinforced thermoplastic polyurethane composite) influence the effectiveness of ACB, shape of geometry and density of the part criteria will affect the efficiency of ACB to obtain maximum energy absorption.

How-How Morphological Diagram Method

Final decision to select ACB conceptual generation idea before producing initial design model of ACB are using hybrid method of how-how morphological diagram method. How –how diagram is an interactive method use to explore relationship underlying a particular problem, where morphological method is a technique to consider all the possible solution for a multi-dimensional and non-quantified complex problem.

Results and Discussion

In this study, automotive crash box (ACB) is a component that installed in a vehicle to absorb kinetic energy during low speed collision. Generally the function of crash box to absorb maximum impact energy by deform prior to the other parts during the crash event to minimize the repair cost and ensure safety of the passengers' life (Nasir Hussain et al. 2017). Figure 1 illustrated ACB system consists of Bumper rails at the most front of the crash system, bumper assemble to the automotive crash box and then crash box fix to the front rail. All parts hold at the position by using screw and bushing. The crash system receive kinetic energy from the impact load during the collision. Each operate segment in Figure 1 painted as an arrow within the diagram because the thick line represents the excessive operate, broken line represents an inadequate operate and thin line represents the traditional operate of the elements. As the structure of ACB would be made by composite material, the structure may not be able to absorb maximum kinetic energy to perform its general function adequately. Thus, in the next stage, the design process of ACB would be focused on the ACB structure for seeking a possible solution of this problem.

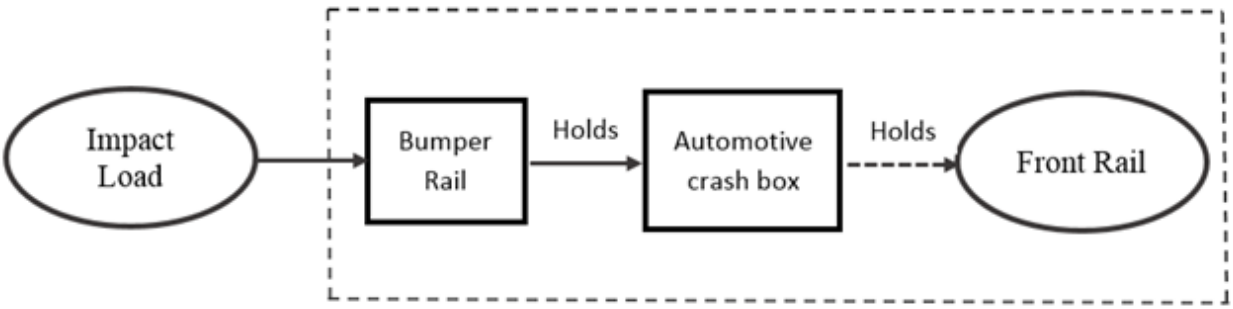

Figure 13. FAD For Automotive Crash Box.

Cause and Effect Analysis for ACB using Ishikawa Diagram.

Nakazawa et al (Y.Nakazawa, K.Tamura, M.Yoshida 2005) summarize force analysis to improve the impact energy absorption or to obtain an axial collapse base on three main points which is high buckling load at the ridge lines, minimize of buckling cycle time and minimization of load fluctuation. Free body diagram FBD shows in Figure 2 illustrate the folding process for ACB, folding start at certain compression area of the ridge line, that compression area then arise plastic buckling known as wrinkle.

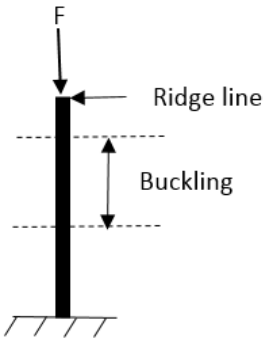

Figure 2. ACB Analysis Force Against Displacement

Subsequently, wrinkle will fold and create another wrinkle at the ridge line under the above wrinkle. From the beginning, the load continuously increase until reaching the maximum value point. The load return back to the minimum value once the wrinkle absolutely fold, the following deformation will repeat the same process causing fluctuation load throughout the collapse, hence provide and axial collapse. Figure 3 illustrated the factor of failure to obtain an axial collapse by using Ishikawa diagram. The most right box is a place to state an effect of the cause failure, the other boxes is a main cause contribute to the failure, then its followed by the details of failure cause for each roots.

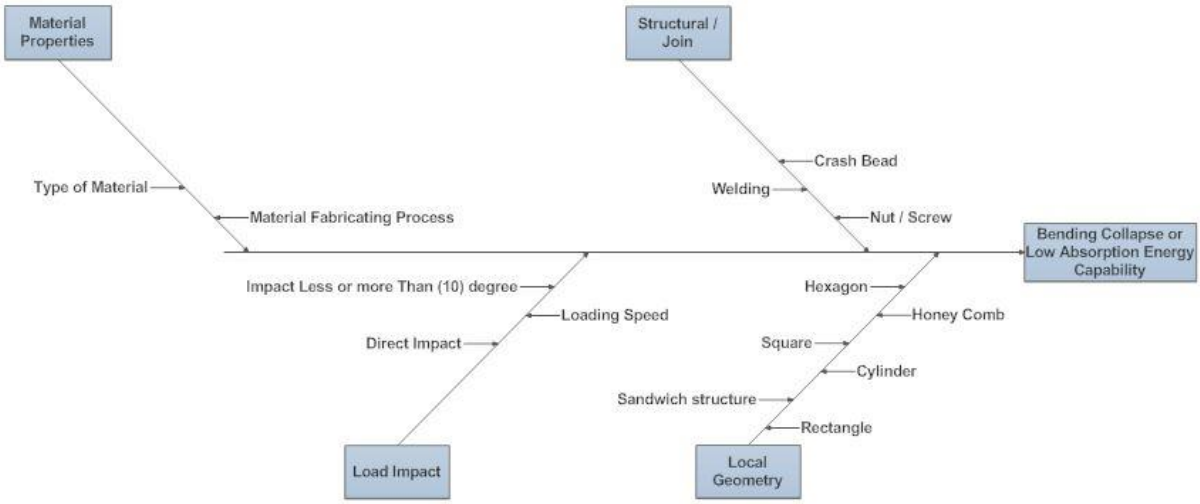

Figure 14. Cause and Effect Analysis for ACB using Ishikawa Diagram (Peroni et al. 2009)(Kim et al. 2014)(Fuganti et al. 2000)

According to the Ishikawa diagram in Figure 3, the failure might come from the structural or joint between crash box and bumper or front rail. Improper installation for ACB using nut and screw could provide misalignment, thus lead load impact smash the ACB slanting to the side way. Besides that, Crash box without crash bead will not provide any fluctuation load, hence provide a bending collapse. In addition, welding join with 6 mm diameter spot at the central of the flange width and 30 mm of the spot pitch will attain a constant progressive axial collapse (Peroni et al. 2009). Material properties is another cause of ACB failure to absorb maximum energy, the properties for materials various depends on types of materials and manufacturing process (Kim et al. 2014). The most material selected by the automotive manufacturer which have high absorption capabilities is steel and aluminium. Material like synthetics composite or natural fiber composite which more user friendly also have a potential to replace aluminium

and steel as ACB structure material due to the high toughness property. Equally important is manufacturing process, material such as Aluminium Carbon fiber reinforced polymer (Al/CFRP) manufactured using hybrid casting joining technology

could increase the specific energy Absorption SEA up to 38% for certain lay-up sequence. Load impact are related to the loading speed and degree of load impact to the ACB structure. The designing of crash box must engage with Federal Motor Vehicle Safety Standard (FMVSS) part 581 bumper test, and the Research Council for Automobile Repairs (RCAR) test to fulfill the strength requirement of the frontal structure (Fuganti et al. 2000).

TRIZ method

TRIZ method presenting contradiction matrix and suggested inventive principle for ACB concept design. In this case, principle use are "the thickness, stiffness and size of the structure increase could improve energy absorption but it will increase more weight".

Table 2. Contradiction Matrix And Suggestion Inventive Principle For ACB Concept Design.

	Worsening Parameter / **Feature to Improve**	**Weight of Stationery**	**Inventive Principles**
14	Strength	40,26,27,1	#40 Composite Material #26 Copying #27 Cheap short-living object #1 Segmentation
2	Area of Stationary	35,30,13,2	#35 Parameter change #30 Flexible shell and thin film #13 The other way round #2 Taking out

Table 1 presenting the principle analysis, the best general suggestion that considered as most appropriate solutions are "# taking out" is defined as an undesirable component or part is disconnected from an object by pull out the only required component or part of an object. "# Parameter change" describe to change from uniform parameters to multiple parameters where each of it particular have own functional requirements.

How-How Morphological Hybrid Method

The hexagonal shape selected as geometry for ACB design in this study due to the benefits offers better than other geometry such as, high performance to absorb energy, easy to manufacture as well as will reduce the cost. ACB Structural selected to assemble using nut and screw due to the benefits offer better than welding such as easy to substitute the damage part, only need well train worker instead of specialist worker, hence reduce the manufacturing cost. The decision made also support by the earlier research such as Liu [8] present the design matrix of crashworthiness for the part with equal geometry could provide higher specific energy absorption SEA for the lightweight part. Moreover, [10][12][13][14] present the hexagonal for ACB structure will perform better SEA value compare with rectangle and square geometry structure.

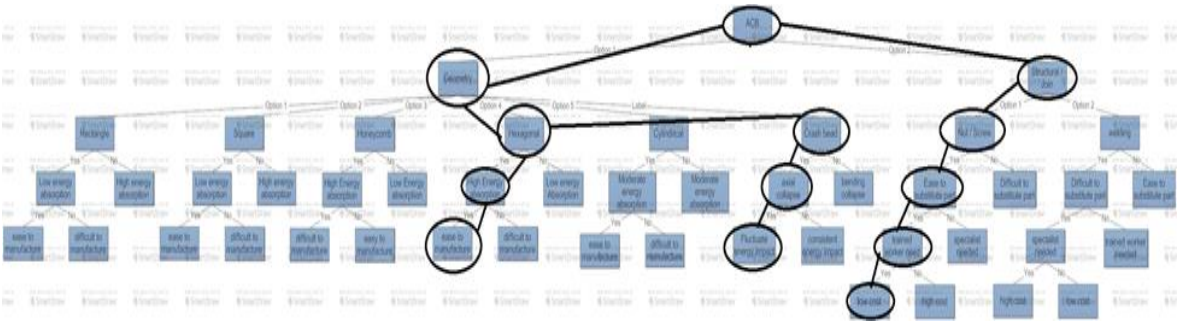

Figure 15. How-How Morphology Diagram To Propose The ACB Conceptual Design.

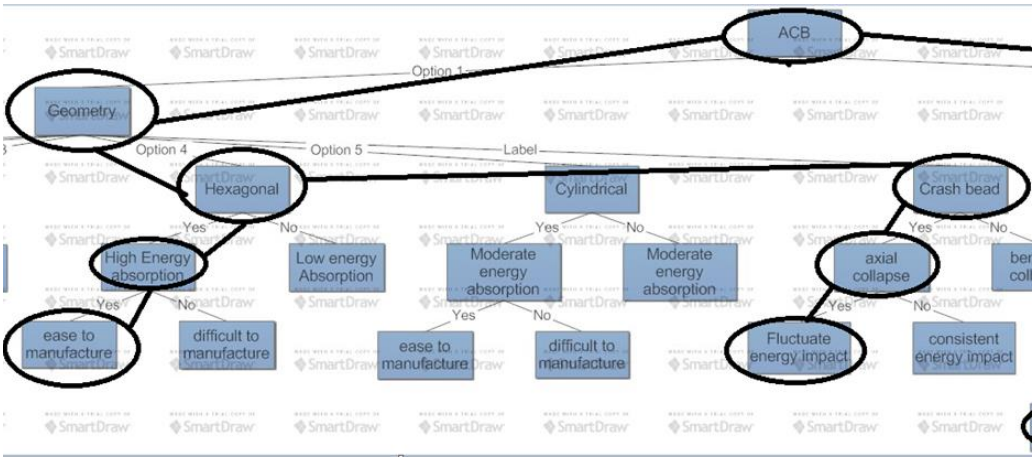

Figure 16. Close Up Solution Decision For Requirements 1 (Geometry)

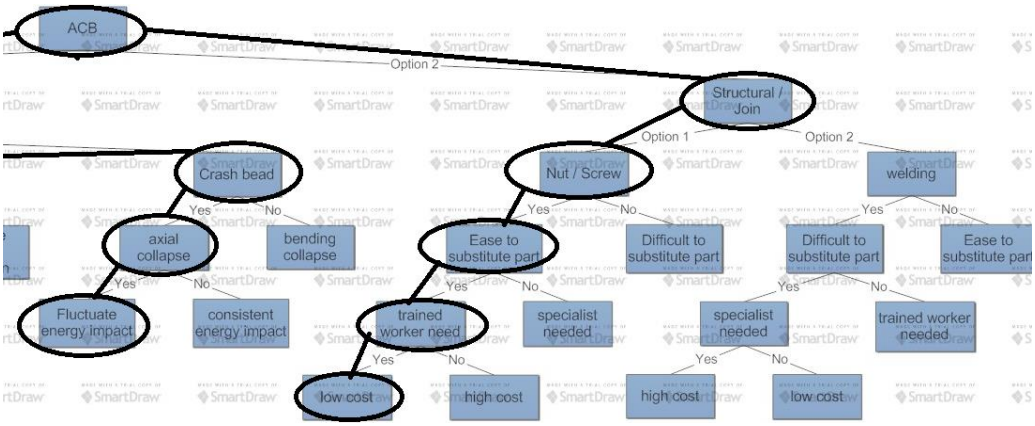

Figure 17. Close Up Solution Decision For Requirements 2 (Structural / Join)

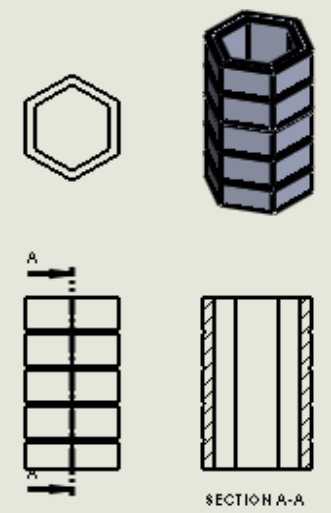

Figure 18. ACB Conceptual Design

Figure 7 shows drawing of final conceptual design selected after undergo selection process, the model shows the hexagonal geometry with hollow structure and crash bead to fluctuate the load impact hence generate axial collapse as well as to efficiently absorb maximum kinetic energy.

Conclusion

Development of ACB had gathered useful method to satisfy the design requirements and technical design specification. Combination TRIZ, How-How diagram and Morphological chart could generate more concept design which would help design engineers to be more creative technically. However, the final ACB conceptual design selected in this study will undergo several alteration for assembly and manufacturing purposes.

Acknowledgements

The authors would like to thank Universiti Putra Malaysia for the financial support provided through the ICOE Grant, research vote number 6369107. As well as to Management and Science University and Ministry of Education of Malaysia for providing the scholarship award to the principal author to carry out this research project.

References

N. Nasir Hussain, S. Prakash Regalla, and Y. V. Daseswara Rao,2017 “Low velocity Impact Characterization of Glass Fiber Reinforced Plastics for Application of Crash Box,” Materials Today Proceedings., vol. 4, no. 2, pp. 3252–3262.

M. A. Maleque and M. S. Salit, Materials Selection and Design. Singapore: Springer, 2013.

P. D. Bois, C. C. Chou, B. B. Fileta, A. I. King, and H. F. Mahmood,2004 Vehicle crashworthiness and occupant protection, American Iron and Steel Institute Michigan.

K. Takagi, M. Kano, Y.Nakazawa, K.Tamura, M.Yoshida,2005 “Development Of Crash-Box For Passenger Car With High Capability For Energy Absorption,” International Conference on Computational Plasticity COMPLAS, vol. 7.

L. Peroni, M. Avalle, and G. Belingardi, 2009“Comparison of the energy absorption capability of crash boxes assembled by spot-weld and continuous joining techniques,” International Journal of Impact Engineering, vol. 36, no. 3, pp. 498–511.

H. C. Kim, D. K. Shin, J. J. Lee, and J. B. Kwon,2014 "Crashworthiness of aluminum/CFRP square hollow section beam under axial impact loading for crash box application," Composite Structures, vol. 112, pp. 1–10.

A. Fuganti, L. Lorenzi, A. Grønsund, and M. Langseth, 2000. "Aluminum Foam for Automotive Applications," Advanced Engineering Materials, vol. 2, no. 4, pp. 200–204.

Y. Liu, 2008 "Optimum design of straight thin-walled box section beams for crashworthiness analysis," Finite Elements in Analysis and Design, vol. 44, pp. 139–147..

F. Tarlochan, F. Samer, A. M. S. Hamouda, S. Ramesh, and K. Khalid, 2013. "Design of thin wall structures for energy absorption applications: Enhancement of crashworthiness due to axial and oblique impact forces," Thin-Walled Structures., vol. 71, pp. 7–17.

L. Qing-fen and W. Hai-dou, 2009. "Finite Element Analysis and Shape Optimization of Automotive Crash-box Subjected to Low Velocity Impact," International Conference on Measuring Technology and Mechatronics Automation Finite, pp. 791–794.

F. Duddeck. and H. Zimmer and Technische, 2014. "New Achievements on Implicit Parameterization Techniques for Combined Shape and Topology Optimization for Crashworthiness based on SFE CONCEPT," Shape and Topology Optimization for Crashworthiness, vol. 44, pp. 456–462.

S. Kumar and H. R. Vitala, 2014. "Evaluation for Energy Absorbing Capacity of Concentric Aluminium Tubes Filled With Foam of Different Density," International Journal of Mechanical and Industrial Technology, vol. 2, no. 1, pp. 113–124.

S. Boria and G. Forasassi, 2008. "Honeycomb sandwich material modelling for dynamic simulations of a crash-box for a racing car," Structures Under Shock and Impact X, vol. 98, pp. 167–176,

N. Tanlak and F. O. Sonmez, 2014. "Thin-Walled Structures Optimal shape design of thin-walled tubes under high-velocity axial impact loads," Thin Walled Structures., vol. 84, pp. 302–312

Proceeding: 5th International Conference on Applied Sciences and Engineering (ICASEA, 2018)
(eISBN 978-967-15744-1-6)
Capthorne Hotel, Cameron Highlands, Malaysia

OPENFOAM IMPLEMENTATION FOR THE STUDY OF STREAMWISE VORTEX-INDUCED VIBRATION-BASED ENERGY HARVESTER FOR SENSOR NETWORKS

Ahmad Adzlan Fadzli Bin Khairi[1,2]
Mohamed Sukri Bin Mat Ali[1]

[1]Wind Engineering for Environment Laboratory, Malaysia-Japan International Institute of Technology, Universiti Teknologi Malaysia, 54100, Kuala Lumpur.
[2]Department of Mechanical and Manufacturing Engineering, Faculty of Engineering, Universiti Malaysia Sarawak, 94300 Kota Samarahan, Sarawak.

Abstract: *The study of streamwise vortex induced vibration has reached a level of maturity that allows it to be harnessed to generate power. However, studies have primarily concentrated on the variables that measured through point-based instruments. This severely limits our understanding of the fluid forcing mechanism that results in the vibration of the elastically supported bluff body. We proposed the usage of computational fluid dynamics, in particular, the open source C++ libraries of OpenFOAM. To implement this successfully to the streamwise vortex-induced vibration problem, which involves near-wall fluid-structure interaction, we explored the method of dynamic mesh handling in OpenFOAM for six degrees of freedom motion of a rigid body fully submerged in fluid. Finally, we argued for the usage of arbitrarily coupled mesh interface to overcome the problem of severely distorted mesh in tight gaps between two walls. We run a short simulation to test this setup and found that the case runs uninterrupted, unlike its former counterpart that relies solely on cell displacement diffusion, suggesting the potential success of a further converged solution of the setup when running on a more powerful machine.*

Keywords: *Openfoam, Vortex Shedding, Vortex Induced-Vibration, Streamwise Vortices*

Introduction

Off-grid operation of sensor networks

The growing demand for real-time monitoring and management of agriculture (PEMANDU, 2014), civil structures (Zahid Kausar, Reza, Saleh, & Ramiah, 2014), machinery (Beeby, Tudor, & White, 2006), and hydrological systems (Aziz & Aziz, 2011) led towards widespread adoption of sensors networks in these disciplines. Under the desired operating conditions, most of the application of the sensors are at sites where power from the national grid is either difficult to source, or non-existent. Sometimes, the issue is not so much on the fact that power lines from the national grid are out of reach, as it is related to the involvedness of the means to distribute the power, *e.g.*, installing/extending power lines, or connecting the power line to the sensor, *e.g.*, for cases where sensors are embedded inside bridges.

Off-grid alternatives for power generation for sensor networks typically rely on one form or another of renewable energy technology. River monitoring in Malaysia, for example, uses solar photovoltaic (PV) panels to power their water depth and discharge sensors. The usage of a renewable energy source relieves the designer of a sensor network not only from the cost, but

also the bureaucracy involved in sourcing power from the national grid - especially when the sensor network is to collect data in remote areas.

For a wide range of operating locations, solar PV panels provide a reliable and economic renewable energy solution to the power source problem for sensor networks. However, PV panels need batteries as part of the power system to be able to provide continuous power to the sensors. This is going to be a problem in the future because the number of sensor networks can only be expected to grow. The growth is foreseeable because: (1) more parties are acknowledging sensor networks as being an integral part of the internet of things (IoT) (Xia, Yang, Wang, & Vinel, 2012), and (2) there is a renewed effort to automate and remotely control aspects of our industrial practices - including agriculture *e.g.*, intelligent palm pollination and shrimp farm management (PEMANDU, 2014).

If solar PV panels become the only go-to technology for renewable energy generation, we must be prepared to face several challenges, one being the disposal of the used batteries (Beeby et al., 2006), and second is theft of the solar PV panels themselves (Azimoh, Klintenberg, Wallin, & Karlsson, 2015; Azimoh, Wallin, Klintenberg, & Karlsson, 2014). We can avoid these problems by opting for an alternative renewable energy technology, such as hydropower generation. Considering the power requirement for sensors are generally low (< 1 W), the method to be employed only needs to: (1) generate that much power, (2) continuously, (3) using inexpensive materials that do not incentivize its theft. Power generation via streamwise vortex-induced vibration (SVIV) is a method that fulfils all the criteria listed above.

Hydropower generation by exploiting SVIV

Streamwise vortex-induced vibration (SVIV) is the name given to the vibration of a cylindrical bluff body that is caused by the alternate shedding of streamwise vortex pairs from the top and bottom surfaces of the cylinder (Shirakashi, Mizuguchi, & Bae, 1989; Zdravkovich, 1983). While the type of vortex shedding from an immersed cylindrical bluff body is typically the Karman vortex, whose vortex axis is parallel to the cylindrical axis (lateral vortex), the streamwise vortex pairs have their axis perpendicular to the axis of the cylinder. The appearance of the streamwise vortex from the cylinder is toggled by placing another cylindrical bluff body downstream perpendicularly, at a certain range of gaps (Bae, Baranyi, Koide, Takahashi, & Shirakashi, 2001; Fox, 1992; Takahashi, Baranyi, & Shirakashi, 1999) between the upstream and downstream cylinders.

There are two forms of streamwise vortices that have been observed: the trailing and necklace vortices. Both exhibit the ability to lock-in to the natural frequency of the system (Tuananh Nguyen, Koide, Takahashi, & Shirakashi, 2010) - thus generating energetic vibration that is key to energy harvesting. A schematic of these two vortices is given in Figure 19.

Sensor networks are required to: (1) operate continuously with (2) minimal maintenance (Discenzo, Chung, & Loparo, 2006). Therefore, the power supply to the sensor network must be robust, with a minimal component count and simple geometric design. To further simplify the geometric design of the SVIV oscillator, Ref. (Kawabata, Takahashi, Haginoya, & Shirakashi, 2013; Koide et al., 2007) replaced the downstream cylinder with a strip-plate, *i.e.* a thin rectangular cylinder, and studied its amplitude and frequency responses. These studies demonstrated the ability to initiate the formation of the streamwise vortices are not strictly dependent on the geometric design of the cylinders - both upstream and downstream. Using

the strip-plate also expands the range of velocity that sustains SVIV, in addition to higher amplitude response, compared to a circular downstream cylinder (KOIDE, KATO, TAKAHASHI, & SHIRAKASHI, 2009).

A laboratory scale energy harvester that utilizes SVIV was developed and tested in Refs. (Koide, Sekizaki, Yamada, Takahashi, & Shirakashi, 2009; Koide, SEKIZAKI, Yamada, TAKAHASHI, & Shirakashi, 2013). The energy harvester exhibits constant power magnitude over a sizeable range of velocities ($1 < U\ (\mathrm{m/s}) < 4$) for a circular cross-section oscillator of diameter 10 mm, length 980 mm, mass ratio $m^* = 17.43$, and Scruton number 7.74. The mass ratio gives the ratio of the mass of the vibrating system to the mass of fluid displaced by the oscillating cylinder, *i.e.* $m^* = m_{system}/m_{displaced} = m_{system}/(\pi D^2 L/4)$, with D and L being the diameter and length of a circular cylinder. The Scruton number Sc is a way to quantify the mass and damping of a vibrating system and it is given by $\mathrm{Sc} = 2m^*\delta$, where δ is the logarithmic decrement of the system.

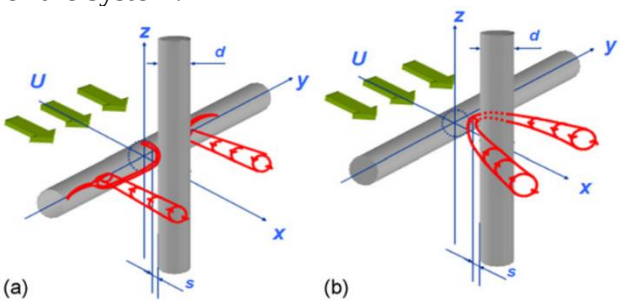

Figure 19. Schematic Of The Two Forms Of The Streamwise Vortex: (A) Trailing Vortex And (B) Necklace Vortex. From (T. Nguyen, Koide, Yamada, Takahashi, & Shirakashi, 2012)**.**

The sizeable operating velocity range partially fulfils the constant operations requirement, and constant power output within this velocity range implies an inherent power regulating mechanism in the system. However, the onset velocity for SVIV in water of about 1 m/s, and the magnitude of power generated currently in the order of mW, usage of the SVIV-based energy harvester remains constrained to singular sensors only. Powering whole sensor networks including the transmission and reception of collected data is still elusive due to insufficient power. To overcome these shortcomings, parametric studies on SVIV control are imperative, and the avenues already explored are reviewed in the next section.

The objectives of this work are threefold: (1) to review the literature and examine the parameters that affect SVIV, (2) to establish the worthwhileness of computational fluid dynamics (CFD) in the study of SVIV, particularly one that uses the open source software OpenFOAM, and (3) to check whether our case set up for an SVIV simulation using arbitrarily coupled mesh interface (ACMI) can run without encountering errors.

Literature review

Aspects of SVIV control

The cruciform arrangement of cylindrical bluff bodies was initially investigated to control the behaviour of Karman vortices from pipe-like structures, the shedding of which causes disruptive vibrations. This method of vibration control does not require any modifications to the pipe-like structures, and the flow upstream the cylinder is virtually left unperturbed - making it relatively simple to retrofit to already existing systems.

However, at certain gaps between the upstream and downstream cylinder in a cruciform arrangement, another type of vortex shedding occurs, whose Strouhal number is 3 to 7 times smaller compared to the Karman vortex. This is true in the two circular cylinders in the cruciform arrangement of Ref. (Shirakashi et al., 1989). When the flow is visualized using smoke streaks in a wind tunnel, the axis of rotation of the vortices being shed was found to be parallel to the free stream (perpendicular to the upstream cylinder axis), hence the name streamwise vortex. The following are several parameters that were found to affect aspects of SVIV.

The *normalized gap* s^* $(= s/D$, s being the gap between the upstream and downstream cylinder) plays a critical role in the control of streamwise vortices. The two documented forms of streamwise vortex, trailing and necklace, is contingent on s^*. The trailing vortex for example, appears when $0 < s^* < 0.25$, and the necklace vortex when $0.25 < s^* < 0.5$, as observed in the wind tunnel experiments of Ref. (Bae, Hirai, Sano, & Shirakashi, 1992), studying the cruciform arrangement of two circular cylinders. The nondimensional vibration amplitude z^* $(= z/D$, where z is the transverse displacement of the upstream cylinder) is also influenced by s^*. There is a region of high $z^*$when $s^* < 0.3$ both at VIV and galloping regions (KOIDE et al., 2009).

On the other hand, *Reynolds number*, Re was observed to affect the nondimensional frequency of vortex shedding, i.e. Strouhal number ($\mathrm{St} = fD/U$, where f and U are the characteristic frequency and velocities respectively). St increases with increasing Re when $\mathrm{Re} < 10000$. However, St ceases to change when $\mathrm{Re} > 10000$ (Bae et al., 2001). Similar experiments were repeated in wind tunnels of different dimensions, and in a water tunnel. The results showed good reproducibility in both mediums (Koide, Oogane, Takahashi, & Shirakashi, 2004).

Mass-damping parameter - or its nondimensional equivalent - Scruton number, Sc, is commonly related to the maximum amplitude and frequency responses of any VIV system. For SVIV, there is a notable lack of data for systematic variation of the mass ratio m^*, and damping δ, most probably due to the exceptionally high initial investment in manpower and capital in developing a cyber-fluidic system that can vary m^* and δ independently (Mackowski & Williamson, 2013; Sun et al., 2017; Sun, Kim, Nowakowski, Mauer, & Bernitsas, 2016). VIV studies that did pursue the effects of mass-damping without cyber-fluidic systems rely on nondimensionalizing these quantities to allow comparison between experimental runs (Koide et al., 2013; T. Nguyen et al., 2012). Nevertheless, a subtle trend has been pointed out in Ref. (T. Nguyen et al., 2012) with respect to damping: the maximum amplitude (frequency) decreases (increases) with increasing damping.

Implementation of computational fluid dynamics (CFD) in SVIV studies

Although the research highlighted above study important aspects of SVIV, they invariably leave out the examination of quantities whose measurement require 2 dimensional (2D) snapshots of the instantaneous velocity field. Example of such quantities is vorticity, circulation, meandering of the separation point (for circular cylinders), reattachment length, and momentum thickness. The best tool available to the researcher for the above purpose is 2D particle image velocimetry (PIV) (Huang, Hsu, & Lin, 2014; van Oudheusden, Scarano, van Hinsberg, & Roosenboom, 2008; Westerweel, 1997). A well-calibrated PIV system enables the collection of time-resolved 2D velocity fields to an uncertainty level of less than 5% (Yen & Yang, 2011).

Despite this, there is a paucity of the adoption of PIV in SVIV studies, perhaps due to the prohibitive cost of procuring such a system. An alternative is to solve for the flow field variables using computational fluid dynamics (CFD).

CFD is the discipline of solving the governing equations of fluid dynamics using numerical methods and approximations. In principle, end users only need: (1) a computer and (2) a solver program to start their practice of CFD. With household access to computers in Malaysia now nearing 70% of the population (Department of Statistics Malaysia, 2016) and near-ubiquitous availability of computers in higher education institutions, requirement (1) for CFD practice can be fulfilled with a modest effort from the researcher. Fulfillment of requirement (2) is even more straightforward: end users can download and install the OpenFOAM (OpenFOAM Foundation, 2014) C++ libraries and begin developing their simulation case right away.

OpenFOAM is highly customizable as it is open-source, and the general public license (GPL) under which it is distributed means that anybody can use it for free. All solver applications in OpenFOAM can be run in parallel, which is indispensable when tackling computationally demanding projects. Parallelization allows the pooling of existing computing resources instead of procuring new ones, aiding initial adoption cost reduction.

Simulation of SVIV using CFD allows detailed analysis of the instantaneous three-dimensional (3D) flow field around the cylinders. To ensure the validity of the simulation, the case must be set up to mimic the real-world conditions as faithfully as possible, while keeping the computational cost at a minimum. Here we note that the phenomenon of SVIV is a 3D, transient, turbulent, fluid-structure interaction (FSI), where the flow influences the motion of the structure and vice-versa. Since there is a marked lack of CFD work in the literature that deals with SVIV, especially ones that employ OpenFOAM, we first need to determine how to implement the features of SVIV into our simulation - most importantly FSI handling and turbulence modelling. Relevant literature on these subjects is reviewed in the following subsections.

General FSI handling in OpenFOAM

Numerical solution of partial differential equations involves the discretization of the independent variables, both spatial and temporal. Among these two, discretizing the spatial extent of the simulation is usually more demanding, and calls for a substantial degree of physical insight. Discretization of the spatial extent of the simulation is commonly referred to as meshing, and this discipline continues to be in active development to this day (J.-F. Remacle, Geuzaine, Com Ere, & Marchandise, 2009; J. F. Remacle et al., 2012).

We want to point out that there only exists a limited amount of documentation for dynamic mesh handling in OpenFOAM (Maric, Hopken, & Mooney, 2014). This lack of documentation, compared to proprietary software, is the earmark open source technology. The common wisdom is that because we can look at the source code, multi-volume documentation of the software is not necessary. Short of going through the source code, users generally figure their way to set up their simulation case by (1) inspecting existing tutorial cases included in their OpenFOAM installation, (2) reading the error messages (3) posting their queries on forums, *e.g.* CFD Online, and (4) referring to case setups shared by other OpenFOAM users. We follow the same steps in this review as well.

A simulation that involves the movement of a rigid body inside a flow requires the surrounding mesh to be able to absorb and follow the motion while retaining the quality of the mesh within an acceptable level, quantified by mesh metrics such as skewness and orthogonality (ANSYS, 2017). In OpenFOAM, handling of mesh motion, *i.e.* dynamic mesh, is done by invoking the dynamicMotionSolverFvMesh class and using the sixDoFRigidBodyMotion solver. The mesh points are then updated according to the motion of the rigid body, by solving the Laplacian of the mesh displacement. In doing so, the displacement of the cells adjacent to the rigid body is diffused to the surrounding mesh. The reader is referred to Ref. (Chen, Andric, & Manni, 2015) for an example of its implementation. Using this method, Ref. (Maruai, Mat Ali, Ismail, & Shaikh Salim, 2017) successfully simulated the transverse vibration of a square cylinder with a downstream splitter plate in a 2D flow domain.

However, diffusion of the cell displacement due to the motion of the rigid body is severely restricted when the rigid body is moving very close to a wall. An SVIV simulation falls under this category, as the vibration only sets in when $s^* < 0.25$. Reference (Koide et al., 2013) used two values of s^*: 0.08 and 0.16 in their experiments, and attempting to simulate these conditions will cause the cell displacement to be highly concentrated within this gap. An immediate consequence of this is that the mesh becomes highly skewed (L. Ding, Bernitsas, & Kim, 2013; Lin Ding, Zhang, Kim, & Bernitsas, 2015), giving negative volumes and introducing severe conservation errors. A snapshot of a severely deformed mesh next to the strip-plate is given in Figure 20, causing the simulation to halt at 0.4 s of flow time. To circumvent this problem, Refs. (L. Ding et al., 2013; Lin Ding et al., 2015) used a generalized grid interface (GGI) (Beaudoin & Jasak, 2008) to allow a sliding mesh interface between two regions interfaced with non-conforming patches.

In the latest version of OpenFOAM (either OpenFOAM v5.0, or OpenFOAM-dev), GGI is implemented under the name arbitrary mesh interface (AMI) and arbitrarily coupled mesh interface (ACMI). The principle and implementation of both AMI and ACMI are discussed in the next subsection.

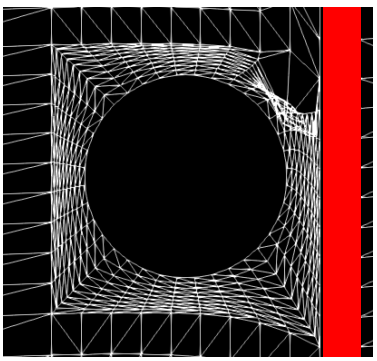

Figure 20. Example Of Severe Deformation Of Mesh Within The Small Gap Between The Cylinder And Strip-Plate. The Red Rectangle Is The Strip-Plate.

Sliding mesh interface in OpenFOAM using AMI and ACMI

OpenFOAM supported the usage of AMI and ACMI since version 2.1.0, and ACMI since version 2.3.0. The idea behind the usage of A(C)MI is that patches no longer need to be conforming, and overlapping patches contribute their transport quantities to the neighbour

patch accor(The OpenFOAM Foundation & Greenshields, 2014).ding to the fraction of overlapping area

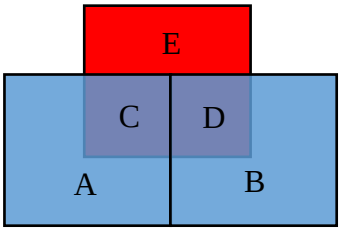

Figure 21. Schematic Of ACMI Implementation. The Non-Overlapping Sub-Patch E Can Be Designated As A Wall.

Figure 21 shows the schematic of the ACMI implementation. The principal patches in this schematic are patches A and B. The ancillary patch is patch E. Regions C and D are where the principal patch overlaps the ancillary, each overlapping 25% of the area of patch E. As such, patches A and B only contributes 25% each of their transport quantities to patch E. This principle is true both in AMI and ACMI handling. The difference between AMI and ACMI is in the treatment of non-overlapping sub-patches. When using ACMI, the non-overlapping part of patch E, *i.e.* top half, can be set to another boundary type - thus integrating two types of boundary treatment within one patch.

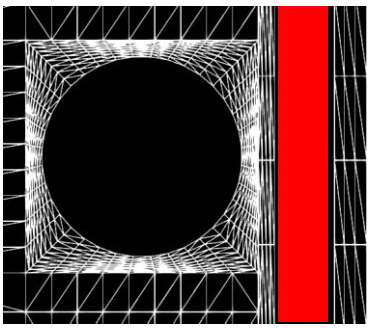

Figure 22. Successful Implementation Of ACMI At The Gap Between The Upstream Cylinder And Strip-Plate.

By implementing ACMI, the mesh on the cylinder side slides on top of the strip-plate side, preventing the severe deformation of the surrounding mesh. This is shown in Figure 22 With the successful implementation of ACMI, we can now set up our simulation case. The details of the simulation are given in the next section.

Simulation setup

We are simulating the occurrence of SVIV as experimented by Ref. (Koide et al., 2013). The value of $D = 10$ mm, $s^* = 0.16$, and the downstream bluff body is a strip-plate of width $w = 10$ mm and thickness $t = 3$ mm. Other mechanical and fluid properties follow that of Ref. (Koide et al., 2013).

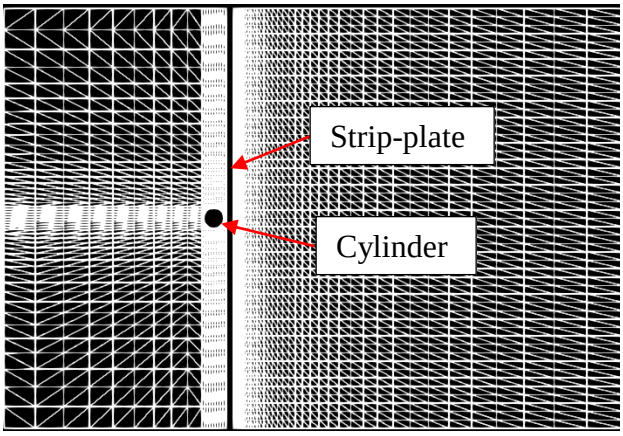

Figure 23. The Mesh Used In This Study. Note That The Strip-Plate Extends From The Bottom To The Top Of The Simulation Domain.

The simulation domain extends 10 diameters (10D) from the top, bottom and upstream surfaces of the circular cylinder. The domain extends 20D from the downstream surface of the circular cylinder. In the lateral direction (direction towards normal to the $x - y$ plane in Figure 23), the domain extends 10D from the sides of the circular cylinder in either direction. The total number of cells is in the order of 3×10^5 cells.

The freestream velocity $U = 1.0\ \mathrm{m/s}$ is chosen as the representative case where SVIV becomes detectable. This is equivalent to $U^* = 23$.

As the actual flow condition under which SVIV takes place is turbulent, a Reynolds averaged Navier-Stokes (RANS) approximation of the turbulence is implemented to offset the computational cost. The one-equation model of Spalart-Allmaras (Allmaras, Johnson, & Spalart, 2012; SPALART & ALLMARAS, 1992; Turbulence, 2011) is chosen as it has a reasonable record of capturing the flow dynamics, and amplitude and frequency response of a circular cylinder excited by Karman vortex, *i.e.* Karman vortex-induced vibration (KVIV). There is also an obvious advantage against 2 or more equation models: the Spalart-Allmaras (S-A) model only adds 1 additional equation to be solved, hence being less computationally expensive.

Implementation of the S-A model in OpenFOAM is done by switching the turbulence model from laminar to RANS and determining the levels of ν_T and $\tilde{\nu}$ through algebraic equations as listed in Ref. (Turbulence, 2011).

The dynamic mesh handling is done by the dynamicMotionSolverFvMesh class, and the solver used for the motion of the cylinder is the sixDoFRigidBodyMotion. A solution of the 3D transient flow field is done using the pimpleDyMFoam application, which handles the solution of pressure and cell displacement using generalized geometric-algebraic multi-grid (GAMG) solver, while the velocity and turbulence viscosity are solved using the stabilized preconditioned biconjugate gradient (PBiCGStab) method.

Results and discussion

The reader is first and foremost reminded that the sole objective of this simulation is to test the case setup using OpenFOAM that implements ACMI and the one-equation turbulence model S-A and make sure that it will not generate errors midway. This is a crucial step before the case can be productively run on a computer cluster, as it minimizes the loss of computing time while accessing a high-performance computing (HPC) cluster due to preventable debugging efforts. We run the simulation for 1060-time steps, with 1-time step equivalent to 0.0001 s of flow time.

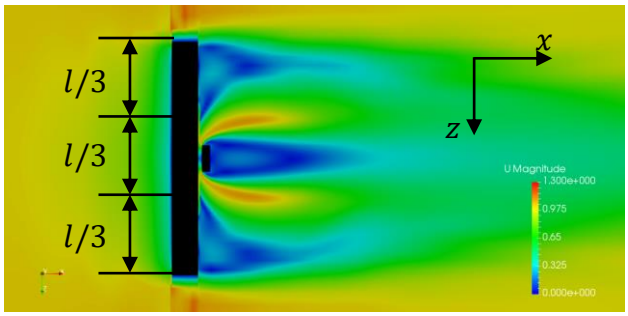

Figure 24. The Velocity Magnitude Field Around The Circular Cylinder And Strip-Plate In The $y/D = 0$ Plane. The Velocities Range From 0 M/S (Blue) To 1.3 M/S (Red).

We present the velocity magnitude field in the $y/D = 0$ plane in Figure 24. The velocity immediately downstream the cylinder is seen to be near zero at the sides of the cylinder (cylinder ends), and this extends towards the middle of the cylinder with a length of approximately one-third the cylinder length ($= l/3$). However, even at this early stage of flow development (1.06 s of flow time), we can already identify a region of high velocity (≈ 1 m/s) located at approximately the middle one-third of the cylinder. This is quite possibly the initial stages of the streamwise vortex formation. The same occurrence is shown from the $y/D = 0.5$ plane in which is the plane at the top surface of the cylinder, shows how the presence of the strip-plate accelerates the flow around it.

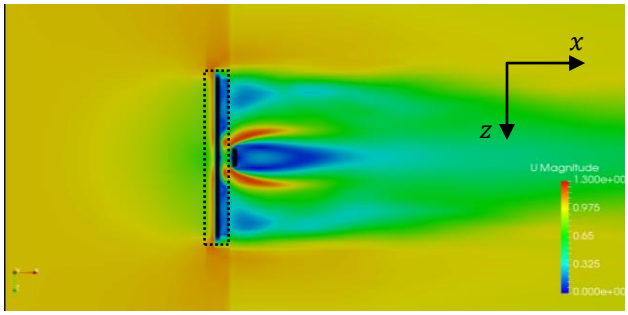

Figure 25. The Velocity Magnitude Field At $y/D = 0.5$ (Top Of The Cylinder). The Dashed Line Gives The Outline Of The Upstream Cylinder.

The most important facet of this result is, however, the fact that the application of ACMI successfully mitigated the severe distortion of the mesh around the juncture between cylinder and strip-plate and allowed the simulation to progress unimpeded.

Admittedly, the mesh in this test simulation is yet to be refined to convergence, and the flow time is yet to be lengthened to a stable solution. But as can be implied from Ref. (Travin, Shur, Strelets, & Spalart, 2000), when testing the application of a new method/simulation setup, grid convergence can be of secondary importance vis-à-vis confirming the applicability of the

method/simulation setup itself. The refinement of the spatial and temporal discretization and the extension of flow time towards a stable solution can always be done promptly after.

Conclusions

In this study, we argued the valuableness of SVIV as the mechanism to drive energy harvesting from flows to sensor networks. We reviewed the literature to establish the parameters that affect the amplitude and frequency response of the SVIV system. We also argued for a wider adoption of CFD as a tool to study SVIV by discussing the potential setups available to the user of the open source CFD toolbox OpenFOAM, to tackle FSI problems.

As a result, we found that aspects of the flow that is critical to the behaviour of SVIV that is 2, or 3 dimensional are generally left out, presumably due to the high initial investment of capital required. We showed the potential of OpenFOAM as a practical solution to this problem by reviewing the working principle of A(C)MI, which lies at the core of a successful simulation involving a sliding mesh. Finally, we demonstrated the applicability of ACMI in simulating the near-wall FSI problem of SVIV, and the simulation results are indicative of the valuable output that can be expected with the further convergence of the solution.

Acknowledgment

The first author acknowledges the Malaysian Ministry of Higher Education and Universiti Malaysia Sarawak for the conferment of a PhD scholarship. This work is supported by a grant numbered R.K130000.7843.4F712.

References

Allmaras, S. R., Johnson, F. T., & Spalart, P. R. (2012). Modifications and clarifications for the implementation of the Spalart-Allmaras turbulence model. *Seventh International Conference on Computational Fluid Dynamics*, (ICCFD7-1902), 1–11. Retrieved from http://www.iccfd.org/iccfd7/assets/pdf/papers/ICCFD7-1902_paper.pdf

ANSYS. (2017). ANSYS Meshing User's Guide. *ANSYS User Guide*, (April). Retrieved from http://www.ansys.com

Azimoh, C. L., Klintenberg, P., Wallin, F., & Karlsson, B. (2015). Illuminated but not electrified: An assessment of the impact of Solar Home System on rural households in South Africa. *Applied Energy*, *155*, 354–364. https://doi.org/10.1016/J.APENERGY.2015.05.120

Azimoh, C. L., Wallin, F., Klintenberg, P., & Karlsson, B. (2014). An assessment of unforeseen losses resulting from inappropriate use of solar home systems in South Africa. *Applied Energy*, *136*, 336–346. https://doi.org/10.1016/J.APENERGY.2014.09.044

Aziz, N. A. A., & Aziz, K. A. (2011). Managing disaster with wireless sensor networks. *13th International Conference on Advanced Communication Technology (ICACT2011)*, (December 2008), 202–207.

Bae, H. M., Baranyi, L., Koide, M., Takahashi, T., & Shirakashi, M. (2001). Suppression of Karman Vortex Excitation of a Circular Cylinder By a Second Cylinder set Downstream in Cruciform Arrangement. *Journal of Computational and Applied Mechanics*, *2*(2), 175–188. https://doi.org/10.1007/s13398-014-0173-7.2

Bae, H. M., Hirai, T., Sano, M., & Shirakashi, M. (1992). Excitation by Vortices Shedding Periodically from Two Cylinders in Cruciform Arrangement. *日本機械学会論文集(B編)*, *58*(551).

Beaudoin, M., & Jasak, H. (2008). Development of a generalized grid interface for turbomachinery simulations with OpenFOAM. In *Open source CFD International conference* (Vol. 2).

Beeby, S. P., Tudor, M. J., & White, N. M. (2006). Energy harvesting vibration sources for microsystems applications. *Measurement Science and Technology*, *17*(12), R175. https://doi.org/10.1088/0957-0233/17/12/R01

Chen, H., Andric, J., & Manni, A. (2015). Proceedings of CFD with OpenSource Software. In H. Nilsson (Ed.), *Proceedings of CFD with OpenSource Software*. Gothenburg. https://doi.org/http://dx.doi.org/10.17196/OS_CFD#YEAR_2015

Department of Statistics Malaysia. (2016). Press Release: Ict Use And Access By Individuals And Households Survey Report, Malaysia, 2015 ICT Services And Equipment Use By Individuals. Retrieved from https://www.dosm.gov.my/v1/index.php?r=column/pdfPrev&id=Q3l3WXJFbG1PNjRwcHZQTVlSR1UrQT09

Ding, L., Bernitsas, M. M., & Kim, E. S. (2013). 2-D URANS vs. experiments of flow induced motions of two circular cylinders in tandem with passive turbulence control for 30,000<Re<105,000. *Ocean Engineering*, *72*. https://doi.org/10.1016/j.oceaneng.2013.06.005

Ding, L., Zhang, L., Kim, E. S., & Bernitsas, M. M. (2015). URANS vs. experiments of flow induced motions of multiple circular cylinders with passive turbulence control. *Journal of Fluids and Structures*, *54*, 612–628. https://doi.org/10.1016/j.jfluidstructs.2015.01.003

Discenzo, F. M., Chung, D., & Loparo, K. A. (2006). Power scavenging enables maintenance-free wireless sensor nodes. In *International Conference on Complex Systems*. Boston. Retrieved from http://www.necsi.edu/events/iccs6/papers/7df7ed07961c3fb28cfd2f851d82.pdf

Fox, T. A. (1992). Interference in the wake of two square-section cylinders arranged perpendicular to each other. *Journal of Wind Engineering and Industrial Aerodynamics*, *40*(1), 75–92.

Huang, R. F., Hsu, C. M., & Lin, W. C. (2014). Flow characteristics around juncture of a circular cylinder mounted normal to a flat plate. *Experimental Thermal and Fluid Science*, *55*, 187–199. https://doi.org/10.1016/j.expthermflusci.2014.03.012

Kawabata, Y., Takahashi, T., Haginoya, T., & Shirakashi, M. (2013). Interference Effect of Downstream Strip-Plate on the Crossflow Vibration of a Square Cylinder. *Journal of Fluid Science and Technology*, *8*(3), 647–658. https://doi.org/10.1299/jfst.8.348

KOIDE, M., KATO, N., TAKAHASHI, T., & SHIRAKASHI, M. (2009). Vibration Control for a Circular Cylinder by a Strip-Plate Set Downstream in Cruciform Arrangement (2nd Report, Generation and Suppression of Vortex Excitation on Elastically Supported Cylinder). *日本機械学会論文集(B編)*, *75*(752), 691–699.

Koide, M., Kato, N., Yamada, S., Kawabata, Y., Takahashi, T., & Shirakashi, M. (2007). Influence Of A Cruciform Arrangement Downstream Strip-Plate On Crossflow Vibration. *Journal of Computational and Applied Mechanics*, *8*(2), 135–148.

Koide, M., Oogane, K., Takahashi, T., & Shirakashi, M. (2004). Experimental Study on Universality of Longitudinal Vortices Shedding Periodically from Crisscross Circular Cylinder System in Uniform Flow. *可視化情報学会論文集*, *24*(4), 15–22.

Koide, M., Sekizaki, T., Yamada, S., Takahashi, T., & Shirakashi, M. (2009). A Novel Technique for Hydroelectricity Utilizing Vortex Induced Vibration. In *Proceedings of the ASME Pressure Vessels and Piping Division Conference*, *PVP2009-77487*.

Koide, M., SEKIZAKI, T., Yamada, S., TAKAHASHI, T., & Shirakashi, M. (2013). Prospect of Micro Power Generation Utilizing VIV in Small Stream Based on Verification Experiments of Power Generation in Water Tunnel. *Journal of Fluid Science and Technology*, *8*(3), 294–308. https://doi.org/10.1299/jfst.8.294

Mackowski, A. W., & Williamson, C. H. K. (2013). An experimental investigation of vortex-induced vibration with nonlinear restoring forces. *Physics of Fluids*, *25*(8). https://doi.org/10.1063/1.4819082

Maric, T., Hopken, J., & Mooney, K. (2014). The OpenFOAM technology primer.

Maruai, N. M., Mat Ali, M. S., Ismail, M. H., & Shaikh Salim, S. A. Z. (2017). Downstream flat plate as the flow-induced vibration enhancer for energy harvesting. *Journal of Vibration and Control*, 107754631770787. https://doi.org/10.1177/1077546317707877

Nguyen, T., Koide, M., Takahashi, T., & Shirakashi, M. (2010). Universality of longitudinal vortices shedding from a cruciform two circular cylinder system in uniform flow. *Journal of Fluid Science and Technology*, *5*(3), 603–616.

Nguyen, T., Koide, M., Yamada, S., Takahashi, T., & Shirakashi, M. (2012). Influence of mass and damping ratios on VIVs of a cylinder with a downstream counterpart in cruciform arrangement. *Journal of Fluids and Structures*, *28*, 40–55. https://doi.org/10.1016/j.jfluidstructs.2011.10.006

OpenFOAM Foundation. (2014). *OpenFOAM - The Open Source CFD Toolbox - User Guide*. *OpenFOAM Foundation*. https://doi.org/10.1023/A

PEMANDU. (2014). ETP Annual Report 2014. Retrieved from www.pemandu.gov.my

Remacle, J.-F., Geuzaine, C., Com Ere, G., & Marchandise, E. (2009). High Quality Surface Remeshing Using Harmonic Maps. *INTERNATIONAL JOURNAL FOR NUMERICAL METHODS IN ENGINEERING Int. J. Numer. Meth. Engng*, *0*, 1–6. https://doi.org/10.1002/nme

Remacle, J. F., Lambrechts, J., Seny, B., Marchandise, E., Johnen, A., & Geuzainet, C. (2012). Blossom-Quad: A non-uniform quadrilateral mesh generator using a minimum-cost perfect-matching algorithm. *International Journal for Numerical Methods in Engineering*, *89*(9), 1102–1119. https://doi.org/10.1002/nme.3279

Shirakashi, M., Mizuguchi, K., & Bae, H. M. (1989). Flow-induced excitation of an elastically-supported cylinder caused by another located downstream in cruciform arrangement. *Journal of Fluids and Structures*, *3*(6), 595–607. https://doi.org/10.1016/S0889-9746(89)90150-3

SPALART, P., & ALLMARAS, S. (1992). A one-equation turbulence model for aerodynamic flows. In *30th Aerospace Sciences Meeting and Exhibit*. https://doi.org/10.2514/6.1992-439

Sun, H., Kim, E. S., Nowakowski, G., Mauer, E., & Bernitsas, M. M. (2016). Effect of mass-ratio, damping, and stiffness on optimal hydrokinetic energy conversion of a single, rough cylinder in flow induced motions. *Renewable Energy*, *99*, 936–959. https://doi.org/10.1016/j.renene.2016.07.024

Sun, H., Ma, C., Kim, E. S., Nowakowski, G., Mauer, E., & Bernitsas, M. M. (2017). Hydrokinetic energy conversion by two rough tandem-cylinders in flow induced motions: Effect of spacing and stiffness. *Renewable Energy*, *107*, 61–80. https://doi.org/10.1016/j.renene.2017.01.043

Takahashi, T., Baranyi, L., & Shirakashi, M. (1999). Configuration and Frequency of Longitudinal Vortices Shedding from Circular Cylinders in Cruciform Arrangement. 可視化情報, *19*(75), 64–72.

The OpenFOAM Foundation, & Greenshields, C. (2014). OpenFOAM 2.3.0: Arbitrary Mesh Interface. Retrieved January 2, 2018, from https://openfoam.org/release/2-3-0/non-conforming-ami/

Travin, A., Shur, M., Strelets, M., & Spalart, P. (2000). Detached-Eddy Simulations Past a Circular Cylinder. *Flow, Turbulence and Combustion*, *63*(1/4), 293–313. https://doi.org/10.1023/A:1009901401183

Turbulence, T. S. (2011). Turbulence Modeling Resource. *Langley Research Center Turbulence Modeling Resource*, *45*(10), 1–8. https://doi.org/https://turbmodels.larc.nasa.gov/

van Oudheusden, B. W., Scarano, F., van Hinsberg, N. P., & Roosenboom, E. W. M. (2008). Quantitative visualization of the flow around a square-section cylinder at incidence. *Journal of Wind Engineering and Industrial Aerodynamics*, *96*(6–7), 913–922. https://doi.org/10.1016/j.jweia.2007.06.030

Westerweel, J. (1997). Fundamentals of digital particle image velocimetry. *Measurement Science and Technology*, *8*(12), 1379–1392. https://doi.org/10.1088/0957-0233/8/12/002

Xia, F., Yang, L. T., Wang, L., & Vinel, A. (2012). Internet of things. *International Journal of Communication Systems*, *25*(9), 1101.

Yen, S. C., & Yang, C. W. (2011). Flow patterns and vortex shedding behavior behind a square cylinder. *Journal of Wind Engineering and Industrial Aerodynamics*, *99*(8), 868–878. https://doi.org/10.1016/j.jweia.2011.06.006

Zahid Kausar, A. S. M., Reza, A. W., Saleh, M. U., & Ramiah, H. (2014). Energizing wireless sensor networks by energy harvesting systems: Scopes, challenges and approaches. *Renewable and Sustainable Energy Reviews*, *38*, 973–989. https://doi.org/10.1016/j.rser.2014.07.035

Zdravkovich, M. M. (1983). Interference between two circular cylinders forming a cross. *Journal of Fluid Mechanics*, *128*(1), 231. https://doi.org/10.1017/S0022112083000464

Proceeding: 5th International Conference on
Applied Sciences and Engineering (ICASEA, 2018)
(eISBN 978-967-15744-1-6)
Capthorne Hotel, Cameron Highlands, Malaysia

REMOVAL OF THE OLD ADHERE MORTAR FROM CRUSHED CONCRETE WASTE AGGREGATE (CCWA) WITH DIFFERENT HCL'S MOLARITY AND ITS EFFECT ON THE PROPERTIES OF THE CCWA

Alodain. Ai. Ab [1]
Ridzuan
A. R. M a,b [1,2]

1 Faculty of Civil Engineering Universiti Teknologi Mara 40450, Malaysia.

2 Institute of Infrastructure Engineering and Sustainable Management, Universiti Teknologi Mara 40450, Malaysia.

Abstract: *Removing the old adhere mortar from the crushed concrete waste aggregate is essential to insure the quality of the CCWA used in the production of new concrete. Pre-soaking the CCWA in HCl solution was reported as an effective technique to remove the old adhere mortar. However, the data on the treatment of the CCWA with HCl failed to address the influence of HCl's molarity on the CCWA properties (such as the aggregate crush value, aggregate impact value and water absorption) and the correlation between the treatment variables such as size of aggregate, time of submerged in HCl, the microstructure of CCWA and the molarity of the HCl. A total of fifteen specimens were prepared of CCWA. one specimen untreated CCWA and fourteen treated specimens, each one of these specimens treated with different HCl's molarity of 0.2, 0.5, 1.0, 2.0, 3.0, 4.0, 5.0, 6.0, 7.0, 8.0, 9.0 10.0, 11.0 and 12.8. experimental program data was analysis with SPSS. A 500x digital microscope used to examine the microstructure surface of the aggregate. The results showed a significant correlation between the HCl's molarity and the properties of the CCWA. The higher HCl molarity results better quality of CCWA. Also, the microscope test showed that a similar microstructure surface of CCWA when treated with 12.8 HCl.*

Keywords: *Surface Treatment, Crushed Concrete Waste Aggregate, Removing The Old Adhere Mortar*

Introduction

The potential benefits of using Crushed Concrete Waste Aggregate (CCWA) in concrete have been widely explored. However, the use of CCWA as substitute material for nature aggregate never been more preferable in the construction industry (Behera, Bhattacharyya, Minocha, Deoliya, & Maiti, 2014; McNeil & Kang, 2013; Raut, Ralegaonkar, & Mandavgane, 2011; Shi et al., 2016). The CCWA contains about 65% natural aggregate and 35% of adhered mortar. The amount of adhered mortar indicates characteristics of original concrete, effectiveness of crushing procedure and the particle size of CCWA (C. . Poon, Shui, & Lam, 2004). There is a mutual correlation between the adhered mortar and the quality of CCWA. adhered mortar is greatly responsible for the poorer properties of the CCWA as compare to the natural aggregate (Behera et al., 2014; McNeil & Kang, 2013; Saravanakumar, Abhiram, & Manoj, 2016) . The water absorption capacity of CCWA is about 3 times more than natural aggregate. Water absorption capacity of CCWA depending on the amount of old adhere mortar attached to the surface of the aggregate particles(He-gong, 2011; Lin, Tyan, Chang, & Chang, 2004; C.-S.

Poon & Chan, 2007; Topçu & Şengel, 2004). CCWA is poorly graded because of its poor particle size distribution. It is either very coarse or very fine, this is due to the inappropriate crushing process. Though The CCWA grading can be controlled with more precise crushing process. The micro-cracks developed in the adhere mortar and fractures developed inside the aggregate as result of the crushing process can't be controlled(Akbarnezhad, Ong, Tam, & Zhang, 2013; Zhang, Zhang, Yan, & Liu, 2017). generally the CCWA has lower mechanical properties (such as low crushing strength and low impact resistance) than natural aggregate due to the presence of old mortar on the surface of the aggregate(Dilbas, Şimşek, & Çakır, 2014; Spaeth & Djerbi Tegguer, 2013; Xiao, Li, Sun, Lange, & Shah, 2013) .

Hence, the main factor that affect the quality of the CCWA is the old cement past remains on the surface of the aggregate, leading to a higher porosity, water absorption and hence a weaker interfacial zone between new cement mortar and aggregates and lower mechanical properties (Tam & Le, 2007). Hence removing the old adhere mortar will promote the move towards sustainability by submerge the CCWA in HCl with various molarities (0.2ml-12.8ml) to remove the old cement paste adhered on the surface of the CCWA. This paper reports the effectiveness of using HCl with various molarities to remove the old cement paste adhered on the surface of the CCWA as treatment method and its' effect on the properties of CCWA such as aggregate crush value, aggregate impact value, water absorption and the relationship between molarity of HCl and size of CCWA.

Experimental Program

Materials

The Crushed Concrete Waste Aggregate (CCWA) was obtained from an old demolished building in Kuala Lumpur Malaysia. Hydrochloric Acid (HCl) with Molar mass of 36.46094 g/mol was used to remove the cement past adhere on the surface of the CCWA. Fourteen specimens of CCWA was prepared and treated with different HCl's molarity and one untreated CCWA. All CCWA aggregate specimens were experimented and compare to natural aggregate. Each of these CCWA specimens was subjected to the same experimental procedure. Table 1 showed the specimens of CCWA linked to different molarity of HCl. Two Jaw crushers at the UiTM laboratory were used to crush CCWA to ensure a good size distribution. In order to have a good size distribution, CCWA was crushed to size 20mm and 10mm. CCWA was sieved and all the undesired particles either eliminated or recrushed again.

Table 1 Specimens Of CCWA Linked To Different Molarity Of Hcl.

CCWA specimens	Description
NA	Natural Aggregate
CCWA0.0H	Untreated CCWA aggregate
CCWA0.2H	CCWA treated with HCL of molarity 0.2 (ml)
CCWA0.5H	CCWA treated with HCL of molarity 0.5 (ml)
CCWA1.0H	CCWA treated with HCL of molarity 1 (ml)
CCWA2.0H	CCWA treated with HCL of molarity 2 (ml)
CCWA3.0H	CCWA treated with HCL of molarity 3 (ml)
CCWA4.0H	CCWA treated with HCL of molarity 4 (ml)
CCWA5.0H	CCWA treated with HCL of molarity 5 (ml)
CCWA6.0H	CCWA treated with HCL of molarity 6 (ml)

CCWA7.0H	CCWA treated with HCL of molarity 7 (ml)
CCWA8.0H	CCWA treated with HCL of molarity 8 (ml)
CCWA9.0H	CCWA treated with HCL of molarity 9 (ml)
CCWA10.0H	CCWA treated with HCL of molarity 10 (ml)
CCWA11.0H	CCWA treated with HCL of molarity 11 (ml)
CCWA12.8H	CCWA treated with HCL of molarity 12.8 (ml)

Treatment of CCWA

Fourteen specimens of CCWA were prepared and oven dried for twenty-four hours. The weight of the oven dried CCWA specimens were recorded. Each CCWA specimen was submerge for 72 hours in HCl with different molarity as illustrated in Table 1. Then the weight of CCWA specimens were recorded at 4 hours, 8 hours, 24 hours, 48 hours, and 72 hours after being oven dried. Then the CCWA specimen returned to the HCl solution after each weight measuring time until the end of the treatment period. The weight loss of the CCWA specimens were recorded at 4 hours, 8 hours, 24 hours, 48 hours, and 72 hours.

Figure 26 Specimens Of CCWA Soaked The Hcl With Different Molarity.

Results and discussion

Treatment of CCWA

The CCWA specimens crushed to size larger than 25mm. the CCWA specimens are submerged in the HCl for three days. the weight loss of the CCWA is calculated after 4, 8, 24, 48, 72 hours. The weight loss is due to dissolving of the old mortar adhere on the surface of the aggregate. Figure 2 showed that the CCWA specimen's loss more weight when the molarity of the HCl increase. Ismail and Ramli (2013) claimed that HCl with molarity of 0.1 and 0.5 are enough for producing a good RCA. However, the experimental results showed that HCl with morality of o.2 and 0.5 loss only 1.7 and 1.8 of total weight of the CCWA. While other specimens that treated with higher HCl molarity record more weight loss by up to 20% of the total weight of CCWA. Tam et al., (2007) reported that the HCl with low molarity removes the loosely adhered mortar that was attached to the original aggregate, which explains the lower percentage of weight loss when 0.2 and 0.5 HCL is used.

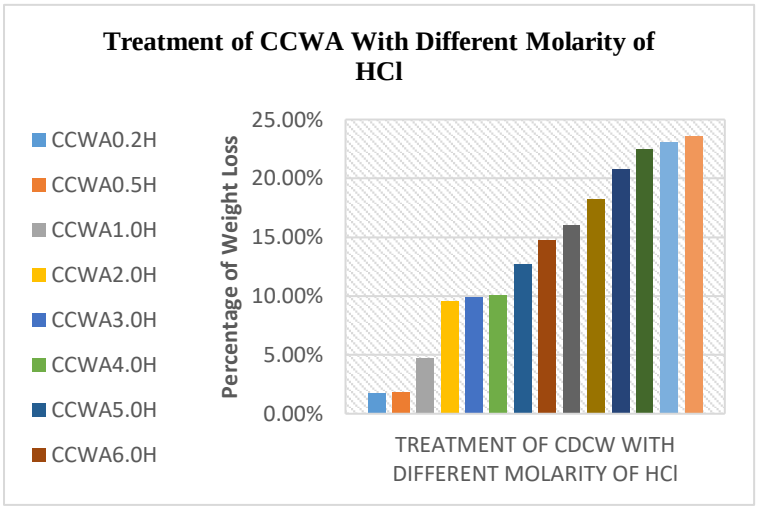

Figure 27 Treatment of 3CCWA With Different

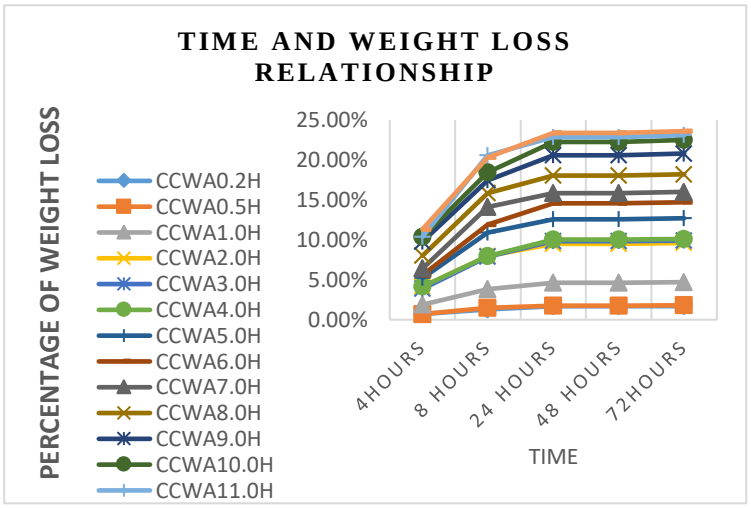

Figure 28 Time and Weight Loss Relationship

Figure 3 showed the development of the CCWA's treatment within the three days. despite the difference in molarity of the HCl, all CCWA specimen stopped reacting with the HCl after 24 hours. (Güneyisi, Gesoğlu, Algın, & Yazıcı, 2014; Ismail & Ramli, 2013, 2014; Tam & Le, 2007) studied the using the HCl as treatment agent to remove the old mortar adhere on the surface of the aggregate. Some of these researches suggested that the RCA to be immerse for 3days, while others reported that 24 hours is sufficient time for the treatment of the RCA. However, there is no study studied the time need to for the CCWA to fully react with HCl.

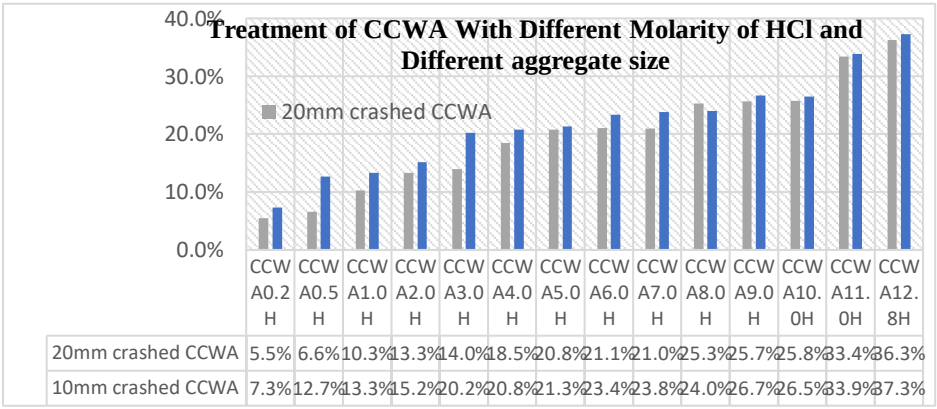

Figure 29 Treatment Of CCWA With Different Molarity Of Hcl And Different Aggregate Size

Figure 4 showed the effect of the HCl with different molarity on the size of the CCWA. Figure 4 showed that there is a relationship between the size of the CCWA and the weight loss. the results from Figure 4 and Figure 6 showed that the HCl has higher corrosion effect on smaller size of aggregate, which lead to approximately 50% more weight loss (old adhere mortar loss). Despite, the molarity of the HCl, the CCWA showed significant weight loss, for instant, the percentage of weight loss increase from 1.7% and 1.8% to 5.6% and 6.7% when 20mm CCWA submerged in HCl with molarity of 0.2 ml and 0.5 ml respectively. the increase in weight loss of the CCWA when smaller size submerged in HCl is due to the increase of the surface area

that react with the HCl. Submerging CCWA in acidic solution such as HCl is an experiment curried out by many research, nevertheless, none of that researches report the size effect on the pre-soaking treatment method (Güneyisi et al., 2014; Ismail & Ramli, 2014; Purushothaman, Amirthavalli, & Karan, 2000a; Saravanakumar et al., 2016; Shi et al., 2016; Tam & Le, 2007; Zaharieva, Buyle-Bodin, Skoczylas, & Wirquin, 2003).

Properties of Treated CCWA

Figure 5 and Figure 6 showed the experimental results of the Aggregate Crush Value (ACV) and Aggregate Impact Value (AIV) conducted on 14 CCWA treated with a different HCl molarity and one of untreated CCWA. The crushing value and impact value indicate to the strength of the aggregate. ACV and AIV are expressed as a percentage of the total weight. A lower percentage indicates tougher and stronger aggregates. From the results of the ACV experiment, the untreated CCWA record the highest value of ACV with 38.6%. treating CCWA improve the ACV value, likewise, the CCWA treated with low molarity showed up to 50% higher than specimens treated with high molarity of HCl. Similarly, Figure 8 showed that the untreated CCWA record the highest value of AIV with 39.1%. treating CCWA improve the ACV value, likewise, the CCWA treated with low molarity showed up to 55% higher than specimens treated with high molarity of HCl. In addition, both the ACV and AIV values showed improvement as the molarity of the HCl increase. The recycled aggregate is reported to have higher ACV and AIV with almost 36% and 31% respectively. also, the treated recycled aggregate recorded to have better ACV AIV with 33% and 29% when treated with HCl of molarity 0.1 ml (Kumar, Dhinakaran, & Ph, 2012; Purushothaman et al., 2000a; Purushothaman, Amirthavalli, & Karan, 2000b).

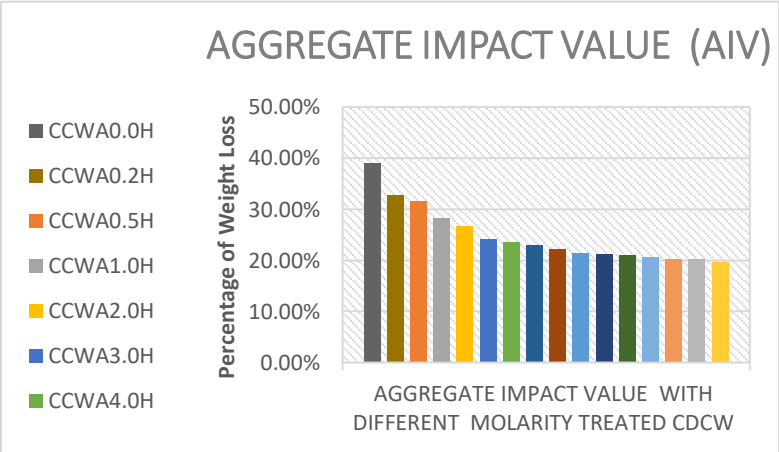

Figure 5 Aggregate Crush Value with Different Type Of Treated CCWA With Different Molarity

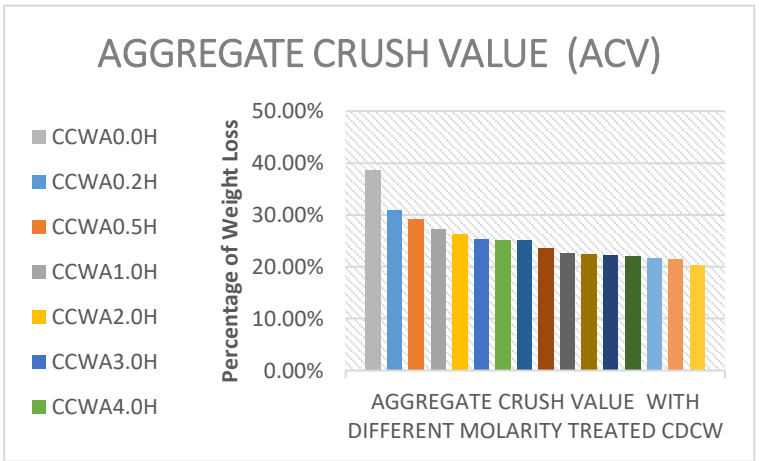

Figure 6 Aggregate Impact Value with Different Molarity Treated CCWA

Figure 30 and Figure 31 showed the experimental results of the water absorption conducted on 14 CCWA treated with a different HCl molarity and one of untreated CCWA. Unexpectedly, the untreated aggregate recorded less water absorption than those specimens treated with HCl of low molarity 0.2ml and 0.5ml. nevertheless, the untreated CCWA showed higher water absorption percentage compere with the specimens treated with HCl of 4ml molarity and higher. The fact that, CCWA treated with HCl of 0.2ml and 0.5 molarity showed higher water absorption proof that the low molarity of HCl increase the porosity of the CCWA, which lead to increase the water absorption. Similar results reported by many researchers that the recycled

aggregate has 3% to 5% higher water absorption compere the natural aggregate. When recycled aggregate treated with pre-soaking in acidic solution, the water absorption some improvement (Çakir, 2014; Çakır & Sofyanlı, 2014; Güneyisi et al., 2014; Kumar et al., 2012; Saravanakumar et al., 2016). Yet the treated recycled aggregate water absorption is higher the nature aggregate. This is due to the remain mortar on the surface of the aggregate. However, when higher concertation of HCl is used to treat the surface of the CCWA the results is very promising. The CCWA treated with HCl of 10ml and above molarity showed a similar water absorption to the natural aggregate.

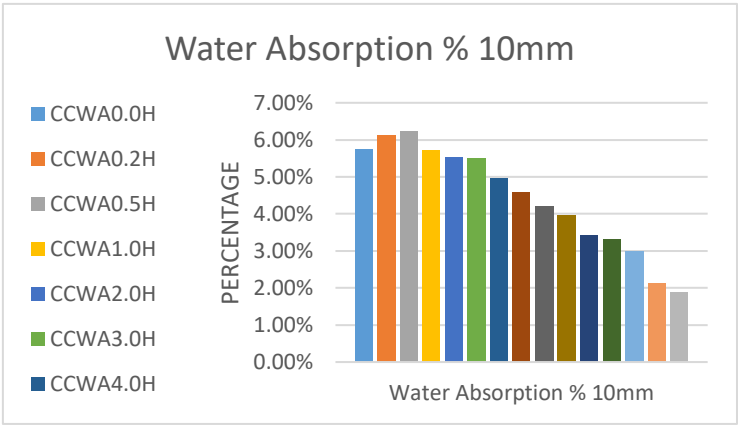

Figure 30 Water Absorption % 10mm

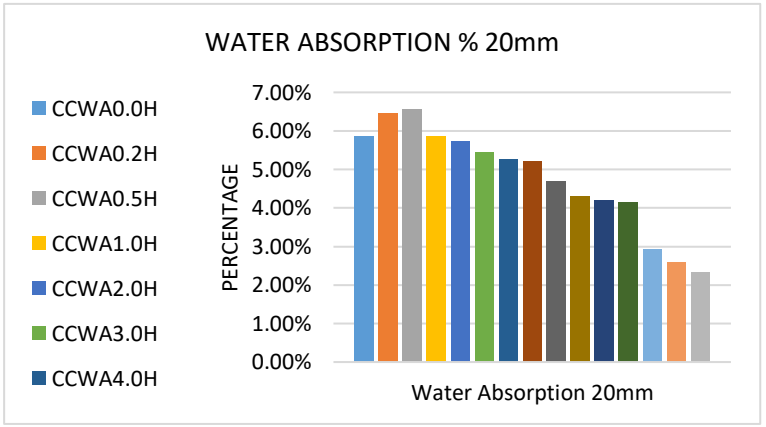

Figure 31 Water Absorption % 20mm

The Microstructure surface of the CCWA

The microstructure surface of the CCWA and the NA was taken by digital microscope, the figures below showed the surface of natural aggregate, untreated CCWA and treated CCWA with different molarity of HCl. The specimens treated with 0.2-4.0 molarity showed higher amount of old mortar adhere to the surface of the aggregate as compare to those specimens treated with molarity of 5.0 and above. Using HCl with molarity of 0.2 and 0.5 helps to remove only the loosely adhere mortar (Ismail & Ramli, 2013; Tam & Le, 2007). The specimens threated with HCl of 0.2ml and 0.5ml molarity Figure 34 and Figure 33 respectively, showed microcracks on the old mortar adhere, which explain the lower properties of the specimens treated when treated with HCl of 0.2ml and 0.5ml molarity. Despite, that increasing the molarity of the HCl helps removing more adhere mortar, all CCWA specimens examined showed an exiting of old mortar on the surface of the CCWA except the those treated with HCl with molarity of 11.0 or higher. Figure 32 and Figure 35 showed that the CCWA treated with CHl of 12.8ml molarity achieved a similar microstructure surface to the natural aggregate.

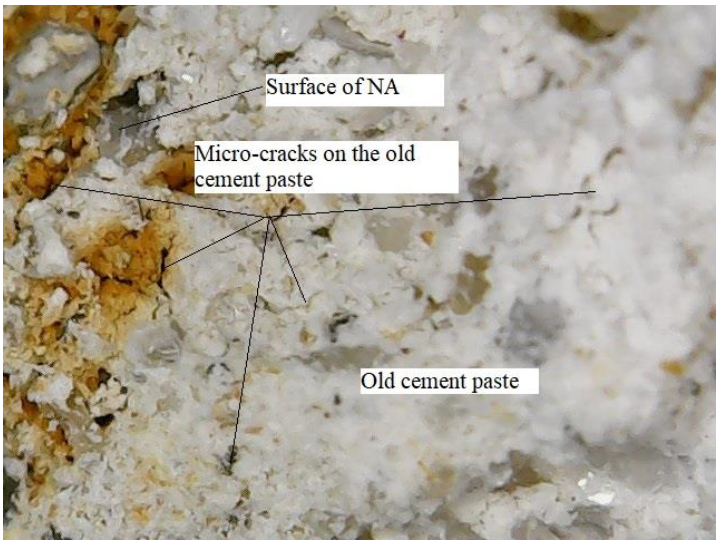

Figure 34 The Microstructure Surface Of The Treated CCWA With Hcl Of 0.2 Ml

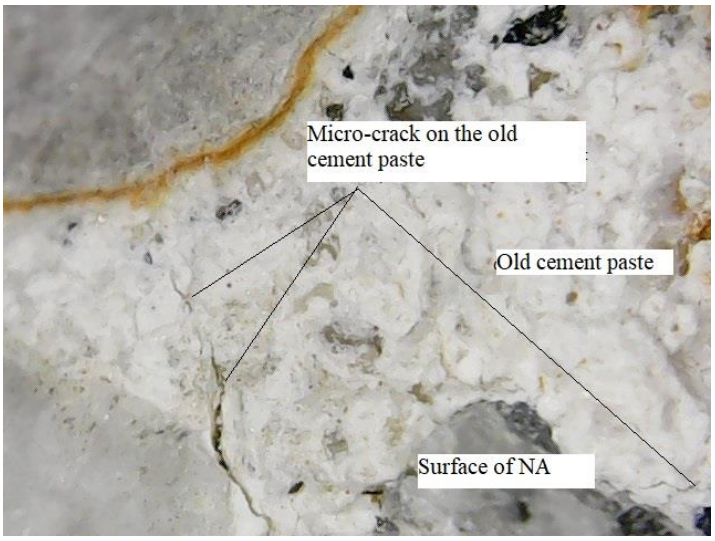

Figure 33 The Microstructure Surface Of The Treated CCWA With Hcl Of 0.5 Ml

Figure 32 The Microstructure Surface Of The Treated CCWA With Hcl Of 12.8 Ml

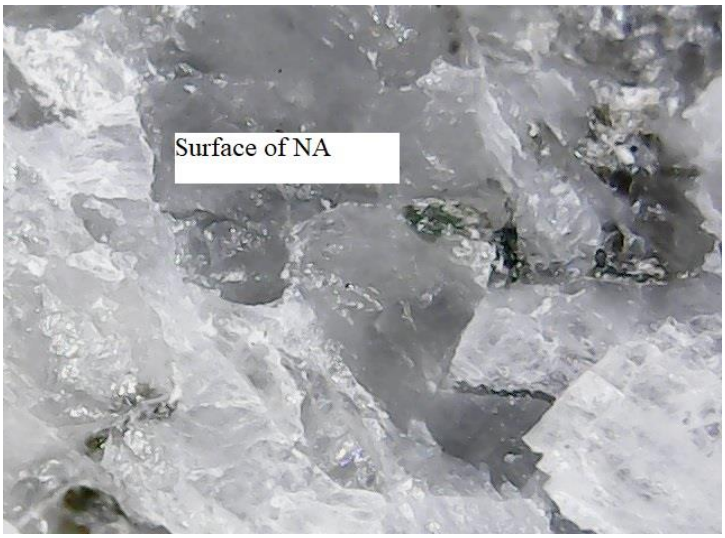

Figure 35 The Microstructure Surface Of The Natural Aggregate

The Correlations Matrix Between Variables

The interpretation of the strength of correlation was based on the description provided by Dudin (2013) The description is as follows:

- If r is +1, perfect positive correlation;
- If r is 0.7 - 0.9, strong positive correlation;
- If r near 0.5, moderate positive correlation;
- If r is 0.1 - 0.3, weak positive correlation;
- If r is 0, no correlation;
- If r is (-0.1) – (-0.3), weak negative correlation; and
- If r near (-0.5), moderate negative correlation;
- If r is (-0.7) – (-0.9), strong negative correlation; and
- If r is -1, perfect negative correlation;

Table 2 showed the correlation matrix between HCl's molarity and the treated CCWA properties (the aggregate crush value, aggregate impact value and water absorption for both 20mm and 10mm). There is a significant correlation (as r = -0.644, -0.698, -0.684 and -0.712) between HCl's molarity and the aggregate crush value, aggregate impact value and water absorption for both 20mm and 10mm respectively with $p < .01$, then we know that there is a moderate negative association between the HCl's molarity, and the treated CCWA properties, if HCl's molarity increases, the properties of the treated CCWA improved. In other word, the using higher HCl molarity to treat the CCWA resulting better CCWA quality, A negative correlation also exists in one decreases and the other also decreases. and the probability of this not being true is less than 1%. That is mean that, over 99% of the time we would expect this correlation to exist.

Table 2 Pearson Correlation between HCl's Molarity, Weight Loss and Properties of CCWA

	HCl Molarity	Aggregate Crush Value	Aggregate Impact Value	Water Absorption 20mm	Water Absorption 10mm
HCl Molarity	1				
Aggregate Crush Value	-.644**	1			
Aggregate Impact Value	-.698**	.984**	1		
Water Absorption 20mm	-.684**	.743**	.767**	1	
Water Absorption 10mm	-.712**	.765**	.789**	.987**	1

**. Correlation is significant at the 0.01 level (1-tailed).
Source: Computed Data Analysis

The relationship between the HCl's molarity and the properties of CCWA

Figure 36 and Figure 37 showed the power relationship between the HCl's molarity and the ACV and the AIV with $R^2 = 0.981$ and 0.987 respectively. While Figure 38 and Figure 39 showed the linear relationship between the HCl's molarity and the water absorption of both 10mm and 20mm of CCWA with $R^2 = 0.928$ and 0.955 respectively This relation help the prediction of the values of ACV, AIV and water absorption when the HCl's molarity change. With such value of R^2 it is safe to say that the probability of this prediction not being true is less than 1%, which mean over 99% of the time we safely expect the prediction to occur.

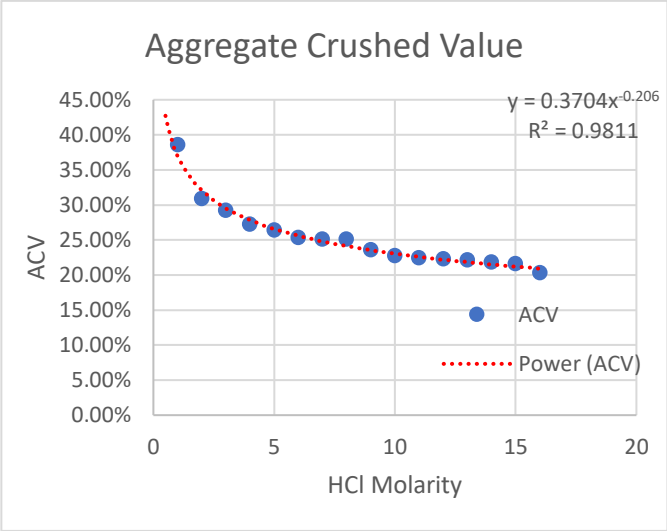

Figure 36 The Relationship Between The Hcl Molarity And The Aggregate Crush Value

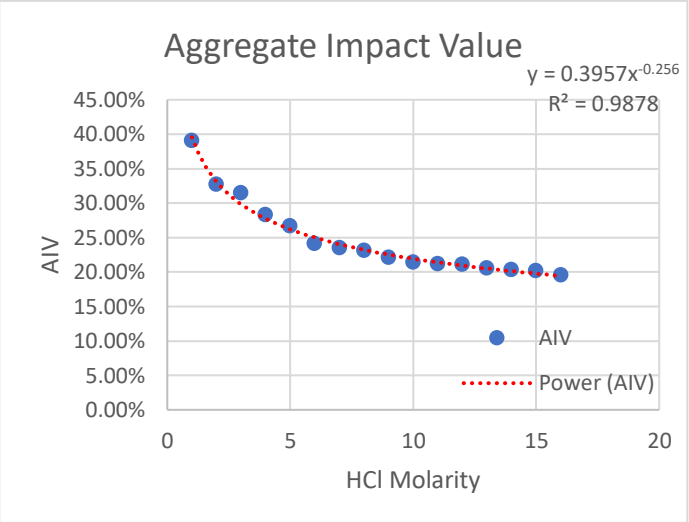

Figure 37 The Relationship Between The Hcl Molarity And The Aggregate Impact Value

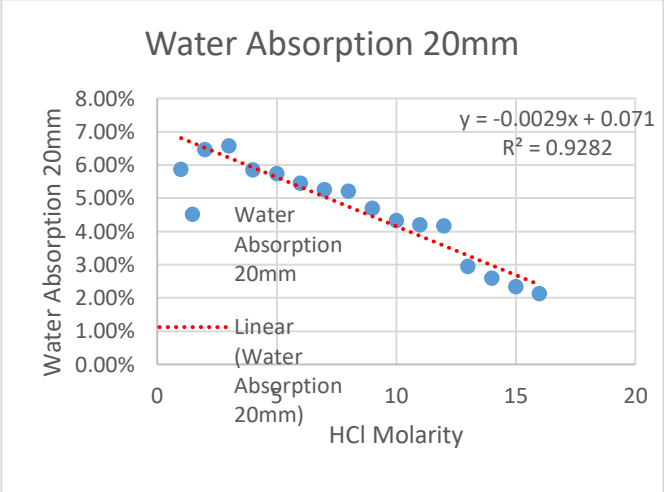

Figure 38 The Relationship Between The Hcl Molarity And The Water Absorption 20mm

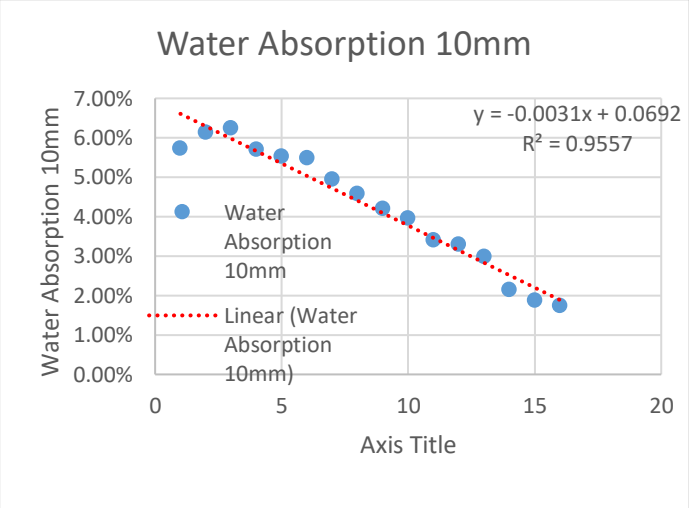

Figure 39 The Relationship Between The Hcl Molarity And The Water Absorption 10mm

Conclusion

Using HCl to remove the adhere mortar is effective. Especially when HCl with molarity of 10 ml or higher is used.

The CCWA's size is also an important factor in the treatment process, as the smaller size of the CCWA shows better results of the treatment.

The experimental program using lower HCl's molarity (0.2ml and 0.5ml) is not effectively improving the properties of the CCWA. In fact, treating the CCWA with lower HCl's concentration cause more microcracks on the old mortar adhere on the aggregate leading to weakening the CCWA even more.

The CCWA treated with the 10-12.8 ml HCl's molarity achieved similar properties to the natural aggregate, while, CCWA treated with lower HCl's molarity inferior properties as compare with the nature aggregate, which cause by the existing of the old adhere mortar on the CCWA.

The experimental program showed a significance influence of the HCl's molarity on the properties of the CCWA.

References

Akbarnezhad, A., Ong, K. C. G., Tam, C. T., & Zhang, M. H. (2013). Effects of the Parent Concrete Properties and Crushing Procedure on the Properties of Coarse Recycled Concrete Aggregates. *Journal of Materials in Civil Engineering*, *25*(December), 1795–1802. https://doi.org/10.1061/(ASCE)MT.1943-5533.0000789.

Behera, M., Bhattacharyya, S. K., Minocha, A. K., Deoliya, R., & Maiti, S. (2014). Recycled aggregate from C&D waste & its use in concrete - A breakthrough towards sustainability in construction sector: A review. *Construction and Building Materials*, *68*, 501–516. https://doi.org/10.1016/j.conbuildmat.2014.07.003

Çakir, O. (2014). Experimental analysis of properties of recycled coarse aggregate (RCA) concrete with mineral additives. *Construction and Building Materials*, *68*, 17–25. https://doi.org/10.1016/j.conbuildmat.2014.06.032

Çakır, Ö., & Sofyanlı, Ö. Ö. (2014). Influence of silica fume on mechanical and physical properties of recycled aggregate concrete. *HBRC Journal*. https://doi.org/10.1016/j.hbrcj.2014.06.002

Dilbas, H., Şimşek, M., & Çakır, Ö. (2014). An investigation on mechanical and physical properties of recycled aggregate concrete (RAC) with and without silica fume. *Construction and Building Materials*, *61*(March 2006), 50–59. https://doi.org/10.1016/j.conbuildmat.2014.02.057

Güneyisi, E., Gesoğlu, M., Algın, Z., & Yazıcı, H. (2014). Effect of surface treatment methods on the properties of self-compacting concrete with recycled aggregates. *Construction and Building Materials*, *64*, 172–183. https://doi.org/10.1016/j.conbuildmat.2014.04.090

He-gong, C. (2011). Analysis of Factors Influencing Durability of Recycled Aggregate Concrete 拘 A Review, 84–87.

Ismail, S., & Ramli, M. (2013). Effect surface treatment of recycled concrete aggregate on properties of fresh and hardened concrete. *2013 IEEE Business Engineering and Industrial Applications Colloquium (BEIAC)*, 651–656. https://doi.org/10.1109/BEIAC.2013.6560211

Ismail, S., & Ramli, M. (2014). Mechanical strength and drying shrinkage properties of concrete containing treated coarse recycled concrete aggregates. *Construction and Building Materials*, *68*, 726–739. https://doi.org/10.1016/j.conbuildmat.2014.06.058

Kumar, P. S., Dhinakaran, G., & Ph, D. (2012). Effect of Admixed Recycled Aggregate Concrete on Properties of Fresh and Hardened Concrete, (April), 494–498. https://doi.org/10.1061/(ASCE)MT.1943-5533.0000393.

Lin, Y.-H., Tyan, Y.-Y., Chang, T.-P., & Chang, C.-Y. (2004). An assessment of optimal mixture for concrete made with recycled concrete aggregates. *Cement and Concrete Research*, *34*(8), 1373–1380. https://doi.org/10.1016/j.cemconres.2003.12.032

McNeil, K., & Kang, T. H. K. (2013). Recycled Concrete Aggregates: A Review. *International Journal of Concrete Structures and Materials*, *7*(1), 61–69. https://doi.org/10.1007/s40069-013-0032-5

Poon, C.-S., & Chan, D. (2007). The use of recycled aggregate in concrete in Hong Kong. *Resources, Conservation and Recycling*, *50*(3), 293–305. https://doi.org/10.1016/j.resconrec.2006.06.005

Poon, C. ., Shui, Z. ., & Lam, L. (2004). Effect of microstructure of ITZ on compressive strength of concrete prepared with recycled aggregates. *Construction and Building Materials*, *18*(6), 461–468. https://doi.org/10.1016/j.conbuildmat.2004.03.005

Purushothaman, R., Amirthavalli, R. R., & Karan, L. (2000a). Influence of Treatment Methods on the Strength and Performance Characteristics of Recycled Aggregate Concrete. *Journal of Materials in Civil Engineering*. https://doi.org/10.1061/(ASCE)MT.1943-5533.0001128.

Purushothaman, R., Amirthavalli, R. R., & Karan, L. (2000b). Influence of Treatment Methods on the Strength and Performance Characteristics of Recycled Aggregate Concrete. https://doi.org/10.1061/(ASCE)MT.1943-5533.0001128.

Raut, S. P., Ralegaonkar, R. V., & Mandavgane, S. a. (2011). Development of sustainable construction material using industrial and agricultural solid waste: A review of waste-create bricks. *Construction and Building Materials*, *25*(10), 4037–4042. https://doi.org/10.1016/j.conbuildmat.2011.04.038

Saravanakumar, P., Abhiram, K., & Manoj, B. (2016). Properties of treated recycled aggregates and its influence on concrete strength characteristics. *Construction and Building Materials*, *111*, 611–617. https://doi.org/10.1016/j.conbuildmat.2016.02.064

Shi, C., Li, Y., Zhang, J., Li, W., Chong, L., & Xie, Z. (2016). Performance enhancement of recycled concrete aggregate - A review. *Journal of Cleaner Production*, *112*, 466–472. https://doi.org/10.1016/j.jclepro.2015.08.057

Spaeth, V., & Djerbi Tegguer, A. (2013). Improvement of recycled concrete aggregate properties by polymer treatments. *International Journal of Sustainable Built Environment*, *2*(2), 143–152. https://doi.org/10.1016/j.ijsbe.2014.03.003

Tam, V. W. Y. T. C. M., & Le, K. N. (2007). *Removal of Cement Mortar Remains from Recycled Aggregate Using Pre-soaking Approaches* (50(1)). Resources Conservation and Recycling.

Topçu, İ. B., & Şengel, S. (2004). Properties of concretes produced with waste concrete aggregate. *Cement and Concrete Research*, *34*(8), 1307–1312. https://doi.org/10.1016/j.cemconres.2003.12.019

Xiao, J., Li, W., Sun, Z., Lange, D. A., & Shah, S. P. (2013). Properties of interfacial transition zones in recycled aggregate concrete tested by nanoindentation. *Cement and Concrete Composites*, *37*(1), 276–292. https://doi.org/10.1016/j.cemconcomp.2013.01.006

Zaharieva, R., Buyle-Bodin, F., Skoczylas, F., & Wirquin, E. (2003). Assessment of the surface permeation properties of recycled aggregate concrete. *Cement and Concrete Composites*, *25*(2), 223–232. https://doi.org/10.1016/S0958-9465(02)00010-0

Zhang, Z., Zhang, Y., Yan, C., & Liu, Y. (2017). Influence of crushing index on properties of recycled aggregates pervious concrete. *Construction and Building Materials*, *135*, 112–118. https://doi.org/10.1016/j.conbuildmat.2016.12.203

Proceeding: 5th International Conference on
Applied Sciences and Engineering (ICASEA, 2018)
(eISBN 978-967-15744-1-6)
Capthorne Hotel, Cameron Highlands, Malaysia

PERFORMANCES OF SANDWICH MEMBRANE IN RECLAMATION OF WATER FROM FINAL DISCHARGED POME

Nurul Ain Mazlan[1]
Khairul Faezah Md Yunos[1]
Mohd Nazli Mohd Naim[1]
Azhari Samsu Baharuddin[1]

[1]Department of Process and Food Engineering, Faculty of Engineering, University of Putra Malaysia, 43400 UPM Serdang, Selangor.

Abstract : *An investigation was made to examine the performance of sandwich configurations of paired ultrafiltration membranes in reclamation of water from final discharged POME. Two membranes were sandwiched together in different configurations without spacer. Two types of membrane were used in this study which were PES and RC with MWCO 5kDa. The sandwich configurations were known as SS-Sandwich, SB-sandwich, where S indicates that the skin layer faces the feed and B indicates that support layer faces towards the feed. The result of single membrane was compared with both sandwich arrangement. SS-sandwich configuration showed the best permeate quality for PES MWCO 5kDa. The pollutant reduced range up to 80%-90% compared to single membrane which were 60%-70% range. The quality of permeate obtained for total dissolved solid (TDS), suspended solid (mg/L), turbidity, BOD_5, COD, were 535 mg/L, <25 mg/L, 0.88 NTU, BOD5 23.3 mg/L, and 48 mg/L. The quality of permeate from SS-sandwich membrane of 5 kDa was beyond reuse standard and approaching drinking water standard for TSS, TDS and turbidity. Therefore it can be concluded that, water reclaimed from treating final discharged from palm oil mill effluent using ultrafiltration technique with right sandwich configuration at optimum operating conditions was successfully complied with WHO reuse water standard.*

Keywords: *Ultrafiltration, Membrane Fouling, Sandwich Membrane, Reclamation*

Introduction

Palm oil industry is a fast growing industry in Malaysia, as Malaysia is the world's largest producer and exporter of palm oil after Indonesia. However, the production of palm oil consumed tonnes of water and half of it end up as effluent. The raw effluent undergoes further treatment before being discharged to the river. The final discharged can be reused for the plant process and therefore reduced the consumption of fresh water and diminishing the amount of discharged effluent (Nuortila-Jokinen, 1999; Pourcelly and Aslan, 2006; Mänttäri and Nyström, Jonsson and Wimmerstedt, 1985, Afonso and de Pinho, 1995). One of the promising technology to treat and reclaim water from final discharged is UF membrane.

In the last decade, ultrafiltration (UF) is a technology experiencing rapid growth and has been recognized as one of the advanced technology. UF membrane widely implemented in various field of industry such as production of pure water, fractionation or concentration in food, pharmaceutical, biotechnology, as well as wastewater treatment (Choi et al., 2005).

Therefore UF may work as reliable tool in treating final discharged effluent and the water reclaimed from this treatment could be reused for the plant process. Thus, the main advantage lie in reduction of cost for water supply for production process. However, based on previous study, the quality of treated POME does not clearly stated whether permeate achieved standard for water reclamation. For instance, study by Wu et al (2007) combined physical conventional treatment with ultrafiltration to treat raw POME. They successfully achieved reduction of TSS, turbidty, TDS, and COD up to 97.3%, 88.2%, 3.1% and 46.9%. Nevertheless, the results was not clearly reported whether the permeate quality achieved standard of water reclamation. Another study by Ahmad et al. (2003) treated POME with membrane technology which were ultrafiltration (UF) and reverse osmosis (RO). They successfully achieved standard discharged regulations, as the water reclaimed can be recycled back to the plant. However, the application of RO membrane increased the cost of application and maintenance. Hence, it not suitable for industrial application. Besides, most of the literature found, treated the raw POME.

Therefore, the idea of sandwich was proposed in this study, to compensate for the imperfection of the pore size distribution of the available commercial membranes. It has been recognised at the wide pore size distribution of most commercial membrane significantly limit the resolving power of the membranes (Cherkasov and Polotsky, 1996) and the broad pore size distribution reduced the effectiveness of membrane in treatment of final discharged. Besides, as the application of UF membrane might reduce the cost compared to RO membrane. In this study, the effect of sandwich configurations of pair ultrafiltration membrane in treating final discharged to reclaim water were examined. The permeate quality and fouling study was compared with those single membrane configuration.

Materials and methods

POME Sample

Samples of final discharged was taken from a local palm oil mill in FELDA Sungai Tengi, Kota Kubu Bharu, The effluent was collected from a pipe before being released into river. The samples was preserved and stored at a temperature of less than 4°C to avoid biodegradation due to microbial action which may affect the result of the experiment. For the analysis and experimental purpose, the temperature of the sample was allowed to reach room temperature. The characteristics of analysis of final discharged was carried out to evaluate the pH, total solid, suspended solid, dissolved solid, chemical oxygen demand (COD), biological oxygen demand (BOD_5), and turbidity. The analytical methods were conducted based on procedures given in the APHA Standard Method for the Examination of Water and Wastewater (Hammer and JR, 2005). Each analysis was performed duplicated.

Ultrafiltration membranes

Membrane used were flat sheet regenerated cellulose (RC) membrane (Merck Milipore USA) with 28.7 cm^2 effective membrane area and diameter 63 mm and polyethersulfone (PES) with membrane (Sartorius) 28.7 cm^2. Molecular weight cut-off of the membrane used were 5 kDa. 2.3 Experimental Set-up and procedure

The experiments were mainly carried out at a fixed conditions, stirring speed 600 rpm, pressure 1.0 bar and pH 8 the. Two flat ultrafiltration membranes of same type were sandwiched together without a spacer, in several different configurations as shown in Figure 1 below, by varying the arrangement of the skin layer (S) and support layer (B) in the sandwich. For SS-

sandwich configuration both skin layer facing up, meanwhile for SB-sandwich configuration the upper layer facing up and the bottom membrane skin layer facing down.

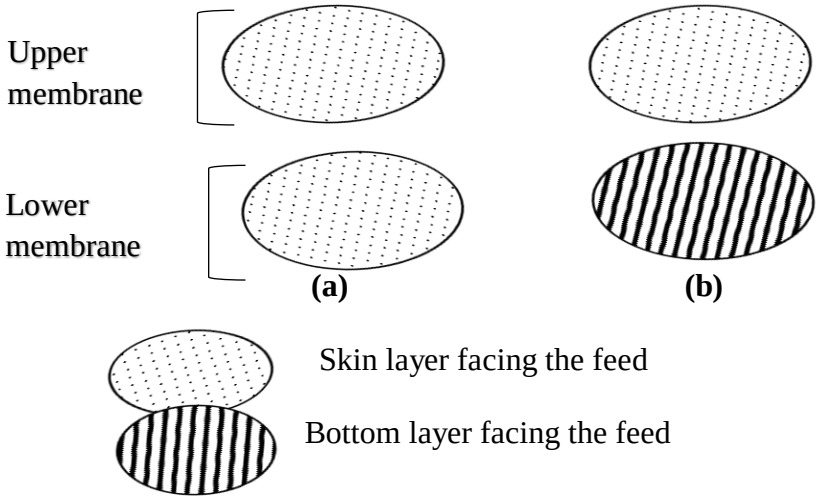

Figure 1: Ultrafiltration Membrane Configurations: (A) SS-Sandwich Membrane (B) SB-Sandwich Membrane.

180 ml of final discharged POME was prepared for each run in ultrafiltration treatment. The experiment performed in batch mode using stirred ultrafiltration cell (Amicon 8200, Milipore USA). For each cycle, the experiment was run in 120 min. The permeate flux was observed by collecting every 20 minutes. The permeate was then further analysed for dissolved solid, turbidity, suspended solid, COD and BOD_5. The details of all analytical methods conducted were based on procedure given in APHA Standard Method for the Examination of Wastewater (Hammer et al., 2005). Each analysis was done twice.

Resistance-in-series model (Tansel et al., 2017)

Darcy's law is used to determine filtration resistance in permeate transport through porous membranes:

$$J = \frac{\Delta P}{\mu R t} \qquad \text{Equation (1)}$$

Where J is the permeate flux ΔP is the trans-membrane pressure (TMP), μ is the viscosity of permeate, and R_t is the total filtration resistance.

R_m is the membrane intrinsic resistance characterized by mainly the pore size and membrane thickness as determined by manufacturing process. Membrane resistance was calculated with the following equation:

$$R_m = \frac{\Delta P}{\mu J w} \qquad \text{Equation (2)}$$

Where R_m is membrane resistance, ΔP is the trans-membrane pressure (TMP), μ is the viscosity of water and J_w pure water flux.

$$R_f = \frac{\Delta P}{\mu p J p} - R_m \qquad \text{Equation (3)}$$

R_f is the most important because it can be reduced by proper techniques in practical application.

Where R_f is membrane fouling, ΔP is the trans-membrane pressure (TMP), μ is the viscosity of permeate and J_w flux of final discharged POME at the end of filtration

$$(R_m + R_p) = \frac{\Delta P}{\mu J a} \quad \text{Equation (4)}$$

Where ΔP is the trans-membrane pressure (TMP), μ is the viscosity of permeate and J_w water flux after membrane was rinsed with distilled water and cleaned with backwash.

Pore blocking resistance was calculated using equation below:

$$R_p = (R_m + R_p) - R_m \quad \text{Equation (5)}$$

While cake resistance was calculated by following equation:

$$R_c = R_f - (R_m + R_p) \quad \text{Equation (6)}$$

Results and Discussion

Effect of sandwich configurations on permeate flux

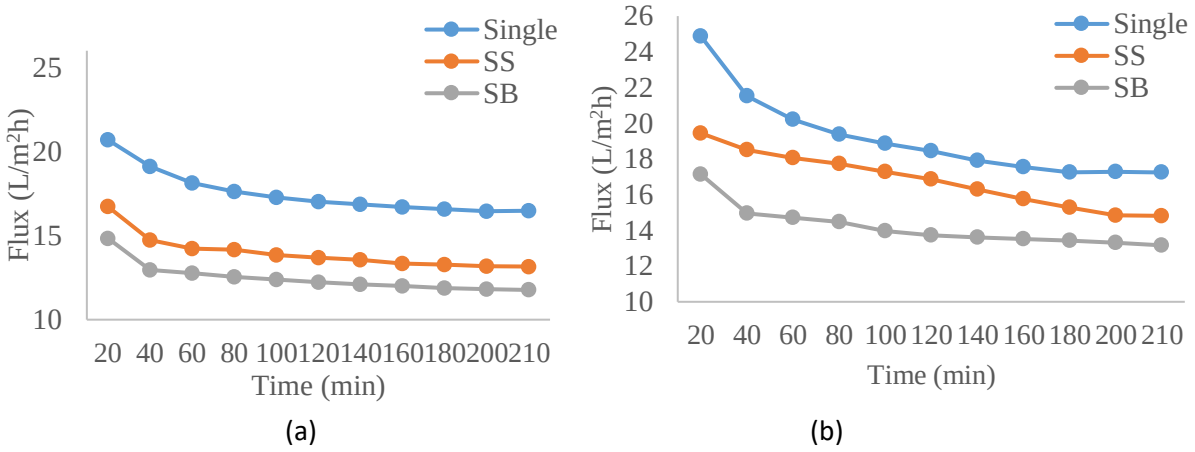

Figure 2: Permeate Flux Of Different Sandwich Configurations (A) PES 5kda (B) RC 5kda

The efficiency of the SS-sandwich and SB-sandwich to treat final discharged POME was evaluated. Figure 2 (a) and (b) compared the permeate flux changes with time between single, SS-sandwich and SB-sandwich membrane for PES and RC membrane. The trend for both configuration of both type of membrane seems to be similar as the permeate flux decreased at early stage of filtration. SS-sandwich membrane experience greater flux decline compared to SB-sandwich, for instance, permeate flux reduction from early to end stage for PES membrane were 30.29% (SS) and 20.7% (SB) respectively and for RC membrane were 31.3% (SS) and 23.2% (SB). It shows that for both type of membrane SS-sandwich experience greater flux decline compared to SB-sandwich membrane. It also suggested that fouling is most likely to occur in SS-sandwich ultrafiltration. The arrangement of SS-configurations which the skin layer of bottom membrane facing the feed increased the possibilities of the solid particles to accumulate on membrane surfaces (Azmi and Yunos, 2014).

Meanwhile, the SB-sandwich configuration results in lower permeate flux than SS-sandwich membrane. This due to reverse direction of bottom membrane caused internal concentration polarization to occur (Field, 2009). The solid particle that build up inside the pores of membrane caused internal intermediate blocking resulted in low permeate flux (Azmi and Yunos, 2014).

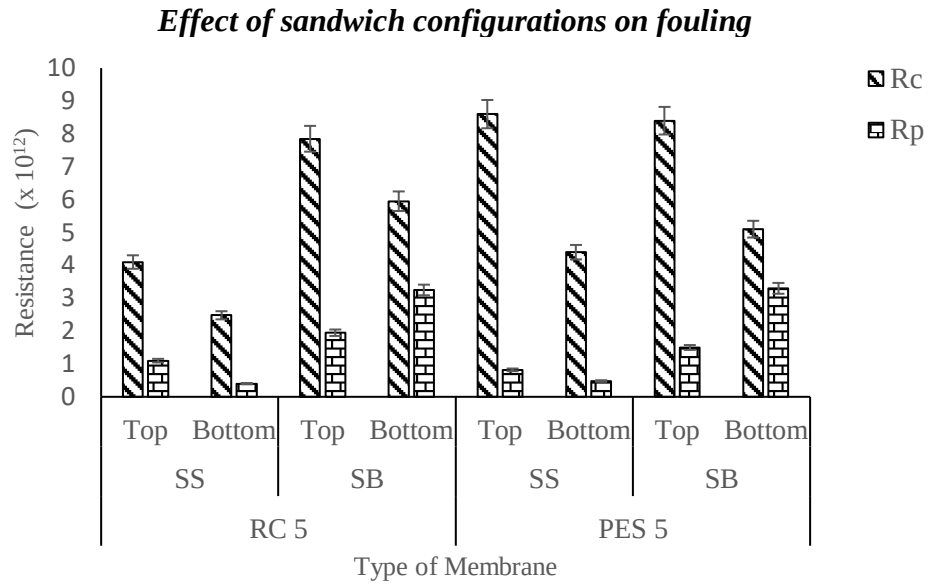

Figure 3: Fouling Resistance Of Sandwich SS-Configuration And SB-Configuration Of Top And Bottom Membrane

As can be seen from Figure 3, when membrane was arranged to SB-sandwich configuration, the cake resistance of upper membrane is higher than bottom membrane. Pore blocking resistance of bottom membrane was higher than top membrane. This is because of the internal concentration polarization most likely to occur when bottom membrane was in reverse direction. Besides, when the support layers with larger pores were arranged towards feed solution, there were more opportunities for the solid particles to enter through these pores (Field et al., 2009). This will caused solid particles which able to pass through the top membrane to build-up inside the pores of the second membrane which resulted in intermediate pore blocking fouling.

Meanwhile, for SS-sandwich configuration, fouling resistance of both R_c and R_p of top membrane was higher than bottom membrane. Both membrane were facing the feed. The particles tend to accumulate on the membrane surface with this arrangement. Since resistances of bottom was reduced, it indicate that the fouling also reduced. There might be some solid particles that able to pass through the membrane was accumulated on the bottom membrane, while most of them was deposited on the top membrane. This proves that the role of second membrane that acts as second barrier suppress the fouling and improve quality of permeate.

Effect of sandwich configurations on permeate quality

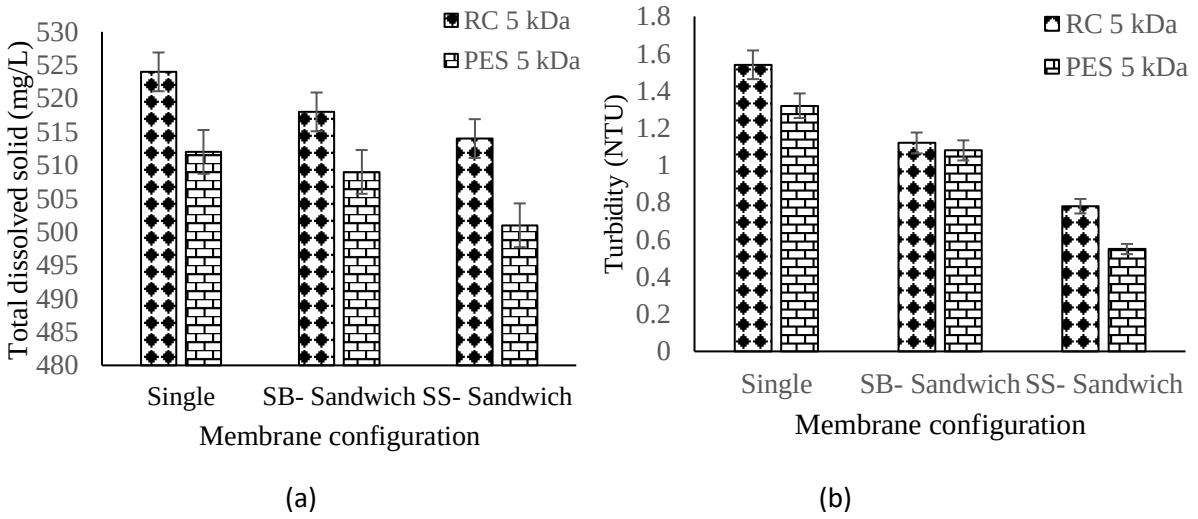

Figure 4: Comparison Of (a) Dissolved Solid And (b) Turbidity In Permeate Of Different Membrane Configuration

Figure 4 (a) above showed that PES membrane consistently showed lowest dissolved solid for all configurations due to hydrophobic characteristics of polyethersulfone typically shows significant surface adsorption (Saha et al., 2006). Dissolved solids tend to adsorp on membrane surface or inside the pores rather than passing through. Membrane with SS-configuration showed lowest dissolved solid concentration compared to SB-configuration. As previously discussed, some dissolved solid particles accumulate on the upper membrane surfaces, some might pass through the first membrane and will accumulate on surface of second membrane. Thus, reduced the possibilities of dissolved solid from passing through the membrane. Besides, dissolved solid concentration at the bottom membrane surface will be less than at the upper membrane surface.

Figure 4 (b) 20 shows only the difference in turbidity between single and sandwich membrane. Generally, all the configurations reduced the turbidity lower than 3 NTU. SS-configurations achieved highest rejection among single membrane and SB-sandwich configuration. From graph above, it can be seen that the lowest turbidity rejection was PES 5kDa membrane by using SS-sandwich configuration. Permeate from this configuration is much clearer if seen by naked eyes. This suggested that SS-configuration was more effective in term of rejecting suspended solid with skin-side-up orientation membrane. Even though this configuration will decreased the permeate flux, the rejection of suspended particles was improved due to the bottom membrane acts as second barrier reduced the possibility of suspended solid to pass through the membrane thus improved the quality of the permeate.

As for SB-configuration, the rejection of particles is lower than SS-configuration. For example the turbidity of PES 5kDa using SB-sandwich turbidity was 1.12 NTU while for SS-configuration was 0.55 NTU. This is due to the fouling which will reduced the flux but improved rejection. For SB-configuration, the bottom membrane in reversed direction, the particles that pass through the upper membrane were clogged throughout the support might be able to penetrate throughout the bottom membrane with the help of transmembrane pressure.

Table 1: Comparison Of Permeate Quality Of Single Membrane, Sandwich Membrane And Water Reuse Guideline

Parameter	Final discharged	5 kDa RC (Single)	5 kDa PES (Single)	5 kDa RC (SS)	5 kDa RC (SB)	PES 5 kDa (SS)	PES 5 kDa (SB)	Final Discharged Limit Standard B	EPA Guideline for water reuse standard
Dissolved solid (mg/L)	890	541	538	535	536	530	533	Not stated	Not stated
Suspended solid (mg/L)	43	<25	<25	<25	<25	<25	<25	≤ 50	≤ 30
BOD_5 (mg/L)	97	33.3	27.7	23.3	28.4	21.8	23.8	50	≤30
COD (mg/L)	170.8	96	62.8	58	62	48	55	100	Null
Turbidity (NTU)	17.6	1.44	1.02	0.88	0.92	0.72	0.58	-	-

Table 1 represents the comparison of the quality final discharged before ultrafiltration, after ultrafiltration with final discharged limit from department of environment and water reuse standard. From the result above, sandwich membrane were effective in improving final discharged compared to single membrane. For example, PES 5kDa membrane, the percentage difference of BOD_5 for permeate after SS-sandwich and SB-sandwich compare to single membrane were 24.9% and 14.08% , for RC 5kDa 30% and 14.7%, Meanwhile, COD value also reduced significantly when compared with single membrane, for instance, PES 5kDa and RC 5kDa using SS-sandwich and SB-sandwich were 23.57%, 12.4%, 39.58% and 35.4% respectively. Dissolved solid concentration which consists of natural organic matter will affected on the BOD_5 and COD values (Wu et al., 2007). The lowest BOD_5 and COD were 21.8 mg/L of permeate was obtained using PES 5kDa with configuration SS-sandwich.

Conclusion

The purpose of this research was to study the performance of sandwich membrane with SS and SB configuration in treating final discharged of POME. The effectiveness of these configurations were evaluated in terms of permeate quality such as dissolved solid, turbidity, COD and BOD_5. From the results it is evident that sandwich membrane treatment process with SS-configuration of PES 5kDa showed the best permeate quality as it able improve permeate quality such as as dissolved solid, turbidity, COD and BOD_5 up to 39.2%, 91.8%, 71.89%, and 77.52% respectively. As a conclusion, the sandwich membrane configuration has shown great potential in reducing some pollutant elements in final discharged compared to single membrane. Besides, the quality of permeate achieved water reused standard thus, can it be reused for many purpose in the mill. Therefore, water security can be sustained and conserved by reclaiming water from final discharge.

References

Afonso M.D., & de Pinho M.N (1995). Treatment of bleaching effluents by pressure-driven membrane processes, a review, in: Caetano, et al., (Eds.), Membrane Technology:Applications to Industrial Wastewater Treatment, *Kluwer Academic Publishers*, pp. 63–79.

Ahmad A.L., Ibrahim N., Ismail S. and Bhatia S.(2003) Removal of suspended solids and residual oil from palm oil mill effluent. *J. Chem. Tech. and Biotech*,78; 971–978.

Azmi, N., & Yunos, K. (2014). Wastewater Treatment of Palm Oil Mill Effluent (POME) by Ultrafiltration Membrane Separation Technique Coupled with Adsorption Treatment as Pre-treatment. *Agriculture And Agricultural Science Procedia*, *2*, 257-264

Chemical, Pharmaceutical, and Biotechnological Applications, CRC Press, Boca

Cherkasov A.N. & Polotsky A.E. (1996) The resolving power of ultrafiltration, *J.Membr. Sci.* 110 (1996) 79–82.

Choi, H., Zhang, K., Dionysiou, D. D., Oerther, D. B., & Sorial, G. A. (2005). Influence of cross-flow velocity on membrane performance during filtration of biological suspension. *Journal of Membrane Science*, 248(1), 189–199.

Field, R. W., Yunos, K. F. M., & Cui, Z. (2009). Separation of proteins using sandwich membranes. *Desalination*, *245*(1-3), 597-605.

Hammer, B. H., & JR, M. J. H. (2005). Water and wastewater technology. Singapore: Prentice Hall.

Jönsson A-S, and Wimmerstedt R. (1985). The application of membrane technology in the pulp and paper industry, *Desalination*, 53:181–196.

Mänttäri M, and Nyström M. (2009). Membranes in the pulp and paper industry, in: A.K. Paddy, A.M. Sastre, S.S.H. Rizvi (Eds.), Handbook of Membrane Separations:

Nuotila-Jokinen, J., Heiskanen, P., Matula, J. (1999) Practical methods to reduce water consumption in a printing paper mill,Wochenbl. Papierfabr, 1392–1395.

Pourcelly G., and Aslan, F. (2006). Industrial liquid effluents in the pulp and paper industry, in: M. Cox, P. Négré, L. Yurramendi (Eds.), A Guide Book on the Treatment of Effluents from the Mining/Metallurgy, Paper, Plating and Textile Industries, INASMETTecnalia On Behalf of the European Commission, Spain pp. 37–73 Raton,

Saha N.K., Balakrishnan, M., Ulbricht. M. (2006) Polymeric membrane fouling in sugarcane juice ultrafiltration: role of juice polysaccharides, *Desalination*,189; 59-70.

Tansel, B., Dizge, N., & Tansel, I. N. (2017). Analysis of high resolution flux data to characterize fouling profiles of membranes with different MWCO under different filtration modes. *Separation and Purification Technology*, *173*, 200-208.

Wu, T., Mohammad, A., Md. Jahim, J., & Anuar, N. (2007). Palm oil mill effluent (POME) treatment and bioresources recovery using ultrafiltration membrane: Effect of pressure on membrane fouling. *Biochemical Engineering Journal*, 35(3), 309–317

Proceeding: 5th International Conference on
Applied Sciences and Engineering (ICASEA, 2018)
(eISBN 978-967-15744-1-6)
Capthorne Hotel, Cameron Highlands, Malaysia

FABRICATION AND PERFORMANCE OF PSF/CA BLEND ULTRAFILTRATION MEMBRANE ON EFFECT OF DIFFERENT POLYMER RATIO

Wan Aisyah Fadilah Wae AbdulKadir[1]
Khairul Faezah Md. Yunos[1]
Abdul Rahman Hassan[2]
Nor Amaiza Mohd Amin[1]

[1]Department of Process and Food Engineering, Faculty of Engineering, University of Putra Malaysia, 43400 UPM Serdang, Selangor
[2]East Coast Environmental Research Institute (ESERI), Faculty of Industrial Design & Technology, Universiti Sultan Zainal Abidin (UniSZA), Kampus Gong Badak, 21300 Kuala Nerus, Terengganu Darul Iman.
Correspondence to: Khairul Faezah Md Yunos (kfaezah@upm.edu.my)

Abstract: *The study is focussed on the fabrication of various polysulfone/cellulose acetate (PSf/CA) polymer ratio with high polymer concentration of 20 wt. % via dry/wet phase inversion technique for membrane performances. These membranes were prepared by blending four different polysulfone/cellulose acetate ratios of 100/0, 90/10, 80/20 and 70/30 in a solvent, known as N-methyl-2-pyrrolidone (NMP). The effect of different polymer ratio on membrane characteristic are discussed in term of flux permeation, morphology, mechanical strength, fourier transform infrared spectroscopy (FTIR) analysis and flux recovery ratio (FRR). The increment of cellulose acetate composition resulted in different behaviours of membrane characteristic. The highest CA ratio (70/30) in PSf/CA composition obtained the highest flux permeation. Meanwhile, the flux recovery of 90/10 wt % membrane achieved the highest flux recovery, 59 % compared to 80/20 wt. % and 70/30 wt. % membranes with values of 12 % and 25 %, respectively. Interestingly, membrane with 80/20 wt. % observed an average improvement in flux permeation with a consistent increased. The formation of uniform finger-like voids in the sublayer of this membrane (80/20) encouraged a good mechanical strength for the membrane structure.*

Keywords: *Blend Membrane, Polysulfone, Cellulose Acetate, Polymer Ratio*

Introduction

Membrane technology has become an alternative and well-known separation technique due to fast process operation, energy efficient and no involvement in any phase change or chemical additives. This advance technology is used in various field such as food, chemical, and pharmaceutical industries (Sivakumar et al., 2005; Sivakumar et al., 2006). The polymeric membrane can be tailor-made in order to obtain the desired pore size distribution. The certain drawbacks of single polymer in the membrane matrix such as hydrophobic characteristic has gained importance and this is improved by fabricating a membrane with multiple components (Kalaiselvi et al., 2013; Kumar et al., 2013). The addition of blending multiple components not only alters the membrane properties but also enhances the flux permeation of the membranes (Arthanareeswaran et al., 2004; Sivakumar et al., 2005). However, the membrane properties are still influenced by the compatibility of the individual polymers with each other and the mixing technique (Sivakumar et al., 2005). The compatibility of the hydrophobic-hydrophilic

balance with the membrane properties can be significantly changed if the membrane is fabricated from multicomponent polymer blends (Moradihamedani & Abdullah, 2017). The combination of cellulose acetate (CA) and polysulfone (PSf) is represented the use of polymer blend membrane that consists of hydrophilic and hydrophobic polymers. Hence, an investigation on the performance of PSf membrane with a hydrophilic polymer has been made to enhance the hydrophilicity of the membrane (Sivakumar et al., 2006).

Polysulfone (PSf) is the most preferred polymer in the fabrication of ultrafiltration membrane. It has excellent mechanical property, a very good chemical and thermal stability as well as high rigidity and creep resistance (Arthanareeswaran et al., 2010; Bowen et al., 2001).
However, the hydrophobic characteristic of PSf polymer has led to the limitation in practical application. Therefore, hydrophilic polymer or additional component has become one of the most approachable materials for membrane modification as blending method is also identified as an attractive route to improve antifouling properties of the membrane (McCloskey et al., 2012). The studies have proved the ability of the cellulose acetate polymer to impart high hydrophilicity to a membrane by reducing fouling properties of the membrane (Saljoughi et al., 2009; Sossna et al., 2007). Besides, CA has high biocompatibility, good toughness, high potential flux and relatively low cost (Saljoughi et al., 2009). Meanwhile, the limitations of CA which are low oxidation and chemical resistance, poor mechanical strength and not applicable in aggressive cleaning can be altered by blending with PSf polymer which facilitates the development of new material with the combination of polymers properties.

Hence, a study on membrane fabrication of polysulfone and cellulose acetate at high polymer concentration (20 wt. %) and the performance of fabricated membranes are reported. The effect of polymer ratios in the polymer matrix on flux permeation, morphology, mechanical strength and flux recovery are discussed and compared with the pure PSf membrane.

Experimental

Materials and methods

Polysulfone (PSf, Ultrason E2010) was supplied by BASF (Ludwigshafen, Germany) in pellet form and used after drying at 60 ^{0}C for 24 hrs. Cellulose acetate (CA, M_w= 100,000 Da) in form of powder was purchased from Acros Organics. N-methyl-2-pyrrolidone (NMP) was obtained from Merck (Germany) and used as a solvent. Distilled water was provided as a non-solvent while ethanol and n-hexane from Merck (Germany) was used as the additional washing step after casting. Bovine serum albumin (BSA, Mw= ~66,000 Da) was received from Sigma Aldrich and used as a module solution for the flux recovery test. Disodium hydrogen phosphate dehydrates ($Na_2HPO_4.2H_2O$) and sodium dihydrogen phosphate monohydrates ($NaHPO_4.2H_2O$) were purchased from Merck (Darmstadt, Germany). Nitrogen gas was supplied by Stable Arm Sdn. Bhd. while other chemicals were commercially analytical grade and used without purification.

Blend membrane preparation

The casting solution of 20 wt. % was prepared by blending different polymer ratios of polysulfone (PSf) and cellulose acetate (CA) in a solvent, known as N-methyl-2-pyrrolidone (NMP) (Table 1) under continuous stirring at 60 ^{0}C for 8 hrs. After the heating process of casting solution was completed, it was kept at rest until no air bubble presence. The casting solutions were then cast on a glass plate with the help of a casting knife by non-solvent induced phase separation (NIPS) technique (Borneman, Gokmen, & Nijhuis, 2001). The thickness of

the spread casting solution was maintained to 200 µm (0.20 ± 0.05 mm) and immediately immersed into coagulation bath (water) at room temperature. The solidified membrane was kept in water for 24 hrs to remove the residual of solvent. Then, this was continued with the additional washing steps with ethanol and n-hexane. In ethanol, this membrane was immersed for another 24 hrs while in n-hexane for a continuous 2 hrs of the washing steps. The membranes were dried for 1 to 3 days at room temperature before undergoing the testing processes.

Table 1: Formulation Of Blend Polymer Ratio Membrane

Membrane	Polymer (20 wt. %)		Solvent (wt. %)
	PSf	CA	NMP
PSf	100	0	80
PSf/CA-10	90	10	80
PSf/CA-20	80	20	80
PSf/CA-30	70	30	80

Characterization

The permeation studies were carried out using a dead-end stirred cell filtration system (Amicon stirred cell, 200 ml). The permeation studies involve compaction test and pure water permeation test. The compaction test of the blend membranes with an effective area of 28.7 cm^2 was initially pressurized with distilled water at 150 kPa for 2 hrs. The water flux was evaluated every 30 mins and continued with pure water permeation test at different transmembrane pressure within 100 to 300 kPa (Hamzah et al., 2014). The flux is calculated using equation (1) (Moradihamedani & Abdullah, 2017; Sivakumar et al., 2006).

$$J_{w1} = \frac{Q}{A \times t} \quad (1)$$

where, Q is the permeate volume (L); A is the membrane area (m^2); and t is the time (h).

The morphology analysis of the blend PSf/CA membranes were captured using Scanning Electron Microscopy of NOVA NANOSEM 230 with User-Friendly Windows xT Software. The membrane were cut and fractured in liquid nitrogen. The fractured membranes were then sputter-coated with gold for 1 to 2 min(s). The cross-section images of the blend membranes were obtained at different magnifications.

The functional groups and chemical structures of the blend membranes were identified using Fourier Transform Infrared Spectroscopy (FTIR) of Varian 3100 FTIR Excalibur Series. The dried membranes were cut into size of 1 cm x 4 cm. These membranes were held in the sample holder and the results were analysed in the transmittance mode. Each bands represent the functional groups of the components presence in the membrane. Different functional groups are represented at different range of infrared radiation wavelength.

The mechanical strength of these blend membranes were measured using TA-XT plus Texture Analyser by Texture Exponent Software Version 2.0.7.0 (Stable Microsystems, Godalming, UK) with stretching rate of 5 mm/min at room temperature. The samples were cut to the size of 63.5 mm x 12.7 mm according to the ASTM D256 standard.

Fouling study

Fouling resistance was studied using stirred cell filtration system. The experiment was carried out with BSA solution to measure the flux recovery ratio (FRR) of the membranes. The BSA solution was prepared at concentration of 0.1 wt. % in phosphate buffer (0.5 M, pH 7.1). The water flux before (J_{w1}) and after (J_{w2}) filtration of BSA solution were calculated at 150 kPa for 30 mins of 5 mins interval. Meanwhile, the intermediate flux of BSA permeate was performed at the same pressure for 1 hr. The backwashing process with distilled water was performed at 200 kPa for 20 mins before continuing with the measurement of water flux of cleaned membrane. The FRR results were calculated to identify the fouling resistance of the membrane using equation (2) (Borneman et al., 2001; Conidi, Cassano, & Drioli, 2011).

$$\text{FRR } (\%) = \left(\frac{Jw2}{Jw1}\right) \times 100\% \qquad (2)$$

where, J_{w1} is the water flux of neat membrane (Eq.1) and J_{w2} is the water flux of cleaned membrane.

Results and Discussion

The results of the blend membranes analysis were explained and discussed. The main focus of this paper is to present the effect of the cellulose acetate composition ratios in the base PSf polymer matrix toward the fouling resistance and the performance behaviour.

Effect of compaction time

The blend membranes of several compositions ratios were compacted with distilled water at 150 kPa for 2 hrs. The water flux of the blend membranes from PSf/CA composition of 100/0 to 70/30 wt. % at different compaction times is presented in Figure 1.

Figure 1 proved that the water flux of blend membranes decrease with increasing compaction time for all polymer ratios. The final 60 mins of compaction times shows an insignificant changes in water flux for PSf, PSf/CA-10 and PSf/CA-20 membranes. This indicates that the blend membranes have approached a complete compaction in the last 60 mins. The decline water flux at the early stages of compaction can be assigned to the reduction in the porosity volume as the arrangement of polymer segments and chains become closer during the compaction process (Sivakumar et al., 2005). However, membrane with polymer ratio of 70/30 wt. % has obtained a sharp reduction after 90 mins of compaction times which is from 89.9 $Lm^{-2}h^{-1}$ to 69.0 $Lm^{-2}h^{-1}$. This is suggested due to the high hydrophilic CA composition that requires extra compaction times for the rearrangement of polymer chains to reduce the porosity volume. High ratio of CA had caused the formation of larger size of pores in the membrane sublayers due to less miscibility of PSf and CA nature. Thus, a high water flux is observed for membrane with 70/30 wt. % composition. Similar relation has reported in a study on the addition of polysulfone in base cellulose acetate polymer blend membrane (Sikder et al., 2009).

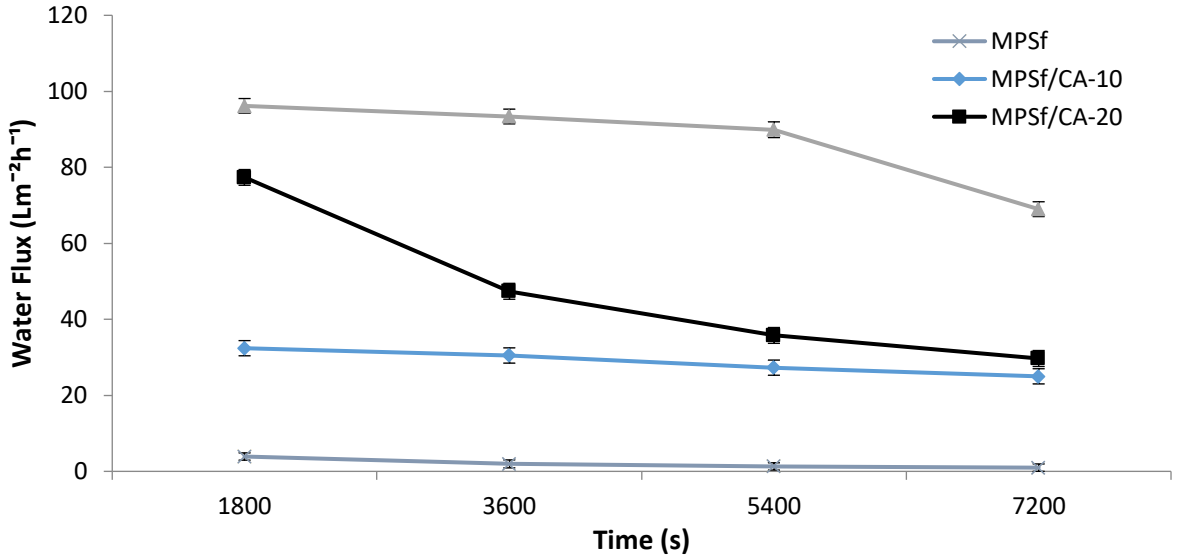

Figure 1: Effect Of Compaction On Water Flux Of Polymer Ratios Blend Membranes

Furthermore, an increase in CA in the casting solution of blend membranes from 10 to 30 wt. % of total polymer has increased the water flux from 3.9 $Lm^{-2}h^{-1}$ to 96.2 $Lm^{-2}h^{-1}$. The relatively higher water flux of the blend membrane with higher CA ratios may occur from a small change of amorphous nature. The higher free energy of the blends had caused a low interaction between PSf and CA chains (partial compatibility) which led to a larger segmental gaps between both polymers (Sivakumar et al., 2005). Likewise, the increase in CA ratios has increased the glass transition temperature, T_g of the blends as PSf has lower T_g than CA which caused the alteration of polymer matrix properties from hard to soft segments (Mahendran et al., 2004). Hence, a higher water flux has been observed for blend membranes with higher CA ratios.

Effect on pure water permeation

The water flux of compacted membranes was measured by the time required for a selected volume of water permeation. Therefore, the effect of cellulose acetate ratios in the casting solution of PSf/CA composition on the pure water permeation (PWP) of the blend membranes are represented in Figure 2.

The blend membrane with 100/0 ratio of PSf/CA composition obtained the lowest flux within the transmembrane pressure (TMP) of 100 to 300 kPa. Further, the water flux of this PSf membrane increases from 6.4 $Lm^{-2}h^{-1}$ to 47.0 $Lm^{-2}h^{-1}$ with increasing TMP. From Figure 2, the increment of CA ratios in the PSf base matrix starts to significantly increase at 150 kPa and above. The addition of CA ratios from 10 to 30 wt. % of total polymer have increased from 47.0 $Lm^{-2}h^{-1}$ to 406.8 $Lm^{-2}h^{-1}$ at 300 kPa of the highest TMP. The influence of CA composition in the casting solution has two main changes on the properties of the blend membrane: (a) improves hydrophilicity and (b) modifies membrane behaviour/morphology. This is acknowledged by the study on the effect of polyethersulfone (PES) in cellulose acetate phthalate blend membrane (CAP) (Rahimpour & Madaeni, 2007). Moreover, the addition of CA improved the hydrophilicity of the membrane and also induced the formation of macrophase in the membrane sublayer which leads to increase the size of membrane pores. The low molecular attractive forces between CA and PSf composition has caused low miscibility between both components which also relates to the formation of larger pore size (Sivakumar et al., 2005). The low viscosity of the membrane solution speeds up the diffusional exchange rate

of the solvent and the non-solvent (Razzaghi et al., 2014). Hence, this enhances the flux of the blend membranes with the addition of higher ratios of cellulose acetate.

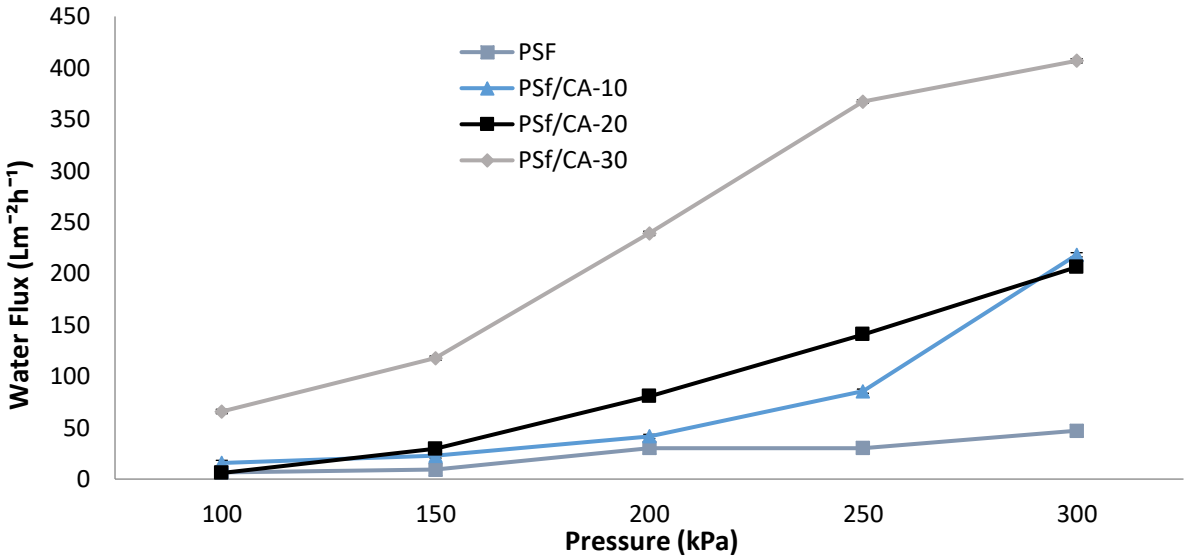

Figure 2: Effect Of The Polymer Ratios On Pure Water Permeation

However, the membrane with 90/10 ratio of 20 wt. % has slightly increased the flux to 218.2 $Lm^{-2}h^{-1}$ compared to 80/20 ratio with value of 206.2 $Lm^{-2}h^{-1}$ at 300 kPa. This happened due to the unstable polymer molecules reaction toward high pressure which reduced compatibility of two different polymers in the casting solution. The less compatible polymers matrix in the casting solution at high pressure would lead to high affinity of blends separation and increased the size of voids in rich polymer regions (Razzaghi et al., 2014). Interestingly, the high concentration (20 wt.%) of polymer matrix of PSf/CA polymer ratio obtained a better flux permeation than the previous study of PSf/CA membrane with 85/15 of 15 wt.% with value of 9.8 $Lm^{-2}h^{-1}$ at 345 kPa (Sivakumar et al., 2006). Besides, the reverse composition of CA/PSf at 80/20 ratio of 17.5 wt. % also obtained a lower flux with value of ~39.0 $Lm^{-2}h^{-1}$at 300 kPa (Sivakumar et al., 2005). This study explored the possibility of increasing PSf polymer had also increased the hydrophobicity of the membrane and resulted in lower flux permeation. Thus, this concludes that CA polymer has the ability to enhance the hydrophilicity of the blend membranes at high polymer concentration depending on the use of molecular weight of supplied CA polymer.

Effect on membrane morphology

The cross-section images were captured by scanning electron microscopy (SEM) on PSf/CA polymer ratios membranes of 100/0, 90/10, 80/20 and 70/30 wt. %. The qualitative results are illustrated in Figure 3 which describes the morphology of each blend membranes on the effect of CA ratios composition. The blend membranes show an asymmetric structure with selective and supporting layers (Hamzah et al., 2014).

The neat PSf membrane (Figure 3 (A)) exhibits a dense skin layer with a small area of sponge-like structure. The image shows micropores finger-like structures in the top layer while a few and large size of finger-like structures in the bottom layer. The neat PSf seems to have less porosity volume compared to other blend membranes with CA compositions. The hydrophobic characteristic of this polymer leads to the less porosity volume of the PSf membrane. This

occurred when high polymer concentration increased the viscosity of the casting solution which inhibited the diffusional exchange rate of NMP (solvent) and water (non-solvent) in sublayer (Hamzah et al., 2014). Thus, it reduced the rate of precipitate exchange and decreased membrane porosity.

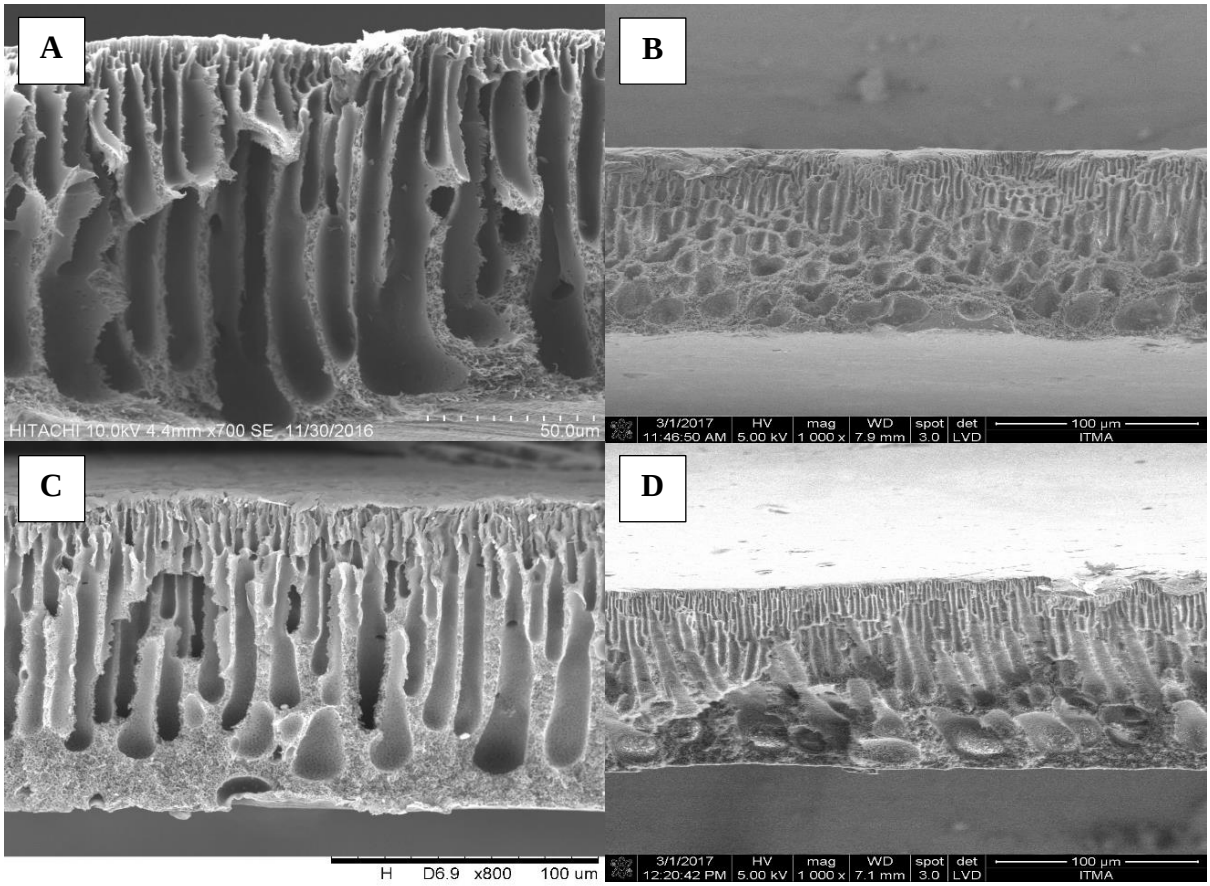

Figure 3: SEM Images Of Blend Membranes. Cross-Section (700 To 1000x); (A) 100/0; (B) 90/20; (C) 80/20; (D) 70/30 Of Psf/CA Polymer Ratios.

The addition of CA ratios in casting solution (Figure 3 (B), (C), and (D)) have obviously altered the morphology of blend membranes. The images displayed macrovoid and porous finger-like structures. Both of PSf/CA-10 (Figure 3 (B)) and PSf/CA-30 (Figure 3 (D)) membranes show a quite similar morphological structure with a combination of finger-like voids and macrovoid for the top and bottom layers of the membranes. However, PSf/CA-10 membrane has a denser skin layer compared to PSf/CA-30 membrane due to the composition of CA polymer. The lower ratio of CA exhibits lower flux permeation. This could be related to the interaction of the polymer matrix and the solvent as well as the kinetic of phase inversion which influenced the morphology of the blend membranes (Amirilargani et al., 2012). This phenomenon was due to an instantaneous demixing during the immersion process of the top surface of the skin layer with the water (non-solvent) and after a while, a delayed demixing occurred due to low exchange rate between solvent and non-solvent (Tseng et al., 2012). Thus, the finger-like voids were formed in the top layer while the delayed demixing had caused the formation of small macrovoid with sponge-like structures in the bottom layer. A previous study reported that the formation of macrovoid might occur when the viscosity of the casting solution was high and it led to a sudden collapsed of finger-like structures formation (Amirilargani et al., 2012). This is

suggested that the morphology of membrane with PSf/CA ratios of 90/10 and 70/30 have exposed to high composition of PSf and CA polymers which caused inconsistency in flux permeation.

Interestingly, the morphology of membrane with 80/20 wt. % was significantly different. The morphology of this membrane was observed to form a uniform finger-like structures with fine tune arrangement. The voids of top and bottom layer are connected to each other. The uniform finger-like voids have seemed to assist the gradual trends of the water flux permeation in the previous sections. Hence, the appropriate selection of 80/20 of PSf/CA ratio has facilitated a good interaction between polymer matrixes during demixing process that formed a well-formed morphology of PSf/CA-20 blend membrane.

Effect on FTIR analysis

Fourier transform infrared (FTIR) was used to analyse specific functional groups and chemical bonds that presence in casting solutions (Ismail et al., 2002; Moradihamedani & Abdullah, 2017). The FTIR spectrum of neat PSf, CA and PSf/CA are presented in Figure 4 (a) to (c).

The existence of PSf in the PSf/CA composition was assigned by the two small transmittance bands at wavenumbers 1294.92 cm^{-1} and 1323.42 cm^{-1}. These bands represent the asymmetric and symmetric stretching mode of sulfonate group. The asymmetric band has slightly stretched to 1294.95 cm^{-1} while symmetric band has slightly bent to 1323.37 cm^{-1} as observes in Figure 4 (c). This changes was claimed due to the existence of multicomponent in casting solution that encouraged the interaction with sulfonate chain. The previous studies had reported the same reason for the modification of PSf membrane (Moradihamedani & Abdullah, 2017; Moradihamedani et al., 2014). Furthermore, the presence of PSf polymer can be determined by the wavenumbers of aliphatic stretching CH_3 and a strong aromatic ether between 3000 to 2800 cm^{-1} and ~1240 cm^{-1}, respectively (Koehler et al., 2000). Besides, the CO bond of PSf chain bands (~1106 cm^{-1}) do not significantly change after adding CA composition in the polymer matrix. Meanwhile, the intensity of the strong aromatic ether is slightly bent when adding CA composition ratio in the casting solution. This is suggested that the interaction of OH bonds (3452.84 to 3366.94 cm^{-1}) in CA chain with the strong aromatic ether in PSf chain has influenced the intensity of the bands form. The phenomenon is proved by the wavenumber of OH bond in pure CA membrane has bent to 3366.94 cm^{-1} after blending PSf and CA together which shows the remaining of OH bonds have decreased in the polymer matrix.

In addition, the presence of CA polymer has been identified by wavenumbers of a small band at approximately between 2700 to 2900 cm^{-1} for CH_2 group and OH bonds around 3500 cm^{-1} (explained in above paragraph) (Moradihamedani & Abdullah, 2017; Pielesz & Binias, 2010). However, the interaction between aliphatic CH_3 of PSf and CH_2 group of CA has shifted the band to 2969.57 cm^{-1} after blending the PSf/CA composition. The significant bands of pure CA membrane at 1065 to 1041 cm^{-1} and ~1746 cm^{-1} are assigned for C-O-C ether chain and carbonyl group (C=O) (Ismail et al., 2002; Moradihamedani & Abdullah, 2017). The unstable double bound of carbonyl group has encourage PSf chain to bind with CA chain which shifts the C=O band to 1738.77 cm^{-1}. The attraction between the molecules inside casting solution had suggested to cause surface segregation which is due to the amphiphilic nature of membrane materials. The affinity of multicomponent materials toward the non-solvent (water) has facilitated the arrangement of hydrophilic segment of membrane materials chain on the membrane surface while the hydrophobic segment of them are intensely embedded in

membrane matrix (Razzaghi et al., 2014). Hence, the amphiphilic PSf/CA membranes produce a higher water flux permeation compared to the neat hydrophobic PSf membrane.

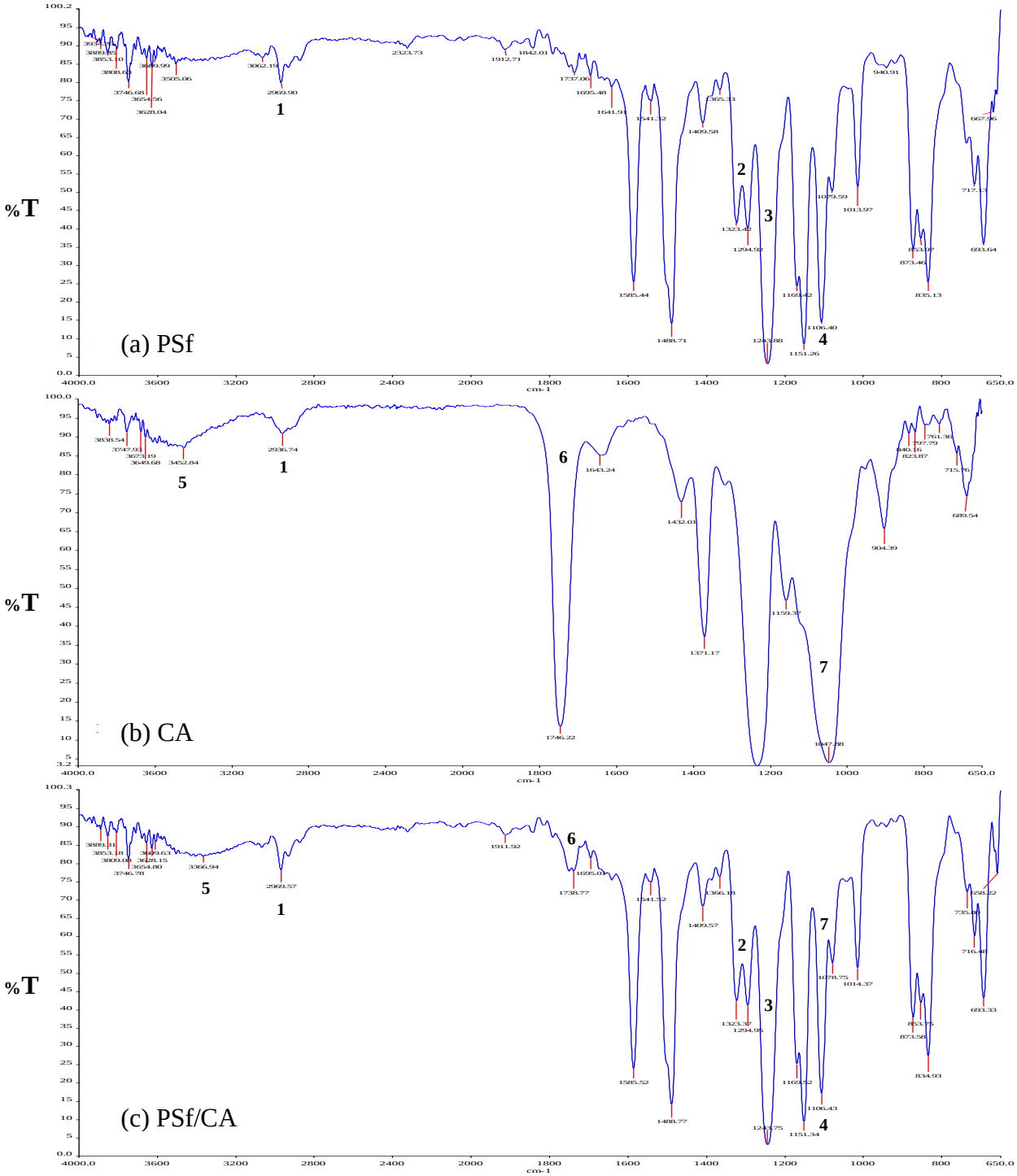

Figure 4: (A) To (C) Represent The FTIR Spectra Of Membrane With Absence And Presence Of Psf And CA Polymers. (1) Aliphatic CH_3 In Psf And CH_2 Group In CA; (2) Sulfonate Group In Psf; (3) Aromatic Ether In Psf; (4) CO Bond In Psf; (5) OH Bond In CA; (6) Carbonyl Groups (C=O) In CA; (7) Ether Chain (C-O-C) In CA

Effect on mechanical properties

The addition of CA in the casting solutions has observed a slight reduction of the mechanical strength of the blend membranes compared to the neat PSf membrane. The lower mechanical strength of CA than PSf polymer has changed the mechanical properties of the blend membrane (Razzaghi et al., 2014). This reduction was due to the entrapment of CA in the polymer matrix which facilitated the formation of voids in the sublayer of blend membrane.

Figure 5 shows the tensile strength of blend membranes, specifically, neat PSf, PSf/CA-10, PSf/CA-20 and PSf/CA-30 which is slightly decreased from 5.1 MPa to 4.7 MPa, 4.7 MPa and 4.9 MPa, respectively. Interestingly, the trend shows that a higher CA ratio obtains a higher tensile strength. The results can relate with the morphology of blend membranes. The numerous finger-like voids in the top layer and small macrovoid in the bottom layer prompted different strength to the membrane structure of PSf/CA-30. The separated voids might help in improving the tensile strength due to the fine arrangement of finger-like voids in the top layer. However, the addition of CA in the casting solution still reduced the tensile strength of blend membranes due to the low mechanical stability of CA polymer which influenced the thickness of the blend membrane (Idris & Ahmad, 2011). Thus, the blend membranes with CA ratios have lower tensile strength than the neat PSf membrane.

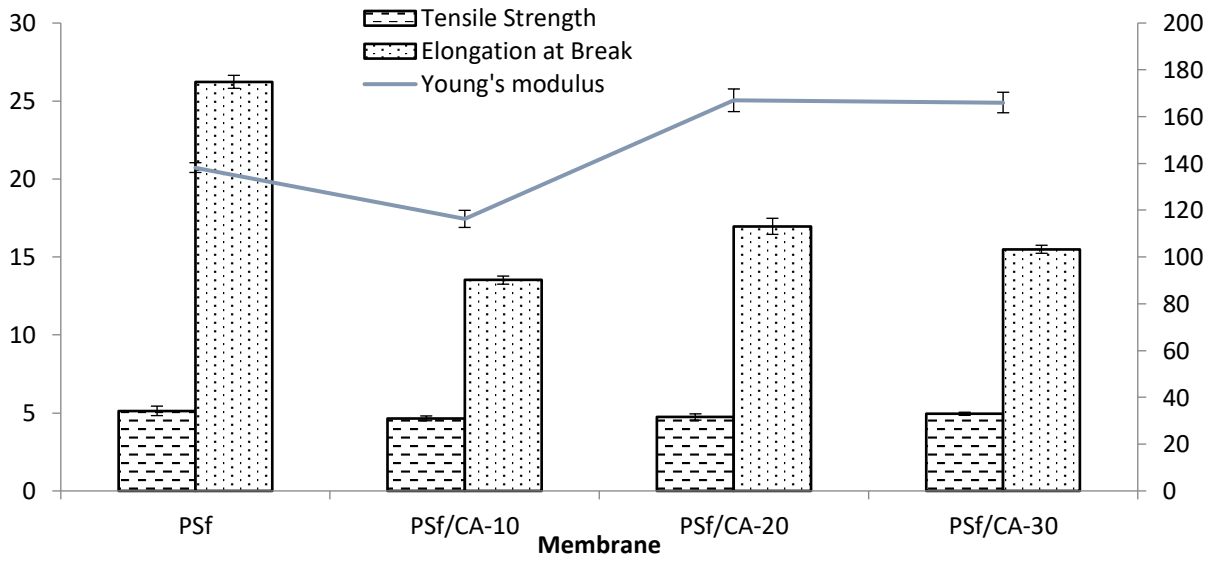

Figure 5: Mechanical Strength Of The Different Polymer Ratios Membranes; Tensile Strength, Young's Modulus And Elongation At Break

A quite similar trend is observed for Young's modulus which shows a fluctuate trend due to the results of elongation at break of blend membranes. The addition of different ratios of CA polymer have reduced the elasticity of the blend membranes as shown in Figure 5. The elasticity of these membranes represent by the elongation at break that decrease from 26.2 % (100/0) to 13.5 % (90/10), 17.0 % (80/20) and 15.5 % (70/30) with increasing CA ratios. However, the addition of CA composition more than 10 % obtains higher elasticity. This explained that the formation of connected finger-like voids from top to bottom layers of PSf/CA-20 membrane has enhanced the elasticity of the membrane structure. Thus, it obtains the highest elasticity compared to 90/10 and 70/30 of CA composition ratios that have macrovoid in the sublayer. However, the highest mechanical strength for the neat PSf membrane is claimed due to the original characteristic of the PSf polymer which has high

strength, rigidity, creep resistance and dimensional stability. This advantages come from the replicating phenelyne rings that presence in the PSf chain (Padaki et al., 2012). Therefore, the morphology of membrane structure has significantly played an important role for the improvement of mechanical strength of the blend membrane. This concludes that the ratio of 80/20 wt. % has a better mechanical strength compared to other blend membranes as it tends to have a greater stretching rate.

Effect on fouling resistance

Fouling study was investigated for further analysis on the different polymer ratios of blend membranes with bovine serum albumin (BSA). The fouling study focuses on the flux recovery ratio (FRR) which represents the surface modification of the blend membranes. In general, the higher the FRR values, the higher the hydrophilicity and antifouling properties of the blend membranes (W. Zhao et al., 2008). FRR values of the blend membranes is presented in Figure 6 (b). The intermediate process between BSA solution filtration and final flux permeation was carried out by backwashing process in order to evaluate a flux of cleaned blend membrane. Thus, the efficiency of the backwashing process can be determined by FRR % parameter for clarification of antifouling property of the blend membranes (Peeva et al., 2011).

The initial flux shows an increasing trend with the addition of higher CA composition ratios while the final flux obtains a different behaviour as seen in Figure 6 (a). The final flux is observed to have higher flux for the blend membranes with higher CA ratios. This behaviour was claimed due to the unstable casting solution which altered the membrane morphology after experienced the backwashing process. The high pressure during backwashing process had disturbed the pore structures. The weak interaction between two polymers in the membrane matrix encouraged the formation of macrovoid (Chakrabarty et al., 2008; S. Zhao et al., 2011) in PSf/CA-10 and PSf/CA-30 which was suggested to occur due to the accumulation of CA molecules in the bottom layer of the blend membranes. Moreover, the presence of second polymer changed the condition of casting solution closed to liquid-liquid demixing boundary which reduced the degree of solubility between polymer matrix and solvent (Aryanti, Khoiruddin, & Wenten, 2013; Reuvers, Berg, & Smolders, 1987). Therefore, these show a possibility of the flux permeation to be affected after BSA permeation and backwashing process.

Furthermore, PSf/CA-30 has no permeates volume for flux calculation. This membrane is observed to be easily fouled. This can be explained by physicochemical properties of the membrane and the feed solution (BSA). The severe fouling might occur when pH of the protein solution was equal to the iso-electric point of the protein and reduced the flux permeation (Ricq, Narc, Reggiani, & Pagetti, 1999). However, a higher and lower pH of the protein solution than the iso-electric point enhanced the flux permeation (Huisman et al., 2000). This clarified that the possibility of BSA solution to obtain an equal value with it iso-electric is high. Besides, the previous study had argued on the hydrophobic behaviour of the protein at the iso-electric point which led to high adsorption on the membrane due to the hydrophobic interaction (Nystrom et al., 1994; Ricq et al., 1999). Therefore, it is clearly assumed that the physicochemical properties between membrane and BSA solution has disturbed the pH and experienced high adsorption in the voids layer of PSf/CA-30 blend membrane.

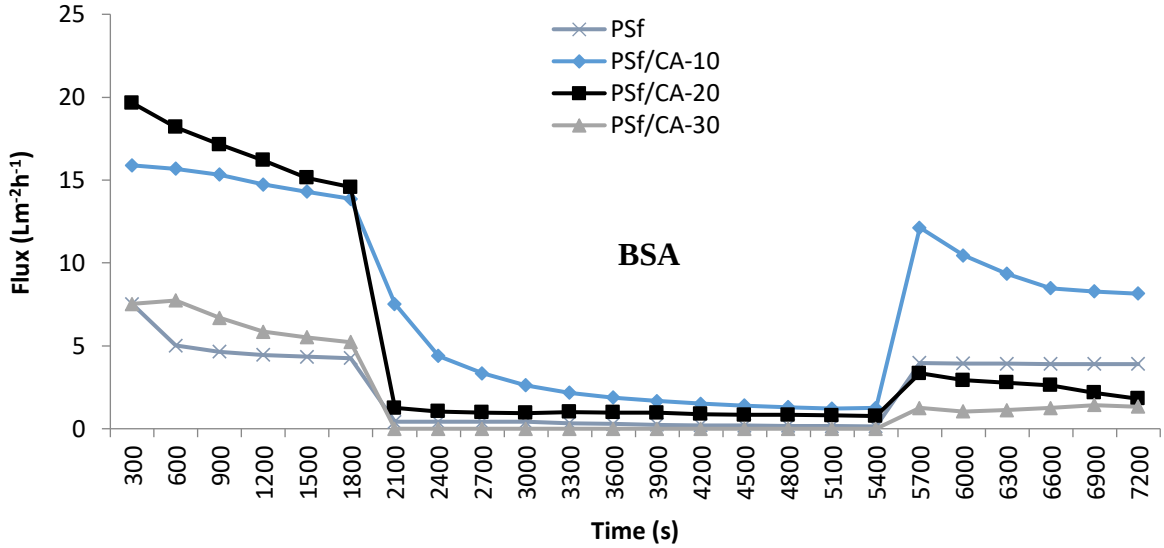

Figure 6 (A): Time-Dependent Flux For Blend Membrane Composition With Different Polymer Ratios. The Ultrafiltration Process Includes Permeation Of Initial Water Permeation, BSA Solution Permeation And Final Water Permeation After Backwashing Process

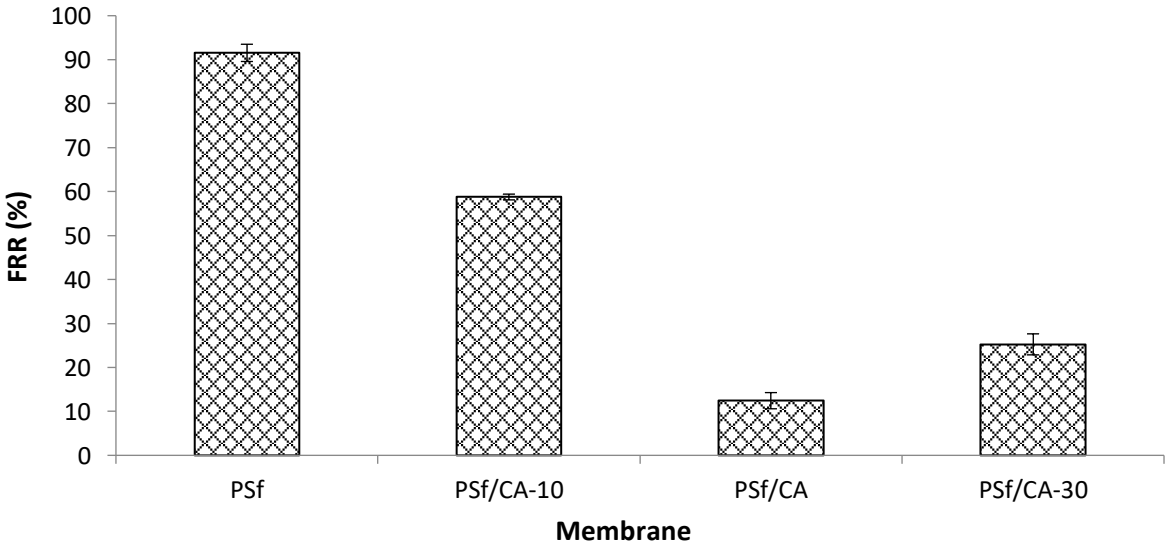

Figure 6 (B): Percentage Of Flux Recovery Ratio (FRR) Of Blend Membranes With Different Polymer Ratios After BSA Solution Permeation

From Figure 6 (b), PSf/CA-10 obtains the highest FRR value (59 %) among the blend membranes with CA ratios. The high pressure during backwashing process has assisted the flux recovery of final flux that observes to achieve merely close to the initial flux. The unstable pore structures of this membrane causes a low separation of BSA molecules as it reaches a higher permeate flux at the first 20 mins of BSA permeation. Thus, it is said that PSf/CA-10 membrane has exposed to reversible fouling which can be removed by physical cleaning (Razzaghi et al., 2014). However, PSf/CA-20 with 20 % of CA ratio has the lowest FRR value of 12 %. This significant reduction was due to the fine arrangement and connected sublayer of finger-like voids which caused a direct blockage of BSA molecules. This pores blockage might need several hours to be completely removed by physical cleaning due to the excessive of BSA molecules inside each finger-like voids which had resulted in a lower final flux permeation compared to the highest initial flux. Moreover, PSf/CA-30 has achieved approximately half of

the FRR value of PSf/CA-10 membrane which is 25 %. The increase of CA ratio up to 30 % has increases the hydrophilicity of blend membrane. The increment of hydrophilic characteristic causes a larger size of pores. However, increase in pore size has increased the effect of fouling (Razzaghi et al., 2014). The increment in pore size was declared to induce an accumulation of BSA molecules in certain pores especially in macrovoid structures. Besides, the explanation on the severe absorption of solute molecules in previous paragraph had also proved the reason of flux reduction. Hence, a higher FRR % was obtained by PSf/CA-30 compared to PSf/CA-20. This concludes that the morphology of different types of voids in membrane sublayer facilitates the flux recovery of the blend membranes as observes in SEM images of PSf/CA-10 and PSf/CA-30 membranes.

Conclusion

The neat PSf membrane and PSf/CA composition membranes were prepared by phase inversion method. Several techniques were carried out for the characterization performances. The results have proved the addition of CA compositions in the polymer matrix influence the properties of blend membranes. The addition of CA composition has improved the hydrophilic characteristic of the blend membranes. In term of water flux permeation, the highest CA ratio (70/30 wt. %) obtained the highest PWP. Meanwhile, the membrane with 80/20 wt. % resulted in lower flux but with a consistent increased than other blend membranes. Further, the morphology analysis of these blend membranes has found that the ratio of 80/20 wt. % membrane forms a uniform arrangement of finger-like voids in the sublayer. This structure is more favourable compared to the membranes with 90/10 wt. % and 70/30 wt. % of PSf/CA composition. The connected finger-like voids of the top and bottom layer facilitates the consistency of flux permeation than the formation of finger-like voids and macrovoid of the separated layers (90/10 and 70/30 wt. %). Besides, the membrane with 80/20 wt. % has also approached a good mechanical strength compared to 90/10 wt. % and 70/30 wt. % which represented by Young's modulus. In term of FRR results, the most recovered flux was obtained by the membrane with 90/10 wt. % with the value of 59 % while membrane with 80/20 wt. % only achieved up to 12 % which was the lowest. Overall, PSf/CA-20 (80/20 wt. %) is highly considered as an appropriate membrane in term of permeation and durable properties compared to other blend membranes as this membrane has shown a high tendency of a good multicomponent interaction inside the polymer matrix.

However, the addition of CA in casting solution has slightly reduced the flux recovery especially for the membrane with 80/20 wt. %. This problem has been considered as a disadvantage for this type of blend membrane. The blend membrane with 80/20 wt. % may improve the FRR % if it incorporates with various additives compositions.

Acknowledgement

The authors acknowledge the financial support provided by Putra Graduate Initiative, Universiti Putra Malaysia (UPM), Malaysia (Vote no. 9477000) with the permission used of facilities in Engineering Properties and Nutraceuticals Laboratory, Faculty of Engineering, Universiti Putra Malaysia.

References

Amirilargani, M., Sabetghadam, A., & Mohammadi, T. (2012). Polyethersulfone/polyacrylonitrile blend ultrafiltration membranes with different molecular weight of polyethylene glycol : preparation , morphology and antifouling properties. *Polymer Advanced Technologies*, *23*, 398–407.

Arthanareeswaran, G., Mohan, D., & Raajenthiren, M. (2010). Preparation, characterization and performance studies of ultrafiltration membranes with polymeric additive. *Journal of Membrane Science*, *350*, 130–138.

Arthanareeswaran, G., Srinivasan, K., Mahendran, R., Mohan, D., Rajendran, M., & Mohan, V. (2004). Studies on cellulose acetate and sulfonated poly (ether ether ketone) blend ultrafiltration membranes, *40*, 751–762.

Aryanti, P. T. P., Khoiruddin, & Wenten, I. G. (2013). Influence of additives on polysulfone-based ultrafiltration membrane performance during peat water filtration. *Journal of Water Sustainability*, *3*(2), 85–96.

Borneman, Z., Gokmen, V., & Nijhuis, H. H. (2001). Selective removal of polyphenols and brown colour in apple juices using PES / PVP membranes in a single ultrafiltration process. *Separation and Purification Technology*, *22–23*, 53–61.

Bowen, W. R., Doneva, T. A., & Yin, H. B. (2001). Polysulfone — sulfonated poly (ether ether) ketone blend membranes : systematic synthesis and characterisation. *Journal of Membrane Science*, *181*, 253–263.

Chakrabarty, B., Ghoshal, A. K., & Purkait, M. K. (2008). Effect of molecular weight of PEG on membrane morphology and transport properties. *Journal of Membrane Science*, *309*, 209–221.

Conidi, C., Cassano, A., & Drioli, E. (2011). A membrane-based study for the recovery of polyphenols from bergamot juice. *Journal of Membrane Science*, *375*(1–2), 182–190.

Hamzah, S., Ali, N., Ariffin, M. M., Ali, A., & Mohammad, A. W. (2014). High performance of polysulfone ultrafiltration membrane : Effect of polymer concentration. *ARPN Journal of Engineering and Applied Sciences*, *9*(12), 2543–2550.

Huisman, I. H., Prádanos, P., & Hernández, A. (2000). The effect of protein – protein and protein – membrane interactions on membrane fouling in ultrafiltration. *Journal of Membrane Science*, *179*, 79–90.

Idris, A., & Ahmad, I. (2011). Cellulose acetate-polyethersulfone (CA-PS) blend ultrafiltration membranes for palm oil mill effluent treatment. *Environmental Earth Sciences*, 1149–1159.

Ismail, A. F., Hassan, A. R., & Cheer, N. B. (2002). Effect of shear rate on the performance of nanofiltration membrane for water desalination. *Songklanakarin Journal Science Technology*, *24*, 879–889.

Kalaiselvi, G., Maheswari, P., Balasubramanian, S., & Mohan, D. (2013). Synthesis , characterization of polyelectrolyte and performance evaluation of polyelectrolyte incorporated polysulfone ultra fi ltration membrane for metal ion removal. *Desalination*, *325*, 65–75.

Koehler, J. A., Ulbricht, M., & Belfort, G. (2000). Intermolecular forces between proteins and polymer films with relevance to filtration. *Langmuir*, *13*, 4162–4171.

Kumar, R., Isloor, A. M., Ismail, A. F., Rashid, S. A., & Al, A. (2013). Permeation , antifouling and desalination performance of TiO 2 nanotube incorporated PSf / CS blend membranes. *Desalination*, *316*, 76–84.

Mahendran, R., Malaisamy, R., & Mohan, D. R. (2004). Cellulose acetate and polyethersulfone blend ultrafiltration membranes . Part I : Preparation and characterizations. *Polymers for*

Advanced Technologies, *15*, 149–157.

McCloskey, B. D., Park, H. B., Ju, H., Rowe, B. W., Miller, D. J., & Freeman, B. D. (2012). A bioinspired fouling-resistant surface modification for water purification membranes. *Journal of Membrane Science*, *413–414*, 82–90.

Moradihamedani, P., & Abdullah, A. H. (2017). High-performance cellulose acetate/polysulfone blend ultrafiltration membranes for removal of heavy metals from water. *Water Science & Technology*, 1–12.

Moradihamedani, P., Ibrahim, N. A., Ramimoghadam, D., Wan Yunus, W. M. Z., & Yusof, N. A. (2014). Polysulfone / zinc oxide nanoparticle mixed matrix membranes for CO_2/CH_4 separation. *Journal of Applied Polymer Science*, *131*, 1–9.

Nystrom, M., Pihlajamiiki, A., & Ehsani, N. (1994). Characterization of ultrafiltration membranes by simultaneous streaming potential and flux measurements. *Journal of Membrane Science*, *87*, 245–256.

Padaki, M., Isloor, A. M., Wanichapichart, P., & Ismail, A. F. (2012). Preparation and characterization of sulfonated polysulfone and N-phthloyl chitosan blend composite cation-exchange membrane for desalination. *Desalination*, *298*, 42–48.

Peeva, P. D., Palupi, A. E., & Ulbricht, M. (2011). Ultrafiltration of humic acid solutions through unmodified and surface functionalized low-fouling polyethersulfone membranes – Effects of feed properties , molecular weight cut-off and membrane chemistry on fouling behavior and cleanability. *Separation and Purification Technology*, *81*(2), 124–133.

Pielesz, A., & Binias, W. (2010). Cellulose acetate membrane electrophoresis and FTIR spectroscopy as methods of identifying a fucoidan in Fucus vesiculosus Linnaeus. *Carbohydrate Research*, *345*(18), 2676–2682.

Rahimpour, A., & Madaeni, S. S. (2007). Polyethersulfone (PES)/ cellulose acetate phthalate (CAP) blend ultrafiltration membranes : Preparation , morphology , performance and antifouling properties. *Journal of Membrane Science*, *305*, 299–312.

Razzaghi, M. H., Safekordi, A., & Tavakolmoghadam, M. (2014). Morphological and separation performance study of PVDF / CA blend membranes. *Journal of Membrane Science*, *470*, 547–557.

Reuvers, A. J., Berg, J. W. A. van den, & Smolders, C. A. (1987). Formation of membranes by means of immersion precipitation-Part I. A model to describe mass transfer during immersion precipitation.pdf. *Journal of Membrane Science*, *34*, 45–65.

Ricq, L., Narc, S., Reggiani, J., & Pagetti, J. (1999). Streaming potential and protein transmission ultrafiltration of single proteins and proteins in mixture : B-lactoglobulin and lysozyme. *Journal of Membrane Science*, *156*, 81–96.

Saljoughi, E., Sadrzadeh, M., & Mohammadi, T. (2009). Effect of preparation variables on morphology and pure water permeation flux through asymmetric cellulose acetate membranes. *Journal of Membrane Science*, *326*, 627–634.

Sikder, J., Pereira, C., Palchoudhury, S., Vohra, K., Basumatary, D., & Pal, P. (2009). Synthesis and characterization of cellulose acetate-polysulfone blend micro fi ltration membrane for separation of microbial cells from lactic acid fermentation broth. *Desalination*, *249*(2), 802–808.

Sivakumar, M., Mohan, D. R., Rangarajan, R., & Tsujita, Y. (2005). Studies on cellulose acetate – polysulfone ultrafiltration membranes : I . Effect of polymer composition. *Polymer International*, *962*, 956–962.

Sivakumar, M., Raju, D., & Rangarajan, R. (2006). Studies on cellulose acetate-polysulfone ultrafiltration membranes II . Effect of additive concentration. *Journal of Membrane Science*, *268*, 208–219.

Sivakumar, M., Susithra, L., Mohan, D. R., & Rangarajan, R. (2006). Preparation and performance of polysulfone- cellulose acetate blend Ultrafiltration membranes Preparation and Performance of Polysulfone-. *Journal of Maromolecular Science*, *43*, 1541–1551.

Sossna, M., Hollas, M., & Scheper, T. (2007). Structural development of asymmetric cellulose acetate microfiltration membranes prepared by a single-layer dry-casting method, *289*, 7–14.

Tseng, H.-H., Zhuang, G.-L., & Su, Y.-C. (2012). The effect of blending ratio on the compatibility, morphology, thermal behavior and pure water permeation of asymmetric CAP/PVDF membranes. *Desalination*, *284*, 269–278.

Zhao, S., Wang, Z., Wei, X., Zhao, B., Wang, J., Yang, S., & Wang, S. (2011). Performance improvement of polysulfone ultrafiltration membrane using PANiEB as both pore-forming agent and hydrophilic modifier. *Journal of Membrane Science*, *385–386*, 251–262.

Zhao, W., Su, Y., Li, C., Shi, Q., Ning, X., & Jiang, Z. (2008). Fabrication of antifouling polyethersulfone ultrafiltration membranes using Pluronic F127 as both surface modifier and pore-forming agent. *Journal of Membrane Science*, *318*, 405–412.

Proceeding: 5th International Conference on Applied Sciences and Engineering (ICASEA, 2018)
(eISBN 978-967-15744-1-6)
Capthorne Hotel, Cameron Highlands, Malaysia

OPTIMIZATION OF OZONATION PROCESS IMPLEMENT PERSULFATE USING AZO DYES

N.A. Razali [1]
C.Z.A. Abidin [1]*
S. A. Ong [1]
M. R. Fahmi [1]
A.H. Ibrahim [1]
S. N. Sabri[1]
S.H. Kow [1]

[1] School of Environmental Engineering, Kompleks Pusat Pengajian Jejawi 3, Universiti Malaysia Perlis, 02600 Arau, Perlis, Malaysia

---

Abstract: *Ozonation (O_3) process aided with other oxidants can be a best method for degradation compounds that presented by azo dyes specifically Acid Orange 52 (AO52). Numerous application of AO52 had been applied in textile industries, cosmetic and pharmaceutical industries. In this work, integration of hydroxyl radical with sulfate radical can enhanced the production of radical useful for colour and COD removal mechanism. It had been proven when its performance of ozonation + persulfate process better than ozonation process only. The effects of operational conditions had been investigated including the fixed initial concentration of AO52, initial pH of the AO52 (2-6), $Na_2S_2O_8$ / sodium persulfate concentration (25-65mM) and contact time (3-25min) on the colour and chemical oxygen demand removal efficiency. By predicting both of responses efficiency, Central Composite Design (CCD) had been applied to achieve the optimization of ozonation process with $Na_2S_2O_8$ / sodium persulfate concentration, second-order polynomial equation was proposed. Good agreement of experimental values were found which is (Colour removal; R^2 = 0.6615, COD removal; R^2 = 0.5453), which proves the appropriateness of the model employed. Hence, success of CCD suggested the optimum conditions of ozonation process at (pH 6,65mM $Na_2S_2O_8$ / sodium persulfate concentration, 25min). Both of process efficiency as a function of independent variables was shown specifically by mathematical modelling equation, interactive effect by cube plot, normal probability plot and ramp. However, the statistical tests are supported also with UV-Vis spectra evolution through each condition. By getting an optimum value, it could be applied in any dyes that contains same organic molecule. Furthermore, the new ozonation approach had been modified based on their factor achievement especially presence of $Na_2S_2O_8$ /sodium persulfate concentration to improve the degradation performances.*

Keywords: *Acid Orange 52(AO52), Ozonation, Sulfate radical, CCD.*

Introduction

Recently, the rapid on-going development of industrial world used of different type of chemicals are been explored just only to meet the trends of fashion requirement. One of the big issues was textile industry processes had been consumed on average about 150 L of water per kilogram of cloth processed (Liu *et al*., 2010). Thus, it had been caused discharge of coloured

textile effluent into the environment in which it's either carcinogenic and/or teratogenic health effects (Tizaoui & Grima, 2011). Practically, this was due to the process had been generated a large flows effluents which contain high COD, large amount of suspended solids, largely fluctuating pH, high temperature, unbound colourants, dye impurities, auxiliaries and surfactants (Zahrim, Tizaoui & Hilal, 2011). As instances of the harmful effluents, azo dyes has been assigned for approximately 70% of all dyestuffs used worldwide by weight, causing them as the largest group of dyes released into the environment (Brillas & Martinez Huitle, 2015). Hence, the degradation process of these dyes and intermediate products completely from dye effluent are crucial to reduce their final discharge flowing to the environment.

As a result, international consensus concerning discharging textile effluent with respect to legislation especially for usage of azo dyes in many countries unfortunately including Malaysia. Therefore, this problem must be immediately to overcome this excess compound appealed around the world where must be considered to their consumption and discharge effluent (Koycyigit & Ugurlu, 2015). This due to this issue was getting recognition from scientists all over the world about their negative effects towards photosynthetic aquatic plant and water bodies (Demirci & Hammaci, 2013; Khosa, Shah & Feng, 2013). It has been conclusively shown azo dyes required a suitable and efficient method for their degradation process. Therefore, the application of azo dyes treatment techniques was increasing including physical, biological and chemical processes had been investigated. Result from Sukanchan (2012) studies have been identified that advanced oxidation processes (AOPs) like ozonation process as one of the efficient chemical process for most of dyes.

However, this method has a number of limitations as example only resulted in significant colour removal, costly if applied in actual field and unable fulfilled the discharge standard of effluents in term of chemical oxygen demand (COD) (Osman & Soubaneh, 2014). Advanced oxidation processes (AOPs) are involved in situ generation of very powerful oxidizing agent such as hydroxyl radical (second highest powerful oxidant after the fluorine) and efficiently for removal of recalcitrant organics from the wastewater (Loeb *et al*., 2012). Among the AOPs, ozonation process can performed well in decolourization due to it occur easy and fast reaction; less harmful; sludge are not formed; decomposition process can convert easily into oxygen and water; and need little space is required (Sharma, Ruparelia & Patel, 2011).The mechanism of this radical is by attacking organic molecules by either abstracting a hydrogen atom or adding hydrogen atom to the double bonds. Hence, if complete mineralization had been completed, formation of different structure of intermediates with lower molecular weight or carbon dioxide and water would occur (Chen *et al*., 2009). Therefore, the selective radicals can be generated by oxidizing agent such as by hydrogen peroxide, $Na_2S_2O_8$/sodium persulfate, ozonation and homogenous or heterogeneous catalyst. The main limitation to another study was investigators are kept suggested several approach to enhance hydroxyl radical production.

This view is supported from this researcher, who argues that hydroxyl radicals are non-selective in nature and able to perform well without any other additives with a wide range of contaminants (Rehman *et al*., 2009). However, AOPs unable to undergoes complete mineralization due to this limitation. By coupling AOPs with $Na_2S_2O_8$/sodium persulfate can be as the most latest improvement to overcome this drawback. In this paper, the integration of oxidation efficiency, ozonation aided with sodium persulfate would obtain a better efficiency of optimum condition in colour and COD removal. Unfortunately, this method of analysis has

a number of limitations studies which unable to know their best of optimum condition, have only focussed on other types of dyes, different experimental condition and aims.

According Buthiyappan *et al*., (2016), many factors had been contributed to the efficiency of dyes degradation such as classes of dye, concentration of solution, temperature, contact time, pH and selection of catalyst. Now, researchers usually delve into applying more extensive statistical mathematical tools and user friendly methods for analysing complex experimental results. To this end, a rigorous approach attempted the response surface methodology (RSM) which is Central Composite Design (CCD) that widely used in many industries for technological operations which provide superior optimization in experimental conditions. CCD in the form of a 2^3 full factorial design was used to develop mathematical equations which utilized for maximizing or minimizing different independent variables by evaluating the effects of multiple factors and their interactions on one or more response variables simultaneously. It would be constructed for performance of the AO52 removal by providing a clear visual aid to improving quantitative evaluation of the integration process of ozonation. In this evaluation, initial pH of AO52, $Na_2S_2O_8$/ sodium persulfate concentration and contact time as the factors affecting the colour and COD removal performance were studied. Consequently, the objectives of this work were to compare performances of ozonation and ozonation + sodium persulfate process, to evaluate the mathematical equation, reconsidering the performances of normal probability plot residual and understanding the interactive effects of different parameters by cube plot dimensional. This data and results could reveal the process of optimization through their ramp suggestion and would improvement in the works already done by researchers.

Methodology

Chemicals and preparation of dye solution

Acid Orange 52, AO52 (Fluka Analytical) as stated in Figure 1, sodium hydroxide, NaOH (HmbG), sulphuric acid, H_2SO_4 (95-98%, Fisher Chemical) and $Na_2S_2O_8$/ sodium persulfate (Sigma Aldrich) has been used along this research. AO52 has been selected due to its low biodegradability and lack of effective treatment. Ultrapure water from Elga Pure-Lab Option-Q water system had been used for the preparation of solutions. When required according condition, the pH of the solution was adjusted using 1M of H_2SO_4 and NaOH. Initial dye concentration was adjusted and as constant variable at 100 mg L^{-1} by dilution with ultrapure water.

Ozonation experiment

Combination of ozonation has been selected in this study was the combination of ozonation process and sodium persulfate. The experimental setup shown in Figure 2 comprised of an oxygen cylinder (99.8% of oxygen concentration), ozone generator (A2ZZ-3G), 2L of glass measuring cylinder as ozone reactor and KI trap. Constant ozone gas was supplied from the bottom of the reactor through a diffuser at a dosage of 2L/min of O_2 inflow at 10g/m^3 of O_3 generation. In ozonation experiment, AO52 with same concentration (100mg/L) undergoes different condition of initial pH (2-6), $Na_2S_2O_8$/sodium persulfate concentration (25-65mM) and contact time (3-25min) were used to investigate their effects towards colour and COD removal. For determination of colour, COD removal as shown in Equation 1 and UV-Vis spectra analysis, the experiments were conducted at room temperature and samples were withdrawn at definite time intervals.

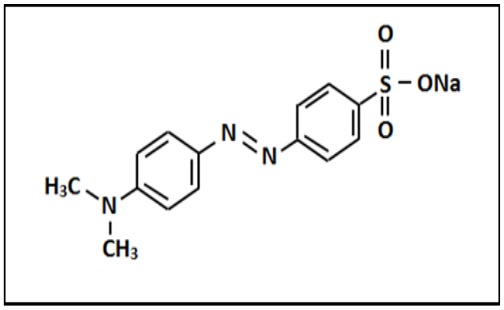

Figure 1: Molecular Structure Of AO52

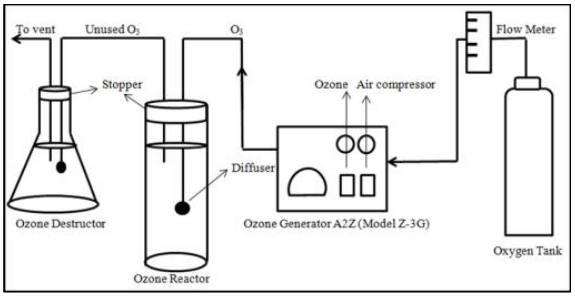

Figure 2: Schematic Diagram Of Ozonation Set-Up

Analytical methods

The solution pH adjusted by Hanna Instrument HI223 pH meter while for absorbance measurements were performed using a UV–Vis spectrophotometer (MesuLabTM), Model ME -UV1100 at wavelengths ranging from 200–800 nm. The maximum visible region (λ max 456 nm) was used as a base to follow AO52 decolourization, using a quartz cuvette. Chemical oxygen demand (COD) was determined with the closed reflux, calorimetric method using HACH DR200 COD reactor and were measured by using HACH DR2800 Spectrophotometer.

$$Colour\ and\ COD\ Removal\ (\%) = [((C_O - C_t)/ C_O)\ \text{x}\ 100] \quad \text{Eq.1}$$

Experimental design

All runs were suggested followed the range as stated in Table 1. It statistically processed using Central Composite Design which helped to optimize the process and obtained good enough precision. Data were acquired from the ozonation experiment and then assessed using RSM (Response Surface Methodology), Design-Expert® (Version 7.1.5) Stat-Ease, Inc., USA). For designing experiments and obtaining optimum conditions for desirable responses, RSM is one of the mathematical and statistical techniques (Kunwar *et al*., 2011).The application of RSM had been applied in different branches of scope like Anupam *et al*., (2011) studies for optimization of various factors for degradation in different pollutants. This current study, three factors with two responses had been applied in Central Composite Design (CCD) based on RSM was used in 20 run of experiments where consist 8 factorial points, 6 axial points and 6 replicates of center points at 5 levels of each variable. The center points were utilized to define the experimental error and the reproducibility of the data.

The experimental plan was based on three factors referred to as face centered central composite design. In this study, the selection of this design as the experimental design because it is more precise for estimating factor effects (Taib *et al*., 2015). Hence, the interaction effect between factors can be evaluated and optimized in the full factor space. It was done to optimize independent variables in this study (A: initial pH), (B: $Na_2S_2O_8$/sodium persulfate concentration) and (C: contact time). The five levels of values for the independent variables were explicit of their coded and uncoded forms in Table 1. The value of independent variables were expressed in their coded as -1, 0, +1 interval shows the low, center, and high level of each variable, respectively. Based on the preliminary screening analysis (Razali *et al*., 2018), the range and levels used in this experiment are constructed in Table 1.

Optimization and Statistical Analysis

By determining the approximately optimum condition, Design Expert software had been predicted the variation of conditions which is independent variables to optimize interest study. The desired goal for each variable was chosen. The optimal of ozonation + persulfate process conditions were chosen based on the condition of attaining highest colour and COD removal for each run. The Design Expert software overlaying all the responses to obtained the optimal condition. Moreover, the optimal condition that depended on the independent variables was also obtained using the predicted equations determined by RSM. By employing the polynomial regression equation, the response surface behaviour was examined for the response function (Y). The generalized response surface model is shown below (Equation 2)

$$Y = \beta_0 + \sum_{i=1}^{k} \beta_i X_i + \sum_{i=1}^{k} \beta_{ii} X_i^2 + \sum_{i=1}^{k-1} \sum_{i=2}^{k} \beta_{ij} X_i X_j + e_i \quad \text{Eq. 2}$$

Where Y represents the response variables to be modeled; β_o is a constant, β_i, β_{ii} and β_{ij} are the linear, quadratic and cross-product coefficients, respectively. X_i and X_j are the levels of the independent variables. k is the number of variables and e is the random error of the model. The statistical significance of the term in the regression equations and best fitted model of response can be achieved by highlighting various statistical parameters such as multiple correlation coefficients (R^2). The fitted polynomial regression equation was expressed in the form of cube plots in order to illustrate the relationship between responses and the experimental variables used.

Table 1: Experimental ranges and levels for parametric optimization process

Symbol	Factor	Goal	Range and level			Response			
			-1	0	+1				
A	Initial pH	In range	2	4	6	1	Colour Removal	%	Optimize
B	($Na_2S_2O_8$) Sodium persulfate concentration	In range	25	45	65	2	COD Removal	%	Optimize
C	Contact time	In range	3	14	25				

Results and Discussions

Differentiate of ozonation and ozonation + sodium persulfate process

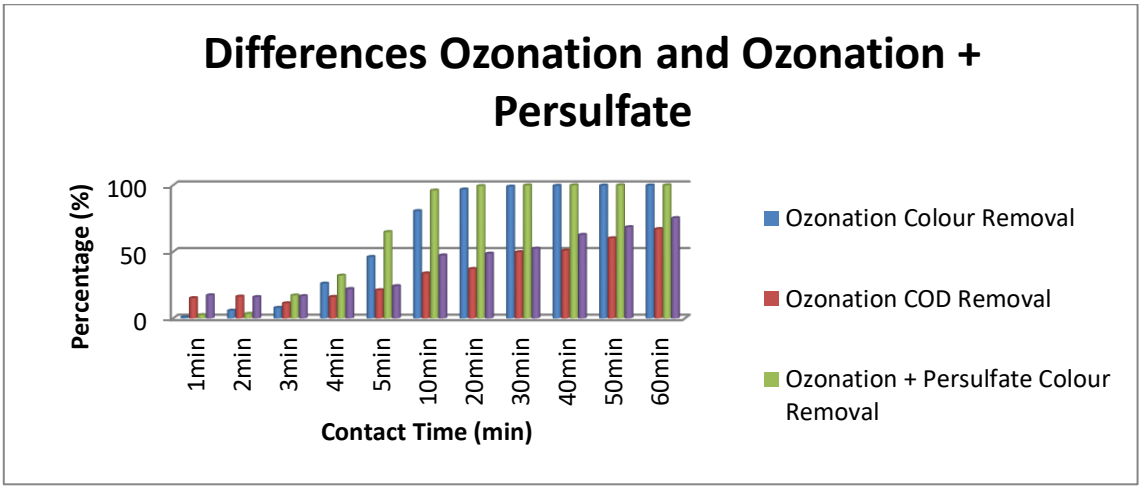

Figure 3: Difference Of Ozonation And Ozonation + Sodium Persulfate Process

In ozonation + persulfate process, sodium persulfate was introduced into ozonation process towards AO52 (500mg/L), which significantly enhanced the performances of ozonation as stated in Figure 3 and provided sulfate radical reaction in degradation process itself , that making ozonation + persulfate process more efficient based on colour and COD removal than ozonation only. With the increasing contact time of process, the decolourization inclined slightly and remained above 90% at 10 min and above. Colour and COD removal rate for both processes increased persistently with increasing contact time and no inhibition process was occurred. However the decolourization rate in ozonation + persulfate process was much higher as compared to ozonation process only due to the average increment was about 31%, which indicated that sodium persulfate might play a synergistic role in the degradation process. As high concentration of AO52 was composed various compound in their structure that make it needed longer contact time to decolourize completely. Equation 3 and 4 showed a comparison how these radical performed in the process (Loeb *et al*., 2012: (Deng & Ezyske. 2011).

Ozonation process	(1) $3O_3 + H_2O \rightarrow 2OH^{\bullet} + 4O_2$	Eq.3
Ozonation + Persulfate process	(1) $3O_3 + H_2O \rightarrow 2OH^{\bullet} + 4O_2$	Eq.4
	(2) $S_2O_8^{2-} + 2H^+ + 2e^- \rightarrow 2HSO_4^-$	

Ozonation + persulfate process gained the highest COD removal at 60 min 75% removal as compared to ozonation process was only about 65%. By introducing sodium persulfate in the ozonation process, it unable to accelerate an accomplished 100% COD removal as compared to colour removal performance. COD Removal average increment of ozonation + persulfate was about 19.85% only. This due to decolourization with ozone would occur rapidly due to the rapid destruction of conjugated chains of dye molecules that functionally for colour only (Tizaoui & Grima, 2011). Furthermore, Yao *et al.*, (2016) stated that mineralization effectiveness usually varies numerously with the type of constituents contain in the wastewater.

Central Composite Design Application

Table 2 : Percentage Of Colour And Cod Removal

Run	A:pH	B: Sodium Persulfate Concentration	C: Contact time	Colour removal (%)		COD removal (%)	
				Experimental	Predicted	Experimental	Predicted
1	4	45	14	99.81	99.55	17.90	25.54
2	2	25	3	68.32	63.46	20.34	23.04
3	2	65	25	99.40	92.04	13.62	19.88
4	6	65	3	74.70	69.17	11.89	19.16
5	6	25	25	99.35	87.62	17.65	22.90
6	4	45	14	99.07	99.55	21.31	25.54
7	6	65	25	99.28	104.60	53.70	51.68
8	4	45	14	99.22	99.55	44.78	25.54
9	2	65	3	19.33	31.52	7.01	2.44
10	6	25	3	63.11	70.93	11.46	5.88
11	4	45	14	99.80	99.55	24.23	25.54
12	2	25	25	99.26	105.25	31.58	24.98
13	4	45	3	77.99	68.37	14.85	15.03
14	4	45	14	99.86	99.55	19.46	25.54
15	6	45	14	98.91	103.04	38.20	33.29
16	4	25	14	99.31	102.10	18.97	23.21
17	4	45	25	99.18	106.97	35.15	32.26
18	2	45	14	98.99	93.03	23.77	25.97
19	4	65	14	99.24	94.62	34.25	27.30
20	4	45	14	99.33	102.99	23.21	28.64

The design of experimental data in Table 2 obtained for this response based on CCD matrix. List of 20 run had been analysed by investigated each run with semi-batch ozonation + persulfate process. Their responses had been determined after calculated the average of triplicate data. Therefore, these data had been compared with the predicted as suggested by CCD. However, there was presented illogical value when the colour removal predicted more than 100% at Run 6, 12, 15, 16, 17 and 20.

Model Fitting and Statistical Analysis

All three independent variables and responses, a quadratic polynomial model was selected and fitted well as suggested by the software. Each response can be represented by a mathematical equation that correlated the response surface as stated in Equation 5 and 6. The optimum condition degradation AO52 was determined by CCD under RSM. Based on the results, higher coefficients of determination for colour and COD removal were (R^2 =0.6615) and (R^2 = 0.543), which confirmed that the quadratic polynomial models are highly significant and acceptable to interpret actual relationship between the responses and variables tested. Furthermore, the calculated R^2 values for studied responses variables got within good range. Hence, there is a close agreement between the experimental values and the theoretical values predicted by the proposed models. The final empirical regression model of the relationship between three tested variables for colour and COD removal were obtained can be expressed using the following equations (Equation (5)-(6)):

Colour removal =

$$94.47 + 5.00\ A - 3.74\ B + 7.55A\ B - 6.27\ AC + 4.68\ BC - 4.96\ A^2 - 4.6\ B^2 \quad \text{Eq. 5}$$

R-squared = 0.6615

COD removal =

$$25.37 + 3.66A + 2.05\ B + 8.47A\ B + 3.77\ A\ C + 3.87\ BC + 0.99A^2 - 3.39\ B^2 \quad \text{Eq. 6}$$

R-squared = 0.5453

where A, B and C are initial pH, $Na_2S_2O_8$/ sodium persulfate concentration and contact time respectively. A negative sign in each equation represented an antagonistic effect of the variables and a positive sign represents a synergistic effect of the variables.

Normal Probability Plot of Studentized Residual for colour and COD Removal

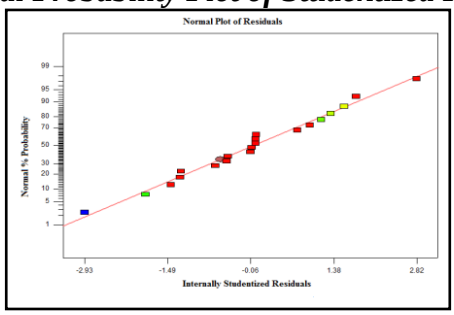

Figure 4: Normal Probability Plot Of Colour Removal

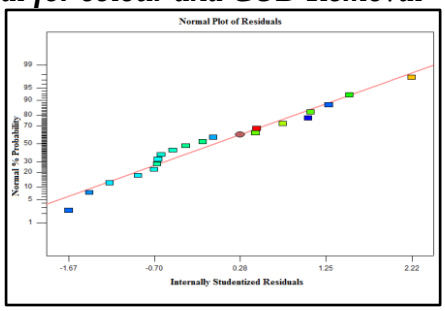

Figure 5 :Normal Probability Plot Of COD Removal

The normal probability plot for colour and COD removal of AO52 were showed in Figure 4 and 5. In this part, the normal probability plot has been indicated that residuals followed a normal distribution. It was apparently shown that residual can be assumed to fit which all runs already scattered followed a straight line that showing errors. Thus, the data collected can support the relevance of the empirical model. Models are reliable has been accepted (Mamun,Aswr & Fahmida., 2017). Different colour of data had been explained through their rank of the performances in which red (optimum), green (average) and blue (lowest) based on data in Table 2.

Interactive Effects of Different parameters

Figure 6 presents the cube plots of colour removal of AO52 dye synthetic wastewater. The data in Figure 6 indicates that at condition (pH 6, 25mM, 3min) resulted highest colour removal which is 97%. Strong evidence of AO52 decolourization can be achieved within 3minutes and found that at (pH 2, 65mM) gave lowest percentage of decolourization which is 57%. It was possible to hypothesise that combination of too high acidic condition with highest $Na_2S_2O_8$/sodium persulfate concentration may give a negative effect towards response. It is because the contribution of unlimited hydrogen ions gave badly influenced to the performance of radicals to breakdown the dye structure. Mamun and their co-workers stated that the oxidants might enhance the degradation of dye because it able to generate number of trapped electrons which can prevents recombination and generates oxidizing radicals. However, tendency of AO52 to be degraded was retarded due to high acidic solutions (pH less than 3). This happened due to high concentration of proton which resulting in lower degradation efficiency (Mamun, Aswr & Fahmida, 2017). The effect of $Na_2S_2O_8$/sodium persulfate concentration strongly affected colour removal efficiency at medium concentration 25-45mM but barely effect the

removal efficiency at high concentration 65mM. The colour removal was ranged from 63.11% to 99.81%.

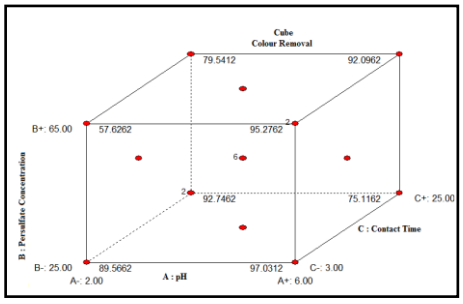

Figure 6: Cube Plots Of Colour Removal

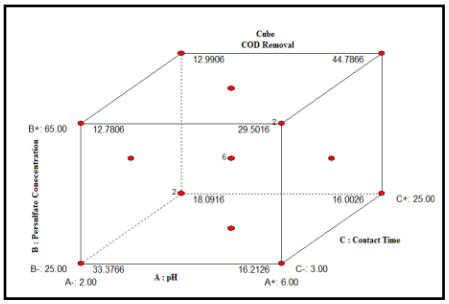

Figure 7: Cube Plots Of COD Removal

Based on Figure 7 the effect of initial pH, $Na_2S_2O_8$/sodium persulfate concentration and contact time on the COD removal was presented. The results, as seen in Figure 7, indicated that about 44% COD removal can be achieved as the condition stated at (pH 2, 65mM, 25 min). The cube plots model exhibited that longer contact time required to enhance the efficiency of COD removal that stated 44.78% in Run 8 as compared to Run 9 which was only 7.01%. There are similarities in significant of contact time as a factor between the present study and those described in ozonation such as crucial factor (Weng & Tao, 2015). On the other hand, $Na_2S_2O_8$ /sodium persulfate had been proved that COD removal of AO52 can exceeds about 44.78% only in 14min in acidic condition rather than the other ozonation only studies needed 150 min for 44.57% respectively (Chen *et al*., 2008).

After all, the optimum conditions of ozonation + persulfate process suitable at (pH 6, 65 mM $Na_2S_2O_8$ / sodium persulfate concentration, 25 min) as stated in Figure 8. In particular, the ozonation + persulfate process of AO52 azo dyes has gained considerable condition due to the facts:

- $\leq$ 65mM $Na_2S_2O_8$ / sodium persulfate concentration: Enhanced hydroxyl radicals in ozonation process by inducing sulfate radical.
- High acidic pH: According to Tizaoui and Grima (2011), increase production of hydroxyl radicals was significant which boost a faster colour removal and H-N-R group of the dye molecule deprotonates, which makes the sites more reactive for the electrophilic attack by ozone. In addition, it more susceptible to electrophilic attacks by molecular ozone and possibly hydroxyl radicals. Unfortunately, at very low acidic pH; the production of hydroxyl radicals from ozone decomposition was negligible because of the very low concentration of hydroxide ions (the initiator of ozone decomposition) make it had been proceed solely through molecular ozone reaction (direct mechanism).
- Longer contact time: This parameter could not give same feedback performances towards colour and COD removal. Since ozonation process itself a fast process that induced the colour removal 100% rapidly when it needs less breakage of compound while COD removal difficult to achieve 80-100% due to it needs longer time to undergo the mineralization process for eliminating all organic products along the process.

Process of Optimization

The priority of operating cost is a vital issue to be considered for each implementation of wastewater treatment method (Cod, 2013). Thus, optimum condition for ozonation aided with $Na_2S_2O_8$ /sodium persulfate with minimum contact time was desired by achieving both of significant responses. Moreover, the frequent initial concentration of wastewater is about 100mg/L that suited with the optimum condition. In present study, by taking operational condition "within range" while for the response as "maximum" to attain maximum efficiency of colour and COD removal approximately 92.09% and 44.77% respectively. The desirability function is achieved 0.855 for the mentioned conditions as optimum. Thus, the validation experiment was done to accomplish, verified and proved the findings which revealing with predicted response values of the mathematical model. The results of predicted and experimental parameter were shown in Table 3 were found within the range and to be not statistically different at 95% confidence level. Based on the optimum conditions, the actual values of colour removal 90% as compared to predicted 92% and 40% for actual COD removal than 44% of its predicted value.

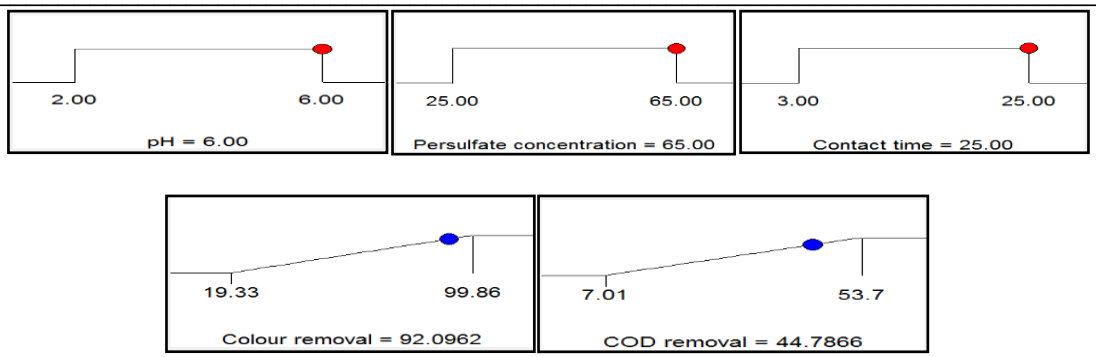

Figure 8: Optimum Condition Derived By RSM For AO52 Degradation

Table 3 : Percentage Of Colour And COD Removal

Variables	Units	Optimum value
Initial pH		6
$Na_2S_2O_8$ /sodium persulfate concentration	mM	65
Contact time	Min	25
Predicted AO52 Removal	%	92
Actual AO52 Removal		90
Predicted COD Removal		44
Actual COD Removal		40

UV-Vis Spectra Changes

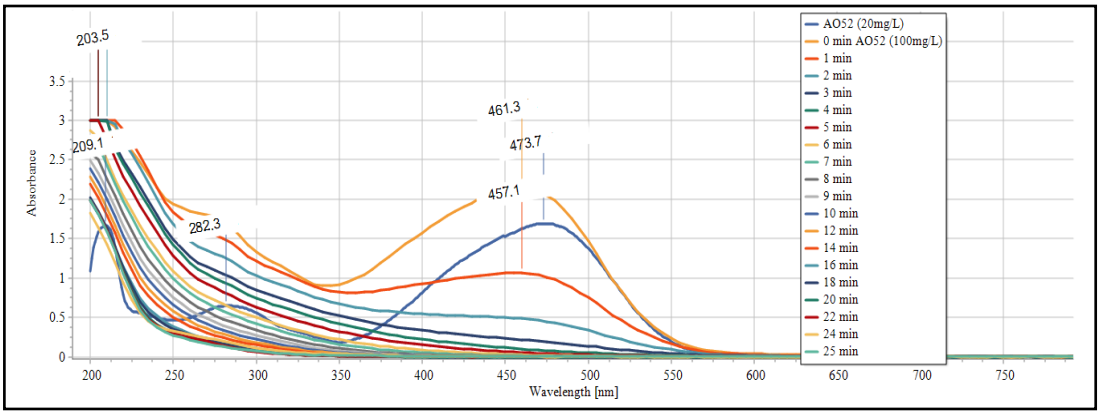

Figure 9: The Evolution Of Absorbance With Reaction Time

Analysis Figure 9 in which UV–Vis absorption spectra along degradation AO52 in aqueous solutions can be shown by using UV–Vis spectrophotometer (MesuLabTM), Model ME - UV1100. Molecular and structural characteristic of AO52 with $Na_2S_2O_8$/sodium persulfate concentration was clarified through UV–vis spectra. Based on the performances of degradation dye solution through its contact time (1min - 25min) were depicted in Figure 8 for enhancing ozonation experiment. Before ozonation process, the absorption spectrum of AO52 in ultrapure water was characterized by one main band in the visible region 474 nm (20 mg/L). It can be prove through its maximum absorption which is 461 nm at 100mg/L was attributed based on its conjugated structure constructed by azo bond. Besides that, other bands were formed in the ultraviolet region located at 282 nm as benzene structures in the molecule.

Along ozonation towards AO52 (100mg/L), the structure had been decreasing which indicated the decomposition of AO52 due to the fragmentation of the azo links by direct ozone attack. Other than that, a new band at wavelength of 203 and 209 nm had been appeared. This had been supported through this study that it was considered suggesting the formation of by-products/intermediates and it was proven through aromatic fragment degradation in the dye molecule (Chen *et al*., 2008).

Conclusion

This research has investigated by ozonation aided with $Na_2S_2O_8$/sodium persulfate degradation of AO52 under various conditions, the following results are significant and five respects conclusions could be drawn:

- Performances of ozonation + persulfate process greater than ozonation process only.
- AO52 was successfully degraded by ozonation aided with $Na_2S_2O_8$/sodium persulfate. Its degradation achieved the optimum condition of ozonation with according condition (pH 6,65mM $Na_2S_2O_8$/sodium persulfate concentration, 25min). The decolorization increased with an increase of contact time.
- Mathematical equation of colour and COD removal of AO52 had been modelled using Central Composite Design and could be analysed their normal probability plot residual.
- In this work, it demonstrated based on statistical analysis degradation of AO52 was significantly accelerated under the oxidative conditions, while its degradation

efficiency was higher based on interactive effects of different parameters by cube plot dimensional.

- This data and results could reveal the process of optimization through their ramp suggestion and would be as improvement in the works already done by researchers. The process of degradation AO52 undergoes C-N cleavages that produced the various intermediates.

Acknowledgement

The authors gratefully acknowledge Ministry of Higher Education (MOHE) Malaysia which providing fundamental research grant scheme (FRGS, Grant Number: 9003-00513 used for financial and technical support to complete the present work.

References

Anupam K, Dutta S, Bhattacharjee C, Datta S. (2011). Adsorptive removal of chromium (VI) from aqueous solution over powdered activated carbon: Optimisation through response surface methodology. *J Chem Eng*, *173*(1), 135–43. doi: 10.1016/j.cej.2011.07.049.

Chen Y, Liu S, Yu H, Yin H, & Li Q.(2008). Radiation-induced degradation of methyl orange in aqueous solutions. *Chemosphere*, *72*, 532–536.

Chen, Kao, Hong, Lin, & Liang. (2009). Application of ozone on the decolorization of reactive dyes – Orange-13 and Blue-19. *Desalination*, *249*, 1238–1242.

Cod, C. (2018). Regional Wastewater Management Plan Understanding the Cost Factors of Wastewater Treatment and Disposal, (March).

Daniel, C. (1959). *Use of Half-Normal Factorial Plots in Interpreting Experiments Two-Level*, 1 (4).

Darvishzadeh T, Priezjev NV. (2012). Effects of cross flow velocity and trans membrane pressure on microfiltration of oil-in-water emulsions". *Journal of Membrane Science, 423*, 1-31.

Demirci, & Hamamci. (2013) Antioxidant responses in Phanerochaete chrysosporium exposed to Astrazone Red FBL textile dye. *Cell Biochemistry and Function*, *31*, 86–90.

Deng & Ezyske. (2011). Sulfate radical-advanced oxidation process (SR-AOP) for simultaneous removal of refractory organic contaminants and ammonia in landfill leachate, *Water Research*, *45*, 6189–6194.

Khosa, Shah, & Feng.(2013). Micellar enhanced ultrafiltration of organic dyes, *Separation Science and Technology*, *48*, 1315–1323.

Kocyigit H., & Ugurlu A. (2015). Biological decolourization of reactive azo dye by anaerobic/aerobic sequencing batch reactor system. *Global NEST Journal*, *17*(X):1–10.

Kunwar, Singha, Gupta, Arun S, & Singha. (2011). Optimizing adsorption of crystal violet dye from water by magnetic nanocomposite using response surface modeling approach. *Journal of Hazardous Materials*, *186*, 1462–1473.

Loeb, Thompson, Drago, Takahara, & Baig. (2012). Worldwide ozone capacity for treatment of drinking water and wastewater: a review. *Ozone Sci Eng*, *34*, 64–77.

Mamun K, Asw R & Fahmida K. (2017). Parameters affecting the photocatalytic degradation of dyes using TiO2: a review. *Applied Water Science*, *7*(4), 1569–1578.

Nouri J, Lorestani B, Yousefi N, Khorasani N, Hasani AH, et al. (2011). Phytoremediation potential of native plants grown in the vicinity of Ahangaran lead- zinc mine. *Environ Earth Sci*. *62*, 639-644.

Osman M & Soubaneh Y. D. (2014). Waste Water Treatment in Chemical Industries: The Concept and Current Technologies. *Journal of Waste Water Treatment & Analysis*, *5*(1), 1–13.

Qian, H. M, Kai Z & Lu X. (2013). Degradation of methyl orange by UV, O3 and UV/O3 systems: analysis of the degradation effects and mineralization mechanism. *Res Chem Intermed*, *39*, 4189–4203.

Razali N. A. , Abidin C. Z., An O. S. , Muhammad F., Ibrahim A. H. , Kow S. H. (2018). Preliminary screening oxidative degradation methyl orange using ozone / persulfate, *34*(2038), 1–9. https://doi.org/10.1051/e3sconf/20183402038.

Rehman S, Ullah R, Butt A.M, Gohar N.D. (2009). Strategies of making TiO2 and ZnO visible light active. J Hazard Mater, 170(2–3), 560–569.

Sharma, S., Ruparelia, J., & Patel, M. (2011). A general review on advanced oxidation processes for waste water treatment. *International Conference on Current Trends in Technology, NuiCONE*, 8–10.

Sukanchan, P. (2012). An overview of ozonation associated with nano-filtration as an effective procedure in treating dye effluents from textile industries with the help of a bubble column reactor. *Research Journal of Chemistry and Environment*, *16* (2), 83–86.

Taib, Siti Husnaa Mohd, Siti Salwa Abd Gani, Mohamad Zaki Ab Rahman. (2015) Mahiran Basri, Amin Ismail, and Rosnah Shamsudin. "Formulation and process optimizations of nano-cosmeceuticals containing purified swiftlet nest." *RSC Advances*, *53* (5), 42322-42328.

Tizaoui, C., & Grima, N. (2011). Kinetics of the ozone oxidation of Reactive Orange 16 azo-dye in aqueous solution. *Chemical Engineering Journal*, *173*(2), 463–473. Retrieved from http://dx.doi.org/10.1016/j.cej.2011.08.014

Yao W, Wang X, Yang H, Yu G, Deng S, Huang J, Wang B, Wang Y. (2016). Removal of pharmaceuticals from secondary effluents by an electro-peroxone process. *Water Res*. *88*, 826-835.

Weng C. H., & Tao H. (2015). Highly efficient persulfate oxidation process activated with Fe0 aggregate for decolorization of reactive azo dye Remazol Golden Yellow.*Arab.J.Chem*,1–41.

Proceeding: 5th International Conference on Applied Sciences and Engineering (ICASEA, 2018)
(eISBN 978-967-15744-1-6)
Capthorne Hotel, Cameron Highlands, Malaysia

NUMERICAL STUDY FOR FLOW OVER A REALISTIC GENERIC MODEL, DRIVAER, USING URANS

Nur Haziqah Shaharuddin[1]
Mohamed Sukri Mat Ali[1]
Shuhaimi Mansor[2]
Sallehuddin Muhamad[3]
Sheikh Ahmad Zaki[1]

[1]Wind Engineering for Environment, Malaysia-Japan International Institute of Technology, UniversitiTeknologi Malaysia, 54100 Kuala Lumpur, Malaysia
[2] Faculty of Mechanical Engineering, Universiti Teknologi Malaysia, 81310 Skudai, Johor, Malaysia
[3]Razak School of Engineering and Advanced Technology, Universiti Teknologi Malaysia, 54100 Kuala Lumpur, Malaysia

---

Abstract *The aim of this study is to present a systematic approach for the grid convergence analysis in simulating flow around a realistic generic model, DrivAer. The numerical simulation is modelled using unsteady Reynolds Averaged Navier-Stokes (URANS) equation. A minimum of three different grid resolutions are considered, which are fine, medium and coarse in order to investigate the grid independency. Richardson extrapolation and Grid Convergence Index (GCI) are introduced to quantitatively evaluate the grid independency. Based on the results between those three different grids, a monotonic convergence criteria has been achieved. The reduction in GCI value indicates that the grid convergence error has been significantly reduced, in which the fine grid has a GCI value less than 7%. Additionally, the result from the fine grid is only 6% difference if compared with previous experimental study.*

Keywords: *CFD, Drivaer, Grid Convergence Index, Openfoam Simulation, URANS*

Introduction

Since 2011, study of flow around a realistic generic vehicle model, DrivAer, has been continuously be the subject of many research (Aljure, Calafell, Baez, & Oliva, 2018; Ashton, West, Lardeau, & Revell, 2016; Guilmineau, 2014; Heft, Indinger, & Adams, 2012a; Shinde, Joshi, & Kishor, 2016). DrivAer is a generic vehicle model proposed by the Technical University of Munchen (TUM), in cooperation with Audi AG and BMW Group. The model has been designed closely similar as the production car. Recently, most of the automotive aerodynamic research usually relied on simplified car models such as the Ahmed Body (Ahmed, Ramm, & Faltin, 1984) and the SAE Type 4 (fullback) model (Cogotti, 1998). These simplified car models could represent data for a basic understanding flow structures. However, the simplified models are unable to produce a detailed flow phenomena similar to a real production car. Shaharuddin et al. (2017) has compared the aerodynamic and flow pattern between the SAE Type 4 (fullback) model and DrivAer Fastback model and confirm that the simplified car model (SAE Type 4) is unable to represent the detailed flow structures but for the DrivAer model, the flow structures are more complex and very similar to a real production car. The DrivAer is introduced by TUM to represent the actual flow behaviour around the car. A study conducted by Heft et al. (2012a) has shown that most of the complex flow structures

occurred around a real production car can be correctly captured by using the DrivAer model, whereas the simplified car models produced a simple flow structures.

Despite the fact that there are many similar investigations have been made numerically by using the DrivAer model, there is still a small variation shown by the results obtained. This could be due to the differences in the construction and distribution of the mesh. Four different meshes have been used by Guilmineau (2014) in order to investigate the flow around a DrivAer fastback model by using the Explicit Algebraic Reynolds Stress Model (EARSM) turbulence model. The coarsest mesh is 19 million cells and the finest mesh is 45 million cells. Results shown that all meshes under-predict the drag coefficient compared to the experimental data. This shows that the used of high number of mesh excessively is not a guarantee to provide a similar result as the experimental data. Additionally, it requires high computational cost and it is impractical for the industry. Therefore, in order to verify that the results obtained are acceptable and reliable, for any numerical study, it is important to investigate the sensitivity of each grid resolution on certain flow properties in a systematic manner.

Computational Fluid Dynamic (CFD) community agree that the source of errors from the numerical simulation is not entirely due to the grid convergence error, but also affected by the other factors. However, the total error can be minimised by reducing the error due to the grid dependency and this should be done systematically. Therefore, the purpose of this study is to present a systematic approach for grid convergence on the simulation of flow around a realistic generic model, DrivAer, by using Grid Convergence Index (GCI) that is based on the Richardson extrapolation.

Methodology

Model Description

The model used in this study is an open-source realistic generic vehicle model, DrivAer, which has a similar exterior design and dimension as the existing passenger cars. Thus, it would provide more realistic results. The detailed geometry of the model is shown in Figure 1. It is a fastback model with a smooth underbody.

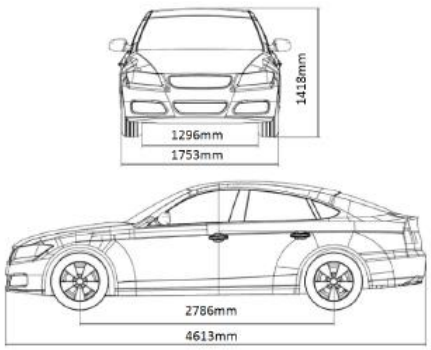

Figure 1: Baseline Configurations In Current Study, Drivaer Fastback (Heft, Indinger, & Adams, 2012b)

The length (L), height (H) and width (W) of the DrivAer Fastback geometry are 4613mm, 1418mm and 1753mm, respectively.

Computational Domain

The size of the numerical wind tunnel (computational domain) is $10\text{L} \times 8\text{H} \times 5.5\text{W}$. The distance from the inlet to the model is 2L. Meanwhile, the distance from the model to the outlet is made large, which is 7L for allowing the wake to dissipate naturally. The model is made attached to non-moving ground. In order to reduce the computational time, only half of the model is simulated. Figure 2 and 3 show the schematic diagram of the computational domain.

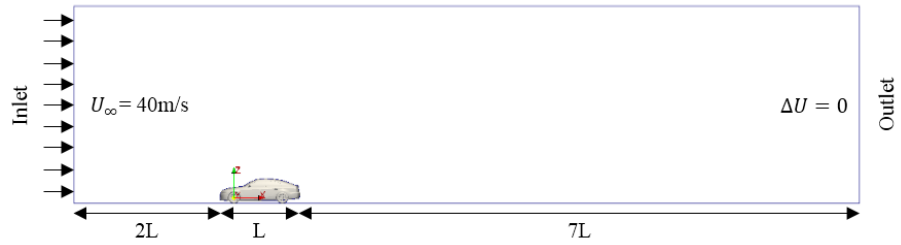

Figure 2: Side view

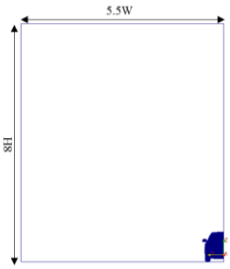

Figure 3: Front view

Free stream velocity (U_∞) in the x-direction is fixed for the inlet condition to drive wind flow through the internal domain. At the upstream floor, slip boundary condition is imposed to prevent the development of boundary layer, while no slip boundary condition is imposed at the downstream to allow the effect of viscosity from the wake interacts with the downstream floor.

Mesh Description

The mesh inside the computational domain is constructed by using the mesh generation utility, *blockMesh*, which is a primary meshing tool provided in the OpenFOAM software, while the mesh refinement around the DrivAer model is generated by using another mesh generation utility that is also supplied with the OpenFOAM, which is *snappyHexMesh* that generates unstructured mesh. Based on the grid refinement factor (r), three different grid resolutions are considered in this study which is fine, medium and coarse grids. Celik, Ghia, Roache, & Freitas (2008) stated that, in order to optimise the accuracy of turbulent flow prediction, a desirable value of r has to be greater than 1.3. The grid refinement factor (r) can be calculated as follows;

$$r_{21} = \frac{h_2}{h_1} \tag{1}$$

$$r_{32} = \frac{h_3}{h_2} \tag{2}$$

where the subscripts 1,2 and 3 indicate the types of grid used which are fine, medium and coarse, respectively. Meanwhile h represents the average cell size, mesh or grid size. For three dimensional (3D), the average cell size can be calculated by using the following equation (Celik et al., 2008);

$$h_{ave} = \left[\frac{1}{N}\sum_{i=1}^{N}(\Delta v_i)\right]^{1/3} \tag{3}$$

where N is the total number of cells used for the computation and Δv_i is the volume of the ith cell. Table 1 shows the grid parameters for the three cases. The mesh generation and distribution for the fine case are shown in Figure 4.

Table 1: Parameters Used For All Cases

Case	Fine (1)	Medium (2)	Coarse (3)
Total No. of Cells, N	4 711 750	2 137 902	851 152
Average cell size, h_{ave}	0.1036	0.1348	0.1833
Refinement ratio, r	r_{21} = 1.30		r_{32} = 1.36

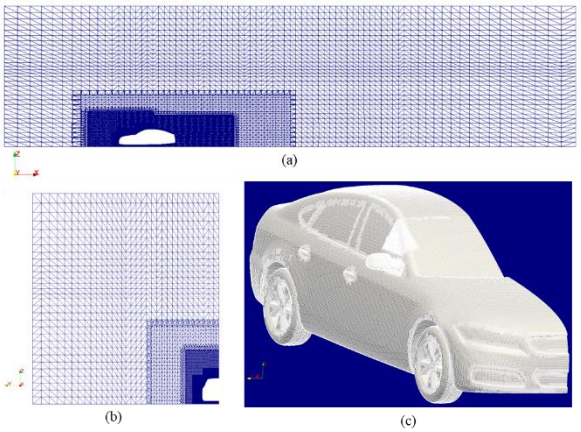

Figure 4: Mesh Generation For The Fine Case. (A) Mesh On The $x-z$ Plane (B) Mesh On The $y-z$ Plane (C) Mesh On The Drivaer Fastback Model.

Numerical Setting

Governing Equation

The governing equations for the turbulent incompressible flow encountered in the current study are the unsteady Reynolds-Averaged Navier-Stokes (URANS) equations as follows;

Continuity:

$$\rho \frac{\partial U_i}{\partial x_j} = 0 \tag{4}$$

Momentum:

$$\rho \frac{\partial U_i}{\partial t} + \rho U_j \frac{\partial U_i}{\partial x_j} = \frac{\partial}{\partial x_j}\left[-\bar{p}\delta_{ij} + \mu\left(\frac{\partial U_i}{\partial x_j} + \frac{\partial U_j}{\partial x_i}\right) - \rho\overline{u_i' u_j'}\right] \tag{5}$$

where $\rho\overline{u_i' u_j'}$ is the Reynolds stress, which then is solved using eddy-viscosity model based on the Boussinesq assumption;

$$-\overline{\rho u_i' u_j'} = \mu_t\left(\frac{\partial \bar{u}_i}{\partial x_j} + \frac{\partial \bar{u}_j}{\partial x_i}\right) - \frac{2}{3}\left(\rho k + \mu_t \frac{\partial \bar{u}_k}{\partial x_k}\right)\delta_{ij} \tag{6}$$

where μ_t the turbulent or eddy viscosity and k is the turbulent kinetic energy.

Turbulence Model

The turbulent kinetic energy (k) and the specific dissipation rate (ω) are solved using the two equations model that is based on Shear Stress Transport (SST) k-ω (Jasak, 1996);

$$\frac{\partial k}{\partial t} + U_j \frac{\partial k}{\partial x_j} = P_k - \beta^* k\omega + \frac{\partial}{\partial x_j}\left[(v + \sigma_k v_T)\frac{\partial k}{\partial x_j}\right] \tag{7}$$

$$\frac{\partial \omega}{\partial t} + U_j \frac{\partial \omega}{\partial x_j} = \alpha S^2 - \beta\omega^2 + \frac{\partial}{\partial x_j}\left[(v + \sigma_\omega v_T)\frac{\partial \omega}{\partial x_j}\right] + 2(1 - F_1)\sigma_{\omega 2}\frac{1}{\omega}\frac{\partial k}{\partial x_i}\frac{\partial \omega}{\partial x_i} \tag{8}$$

where v_T is kinematic eddy viscosity and it is defined as;

$$v_T = \frac{a_1 k}{\max(a_1\omega, SF_2)} \tag{9}$$

Boundary Condition

A uniform velocity, $U = 40m/s$, is imposed at the inlet as well as at the top and side of the computational domain as stated in Table 2. Based on the length (L) of the DrivAer Fastback model, the Reynolds number is, *Re = 4.87 x 10^6* which make the flow is fully turbulent. The flow is assumed incompressible as the Mach number is below than 0.3.

Table 2: Numerical Boundary Conditions For Drivaer Model

	Inlet	Outlet	Top	Side	Downstream & DrivAer Fastback	Upstream
$k\ (m^2 s^2)$	fixedValue (0.0016)	zeroGradient	fixedValue (0.0016)	fixedValue (0.0016)	kqRWallFunction	slip
$\omega\ (s^{-1})$	fixedValue (4.36)	zeroGradient	fixedValue (4.36)	fixedValue (4.36)	omegaWallFunction	slip
$nut\ (m^2/s)$	fixedValue (3.69×10^{-4})	zeroGradient	fixedValue (3.69×10^{-4})	fixedValue (3.69×10^{-4})	nutkWallFunction	slip
$p\ (kg/ms^2)$	zeroGradient	0	zeroGradient	zeroGradient	0	slip
$U\ (m/s)$	fixedValue (40)	zeroGradient	fixedValue (40)	fixedValue (40)	zeroGradient	slip

Some important settings used in the OpenFOAM software are shown in Table 3. The discretization schemes used are at least in the second-order accuracy and this has been applied to all equations.

Table 3: Solver Settings Used In Openfoam

Discretization	Scheme
Temporal discretization	Backward (2nd order implicit)
Gradient	Central differencing (2nd order)
Divergence	QUICKV (3rd order)
Laplacian	Gauss linear differencing scheme (2nd order unbounded)
Pressure-velocity Coupling	PIMPLE
Turbulence model	URANS SST *k-ω*

Table 4 shows three different time step used based on the different grid cases in order to ensure that the Courant-Fredichs-Lewy (CFL) number always below 0.8.

Table 4: Time Step For All Cases

Case	Fine (1)	Medium (2)	Coarse (3)
Time step (Δt)	0.000005	0.000025	0.00003

Results and Discussions

Richardson Extrapolation

Richardson extrapolation (Richardson & Gaunt, 1927) is used to calculate a higher-order estimate of the continuum value (value at zero grid spacing) from a series of lower-order discrete values. In grid refinement study, the value estimated from the Richardson extrapolation is obtained if the cell grid size tends to zero ($h \to 0$). Extrapolation is made at least from the comparison between two different grid resolutions results. Nevertheless, Stern, Wilson, Coleman & Paterson (2001) stated that a minimum of three grid resolutions are required for a convergence study.

The Richardson extrapolation can be generalised by p^{th} – order methods (Roache, 1994);

$$f_{RE} \approx f_1 + \left[\frac{(f_1 - f_2)}{(r^p - 1)}\right] \tag{10}$$

where r is the grid refinement ratio as mentioned in (1) and (2).

From (10), the extrapolated value is varied due to different order of accuracy (p) that can be estimated as follows;

$$p = \frac{1}{\ln(r)}\left|\ln\left|{}^{\varepsilon_{32}}/_{\varepsilon_{21}}\right| + q(p)\right| \quad (11)$$

$$\varepsilon_{32} = f_3 - f_2 \quad (12)$$

$$\varepsilon_{21} = f_2 - f_1 \quad (13)$$

$$q(p) = \ln\left(\frac{r_{21}^{p} - s}{r_{32}^{p} - s}\right) \quad (14)$$

$$s = 1.sign\left({}^{\varepsilon_{32}}/_{\varepsilon_{21}}\right) \quad (15)$$

Note that $q(p) = 0$ if the grid refinement ratio is constant (i.e., $r_{21} = r_{32}$). However, the grid refinement ratio in the current study is not constant ($r_{21} \neq r_{32}$) as shown in Table 1 and therefore the extrapolated value differs based on the order of accuracy (p).

In order to evaluate the extrapolated value of these resolutions, the convergence condition must be first determined, where there are three possible convergence conditions;

1. Monotonic convergence ($0 < R < 1$)
2. Oscillatory convergence ($R < 0$)
3. Divergence ($R > 1$)

where R is the convergence ratio that is defined as follows;

$$R = \frac{\varepsilon_{21}}{\varepsilon_{32}} \quad (16)$$

Grid Convergence Index

Grid Convergence Index (GCI) provides a uniform manner in reporting the results of grid convergence studies (Roache, 1994) in which it will gives a result that approaches the actual result as the grid size approaches to zero. It is based on the estimated fractional error derived from the generalised Richardson Extrapolation. GCI represents the percentage of the computed value that is away from the value of the asymptotic numerical value and how much the resolution would be affected with a further grid refinement. A small value of GCI shows that the computation is within the asymptotic range. There have been many published studies that showing the GCI results for many fundamental and engineering problems (Ali, Doolan, & Wheatley, 2009; Celik et al., 2008; Ishak, Ali, & Shaikh Salim, 2017; Maruai, Ali, Ismail, & Zaki, 2018; Roache, 1994). However, there is still no reported study on the GCI for a numerical simulation of a realistic car model. The GCI result is important as it can be the benchmark for future numerical study.

The GCI for the fine grid resolution is calculated as follows;

$$GCI_{i+1,i} = F_s \frac{\left|\varepsilon_{i+1,i}\right|}{f_i(r^p - 1)} \times 100\% \quad (17)$$

where F_s is the safety factor. According to Wilcox (2006), for comparisons between three or more grids, the safety factor considered is 1.25.

The percentage error between the simulation value and the extrapolated value based on Richardson extrapolation is calculated as follows;

$$E_i = \left|\frac{f_i - f_{RE}}{f_{RE}}\right| \times 100\% \quad (18)$$

For a better analysis, it is suggested to consider three levels of grid resolution in order to correctly evaluate the order of convergence and to ensure that the solutions are within the asymptotic range of convergence. Studies on grid refinement by Ali et al. (2009), Ishak et al. (2017) and Maruai et al. (2018) have also considered three level of grid resolutions in which their results show that the grid refinement is achieving a monotonic converged criteria that indicates the grid convergence error is progressively reduced.

Table 5: Comparison Of Forces Coefficient Parameter Between The Three Mesh Resolutions And The Extrapolated Value Based On Richardson Extrapolation Calculation

Case	Fine (f_1)	Medium (f_2)	Coarse (f_3)	f_{RE}
Drag Coefficient, C_{Dmean}	0.2456	0.2524	0.2652	0.2333
f_i/f_{RE}	1.0527	1.0819	1.1367	
Error (%)	5.2718	8.1865	13.6730	
Lift Coefficient, C_{Lmean}	-0.0510	-0.0490	-0.0436	-0.0539
f_i/f_{RE}	0.9462	0.9091	0.8089	
Error (%)	5.3518	9.0635	19.0851	

The results of forces coefficient parameter obtained from the simulation of the three grid resolutions and its corresponding extrapolated values based on Richardson Extrapolation equation are represented in Table 5. Two parameters are considered which are, the mean drag and mean lift coefficients. Both forces coefficient are calculated once a statistically steady data is obtained. Percentage error for the three grid resolutions also are calculated using Equation (18) in which the fine mesh gives the percentage of error below 6%.

Table 6: Order Of Accuracy And Grid Convergence Index For Three Grid Resolution Based On Forces Coefficient Parameter

Case	$\lvert\varepsilon_{32}\rvert$	$\lvert\varepsilon_{21}\rvert$	R	p	GCI_{32}(%)	GCI_{21}(%)
C_{Dmean}	0.0132	0.0070	0.5313	1.6708	9.4588	6.2598
C_{Lmean}	0.0054	0.0020	-0.0539	2	16.2486	7.0680

Table 6 summarises the order of accuracy and Grid Convergence Index (GCI) values. The convergence ratio for both parameter, drag and lift, shows that the refinement condition is monotonic as the value is in the range of $0 < R < 1$. The GCI value between fine and medium grid is relatively small compared to the GCI value between medium and coarse grid. This indicates that the dependency of the numerical simulation on the cell size has been reduced and the fine grid is nearly grid independent. In addition, further refinement of the fine grid resolution will not give a great impact on the simulation results.

The comparison between the mean drag coefficient C_{Dmean} and the Richardson extrapolation value for all three grids are shown in Figure 5. The discrepancy between the resolution and the extrapolated value becomes smaller as the grid is refined. The ratio between the result obtained using the fine grid with the estimated value using the Richardson extrapolation is $f_1/f_{RE} = 1.0527$. This corresponds to a minimum error of $E_1 = 5.2718\%$ as compared to the extrapolated value. Percentage errors between the three different grid resolutions are shown in Figure 6. The error values also have shown a reduction when approaching the fine grid.

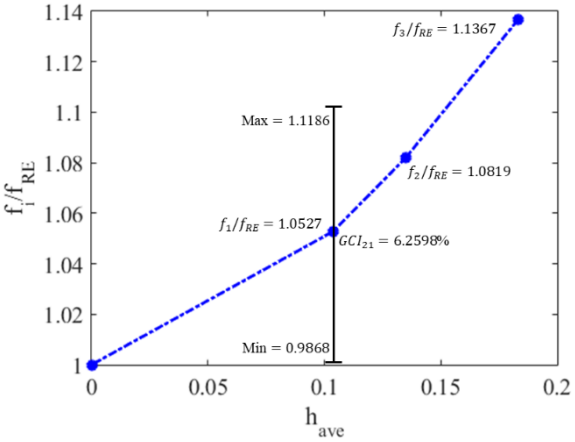

Figure 5: Extrapolated Value Of C_{Dmean}

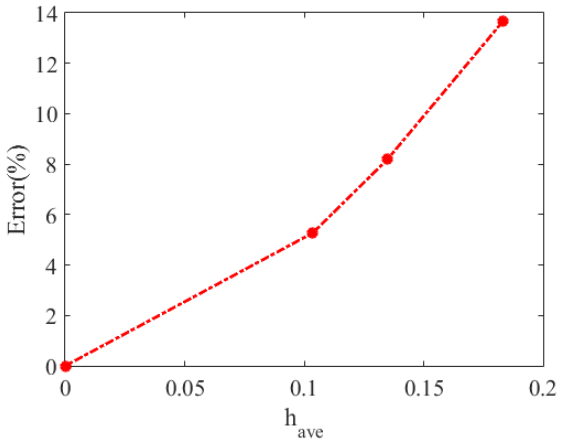

Figure 6: Percentage Error For C_{Dmean}

From the calculation between the GCI and extrapolated value for fine grid, for an applicable and reliable grid or mesh, the maximum and minimum values for the extrapolated values are 1.1186 and 0.9868, respectively.

Result from mean lift coeffcient C_{Lmean} also has shown that there is a reduction in the GCI value for fine grid when compared with coarse order grid resolution ($GCI_{21} < GCI_{32}$). According to the GCI value of fine grid and based on ratio between the fine grid and the extapolated value, its maximum and minimum values are 1.0131 and 0.8793, respectively as shown in Figure 7. The percentage error also is decreased when the grid becomes finer as observed in Figure 8 where the error for fine grid is 5.3518%.

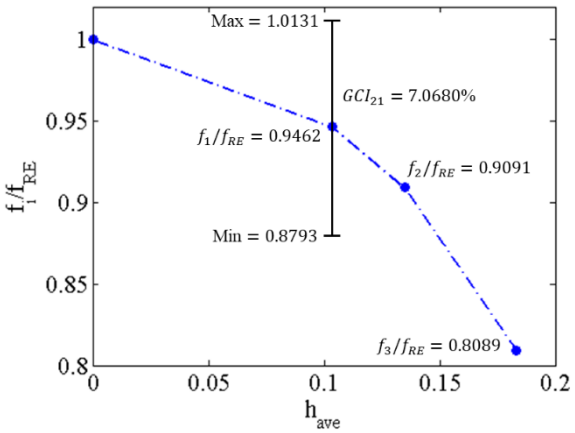

Figure 7: Extrapolated Value Of C_{Lmean}

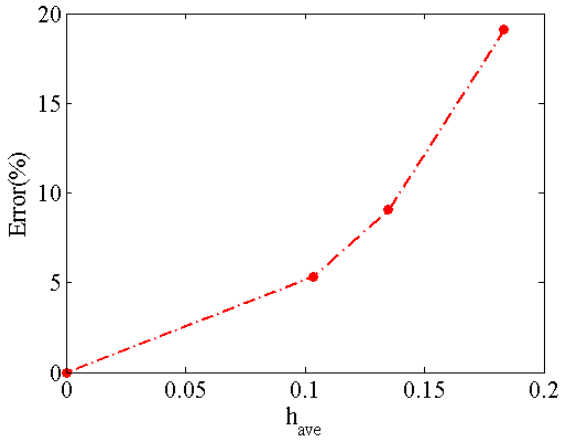

Figure 8: Percentage Error For C_{Lmean}

Forces Coefficient and Flow Visualisation

In order to reduce the computational cost, the cell size near the surface is properly treated by using the wall function. The overall number of grids can be minimized, especially at the near-wall regions while maintaining the accuracy of the computational result (Ishak et al., 2017). The corresponding average y^+ values on the DrivAer Fastback body and ground floor (downstream) for all cases are shown in Table 7. On the body, the y^+ values are on the log-law region which is in the range of $30 < y^+ < 300$. Meanwhile a greater y^+ is generated at the ground floor, but the values are still accepted since the main focused is given on the mesh generation around the model. Generally, fine grid case has shown a lower y^+ values compared to the other two cases and its distribution of y^+ on the body can be observed in Figure 9.

Table 7: The y^+ Values On The Wall For All Cases

Case	Body			Ground Floor		
	y^+min	y^+max	y^+avg	y^+min	y^+max	y^+avg
Fine (f_1)	0.5412	675.2739	54.7379	1.0030	8085.6739	428.8274
Medium (f_2)	0.7472	566.4583	112.8169	4.5087	9076.7770	702.3972
Coarse (f_3)	1.3404	974.7539	153.9980	0.1786	7722.4127	738.3401

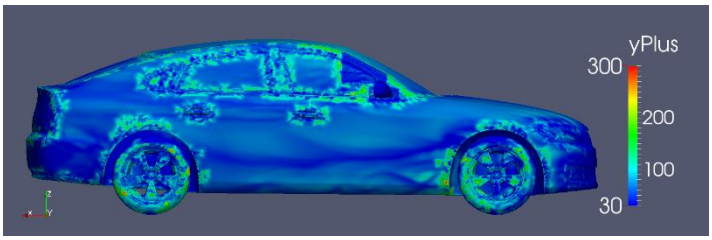

Figure 9: Distribution Of y^+(Yplus) On The Drivaer Fastback Model

Table 8 compares the drag coefficient (C_D) results of current study for the fine grid case with previous available data. It shows that the results obtained in the current study for the unsteady case has a good agreement with the experimental results provided by Guilmineau (2014) and Heft et al. (2012a). Overall, current results obtained are below 6% difference compared to the previous studies.

Table 8: Comparison Of Drag Coefficient (C_D) Between Current Study And Previous Studies

Turbulence Model	Method	Drag Coefficient (C_D)	%Δ
Current (Fine)	*k-ω* SST (Steady)	0.2542	2.61%
Current (Fine)	*k-ω* SST (Unsteady)	0.2456	5.90%
Heft et al. (2012a)	*k-ω* SST (Steady)	0.2410	7.66%
Guilmineau (2014)	RANS (EARSM) (Steady)	0.2573	1.42%
Shinde et al. (2016)	*k-ω* SST (Steady)	0.2510	3.83%
Ashton et al. (2016)	*k-ω* SST (Steady)	0.2600	0.38%
Ashton et al. (2016)	Realisable k-ε (RKE) (Steady)	0.2440	6.51%
Heft et al. (2012a)	Experiment	0.2430	6.90%
Guilmineau (2014)	Experiment	0.2610	-

Result from the URANS numerical simulation for the vortex structure around the DrivAer Fastback model using the iso-surface of the second invariant of velocity gradient (Q) is shown in Figure 10. Compared to the current study that used only 4.7 million cells, the flow characteristics captured a similar flow pattern as the study done by Guilmineau (2014) which has been done with a total of 45 million number of cells using RANS approach. Note that different contours are used between both figures. However similar pattern of A-pillar vortex is observed in both figures, in which a conical shape that elevated downstream is formed. Moreover, it is clearly can be observed that the flow is detached at the side view mirror and at the A-pillar. A long conical wake is produced near the side view mirror and also there are vortex structures generated by the wheels and at the rear end of the model. Similar flow structures are also observed by Aljure et al. (2018).

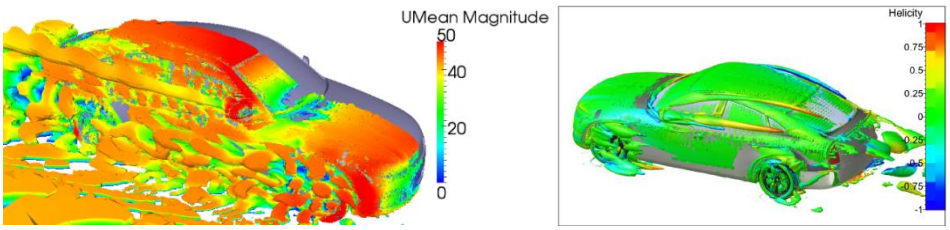

Figure 10: Iso-Surface Of The Second Invariant (Q) Based On Mean Velocity Magnitude. Current Study (Left), Study By Guilmineau (Right) (Guilmineau, 2014)

Figure 11 shows the streamlines at the symmetry of the DrivAer Fastback model that is constructed using the time-averaged velocity flow field. The flow remains attached at the rear window and two counter rotating vortices are observed at the wake of the model. This result also very similar to the study done by Guilmineau (2014).

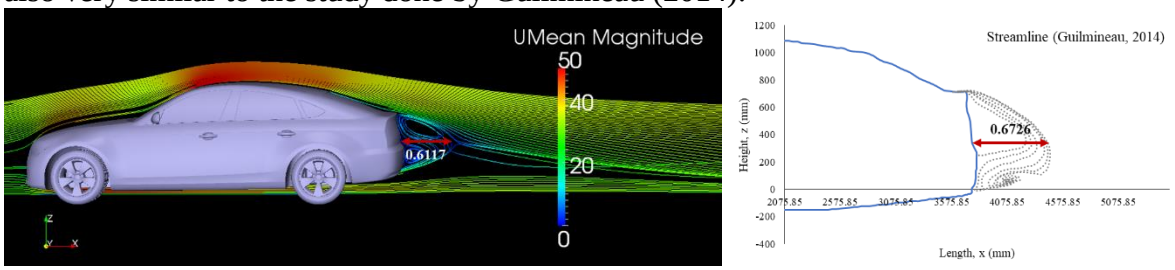

Figure 11: Streamlines At The Symmetry Of The Model. Current Study (Top), Study By Guilmineau (Bottom) (Guilmineau, 2014)

By comparing the wake length for the DrivAer Fastback model with Guilmineau (2014), it can be seen that the wake length produced by current study is only about 9% shorter than the study done by Guilmineau. The pressure coefficient results obtained from the fine grid is also compared with the experimental and numerical data by Guilmineau (2014) study. The dimensionless pressure coefficient is defined as;

$$c_p = \frac{p - p_\infty}{0.5\rho u_\infty^2} \tag{19}$$

where p is the local static pressure and p_∞ is the free stream static pressure.

The pressure coefficient distribution on top and bottom of the symmetry plane of the DrivAer Fastback model are shown in Figure 12 and Figure 13, respectively. Generally, the pressure coefficient for current study has shown a good agreement as the experimental data provided by Guilmineau (2014). Meanwhile, there is only a small discrepancies observed when compared with the numerical data.

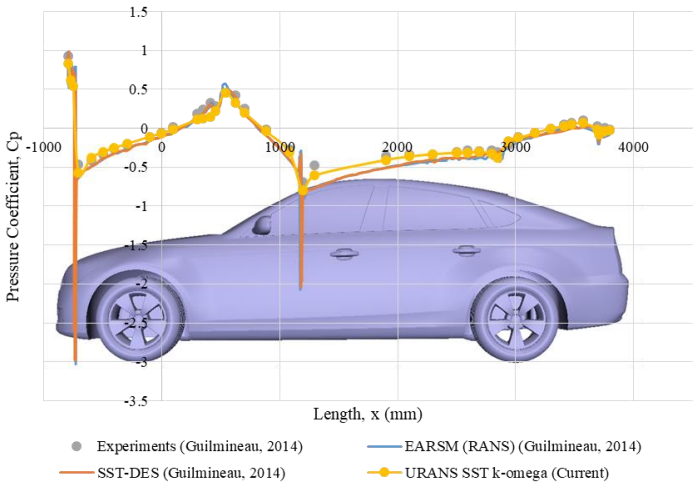

Figure 12: Pressure Coefficient (Cp) Distribution On Top Of Drivaer Fastback Model At The Symmetry Plane

Figure 12 compares the pressure coefficient along the top surface of the model between the current study and previous experimental and numerical studies by Guilmineau (2014). Current study is able to reproduce the same pressure distribution as the previous experimental study. A stagnation point is observed at the beginning of the measurement points where a sudden drop in pressure is observed. This is due to the flow separation occurred in front of the model (Aljure et al., 2018). The flow then recover at which the pressure slowly increased with distance downstream. At the junction between the hood and windshield, a peak in pressure is observed as the flow tends to separate before the pressure slowly decreasing over the windshield. This is a point where the favourable presure gradient starts to occur. In current study, speedy pressure recovery behaviour is observed in front of the roof junction and it continues to increase gradually further downstream. The pressure then rises slowly at the rear window and a sudden decrease in pressure is found at the end of the model that shows that there is a flow detachment created.

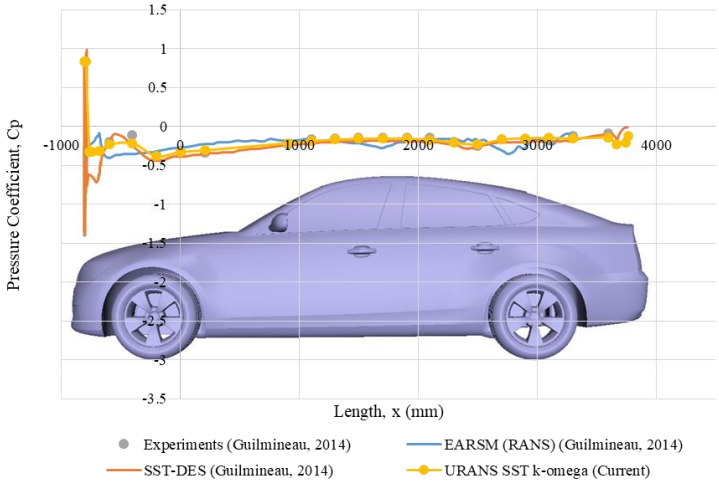

Figure 13: Pressure Coefficient (Cp) Distribution Below Of Drivaer Fastback Model At The Symmetry Plane

A good agreement with the previous experimental and numerical studies is also observed for the pressure distribution along the bottom surface of the model where the pressure coefficient gives a negative value starting from the beginning of the front wheels. The current study gives a better similarity with the previous experimental results. Based on the previous numerical study (Guilmineau, 2014), small differences observed in front of the model is due to the different meshes used.

Conclusion

The grid convergence of flow around a realistic generic model, DrivAer has been numerically analysed that is based on a systematic assessment of computation grid refinement through the Grid Convergence Index (GCI) and Richardson extrapolation calculation. Based on the analysis performed, the calculated value of GCI gradually reduced as the grid system is refined. Results from the fine grid for both parameter have shown that the grid is appropriate to be used for further analysis. This is due to the GCI value of fine grid is less than 7%. Additionally, the drag coefficient obtained in the current study for the fine grid shows a good agreement with the previous studies with only less than 6% difference. Flow visualisation results also have captured the similar characteristics as the previous experimental study. The results of pressure coefficient on top and at bottom of the DrivAer Fastback model also have shown a similar pattern as the previous experimental results. Therefore, it can be concluded that the results of current study are practicable for further studies. Additionally, the study shows that by properly refining the grid systematically, the use of excessive number of grid can be prevented through a systematic mesh refining using Richardson extrapolation and Grid Convergence Index (GCI) method. Small number of grid usage reduces the simulation time and reduces the computational costs at once that are preferred by the industries.

Acknowledgements

This research is financially supported by the Ministry of Higher Education (MOHE) Malaysia under the Research University Grant (RUG) project of Universiti Teknologi Malaysia (Vot No. R.K130000.7843.4F712), High Performance Computer (HPC) Universiti Teknologi Malaysia for the use of their supercomputer facilities and also Malaysia-Japan International Institute of Technology (MJIIT) Incentive.

References (APA Sixth Edition)

Ahmed, S. R., Ramm, G., & Faltin, G. (1984). Some Salient Features of The Time-Averaged Ground Vehicle Wake. *SAE Technical Paper Series (840300)*.

Ali, M. S. M., Doolan, C. J., & Wheatley, V. (2009). Grid Convergence Study for a Two-Dimensional Simulation of Flow Around a Square Cylinder At a Low Reynolds Number. *Seventh International Conference on CFD in the Minerals and Process Industries CSIRO*, (December), 1–6.

Aljure, D. E., Calafell, J., Baez, A., & Oliva, A. (2018). Flow over a realistic car model: Wall modeled large eddy simulations assessment and unsteady effects. *Journal of Wind Engineering and Industrial Aerodynamics*, *174*(December 2017), 225–240. https://doi.org/10.1016/j.jweia.2017.12.027

Ashton, N., West, A., Lardeau, S., & Revell, A. (2016). Assessment of RANS and DES methods for realistic automotive models. *Computers and Fluids*, *128*, 1–15. https://doi.org/10.1016/j.compfluid.2016.01.008

Celik, I., Ghia, U., Roache, P. J., & Freitas, C. (2008). Procedure for Estimation and Reporting of Uncertainty Due to Discretization in CFD Applications. *Journal of Fluids Engineering*,

130(7), 78001. https://doi.org/10.1115/1.2960953

Cogotti, A. (1998). Parametric Study on the Ground Effect of a Simplified Car Model. *SAE Paper* (980031)

Guilmineau, E. (2014). Numerical Simulations of Flow around a Realistic Generic Car Model. *SAE International Journal of Passenger Cars - Mechanical Systems*, *7*(2), 2014-01–0607. https://doi.org/10.4271/2014-01-0607

Heft, A. I., Indinger, T., & Adams, N. A. (2012a). Experimental and Numerical Investigation of the DrivAer Model. *Proceedings of the ASME 2012 Fluids Engineering Summer Meeting, July 8-12*(FEDSM2012-72272), 1–11.

Heft, A. I., Indinger, T., & Adams, N. A. (2012b). Introduction of a New Realistic Generic Car Model for Aerodynamic Investigations. https://doi.org/10.4271/2012-01-0168

Ishak, I. A., Ali, M. S. M., & Shaikh Salim, S. A. Z. (2017). Mesh size refining for a simulation of flow around a generic train model. *Wind and Structures, An International Journal*, *24*(3), 223–247. https://doi.org/10.12989/was.2017.24.3.223

Jasak, H. (1996). *Error Analysis and Estimation for the Finite Volume Method with Applications to Fluid Flows*. *Direct*. https://doi.org/10.1016/S0020-7683(02)00168-3

Maruai, N. M., Ali, M. S. M., Ismail, M. H., & Zaki, S. A. (2018). Flow-induced vibration of a square cylinder and downstream flat plate associated with micro-scale energy harvester. *Journal of Wind Engineering and Industrial Aerodynamics*, *175*, 264–282. https://doi.org/10.1016/j.jweia.2018.01.010

Richardson, L. F., & Gaunt, J. A. (1927). The Deferred Approache to the Limit. Part I. Single Lattice. Part II. Interpenetrating Lattices. *Philosophical Transactions of the Royal Society of London. Series A, Containing Papers of a Mathematical or Physical Character*, *226*, 299–361.

Roache, P. J. (1994). Perspective: A Method for Uniform Reporting of Grid Refinement Studies. *Journal of Fluids Engineering*, *116*, 405–413.

Shaharuddin, N. H., Ali, M. S. M., Mansor, S., Muhamad, S., Zaki, S. A., & Usman, M. (2017). Flow simulations of generic vehicle model SAE type 4 and DrivAer Fastback using OpenFOAM. *Journal of Advanced Research in Fluid Mechanics and Thermal Sciences*, *37*(1), 18–31.

Shinde, G., Joshi, A., & Kishor, N. (2016). Numerical Investigations of the DrivAer Car Model using Opensource CFD Solver OpenFOAM Numerical Investigations of the DrivAer Car Model using Opensource CFD Solver OpenFOAM Abstract : In *Tata Consultancy Services, Pune, India* (pp. 0–12).

Stern, F., Wilson, R. V., Coleman, H. W., & Paterson, E. G. (2001). Comprehensive approach to verification and validation of CFD simulations part 1: Methodology and procedures. *Journal of Fluids Engineering*, 123(4), 793-802

Wilcox, D. C. (2006). Turbulence Modelling for CFD, 3rd Ed., DCW Industries, Inc.

Proceeding: 5th International Conference on Applied Sciences and Engineering (ICASEA, 2018)
(eISBN 978-967-15744-1-6)
Capthorne Hotel, Cameron Highlands, Malaysia

NOISE MEASUREMENT IN ANECHOIC WIND TUNNEL OF ROD-AIRFOIL WITH LEADING EDGE SERRATIONS

Siti Ruhliah Lizarose Samion[1]
Mohamed Sukri Mat Ali[1]

[1]Malaysia-Japan International Institute of Technology, University of Technology Malaysia, 54 100 Kuala Lumpur, MALAYSIA

Abstract: *Turbulent flow interaction with the leading edge of an airfoil generates a well-known leading edge noise. The present work is an experimental investigation of reducing the leading edge noise by adapting serrations on the leading edge of NACA0012 airfoil. A rod is placed upstream of the airfoil to magnify the turbulence flow-leading edge interaction. Locations and the size of the serrations are two parameters being investigated for the noise reduction. The study found that a noise reduction up to 3.5 dB is obtained when the size of the serration is wider. Additionally, more sound reduction can be obtained when the angle of attack is increased.*

Keywords: *Airfoil, Leading Edge Noise, Leading Edge Serrations*

Introduction

Airfoil geometry is a common part in many engineering applications, but it is also responsible for the generation of what we call as airfoil self-noise. In a strong perturbed flow, the airfoil-turbulence interaction noise (ATIN) is prominent (Paterson 1976; Oerleman 2004; Moreau 2005). The important devices involving such noise are the rotor configurations of turbo engines, helicopter rotors, and wind turbines in which the downstream airfoil blades lie in the wake of upstream blades.

The airfoil experiences fluctuating lift as a result of the unsteady pressure field produced by the airfoil in response to the turbulence. The pressure fluctuations are generated by the interaction between the turbulent eddies and the solid surface of the airfoil. Thus part of the noise generated by this interaction is radiated to the far field and is referred to as the leading edge noise or the ATIN in this study. ATIN is mostly noticeable in the low frequency version. This is because the noise generation mechanism is dominated by the large turbulent structures.

In most experimental investigation, the upstream turbulence is generated and conveyed downstream to the airfoil by a vortex generator to create the turbulent-leading edge interaction as in the real condition. The turbulence-generating-grid is also a common mechanism by researchers to have the turbulence with a full spectrum of wave number. Jackson et al. (1973) experimentally investigated the lift on both a two-dimensional wing and a finite aspect ratio wing subjected to grid turbulence in a closed return, low-speed wind tunnel. Turbulence was generated by a square grid of rectangular bars with 25.4 mm wide vertical bars and 6.35 mm wide horizontal bars. Paterson and Amiet (1976) implemented homogeneous, isotropic turbulence field in their experiment in an open-jet, open-circuit wind tunnel with two scales anechoic chambers. The turbulence was generated using a grid with 2.54 cm bars perpendicular

to the free-stream and 1.91 cm bars parallel to the free-stream. The grid has a mesh size of 13.3 cm and solidity of 0.35 and was located 11.7 mesh lengths upstream of the airfoil which allowed the turbulence to become isotropic before reaching the airfoil. Their turbulence scale was approximately 15% of the airfoil chord and had 4% turbulence intensity. They obtained that the noise associated with the interaction of the turbulence and the airfoil was an order of magnitude higher than other noise sources as the peak in the unsteady pressure was located close to the leading edge. Other several experimental investigations, like McKeough and Graham (1980), Mish et al. (2003), Oerlemann & Migliore (2004), Moreau et al. (2005), Narayanan et al. (2014) and Chaitanya et al. (2015, 2017) also used grid generated turbulence in their airfoil leading edge noise experiments. However the experimental studies of the interaction of grid-generated turbulence have created somewhat a confusing picture of the effects of the turbulence interaction with the unsteady surface. For instance, the measurement of Oerlemann's (2004) showed up to 5 dB increased in the noise sound level as the AOA was increased from 0° to 8° for a variety of airfoils while the experimental results of Moreau et al. (2005) showed almost no AOA effects on the radiated noise. This can explain the discrepancies of the far field noise measurements and the challenges to understand the interaction of turbulence with the noise generated at the leading edge. More recent experimental studies using the leading edge (LE) serrations as the ATIN reduction treatments, like Chaitanya et al. (2015, 2017), they correlated the measured turbulence spectrum with that of Von Karman's for longitudinal isotropic turbulence by Pope (1984) and confirmed the turbulence generated in the isotropic is in a good degree. They presented performance of the LE serrations on the ATIN reduction and showed somewhat good correlation of the serrations geometry on the reduction mechanism with the turbulence length scale Λ, from their experiment.

Gruber et al. (2013) used tandem airfoil configurations in an experiment to decompose the interaction noise due to the turbulent wake of upstream airfoil, and investigate its reduction due to the presence of leading edge serrations on the downstream airfoil. This study for the first time combined two airfoils to imitate a rotor-stator broadband interaction in a turbofan aircraft engine. The reductions of ATIN level has been obtained to be up to 6 dB.

In a numerical study, few types of synthetic eddy method have been implemented for inflow turbulence generation. One of them is the vortical disturbance. Turner and Kim (2016) modelled a single spanwise vortex filament as the vertical disturbance. Through this approach, the resulting sound spectra are smooth making essential trends much easier to identify. Also, it is divergence free if compared to other approaches that are based on a single inflow disturbance that contain a range of frequencies. Turner and Kim (2016) has made it easier explained on the discrepencies between the peak and the root of LE serrations.

Therefore the turbulence physics upstream of airfoil is an important feature in the ATIN study as it plays the main role in the generating mechanism. Thus, it is much appreciated if any investigation of ATIN reduction can correlate the upstream turbulent characters with the reduction mechanism. The LES generally is the most promising Computational Fluid Dynamic (CFD) method to correctly predict the flows. However, extensions of the LES techniques to the prediction of ATIN generated by high Reynolds number flows in complex geometries have first to be benchmarked on relevant test cases. Such a test case must be based on geometry that contains some of the aerodynamic mechanisms encountered in ATIN applications, but remain simple enough from the computational point of view in order to achieve parametric study purposes. The rod-airfoil configuration is a relevant benchmark case for the ATIN

investigation. Jacob et al. (2005) was among the pioneer to introduce this rod-airfoil configuration. This is because at high Reynolds numbers, the rod sheds the well-known von Karman vortex street which acts as an oncoming turbulence disturbance onto the airfoil.

The rod flows had been extensively studied since the early work of Strouhal (1878) on Aeolian tones, and a complete review of this topic has been published by Zdravkovich (1997). However, although the von Karman street can be regarded as a gust, very few investigations concerning rod-airfoil configuration are reported in the literature. Stapountzis et al. (1999) and Cambanis (2001) focused on airfoil in the near wake of a very large rod (rod diameter ≈ airfoil chord length) in the context of wind turbine. Jacob et al. [14] highlighted three strong dimensional effects responsible for spectral broadening around the rod vortex shedding frequency in the subcritical regime, and identified that the airfoil leading edge was the main contributor to the noise emission in a rod-airfoil configuration due to vortex-structure interaction. Takagi et al. (2006) investigated the influence of the cylinder transverse location on the turbulent development of the flow around the airfoil. They found that the transverse location of the cylinder impacted on the radiated acoustic field. To identify the flow features responsible for the noise generation, Henning et al. (2008, 2009) performed dual PIV and simultaneous far-field microphone measurements. Based on their correlation technique, the regularities in the near field fluctuations are related to the radiated sound. Further comparison done by Lorenzoni et al. (2009) revealed the ability of rod-airfoil configuration to predict reasonably well compared with the real case, especially the magnitude of the tonal peak of emission and the narrow band spectrum around it. Microphone array measurements have also been done to investigate the influences of the rod diameter and the streamwise gap between the rod and the airfoil leading edge on the broadband noise generation frequencies higher than the vortex shedding frequency (Giesler, 2004). The results showed that the noise generation for the lower frequencies depended more strongly on the cylinder diameter than on the streamwise gap.

Moreover, further understanding on the details of the rod-airfoil interactions have been gained through numerical simulations too (Casalino et al. 2003; Sorguven et al. 2003; Boudet et al. 2005; Magagnato et al. 2003; Greschner et al. 2008; Berland et al. 2010, 2011). Berland (2011) found good agreement between calculation and experiment when they used direct noise calculation based on the compressible LES. The dominant noise source on the rod-airfoil model was found to be caused by impingement of Karman vortices upon leading edge of airfoil. Hence, modification of the leading edge (LE) aerodynamics can be expected to modify both the turbulent flow and the sound emission of the rod-airfoil configuration. One of the treatment implemented on the LE of airfoil is the introduction of the LE serrations. The LE serrations are inspired biologically from the silent flight of the barn owl. Many studies have proved the noise reduction promoted by LE serrations (Haeri et al. 2014; Hansen et al. 2011; Hersh et al. 1974; Johari et al. 2007; Yong Li et al. 2014).

The use of microphone array can accurately localize noise source and determine the dominant noise at different configurations, whereas the PIV technique reveals the corresponding flow physics of the noise generation, but the use of numerical studies can also give a good flow physics behavior based on the LES. Hence, the experimental results of current study aim to provide early expectation of using LE serrations in the NACA0012 ATIN reduction treatment before further numerical investigations can be done by the author. Current study takes the rod-airfoil configuration as the experiment case study and implemented LE serrations on the LE to investigate the noise perfornance. The experimental procedure is described in Section 2 and

Section 3. The noise results are presented in Section 4. Finally the conclusion from the study is given in the last section.

Experimental facilities and setup

The experiments were conducted using the anechoic open-return wind tunnel (AWT) at the University of New South Wales. The schematic diagram of the experimental setup is shown in Fig. 1. The facility contains a three-dimensional contraction which goes from 1.07 m × 1.07 m to 0.455 m × 0.455 m. The contraction area ratio is 5:5:1 with turbulence intensity of $Tu =$ 0.6%. The section for mounting the test case is surrounded with a chamber with walls line with foam blocks which provide an anechoic environment.

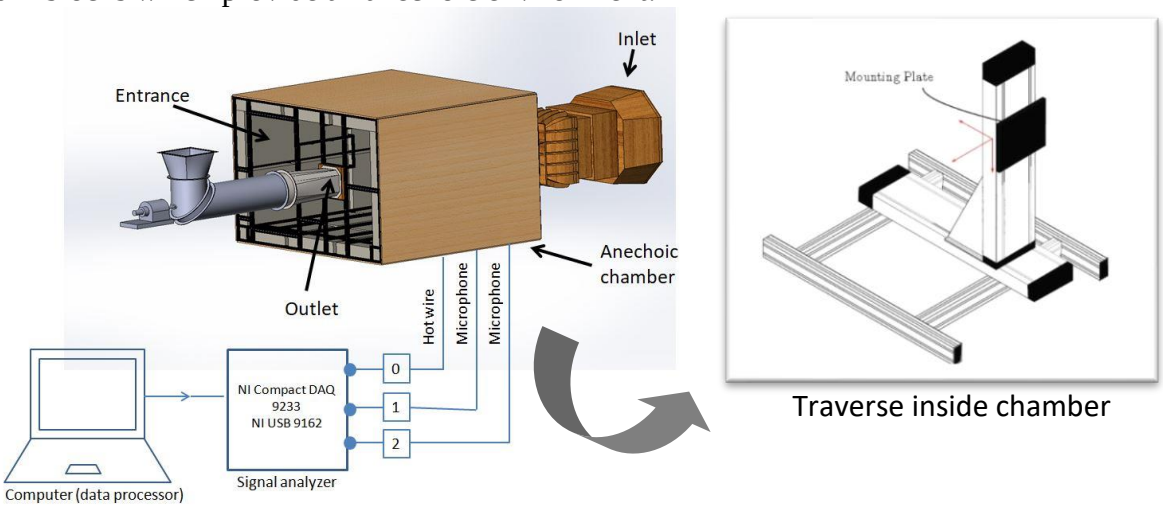

Figure 40 Schematic Diagram Of Experimental Setup.

Rod-airfoil configuration setup

The rod and airfoil have a span of 455 mm and are mounted in such a manner that the ends were fixed at the mounting plates as shown in Fig. 2. In this study, the coordinate system origin is located in the center of the outlet as shown in pink lines in the sketched figure. Axis x is aligned with the streamwise direction of the flow, axis y is the cross-stream direction, and pointing to the wind tunnel wall is z the spanwise direction. For current experiment, the free stream velocity of the jet is set at 15 m/s.

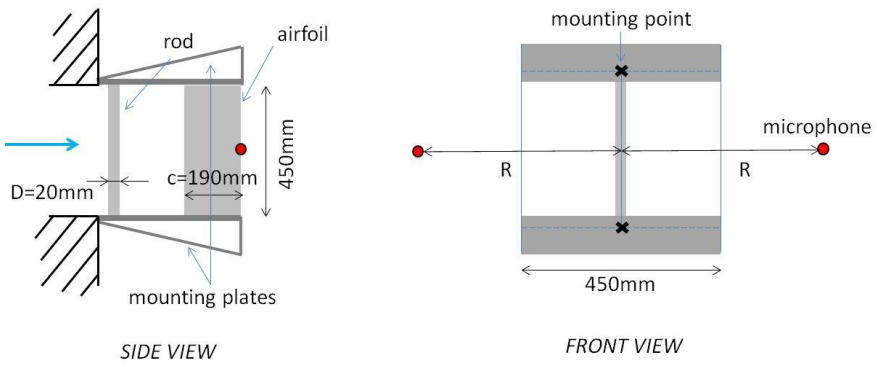

Figure 41 Sketch-Up Of Rod-Airfoil Configuration

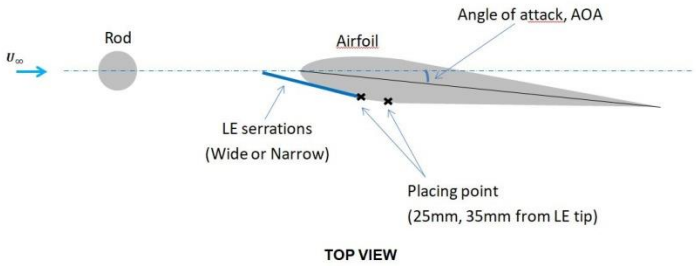

Figure 3 Schematic Diagram Of Leading Edge Serrations Used In Current Study

Hot wire anemometer for velocity profile measurement

The hot wire anemometer is used to perform wake survey of the streamwise velocity downstream of the problem configuration (in this study the airfoil wake). Hot wire is a thin cylindrical wire made from tungsten wire with thin platinum coating on its surface. The hot wire compute flow velocity from its relationship between local flow velocity and the convective heat transfer from the heated elements. When air flows over the wire, heat transfer from the wire will act to reduce the wire's temperature and unbalance the bridge. By simultaneously powering the wire and supplying it with current at the same rate at which heat is lost, the bridge can re-balance itself at a rate much faster than the smallest eddies in the flow, and the temperature of the wire can be kept virtually constant in time. The heat loss from the wire (which is directly proportional to the bridge voltage) is then monotonically related to the velocity of the flow.

A miniature wire probe with wire length of 1.2 mm diameter and of 5 μm is used. The hot wire is held by a self-designed traverse (shown in figure) and is connected to the signal analyzer the NI 9233 compact DAQ. Each velocity record is sampled at 2^{15} Hz for 15 seconds. This hot wire is calibrated inside of the AWT. For a calibration, the hot wire is placed on the traverse arm and positioned in the core of the wind tunnel. The wind tunnel is then run at 30 different velocities ranging from zero to 15 m/s. The velocity of the tunnel is monitored using a pitot tube connected to a Baratron transducer via long plastic tubing.

A careful calibration of the constant temperature anemometer is crucial to guarantee high reliable data. In current study, calibration is done to provide relation between velocity and output voltage of the CTA signal. For this purpose, the hot wire is exposed to varying flow speeds at the measurement location while a pitot tube, located to the hot wire measures the dynamic pressure. Use of the ambient temperature and barometric pressure enables the determination of the flow velocity in accordance to the equation below:

$$U_0 = \sqrt{\frac{2 \cdot p_{\mathrm{dyn}}}{\rho}} \qquad (1)$$

Relating the output voltage of the anemometer to the measured flow speed yields a calibration curve to be used for further hot wire measurements. The curve fit is performed by use of a polynomial function of 4th order (Eq. (2)) or the King's Law (Eq. (3)) whereas the polynomic form is expected to yield a higher accuracy. For a calibration in a velocity range of 0 m/s to 20 m/s measurement points where the most points cover the low to intermediate velocity region due to the higher gradient in voltage.

$$E = C_0 + C_1E + C_2E^2 + C_3E^3 + C_4E^4 \quad (2)$$
$$E^2 = C_0 + C_1(U)^n \quad (3)$$

Where E is the output voltage, C_0 to C_4 are calculated constants, U the flow velocity and n the scaling power of the velocity.

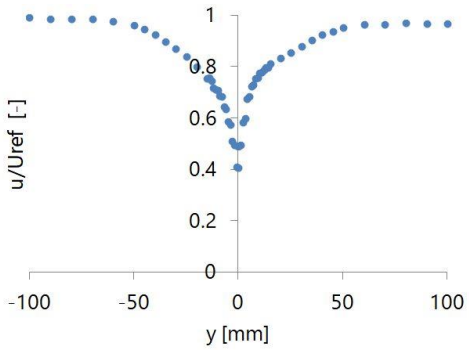

Figure 4 Velocity profile at x=10mm downstream the airfoil

Microphone setup for sound measurement

To measure the flow-induced noise, GRAS 40PH microphones are used. The microphones are held using microphone holder (as presented in Fig. 5). The microphone's frequency range is ±1 dB range between 50-20000 Hz as stated in the transducer documentations. The microphones are located at a distance R=500 mm away from the trailing edge of airfoil at 90 and 180 degree angles to the flow direction directly above and below the airfoil.

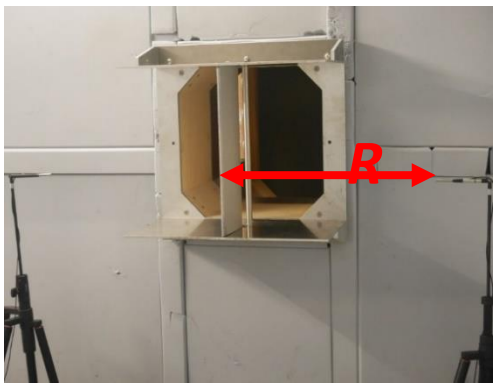

Figure 5 Microphones Position For Sound Measurement

The acoustic pressure is sampled at 51 200 Hz for 10 seconds using a DAQ with an automatic anti-aliasing filter. Noise measurement from the microphone is obtained in the form of sound pressure fluctuations in Pascal. The sound pressure level in decibels is then calculated using (1).

$$SPL = 20 \log\left(\frac{P\prime}{P_{\text{ref}}}\right) \text{ [dB]} \quad (4)$$

The reference pressure is $P_{\text{ref}} = 2.0 \times 10^{-5}$ [Pa].

Noise Control Setup

Two parameters are being investigated in the effect of sound radiation. They are the serrations wideness (λ) and the location of the serrations (y) are placed are as presented in Fig. 3. The gap between the rod and airfoil is G=3.5D agreeing the study of Y. Li whom proved that at G $\geq$ 3.3D the airfoil experience fully developed vortex in the wake of the rod (Yong Li et al. 2014). The narrow serrations have constant amplitude of 33.09 mm and wavelength of 8.27 mm, while the wide serrations have the same amplitude but a double wavelength of the narrow serrations'. The serrations are placed at pressure surface of the airfoil. This concept was previously investigated by Hersh et al. (1974). In all cases, the influence of different angles of attack is also investigated.

Table 5 Noise Control Setup

Type of serrations λ	Wide	Narrow
Placing point, y	25mm, 35mm from LE	25mm, 35mm from LE
AOA	0°~30°	0°~30°

Results

This section summarizes the results of several tests using the aforementioned microphone to identify the serrations effect on the noise generation. The parametric study (including the wideness of serrations and effects of serrations location) is made by comparing the sound spectra in decibels and the integration of sound spectra at different range of sound frequency with the clean rod-airfoil case (without serrations).

Sound pressure fluctuations

Fig. 6 shows the time history of sound pressure of the background environment of the tunnel. The background sound is needed prior to observed the changes in the noise level when the rod-airfoil is placed inside the wind tunnel.

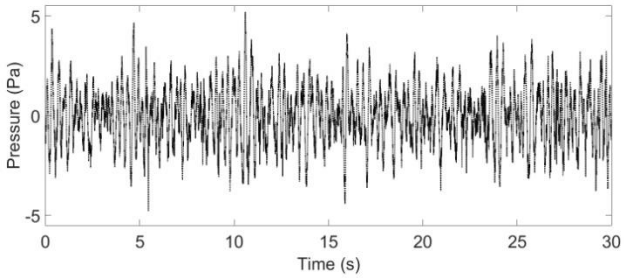

Figure 6 Sound Pressure Fluctuations Of Background Noise (Without Any Test Case)

Sound spectrum

The sound pressure fluctuation is then transformed using FFT to get the spectra as shown in Fig. 7. The figure depicts sound spectrum density of the baseline case. Sound from the rod-airfoil configuration and the airfoil only cases are compared. The case with upstream rod shows the presence of a tonal peak at a low frequency. The tonal peak is explained due to the vortex shedding of the upstream rod. The interaction between the rod wakes with the leading edge of the airfoil is believed to be the generation mechanism of airfoil-turbulence interaction noise [14]. Current study has taken the integral of the spectra at two different frequency ranges; namely the tonal noise (at frequency in the vicinity of the tonal peak Strouhal number) and the broadband noise (at frequency other than the tonal range). Hence, the tonal noise is calculated to be 1.79 dB and the broadband noise is 2.09 dB. The integral equations for tonal noise and broadband noise are as in Eq. (5) and Eq. (6) respectively. These values will be the baseline

case for reference in order to identify the effect of serrations on the noise reduction.

$$Tonal\ N\ [dB] = \int_{St=0.1}^{St=0.3} SP\ (St)\ d\ St \quad (5)$$

$$Broadband\ N\ [dB] = \int_{St=0.3}^{St=1.0} SP\ (St)\ d\ St \quad (6)$$

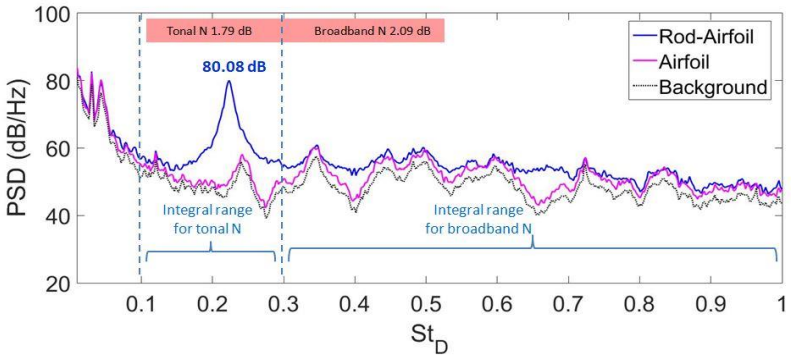

Figure 7 Sound Spectrum Density Of Baseline Case (Clean Rod-Airfoil Configuration)

Fig. 8 represents the sound spectra for cases with the leading edge serrations at two respective angles of attack i.e. AOA=0° and AOA=12°. There is not much obvious reduction if seen from the sound spectra if seen in overall. However, results of the case when angle of attack AOA=12° show that the LE serrations give better noise reduction effect at higher AOA. If seen from the integral values, wide serrations (highlighted in green box) have a bigger noise reduction if compared to that of the narrow serrations. The narrow serrations even increased some noise in the broadband part at zero angle of attack.

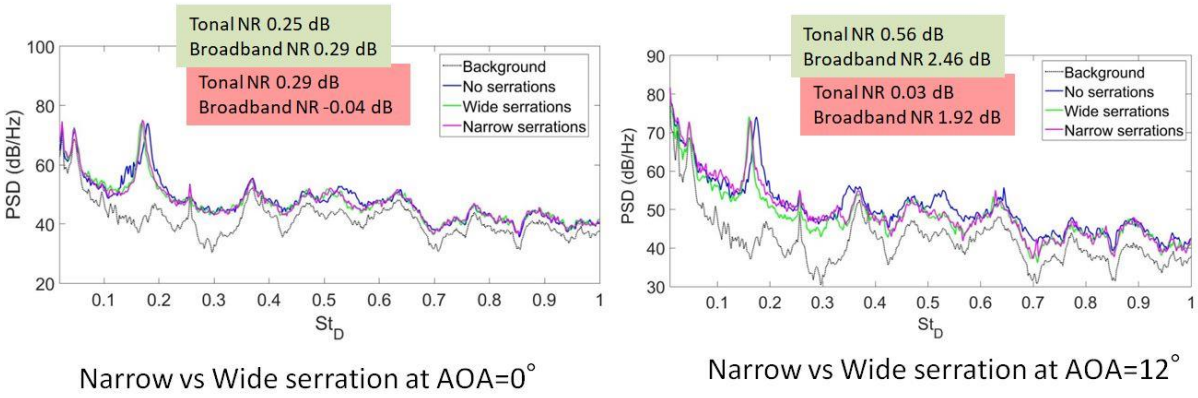

Figure 8 Sound Spectra Results For Case Of Wide Vs Narrow LE Serrations

Integration of Sound spectrum

The relation of the sound reduction ($\Delta\ SPL$) with the angles of attack can be further investigated by referring to the lines in Fig. 9. LHS shows the tonal sound and RHS shows the broadband sound. The LE serrations of current study seem to give better noise reduction at angles of attack in the range of approximately 10° to 25°. Highest noise reduction is when the angle of attack is at 12°. Whereas at lower angles of attack cases, the serrations seem to has increased the noise generation.

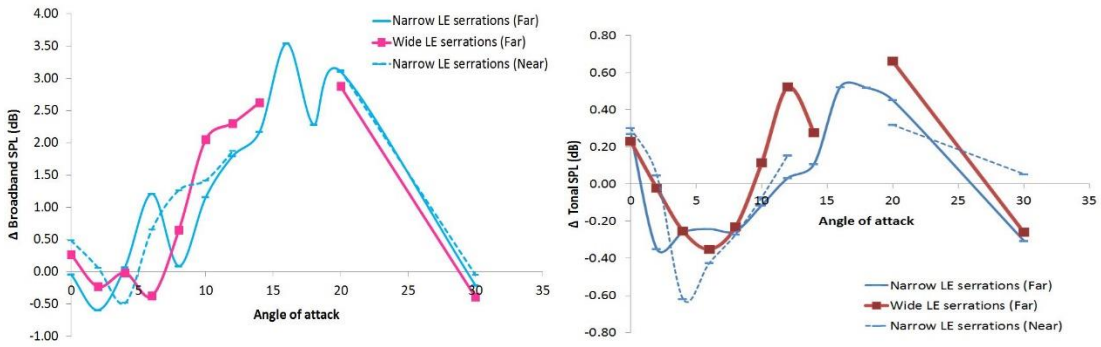

Figure 9 Tonal (LHS) And Broadband (RHS) Sound Levels At Different Angles Of Attack

Conclusion

The noise measurement setup of rod-airfoil configuration has been discussed and the LE serrations effect on the noise generation of rod-airfoil has been assessed. Wider serration gives better noise reduction and the LE serrations give good reduction at higher angle of attack. For the future planning, the noise increment and reduction that the LE serrations promote at different angle of attack can be further explained based on the flow behaviours and physics point of view.

Acknowledgement

The author would like to acknowledge University Teknologi Malaysia for the Ainuddin Wahid Scholarship award. Additionally, the research is also sponsored by Malaysia of Higher Education (MOHE) under the Research Grant project of Universiti Teknologi Malaysia (Vot No.R.K130000.7843.4F712). Special thanks to University of New South Wales (UNSW) for the use of wind tunnel facilities and also Assoc Prof Con Doolan for his supervision during the research attachment in UNSW Sydney.

References

Berland, J., Lafon, P., Crouzet, F., Daude, F., Bailly, C. (2010) *Numerical insight into sound sources of a rod–airfoil flow configuration using direct noise calculation*. AIAA 3705.

Berland, J., Lafon, P., Crouzet, F., Daude, F., Bailly, C.(2011) *A Parametric study of the noise radiated by the flow around multiple bodies: direct noise computation of the influence of the separating distance in rod–airfoil flow configurations.* AIAA 2819.

Boudet, J., Grosjan, N., Jacob, MC (2005) *Wake-airfoil interaction as braodband noise source: A large eddy simulatino study*.International Journal of Aeroacoustics Vol. 4, No. 1 pp. 93-115

Cambanis, VP., Stapountzis, H. (2001) *An experimental study on FLUENT simulation of the horizontal axis wind turbine (HAWT) blade-tower dynamic interaction*. 2nd Southeastern Europe Fluent Users Group Meeting. November 1-2, Bucharest, Romania.

Casalino, D., Jacob, M. and Roger, M. (2003) *Prediction of Rod-Airfoil Interaction Noise using the Ffowcs-William Hawkings Analogy*. AIAA Journal ; 41 (2)

Chaitanya, P., Naraynan, S., Joseph, P., Vanderwel, C., Turner, J., Kim, JW., and Ganapathisubramani, B (2015) *Broadband noise reduction through leading edge serrations on realistic airfoils.* AIAA Aviation Forum 22-26 June. Dallas, TX.

Chaitanya, P., Joseph, P., Narayanan, S., Vanderwel, C., Turner, J.,Kim, JW. and Ganapathisubramani (2017) *Performance and mechanism of sinusoidal leading edge*

serrations for the reduction of turbulence-airfoil interaction noise. Journal of Fluid Mechanics. Vol. 818, pp. 435-464

Giesler, J. amd Sarradj, E. (2004) *Measurement of broadband noise generation on rod-airfoil configurations.* AIAA. 3308

Greschner, B., Thiele, F., Jacob, M.C., Casalino, D. (2008) *Prediction of sound generated by a rod–airfoil configuration using EASMDES and the generalised Lighthill / FW–H analogy* Computers & Fluids Vol. 37, No.4, pp. 402–413.

Gruber, M., Joseph, M. and Azarpeyvand, M. (2013) *An expermiental investigation of novel trailing edge geometries on airfoil trailing edge noise reduction*. AIAA Paper 2013-2011.

Haeri, S., Kim, J. W., Narayanan, S. and Joseph, P.(2014) *3D calculations of aerofoil–turbulence interaction noise and the effect of wavy leading edges*. AIAA Paper 2325.

Hansen, K. L., Kelso, R. M. and Dally, B. (2011) *B.Performance variations of leading-edge tubercles for distinct airfoil profiles.* AIAA J. Vol. 49, No. 1, pp. 185–194.

Hersh, A. S., Soderman, P. T. and Hayden, R. E. (1974) *Investigation of acoustic effets of leading edge serrations on airfoils*. J. Aircraft Vol. 11, No. 4, pp.197–202.

Henning, A, Kaepernick, K., Ehrenfried, K., Lauterbach, A., Kroeber, S.(2008) *Investigation of aeroacoustic noise generation by simultaneous particle image velocimetry and microphone measurements.* Experiments in Fluids 45. 1073-1085

Henning, A., Koop, L. Ehrenfried, K. Lauterbach, A., Kroeber, S.(2009) *Simultaneous multiplane PIV and microphone array measurements on a rod-airfoil configuration.* AIAA 3184

Jackson, R., Graham, JMR., and Maull, DJ (1973) *The lift on a wing in a turbulent flow* Aeronautical Quarterly, Vol. 24, Pt. 3, pp. 155-166

Jacob, MC., Boudet, J., Casalino, D., and Michard, M (2005) *A rod-airfoil experiment as benchmark for broadband noise modeling*. Theorotical and Computational Fluid Dynamics (10) 171-196

Johari, H., Henoch, C., Custodio, D. and Levshin, A. (2007) *Effects of leading-edge protuberances on airfoil performance*. AIAA J. Vol. 45, No. 11, pp. 2634–2642

Lorenzoni, V., Moore, P. Scarano, F., Tuinstra, M.(2009) *Aeroacoustic analysis of a rod-airfoil flow by means of time-resolve PIV*. AIAA 3298

Magagnato, F.,Sorğuven, E., Gabi,M. (2003) *Far-field noise prediction by large-eddy simulation and Ffowcs–Williams and Hawkings analogy* AIAA 3206.

McKeough, PJ. And Graham, JMR. (1980) *The effect of mean loading on the fluctuating loads induced on airfoils by a turbulent stream.* Aeronautical Quarterly, Vol. 31, pp. 56-69

Mis, PF (3003). *An experimental investigation of unsteady surface pressure on single and multiple airfoils.* PhD Dissertation, Virginia Tech, Blacksburg, VA.

Moreau, S., Roger, M. and Jurdic, V (2005) *Effect of an angle of attack and airfoil shape on urbulence-interaction noise.*AIAA paper no. 2973, 11th AIAA/CEAS Aeroacoustics Conference Meeting and Exhibit, May 22-25, Monterey, CA.

Narayanan, S., Haeri, S. and Joseph, P (2014) *3D calculations of airfoil-turbulence interaction noise and the effect of wavy leading edges*. AIAA/CEAS Conference.

Oerleman, S. and Migliore, P (2004) *Wind tunnel aeroacoustic tests of six airfoils for use on small wind turbines.* NREL/SR-500-35339

Olsen, W and Wagner, J (1982) *Effect of thickness on airfoil surface nosie.*AIAA Journal Vol. 20, No. 3, pp. 437-439

Paterson, RW. And Amiet, RK (1976) *Acoustic radaition and surface pressure characteristics of an airfoil due to incident turbulence*. NASA CR-2733

Petersen (Ed) James & James, pp. 172-175.Sorguven,E., Magagnato, F., Gabi, M. (2003) *Acoustic prediction of a cylinder and airfoil configuration at high Reynolds numbrs with LES and FWH.* ERCOFTAC Bulletic 58, pp. 47-50

Pope, SB. (1987) *PDF methods for turbulent reactive flows*. Progress in Energy and Combustion Science 1984. Vol. 11, Issue 2, pp. 119-192

Stapountzis, H., Yakinthos, K., Goulas, A., Kallergis, LS., Kambanis, V. (1999) *Cylinder wake airfoil interaction with application to downwind HAWT*. Proc. Eur. Wind Wnergy Conf. EL

Strouhal, V. (1878) *Ueber eine besondere Art der Tonerregung. Annalen der Physik und Chemie* ; n5 (10) 216-251

Takagi, Y., Fujisawa, N., Nakano, T., Nashimoto, A. (2006) *Cylinder wake influence on the tonal noise and aerodyanmic characteristics of a NACA 0018 airfoil*. Journal of Sound and Vibration 297, pp. 563-577

Turner, JM and Kim, JW (2016). *Towards understanding airfoils with wavy leading edges interacting with vortical disturbances.* 22nd AIAA Aeroacoustic Conference 10 May – 1 June, Lyonn, France.

Yong Li, Wang, XN, Chen, ZW and Liu, ZC (2014). *Experimental study of vortex-structure interaction noise radiated from rod-airfoil configurations*. Journal of Fluids and Structures Vol. 51, pp. 313-325

Zdravkovich, MM. (1997) *Flow around circular cylinders.* V1 Oxford Univesity Press, Oxford

Proceeding: 5th International Conference on Applied Sciences and Engineering (ICASEA, 2018)
(eISBN 978-967-15744-1-6)
Capthorne Hotel, Cameron Highlands, Malaysia

MICROWATT ENERGY HARVESTING BY EXPLOITING FLOW-INDUCED VIBRATION

Zinnyrah Methal[1]
Mohamed Sukri Mat Ali
Nurshafinaz Mohd Maruai
Rasli Abd Ghani

[1]Malaysia-Japan International Institute of Technology, Universiti Teknologi Malaysia, Malaysia

---

Abstract: *The green technology approaches by harvesting energy from aerodynamic flow-induced vibrations using a flexible square cylinder is experimentally investigated. The practicability of flow-induced vibration system to supply a sufficient base excitation vibration in microwatt scale is evaluated through a series of wind tunnel tests with different velocities. Test are performed for low Reynolds number 3911< Re <13,762 and damping ratio $\zeta = 0.0052$. The experiment setup is able to replicate the pattern of vibration amplitude for isolated square cylinder with previous available study. Then, the experimental setup is used to study the effect of vibration cylinder in harvesting the fluid energy. A prototype of electromagnetic energy harvesting is invented and fabricated to test its performance in the wind tunnel test. Test results reveal that the harnessed power is corresponding to vibration amplitude flow pattern, but the power obtained is much lower than the vibration amplitude due to the power dissipation at the resistor. The best condition for harnessing power is identified at $U_R = 7.7$ where the Karman Vortex-Induced Vibration (KVIV) is the largest.*

Keywords: *Square Cylinder, Green Technology, Flow-Induced Vibration, Energy Harvesting*

Introduction

Flow-induced vibration (FIV) is claimed to cause large number of problems, especially in civil structural design (Jungao Wang, Fu, Baarholm, Wu, & Larsen, 2015) such as risers in marine technology (G. K. Lee, 2014), buildings and bridges (Arioli & Gazzola, 2013) and heat exchanger tube bundle (M. Li, Tang, Wang, Zhao, & Tao, 2017). Commonly, this FIV is occurring when the structure is analogous to a body supported with a spring-damper system that is then contacting with a fluid flow (Blevins, 1977). The flow pattern found near the body is based on the Reynolds number. When the flow exceeds Reynolds number of 40, unstable separation of fluid flow from the surfaces of the body will cause instability in the flow field (Sudhakar & Vengadesan, 2012). The vortices that is usually fully attached when Re is low appears to detach periodically from the surface of body and this circumstance explains the definition of von-Karman vortex shedding, VKVS (Sudhakar & Vengadesan, 2012). The vortex shedding induces oscillating to the structure that thus generates vibrations. At a certain free stream velocity, the vibration frequency is equal to the natural frequency of the structure once the resonance is met. Therefore, there are various studies in developing an effective wake control for suppression of vortex shedding which can be grouped into two: active vibration control (Bao & Tao, 2013; Chen et al., 2013; Jin-jun Wang, Choi, Feng, Jukes, & Whalley, 2013) and passive vibration control (Ismail et al., 2017; Maruai et al., 2017; Sudhakar & Vengadesan, 2012).

From a totally different viewpoint, an approach to harvest energy from VKVS has been studied in recent years to manipulate and enhance its possibility as a new ideal energy source (Demori, Ferrari, & Id, 2017; Jung & Lee, 2011; H. Liu, Zhang, Kathiresan, Kobayashi, & Lee, 2012; Yu, Hu, & Wang, 2012). There are several types of transducer that can be used to convert the mechanical energy to the electrical power such as electromagnetic (Ali, Arafa, & Elaraby, 2013), electrostatic (Najar, Nayfeh, Abdel-Rahman, Choura, & El-Borgi, 2010) and piezoelectric transducer (M. Liu, Xiao, & Yang, 2015; Sirohi & Mahadik, 2012; S. Li et al., 2011; Akaydin, Elvin, & Andreopoulos, 2010). However, most of the studies have focus on a flexible piezoelectric transducer due to its convenient mechanism to operate the energy harvester system in the optimum condition (Demori et al., 2017; Liu et al., 2012; Wang, 2014). Studies on different cross section geometries are also have an attention in many years based on the fact that the flow behavior appears on the wake of bluff body will be affecting by the bluff body shape. Basically, the considered shape are circular cylinder, rectangular cylinder, triangular cylinder and square cylinder. But, a square cylinder has been acknowledged more due to its accessibility to the onset of galloping (A Abdelkefi, Scanlon, Mcdowell, & Hajj, 2013; Abdessattar Abdelkefi, Hajj, & Nayfeh, 2012; Abdessattar Abdelkefi, Hasanyan, Montgomery, Hall, & Hajj, 2014; Abdessattar Abdelkefi, Yan, & Hajj, 2013; Jung & Lee, 2011). Therefore, the recent studies has shown the interest to improve the fluctuation of the body using a square cylinder in an effort to obtain higher performance of the energy harvester (A Abdelkefi et al., 2013; Gao et al., 2011).

An electromagnetic induction is literally having a potential to be used as a transducer in exploiting the energy from a relative body motion in the magnetic field , but only gained the interest from a limited past studies. Jung & Lee, (2011); Jung, Lee, & Jang, (2009) performed an experimental study on the concept of electromagnetic energy harvesting from a wake galloping. The study found the relation between the harvested energy and the aerodynamic instability (i.e., wake galloping). An approach to experimentally study the galloping oscillations-based electromagnetic wind generator has been investigated by Ali et al., (2013) with different cross-section geometries. In the latest study by Maruai et al., (2017), different cross geometries are considered and a detached flat plate is placed downstream of the body in the objective to amplify the vibration so that the harvested energy can be amplified. The study reveals that a downstream body with a relevant gap separation are able to magnify the amplitude vibration. Blazewicz & Bies, (1996) and Ozono, (2013) are also supported the findings. However, both study by Ali et al., (2013) and Maruai et al., (2017) did not consider the effect of transducer on the overall performance of the harvested energy where in the actual case, the energy harvester performance may be affected by the installation of the transducer.

This manuscript presents the experimental study of a complete energy harvesting system by using an electromagnetic transducer that is utilized from VKVS. The design are targeted for low power consumption applications, such as wireless sensor network (WSN) (Beeby et al., 2006; Tang, He, Member, Li, & Dong, 2016) and also for the purpose of health monitoring applications (Davidson & Mo, 2014; Weinstein et al., 2012). The detail of the experimental setup to measure the velocity, displacement and output voltage are also presented in this paper.

Experimental Apparatus and Measurements

Arrangement of the experimental study and the framework that involved in this study are shown in Fig. 1. The test section is having a square cross-section and lengths of 0.36 m × 0.36 m and 0.8 m, respectively. The bluff body under investigation is a square cylinder with side lengths D = 26 mm and spanwise length of L = 0.349 mm. The cylinder is hollow and it is supported to the wind tunnel by a steel rod at each end of the cylinder and the length of supported steel rod is 0.105 m length. The steel rods pass through the opening slot on the side walls of the test section and elastically supported by two parallel twin spring plates at both ends outside the wall test section to allow the square cylinder moves in a transverse direction of the incoming airflow. The dimension of the spring plate is 0.5 m × 0.004 m × 0.001 m. To prevent the end effect so that the cylinder will acting as an infinite length, an end plate (circular disk) is used at each of the cylinder end. The experimental conditions are listed in Table 1.

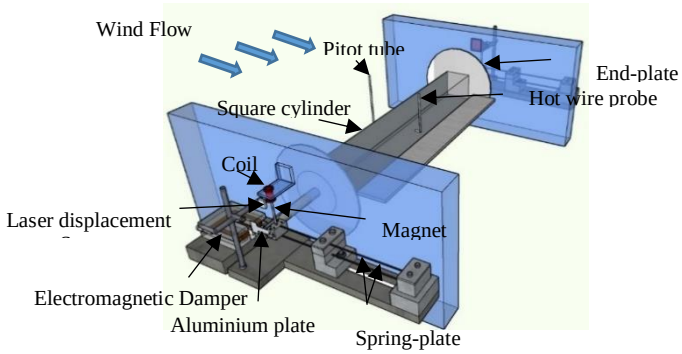

Figure 1: Arrangement Of The Experimental Apparatus And The Coordinate System Used In This Study.

Table 1: Experimental Conditions.

Parameter	Specification
Square cylinder side length, D[m]	0.026
Mass per unit length [kg/m]	0.34
Mass damping ratio,m*	428.15
Spring constant, k [N/m]	1189.75
Logarithmic damping factor, δ	0.0305
Damping ratio, ζ	0.0052
Natural frequency, f_n[Hz]	15.9
Free flow velocity, U [m/s]	2.37-9

Free stream velocity measurement

The selected device for measuring the air velocity of the airflow is by using the pitot tube. The pitot tube is having ellipsoidal sensing tip (NPL Modified Ellipsoidal Pitot Tube) and it is assembled from a co-axial tubing. This design provides the most accurate velocities measurement for high-velocity flow like is being conducted for this experiment. Pitot tube enables the concurrent measurement of the pressure induced by the moving air particle hitting the tip of the pitot tube and the stagnant pressure of the static air. According to Jr (1998), this devices able to correct the errors in static pressure reading that is caused by pressure distribution when it is subjected to airflow. Fig. 2 shows the basic pitot tube construction with L-shaped that is used in this experiment.

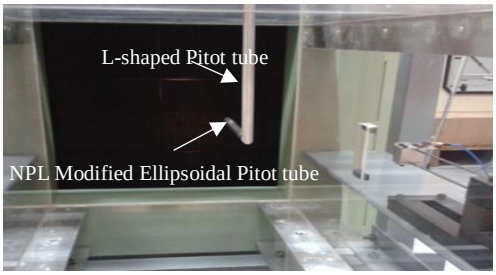

Figure 2: Basic Pitot Tube Construction.

It should be noted that the pitot tube is physically measuring the pressure generated by the air mass moving around the tip, thus the pressure gauge is required. To obtain the accurate measurement, the sensing tip must be pointed directly into the moving air flow. In addition for a better measurement, the pitot tube is located at the average velocity point in the moving air to reduce the effect of frictional drag due to the pipe wall. The free flow velocity, U is obtained from the Bernoulli's Equation as follows.

Bernoulli's Equation:

Static pressure + Dynamic pressure = Total pressure

$$\left(P_s + \rho \frac{U^2}{2} \right) = P_T \tag{1}$$

$$U = \sqrt{2\,(P_T - P_s)\,/\,\rho} \tag{2}$$

where P_s is the static pressure [pa], P_T is the total pressure [pa], ρ is the density of air [kg/m^3] and U is airflow velocity profile [m/s].

Free stream velocity measurement

To measure the vortex shedding frequency in the wake of the cylinder, the hot wire probe with a single-wire sensor that is attached to two support needles is used as shown in Fig. 3.

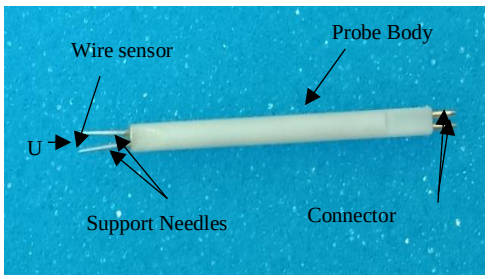

Figure 3: Hot wire probe with a single-wire sensor type.

The position of the hot wire probe in the wind tunnel is similar to Kawabata & Takahashi, (2013) with x/D = 1.5, y/D = 1.25, z/D = 0.4 from the center of the square cylinder. According to Dryden and Kuethe, (1929), the two support needles should confront directly into the moving airflow in order to obtain the accurate readings. When the current is passed through the thin wire, heat will be generated. Due to the change in velocity, U, the convective heat transfer coefficient from the electrical package and the wire temperature will change until eventually reach a thermal equilibrium. Afterwards, the signal will be transmitted to the Constant Temperature Anemometer (CTA). CTA is work based on the fact that probe's resistance will be proportional to the temperature of the hot wire and it is capable of measuring the flow and turbulence with low to medium velocity and moderate fluctuation frequencies. The CTA is also equipped with data noise reduction system. For high precision measurement, NI USB-9215 Series is used to build data acquisition and instrument control application using the LabVIEW. Physically, the hot wire measures the stream wise velocity in the wake of the square cylinder. The vortex shedding frequency is obtained by doing a series of power spectrum analysis of the fluctuation velocity. The peak on the spectrum indicates the frequency of the vortex shedding.

Displacement measurement

A laser displacement sensor with a diffuse reflective sensing sensor is used to measure the displacement at each end of the cylinder. Data acquisition and data analyzing are conducted using the LabVIEW software with NI USB-9215 Series as an interphase. To find the elastic properties of the system (natural frequency, f_n, logarithmic damping factor, δ and spring constant, K), free damping oscillations are conducted in static air as shown in Fig. 4. To calibrate the laser displacement sensor, height gauge is used as signify in Fig. 5.

Figure 4: Free Damping Oscillations In Static Air

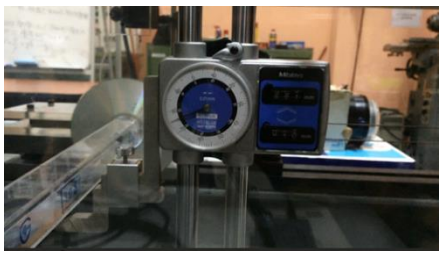

Figure 5: Laser Calibration Method By Using The Height Gauge

Modelling the energy harvester system with electromagnetic damper system and electromagnetic induction

The energy harvester consists of a customized permanent magnet (5 × neodymium, Ø 4 mm × 10 mm) that is glued to the movable square cylinder. The circular coil is fixed above the permanent magnet, thus the position is confirmed to be in the middle of circular coil. Specifications of the coil is presented in Table 2. The method for controlling the vibrations using electromagnetic damper has been investigated experimentally. The width of aluminum thin-plate will be inserted for every 1 mm interval ($\Delta\ L_d$ = 1 mm) into the electromagnetic damper and free damping oscillations in static air is applied to identify the relevant damping factor that is applicable in this experiment. The effect of electromagnetic induction is also has been considered during the free damping test. Fig.6 shows the schematic modelling of energy harvester with electromagnetic damper while Fig.7 shows the equivalent circuit model in this study.

Table 2: Coil Specifications.

Coil type	Specification	Specification
Copper	No. of turns, N_t	400
	Resistance, [mΩ]	0.49
	Inductance, L [H]	0.00837
	Wire diameter d_w [mm]	0.4
	Outer diameter coil, d_o [mm]	20.7
	Inner diameter coil, d_i [mm]	14.9
	Height of coil, h_c [mm]	40
	Total wire length, L_w [m]	9.61

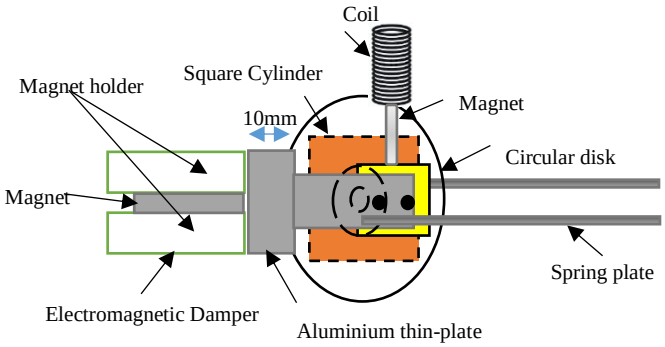

Figure 6: Schematic Modelling Of Energy Harvester With Electromagnetic Damper.

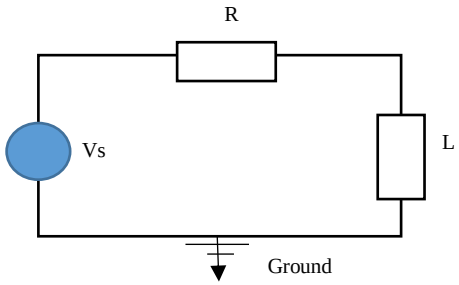

Figure 7: Equivalent Circuit Model

Mathematical modelling

In this part, a mathematical modelling for experimental power [P_e] is introduced as follows:

- Resistance [R]

$$R = \rho L_T / A \tag{3}$$

where R is electrical resistance of coil[Ω], ρ is resistivity of the copper coil in [Ω·m], L_c is the length of coil [m] and A is the cross-sectional area of coil [m^2]

- Power [P_e]

$$V_{emf} = I / R \tag{4}$$

Hence,

$$I = V_{emf} / R \tag{5}$$

Substitute I value into the power equation,

$$P = VI \tag{6}$$

where P is the power output [W] and V is the emf voltage. Noted that the V value is obtained from the experimental result.

Experimental results

In a series of experimental studies of flow-induced vibration, the square cylinder is flexible and it is subjected to wind stream velocities within 2.37 m/s to 9 m/s that is corresponding to wind speed velocity in Malaysia (Petinrin & Shaaban, 2015). The equivalent reduced velocities [$U_R = U\ f_n/D$] is determined in the range of $5.5 < U_R < 19.5$. The study has been conducted similar to Ismail et al., (2017); Maruai et al., (2017); Kawabata et al., (2013). Therefore, a comparison are made to validate the experimental setup as listed in Table 3. The square cylinder side length (D), effective mass ($m_{e)}$, and spring stiffness (k) have chosen to be consistent with the previous studies and were kept as close as possible for this validation purposes.

Table 3: Damping Factor Calibration.

Physical parameter	Kawabata et al. (2009)	Ismail et al. (2017)	Maruai et al. (2017)	Current study
Square cylinder side length, D [m]	0.0260	0.0260	0.0260	0.0260
Effective length [m]	0.3150	0.3150	0.3150	0.3150
Effective mass,m_e [kg]	0.11	0.15	0.15	0.12
Mass ratio, m^*	585	587.56	587.56	428.15
Spring stiffness, k [N/m]	1181	1173	1173	1189
Logarithmic damping factor, δ	0.027	0.0275	0.0275	0.0305
Damping ratio, ζ	0.0047	0.0047	0.0047	0.0052
Natural frequency, f_n [Hz]	16.5	14.2	14.2	15.9
Scruton number, Sc	35.1	32.3	32.3	26.1
Free flow velocity, U [m/s]	1.8-16.5	2.37-9	2.37-9	15.92.37-9

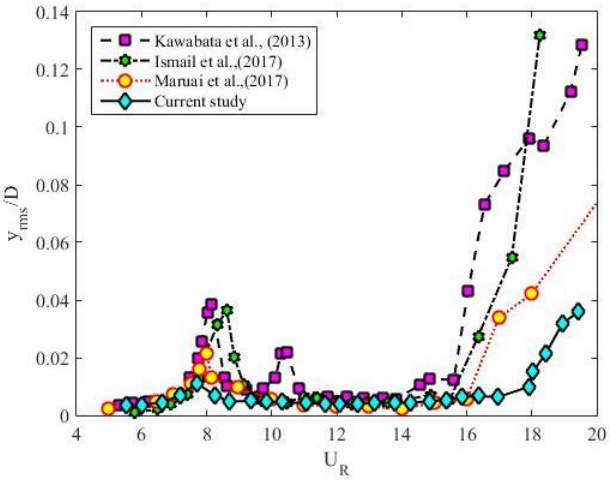

Figure 8: – RMS Transverse Amplitude With Reduced Velocity, U_R..

For flow across an isolated square cylinder with one degree of freedom, there are two types of flow-induced vibration are predicted, Karman vortex-induced vibration (KVIV) and galloping. The current study is able to replicate the vibration behavior with reduce velocities as predicted by Sarpkaya, (2004) when the regions of KVIV is occurred at lower branch velocity region

while galloping is at higher branch velocity region. However, the occurrence of the peak vibration in the KVIV region is shifted to earlier reduced velocity compare to the other studies due to the different value in damping ratio (ζ) as shown in Fig. 8.

Power harnessing

From the results presented in Fig. 9, the power harnessed by the electromagnetic converter from flow-induced vibration is calculated using the equation 3-6. It shows that the harnessed power flow pattern is equivalent to the amplitude ratio $(\mathbf{Y_{rms}/D})$ and this theory is supported by Maruai et al., (2017). According to the data, the ideal U_R to harness the power is at U_R = 7.7 which is in the Karman Vortex Induced Vibration region. The power identified at that particular U_R is about 5.224 mW after the value of resistor and inductance has been considered. The determined power value across the U_R is observed between 0.3265 mW-73.47mW within 5.5 $\leq U_R \leq$ 20.

In Fig 10, three different frequencies are plot in the same graph for $\boldsymbol{U_R}$ = 7.7. Apparently, the PSD analysis shows that the energy frequency is the lowest among the three frequencies. Thus, the harnessed power is expected to loss due to the resistor that is equipped in the circuit or through the mechanical devices during the vibration.

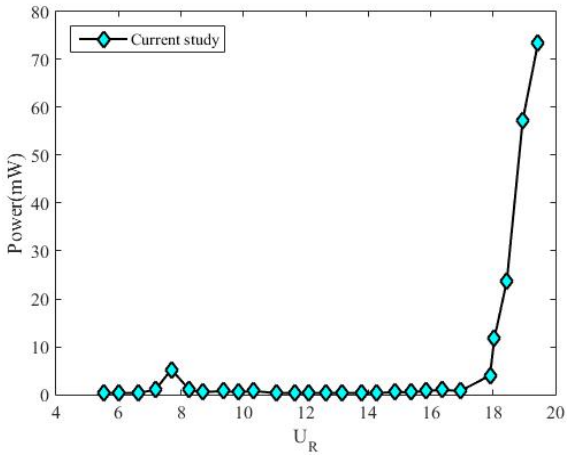

Figure 9: Power Against U_R

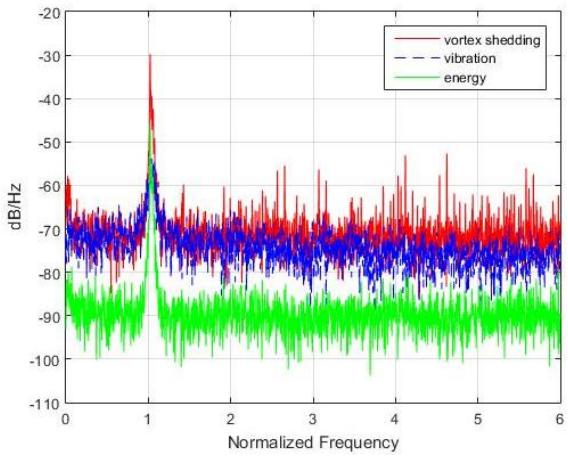

Figure 10: PSD At U_R = 7.7.

Conclusion

In this paper, the feasibility study of flow-induced vibration for generating a green technology is extensively investigated. In order to design the portable energy harvester based electromagnetic transducer, the characteristics and mechanisms of various aerodynamic instability have been studied clearly before approaching the next step which is to design the energy harvesting device that is appropriated to test under the wind tunnel. As seen from the test results, the average generated power can be obtained in the range of 0.3265 mW-73.47mW under the wind speed 2.3 – 9 m/s. However, the ideal wind speed to harness the power is obtained at wind speed 3.3 m/s which is equal to $\boldsymbol{U_R}$ = 7.7. For this proposed devices, the electromagnetic induction can be easily increased, thus more power can be produced with the right configuration. Therefore, the advantages of the proposed energy harvesting device is promising and it could be effectively used as a power supply for powering up low power electronic devices like the wireless sensor network under the moderate wind conditions.

Acknowledgements

The research was fully sponsored by Malaysia of Higher Education (MOHE) under the Research University Grant project of Universiti Teknologi Malaysia (Vot No. R.K130000.7843.4F712). Special thanks to Mara-Japan Industrial Institute, Beranang (MJII) for the use of the laboratory facilities for the purpose of wind tunnel testing.

References

Abdelkefi, A., Hajj, M. R., & Nayfeh, A. H. (2012). Power harvesting from transverse galloping of square cylinder. Nonlinear Dynamics, 70(2), 1355–1363. https://doi.org/10.1007/s11071-012-0538-4

Abdelkefi, A., Hasanyan, A., Montgomery, J., Hall, D., & Hajj, M. R. (2014). Incident flow effects on the performance of piezoelectric energy harvesters from galloping vibrations. Theoretical and Applied Mechanics Letters, 4(2), 22002. https://doi.org/10.1063/2.1402202

Abdelkefi, A., Scanlon, J. M., McDowell, E., & Hajj, M. R. (2013). Performance enhancement of piezoelectric energy harvesters from wake galloping. Applied Physics Letters, 103(3), 3–8. https://doi.org/10.1063/1.4816075

Abdelkefi, A., Yan, Z., & Hajj, M. R. (2013). Modeling and nonlinear analysis of piezoelectric energy harvesting from transverse galloping. Smart Materials and Structures, 22(2). https://doi.org/10.1088/0964-1726/22/2/025016

Abdelkefi, A., Hajj, M. R., & Nayfeh, A. H. (2013). Piezoelectric energy harvesting from transverse galloping of bluff bodies. Smart Materials and Structures, 22(1). https://doi.org/10.1088/0964-1726/22/1/015014

Akaydin, H. D., Elvin, N., & Andreopoulos, Y. (2010). Journal of Intelligent Material Systems and Structures Energy Harvesting from Highly Unsteady Fluid. https://doi.org/10.1177/1045389X10366317

Ali, M., Arafa, M., & Elaraby, M. (2013). Harvesting Energy from Galloping Oscillations. Proceedings of the World Congress on …, III. Retrieved from http://www.iaeng.org/publication/WCE2013/WCE2013_pp2053-2058.pdf

Arioli, G., & Gazzola, F. (2013). Old and new explanations of the Tacoma Narrows Bridge collapse. Atti XXI Congresso AIMETA, Torino, 10.

Bao, Y., & Tao, J. (2013). Active control of a cylinder wake flow by using a streamwise oscillating foil Active control of a cylinder wake flow by using a streamwise oscillating foil, 53601. https://doi.org/10.1063/1.4802042

Beeby, Tudor, & White, (2006). Energy harvesting vibration sources for microsystems applications, 175. https://doi.org/10.1088/0957-0233/17/12/R01

Blazewicz, A. M., & Bies, D. A. (1996). Interaction between a Vortex Wake and an Immersed Rectangular Plate, 1777(95), 209–220.

Blevins, R. D. (1977). Flow induced vibration, 363.

Blevins RD. 1990. Flow-Induced Vibrations. New York: Van Nostrand Reinhold

Chen, W., Xin, D., Xu, F., Li, H., Ou, J., & Hu, H. (2013). Suppression of vortex-induced vibration of a circular cylinder using suction-based flow control. Journal of Fluids and Structures, 42, 25–39. https://doi.org/10.1016/j.jfluidstructs.2013.05.009

Dai, H. L., Abdelkefi, A., & Wang, L. (2014). Piezoelectric energy harvesting from concurrent vortex-induced vibrations and base excitations. Nonlinear Dynamics, 77(3), 967–981. https://doi.org/10.1007/s11071-014-1355-8

Davidson, J., & Mo, C. (2014). Recent Advances in Energy Harvesting Technologies for Structural Health Monitoring Applications, 2014.

Demori, M., Ferrari, M., & Id, V. F. (2017). Autonomous Sensors Powered by Energy Harvesting from von Karman Vortices in Airflow, 10–12. https://doi.org/10.3390/s17092100

Ding, L., Zhang, L., Wu, C., Mao, X., & Jiang, D. (2015). Flow induced motion and energy harvesting of bluff bodies with different cross sections. Energy Conversion and Management, 91, 416–426. https://doi.org/10.1016/j.enconman.2014.12.039

Gao, X., Shih, W., & Shih, W. Y. (2011). Flow Energy Harvesting Using Piezoelectric Cantilevers with Cylindrical Extension, (c).

Ismail, M. H., Ali, M. S. M., Shaikh, S. A. Z. S., Shirakashi, M., & Muhamad, S. (2017). Flow induced vibration of a square cylinder with high scruton number. ARPN Journal of Engineering and Applied Sciences, 12(10), 3068–3075. https://doi.org/10.1016/B978-0-7020-2797-0.00001-1

Jr, R. K. (1998). Air velocity and Flow measurement using a Pitot tube, 37.

Jung, H., & Lee, S. (2011). The experimental validation of a new energy harvesting system based on the wake galloping phenomenon, 55022. https://doi.org/10.1088/0964-1726/20/5/055022

Jung, H., Lee, S., & Jang, D. (2009). Using Aerodynamic Instability, 45(10), 4376–4379.

Kawabata, Y., & Takahashi, T. (2013). Science and Technology Interference Effect of Downstream Strip-Plate on the Crossflow Vibration of a Square Cylinder *, 8(3), 647–658. https://doi.org/10.1299/jfst.8.348

Lee, G. K. (2014). A Finite Element Tool for Investigation of Vortex-Induced Vibration of Marine Risers, (June).

Lee, J. H., Bernitsas, M. M., & Viv, H. (2011). High-damping, high-Reynolds VIV tests for energy harnessing using the VIVACE converter. Ocean Engineering, 38(16), 1697–1712. https://doi.org/10.1016/j.oceaneng.2011.06.007

Li, M., Tang, S., Wang, F., Zhao, Q., & Tao, W. (2017). Gas-side fouling, erosion and corrosion of heat exchangers for middle/low temperature waste heat utilization: A review on simulation and experiment. Applied Thermal Engineering. https://doi.org/10.1016/j.applthermaleng.2017.07.095

Li, S., Yuan, J., Lipson, H., Li, S., Yuan, J., & Lipson, H. (2011). Ambient wind energy harvesting using cross-flow fluttering, 26104, 2–5. https://doi.org/10.1063/1.3525045

Liu, H., Zhang, S., Kathiresan, R., Kobayashi, T., & Lee, C. (2012). Development of piezoelectric microcantilever flow sensor with wind-driven energy harvesting capability Development of piezoelectric microcantilever flow sensor with wind-driven energy harvesting capability, 223905, 1–4. https://doi.org/10.1063/1.4723846

Liu, M., Xiao, L., & Yang, L. (2015). Experimental investigation of flow characteristics around four square-cylinder arrays at subcritical reynolds numbers. International Journal of Naval Architecture and Ocean Engineering, 7(5), 906–919. https://doi.org/10.1515/ijnaoe-2015-0063

Maruai, N. M., Mat Ali, M. S., Ismail, M. H., & Shaikh Salim, S. A. Z. (2017). Downstream flat plate as the flow-induced vibration enhancer for energy harvesting. Journal of Vibration and Control, (August 2016), 107754631770787. https://doi.org/10.1177/1077546317707877

Najar, F., Nayfeh, A. H., Abdel-Rahman, E. M., Choura, S., & El-Borgi, S. (2010). Dynamics and global stability of beam-based electrostatic microactuators. JVC/Journal of Vibration and Control, 16(5), 721–748. https://doi.org/10.1177/1077546309106521

Ozono, S. (2013). Flow control of vortex shedding by a short splitter plate asymmetrically arranged downstream of a cylinder Flow control of vortex shedding by a short splitter plate

asymmetrically arranged downstream of a cylinder, 2928(1999), 9–16. https://doi.org/10.1063/1.870151

Petinrin, J. O., & Shaaban, M. (2015). Renewable energy for continuous energy sustainability in Malaysia. Renewable and Sustainable Energy Reviews, 50, 967–981. https://doi.org/10.1016/j.rser.2015.04.146

Raghavan, K., & Bernitsas, M. M. (2011). Experimental investigation of Reynolds number effect on vortex induced vibration of rigid circular cylinder on elastic supports. Ocean Engineering, 38(5–6), 719–731. https://doi.org/10.1016/j.oceaneng.2010.09.003

Sarpkaya, T. (2004). A critical review of the intrinsic nature of vortex-induced vibrations. Journal of Fluids and Structures, 19(4), 389–447. https://doi.org/10.1016/j.jfluidstructs.2004.02.005

Sirohi, J., & Mahadik, R. (2012). Harvesting Wind Energy Using a Galloping Piezoelectric Beam. Journal of Vibration and Acoustics, 134(1), 11009. https://doi.org/10.1115/1.4004674

Sudhakar, Y., & Vengadesan, S. (2012). Vortex shedding characteristics of a circular cylinder with an oscillating wake splitter plate. Computers and Fluids, 53(1), 40–52. https://doi.org/10.1016/j.compfluid.2011.09.003

Tang, Q., He, Q., Member, S., Li, M., & Dong, C. (2016). Wireless Alarm Microsystem Self-Powered by Vibration-Threshold-Triggered Energy Harvester, 63(4), 2447–2456.

Vandiver, J. K. (2012). Damping Parameters for flow-induced vibration. Journal of Fluids and Structures, 35, 105–119. https://doi.org/10.1016/j.jfluidstructs.2012.07.002

Wang, J., Choi, K., Feng, L., Jukes, T. N., & Whalley, R. D. (2013). Progress in Aerospace Sciences Recent developments in DBD plasma fl ow control. Progress in Aerospace Sciences, 62, 52–78. https://doi.org/10.1016/j.paerosci.2013.05.003

Wang, J., Fu, S., Baarholm, R., Wu, J., & Larsen, C. M. (2015). Out-of-plane vortex-induced vibration of a steel catenary riser caused by vessel motions. Ocean Engineering, 109, 389–400. https://doi.org/10.1016/j.oceaneng.2015.09.004

Weinstein, Cacan, So & Wright. (2012). Vortex shedding induced energy harvesting from piezoelectric materials in heating , ventilation and air conditioning flows, 45003. https://doi.org/10.1088/0964-1726/21/4/045003

Yu, M. L., Hu, H., & Wang, Z. J. (2012). Experimental and Numerical Investigations on the Asymmetric Wake Vortex Structures of an Oscillating Airfoil, (January)

Proceeding: 5th International Conference on Applied Sciences and Engineering (ICASEA, 2018)
(eISBN 978-967-15744-1-6)
Capthorne Hotel, Cameron Highlands, Malaysia

EFFECTS OF MICROWAVE FINISH DRYING ON THE TEXTURAL CHARACTERISTICS OF BUFFALO JERKY

C. Y. W. Michelle[1]
M. Nor Afizah[1]
Z. A. N. Hanani[1]
M. R. Ismail-Fitry[1]*

[1]Department of Food Technology, Faculty of Food Science and Technology, Universiti Putra Malaysia, 43400, Serdang, Selangor, Malaysia.
*ismailfitry@upm.edu.my

Abstract: *Jerky, a ready-to-eat snack, known for its high protein and low-fat content. Current methods used in jerky processing take 6-10 hours in a conventional oven, dehydrator or smokehouse. In this study, whole buffalo meat was sliced to 5mm and 6mm and cured in three different salt concentrations of 1.0%, 1.5% and 2.0% for 24 hours at 4°C. The effects of microwave finish drying (5, 10 and 15 seconds) were examined after samples were dried in a convection oven for three hours. Cured buffalo slices showed significant ($p<0.05$) lower initial moisture content compared to uncured slices. This is due to the effect of salt which increased the protein solubility thus reducing its moisture content. Buffalo jerky treated with 2.0% salt showed the lowest final moisture content and the highest weight loss. Analysis of the texture characteristics showed that lower salt content and higher microwave duration produced softer buffalo jerky. Thus, microwave finish drying is capable of reducing the moisture content without negatively impacting the texture of buffalo jerky.*

Keywords: *Beef Jerky, Salt Concentration, Drying, Oven, Microwave*

Introduction

High protein meat-based snack such as jerky has gained interest globally as consumers are more health conscious. Due to its low water activity, it is shelf stable. Meat jerky can be made from any lean meat. The most popular jerky is made of beef or pork. There are two ways to prepare meat jerky, one by slicing the meat into strips and another by grinding the meat before moulding it into strips. The product from the former method is also known as whole meat jerky and the latter is known as restructured jerky (Kim et al., 2010; Jang et al., 2015).

The influence of drying and curing on beef and pork jerky has been studied over the years. Though beef and buffalo seem to be similar, the composition of the meat differs vastly (Nanda & Nakao, 2003). Currently, in Malaysia, most of the buffalo meats are imported from India. Since the price of buffalo meat is lower compared to beef, it is commonly used in food industry. Based on the research done by Kandeepan et al. (2009), young male buffalo meat is more suitable for processing due to its higher moisture, water holding capacity and collagen solubility. However, recent studies on buffalo meat are still limited.

Generally, jerky is prepared by curing and drying over a period of time, which reduces the water activity to approximately 0.70-0.85. The drying process consumes between 6 to 10 hours at 60°C in dryer, smokehouse or oven. Therefore, the reduction of processing time would lead to substantial reduction in cost, thus increasing the production efficacy.

To date, there are no studies that have been conducted to investigate the assistance of microwave to reduce the drying time of whole buffalo jerky. Therefore, in this study, an attempt was made to explore the fusion of oven and microwave to reduce the drying time in the preparation of buffalo jerky. The effect of different brine concentration and jerky thickness were also investigated.

Materials and methods

Sample preparation

Frozen buffalo meats (Bubalus bubalis) were obtained from a local supermarket. The excess and visible fat were trimmed off from the meat. The frozen buffalo meat was sliced to 5mm and 6mm thick pieces, using a meat slicer (Duegi Affettatrici, Italy). The slices were then cut into 50mm x 20mm. The meat slices were frozen at -18°C until use. Samples were thawed at 4°C prior to curing.

Experimental design

The mixture for curing consisted of water, salt, sugar and sodium nitrate was prepared. Buffalo meat slices were cured for 24 hours at 4°C. All experiments were done in triplicates. The cure formulations are shown in Table 1.

Table 1: Formulations For Buffalo Jerky Curing

Cure agents	Thickness of sample					
	5mm			6mm		
Salt	1.0%	1.5%	2.0%	1.0%	1.5%	2.0%
Sugar	1.0%	1.0%	1.0%	1.0%	1.0%	1.0%
Sodium nitrate	0.02%	0.02%	0.02%	0.02%	0.02%	0.02%
Water	3.0%	3.0%	3.0%	3.0%	3.0%	3.0%

Drying treatment

Table 2: Process Parameters Used For Convection Oven And Microwave Finish Drying

Treatment	Drying time (hours)	Drying time (seconds)
	Convection dryer (70°C)	Microwave (800W power)
1	3	5
2	3	10
3	3	15

Drying treatments were carried out in a laboratory-scale cabinet dryer (M-CD0106, Malchem, Malaysia) which was designed to dry and heat using convective energy. A setting of 70°C air temperature and level 5 fan speed was used to dry the samples for 3 hours. After 3 hours, the samples were removed and placed in the microwave (NN-ST342M, Panasonic, Malaysia). All experiments were conducted in triplicates. Table 2 shows the process parameters used in microwave drying.

Physical parameters measurement

Moisture content

The moisture contents of the sample were measured using Precisa Moisture Content Analyser (Precisa Gravimetrics, Switzerland). The buffalo jerky slices were cut into 10 mm x 10 mm to be placed into the device.

Weight loss measurement

Initial and final weights were measured and the weight loss was calculated by using this formulation:

Weight loss percentage = (Initial weight – Final weight)/ Initial weight × 100%

Texture Profile Analysis (TPA)

Texture measurement on jerky samples was conducted using a computer-assisted TA-XT2i Texture Analyzer (Stable Micro System, UK), fitted with Warner-Bratzler blade. The method was to determine hardness, springiness and chewiness. A piece of buffalo meat jerky measuring 20 x 50 mm was placed on the platform, with the fibres of the meat parallel to the direction of the blade. A 30 kg load cell with 50% strain was used to compress the sample. The settings of the texture analyser were as follows; pre-test speed of 5.0mm/s; test speed 2.0mm/s, post-test 5.0mm/s.

Statistical analysis

All data were analysed using two-way analysis of variance (ANOVA), using Minitab 17. Differences were considered significant at $p < 0.05$.

Results and discussion

Moisture content

The moisture content for sliced buffalo jerky was tabulated in Table 3. Samples with the highest mean were showed by the lowest salt concentration and vice versa. Data significantly ($p<0.05$) showed that the higher the salt concentration, the lower the final moisture content. This is seen throughout all different microwave treatment and both jerky thickness. It can be due to the osmotic effect which was theorized by Offer et al. (1989) which stated that myosin depolymerised in the presence of salt or with acid marinades. A weakening of muscle protein will lead to a poor water holding capacity due to the decrease of hydrogen bonding and hydration of ionic groups, thus increasing water molecules to be released from jerky (Damodaran, 2008). When the temperature is raised during the drying process, higher water molecules were lost. The moisture content of all samples decreases after curing steps due to moisture diffusion and decreased further due to evaporation when heat is applied (Yalcìn & Seker, 2016). The thickness and porosity of a material also affect the movement of water molecules (Berk, 2013). Overall result showed that 6mm buffalo jerky has higher final moisture content compared to the 5mm dried buffalo jerky.

However, it is also noted that the output power has a crucial effect on drying rate. In this research, the output is maintained at one level. Therefore, there are no significant differences ($p>0.05$) between the final moisture content between samples exposed to different microwave time, except for uncured buffalo slices. The salt compound found in the cured mixture interact with free water found in the buffalo slices thus reduces the concentration of water available for evaporation (Shrestha & Nummer, 2016). Studies have also shown that too high microwave

power has also been associated with physical damage to products such as charring and uneven temperature (Hu et al., 2006; Pereira & Vicente, 2010). These physical damages are the result of the continuous increase in sample temperature. It is also discovered that microwave output power will affect the characteristics of the surrounding air rapidly increasing the temperature of the water vapour in the air reducing the drying rate (Hemis et al., 2016). Hence, it is difficult to control the quality and drying rate of buffalo jerky when higher power output is applied.

Table 3: Moisture Content Of 5mm And 6mm Buffalo Strips[1]

Strip size	Salt concentration (%)	O-MW treatment[2]			
		Control	1	2	3
5 mm	0	78.97^{aA} ± 1.53	35.77^{aB} ± 0.78	32.83^{aC} ±0.63	31.85^{aC} ± 0.77
	1.0	67.02^{bA} ± 0.67	29.11^{bB} ± 0.95	28.54^{bB} ± 1.32	30.40^{abB} ± 0.82
	1.5	66.44^{bA} ± 1.04	27.63^{bcB} ± 0.49	28.38^{bB} ± 0.72	29.29^{bcB} ± 0.82
	2.0	66.81^{bA} ± 2.01	25.81^{cB} ± 0.83	26.46^{bB} ± 0.82	27.79^{cB} ± 0.97
6 mm	0	76.20^{aA} ± 2.85	36.21^{aB} ± 1.14	33.54^{aC} ± 0.67	32.58^{aC} ± 1.23
	1.0	70.41^{bA} ± 1.21	30.87^{bB} ± 0.41	29.64^{bB} ± 0.49	31.35^{aB} ± 1.40
	1.5	69.76^{bA} ± 0.95	28.02^{cB} ± 1.38	29.56^{bB} ± 0.13	27.91^{bB} ± 0.53
	2.0	69.30^{bA} ± 0.68	26.90^{cB} ± 0.74	26.54^{cB} ± 1.20	26.45^{bB} ± 0.49

[1]Means ± SD with different superscripts row-wise (capital letter) and column-wise (small letter) are significantly different ($p<0.05$) within the same strip size
[2]O-MW treatment 1 = 3 hours oven + 5 seconds microwave; O-MW treatment 2 = 3 hours oven + 10 seconds microwave; O-MW treatment 3 = 3 hours oven + 15 seconds microwave

Weight loss

Weight loss (%) data were shown in Table 4. The overall trend showed an increasing weight loss as salt concentration increases. The highest weight loss for 5mm buffalo jerky is recorded by samples treated with 2.0% salt concentration and exposed to 15 seconds microwave. There are significant differences between the percentages of weight loss of buffalo jerky as salt concentration increases. This can be seen in all three different oven-microwave treatments, although varying microwave time did not significantly affect the weight loss.

A similar trend is recorded for 6mm buffalo jerky. Nevertheless, for 6mm buffalo jerky strip, treated with 1.5% salt concentration showed a contrast result. Weight loss for the samples showed significant differences when treated with different microwave time. For both 5mm and 6mm, there was no significant interaction between salt concentration and oven-microwave time, though salt concentration showed a significant effect ($p<0.05$).

Table 4: Weight Loss (%) Of Dried 5mm And 6mm Buffalo Jerky[1]

Strip size	Salt concentration (%)	O-MW treatment[2]		
		1	2	3
5 mm	0	$51.00^{cA} \pm 1.61$	$51.73^{cA} \pm 0.55$	$53.27^{cA} \pm 2.23$
	1.0	$56.45^{bA} \pm 1.43$	$53.25^{bcA} \pm 2.78$	$54.48^{cA} \pm 0.74$
	1.5	$58.78^{bA} \pm 0.86$	$58.25^{abA} \pm 0.95$	$61.26^{bA} \pm 1.62$
	2.0	$63.35^{aA} \pm 1.47$	$62.66^{aA} \pm 2.51$	$66.95^{aA} \pm 3.06$
6 mm	0	$51.41^{cA} \pm 1.26$	$52.81^{cA} \pm 1.50$	$52.66^{cA} \pm 1.64$
	1.0	$52.76^{bcA} \pm 3.21$	$52.75^{bA} \pm 0.80$	$52.69^{cA} \pm 1.07$
	1.5	$58.36^{abA} \pm 1.13$	$53.47^{bAB} \pm 2.64$	$56.81^{bB} \pm 1.66$
	2.0	$62.91^{aA} \pm 2.83$	$64.63^{aA} \pm 3.26$	$65.64^{aA} \pm 1.45$

[1]Means ± SD with different superscripts row-wise (capital letter) and column-wise (small letter) are significantly different ($p<0.05$) within the same strip size
[2]O-MW treatment 1 = 3 hours oven + 5 seconds microwave; O-MW treatment 2 = 3 hours oven + 10 seconds microwave; O-MW treatment 3 = 3 hours oven + 15 seconds microwave

The results indicated that microwave did reduce moisture content, which contributed to most of the weight loss. Water loss from buffalo jerky is mainly due to sudden volumetric heating, generating high pressure in the strips. Exposure to microwave generates large vapour pressure gradients between the internal and the surface of the buffalo jerky, which propel the movement of inner moisture to the surface (Monteiro et al., 2016). This is consistent with the results obtained by Maskan (2000), which suggested that microwave energy should be applied in the falling rate period for finish drying.

Texture Profile Analysis

The texture profile analysis was carried out to determine the textural characteristics of buffalo jerky. Main parameters that are concentrated in this test were hardness, chewiness, cohesiveness, springiness and resilience. Table 5 showed the changes in hardness level when buffalo jerky is cured in different salt concentration and dried in a different duration of microwave treatments. Overall, uncured strips showed lower hardness level compared to the cured strips.

Table 5: Hardness Of Dried 5mm And 6mm Buffalo Jerky[1]

Strip size	Salt concentration (%)	O-MW treatment[2]		
		1	2	3
5 mm	0	$3003.16^{bA} \pm 139$	$2889.75^{bA} \pm 16$	$3305.50^{aA} \pm 830$
	1.0	$3967.90^{abA} \pm 342$	$3046.54^{bA} \pm 86$	$3244.50^{aA} \pm 527$
	1.5	$4756.50^{abA} \pm 232$	$5059.90^{aA} \pm 328$	$4204.10^{aA} \pm 377$
	2.0	$5996.90^{bA} \pm 1034$	$5415.80^{aA} \pm 400$	$5504.70^{aA} \pm 877$
6 mm	0	$3001.60^{cA} \pm 301$	$2880.71^{cA} \pm 131$	$3407.70^{cA} \pm 154$
	1.0	$3412.00^{cA} \pm 190$	$4131.60^{bA} \pm 226$	$3728.80^{cA} \pm 210$
	1.5	$4981.92^{bA} \pm 57$	$5201.24^{aA} \pm 48$	$5267.40^{bA} \pm 210$
	2.0	$6100.40^{aA} \pm 279$	$5975.60^{aA} \pm 311$	$6262.29^{aA} \pm 71$

[1]Means ± SD with different superscripts row-wise (capital letter) and column-wise (small letter) are significantly different ($p<0.05$) within the same strip size
[2]O-MW treatment 1 = 3 hours oven + 5 seconds microwave; O-MW treatment 2 = 3 hours oven + 10 seconds microwave; O-MW treatment 3 = 3 hours oven + 15 seconds microwave

The data showed that the effect of salt significantly affects ($p<0.05$) the texture. Increasing the concentration of salt may increase the hardness of the buffalo jerky. There are possibilities of hardening reactions and interaction of protein due to the moisture loss during heating. Higher concentration of salt also promotes the loss of water, therefore increases hardening and protein binding which results in harder jerky. This is supported by studies done by Church et al. (2013), stated that the application of microwave did not produce a softer beef jerky.

Chewiness refers to the work needed to be done during mastication. The chewiness for all samples of dried buffalo jerky is found to be high, all recorded above 1000g. A simple paired T-test revealed that there were no significant differences ($p>0.05$) between the two thickness (5mm and 6mm). The results indicated that the sample thickness insignificantly affects the chewiness of buffalo jerky. There was also no significant effect ($p>0.05$) of increasing salt concentration on the chewiness of buffalo jerky for most of the designs except for 6mm buffalo jerky, exposed to 10 seconds microwave.

The chewiness is due to the cross-linkage and protein binding during the drying process. Since buffalo meat is considered as tough meat due to its high collagen content, the addition of tenderizers or humectant may assist in achieving tenderer buffalo jerky (Amin et al., 2014; Kim et al., 2010; Naveena et al., 2011).

Table 6: Chewiness Of Dried 5mm And 6mm Buffalo Jerky[1]

Strip size	Salt concentration (%)	O-MW treatment[2]		
		1	2	3
5 mm	0	$1085.20^{aA} \pm 272.30$	$1282.10^{aA} \pm 247.10$	$1320.07^{aA} \pm 93.61$
	1.0	$1314.50^{aA} \pm 230.90$	$1595.80^{aA} \pm 298.00$	$1597.19^{aA} \pm 79.07$
	1.5	$1447.22^{aA} \pm 78.17$	$1557.40^{aA} \pm 143.60$	$1621.10^{aA} \pm 203.70$
	2.0	$1688.25^{aA} \pm 79.20$	$1829.70^{aA} \pm 193.20$	$1693.10^{aA} \pm 149.10$
6 mm	0	$1176.50^{aA} \pm 267.90$	$1203.10^{bA} \pm 147.70$	$1369.56^{aA} \pm 86.88$
	1.0	$1490.78^{aA} \pm 70.53$	$1600.04^{abA} \pm 45.34$	$1431.50^{aA} \pm 314.70$
	1.5	$1504.20^{aA} \pm 417.70$	$1601.08^{abA} \pm 35.22$	$1876.85^{aA} \pm 140.95$
	2.0	$1870.43^{aA} \pm 6.88$	$1878.80^{aA} \pm 161.90$	$2160.80^{aA} \pm 196.60$

[1]Means ± SD with different superscripts row-wise (capital letter) and column-wise (small letter) are significantly different ($p<0.05$) within the same strip size
[2]O-MW treatment 1 = 3 hours oven + 5 seconds microwave; O-MW treatment 2 = 3 hours oven + 10 seconds microwave; O-MW treatment 3 = 3 hours oven + 15 seconds microwave

There is also no significant difference ($p>0.05$) between the springiness of buffalo jerky throughout the different oven-microwave treatment. The p-value across 1.0% salt concentration for 5mm strips is 0.45, which suggests that the contrasting microwave treatment time did not affect the springiness of buffalo jerky. Similarly, the p-value for 6mm strips is 0.39, which indicates the same. Varying salt concentration showed no consistent effect on the springiness of the dried buffalo jerky. Based on Zochowska-Kujawska (2016), dry-cured deer muscles with lower salt content showed lower hardness, cohesiveness, springiness and chewiness.

Table 7: Springiness Of Dried 5mm And 6mm Buffalo Jerky[1]

Strip size	Salt concentration (%)	O-MW treatment[2]		
		1	2	3
5 mm	0	$0.81^{aA} \pm 0.01$	$0.84^{aA} \pm 0.02$	$0.83^{aA} \pm 0.06$
	1.0	$0.77^{abA} \pm 0.02$	$0.77^{abA} \pm 0.03$	$0.74^{aA} \pm 0.01$
	1.5	$0.71^{bcA} \pm 0.01$	$0.77^{abA} \pm 0.05$	$0.73^{aA} \pm 0.02$
	2.0	$0.67^{cA} \pm 0.02$	$0.69^{bA} \pm 0.02$	$0.69^{aA} \pm 0.05$
6 mm	0	$0.81^{aA} \pm 0.01$	$0.82^{aA} \pm 0.04$	$0.80^{aA} \pm 0.04$
	1.0	$0.76^{abA} \pm 0.01$	$0.79^{abA} \pm 0.01$	$0.77^{aA} \pm 0.04$
	1.5	$0.78^{aA} \pm 0.03$	$0.74^{abA} \pm 0.01$	$0.75^{abA} \pm 0.02$
	2.0	$0.69^{bAB} \pm 0.02$	$0.70^{bA} \pm 0.01$	$0.64^{bB} \pm 0.01$

[1]Means ± SD with different superscripts row-wise (capital letter) and column-wise (small letter) are significantly different ($p<0.05$) within the same strip size
[2]O-MW treatment 1 = 3 hours oven + 5 seconds microwave; O-MW treatment 2 = 3 hours oven + 10 seconds microwave; O-MW treatment 3 = 3 hours oven + 15 seconds microwave

Conclusion

Different microwave treatments and curing of buffalo strips in different concentrations of salt had significantly affected the moisture content of the dried buffalo jerky. Increasing the microwave duration and the salt concentration is found to increase the rate of moisture loss. The increase of salt concentration also affects the textural characteristics, as the hardness of buffalo jerky is found to be higher when cured in higher salt concentration. However, the changes of microwave treatment duration did not significantly affect the textural parameters of buffalo jerky. It can be concluded that the use of microwave reduced the drying time needed for the preparation of buffalo jerky without negatively impacting the texture of buffalo jerky. Traditional convective drying assisted by microwave demonstrated superior efficiency in dehydrating buffalo jerky sample, compared to traditional oven processing. This translates to substantial energy saving.

References

Amin, T., Bhat, S. V. & Sharma, N. (2014). Technological advancements in meat tenderization-A review. *Journal of Meat Science and Technology*, 2: 1–9.

Berk Z. (2013). *Food Process Engineering and Technology*. San Diego, CA: Elsevier Inc.

Church, J. S., MacIntyre, C. M., Archambault, W. R., Moote, P. E., Cochran, J. L., Durance, T. D. & Hamme J. D. V. (2013). Effect of radiant energy vacuum on physical and microbial properties of beef jerky. *Journal of Food Science and Engineering*, 3: 33–39.

Damodaran, S. (2008). In Damodaran, S. & Parkin, K. L. (Eds.), *Fennema's Food Chemistry* (5th ed.) (pp. 231–269). Boca Raton, FL: CRC Press.

Halling, P. J. (1992). Salt hydrates for water activity control with biocatalysts in organic media. *Biotechnology Techniques*, 6(3): 271–276.

Hemis, M., Choudhary, R., Becerra-Mora, N., Kohli, P. & Raghavan, V. (2016). Modelling of microwave assisted hot-air drying and microstructural study of oilseeds. *International Journal of Agricultural and Biological Engineering*, 9(6): 167-177.

Hu, Q., Zhang, M., Mujumdar, A. S., Xiao, G. & Sun, J. (2006). Drying of edamames by hot air and vacuum microwave combination. *Journal of Food Engineering*, 77: 977-982.

Jang, S. -J., Kim, H. -W., Hwang, K. -E., Song, D. -H., Kim, Y. -J., Ham, Y. -K., Lim, Y. -B., Jeong, T. -J., Kim, S. -Y. & Kim, C. -J. (2015). Effects of Replacing Sucrose with Various Sugar Alcohols on Quality Properties of Semi-dried Jerky. *Korean Journal for Food Science of Animal Resources*, 35(5): 622–629.

Kandeepan, G., Anjaneyuly, A. S.,R., Kondaiah, N., Mendiratta, S. K. & Lakshmanan V. (2009). Effect of age and gender on the processing characteristics of buffalo meat. *Meat Science*, 83: 10-14.

Kim, G. D., Jung, E. Y., Seo, H. W., Joo, S. T. & Yang, H. S. (2010). Textural and sensory properties of pork jerky adjusted with tenderizers or humectant. *Korean Journal of Food Science and Animal Resource*, 30: 930-937.

Maskan, M. (2000). Microwave/air and microwave finish drying of banana. *Journal of Food Engineering*, 44: 71-78.

Monteiro, R. L., Carciofi, B. A. M. & Laurindo, J. B. (2016). A microwave multi-flash drying process for producing crispy bananas. *Journal of Food Engineering*, 178: 1–11.

Nanda, A. S. & Nakao, T. (2003). Role of buffalo in the socioeconomic development of rural Asia: Current status and future prospectus. *Animal Science Journal*, 74(6): 443-455.

Naveena, B. M., Kiran, M., Reddy, K. S., Ramakrishna, C., Vaithiyanathan, S. & Devatkal, S. K. (2011). Effect of ammonium hydroxide on ultrastructure and tenderness of buffalo meat. *Meat Science*, 88:727-732.

Offer, G., Knight, P., Jeacocke, R., Almond, R., Cousins, T., Elsey, J., Parsons, N., Sharp, A., Starr, R. & Purslow, P. (1989). The structural basis of the water-holding, appearance and toughness of meat and meat products. *Food Microstructure*, 8: 151-170.

Pereira, R. N. & Vicente, A. A. (2010). Environmental impact of novel thermal and non-thermal technologies in food processing. *Food Research International*, 43 (7): 1936-1943.

Shrestha, S. & Nummer, B. (2016). Survival of Salmonella spp. in low water activity chicken base paste and powder formulated at different salt levels. Food Control, 59: 663-668.

Yalcin, M. Y. & Seker, M. (2016). Effect of salt and moisture content reduction on physical and microbiological properties of salted, pressed and freeze dried turkey meat. *LWT-Food Science and Technology*, 68: 153-159.

Zochowska-Kujawska, J. (2016). Effect of fibre type and structure of longissimus lumborum (L1), biceps femoris (Bf) and semimembranosus (Sm) deer muscles salting with different NaCl addition on proteolysis index and texture of dry-cured meat. *Meat Science*, 121: 390–396.

Proceeding: 5th International Conference on Applied Sciences and Engineering (ICASEA, 2018)
(eISBN 978-967-15744-1-6)
Capthorne Hotel, Cameron Highlands, Malaysia

POTENTIAL USE OF FISH COLLAGEN HYDROLYSATE AS FAT REPLACER IN BUFFALO PATTIES

Fakhriyah Nur Ibrahim[1]
Radhiah Shukri[1]
Masni Mat Yusoff[1]
Mohammad Rashedi Ismail-Fitry[1]*

[1]Department of Food Technology, Faculty of Food Science and Technology, Universiti Putra Malaysia, 43400, Serdang, Selangor, Malaysia.
*ismailfitry@upm.edu.my

Abstract: *Pork and bovine collagen incorporated into meat products showed promising functional properties as food ingredients but has the halal issue. This study was to investigate the effect of incorporating fish collagen hydrolysate (FCH) as a fat replacer in buffalo patties and evaluate its proximate values, texture and colour properties. There were five different formulations and labelled as control (10% fat, 0% FCH), A (7.5% fat, 2.5% FCH), B (5% fat, 5% FCH) and D (0% fat, 10% FCH). Formulation with higher FCH percentage has higher protein content and ash, while the moisture content of beef patties was reduced at higher FCH percentage. The fat content of buffalo patties shows significantly different ($p>0.05$) in which the control, formulation A and B showed increment from 3.44% to 4.49%, however, the amount of fat decreased with formulation C and D with a fat of 2.46% and 3.11%, respectively. The cohesiveness of the buffalo patties with 75% and 50% of FCH is significantly different ($p<0.05$) compared to the control and other formulations. While, other texture attributes such as hardness, adhesiveness and springiness showed no differences among each other ($p>0.05$). Raw beef patties with higher FCH content were darker compared to patties with a lower percentage of FCH. There were no significant different ($p>0.05$) of yellowness and redness of buffalo patties with or without FCH incorporation before and after cooking. As the conclusion, fish collagen hydrolysate has the potential use as a fat replacer in the production of low-fat patties.*

Keywords: *Buffalo Patties, Fat Replacer, Fish Collagen Hydrolysate, Halal Collagen.*

Introduction

Fats play a vital role in sensory and structural benefits in food products. Consumer preferences often food that could give the mouthfeel, satiety, satisfaction, full of aroma in which generally contributed by fat in food (Ognean et al., 2006; Keeton, 1994). In the nutrition standpoint, fat intake contributes to major energy needs of human (Tokusoglu and Unan, 2003). However, due to health awareness, consumer nowadays privilege healthier version of food for their consumption. Low-fat food, low sugar food often becomes primary selection amongst educated, urban consumer whom concern on their health risk. The traditional way to replaced fat in food is via water substitution (Ognean et al., 2006). However, due to technology advancement in food processing, scientist found many carbohydrates, protein-based, synthetic compounds and food additives that can be used as the fat replacer or fat substitutes (Tokusoglu and Unan, 2003; Keeton, 1994).

Collagen proteins are the most abundant in the human and animal body vital proteins of connective tissue, skin, tendons, cartilage, ligaments, cornea, teeth, nails and hair (Dybka and Walczak, 2009; Barzideth et al., 2014; Hashim et al., 2015). The main sources of collagen peptides are bovine hide, bone, pigskin and marine sources (Dybka and Walczak, 2009; Hashim et al., 2015). Collagen hydrolysates are processed via hydrolysis until soluble peptide was achieved (Dybka and Walczak 2009). In the food industry, many studies have been conducted to study the physicochemical, microbiological and sensory property of meat product incorporated with collagen. As an example, Sousa et al. (2017) investigated the use of bovine hydrolysed collagen powder as the fat replacer in frankfurter. Schilling et al. (2003) had investigated the use of pork collagen in improving the functionality of sucuk. However, the use of fish hydrolysed collagen as fat replacer has not yet been explored. Due to halal issues of existing collagen derived from bovine (due to slaughtering by non-muslim) and other non-halal issues revolving around collagen as raw material, fish collagen hydrolysate is seen as a potential field of study in which commonly produced from waste i.e scales, skin and viscera could solve the issue with beneficial properties.

The demands on the production of low-fat meat products are rising due to awareness of healthy eating habits and health risks associated with inappropriate diets and food consumptions. Using fat substitute to replace fat in meat and low-fat meat product processing has been implemented decades. Collagen and collagen hydrolysate is a protein-based fat substitute in which has been seen as a potential fat replacer in low-fat beef patties processing. Due to halal issues of collagen and its hydrolysate derived from chicken, bovine and pork, collagen and its derivatives from marine i.e fish waste seen as alternatives fat replacer in producing low-fat beef patties. However, the effect of using fish collagen hydrolysate in beef patties need to be further investigated in which to what extent it affects the physicochemical and sensory level of beef patties upon its incorporation. Hence, following objectives has been proposed for this study:

To evaluate physicochemical alteration resulted from fish hydrolysed collagen incorporation as the fat replacer in beef patties.
To determine sensory acceptance of using fish hydrolysed collagen as the fat replacer in beef patties.

Materials and methods

Buffalo patties formulation

The meat for the patties was obtained from Pasar Borong Selangor (frozen buffalo topside). The visible fats were initially removed from the meat. The meat and fat were grounded separately in a grinder (standard size hole opening in the grinder plate). After grinding, the meat was divided in 500g and packed frozen at -18^{o}C until further processing and analysis. The ingredients used in the formulation as shown in Table 1 consist of sodium tripolyphosphate (STPP), cornstarch, sugar, salt, white pepper and garlic powder. STPP was purchased from Meilun Sdn Bhd, Klang, Selangor while all other ingredients were purchased from Giant Hypermarket, Serdang, Selangor. The fish collagen hydrolysate (FCH) was obtained from Industri Az-Zahrah Sdn. Bhd., Bangi, Selangor as the sample of in the weight of 700 g in nylon packaging.

Table 1: The Ingredients Used To Formulate Buffalo Patties.

Raw materials and ingredients (%)	Control	A	B	C	D
Buffalo Meat	70.00	70.00	70.00	70.00	70.00
Cornstarch	3.50	3.50	3.50	3.50	3.50
Salt	1.20	1.20	1.20	1.20	1.20
Garlic	0.50	0.50	0.50	0.50	0.50
Sugar	1.00	1.00	1.00	1.00	1.00
White pepper	0.50	0.50	0.50	0.50	0.50
Sodium tripolyphosphate (STPP)	0.30	0.30	0.30	0.30	0.30
Buffalo fat	10.00	7.50	5.00	2.50	0.00
Warm water	13.00	13.00	13.00	13.00	13.00
Fish Collagen Hydrolysate (FCH)	0.00	2.50	5.00	7.50	10.00

Control (10% fat, 0% FCH), A (7.5% fat, 2.5% FCH), B (5% fat, 5% FCH), C (2.5% fat, 7.5% FCH) and D (0% fat, 10% FCH).

Preparation of buffalo patties

The meat and other ingredients were mixed using (Fresh Mixer) for an average of 15 minutes. The corn starched was the first ingredient added was hydrated with warm water at the portion of 1:2. Then, STPP and other ingredients were added simultaneously followed with FCH. Finally, water was added. For individual patties, the meat mixture was weighed manually using patties moulder of 80g each. The 80g portion was pressed into a mould at 10 cm diameter each. After moulding, all samples were kept frozen on a metal tray at -18^{o}C for 24 hours before being packaged into a plastic bag at -18^{o}C until further analysis.

Physicochemical analysis

Compositional analysis of Fat, Moisture Content, Ash and Protein

The compositional analysis of the cooked buffalo patties was analysed as stated by Nissar et al. (2009). The fat (ether extractable), ash, protein content and moisture content were determined according to the standard AOAC (1995) procedures using a hot air oven, a furnace, a Soxhlet extraction apparatus and a Kjeldahl accordingly.

Texture Profile Analysis (TPA)

For Texture Profile Analysis (TPA) of cooked and uncooked beef patties sample, TA-XT2 texture analyser was used with using blade set warner bratzler probe p/75 with compression degree of 75 % with pre-test speed of 1.00 mms-1, test speed of 3.00 mms-1 and post-test speed of 5.00 mms-1 as described by Bourne (1978) with minor amendments for hardness (N), springiness, cohesiveness and chewiness determinations as indicated by Bourne. (1979).

Colour measurements

The colour of the raw and cooked samples was measured by using colorimeter (Minolta Chromameter) as stated in Phrabu et al. (2004). The raw sample was thawed at room temperature for 30 minutes to 1 hour before analysis while for the cooked sample, the colour assessment was conducted after 30 min to 1 hour after cooking preparation. The cooked patties were left at room temperature before analysis. The colorimeter was calibrated using white A4 paper with a reading of l (lightness-darkness), a (redness-greeness) and b (yellowness-blueness) of 66.88, 69.94 and 81.22. All readings were taken triplicate for each sample.

Statistical analysis

Each parameter was analyzed in triplicate. Data were collected and analyzed by using Minitab® 17 Statistical Software as used by Sousa et al. (2017) with some modification. A multifactor analysis of variance (ANOVA) was used to evaluate the effect of collagen at different percentage added on beef patties.

Results and discussion

Compositional analysis

Table 2: Compositional Analysis Of Cooked Buffalo Patties Formulated With Different Percentage Of FCH As The Fat Replacer

Treatment Variables	Control	A	B	C	D
Moisture	71.04±0.15^{a}	69.18±0.37^{a}	68.10±0.21^{ab}	65.51±0.32^{b}	65.35±1.87^{b}
Protein	17.59±0.12^{c}	17.49±0.67^{c}	23.40±0.13^{b}	22.14±1.07^{b}	26.68±0.86^{a}
Fat	3.44±0.04^{c}	4.80±0.03^{a}	4.49±0.11^{b}	2.46±0.06^{e}	3.11±0.09^{d}
Ash	2.13±0.08^{a}	2.10±0.10^{a}	2.14±0.13^{a}	2.26±0.04^{a}	3.06±1.01^{a}

Means that do not share a letter are significantly different at level $p<0.05$. Control (10% fat, 0% FCH), A (7.5% fat, 2.5% FCH), B (5% fat, 5% FCH), C (2.5% fat, 7.5% FCH) and D (0% fat, 10% FCH).

The compositional analysis of cooked buffalo patties formulated with different percentage of FCH was presented in table 2. The moisture content of the patties formulated with different percentage was significantly decreased ($p<0.05$) as the FCH increased at the level of more than 50%. The range of moisture content of the buffalo patties was from 63.35% to 71.04%. From a study conducted by Verma et al. (2015), the moisture content in cooked ground pork patties was reduced as the fat content is higher was contradicting with the data obtained from the experimentation. This result was similarly obtained by Troutt et al. (1992) on the study of ground beef patties. FCH is a fish collagen extracted from fish scales and undergone further hydrolysis treatment in which being converted to peptides molecule of smaller sizes (Mahboob, 2015). Collagen extracted from waste such as visceral, skin and scale has three most abundant amino acid namely proline, hydroxyproline and alanine that made up most of the collagen peptides. These might suggest properties of FCH in binding water might be differred from documented properties of collagen and gelatine as results obtained from this experiment, FCH does not act as hydrocolloid with good water holding the capacity to retain water and hence contribute to higher moisture content. This issue can be further investigated in for future reference.

Interestingly, data obtained for protein content in buffalo patties formulated with different FCH percentage was consistent with its protein increment in which significantly different ($p<0.05$) as higher FCH incorporation resulted in higher protein content in the patties. The highest protein content was determined with formulation incorporated with 100% FCH with the value of 26.63. The significant differences ($p<0.05$) were observed between the patties with different percentage of FCH in which patties with 75% FCH and 25% fat depicts lowest fat reading of 2.46 when compared to control formulation of 0% FCH and 100% fat. Patties handling, storage, processing and sampling might contribute to the interesting result obtained with moisture content and fat analysis. The incorporation of FCH at different percentage was not significant ($p>0.05$) with the ash value obtained.

Texture analysis

Table 3: Texture Profile Analysis Of Cooked Buffalo Patties Formulated With Different Percentage Of FCH As The Fat Replacer

Treatment Variables	Control	A	B	C	D
Hardness	1606.3±28.2[a]	1877.4±79.5[a]	723.90±3.30[a]	2381±1254.10[a]	1167.0±194.20[a]
Adhesiveness	-151.80±43.10[a]	-214.70±99.22[a]	-207.50±118.70[a]	-257.70±211.00[a]	-137.10±5.40[a]
Springiness	0.35±0.03[a]	0.73±0.40 [a]	1.13±0.57 [a]	1.04±1.09 [a]	1.37±1.22 [a]
Cohesiveness	0.28±0.04[ab]	0.30±0.08[ab]	0.39±0.09[b]	0.17±0.05[a]	0.33±0.09[ab]
Gumminess	412.10±32.30 [a]	470.00±5.80 [a]	388.60±172.30 [a]	518.80±264.80 [a]	282.10±82.80 [a]
Resilience	147.10±7.10 [a]	341.0±182.30 [a]	381.4±44.60 [a]	440.6±330.00 [a]	437.00±495.00 [a]

Means that do not share a letter are significantly different at level $p<0.05$. Control (10% fat, 0% FCH), A (7.5% fat, 2.5% FCH), B (5% fat, 5% FCH), C (2.5% fat, 7.5% FCH) and D (0% fat, 10% FCH).

The mean values of TPA parameters are depicted in table 3. Overall, the significant differences ($p>0.05$) was observable only on the cohesiveness parameter of the buffalo patties formulated with different percentage of FCH. Other parameters such as hardness, adhesiveness, springiness, gumminess and resilience of the buffalo patties were not significant ($p<0.05$). However, there was an observable trend in such parameters even though there were not significant. For hardness, springiness, gumminess and resilience, there were observed that buffalo patties formulated with higher FCH percentage of 50-75% depicts higher value compared to formulation with lesser or no FCH. A similar result of chewiness of Frankfurt sausages formulated with collagen from pig skin and wheat fat and sausages incorporated with hydrolyzed bovine collagen (Choe et al. 2013, Sousa et al. 2017).

Interest result was denoted with the cohesiveness of the buffalo patties in which formulation with 75% FCH resulted in lowest cohesive parameter while formulation with 50% FCH being the most cohesive. Moreover, Crehan et al. (2000) found that fat reduction in sausages increase springiness consistent with data obtained from the experimentation, however, decrease in adhesiveness was not observed with buffalo patties with lower fat content. Same goes with the result obtained by Noriham et al. (2016) in which the usage of okara flour as fat replacer reduced hardness, cohesiveness, springiness and chewiness of sausages formulation as fat was reduced throughout formulations. The result obtained from the experiment suggest incorporation of FCH in patties dictates by the property of the hydrolyzed collagen in which might work similarly like carrageenan in which capable in improving the cohesiveness of cooked sliced meat (Daud et al. 2016).

Colour measurements

Colour is one of the extrinsic factors that influence customer satisfaction and preferences towards meat products (Troy and Kerry 2010). Based on table 4 above, there was no significant difference observed with the lightness (L*), redness (a*) and yellowness (b*) of the buffalo patties of different percentage of FCH for raw patties. However, the observable trend within all patties were, the higher the FCH percentage, the darker the buffalo patties, the redness was reduced and the yellowness reduced within the range of 8.74 to 11.50 for L*, 7.91 to 10.52 for a* and 6.14 to 7.92 for b*.

Table 4: Colour Measurements Of Raw And Cooked Buffalo Patties Formulated With Different Percentage Of FCH

Treatments Variables		Control	A	B	C	D
Raw patties	Lightness (L*)	11.50±1.16[a]	10.57±2.70[a]	8.77±1.90[a]	9.49±1.59[a]	8.74±0.74[a]
	Redness (a*)	10.52±1.14[a]	9.76±2.53[a]	8.02±1.84[a]	8.56±1.71[a]	7.91±0.74[a]
	Yellowness (b*)	7.92±0.83[a]	7.41±1.14[a]	6.14±1.23[a]	6.63±1.19[a]	6.11±0.42[a]
Cooked patties	Lightness (L*)	36.61±0.27[a]	34.81±1.46[a]	31.80±1.51[b]	29.63±0.44[b]	30.49±0.38[b]
	Redness (a*)	6.54±0.34[a]	7.28±0.41[a]	7.14±0.80[a]	7.52±0.60[a]	7.51±0.85[a]
	Yellowness (b*)	9.96±0.34[a]	11.85±1.96[a]	12.37±1.46[a]	8.89±1.40[a]	10.66±1.73[a]

Means that do not share a letter are significantly different at level $p<0.05$. Control (10% fat, 0% FCH), A (7.5% fat, 2.5% FCH), B (5% fat, 5% FCH), C (2.5% fat, 7.5% FCH) and D (0% fat, 10% FCH).

An interesting observation was found with cooked patties in which the patties lightness were significantly different ($p<0.05$) as the amount of FCH increased. The lowest lightness (darkest) was observed with patties of 7.5% FCH while the lightest patties were with control formulation of % FCH. As consumer perception is dictated by colour especially for meat produce (the more red, the fresher the product) whereas for the cooked meat product, for example with cooking preparation via grilling, the darker (brown) the meat, the more palatable the product. Not only that, as FCH is a protein-based fat replacer, the reduced in the lightness of the product might contribute to the fat of higher protein content and the process of Maillard browning might take place as the protein content might be increased. Others parameter of a* and b* of the cooked patties were not significant.

Conclusion

As the conclusion, buffalo patties with the formulation with 75% FCH were most reduced in fat, relatively high protein and moisture content. In term of texture analysis, there were no significant effects ($p>0.05$) observed on the incorporation of FCH at different percentage when compared to control formulation except for the cohesiveness of the buffalo patties. From the result obtained the most cohesive patty was with the formulation of 50% FCH. The cohesiveness of meat product had been determined with gelatine and collagen incorporated products by the previous studies. This suggests FCH might have a character that contributes to the cohesiveness of meat product. The observable significant result was only seen on the lightness of the cooked buffalo patties ($p<0.05$) in which other parameters in colour analysis were not significant with the colour analysis on the buffalo patties. The cooked patties of higher FCH incorporated, the patties appear to be darker in colour. This observation might result from the characteristic of the FCH as a protein-based fat replacer. The higher protein content for higher FCH % incorporated may contribute to this result due to Maillard Browning reaction. FCH could be used as the fat replacer for producing buffalo patties as its offer acceptable quality and halal status.

References

Barzideh, Z., Latiff, A. A., Gan, C. Y., Abedin, M., & Alias, A. K. (2014). ACE inhibitory and antioxidant activities of collagen hydrolysates from the ribbon jellyfish (Chrysaora sp.). *Food Technology and Biotechnology*, 52(4), 495-504.

Bourne, M. C., Kenny, J. F., & Barnard, J. (1978). Computer-assisted readout of data from texture profile analysis curves. *Journal of Texture Studies*, 9(4), 481–494.

Choe, J. H., Kim, H. Y., Lee, J. M., Kim, Y. J., & Kim C. J. (2013). Quality of frankfurter-type sausages with added pig skin and wheat fiber mixture as fat replacers. *Meat Science*, 93 (4), 849-854

Crehan, C. M., Hughes, E., Troy, D. J., & Buckley, D. J. (2000). Effects of fat level and maltodextrin on the functional properties of frankfurters formulated with 5, 12 and 30% fat. *Meat Science*, 55(4), 463–469.

Daud, N. A., Ghassem, M., Fern, S. S., & Babji, A. S. (2016). Functional bioactive compounds from freshwater fish, edible birdnest, marine seaweed and phytochemical. *American Journal of Food and Nutrition*, 6(2), 33-38.

Dybka, K., & Walczak, P. (2009). Collagen hydrolysates as a new diet supplement. *Food Chemistry and Biotechnology*, 73, 83-92.

Hashim, P., Mohd Ridzwan, M. S., Bakar, J., & Mat Hashim, D. (2015). Collagen in food and beverage industries. *International Food Research Journal*, 22(1), 1-8.

Keeton, J. T. (1994). Low-fat meat products technological problems with processing. *Meat Science*, 36, 261–276.

Mahboob, S. (2015). Isolation and characterization of collagen from fish waste material - skin, scales and fins of Catla catla and Cirrhinus mrigala. *Journal of Food Science and Technology-Mysore*, 52(2), 4296-4305.

Nissar, P. U., Chatli, M. K., & Sharma, D. K. (2009). Efficacy of tapioca starch as a fat replacer in low-fat buffalo meat patties. *Buffalo Bulletin*, 28(1), 18-25.

Noriham, A., Muhammad Ariff Aizuddin, R., Noorlaila, A., & Faris Zakry, A. N. (2016). Potential use of okara as meat replacer in beef sausage. *Jurnal Teknologi*, 78(6–6), 13–18.

Official methods of analysis, 16th Ed. Association of Official Analytical Chemists, Washington, DC.

Ognean, C. F., Darie, N., & Ognean, M. (2006). Fat Replacers – Review. *Journal of Agroalimentary Processes and Technologies*, XII(2), 433–442.

Phrabu, G., Doerscher, D., & Hull, D. (2004). Utilization of pork collagen protein in emulsified and whole muscle meat products, *Journal of Food Science*, 69 (5), 388-392.

Schilling, M. W., Mink, L. E., Gochenour, P. S., Marriott, N. G., & Alvarado, C. Z. (2003). Utilization of pork collagen for functionality improvement of boneless cured ham manufactured from pale, soft, and exudative pork. *Meat Science*, 65(1), 547–553.

Sousa, S. C., Fragoso, S. P., Penna, C. R. A., Arcanjo, N. M. O., Silva, F. A. P., Ferreira, V. C. S., Barreto, M. D. S., & Araujo, I. B. S. (2017). Quality parameters of frankfurter-type sausages with partial replacement of fat by hydrolyzed collagen. *LWT - Food Science and Technology*, 76, 320–325.

Troutt, E. S., Hunt, M. C., Johnson, D. E., Claus, J. R., Kastner, C. L., Kropf, D. H., & Stroda, S. (1992). Chemical, physical, and sensory characterization of ground beef containing 5 to 30 percent fat. *Journal of Food Science*, 57(1), 25–29.

Verma, A. K., Chatli, M. K., Kumar, D., Kumar, P., & Mehta, N. (2015). Efficacy of sweet potato powder and added water as fat replacer on the quality attributes of low-fat pork patties. *Asian-Australasian Journal of Animal Sciences*, 28(2), 252–259

Proceeding: 5th International Conference on Applied Sciences and Engineering (ICASEA, 2018)
(eISBN 978-967-15744-1-6)
Capthorne Hotel, Cameron Highlands, Malaysia

APPLICATION OF VARIOUS MECHANICAL TREATMENTS FOR MEAT TENDERIZATION

Mohamad Afifi Ismail[1]
Gun Hean Chong[1]
Mohammad Rashedi Ismail-Fitry[1]*

[1]Department of Food Technology, Faculty of Food Science and Technology, Universiti Putra Malaysia, 43400, Serdang, Selangor, Malaysia.
*ismailfitry@upm.edu.my

Abstract: *Meat tenderness is an important quality attribute that influences consumer acceptance. The application of mechanical treatment by mean to reduce toughness of meat cuts has gained much interest recently, with an intention to make use the lower grade meat cuts. This review deliberates the function, mechanism and numerous types of mechanical work in meat tenderization. The mechanical work employs to make meat softer by loosening the muscle structure and disrupting muscle cell. Previous studies have thoroughly examined the use of mechanical treatment (such as massaging, tumbling, and grinding) as an effective meat tenderization technique. Besides that, current research on newly emerging processing technology such as high-pressure process (HPP) also shows potential to be explored. The application of mechanical work has shown impressive outcomes by reducing the shear force value that represents hardness of meat. The present paper also described the physical, biochemical and the structural changes of the meat. Finally, the improvements in the meat tenderness by using various type of mechanical work are presented in this paper.*

Keywords: *Food Technology, Meat Tenderization, Mechanical Work*

Introduction

According to FAO, the world food consumption of meat in the year 2015 was 41.3 kg per capita, and it has been projected to be 45.3 kg per capita for the year 2030. The raised of interest in meat consumption forces the meat industry to provide consistent supplies of high-quality meat and meat products. Meat quality is a multi-dimensional concept that can be defined based on the nutritional, compositional quality and palatability factors (Kerry, Kerry, & Ledward, 2002). Other factors such as visual appearance, smell, firmness, juiciness, tenderness and flavour also affect consumer selection. The eating quality perceived by a consumer is highly subjective. Meat tenderness is generally recognized as the most influential factor affecting the meat or meat product palatability (Huffman et al., 1996). Tender meats are more acceptable by consumers. Hence, the improvement in tenderness would increase the commercial value of the final meat product.

Lean meat basically composed of muscle fibers. Muscle in meat consists of two main components which are myofibers and connective tissue (Lawrie & Ledward, 2006). Hence, meat tenderness is greatly affected by the structural integrity of these muscle protein (Kerry et al., 2002). The different type of muscles showed variation in tenderness (Kiran et al., 2015).

Meat tenderness is contributed by various pre-slaughtering factors such as the species, genetic, nutrition and age of the animal. Meanwhile, the post-slaughtering factors are post mortem shortening, conditioning, processing and cooking method (Lawrie & Ledward, 2006). Previous studies found that meat tenderness is mainly associated with the structural integrity of myofibrillar and connective tissue proteins (Nishimura, Hattori, & Takahashi, 1995)

Meat tenderization is a decisive technique employed to reduce toughness of certain lower grade meat cuts or other parts. This technique would be valuable to the processor as they can supply consistently a tender product, thus satisfying consumer demands. In order to improve the tenderness of the meat, a number of tenderizing methods have been investigated, which basically involve chemical, enzymatic and physical treatments. The earlier practice of meat tenderization commonly involved an aging process by holding the whole carcass for a period of 7 to 12 days under chilled conditions depending on the meat cuts and the age (Koohmaraie, 1996). The cooler conditioning leads to structural weakening of muscle protein by the endogenous proteases (Huff Lonergan, Zhang, & Lonergan, 2010).

Technological advancement provides a great contribution to meat processing as the use of mechanical equipment to tenderize meat were evolved. There are various mechanical treatments that are applicable to meat industry such as tumbling, massaging, grinding and injecting. These mechanical disruptions are sufficient to loosen the muscle structures, disrupt muscles cells and destroy the connection between the myofibers and the connective tissues (Heinz & Hautzinger, 2007). Hence, the post-mortem processing technology employs able to improve the meat tenderness.

Meat tenderization is important to ensure the best quality of meat product. Besides that, this method can ensure the lower grade meat cuts will be fully utilized by improving its texture. It also can maximize the use of all parts of the carcass and increase the profits. These lower grade meat cuts usually used for the production of value-added meat products. Therefore, this review aimed to discuss the variety of mechanical work in meat processing and their role in meat tenderization.

Meat Tenderness and Factor Influence Meat Toughness

Tenderness is the most important organoleptic characteristics of meat, that defined as the toughness and resistance to cut (Lawrie & Ledward, 2006). Kerry et al. (2002) stated that meat tenderness is related to the strength of the structural components of the muscle fiber. Tornberg (1996) elaborated that meat tenderness can be referred to the mechanical properties of meat, which involves the structural components; myofibrillar mass, sarcoplasmic proteins and connective tissue. Meat tenderness can be evaluated by instrumental methods and sensory.

Factors contribute to meat tenderness can be classified into two; pre-slaughter and post-slaughter. The pre-slaughter factors for example species, breed, age, sex, feeding and management, genetic influence and stress conditions significantly influenced the meat tenderness. Meanwhile, post-slaughter factors include postmortem glycolysis, postmortem shortening, conditioning, processing and cooking methods might contribute to the meat tenderness (Lawrie & Ledward, 2006). Kandeepan, Anjaneyulu, Kondaiah, Mendiratta, & Lakshmanan (2009) found that spent male and spent female buffaloes had higher shear force value and muscle fiber diameter than young buffalo meat. The sensory evaluation also marked the less tenderness of meat chunks from spent male and spent female buffaloes. The specific

muscles from old animals significantly tougher compared to young animals due to the strength of connective tissues and lack of endogenous enzymes capacity to tenderize the meat. As animals matured, collagen becomes more cross-linked and heat resistant and more variation in tenderness is expected. Neath et al. (2007) demonstrated that water buffalo meat and beef had different in tenderness; however, the rate of tenderizing during 2, 4, 7, and 14 days postmortem did not differ significantly.

Takahashi (1996) explained that meat tenderness is due to structural and biochemical properties of skeletal muscle fibers; myofibrils and intermediate filaments, and the intramuscular connective tissue; endomysium and perimysium, which are composed of collagen fibrils and fibers. Intramuscular connective tissue acts to maintain skeletal muscle fiber integrity. Hence, meat toughness could result from the properties of endomysium and perimysium. Purslow (2005) also described that meat toughness is associated with the collagen content. Berry & Abraham (1996) reported that the patties produced from high connective tissue trimmings exerted some influence on sensory scores of tenderness.

Method of improving meat tenderness

Generally, the tenderness has been accepted as a critical criterion for good quality of meat, thus any approach that serves positive impact on meat tenderness would be beneficial for further investigation. Meat tenderization is the process of reducing meat toughness of certain cuts. Meat tenderization is vital for the meat industry to ensure that lower grade meat cuts can be fully utilized, thus increase capitals. Treatments to improve tenderness of round muscle would add value to the whole carcass by enabling processors to market consistently tender products, increasing returns to the processor and satisfying consumer demands.

Previous studies had reported the application of various techniques aimed to tenderize meat, which involved the use of physical forces; mechanical meat tenderizer (Jeremiah, Gibson, & Cunningham, 1999), chemical; calcium chloride (Gerelt, Ikeuchi, Nishiumi, & Suzuki, 2002) or exogenous enzymes; papain, bromelain, ficin (Sullivan & Calkins, 2010). Methods of meat tenderization had been the subject of many studies, and the technologies keep on developed time after time.

Traditional Aging Method.

Aging had been practiced for many years and proved to be effective in tenderizing meats. Aging is the practice of storing meat beyond the normal time taken for setting and cooling to enhance tenderness (Dransfield, 1994). Meat industry generally utilizes two type of aging; wet (vacuum) and dry aging. According to Bowker, Eastridge, & Solomon (2014), Warner-Bratzler shear force (WBSF) value of boneless strip loins that aged for 7 days (38.1 N) and 14 days (33.3 N) at 4°C were significantly lower compared to steaks that aged for 0 day (57.0 N). However, the WBSF values of the samples aged for 7 and 14 days did not differ significantly between each other's. Another study also found that WBSF value decreased significantly from 1 to 21 days of aging in all breeds (Friesien, Podolian, and Romagnola x Podolian crossbred young bulls) reaching the lowest values at 21 days (Marino et al., 2013). The improvement in tenderness with aging was directly attributed to postmortem proteolysis. Meat tenderization happens due to structural weakening of the myofibrils, the intermediate filaments and the intramuscular connective tissue; endomysium and perimysium during post-mortem aging. The ultrastructural changes weaken the myofibers integrity in the muscle tissue (Takahashi, 1996).

However, there are some limitations of this process as this practice is very time and energy consuming. Besides that, the meat will easily spoiled and develop off-flavour when held at higher temperature. The high processing costs and a huge area for storage at refrigerated conditions are required to implement this technique.

Mechanical Tenderization

In the meat industry, most of the processing involves the use of mechanical or physical force for the purpose of reducing meat particle size, softening the meat and mixing the ingredients (Heinz & Hautzinger, 2007). Common mechanical treatments were tumbling, massaging, grinding and needle/blade injection. The mechanical work during the process had a significant impact on the meat quality especially textural attribute; tenderness. The mechanical work capable to alter the physical structure of muscle fibers and is effective in tenderizing meat. The application of mechanical treatment in tenderizing the meat had been reported by many researchers previously.

Tornberg (2013) reported that mechanical treatment applied effectively can cause the loosening the muscle structure, disrupting muscle cells and destroying the connection between the myofibers and the connective tissues. Tougher meat cuts usually were treated by removing the connective tissues. Apart from that, the connective tissues structure can be disrupted by blade tenderization and grinding as well. Many reports have shown that the mechanical tenderization especially the blade tenderization can significantly improve the tenderness of less tender cuts of meat. In the processing of burgers, the process of grinding is employed to reduce the particle size prior to the mixing process. Grinding process also was effective in disrupting and reducing the connective tissue of muscle fiber (Wells, Berry, & Douglass, 1980). Physical treatments such as tumbling and massaging applied on meat also were aim to disintegrate the muscle structure so that salt and phosphate can reach the myofibrillar proteins (Cassidy et al., 1978).

Massaging

Massaging usually involves a stationary drum with paddles rotating around the vertical axle. This process does not involve free falling of meat contents. Consequently, the process mainly involves muscle tissue rubbing other muscle tissue and the smooth surface of the drum. As massaging time increases, the amount of protein and fat in the exudate also increases. This effect is more pronounced in the presence of salt and phosphate.

The improvement in product yield and reduction in shear force of restructured pork blocks were recorded as the massaging time increase from 6 min to 10 min (Gurikar, Lakshmanan, Gadekar, Sharma, & Anjaneyulu, 2014). In the processing of restructured meat product, tumbling and massaging are the crucial steps because these techniques help to extract salt-soluble protein thus enhance the tenderness, juiciness and slicing characteristics.

Zochowska-Kujawska et al. (2007) presented that massaging was effectively utilized to reduce the hardness of young and wild boars muscle. The rate of changes in textural properties and structural elements during massage is highly depended on muscle type and age of the animals.

Lachowicz, Sobczak, Gajowiecki, & Żych (2003) demonstrated that by increasing the massaging time it can result in a decrease of textural characteristics and the rheological parameter of the muscles. Their study also found that different type of muscles (*Biceps femoris*, *Semimembranosus*, *Quadriceps femoris*) had a different rate of changes in textural

characteristics, rheological properties, and structural elements during the massage. The cause of the reduction in hardness and chewiness might be attributed to the swelling of myofibrillar protein and loosening of the connective tissue.

Tumbling

Tumbling involves the physical process of meat rotating in a drum, falling and making contact with metal walls and paddles. This process involves a transfer of kinetic energy and consequently causes alterations in muscle tissue. Tumbling usually applied for the processing of meat products such as whole-muscle or reconstituted hams. Rotating drum equipped with steel paddles inside the drum is applied to slowly move the meat pieces. This mechanical process is assisted by the addition of salt and phosphates to liberate muscular protein from the meat tissue (protein extraction).

The advantages of tumbling that mostly discuss are the formation of a protein exudate during the process. Protein exudate is a fluid that naturally expressed from muscle tissue that comprised primarily of sarcoplasmic proteins. The protein exudate acts as a sealer when the protein is denatured during thermal processing. The previous researcher explained the relationship between muscle exudate and meat tenderness (Bowker et al., 2014).

Cassidy et al. (1978) found that tumbling caused an increase in cell membrane disruption in both surface and deep muscle regions. Besides that, their study also outlined the effect of continuous tumbling and intermittent tumbling. They found that intermittent tumbling caused the nuclei of the hams more disorganized and the striation patterns of the hams less clear compare to continuous tumbling. This could be explained that rest period provides greater diffusion and sufficient time for salt and phosphate to exhibit the maximum effect. Once the cell membranes have been broken, the myofibrillar protein can migrate to the surface since salt and phosphate aid in solubilization. This protein exudate promotes cohesion in the cooked product.

The previous study conducted by Gao et al. (2015) had proved that the fresh whole pork loins (*Longissimus dorsi*) sample treated with different tumbling marination treatment; conventional static marination, vacuum continuous tumbling marination and vacuum intermittent tumbling marination significantly reduced the textural parameter of hardness compared to control samples. Besides that, tumbling treatment also resulted in higher score sensory attributes of tenderness and juiciness for pork chops. Another study also found that the decreased in shear force and hardness value of injected roast beef (*semimembranous* muscle) that were tumbled with increases time (0, 2, and 16 hours) (Pietrasik & Shand, 2004).

Grinding

Particle size reduction involves grinding, chopping, flaking, and mechanical desinewing have a great contribution to attributes of tenderness. Grinding or mechanical desinewing is the process to remove and reduce the amount of connective tissue in boneless beef shanks, plates, and chucks. Purslow (2005) summarized that the toughness of meat mostly associated with the composition and distribution of intramuscular connective tissues in muscle tissues. The process of grinding capable to disrupt and reduce connective tissues link in muscle tissue thus leads to reduce in toughness.

Wells, Berry, & Douglass (1980) investigated that smaller aperture size (0.19 cm) reduced the total collagen and increased the tenderness attributes of patties in contrast with larger aperture sizes (0.25cm and 0.32cm). Grinding is common processing technique applied for tough meat cuts, especially from old cattle. Grinding process is effective to improve meat tenderness of tough meat cuts that not economically profitable for fresh consumption. Chuck and round are generally known as the tough meat cuts that always are used for the production of value-added products.

Suman and Sharma (2003) found that cooking yield, pH, proximate composition and dimensional changes of buffalo meat patties prepared from difference grind size which were 3, 4 or 6 mm did not differ significantly. However, the increase in grind size caused the significant increase in shear force value. The sensory of juiciness, texture and overall acceptability were higher for patties prepared by using 3 mm grind sizes compared to 4 and 6 mm grind sizes.

Berry, Bigner-George, & Eastridge (1999) demonstrated that hot-processed beef patties prepared by using 0.32 cm grind size showed significant improvement in tenderness compared to patties prepared by using 0.40 cm grind size. The sensory evaluation also indicated higher tenderness for patties produced from smaller aperture size. The smaller grind size created softness, faster sample breakdown in chewing and a greater number of smaller size chewed pieces in contrast to the larger grind size.(Berry et al., 1999)

Wells et al. (1980) reported that the amount of connective tissue and collagen in patties were decreased by using smaller aperture size (0.19 cm). Their research also outlined that the mechanical desinewing may remove connective tissue, but did not significantly impact on the palatability or shear force value. Mechanical desinewing operates by forcing the meat through a smaller aperture and this technique might improve tenderness attribute of beef patties. The only limitation of this technique is the major lost in the market value of minced meats compare to unprocessed meat used for fresh consumption such as steaks.

Blade and needle tenderization

Needle or blade tenderization is performed using a set of needles/blades that function to cuts and punctures the muscle fibers and connective tissues, and this mode of action leads to reduced meat toughness. Needle tenderization is widely applied on wholesale cuts such as steak and roasts. Previous study indicated that most of the mechanically tenderized meat cuts obtained higher sensory scores for tenderness and flavour (Pietrasik & Shand, 2004). Mechanical treatment through blade tenderization disrupted the muscle structure; disintegrated external surfaces of meat pieces and released the myofibrillar proteins, thus making this technique sufficient to tenderize tough meat cuts like round and chuck. This technique is important since it can improve the tenderness less acceptable meat cuts.

Obuz, Akkaya, Gök, & Dikeman (2014) observed that the boneless strip loin (*Longissimus lomborum* muscle) that underwent blade tenderization resulted in lower Warner-Braztler shear force value in comparison to the control loins. However, blade tenderization treatment had higher weight loss than the control loins. The disruption of the muscle structure might allow moisture to escape from the interior of meat to the exterior easier. Narsaiah et al. (2011) demonstrated that the use of handheld blade tenderizer to incise the goat meat resulted in lower shear force value compared to the controls.

Pietrasik & Shand (2004) investigated the influence of blade tenderization prior to injection on beef roasts and reported that it can be effectively utilized to reduce the shear force and hardness of *semimembranosus* muscles. Their study indicated that the mechanical tenderizer causes sufficient disruption of the muscle fibers and connective tissue to reduce shear force values.

Hayward, Hunt, Kastner, & Kropf (1980) reported that blade-tenderizer significantly reduced the shear force of beef *longissimus* steaks in contrast with control samples. It can be explained that the tenderness improved because of the decreased in the structural strength of both myofibrillar and connective components.

Based on the study conducted by Seideman, Smith, Carpenter, & Marshall (1977), blade tenderization significantly reduced the shear force, detectable connective tissues and increased rating for tenderness of both *semitendinosus* and *psoas major* muscles. The blade incision of blade tenderization method is the cause for the disruption of connective tissue, which increase the muscle tenderness.

There were some limitations with this technique as mechanical disruption caused potential microbial cross-contamination and colour changes in the penetration area. The needle tenderizer in a large-scale plant usually is huge and expensive. Previous studies also highlight that blade tenderization caused higher drip loss and reduced shelf life.

High-Pressure Processing (HPP)

According to Bolumar, Enneking, Toepfl, & Heinz (2013), the HPP effect is due to the disruptive nature induced by the pressure that causes dissociation of the myofibrillar proteins. There are many researchers had reported the effectiveness of high-pressure processing for meat tenderizing. The tenderizing effect was understandably due to the structural changes of the myofibrils by the high pressure.

Sikes & Tume (2014) reported that the HPP-heat treated samples would be juicier and more succulent than the heat-only samples. Combination of pressure and heat treatment resulted in a significant reduction in toughness of the meat. They demonstrated that beef steaks heated at specified temperatures and combined with pressure at 200 MPa had lower peak shear force in contrast with heat-only samples. This could explain why the HPP-heat treated meat was tenderer than heat-only treated samples.

Ma & Ledward (2004) observed that the hardness of post rigor beef *longissimus dorsi* was largely decreased when heated at 200 MPa pressure and higher temperature (60°C and 70°C). Meanwhile, there were no significant changes in hardness of beef samples when the pressure applied at ambient temperature (20°C). Hence, it can be suggested that treatment of pressure alone without manipulating the temperature did not affect tenderness.

Jung, De Lamballerie-Anton, & Ghoul (2000) reported that high-pressure treatment at low temperature (10°C) contributed to the tenderness of bovine muscle (*Biceps femoris*). The improvement in tenderness attributed to the ultrastructural changes examined through electron micrographs. The samples showed contracted sarcomeres with structural smoothness but disorganization of thick and thin filaments after treatment at 325 MPa. It can be explained that the ultrastructural changes is highly depended on the intensity of the pressure.

Previous study conducted by Ueno, Ikeuchi, & Suzuki (1999) found that the smooth surface associated with the disappearance of the wavy structure was observed in the sample pressurized at 100 MPa, and these changes increased with increasing pressure (200 MPa, 300MPa and 400MPa) applied to the muscle. The deformation of the honeycomb-like structure of endomysium was accelerated with the increase of pressure applied to muscle samples. The structural changes of intramuscular connective tissue by high pressure exert a significant effect on tenderness.

Sun & Holley (2010) outlined that high pressure can modify the structure and function of proteins. The structural changes will affect the texture of the muscle. Simultaneous application of pressure and heat to meat has been shown to improve tenderness but still, the effectiveness is depending on the temperatures and pressures used.
From the compilation of the previous studies, it can be summarized that the application of high pressure to improve meat tenderness showed great potential. The condition for treatment such as pressure and temperature need to be understood so that they can be optimized.

The problem associated with the application of HPP on meats usually are the changes in colour due to muscle protein denaturalization at the pressure required for meat tenderization. According to consumer perspective, the HPP-treated meat is less accepted as fresh meat. Besides that, the application of HPP requires a high initial investment. Thus, these techniques less familiar in industrial scale for meat tenderization.

CONCLUSION

As the conclusion, there are various mechanical treatments available for meat tenderization. The effectiveness of each technique varies depending on the type of muscle. The technology advancement contributes to the improvement of the methods. The use of technology combined with mechanical treatment will provide a greater effect on meat tenderizing.

REFERENCE

Berry, B. W., & Abraham, H. C. (1996). Sensory, shear force and cooking properties of commercially processed ground beef patties. *Food Quality and Preference*, *7*(1), 55–59. https://doi.org/10.1016/0950-3293(95)00007-0

Berry, B. W., Bigner-George, M. E., & Eastridge, J. S. (1999). Hot processing and grind size affect properties of cooked beef patties. *Meat Science*, *53*(1), 37–43. https://doi.org/10.1016/S0309-1740(99)00034-0

Bolumar, T., Enneking, M., Toepfl, S., & Heinz, V. (2013). New developments in shockwave technology intended for meat tenderization: Opportunities and challenges. A review. *Meat Science*, *95*(4), 931–939. https://doi.org/10.1016/j.meatsci.2013.04.039

Bowker, B. C., Eastridge, J. S., & Solomon, M. B. (2014). Measurement of Muscle Exudate Protein Composition as an Indicator of Beef Tenderness. *Journal of Food Science*, *79*(7), 1292–1297. https://doi.org/10.1111/1750-3841.12496

Cassidy, R. O., Ockerman, H. W., Krol, B., Van Roon, P. S., Plimpton, R. F., & Cahill, V. R. (1978). Effect of tumbling method, phosphate level and final cook temperature on histological characteristics of tumbled porcine muscle tissue. *Journal of Food Science*, *43*(5), 1514–1518.

Dransfield, E. (1994). Optimisation of tenderisation, ageing and tenderness. *Meat Science*, *36*(1–2), 105–121. https://doi.org/10.1016/0309-1740(94)90037-X

Gao, T., Li, J., Zhang, L., Jiang, Y., Song, L., Ma, R., … Zhou, G. (2015). Effect of different

tumbling marinade treatments on the water status and protein properties of prepared pork chops. *Journal of the Science of Food and Agriculture*, *95*(12), 2494–2500. https://doi.org/10.1002/jsfa.6980

Gerelt, B., Ikeuchi, Y., Nishiumi, T., & Suzuki, A. (2002). Meat tenderization by calcium chloride after osmotic dehydration. *Meat Science*, *60*(3), 237–244. https://doi.org/10.1016/S0309-1740(01)00126-7

Gurikar, A. M., Lakshmanan, V., Gadekar, Y. P., Sharma, B. D., & Anjaneyulu, A. S. R. (2014). Effect of meat chunk size, massaging time and cooking time on quality of restructured pork blocks. *Journal of Food Science and Technology*, *51*(7), 1363–1369. https://doi.org/10.1007/s13197-012-0644-9

Hayward, L. H., Hunt, M. C., Kastner, C. L., & Kropf, D. H. (1980). Blade tenderization effects on beef longissimus sensory and instron textural measurements. *Journal of Food Science*, *45*(4), 925–935. https://doi.org/10.1111/j.1365-2621.1980.tb07480.x

Heinz, G., & Hautzinger, P. (2007). *Meat processing technology for small-to medium-scale producers*. *RAP Publication (FAO)*.

Huff Lonergan, E., Zhang, W., & Lonergan, S. M. (2010). Biochemistry of postmortem muscle - Lessons on mechanisms of meat tenderization. *Meat Science*, *86*(1), 184–195. https://doi.org/10.1016/j.meatsci.2010.05.004

Huffman, K. L., Miller, M. F., Hoover, L. C., Wu, C. K., Brittin, H. C., & Ramsey, C. B. (1996). Effect of Beef Tenderness on Consumer Satisfaction with Steaks Consumed in the Home and Restaurant. *Journal of Animal Science*, *74*(1), 91–97. https://doi.org/10.2527/1996.74191x

Jeremiah, L. E., Gibson, L. L., & Cunningham, B. (1999). The influence of mechanical tenderization on the palatability of certain bovine muscles. *Food Research International*, *32*(8), 585–591. https://doi.org/10.1016/S0963-9969(99)00134-9

Jung, S., De Lamballerie-Anton, M., & Ghoul, M. (2000). Modifications of Ultrastructure and Myofibrillar Proteins of Post-rigor Beef Treated by High Pressure. *LWT - Food Science and Technology*, *33*(4), 313–319. https://doi.org/10.1006/fstl.2000.0654

Kandeepan, G., Anjaneyulu, A. S. R., Kondaiah, N., Mendiratta, S. K., & Lakshmanan, V. (2009). Effect of age and gender on the processing characteristics of buffalo meat. *Meat Science*, *83*(1), 10–14. https://doi.org/10.1016/j.meatsci.2009.03.003

Kerry, J., Kerry, J., & Ledward, D. (2002). *Meat processing: Improving quality (Vol. 76)*. *Woodhead Publishing*. https://doi.org/10.1533/9781855736665.1.137

Kiran, M., Naveena, B. M., Reddy, K. S., Shashikumar, M., Reddy, V. R., Kulkarni, V. V., … More, T. H. (2015). Muscle-Specific Variation in Buffalo (Bubalus bubalis) Meat Texture: Biochemical, Ultrastructural and Proteome Characterization. *Journal of Texture Studies*, *46*(4), 254–261. https://doi.org/10.1111/jtxs.12123

Koohmaraie, M. (1996). Biochemical factors regulating the toughening and tenderization processes of meat. *Meat Science*, *43*, 193–201. https://doi.org/10.1016/0309-1740(96)00065-4

Lachowicz, K., Sobczak, M., Gajowiecki, L., & Żych, A. (2003). Effects of massaging time on texture, rheological properties, and structure of three pork ham muscles. *Meat Science*, *63*(2), 225–233. https://doi.org/10.1016/S0309-1740(02)00073-6

Lawrie, R. A., & Ledward, D. A. (2006). *Lawrie's Meat Science*. *Lawrie's Meat Science*. https://doi.org/10.1533/9781845691615.358

Ma, H. J., & Ledward, D. A. (2004). High pressure/thermal treatment effects on the texture of beef muscle. *Meat Science*, *68*(3), 347–355. https://doi.org/10.1016/j.meatsci.2004.04.001

Marino, R., Albenzio, M., della Malva, A., Santillo, A., Loizzo, P., & Sevi, A. (2013). Proteolytic pattern of myofibrillar protein and meat tenderness as affected by breed and aging time. *Meat Science*, *95*(2), 281–287. https://doi.org/10.1016/j.meatsci.2013.04.009

Narsaiah, K., Jha, S. N., Devatkal, S. K., Borah, A., Singh, D. B., & Sahoo, J. (2011). Tenderizing effect of blade tenderizer and pomegranate fruit products in goat meat. *Journal of Food Science and Technology*, *48*(1), 61–68. https://doi.org/10.1007/s13197-010-0127-9

Neath, K. E., Del Barrio, A. N., Lapitan, R. M., Herrera, J. R. V., Cruz, L. C., Fujihara, T., … Kanai, Y. (2007). Difference in tenderness and pH decline between water buffalo meat and beef during postmortem aging. *Meat Science*, *75*(3), 499–505. https://doi.org/10.1016/j.meatsci.2006.08.016

Nishimura, T., Hattori, A., & Takahashi, K. (1995). Structural Weakening of Intramuscular Connective-Tissue During Conditioning of Beef. *Meat Science*, *39*(1), 127–133.

Obuz, E., Akkaya, L., Gök, V., & Dikeman, M. E. (2014). Effects of blade tenderization, aging method and aging time on meat quality characteristics of Longissimus lumborum steaks from cull Holstein cows. *Meat Science*, *96*(3), 1227–1232. https://doi.org/10.1016/j.meatsci.2013.11.015

Pietrasik, Z., & Shand, P. J. (2004). Effect of blade tenderization and tumbling time on the processing characteristics and tenderness of injected cooked roast beef. *Meat Science*, *66*(4), 871–879. https://doi.org/10.1016/j.meatsci.2003.08.009

Purslow, P. P. (2005). Intramuscular connective tissue and its role in meat quality. *Meat Science*, *70*(3), 435–447. https://doi.org/10.1016/j.meatsci.2004.06.028

Seideman, S. C., Smith, G. C., Carpenter, Z. L., & Marshall, W. H. (1977). Blade tenderization of beef psoas major and semitendinosus muscles. *Journal of Food Science*, *42*(6), 1510–1512. https://doi.org/10.1111/j.1365-2621.1977.tb08413.x

Sikes, A. L., & Tume, R. K. (2014). Effect of processing temperature on tenderness, colour and yield of beef steaks subjected to high-hydrostatic pressure. *Meat Science*, *97*(2), 244–248. https://doi.org/10.1016/j.meatsci.2013.12.007

Sullivan, G. A., & Calkins, C. R. (2010). Application of exogenous enzymes to beef muscle of high and low-connective tissue. *Meat Science*, *85*(4), 730–734. https://doi.org/10.1016/j.meatsci.2010.03.033

Suman, S. P., & Sharma, B. D. (2003). Effect of grind size and fat levels on the physico-chemical and sensory characteristics of low-fat ground buffalo meat patties. *Meat Science*, *65*(3), 973–976. https://doi.org/10.1016/S0309-1740(02)00313-3

Sun, X. D., & Holley, R. A. (2010). High hydrostatic pressure effects on the texture of meat and meat products. *Journal of Food Science*, *75*(1), R17–R23. https://doi.org/10.1111/j.1750-3841.2009.01449.x

Takahashi, K. (1996). Structural weakening of skeletal muscle tissue during post-mortem ageing of meat: the non-enzymatic mechanism of meat tenderization. *Meat Science*, *43*, 67–80. https://doi.org/10.1016/0309-1740(96)00056-3

Tornberg, E. (1996). Biophysical aspects of meat tenderness. *Meat Science*, *43*(SUPPL. 1), 175–191. https://doi.org/10.1016/0309-1740(96)00064-2

Tornberg, E. (2013). Engineering processes in meat products and how they influence their biophysical properties. *Meat Science*, *95*(4), 871–878. https://doi.org/10.1016/j.meatsci.2013.04.053

Ueno, Y., Ikeuchi, Y., & Suzuki, A. (1999). Effects of high pressure treatments on intramuscular connective tissue. *Meat Science*, *52*(2), 143–150. https://doi.org/10.1016/S0309-1740(98)00161-2

Wells, L. H., Berry, B. W., & Douglass, L. W. (1980). Effects of grinding and mechanical desinewing in the manufacture of beef patties using conventionally chilled and hot boned and rapidly chilled mature beef. *Journal of Food Science*, *45*(2), 163–167. https://doi.org/10.1111/j.1365-2621.1980.tb02567.x

Zochowska-Kujawska, J., Lachowicz, K., Sobczak, M., Gajowiecki, L., Kotowicz, M., Zych, A., & Medrala, D. (2007). Effects of massaging on hardness, rheological properties, and structure of four wild boar muscles of different fibre type content and age. *Meat Science*, *75*(4), 595–602. https://doi.org/10.1016/j.meatsci.2006.09.018

Proceeding: 5th International Conference on Applied Sciences and Engineering (ICASEA, 2018)
(eISBN 978-967-15744-1-6)
Capthorne Hotel, Cameron Highlands, Malaysia

REVIEW ON DIFFERENT EXTRACTION METHODS OF POLYPHENOL COMPOUNDS FROM POMEGRANATE (PUNICA GRANATUM)

S. Jauhar[1]
M. A. R. Nor-Khaizura[2]
W. Z. W. Ibadullah[2]
M. R. Ismail-Fitry[1]*

[1]Department of Food Technology, Faculty of Food Science and Technology, Universiti Putra Malaysia, 43400, Serdang, Selangor, Malaysia.
[2]Department of Food Science, Faculty of Food Science and Technology, Universiti Putra Malaysia, 43400, Serdang, Selangor, Malaysia.
*ismailfitry@upm.edu.my

Abstract: *Recently natural polyphenol compounds (PCs) of plants, gained wide consideration of scientists, companies and public people because of its unique pharmaceutical and preservative benefits in the physiological system. They can prevent mortal and serious diseases such as cancer, cardiovascular and Alzheimer. However, defining a suitable source of PCs and their proper, economic and efficient extraction method are still a challenge. The aim of this study was to review PCs as an important antioxidant, the significance of pomegranate as a source of natural PCs. This study also covers different types of PCs extraction methods such as solid-liquid extraction (SLE) method as a conventional extraction which using Soxhlet apparatus and several solvents and advanced methods such as microwave-assisted extraction (MAE), supercritical fluid extraction (SFE), accelerated solvent extraction (ASE), ultrasound-assisted extraction (UAE) and high hydrostatic pressure extraction (HHPE). Simple and developed analytical method of PCs is also reviewed in the study. SLE method is an easy and simple method but, it uses lots of chemicals and is not suitable for all kinds of PCs extraction. UAE is using for quick extraction PCs, SFE is green extraction method uses less solvent and have a good result but it needs high technology. ASE method is a proper alternative for Soxhlet extraction method for its quick result. MAE method has high extraction result but is not suitable for some thermolabile PCs.*

Keywords: *Antioxidants, Polyphenol, Extraction Methods, Pomegranate*.

Introduction

Antioxidant molecules are known as inhibitor substance of oxidation, causes cell destroying inside a physiological system including human and different types of foods. Oxidation process produces free radicals which are highly reactive species and contains one or more unpaired electron in its outer shell (Brar, Dhillon, & Soccol, 2014). Free radicals inside live organisms are reacting during the oxidation process. They can easily react and destroy cells and tissues. Antioxidants prevent spreading reaction by donation of hydrogen radical to other available free radicals and can effectively reduce food lipid oxidation and rancidity without any sensory and nutrition value damage (Kumar, Yadav, Ahmad, & Narsaiah, 2015). Plant polyphenol as natural antioxidants are widely used as it showed considerable health benefits such as anti-

carcinogenic, anti-microbial, antioxidant, antiviral, antitumor, anti-inflammatory, antipyretic, analgesic characteristics (Rajbhar, Dawda, & Mukundan, 2015).

Recently plant polyphenols compound (natural antioxidant) has achieved remarkable significance for its food conservative traits, free radical scavenging and containing health benefits for several diseases (Ameer, Shahbaz, & Kwon, 2017; Pinelo et al., 2007). Due to public awareness, health benefits and consumer high demand the international market of polyphenol compound is remarkably increasing, it was estimated $757 million in 2015 and it is predicted to reach $1,121 million by 2022. The high consumption rate of plant-rich of polyphenol compound by patients and elder peoples also had an important role in the global market growing (Prasad Eswara, 2017). The use of preservative as food conservation become prevalent and plays a critical role in the food industries. Even though many types of preservatives have been applied for food protection, consumer demands for natural food preservative are still increasing (Carocho, Morales, & Ferreira, 2018).

Preservatives are divided into artificial and natural. Artificial preservatives are the cause of toxicology and carcinogen. So the companies and consumers are preferring natural antioxidant as a food preservation (Kumar et al., 2015). Fruit and some plants containing high phenolic compounds are suitable to be used as preservatives or antioxidants. Pomegranate is one of those which presented stronger antioxidant properties among the fruits, all parts of this fruit comprises a high antioxidants concentration. Pomegranate's peel is a decent source of tannins, anthocyanin, and flavonoids (Karre, Lopez, & Getty, 2013). Çam & Durmaz (2009) reported that pomegranate has high antioxidant traits among many common fruits.

Several methods have been used for the extraction of polyphenol compound from numerous types of plants. Extraction through Soxhlet apparatus with different polar solvent such as water, methanol, ethanol or ethyl acetate is a conventional method. There are some advanced methods of extraction such as microwave-assisted extraction (MAE), supercritical fluid extraction (SFE), accelerated solvent extraction (ASE), ultrasound-assisted extraction (UAE) and high hydrostatic pressure extraction (HHPE), which showed different quantitative and qualitative results (Xu, Wang, Pu, Tao, & Zhang, 2017). However, developing a unique standard method for extraction of different types of plants is still challenging. Scientists are trying to find an efficient, cost-effective and eco-friendly method for polyphenol extraction (Ameer et al., 2017).

This study aims to review the importance of polyphenol as food and health benefited antioxidant, the significance of pomegranate as a strong antioxidant against autoxidation inside the biological system and different types of simple and advanced polyphenol extraction methods, to provide useful information for relevant research and companies.

Literature review

Polyphenol compounds

Polyphenols compounds are secondary metabolites which have been widely used as antioxidants; especially for oxidative and microbial spoilage prevention, there are more than 8000 phenolic compounds around the world (Gropper, Smith, & Groff, 2009). Plant-derived polyphenols are secondary metabolites being existed naturally through Shikimate/phenylpropanoid pathway to cope with biotic and abiotic environmental stress, such

as temperature, pathogens, and several other factors. Meaning of phenol in chemistry is phenyl ring bearing one or more hydroxyl group (Lattanzio, 2013).

Recently, working on polyphenols compound extraction fascinated attention as a natural product because of its distinct importance. The attention could be justified as a recognized capacity of this compound for scavenging free radicals which are causes of abundant diseases (Pinelo et al., 2007). Polyphenol compounds could be found in abundant plants such as fruits, vegetables, and herbs. Among plants, the fruits are recognized as a leading source of phenolic compounds for example peaches, cherries, apples, plums, citrus fruit, apricots, berries, grapes and tropical fruits (Li et al., 2014). Polyphenol compound can be found in different types of vegetables such as: soybeans, carrots, olives, capers, tomato, bean, artichoke, cauliflower, broccoli, spinach and onions (Duthie, Duthie, & Kyle, 2000; Fresco, Borges, Marques, & Diniz, 2010; Mocanu, Nagy, Szöllosi, & Mayence, 2015; Weichselbaum & Buttriss, 2010). There are other significant sources of phenolic in different types of beverages for example: coffee, beer, black and green tea, cocoa, grains, nuts and fruit juices grains and nuts (Bravo, 2009; Fresco et al., 2010; Mocanu et al., 2015; Weichselbaum & Buttriss, 2010). Also there are different herbs and spices which have high level of polyphenols for example: turmeric, celery, parsley, mint, rosemary, thyme, curry, ginger, clove bud, sage and dill (Fresco et al., 2010; Mocanu et al., 2015; Pérez-Jiménez, Neveu, Vos, & Scalbert, 2010; Weichselbaum & Buttriss, 2010).

Phenols are normally soluble in polar organic solvents; the glycoside phenols are water soluble. By increasing hydroxyl group water solubility is increasing. Some phenolic are soluble in sodium carbonate and sodium hydroxide. Phenol with a few hydroxyl groups is soluble in ether, chloroform, ethyl acetate, methanol, and ethanol. Methanol, ethanol, water, alcohol are normally used for chemical analysis of phenol (Lattanzio, 2013). Polyphenol compounds are further divided into several classes such as phenolic acid, polyphenols, flavonoids, lignans, stilbenes and tannins (Mocanu et al., 2015).

Pomegranate

Pomegranate is related to Punicaceae family (Erkan & Kader, 2011). Some recent studies propose reassessment on its taxonomy to place it in Lythraceae family. Pomegranate is related to Rodidae subclass, Myrtales order and Punica genus, the pomegranate is unlike other plants has only two species granatum or Lythraceae and protopunica. The Punica protopunica species is only found in Socotra island of Arabian Peninsula. Punica granatum means seeded apple which is derived from Pommum (apple) and grantus (grainy) (Teixeira da Silva et al., 2013). A different region named pomegranate and has more than 500 cultivars, in some places, there is a different name for same basic genotype cultivars (Braidy, 2015). Pomegranate has a small tree and included in shrub category, the pomegranate is evergreen in the tropics and is deciduous in a subtropical climate. The pomegranate plant is deciduous, and have small, narrow, oblong leaves and short stems. This plant has granular fruit, with green/red of white skin, each grain contains juice which is covered by a smooth membrane (Erkan & Kader, 2011).

Health benefits and medicinal use of pomegranate

Medicinal using of pomegranate has a long history, different parts of pomegranate were used for several diseases treatments. Pomegranate root extracts full of tannin were used by ancient Egyptian to release tapeworms from human intestines. Hippocrates treat abundant disease through pomegranate extracts such as digestion problems, reducing skin and eye inflammation

(Braidy, 2015). Phytochemicals of pomegranate were used as pharmaceutical, pharmacological and medicinal bioactivities to heal anti-diarrheal, helminthic, anti-diabetic, antibacterial, anticancer, anti-neoplastic, antiviral, antioxidant, hypolipidemic, digestive and vascular protection (Teixeira da Silva et al., 2013). He points out some phytochemicals such as flavonoids, alkaloids, tannins, organic acids, steroids, and triterpenes. According to Smith, (2014) recent research of pomegranate suggests different parts of pomegranate for healing several diseases for example diabetes, cardiovascular disease, male infertility, Alzheimer, infant brain ischemia, erectile dysfunction, dental conditions, cancer, obesity, protection from UV radiation and arthritis. According to Table 1 different parts of pomegranate (juice, seed oil, peel, leaves, flower, bark, and roots) has several constituents of chemical sources, which are important for human health (Jurenka, 2008). Akhtar, Ismail, Fraternale, & Sestili (2015) reported that data from literature indicate 124 different phytochemicals which can be found in pomegranate fruit; among these phytochemicals, high molecular weight polyphenols (e.g. ellagitannins and the pomegranate-peculiar punicalagin) are likely to mediate the protective effects against a wide range of oxidative and inflammatory disorders, including cancer (Erkan & Kader, 2011).

Table 1: Pomegranate Ingredients From Its Different Sources.

Pomegranate parts	Ingredients
Peel and pericarp	Anthocyanidins, phenolic punicalagins, gallic acid, catechin, flavones, flavonones.
Juice	Rutin, quecertin ,anthocyanins, glucose, ascorbic acid, ellagic acid, gallic acid, catechin, minerals, amino acids,
Seed oil	Sterols, ellagic acid, , 95% punicic acid
Flowers	Gallic acid, urosolic acid, triterpenoids including maslinic and Asiatic acid
Roots and bark	Piperidie alkaloids, Ellagitannins, punicalin and punicalagin
Leaves	Apigenin, Tannins, flavone glycosides, luteolin,

Pomegranate peel polyphenol compounds

The pomegranate peel might be considered as the major source of natural antioxidant and its extract possess a relatively high antioxidant activity (Yasoubi, Barzegar, Sahari, & Azizi, 2007). Due to high of its healing characteristic, pomegranate peel has been used since ancient time for several diseases.In addition to its healing value, it also has high nutrition importance which includes vitamins A, B6, C, E, folate, potassium and oxalic acid. In recent years more medicinal values of pomegranate peel have been investigated such as abortifacient, analgesic, anti-amoebic, antibacterial, anticonvulsant, antifungal, antimalarial, anti-mutagenic, antiviral, antispasmodic, diuretic, hypoglycemic, hypothermic, and antioxidant activities (Al-Rawahi, 2014).

Li et al., (2006) argued that pomegranate peel accounts for about 50% of fruit weight is characterized by the presence of 63 high molecular weight phenolic, ellagitannins, proanthocyanidins, complex polysaccharides, flavonoids and appreciable quantities of microelements that on the whole, exhibit strong anti-mutagenic, antioxidant, antimicrobial and apoptotic properties.

Polyphenol extraction methods

There are several types of polyphenol compound extraction methods. According to the nature of the plant and effective antioxidant activity, different methods can be used; it can be divided into simple or usual methods and advanced methods with the help of modern technology. The simple methods included solid-liquid extraction (SLE) and heat reflux extraction. Advanced methods of extraction are: ultrasound-assisted extraction (UAE), microwave-assisted extraction (MAE), supercritical fluid extraction (SFE), accelerated solvent extraction (ASE) and high hydrostatic pressure extraction (HHPE) (Xu et al., 2017).

Xu et al., (2017)concluded that SLE is a simple and easy method but it needs chemicals and has low efficiency. SFE is an environmentally friendly extraction method but some demotivation factors for this method are required high expenses for investment and it might be not suitable for some polar polyphenol compounds extraction. In SFE method, normally supercritical CO^2 liquid is used but because of the non-polarity trait of this substance, some polar fluids such as ethane, butane, pentane, nitrous oxide, ammonia, trifluoromethane, and water are also used.

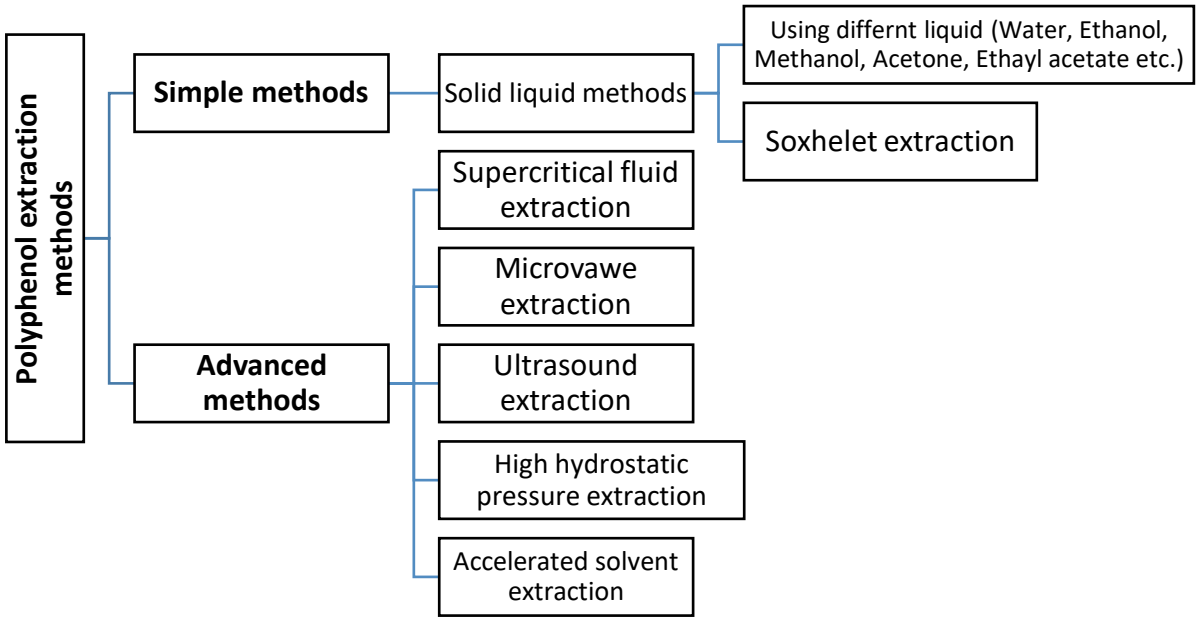

Figure 1: Different Polyphenol Extraction Methods.

Due to highly selectivity, highly extractive rate and low critical point the SFE is the remarkable alternative for the extraction of natural thermosensitive bioactive compounds, which does not generate toxic residues (Cavalcanti, Navarro-Díaz, Santos, Rostagno, & Meireles, 2012).

Solid-liquid extraction method (SLE)

Solid-liquid extraction is a simple method which has been used for a long time. It does not need modern technology and can be conducted easily through simple tools. In this method, different types of polar solvent can be used to extract target ingredients of a substance. Polar solvents such as methanol, ethanol, acetone, chloroform and ethyl acetate are generally used for solid-liquid extraction of polyphenol compound. Extraction without using water showed different antioxidant activities and different amount of yield but by using water for extraction of dried

pomegranate peel extract with ethyl acetate, acetone and methanol exhibited higher antioxidant activities. Methanol has higher polarity then other solvents, the phenolic result of this solvent showed higher antioxidant activity (Ismail, Sestili, & Akhtar, 2012). There are some important variables in SLE method which are necessary to be considered. The solvents such as ethanol, methanol, water or ethyl acetate are strongly depended on contact time, stirring, and temperature (Pinelo, Del Fabbro, Manzocco, Nuñez, & Nicoli, 2005). Al-Rawahi, Rahman, Guizani, & Essa (2013) concluded that in comparison of different extraction methods; methanol extraction of pomegranate peels exhibited a higher capacity for extracting phenolic compounds than water and ethanol. However, some researches preferred ethanol extraction because it is safe and help water to be evaporated (Rababah, Banat, Rababah, Ereifej, & Yang, 2010). Masci et al., (2016) evaluated several extraction methods and they extracted good yields of the polyphenolic compound of pomegranate peel by using soxhlet apparatus with ethyl acetate for 6 h. For antioxidant activity they resulted with polyphenol extracted from ethyl acetate and Soxhlet extraction methods has the same antioxidant activities but these methods showed stronger antioxidant activities among others.

The solid-liquid extraction method is a simple method which can be implemented without developed technology. Using liquid the methanol yielded a high amount of polyphenol compound but if it remained, the compound inside the product will be harmful to the health of humans and animal. Ethanol or ethyl acetate are preferred by producing a good yield and antioxidant activities. Using ethyl acetate in Soxhlet might be preferred because this method resulted in high phenolic contents and good antioxidant activities.

Supercritical Fluid Extraction method

One of the advanced environmental friendly extraction methods for solid or liquid substance is Supercritical Fluid Extraction (SFE) method, desirable separation of components can be extracted through this analytical technique (Herrero, Mendiola, Cifuentes, & Ibáñez, 2010). This method produces solvent between vapour and liquid phase, through temperature and pressure conditions. By this situation physical changes accruing inside the solvent such as diffusivity, compressibility, gas-like viscosity, liquid-like densities and reduction in surface tension. However, several extraction solvents have been used for SFE methods such as sulfur hexafluoride, fluoroform, ammonia, n-pentane, propane, ethane, nitrous oxide and water, but the most commonly used extraction solvent is carbon dioxide (Zougagh, Valcárcel, & Ríos, 2004).

Pinelo et al. (2007) used CO^2 as extraction solvents for its economical, non-toxic value and volatile solvent, which have the modest critical condition. Using ethanol as a co-solvent with CO^2 resulted in high extraction of polyphenols than pure carbon dioxide because CO^2 is not a polar solvent and ethanol has high polarity. The efficient extraction was correlated with temperature (40-60°C) and pressure (10-30mPa). Although peak polyphenols was extracted at 60°C and 10MPa (Castro-Vargas, Rodríguez-Varela, Ferreira, & Parada-Alfonso, 2010). Selectivity of SFE method is more than other extraction methods, also the production of a less toxic product is another merit of this technique but, the main disadvantage is, it is not applicable to polar solvent and it needs more investment than other methods (Xu et al., 2017).

Ultrasound-assisted extractions (UAE)

The wave sound of ultrasound is produced by rarefaction and compression process which produces high frequency 2 MHz or greater sound (Watson, 2014). The ultrasound-assisted extraction method is derived from ultrasonic processing technology which has been used in the food industry as a novel and promising technology. It has several chemical and physical effects for improving efficiency in food processing operations. This technology is also used as a diagnostic technology for the food quality control process. UAE method is economic and beneficial technology which does not need for expensive equipment. It provides sonication in food extraction process, which is produced through sound waves and generates cavitation bubbles near the sample tissue, so it disrupts plant cell walls and releasing its cell contents (Cheng, Zhang, Xu, Adhikari, & Sun, 2015).

There are some variables which have an influence on extraction efficiency such as sonication time, ultrasonic wave frequency, the property of the solvent and temperature (Xu et al., 2017). Cheng et al., (2015) stated that cavitation is very important variable because moreover to the production of cavitation bubbles it occurs microstreaming as well. Than main advantages of this method can be summarized as: it is easy to be used and simple, at mild/low temperature the extraction yield and rapid extraction of heat sensitive ingredients are increasing, it needs less time for extraction process in comparison to conventional extraction methods such as Soxhlet, it needs less equipment and also it is an economic method. The main disadvantages are: in dynamic extraction, the dilution of the extract is not possible, high ultrasound wave causes harmful effects for active ingredients and undesirable changes (Ameer et al., 2017; Watson, 2014; Xu et al., 2017).

Microwave-assisted extraction (MAE)

Microwave-assisted extraction is another advanced method which is widely used for extraction of polyphenol compound from different types of plants. It analyzes the sample directly through microwave energy (Fang, Wang, Hao, Li, & Guo, 2015). The wave's microwaves have 1m to 1 mm lengths range, which are equal to 300 MHz (0.3 GHz) to 300 GHz frequencies and produces through the radio. Polar molecules are warm up by this wavelengths through the double mechanism of dipole rotation and ionic conduction (Watson, 2014). Important variables of MAE method are extraction time, solvent property, dielectric constant, microwave power and solubility. The solvent property is an important variable because more microwave energy can be absorbed by the high dielectric solvent. Generally, water, ethanol, and methanol are using for polyphenol extraction (Fang et al., 2015).

The MAE process is started through the generation of the electromagnetic wave from a cavity called magnetron. It is continued with the interaction between tissue cell wall, matrix inside the plant and emitted radiation waves and moisture inside plant matrix will be heating up due to absorption of characteristic photonic energy of electromagnetic waves. Evaporation of the plant matrix is started through electromagnetic energy, therefore remarkable pressure applies to cell walls of the plant at subcellular and cellular levels, so plant swelling is started during the process. A structural change occurs inside plant matrix and by interrupting plant cell wall increases in the mass moving of solutes thus, phytochemical are leaching from the cellular matrix of the plant (Ameer et al., 2017). Merits of this method are: it uses less extraction solvent, the extracted PCs through this method showed high antioxidant activity and need short time for extraction. This method is not applicable to the PCs which have more OH groups and heat sensitive also oxidation of PCs is occurring during this extraction process (Xu et al., 2017).

Accelerated solvent extraction method (ASE)

Accelerated solvent extraction (ASE) or pressurized liquid extraction is another innovative method which extracts polyphenols of plants through high pressure and temperature. The solvent is rapidly diffusing into plant cells by high pressure and temperature and prevent degradation of polyphenol compound. In comparison to conventional methods, it provides quick extraction and needs a small amount of solvents (Rodríguez-Solana, Salgado, Domínguez, & Cortés-Diéguez, 2015). In this method, high pressure (3–20 MPa) and high temperature (25–200°C) are used (Watson, 2014). Generally, ASE method is similar to Soxhlet or other conventional method and have the similar results, but it is used to reduce laboratory time and amount of solvent. This method uses high pressure for preventing solvent under its boiling point and slightly high temperature in the extraction process. So, this method is considered as good replacer to old extraction methods (Rodríguez-Solana, Salgado, Domínguez, & Cortés-Diéguez, 2014). Merits of this method are: target phytochemical can be extracted quickly from solid plant matrix in short time, increase the solubility of solvent and reduce its viscosity in high pressure and temperature and requires the small amount of solvent. The disadvantage is: it needs high pressure and temperature, the requirement of high technology and has no efficiency for extraction of heat sensitive PCs (Ameer et al., 2017; Xu et al., 2017).

High hydrostatic pressure extraction (HHP)

High hydrostatic pressure is another advanced method of extraction which is used for extraction of plant polyphenol compound. The pressure uses in this method facilitate rapid diffusion of solvent into plant cell wall and causes leakage of cell components (Lee et al., 2011). HHP extraction method is derived from the high-pressure processing of food, which uses law heat treatment for food processing. This method also has a good result on heat sensitive plants, they will be damaged by the high rate of heating or lose another biological value. The heat-sensitive plants cannot be extracted through traditional method but, its extraction is possible through HHP method. The solvent of HHP method should be selected according to extracting ingredients of the plant because the polarity of the solvents is different (Shouqin, Junjie, & Changzhen, 2004).

Conclusion

Natural polyphenol compound is effective antioxidants which are produced in several types of plants such as fruit, vegetables, and beverages. Fruits are the main source of phenolic which can provide abundant types of PCs. There are some important antioxidants which can provide inside the human body or other physiological system, but natural polyphenol compound should be eaten within food or drinks. Pomegranate is the suitable source of PCs, which have the capacity to scavenge free radicals inside the organism and avoid different mortal disease. There are simple and advanced methods of PCs extraction that could be applied to pomegranate. SLE method is an easy and simple method but, it uses lots of chemicals and is not suitable for all kinds of PCs extraction. Methanol extraction resulted in high antioxidant activity while water extraction showed a high quantitative result, using Soxhlet apparatus with ethyl acetate showed the suitable result. SFE is green extraction method uses less solvent and have a good and specific result, but it needs high technology. UAE is using for quick extraction PCs and it is simple to use no need for more equipment. ASE method is a proper alternative for Soxhlet extraction method for its quick result. MAE method has high extraction result but is not suitable

for some thermolabile PCs. The importance of HHP extraction method is that have a good result in heat sensitive plants but need high technology.

References

Akhtar, S., Ismail, T., Fraternale, D., & Sestili, P. (2015). Pomegranate peel and peel extracts: Chemistry and food features. *Food Chemistry*, *174*(November), 417–425. https://doi.org/10.1016/j.foodchem.2014.11.035

Al-Rawahi, A. (2014). Phenolic Constituents of Pomegranate Peels (Punica granatum L.) Cultivated in Oman. *European Journal of Medicinal Plants*, *4*(3), 315–331. https://doi.org/10.9734/EJMP/2014/6417

Al-Rawahi, A. S., Rahman, M. S., Guizani, N., & Essa, M. M. (2013). Chemical Composition, Water Sorption Isotherm, and Phenolic Contents in Fresh and Dried Pomegranate Peels. *Drying Technology*, *31*(3), 257–263. https://doi.org/10.1080/07373937.2012.710695

Ameer, K., Shahbaz, H. M., & Kwon, J. H. (2017). Green Extraction Methods for Polyphenols from Plant Matrices and Their Byproducts: A Review. *Comprehensive Reviews in Food Science and Food Safety*, *16*(2), 295–315. https://doi.org/10.1111/1541-4337.12253

Braidy, N. (2015). *Pomegranate old age remedy for today's diseases*. New York: Nova Science Publishers, Inc.

Brar, S. K., Dhillon, G. S., & Soccol, C. R. (2014). *Biotransformation of waste biomass into high-value biochemicals*. *Biotransformation of Waste Biomass into High-Value Biochemicals* (Vol. 9781461480). https://doi.org/10.1007/978-1-4614-8005-1

Bravo, L. (2009). Polyphenols: Chemistry, Dietary Sources, Metabolism, and Nutritional Significance. *Nutrition Reviews*, *56*(11), 317–333. https://doi.org/10.1111/j.1753-4887.1998.tb01670.x

Çam, M., & Durmaz, G. (2009). Classification of eight pomegranate juices based on antioxidant capacity measured by four methods, *112*, 721–726. https://doi.org/10.1016/j.foodchem.2008.06.009

Carocho, M., Morales, P., & Ferreira, I. C. F. R. (2018). Antioxidants: Reviewing the chemistry, food applications, legislation and role as preservatives. *Trends in Food Science and Technology*, *71*(October 2017), 107–120. https://doi.org/10.1016/j.tifs.2017.11.008

Castro-Vargas, H. I., Rodríguez-Varela, L. I., Ferreira, S. R. S., & Parada-Alfonso, F. (2010). Extraction of phenolic fraction from guava seeds (Psidium guajava L.) using supercritical carbon dioxide and co-solvents. *Journal of Supercritical Fluids*, *51*(3), 319–324. https://doi.org/10.1016/j.supflu.2009.10.012

Cavalcanti, R. N., Navarro-Díaz, H. J., Santos, D. T., Rostagno, M. A., & Meireles, M. A. A. (2012). Supercritical Carbon Dioxide Extraction of Polyphenols from Pomegranate (Punica granatum L.) Leaves: Chemical Composition, Economic Evaluation and Chemometric Approach. *Journal of Food Research*, *1*(3), 282. https://doi.org/10.5539/jfr.v1n3p282

Cheng, X., Zhang, M., Xu, B., Adhikari, B., & Sun, J. (2015). The principles of ultrasound and its application in freezing related processes of food materials: A review. *Ultrasonics Sonochemistry*, *27*, 576–585. https://doi.org/10.1016/j.ultsonch.2015.04.015

Duthie, G. G., Duthie, S. J., & Kyle, J. A. M. (2000). Plant polyphenols in cancer and heart disease: implications as nutritional antioxidants. *Nutrition Research Reviews*, *13*(1), 79. https://doi.org/10.1079/095442200108729016

Erkan, M., & Kader, A. A. (2011). *Postharvest Biology and Technology of Tropical and Subtropical Fruits*. *Postharvest Biology and Technology of Tropical and Subtropical*

Fruits. https://doi.org/10.1533/9780857092618.287

Fang, X., Wang, J., Hao, J., Li, X., & Guo, N. (2015). Simultaneous extraction, identification and quantification of phenolic compounds in Eclipta prostrata using microwave-assisted extraction combined with HPLC-DAD-ESI-MS/MS. *Food Chemistry*, *188*, 527–536. https://doi.org/10.1016/j.foodchem.2015.05.037

Fresco, P., Borges, F., Marques, M. P. M., & Diniz, C. (2010). The anticancer properties of dietary polyphenols and its relation with apoptosis. *Current Pharmaceutical Design*, *16*(1), 114–134. https://doi.org/10.2174/138161210789941856

Gropper, S. S., Smith, J. L., & Groff, J. L. (2009). *Advanced Nutrition and Human Metabolism*. *Children* (Vol. 81). https://doi.org/10.1016/j.plefa.2009.05.011

Herrero, M., Mendiola, J. A., Cifuentes, A., & Ibáñez, E. (2010). Supercritical fluid extraction: Recent advances and applications. *Journal of Chromatography A*. https://doi.org/10.1016/j.chroma.2009.12.019

Ismail, T., Sestili, P., & Akhtar, S. (2012). Pomegranate peel and fruit extracts: A review of potential anti-inflammatory and anti-infective effects. *Journal of Ethnopharmacology*, *143*(2), 397–405. https://doi.org/10.1016/j.jep.2012.07.004

Jurenka, J. S. (2008). Therapeutic applications of pomegranate (Punica granatum L.): a review. *Alternative Medicine Review : A Journal of Clinical Therapeutic*, *13*(2), 128–144.

Karre, L., Lopez, K., & Getty, K. J. K. (2013). Natural antioxidants in meat and poultry products. *Meat Science*, *94*(2), 220–227. https://doi.org/10.1016/j.meatsci.2013.01.007

Kumar, Y., Yadav, D. N., Ahmad, T., & Narsaiah, K. (2015). Recent Trends in the Use of Natural Antioxidants for Meat and Meat Products. *Comprehensive Reviews in Food Science and Food Safety*, *14*(6), 796–812. https://doi.org/10.1111/1541-4337.12156

Lattanzio, V. (2013). Phenolic compounds: Introduction. In *Natural Products: Phytochemistry, Botany and Metabolism of Alkaloids, Phenolics and Terpenes* (pp. 1543–1580). https://doi.org/10.1007/978-3-642-22144-6_57

Lee, H. S., Lee, H. J., Yu, H. J., Ju, D. W., Kim, Y., Kim, C. T., … Suh, H. J. (2011). A comparison between high hydrostatic pressure extraction and heat extraction of ginsenosides from ginseng (Panax ginseng CA Meyer). *Journal of the Science of Food and Agriculture*, *91*(8), 1466–1473. https://doi.org/10.1002/jsfa.4334

Li, A. N., Li, S., Zhang, Y. J., Xu, X. R., Chen, Y. M., & Li, H. Bin. (2014). Resources and biological activities of natural polyphenols. *Nutrients*. https://doi.org/10.3390/nu6126020

Li, Y., Guo, C., Yang, J., Wei, J., Xu, J., & Cheng, S. (2006). Evaluation of antioxidant properties of pomegranate peel extract in comparison with pomegranate pulp extract. *Food Chemistry*, *96*(2), 254–260. https://doi.org/10.1016/j.foodchem.2005.02.033

Masci, A., Coccia, A., Lendaro, E., Mosca, L., Paolicelli, P., & Cesa, S. (2016). Evaluation of different extraction methods from pomegranate whole fruit or peels and the antioxidant and antiproliferative activity of the polyphenolic fraction. *Food Chemistry*, *202*, 59–69. https://doi.org/10.1016/j.foodchem.2016.01.106

Mocanu, M. M., Nagy, P., Szöllosi, J., & Mayence, A. (2015). Chemoprevention of breast cancer by dietary polyphenols. *Molecules*. https://doi.org/10.3390/molecules201219864

Pérez-Jiménez, J., Neveu, V., Vos, F., & Scalbert, A. (2010). Identification of the 100 richest dietary sources of polyphenols: An application of the Phenol-Explorer database. *European Journal of Clinical Nutrition*, *64*, S112–S120. https://doi.org/10.1038/ejcn.2010.221

Pinelo, M., Del Fabbro, P., Manzocco, L., Nuñez, M. J., & Nicoli, M. C. (2005). Optimization

of continuous phenol extraction from Vitis vinifera byproducts. *Food Chemistry*, *92*(1), 109–117. https://doi.org/10.1016/j.foodchem.2004.07.015

Pinelo, M., Ruiz-Rodríguez, A., Sineiro, J., Señoráns, F. J., Reglero, G., & Núñez, M. J. (2007). Supercritical fluid and solid-liquid extraction of phenolic antioxidants from grape pomace: A comparative study. *European Food Research and Technology*, *226*(1–2), 199–205. https://doi.org/10.1007/s00217-006-0526-3

Prasad Eswara. (2017). *Polyphenol Market by Product Type (Apples, Green Tea, Grape Seed, and Others) and Application (Functional Beverages, Functional Food, Dietary Supplements, and Others) - Global Opportunity Analysis and Industry Forecast, 2014-2022*. Retrieved from https://www.alliedmarketresearch.com/polyphenol-market

Rababah, T. M., Banat, F., Rababah, A., Ereifej, K., & Yang, W. (2010). Optimization of extraction conditions of total phenolics, antioxidant activities, and anthocyanin of oregano, thyme, terebinth, and pomegranate. *Journal of Food Science*, *75*(7). https://doi.org/10.1111/j.1750-3841.2010.01756.x

Rajbhar, K., Dawda, H., & Mukundan, U. (2015). Polyphenols : Methods of Extraction. *Sci. Revs. Chem. Commun*, *5*(1), 1–6. Retrieved from http://www.tsijournals.com/articles/polyphenols-methods-of-extraction.pdf

Rodríguez-Solana, R., Salgado, J. M., Domínguez, J. M., & Cortés-Diéguez, S. (2014). Characterization of fennel extracts and quantification of estragole: Optimization and comparison of accelerated solvent extraction and Soxhlet techniques. *Industrial Crops and Products*, *52*, 528–536. https://doi.org/10.1016/j.indcrop.2013.11.028

Rodríguez-Solana, R., Salgado, J. M., Domínguez, J. M., & Cortés-Diéguez, S. (2015). Comparison of soxhlet, accelerated solvent and supercritical fluid extraction techniques for volatile (GC-MS and GC/FID) and phenolic compounds (HPLC-ESI/MS/MS) from lamiaceae species. *Phytochemical Analysis*, *26*(1), 61–71. https://doi.org/10.1002/pca.2537

Shouqin, Z., Junjie, Z., & Changzhen, W. (2004). Novel high pressure extraction technology. *International Journal of Pharmaceutics*, *278*(2), 471–474. https://doi.org/10.1016/j.ijpharm.2004.02.029

Smith, R. E. (2014). *Pomegranate: Botany, Postharvest Treatment, Biochemical Composition and Health Effects*. Nova Science Publishers, Inc.

Teixeira da Silva, J. A., Rana, T. S., Narzary, D., Verma, N., Meshram, D. T., & Ranade, S. A. (2013). Pomegranate Biology And Biotechnology: A Review. *Scientia Horticulturae*, *160*, 85–107. https://doi.org/10.1016/j.scienta.2013.05.017

Watson, R. R. (2014). *Polyphenols in Plants: Isolation, Purification and Extract Preparation*. *Polyphenols in Plants: Isolation, Purification and Extract Preparation*. https://doi.org/10.1016/C2011-0-08711-2

Weichselbaum, E., & Buttriss, J. L. (2010). Polyphenols in the diet. *Nutrition Bulletin*, *35*(2), 157–164. https://doi.org/10.1111/j.1467-3010.2010.01821.x

Xu, C. C., Wang, B., Pu, Y. Q., Tao, J. S., & Zhang, T. (2017). Advances in extraction and analysis of phenolic compounds from plant materials. *Chinese Journal of Natural Medicines*, *15*(10), 721–731. https://doi.org/10.1016/S1875-5364(17)30103-6

Yasoubi, P., Barzegar, M., Sahari, M. A., & Azizi, M. H. (2007). Total Phenolic Contents and Antioxidant Activity of Pomegranate (Punica granatum L.) Peel Extracts. *J. Agric. Sci. Technol*, *9*, 35–42.

Zougagh, M., Valcárcel, M., & Ríos, A. (2004). Supercritical fluid extraction: A critical review of its analytical usefulness. *TrAC - Trends in Analytical Chemistry*. https://doi.org/10.1016/S0165-9936(04)00524-2

Proceeding: 5th International Conference on Applied Sciences and Engineering (ICASEA, 2018)
(eISBN 978-967-15744-1-6)
Capthorne Hotel, Cameron Highlands, Malaysia

ANALYSIS THE INFLUENCE OF HEART RATE AND MUSCLE ACTIVITY TOWARDS MUSCLE FATIGUE IN LAYUP WORKERS

Noor'Ain Azizan[1]
Ruzy Haryati Hambali[1]
Seri Rahayu Kamat [1,2]
Nur Syafiqah Rayme[1]

[1]Advanced Manufacturing Centre, Fakulti Kejuruteraan Pembuatan, Universiti Teknikal Malaysia Melaka, Melaka, Malaysia.
[2] Tokushima Malaysia Academic Centre (TMAC), Tokushima University, 2-1 Minamihosanjma-cho, 770-8506, Japan.

Abstract: *Repetitive movement can lead to the pain muscle, nerves, and tendons that cause by repetitive overuse of working task. The muscle will fatigue due to; repetitive movement, force that been applied, posture during working and duration of working. The stress level during working can influent the energy performance usage during working. The aim of this paper is to analyse the influence of heart rate and muscle activity of workers in composite manufacturing towards muscle fatigue. The data was collected for a worker in hand layup department and the Qualitative method was used in a way to investigate the working load and level of pain received by their body. Then, the Qualitative data was sorted and the respondent proceeded for a Quantitative method which involves muscle activity analysis and heart rate analysis. The tools that were used to conduct these experiments were surface electromyography (sEMG), Wristwatch with chest strap and perceived stress scale (PSS). The experimentation used to calculate the average reading of heart rate and muscle activity during working and detect the duration the muscle to start fatigue. Moreover, this paper analysed the relationship between heart rate and muscle activity through the duration of working. As an overall finding of this research, it was shown that the heart rate of the workers influence the muscle activity of workers and has high potential relationship to the fatigue of muscles of the workers in the layup department.*

Keywords: *Muscle Activity, Repetitive Movement, Surface Electromyography (Semg), Heart Rate, Fatigue*

Introduction

In composite manufacturing, most of the working task faced by the worker is manual where it is more one handmade skill, without the aid of any facilities machines. The posture of their bodies during handling this task was the key factor of this research. Nowadays, in the industry field, there is a high demand for production hence, the body will back to its normal state of parameter index after the working hours. This threat is normally known as a stressor because it is a set of conditions where the stress response is occurring in humans. Therefore, the stress can be summarized, as the body's physiological response to a stressor and strain is the body's longer-term reaction to chronic stress. Some known occupational stress is workloads and shift schedule. In addition, the more the task that is exposed to the physical danger, the more possibility they will contribute to the stress of a job. Based on previous study (Carneiro et al.,

2012), occupational stress has the connective effect to various medical related illnesses such as hypertension, depression and musculoskeletal disorder (MSD). As a result, this problem affects the health and performance of the organization because there are challenged by work stress if a large number of workers are stressed.

Based on the survey from European working conditions (EWCS), reported that the issues among industrial workers, where more than 40% were suffered from the muscular pains while they are performing a routine work. Most of working task is repetitive work or called arm movement activities. Besides that, the awkward posture is a common risk that has high probability may face by the worker. About 63% of workers in the industry being exposed to the ergonomics risk (Chander & Cavatorta, 2017). Moreover, the level of ergonomics risks issues is depending on the frequency and duration of the exposure been done such as workload factors with the awkward working posture and repetitive in the movement activities. The tools have been used in this paper include observation methods, subjective method (physiological) and physical methods. According to the study Occupational Repetitive Action tool (OCRA) in 1998, evaluated repetitive handling frequently by upper limb may lead to high ergonomic risk among the workers in industry (Otto & Battaia, 2017).

Through questionnaires, an assembly worker in a truck axle assembly reported through questionnaires had been facing the trouble with musculoskeletal disorders during the one year working. Low back disorders (LBDs) are normally the common symptom of all musculoskeletal disorders for the workers. The risk of back failure increases for workers whose jobs include lifting with a rotated trunk (Zara et al., 2015).

In the study by Padula et al. (2017), the workers involve both genders average age between 18 to 65 years old, with this samples ranging from 11 to 957 workers and within 25 workstations. Other than that, high-hazard job that has been assigned and better recovery time from combined exhaustion were observed when job rotation has been within two hours. To reduce the workload by development, breaks of ten minutes' durations have been proposed between the rotations. Biomechanical in risk factor that been relating to the repetitive motion may lead to higher possibility to get an injury.

This aim of this paper is to investigate the relationship between the psychophysical experience of muscle activity and stress level based on heart rate of workers toward fatigue in hand layup process.

Methods

Participants

The involved respondents participated which from layup department and that had been chosen as experimental workstation. This respondent was chosen through body-mass index (BMI) calculation and male respondents because this workstation occupied by male workers only. The task chosen for the experimental set was a repetitive movement of hand layup process. The third step of data collection was the level of comfort survey, heart rate analysis and muscle activity analysis. The survey involves 31 respondents and other analysis been filtered the respondents based on BMI and worst level of comfort.

Instrumentations

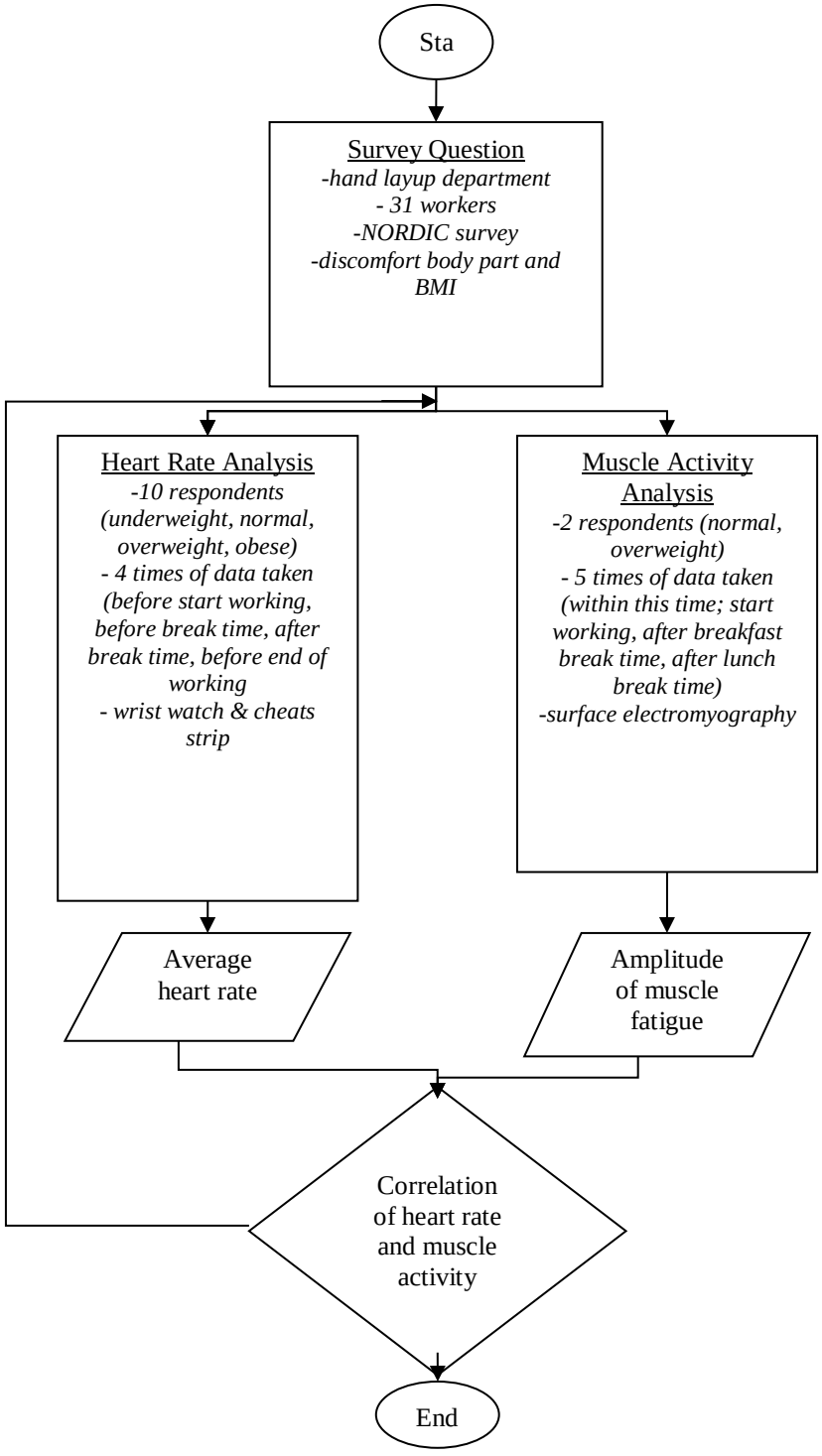

Figure 1: Flowchart Of Research

Figure 1 above shows the flowchart of this research in a way to see the relationship between heart rate and muscle activity. The basic survey was conducted to identify the working activities and discomforts on body parts experienced by respondents after working. The survey form was distributed to workers in layup department involving 31 total respondents. Based on Halim et al. (2010) framework of survey guideline, the survey data is used to analyse and identify the discomfort area in body based on physical workload. From the 31 respondents that involved in this survey, and the data been analysis and sorted out based on discomfort on body parts and body-mass index (BMI) categories which; underweight, normal, overweight and obesity. Ten respondents have been chosen from this sorted data survey and will go through for heart rate analysis and muscle activity analysis. The wristwatch is provided with a chest strap to detect the heart rate. While conducting the PPS survey, the heart rate is also collected to see how stressful the workers when working in this department. The manipulated variable for this experiment is time taken during respondents working which are before start working, before rest time, after rest time and lastly before end of working day.

For muscle activity, there are five muscles that were involved in this experiment; thoracic erector spine, lumbar erector spine, multifidus lumbar, gastrocnemius and soleus (Kang et al., 2013). This experiment also analyse trapezius muscle because it related to hand layup process. The experiment was taken during layup process for one hour and repeated by five times using surface electromyography (EMG) for muscle reaction while working. The data taken within this time; start working, after breakfast break time, after lunch break time based on time cycle of the production. The respondents that involved same as heart rate respondents, but for this analysis only take two BMI categories because of time constraints of production.

Data Analysis

These heart rate and muscle activity data were analysed using Statistical Package for Social Sciences (SPSS) software to get the correlation between heart rate and also muscle activity.

Results

The survey form was distributed to workers in layup department involving 31 total respondents. The purpose of this evaluation was to identify the problems related to ergonomic issues experienced by workers at the workstation. Most of the questions were closely related to the problem of discomfort in any part of body. Based on these questions, an experimental test was conducted to determine the fatigue muscle of the spine and legs. Furthermore, the function of the questionnaire was to be used as evidence for validations after two experimental validations on muscle fatigue and stress-related to heart rate would be conducted on the next stage of the overall research. This repetitive movement will cause muscle pain due to long periods take the same task and posture (Delitto et al., 2012).

Table 1: Level Of Comfort For Each Body Regions

Body region	(%)
Arm	2
Wrist	1
Elbow	1
Fingers	1
Shoulders	8
Neck	7
Spine	15
Thighs	7
Knees	3
Calf	14
Legs	12
Heels	2
Footprints	3
Lower back	11
Waist	5
Overall back	8

Table 1 shows the level of comfort for each body parts. Most of respondents have felt pain in the body part while performing their job task. Based on result, the respondents feel discomfort mostly at spine, calf, leg and lower back. Plus, the shoulder was also affected due to the hand layup process procedures that use high forces for applying ply. The level of discomfort on body parts been classified through this Table 1.

Heart rate reading

The reading of the heart rate has been taken for respondents that have critical issues discomfort level and BMI calculation. From literate review exaggerated systolic blood pressure (SBP) will respond to exercise and heavy movement is a factor for the future in develop of hypertension and associated a greater cardiovascular disease (Cho et al., 2012) (Spartano et al., 2016). Therefore, this experimental taken in four different times of working in order to get the average reading data per person. After the experimental done, the watch technology can provide the graph for an overall rate of reading heart rate path of a person working per day through its software. Figure 2 shows the overall average heart rate on the ten respondents has been tested based on BMI category. The highest heart rate average during the initial working task and after break time for all BMI category. This because the workers been exposed to their work plan that was distributed. The working task is considered as high-intensity exercise increases the heart rate of the respondents and this related to their BMI as well. The underweight respondents have a higher pulse because of the metabolism of their body compared to other. In addition, most of respondents were already tired and no motivated to continue their work which are mostly related to the physiological of the workers in performing the job scope given. It showed that the mind behaviour was related to the rate of productivity of a person which detected by heart rate result.

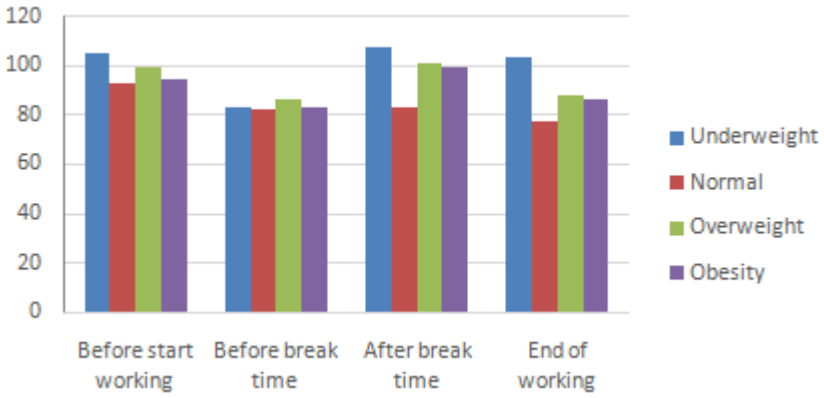

Figure 2: Average Heart Rate Of Respondent

Muscle activity while working

The muscle activity test was done for two BMI categories, which are normal and overweight that being tested based on result of questionnaire because of limitation of production cycle time within this research. The data was taken for one hour and repeated five times consequently during hand layup process. There are 12 muscles (both sides of human body) involved in this testing and had been analysed using Delsys Trigno Wireless EMG System. Figure 3 and Figure 4 below shown two data from BMI categories which are normal and overweight.

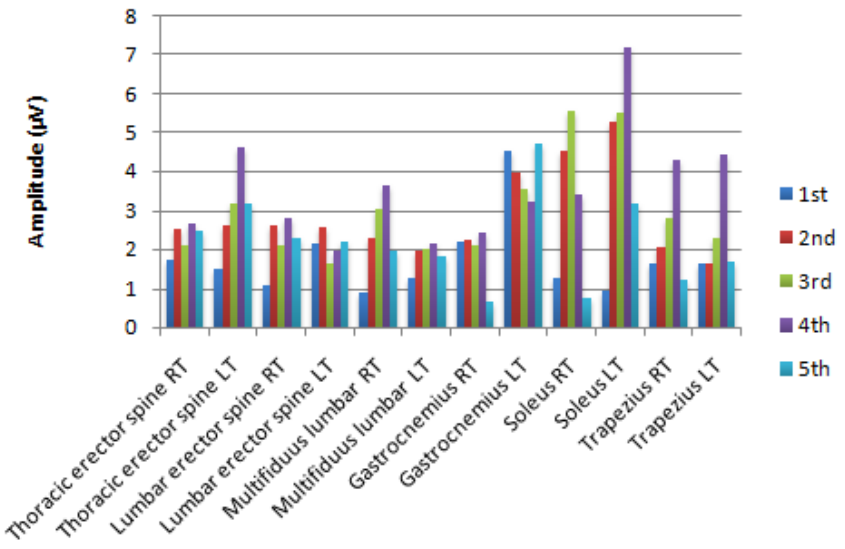

Figure 3: Muscles Activity For Normal Category

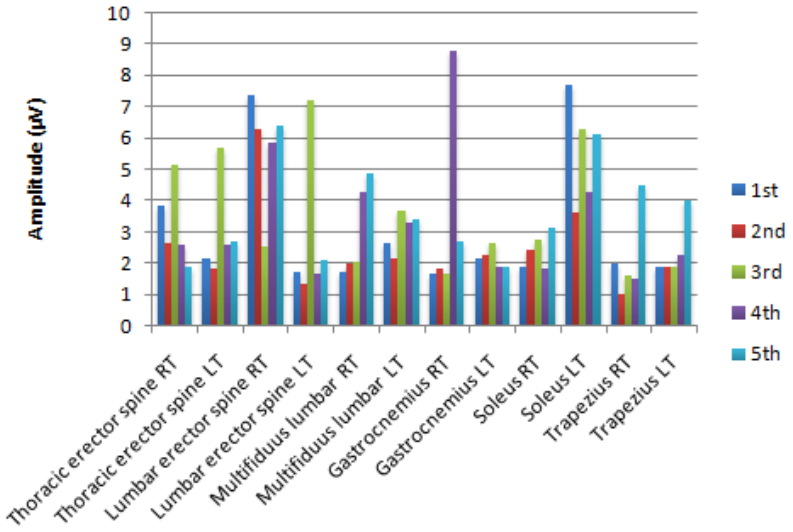

Figure 4: Muscles Activity For Overweight Category

Based on Figure 3 and Figure 4, it shows that the muscle involves fatigue when the working task was done. The Figure 3 and Figure 4, shows the muscle amplitude started to increase while conducting the works, it detects normally by using amplitude and frequency of the signal (Freitas, 2008). The Freitas (2008) stated that the amplitude of EMG signals increases through the time when the fatigue increases, otherwise the mean power frequency decreases. This showed that the muscle involve fatigue when respondents did their work repetitive time by time. For normal respondent, the spine muscles, lumbar muscles, soleus and trapezius show the muscle become fatigue in peak time until the end of work. While for overweight, the muscle that tends to fatigues are spine muscles, lumbar muscles and gastrocnemius. Table 2 shows the muscle that contract and fatigue during the experimental process.

Table 2: Muscles Activity During Experiment Process

Muscles	Normal respondent	Overweight respondent
Thoracic erector spine RT	Fatigue	Fatigue
Thoracic erector spine LT	Fatigue	Fatigue
Lumbar erector spine RT	Fatigue	Contraction
Lumbar support spine LT	Contraction	Fatigue
Multifiduus lumbar RT	Fatigue	Contraction
Multifiduus lumbar LT	Fatigue	Fatigue
Gastrocnemius RT	Fatigue	Fatigue
Gastrocnemius LT	Contraction	Fatigue
Soleus RT	Fatigue	Contraction
Soleus LT	Fatigue	Contraction
Trapezius RT	Fatigue	Contraction
Trapezius LT	Fatigue	Contraction

Correlation of heart rate and muscle activity

The significant values of heart rate value and muscle activity have been analysed through SPSS analytical software. Based on the analysis, the average of heart rate had a relationship with muscle activity. Table 3 shows the significance of heart rate and muscle activity. Heart Rate (HR) describes as the heart rate of respondent while Electromyography (EMG) describes as the muscle activity of respondent. HR have four times of data taken which includes; before start working (HR1), before break time (HR2), after break time (HR3) and end of working (HR4). EMG have five set of hand layup process in one day of working which have; start working

(EMG1), after breakfast break time (EMG2 & EMG3), after lunch break time (EMG4 & EMG5).

Table 3: The Significance Of Heart Rate And Muscle Activity

	HR 1	HR 2	HR 3	HR 4	EMG 1	EMG 2	EMG 3	EMG 4	EMG 5
HR 1		0.511	0.606	0.123	0.158	0.190	0.235	0.090	0.769
HR 2	0.511		0.735	0.235	0.117	0.688	0.257	0.715	0.426
HR 3	0.606	0.735		0.017*	0.534	0.660	0.538	0.713	0.029*
HR 4	0.123	0.235	0.017*		0.632	0.995	0.638	0.513	0.035*
EMG 1	0.158	0.117	0.534	0.632		0.794	0.728	0.441	0.108
EMG 2	0.190	0.688	0.660	0.995	0.794		0.000**	0.021*	0.404
EMG 3	0.235	0.257	0.538	0.638	0.728	0.000**		0.012*	0.775
EMG 4	0.090	0.715	0.713	0.513	0.441	0.021*	0.012*		0.291
EMG 5	0.769	0.426	0.029*	0.035*	0.108	0.404	0.775	0.291	

*. Correlation is significant at the 0.05 level (2-tailed).

**. Correlation is significant at the 0.01 level (2-tailed).

The heart rate of respondents decreases in the evening because of the pressure and work task that was done through the day. The heart rate of respondents influenced by the working task and stress during working. Moreover, the muscle activity of the respondents getting slow in the amplitude through EMG, it shows the significant effect on heart rate at the end of working at duration of 3pm to 5pm. This because the energy of workers been use during working and muscle start to fatigue towards the end of working day. The relationship of heart rate and muscle activity connected at the end of working day because the workers start to feel tired and suggested there is a need for a break to refresh back their energy to start back the work for the workers that have overtime for working. In this stage most of workers faced a critical phase with the workload, stress level and working posture that made them feeling discomfort. This duration also can be a framework for industry, as a guideline for them in order to improve the production quality.

Conclusion

In a nutshell, the discomfort had been identified through survey questions whether the upper and lower back (spine area) of body was in discomfort felt by respondents. The working postures of the workers are bending in this hand layup process and it been done repetitively along with working days. Therefore, the unrealized works in daily work beyond the limits of the human ability to bend the body that will affect the psychophysical experienced and stress level workers toward the fatigue. The muscle activity of workers been analyse and show that 83% of muscle tended to fatigue while finishing their work task while for heart rate data 11% slightly decrease before break time and another at the end of work while it decrease 7% average of heart rate. This shows the workers are fatigue and needs rest to counter back the energy and prevent injuries in a way to make a better performance and healthy working environment. The relationship between heart rate and muscle activity show it has significant, this due to the biomechanics of human body. This analysis can be one of a way to improve the health of working by eliminating the risk of getting MSD. Due to the repetitive movement, it can be suggested to the company to redesign a comfort tools like lumbar support that can reduce the discomfort of body thus, limit motion is required and less energy required forcing the body that can help in reducing fatigues.

References

Carneiro, P., Braga, C. A., & Barroso, M. (2012). Work-related musculoskeletal disorders in home care nurses: study of the main risk factors. *International Journal of Industrial Ergonomics*, *61*, 22-28.

Chander, S. D., & Cavatorta, P. M. (2017). An observation method for Postural Ergonomic Risk Assessment (PERA). *International Journal of Industrial Ergonomics*, *57*, 32-41.

Delitto, A., George, Z. S., & etc. (2012). Clinical Practice Guidelines Linked to the International Classification of Functioning, Disability, and Health from the Orthopaedic Section of the American Physical Therapy Association**.** *Journal of Orthopaedic & Sport Physical Therapy*, 42(4), A1-A57.

Freitas, I. (2008). Fatigue detection in EMG signals. THESIS Graduation in the Master Degree. Faculty Electrical and Computer Engineering Universidade Tecnica de Lisboa. 2008.

Halim, I., Omar, R. A., Saman, M. Alias., Othman, I., & Ali, A. (2010). Development of a questionnaire for prolonged standing jobs at manufacturing industry. *Advances in Human Factors, Ergonomics, and Safety in Manufacturing and Service Industries*, *26*, 253-263.

Kang, H. M., Choi, H. S., & Oh, S. J. (2013). Postural taping applied to the low back influences kinematics and EMG activity during patient transfer in physical therapists with chronic low back pain. *Journal of Electromyography and Kinesiology*, 23(4), 787-793.

Cho, M. S., Jang, S., Lee, C. H., & Park, C. (2012). Association of early systolic blood pressure response to exercise with future cardiovascular events in patients with uncomplicated mild-to-moderate hypertension. *Hypertension Research*, *35*(9), 922-927. doi:10.1038/hr.2012.52.

Otto, A., & Battaia, O. (2017). Reducing physical ergonomic risks at assembly lines by line balancing and job rotation: A survey. *Computers & Industrial Engineering*, *111*, 467-480.

Padula, S. R., Comper, C. L. M., Sparer, H. E., & Dennerlein, T. J. (2017). Job rotation designed to prevent musculoskeletal disorders and control risk in manufacturing industries: A systematic review. *Applied Ergonomics*, 58, 386-397.

Spartano, L. N. PhD., Lyass, A. PhD., Larson, G. Martin. ScD., Lewis, D. G. MD., & Vasan, S. R. MD. (2016). Submaximal Exercise Systolic Blood Pressure and Heart Rate at 20 Years of Follow-up: Correlates in the Framingham Heart Study. *Journal of American Heart Associaton*, 5(6).

Zare, M., Bodin, J., Cercier, E., Brunet, R., & Roquelaure, Y. (2015). Evaluation of ergonomic approach and musculoskeletal disorders in two different organizations in a truck assembly plant. *International Journal of Industrial Ergonomics*, 50, 34-42.

Proceeding: 5th International Conference on Applied Sciences and Engineering (ICASEA, 2018)
(eISBN 978-967-15744-1-6)
Capthorne Hotel, Cameron Highlands, Malaysia

OBSERVATION OF SPACE CHARGE FORMATION IN XLPE/MGO NANOCOMPOSITE

A. N. Ramani [1,3]
A. M. Ariffin[1]
Muhamad Safwan Abd Rahman[1]
Ahmad Basri Abd Ghani[2]
Kyairul Azmi Baharin[3]

[1]College of Engineering, Universiti Tenaga Nasional, Jalan Ikram-Uniten, 43000 Kajang, Selangor, Malaysia.
[2]TNB Research Sdn. Bhd.
[3]Faculty of Electrical Engineering, Universiti Teknikal Malaysia Melaka, Hang Tuah Jaya, 76100 Durian Tunggal, Melaka, Malaysia.

Abstract: *The presence of space charges that tend to distort the local electric field distribution in insulation materials have become a major concern. Preceding research works have proven that electric properties of polymer insulation can be improved by the addition of nano-sized inorganic filler. This work investigates the space charge distribution of Cross Linked Polyethylene (XLPE) nanocomposites mixed with nano-sized MgO filler. The distribution is measured using the Pulsed Electro-Acoustic (PEA) system. The results indicate that the introduction of MgO nanoparticles improves the space charge suppression substantially compared to unfilled XLPE.*

Keywords: *Nanocomposite, Polyethylene, Nanodielectric, Space Charge, PEA method*

Introduction

In recent years, polymeric nanocomposites have been regarded as the next generation insulation material with the intention to enhance insulation performance by increasing its electrical properties, especially improving the suppression of space charge injection and controlling of dissipation (Wu et al., 2011). Nano-sized particles have been proven as an effective method to suppress the space charge accumulation in dielectric composites (Wu, Lv, Wang, Tu, & Dissado, 2012). Currently, the mechanism of inorganic particles on the electrical and mechanical properties of polymers is of great interest. Several reports revealed that the interfaces between additives and the polymer bulk account for the space charge suppression (Li, Xu, Du, & Preparation, 2016).

In polymer nanocomposites, chemically dissimilar components are combined at the nanometer scale, and stronger interactions between the polymer and nanoparticles produce markedly improved materials with better electrical, mechanical and thermal performances than the conventional filled polymer composites (Chen, Zhang, & Stevens, 2007). In recent years, polymer nanocomposites have been extensively studied in optical, thermal and mechanical properties, but there has been relatively little research into dielectric properties. Considering polymers and polymer composites as traditional electrical insulating materials, but with some exceptions, few polymer nanocomposites are used in electrical insulation industry. Therefore, it is very important to investigate the dielectric properties of polymer nanocomposites.

The formation of space charge may distort the electrical field and distribution throughout the cable insulation thickness which may lead to the premature failure of the cable insulation at stresses below the anticipated value (Lau & Chen, 2006). This condition becomes more severe during dc application.

Experiment

Materials

The base polymer used was an additive free cross linked polyethylene (XLPE) with a grade of 4201R and a density of 0.9–1.0 g/cm^3 provided by Borealis AG, Austria. The nanoparticles used was Magnesium Oxide (MgO) with a density of 5.61 g/cm^3 and particle size in the range of 10 to 30 nm were used, supplied by US Research Nanomaterial, USA. The weight percentage of nanoparticles in MgO is varies at 1%, 2% and 3%.

Figure 1 Below Shows The Example Of Cylindrical Thin Film Samples With An Average Thickness Of 200 µm And A Diameter Of 70 Mm.

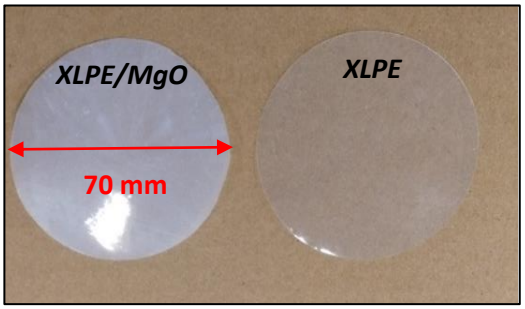

Sample Preparation

Unfilled XLPE and nanoparticles were melt-blended in a twin-screw extruder at 130°C after dried in an oven for 16 hours at 55°C. After that, the nanocomposites were press moulded at 185°C and at a pressure of 10 MPa to produce thin films. Then, the samples were removed from the press and cooled down for 180 seconds to room temperature. Before the test for space charge measurement, the samples were put in a vacuum oven for 24 hours at 60°C due to uniform initial conditions. For the FTIR analysis, the samples can be used directly.

Space Charge Measurements

In this experiment, space charge measurement was performed for two different times which are at 30 minutes and at 60 minutes using a pulsed electro-acoustic (PEA) system (Maeno, 2003) supplied by Techimp. All measurements were carried out at room temperature, the pulsed length of 10 ns, pulse amplitude is 400 V and a DC electric field of 25 kVmm^{-1}. A semi-conductive layer was sandwiched between the upper brass electrode and samples to reduce mismatch acoustic impedance. The high voltage pulse module supplied a pulsed length of 10 ns, 400 V, at 150 Hz. Calibration was conducted at a DC field of 10 kV mm^{-1} with a short period as to minimize its influence on space charge accumulation.

FTIR Measurements

Fourier transform infrared (FTIR) spectroscopy was used to identify the unfilled XLPE and inorganic materials in nanocomposite by producing an infrared absorption spectrum. Infrared spectra were collected using a Bruker Tensor 27 equipped with a KBr beamsplitter (Pike Miracle single-bounce) with using a DTGS (deuterated tri-glycine sulphate) detector. For this

testing, spectra were collected over the range of 400 to 4000 cm^{-1} with the co-addition of 32 scans at a spectral resolution of 4 cm^{-1}.

Results

Structure and Morphology

Figure 2 shows FTIR absorbance spectrum of the XLPE/MgO with 1 wt% to 3 wt% in comparison to unfilled XLPE spectrum. The absorption band at 1263 cm^{-1} exhibits characteristics of the bending mode of vibration in water (HOH) and the sharp and shallow band observed in the band at 2848 cm^{-1} shows the stretching mode of vibration in hydroxyl group (O-H). The peak wavenumber of 2916 cm^{-1} represents the existence of the brucite phase of $Mg(OH)_2$ (B. Vijayalakshmi, V. Lakshmipriya, K. P. Radha, B. Natarajan, V. Ramadas, 2016). Also, the wavenumber of 1463 cm^{-1} indicates to the Mg-O stretching vibration.

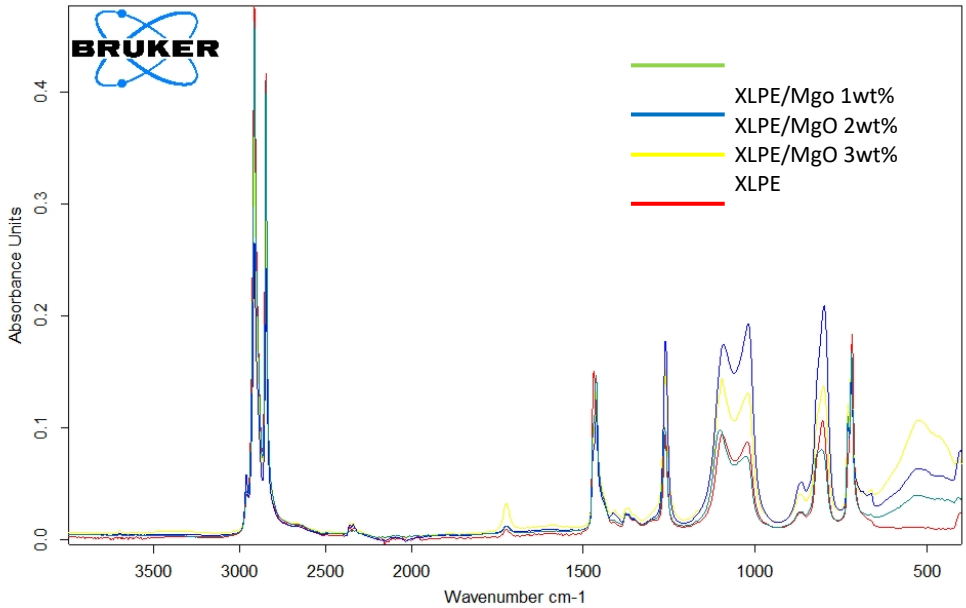

Figure 2: FTIR Spectra Of XLPE/Mgo Nanocomposites With Different Weight Percentage

Figure 3 shows the space charge distributions of XLPE/MgO containing 1 wt%, 2 wt% and 3 wt% nanofiller at an applied DC voltage of 25 $kVmm^{-1}$. Space charge distribution of an unfilled XLPE sample used for reference shows a minimal amount of homocharge development existing near the cathode. Also, as revealed by the graph, the injected space charge starts to form in the sample and then accumulates obvious homocharge at both electrodes. Besides that, the charge density in nanocomposites were reduced at both electrodes when compared with unfilled XLPE. The similar profiles of space charge distribution as a function of time shows that almost all types of samples had similar properties which is homocharge accumulation near both cathode and anode. The amount of charge formed is quite similar for both electrodes.

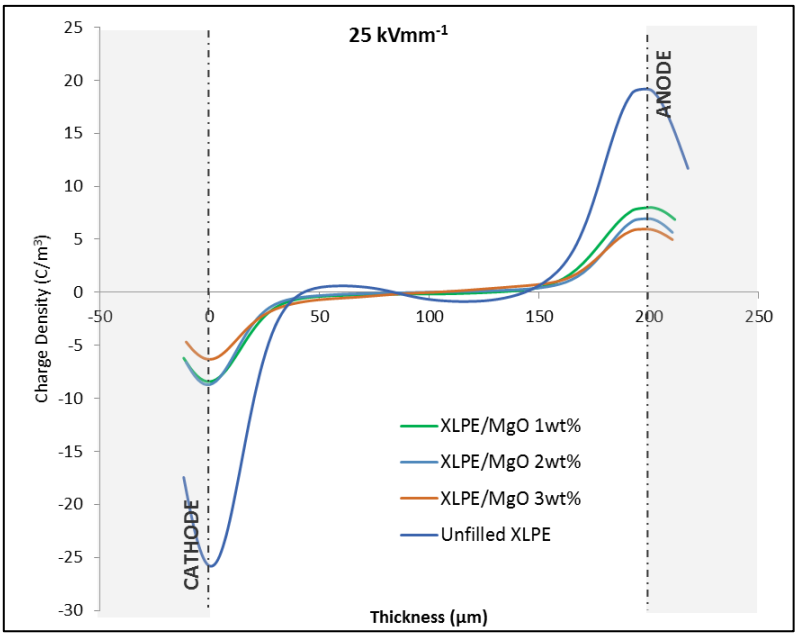

Figure 3: Space Charge Measurements In XLPE And Mgo Nanocomposite

Refering to the result in Table 1, it can be expected that the adding of the larger content of Magnesium Oxide nano filler to XLPE is more effective in suppressing the charge injection. With the addition of 3 wt% MgO, the charge injected in cathode are reduced to 75.53% while 68.9% reduction is obtained at the anode because the metal oxide nano-sized filler acts as a trap side under high DC voltage as mentioned in (Arakane et al., 2012). Therefore, these experiments show that the sample with the higher contents of the filler is expected to show better performance of the suppression effect.

Table 1: Percentage Reduction Of Charge Density By Mgo Nanofillers

Material	At cathode (C/m^3) %	At anode (C/m^3) %
XLPE/MgO 1 wt%	67.4	62.54
XLPE/MgO 2 wt%	66.33	65.14
XLPE/MgO 3 wt%	75.53	68.9

For this case, it can be seen that homocharge development when applied with 25 $kVmm^1$ is obviously in all the nanocomposites sample the charge magnitude decreasing with increasing of MgO contents.

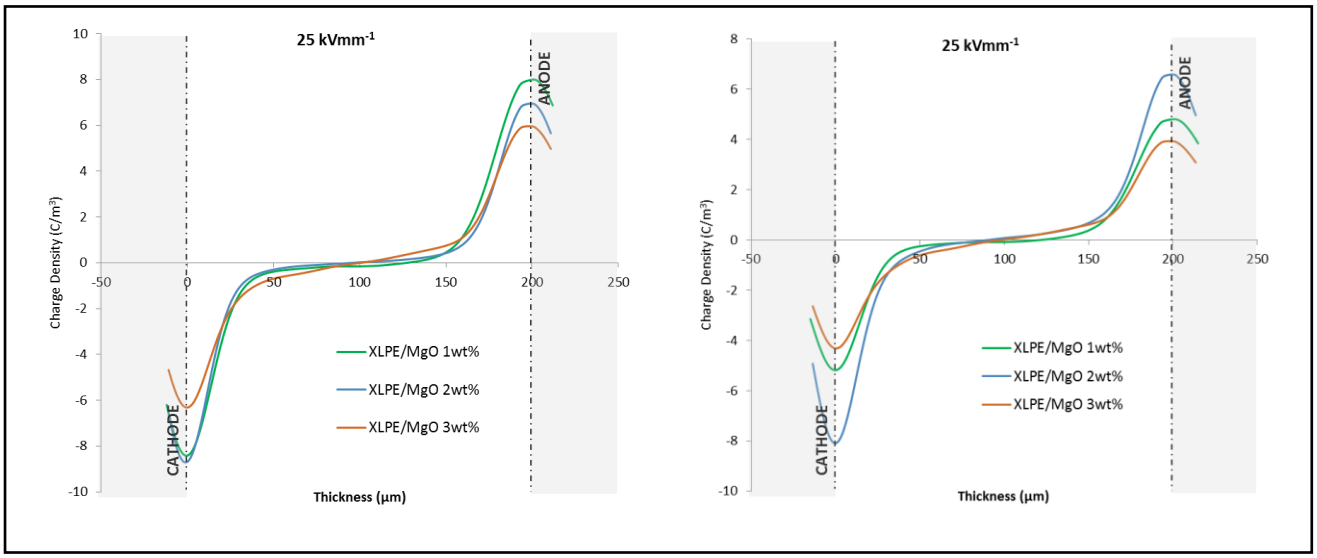

Figure 4: Space Charge Measurements In XLPE And Its Mgo Nanocomposite At (A) After 30 Minutes Voltage Application And (B) After 60 Minutes Voltage Application

Figure 4 shows the space charge distribution after 30 minutes and 60 minutes polarization. This shows the suppression of injected charge at both electrodes after voltage application. The space charge distribution is consistent with the results shown in Figure 3. For sample XLPE/MgO with 1 wt% charges injected at the cathode reduced about 38.4% and at anode is 39.92%. The sample with 2 wt% has slightly lower reduction at the cathode and anode around 6.93% and 5.24% respectively. The sample with 3 wt% also has a substantial drop at the cathode and anode with values around 31.67% and 34.01% respectively.

Conclusion

In this study, the effect of nanofiller on space charge distribution of XLPE loaded with different weight contents of nano-sized MgO has been investigated under high 25 kVmm^{-1} DC voltage using the PEA technique. The introduction of nanocomposites will reduce carrier injection that contributes to the suppression of space charge accumulation. The amount of injection charge in the samples and its duration of time were observed. The experimental result revealed that the homocharge is formed and this injection charge is suppressed when nanofillers are added. The space charge distribution on the sample with 3 wt% suppresses 75.53% more compared to the others. Also it can be seen that the amount of charge in the sample decreases with the duration of the applied voltage.

Acknowledgements

The author acknowledge Ministry of Education, Malaysia and Universiti Teknikal Malaysia Melaka for their support. This work also was supported by TNB Research.

References

Arakane, T., Motchizuki, T., Adachi, N., Miyake, H., Tanaka, Y., Kim, Y. J., … Lee, G. J. (2012). Space charge accumulation properties in XLPE with carbon nano-filler. In *IEEE International Conference on Condition Monitoring and Diagnosis* (pp. 328–331). http://doi.org/10.1109/CMD.2012.6416444

B. Vijayalakshmi, V. Lakshmipriya, K. P. Radha, B. Natarajan, V. Ramadas, C. M. (2016). Synthesis and Optical Characterization of MgO Nanoparticles using Chemical Precipitation Method. *International Research Journal of India*, *II*(IV), 6. Retrieved from http://irji.in/images/Muthuselvi.pdf

Chen, G., Zhang, C., & Stevens, G. (2007). Space charge in LLDPE loaded with nanoparticles. In *Annual Report - Conference on Electrical Insulation and Dielectric Phenomena, CEIDP* (pp. 275–278). http://doi.org/10.1109/CEIDP.2007.4451554

Lau, W. S., & Chen, G. (2006). Simultaneous space charge and conduction current measurements in solid dielectrics under high dc electric field. *IEEE International Conference on Condition Monitoring and Diagnosis*. Retrieved from http://eprints.ecs.soton.ac.uk/12733/

Li, J., Xu, H., Du, B., & Preparation, A. S. (2016). Space Charge Accumulation Characteristics in Ethylene-Vinyl Acetate Copolymer Filled with ZnO Nanoparticles. In *IEEE International Conference on Dielectrics*. http://doi.org/10.1109/ICD.2016.7547574

Maeno, T. (2003). Portable space charge measurement system using the pulsed electrostatic method. In *IEEE Transactions on Dielectrics and Electrical Insulation* (Vol. 10, pp. 331–335). http://doi.org/10.1109/TDEI.2003.1194119

Wu, K., Chen, X., Liu, X., Wang, X., Cheng, Y., Dissado, L. A., & Sample, A. (2011). Study of the space charge behavior in polyethylene nano-composites under temperature gradient. *International Conference on Electricity Insulation Material*, (50907050), 84–87.

Wu, K., Lv, Z., Wang, X., Tu, D., & Dissado, L. A. (2012). Study on suppression mechanism of space charge accumulation in nano-doped LDPE. *Annual Report - Conference on Electrical Insulation and Dielectric Phenomena, CEIDP*, 299–302. http://doi.org/10.1109/CEIDP.2012.6378780

Proceeding: 5th International Conference on Applied Sciences and Engineering (ICASEA, 2018)
(eISBN 978-967-15744-1-6)
Capthorne Hotel, Cameron Highlands, Malaysia

ACID-MODIFIED ADSORBENTS FROM SUSTAINABLE GREEN-BASED MATERIALS FOR CRUDE OIL REMOVAL

Z. Nazlina[1]
Z. Nabilah[2]
Y.S. Lim[1]
Y.K. Teng[1]
A.A. Ahmed Abdulkarim[1]
N.S. Nasri[3]
K.S.N. Kamarudin[3]

[1]Chemical Engineering Programme, Faculty of Engineering and the Built Environment, SEGi University, 47810 Kota Damansara, Selangor Darul Ehsan, Malaysia
[2]Shizen Conversion & Separation Technology iKohza, Department of Chemical Process Engineering (CPE), Malaysia-Japan International Institute of Technology (MJIIT), Universiti Teknologi Malaysia (UTM) Kuala Lumpur, Jalan Sultan Yahya Petra (Jalan Semarak), 54100 Kuala Lumpur, Wilayah Persekutuan, Malaysia.
[3]Department of Energy Engineering, Faculty of Chemical and Energy Engineering, Universiti Teknologi Malaysia, 81310 Johor Bahru, Johor, Malaysia.

***Abstract*:** *This research was carried out to study the sorption capacity of crude oil using acid-modified green-based adsorbents originated from kenaf core and coconut shell. The adsorbent modification was impregnated in the lauric acid, phosphoric acid, and citric acid solution via the conventional method known as wetness impregnation technique. A comparison study of oil sorption capacity between acid-modified kenaf core and acid-modified coconut shell were conducted to identify a better adsorbent for crude oil adsorption. Variable Pressure Scanning Electron Microscopy (VPSEM) equipped with Energy Dispersive X-Ray Spectroscopy (EDX) were utilized to study the morphological characteristics and element compositions for both the unmodified and acid-modified adsorbents. Besides, Fourier Transform Infrared Spectroscopy (FTIR) was used to address the presence, absence, and/or shrink of certain functional groups for both unmodified and acid-modified adsorbents. Based on these three acids used, lauric acid was the best acid modifier than phosphoric acid and citric acid that performed the highest oil adsorption capacity. The VPSEM images of acid-modified adsorbents determined the presence of new pores and thinner walls across the hollow fibres compared to the unmodified adsorbent. Besides, FTIR results proved the presence of new peaks on the green-based adsorbents that confirmed the successful of acid impregnation procedure. This study have proposed that acid-modified green-based adsorbents has high potential to tackle the issues of crude oil spillage. The higher adsorption performance of kenaf core than coconut shell demonstrates that kenaf core can be a low-cost and competitive adsorbent in various applications and expertises.*

Keywords: *Crude oil, Sorption Capacity, Acid-Modified Adsorbent, Lauric acid, Citric acid, Phosphoric acid*

Introduction

Crude oil is a naturally occurring mixture of hundreds of different hydrocarbon compounds trapped in subsurface rock. It is a mixture of hydrocarbons, which range from almost solid to gaseous. These hydrocarbons were created millions of years ago from the dead

plant and algae material and settled at the bottom of streams, lakes, seas and oceans, forming a thick layer of organic material. Subsequent sedimentation covered this layer and change it into petroleum that extracted from the subsurface today (Holmager, 2010). Crude oil spillage is one of the major disastrous around the world that effects the aquatic life and caused water pollution. One of the world largest oil spill disastrous, The Deepwater Horizon oil spill released 4 million barrels of crude oil into Gulf of Mexico (Carey, 2016).

Numerous approaches for oil spillage cleaning had been reported in the literature which includes the filtration (ultra and micro), reverse osmosis, gravity separation, activated sludge treatment, various flotation methods (dissolved air, column floatation, gas-aphrons, electro and induced air), membrane bioreactors, biological treatment, chemical coagulation, electron-coagulation, coalescences and adsorption. Among all the approaches, adsorption is believed to be the optimal oil spill clean-up as its relatively low cost, excellent oil-removing ability, and eco-friendliness (Sabir, 2015).

Adsorption is defined as the adhesion of a chemical species onto the surface of particles. In adsorption process, the gas or liquid particles known as adsorbates, bind to the solid or liquid surface which called as adsorbent. Adsorbent used for oil spillage clean-up can be classified into three basic categories which are inorganic mineral products, organic synthetic products, and organic vegetable products. Inorganic mineral products including zeolites, silica, graphite, and organic synthetic products such as polypropylene and polyurethane. Wood fibre, cotton fibre, kenaf, ground corncobs, and other carbon-based products are classified under the organic vegetable products or known as natural organic sorbents (Behnood et al, 2013).

Organic vegetable or natural organic sorbent had been investigated for the removal of oil spillage due to its advantages which include environmental friendly, cost effectiveness, and relatively easy disposal. Despite of their advantages, several natural sorbents suffer drawback in term of high water uptake due to low hydrophobicity. Therefore, numerous researches had been done to improve the hydrophobicity of natural sorbents. In fact, this research is conducted to study the performance of crude oil adsorption of kenaf core and coconut shell by improving its surface chemistry using acid modification approach. In this study, the surface chemistry for both acid-modified samples were characterized via different characterization techniques such as morphological and structural techniques prior crude oil adsorption study in batch reaction. The hydrophobicity property of the modified green-based material was the main consideration.

Materials and Method

Material

Kenaf core was procured from National Kenaf and Tobacco Board (NKTB), Kelantan whilst coconut shell was obtained from UTM-MPRC Institute for Oil and Gas. Kenaf core and coconut shell were selected due to its environmental friendly, easily reachable in Peninsular of

Malaysia, and more affordable as compared to other adsorbents. All of these materials shall be prepared in a suitable particle size for the experimental purpose.

Preparation of Adsorbents

Kenaf core and coconut shell were milled, grinded, and sieved to obtain smaller particle sizes. The particle sizes were varied in the series of ranges below than 150 µm, 150 to 212 µm, 213 to 600 µm, 601 µm to 1.18 mm, and above 1.18 mm. The sieving procedure was conducted at Shizen Conversion and Separation Technology Laboratory, UTM Kuala Lumpur. The previous study reported by Zaveri (2004) found that the particle sizes range of 106 to 840 µm achieves the highest water adsorption rate than other particle sizes. Besides, Zaini (2016) also revealed that kenaf core in range of 300 to 500 µm was the best size to adsorb CO_2 than other particle sizes. Based on these references, this study was proceeded by selecting kenaf core in range of 213 to 600 µm. The sieved samples were kept in a tight container at room temperature in order to prevent any contamination. For the preparation of acid-modified samples, 2 g of kenaf core and coconut shell, respectively was immersed in a 1.0 M and 200 ml of lauric acid, citric acid, and phosphoric acid for six hours in the separated beakers. The mixture was stirred continuously for six hours throughout the impregnation technique by using a magnetic stirrer. The prepared sample was filtered, collected, and dried at 105°C in an oven to remove moisture.

Characterization of Acid-Modified Sample

The prepared acid-modified sample was characterized via Variable Pressure Scanning Electron Microscope (VPSEM) equipped with Energy Dispersive X-ray Spectroscopy (EDX), and Fourier Transform Infrared Spectroscopy (FTIR). VPSEM provides surface topographical of the prepared surface chemistry sample at magnification of 1000X. Meanwhile, EDX analysis was conducted to determine the element compositions of the samples. In addition to that, FTIR was also conducted to identify the presence, absence, or shrink of certain functional groups on the acid-modified sample.

Batch Oil Adsorption Study

The unmodified and acid-modified coconut shell and kenaf core were used as crude oil adsorbents and the experiment was carried out at room temperature. A water-oil mixture was prepared by adding the tap water with crude oil in a fix proportion. Then, 2 g of the prepared acid-modified sample was poured into the water contaminated solution and left without stirring for 60 minutes to make sure all the crude oil is adsorbed by the sample. After 60 minutes, the sample with adsorbed crude oil was removed using a filter paper. The filtered sorbent was dried in oven at 105°C to remove the extra moisture. The batch adsorption test was repeated by using different proportions of crude oil and water from 10000 to 50000 mg/L. The amounts of crude oil adsorbed and oil sorption capacity at different crude oil-water concentrations is determined by weight differences before and after contacting the oil. The oil sorption capacity equation is:

$$S = \frac{m_f - m_i}{mi} \quad (1)$$

Where, S is the oil sorption capacity (g/g), m_f is the mass of sorbent after crude oil adsorption, and m_i is the initial mass of sorbent before crude oil adsorption (Santos et al., 2017; Sandeep et al., 2011).

Determination of Volatile Loss

Loss of volatile compound was determined by measuring 0.5 g of crude oil in petri dish and dried in oven at 105ºC for six hours. After six hours, the weight of crude oil was measured. This process was repeated until the weight of crude oil was maintain.

Results and Discussion

Characterization Study of Acid-Modified Samples

Morphological Analysis

In this study, VPSEM analysis was conducted to observe the morphology of the acid-modified samples. Table 1 presents the cross-sectional area of the prepared acid-modified kenaf core and acid-modified coconut shell samples. These morphologies would give information on the surface structure available for trapping the oil adsorbates.

Table 1: Cross-Sectional Area of Unmodified and Modified Kenaf Core and Coconut Shell.

Sample	Kenaf core	Coconut shell
Precursor (raw)	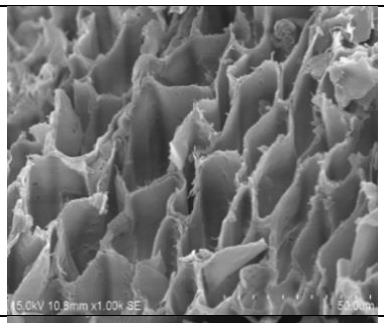	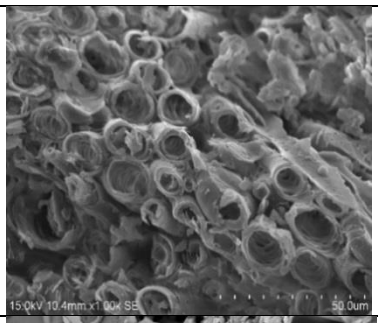
Lauric acid-modified	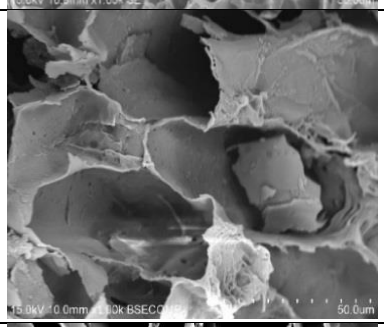	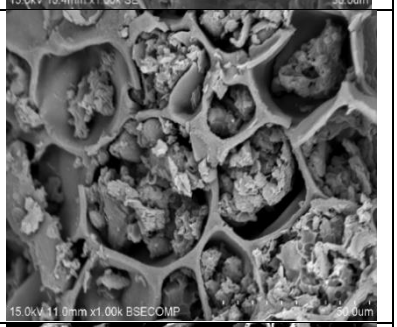
Citric acid-modified	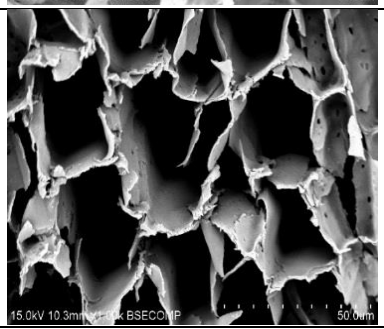	

Phosphoric acid-modified	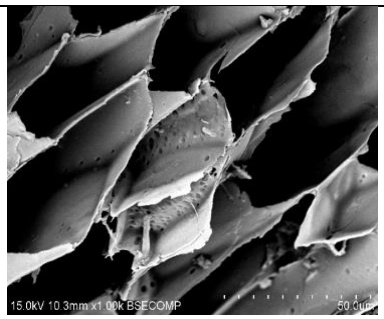	

From the observed morphologies, all the acid-modified kenaf core and acid-modified coconut shell samples exhibit the thinner wall across the hollowed fibre compared to its precursor. This is due to the stretching of cellulosic compounds caused by the acid modification. The stretching of cellulosic compounds cause the hydrophilic nature of plant to reduce, alternatively increases the hydrophobicity character. As the wall of the hollowed fibre become thinner, the oil sorption capacity is expected to be improved. Similar finding was found by Idan et al, (2017) where the pore size for the natural kenaf core fibre is smaller than the modified kenaf core fibre. The pore size is bigger due to dissolved lignin and hemicellulose in the solution.

Fourier Transform Infrared Spectroscopy Analysis

The FTIR spectra of acid-modified kenaf core samples are shown in Figure 1. In order to distinguish the changes of structure after acid modification procedure, the FTIR spectra of the kenaf core precursor is taking into consideration. The changes of structure could define the effect of acid modification on the surface chemistry of kenaf core.

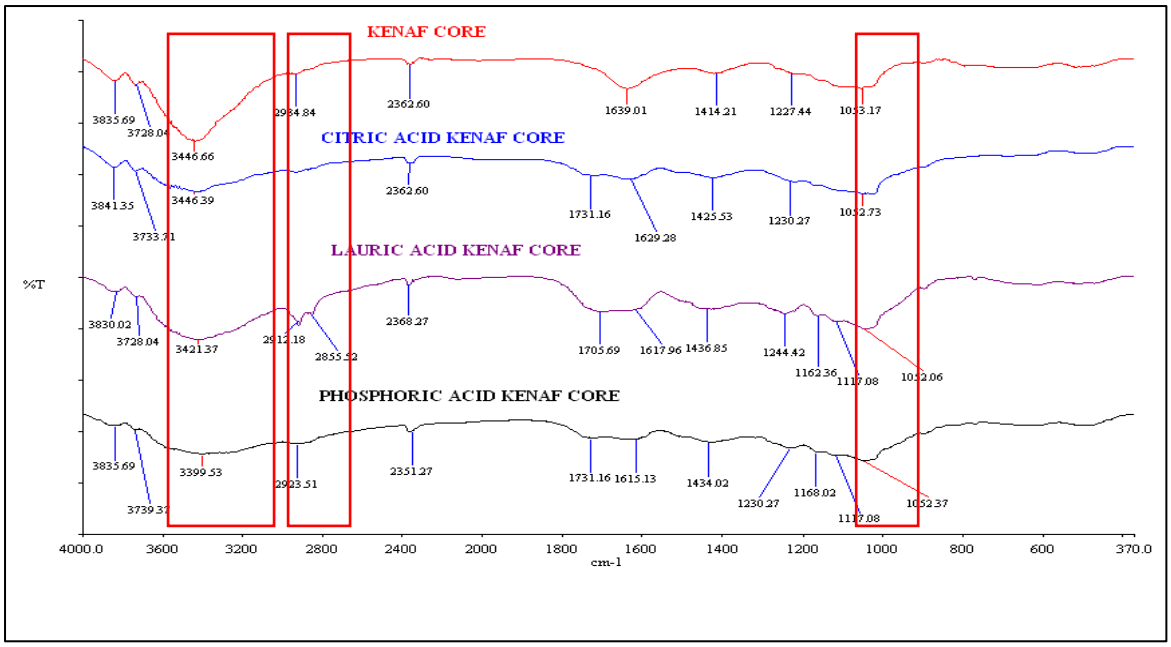

Figure 1: FTIR results for unmodified and modified kenaf core.

For all the acid-modified kenaf core, the shrinkages of broad inverted peak in the range of 3300 up until 3500 cm^{-1} defines the stretching of hydrogen bonding (O-H) of cellulose and hemicellulose compounds after the impregnation of acid modification. The presence of peak at 2912.18 cm^{-1} and 2855.52 cm^{-1} for lauric acid-modified, 2923.51 cm^{-1} for citric acid-modified

and phosphoric acid-modified represents the presence of methyl CH_3 and CH_2 groups after acid modification (Teas et al., 2001). This is caused by the link formation between long alkyl chain of cellulose and hemicellulose compounds. The presence of peaks at 1052.06 cm^{-1} for the lauric acid-modified, 1052.73 cm^{-1} for the citric acid-modified, and 1052.37 cm^{-1} for the phosphoric acid-modified signifies the presence of C–O–C stretching of celluloses and C–O stretching of hemicelluloses (Pandey and Pitman, 2003). Based on this FTIR spectra analysis, the change of

surface chemistry of the acid-modified kenaf core prove that the modification was successfully executed via wetness impregnation technique.

Figure 2 indicates the FTIR spectra of the acid-modified coconut shell samples. The acid-modified coconut shell samples had been compared to the coconut shell precursor to detect any structural changes after completing acid modification procedure.

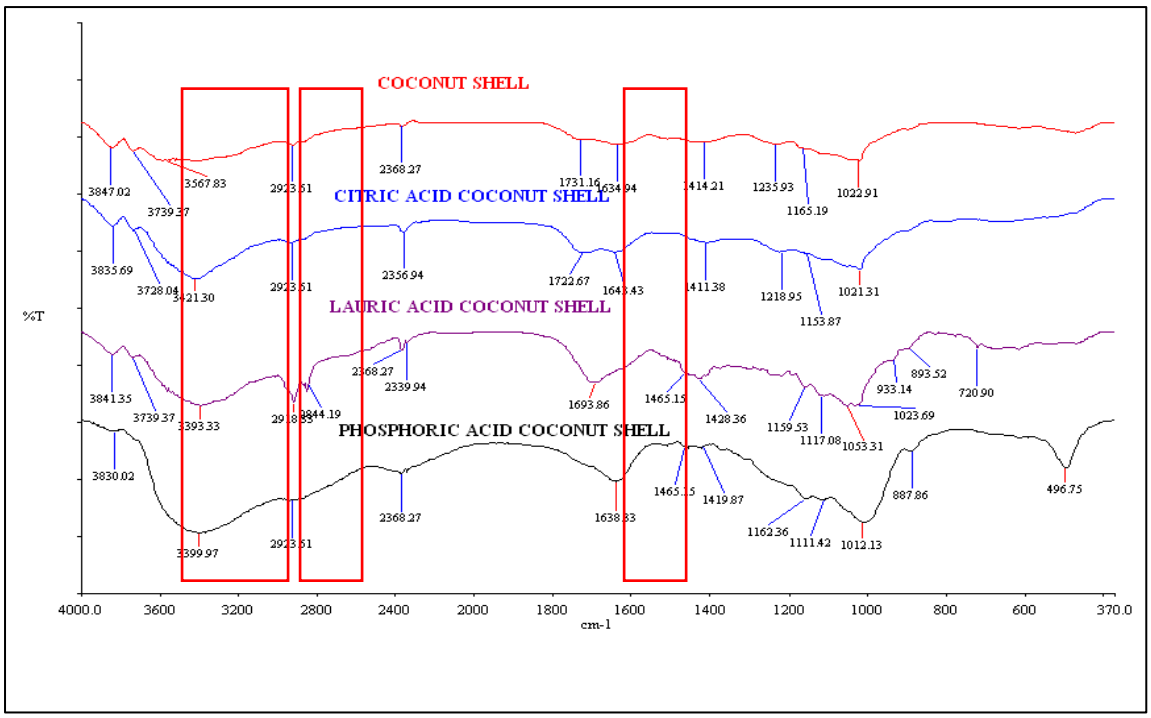

Figure 2: FTIR results for unmodified and modified coconut shell.

For acid-modified coconut shell samples, an obvious peak was observed at 3393.33 cm^{-1}, 3421.30 cm^{-1}, and 3399.97 cm^{-1} for lauric acid-modified, citric acid-modified,and phosphoric acid-modified, respectively. These results indicates the same trend as acid-modified kenaf core which the presence of these peaks are due to the stretching of hydrogen bond (O–H) of cellulose and hemicellulose compounds after acid modification procedure. Besides, the presence of peak observed at 1693.86 cm^{-1} for lauric acid-modified, 1643.43 cm^{-1} for citric acid-modified, and 1638.33 cm^{-1} for phosphoric acid-modified attribute to the stretching of C=C. The presence of peaks in the range from 2900 cm^{-1} to 3000 cm^{-1} for all the acid-modified coconut shell samples is due to the presence of alkyl CH_3 and CH_2 groups. Finally, the presence of peaks at 1000 cm^{-1} to 1100 cm^{-1} denotes the presence of C–O–C stretching of celluloses and C–O stretching of hemicelluloses.

Energy Dispersive X-Ray Spectroscopy Analysis

The elemental composition analysis provides information on the surfaces chemistry of the prepared acid-modified adsorbent samples. Table 2 (as presented in below) summarizes the elemental compositions present on the surface chemistry of each prepared acid-modified kenaf core and acid-modified coconut shell samples. The element composition of each prepared acid-modified samples were compared to the precursor sample to distinguish the amount of elements that had been increased or degraded after undergone acid-modification procedure.

Table 2: Elemental Composition of Kenaf Core and Coconut Shell.

Adsorbents	Elemental Compositions					
	C	O	Na	Mg	K	P
Unmodified Kenaf Core	52.34	46.00	0.43	0.21	1.02	-
Lauric Acid Modified Kenaf Core	63.73	36.03	0.00	0.11	0.13	-
Citric Acid Modified Kenaf Core	54.30	45.70	0.00	0.01	0.00	-
Phosphoric Acid Modified Kenaf Core	55.00	34.16	0.00	0.03	0.00	1.64
Unmodified Coconut Shell	52.34	46.00	0.43	0.21	1.02	-
Lauric Acid Modified Coconut Shell	65.07	34.37	0.00	0.33	0.20	-
Citric Acid Modified Coconut Shell	58.15	41.83	0.00	0.00	0.02	-
Phosphoric Acid Modified Coconut Shell	57.01	37.07	0.00	0.16	0.16	5.60

Based on Table 2, it can be seen that the carbon element (C) in the acid-modified kenaf core and acid-modified coconut shell samples is increased and oxygen element (O) is degraded. This is due to the presence of alkyl CH_2 and CH_3 functional groups in the lauric acid and citric acid. Both the lauric acid modification samples reveal the highest increment of carbon element (C) among all the modified samples that can be explicated by the presence of long hydrocarbon chain in the lauric acid. For phosphoric acid-modified sample, the presence of phosphate group (P) proved that the kenaf core and coconut shell samples were successfully impregnated using phosphoric acid. According to Bello et al. (2015), adsorbent with the highest amounts of carbon was the most efficient in adsorbing dyes, heavy metals, and organic pollutants. This EDX data showed that the surface chemistry of acid-modified sample was affected after the impregnation of acid modifier.

Effect of Initial Crude Oil Concentration

In order to study the adsorption performance of acid-modified natural-based adsorbent, the oil-water concentration was prepared from 10 g/L to 50 g/L. The acid-modified adsorbent was poured without further stirring to let the process running naturally. The crude oil adsorption capacity achieved by acid-modified kenaf core and coconut shell are shown in Figure 3 and 4.

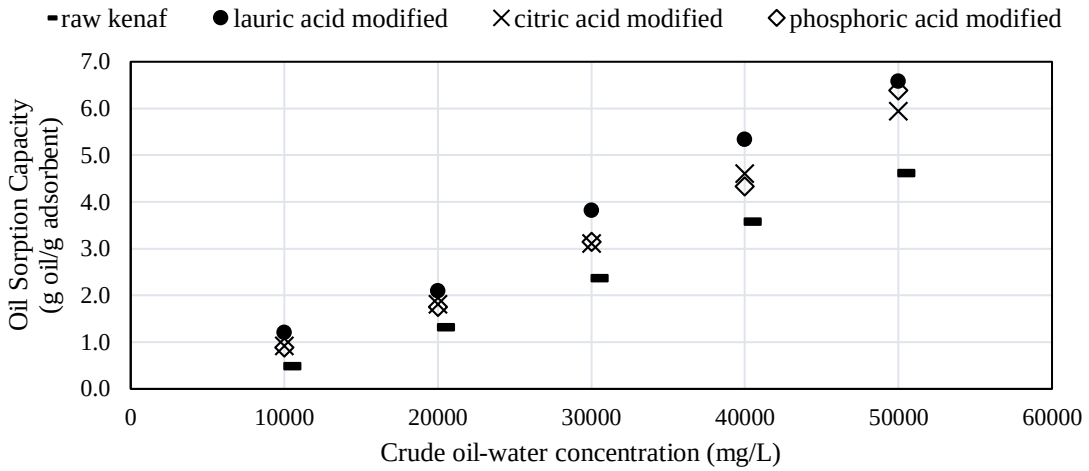

Figure 3: Crude oil adsorption capacity of unmodified and acid modified-kenaf core adsorbents.

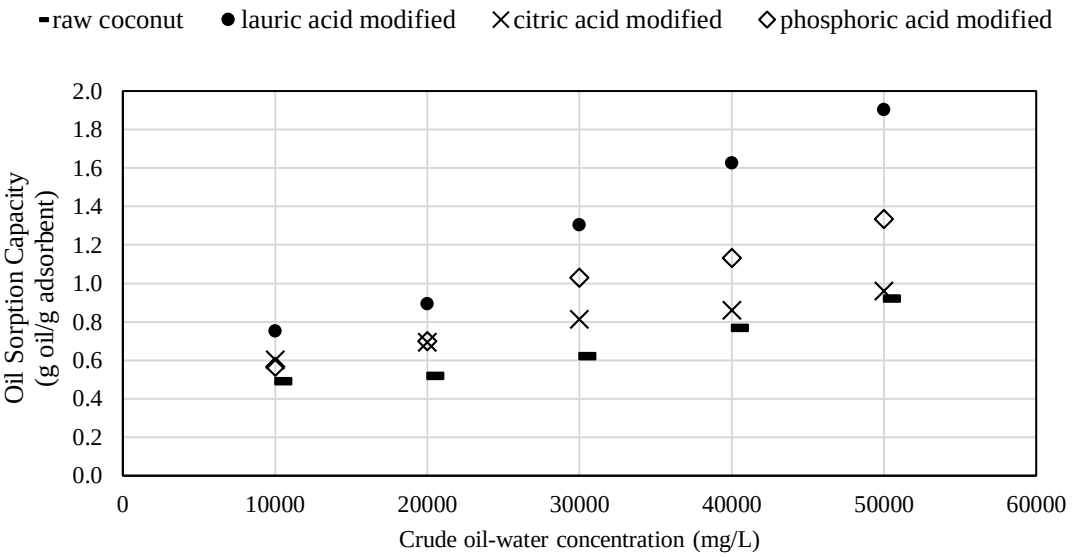

Figure 4: Crude oil adsorption capacity of unmodified and acid modified-coconut shell adsorbents.

The oil adsorption capacity is the amount of crude oil adsorbed (in gram) per weight of sorbent used (in gram). The oil adsorption capacity is defined as the oil uptake capacity or the sorbency ratio that represents the mass of liquid uptaken per mass of sorbent used (Teng, 2018). It means that the higher the amount of oil adsorption capacity, the higher the amount of oil that has being adsorbent from the prepared solution. Based on the Figure 3 and 4, the oil sorption capacity of the unmodified and acid-modified kenaf core and coconut shell adsorbents are increased with respect to the increasing of oil-water concentrations. The achieved results also reveal that the acid-modified adsorbents show a better oil sorption capacity than the unmodified adsorbents, valid for both kenaf core and coconut shell adsorbents. The unmodified kenaf core and coconut shell were found to show poor efficiency for crude oil adsorption with the capacities uptake at 10000 mg/L of 0.88 g/g and 0.57 g/g, respectively. Generally, the agricultural waste products usually exhibits low sorption capacity due to the presence of numerous hydroxyl groups on its surface (Sidik et al., 2012; Gong et al., 2006). The existence of hydroxyl groups on the surface of kenaf core and coconut shell are hypothesized to repel the crude oil molecules during the adsorption process, thus reduced the oil sorption capacity. At oil-water concentration of 10000 mg/L, the lauric acid modifier presents the higher oil sorption capacity for both kenaf core and

coconut shell adsorbents as compared the citric acid and phosphoric acid modified sorbent with the oil capacities for lauric acid-modified kenaf core was 1.20 g/g, and acid-modified coconut shell was 0.75 g/g. Based on this pattern, the oil sorption capacities for those two acid-modified adsorbents were kept increasing with respects to the oil-water concentrations from 10000 until 50000 mg/L. It was due to the higher hydrophobicity characteristics present by the lauric acid. In order to describe the hydrophobicity characteristics, Figure 5 exhibits the molecular structure of lauric acid, citric acid, and phosphoric acid, respectively.

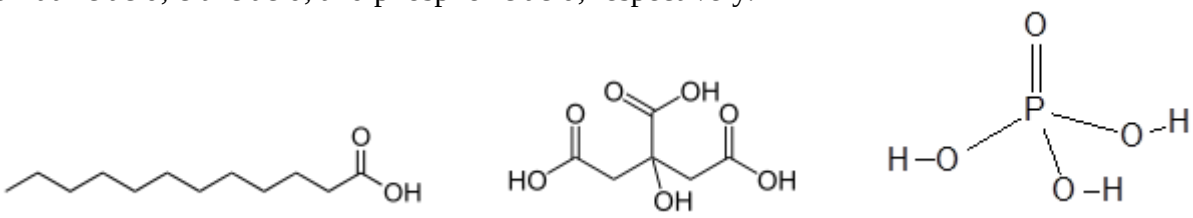

Lauric acid Citric acid Phosphoric acid

Figure 5: Molecular structure of different acids used for the modification.

.

As indicated on Figure 5, lauric acid has the longest alkyl chains which promoting the strongest hydrophobicity characteristics to the oil-water mixture. The stronger hydrophobicity character of the modified adsorbent, the higher tendency for the modified adsorbent to repel the molecule of water away from its surface. As a consequence, the higher of oil molecules interacted to the surface, hence increased the oil sorption capacity of the modified adsorbent. Sidik et al. (2012) also explicated that the introduction of lauric acid chain to the agricultural waste materials will substitutes the existing hydroxyl groups which then led to the creation of non-polar layer of the surfaces. The presence of these non-polar surfaces increased the hydrophobicity degree as well as the contact area to the oil molecules which was believed to provide the superior sites for the oil adsorption uptake, hence improves the oil sorption capacity of the adsorbent.

Conclusion

This study concludes that acid-modified green-based adsorbent demonstrate the higher oil sorption capacity by introducing the non-polar layer on its surfaces. The introduction of this non-polar layer on the surface increased the hydrophobicity degrees of the modified adsorbent, thus enhance the oil adsorption capacity of the acid-modified adsorbent. This study proves that the acid modification technique is one of the improvements that can be used to enhance the oil adsorptive capability of kenaf core and coconut shell.

Acknowledgements

The authors would like to dedicate their gratitude to SEGi University, Kota Damansara Selangor for the financial assistance and hospitalities. Besides, the authors also appreciated the financial supports given under the Research University Grant (GUP Tier 2) vote no. 13J72 and the facilities provided by the Malaysia-Japan International Institute of Technology (MJIIT), University Teknologi Malaysia (UTM), specially SHIZEN iKohza throughout this research.

References

Ali, A., Shaker, K., Nawab, Y., Jabbar, M., Hussain, T., Militky J. and Baheti, V. (2016). Hydrophobic Treatment of Natural Fibres and their Composites-A Review. *Journal of Industrial Textiles*, https://doi.org.10.1177/1528083716654468.

Behnood, R., Anvaripour, B., Fard, N.J.H. and Farasati, M. (2013). Application of Natural Sorbents in Crude Oil Adsorption. *Iranian Journal of Oil & Gas Science and Technology*, 2(4), 1-11.

Bello, O.S., Adegoke, K.A. and Akinyunni, O.O. (2015). Preparation and characterization of a novel adsorbent from Moringa oleifera leaf. *Applied Water Science*, 7(3), 1295-1305.

Carey, B. (2016). Deepwater Horizon oil spill impacted bluefin tuna spawning habitat in Gulf of Mexico, Stanford and NOAA researchers find.

Gong, R., Jin, Y., Chen, F. and Liu, Z. (2006). Enhanced Malachite Green Removal from Aqueous Solution by Citric Acid Modified Rice Straw. *Journal of Hazardous Materials*, 137, 865–870.

Holmager, M. (2010). "Offshore Book: An Introduction to the Offshore Industry. *Offshore Center Danmark*.

Idan, I.J., Abdullah, L.C., Mahdi, D.S., Obaid, M.K. and Md. Jamil, S.N.A.B. (2017) Adsorption of Anionic Dye Using Cationic Surfactant-Modified Kenaf Core Fibers. *Open Access Library Journal*, https://doi.org.10.4236/oalib.1103747

Noraisah, J., Siew Ling, E., Rizafizah, O. and Suria, R. (2015). Modification of Oil Palm Plantation Wastes as Oil Adsorbent for Palm Oil Mill Effluent. *The Malaysian Journal of Analytical Science*, 19 (1), 31-40.

Pandey, K.K. and Pitman, A.J. (2003) FTIR studies of the changes in wood chemistry following decay by brown-rot and white-rot fungi. *International Biodeterioration and Biodegradation*, 52, 151-160

Sabir, S. (2015). Approach of Cost-Effective Adsorbents for Oil Removal from Oily Water. *Critical Reviews in Environmental Science and Technology*, 45(17), 1916-1945.

Sidik, S. M. Jalil, A. A., Triwahyono, S., Adam, S. H., Satar, M. A. H., Hameed, B. H. (2012). Modified oil palm leaves adsorbent with enhanced hydrophobicity for crude oil removal. *Chemical Engineering Journal*, 203, 9-18.

Teas, C., Kalligeros, S., Zanikos, F., Stournas, S., Lois, E. and Anastopoulos, G. (2001). Investigation of the effectiveness of absorbent materials in oil spills clean up. *Desalination*, 140(3), 259–264.

Zaveri, M. (2004). *Absorbency Characteristics of Kenaf Core Particles*. North Carolina State University.

Zaini, N. (2016). Amine-Functionalized Kenaf as Carbon Dioxide Adsorbent in Pressure Swing Adsorption System. PhD Thesis. Universiti Teknologi Malaysia, Malaysia.

Proceeding: 5th International Conference on Applied Sciences and Engineering (ICASEA, 2018)
(eISBN 978-967-15744-1-6)
Capthorne Hotel, Cameron Highlands, Malaysia

EXPERIMENTAL EVALUATION OF CRUDE OIL USING SAWDUST-LIGNIN SURFACTAN

Ali Ali Mohammed Alkaboos[1]
Farhana Bt Abdul Barri[2]

[1]Chemical and Petroleum Engineering Department, UCSI University, Malaysia.
[2]Head Of Programme Of Chemical and Petroleum Engineering Department, UCSI University, Malaysia.

Abstract: *The limited supply and increasing cost of petroleum-based surfactants for chemical enhanced oil recovery have led to study renewable resources as sources of sawdust-lignin surfactant. Sawdust is a waste material from wood industry. The use of various sawdust types is being extensively explored as biomass and other industries, in reducing waste materials. Sawdust has been found to contain lignin component, which is the second most abundant organic chemical on Earth. Lignin possesses the properties and characteristics as a surfactant which enhances Enhanced Oil Recovery (EOR) properties such as Du Nouy ring and Sessile drop test were carried out to measure the interfacial behavior and the wettability of the sample, respectively. Lignin was extracted using catalysts solvents such as Acetic Acid, Formic Acid, Peroxy Acetic Acid, and Peroxy Formic Acid. The extracted lignin from sawdust had lower the IFT value of crude oil from 24.7 mN/m to 9.705 mN/m. As a result, the extracted lignin had reduced 60.06% of IFT value of crude oil successfully. Moreover, the contact angle of crude had been reduced by the following: a) MOO308 Carbonate sample from 167.97 o to 137.64 b) Cp8 Carbonate sample from 168.38 o to 138.71 c) sample 9 Sandstone 168.21 o to 141.32 d) sample 6-11 Sandstone from 166.65 o to 141.78. All the reduction above was observed when the lignin surfactant was added. Therefore, the sand pack for EOR methods (tertiary recovery) was 33.3%.*

Keywords*: IFT, CMC, Formic acid, Acetic Acid, Sawdust*

Introduction

Oil recovery may consist of certain specific steps. These steps may vary according to its needs. The steps may be specified into 3 phases which is the primary, secondary and tertiary recovery. At the primary phase of oil recovery, oil is extracted up to the surface by natural pressure that is present in the wellbore. The pressure will help the oil to be driven out up to the surface by the help of density measures. The oil extraction range is from 10 to 20% of the oil available in the field. For the secondary phase of oil recovery, the usage of water will be put into account. This method is well known to be called as water-flooding technique where the oil will be displaced by water hence will lift the oil up to the surface in order to recover oil up to the surface. In this technique, the injected water or steam displaces the oil and sends it to the wellbore by having differential in density. 10%-30% of oil can be recovered additionally by having to implement an injection well in the secondary phase. For the tertiary phase of oil recovery, additional chemical and method may be put into practice and this will be unpredictable as the price of oil fluctuates and this method can be costly. This method will be evaluated to see whether the oil recovery is very much needed for it has to be economical and does not provide loss to the company (Taber, Martin, & Seright, 1996).

Sawdust is a naturally occurring composite material which grows abundantly Generally in most of the tropical countries. It's considered a composite material as it contains cellulose fibers wrapped within a lignin matrix. In Asian Countries, bamboo was employed for household utilities such as containers, Chopsticks, woven mats, fishing rods, cricket boxes, handicrafts, chairs. Bamboo contains others organic makeup from added to cellulose and Lignin it comprises about 2 - 6 percent, 2& 2 deoxidized saccharide ,2 - 4% fat and 0.8 - 6 % protein (Zhao et al., 2012).

Sulphite lignin One of the most abundant form of advertisement lignin available is Sulphite lignin because traditionally this is the most used form of pulping process. Initially it originated based on using calcium bisulphite, a cheap pulping chemical. The dearth of suitable technology for its regeneration with this compound from the spent pulping liquor propitiated that the development of uses such as calcium lignosulphonate. The sulphite pulping technology evolved to encompass the usage of different sulphites and bisulphites, such as magnesium, ammonium and sodium. During the time, the sulphite pulping process started to be substituted with the kraft pulping, and it is more versatile and generates more powerful pulps, also features a robust chemical recovery procedure (Gosselink, De Jong, Guran, & Abächerli, 2004).

Experimental Procedure

In this section, discussion about the on how the extraction of lignin using the apparatus and materials will be stated as shown in Figure 1. In brief sawdust will be extracted for lignin and lignin will be used to reduce the interfacial tension of the crude oil by having to use the Sessile drop method. The wettability alteration of lignin can also be observed through the addition of lignin by having to observe it under microscopic lens. Sandpack using different concentration of lignin 2wt% to 5wt% as a chemical flooding to identify total oil recovery. This observation will then be noted and the difference between the interfacial tension and the wettability will be discussed.

Figure 1: Experimental flow diagram

Extraction (Formic acid/ Acetic Acid)

Small sized bamboo sawdust was placed in the conical flask. 85% by volume of organic acid with a ratio of 70:30 (formic acid: acetic acid) was added to the bamboo sawdust with a ratio of 1:8 fiber to liquor. The mixture was then left to boil on a hot plate. Once boiled, the mixture was left to cool at ambient (room) temperature. Fibers present in the mixture were filtered off using a Buchner funnel and was washed with 80% formic acid and followed by hot distilled water Irimia R, Gottschling M (2016).

Peroxy Formic AND Peroxy Acetic (Pfa/Paa) ACID TREATMENT

Treated formic acid/acetic acid were further delignified with a mixture of PFA/PAA in a hot water bath (80ºC) . The PFA and PAA were prepared by adding 8ml of 35% of H2O2 with 85% of formic acid or acetic acid. The delignified fibres were then filtered in order to separate the cooking liquor from the cellulose and was washed with hot water Irimia R, Gottschling M (2016).

Bleaching

Delignified fibers were bleached with 14ml (35%) H2O2 solution (pH11-12) in the hot water bath. Pulp was washed with distilled water to remove residual lignin. This step was repeated until the lignin was removed completely Irimia R, Gottschling M (2016).

Isolation of lignin

The spent liquor was heated up to 105ºC after pulping and delignification process. Dissolved lignin in the formic acid was precipitated by adding distilled water (5 times more than the volume of the concentrated liquor) and the precipitation was then filtered using a Buchner funnel. The precipitated lignin was washed with distilled water and dried in a vacuum over P2O5.Lignin was collected Irimia R, Gottschling M (2016).

Additive Mixing

The order of chemicals mixed is shown in Table 1. The way of adding chemicals and mixing time for each chemical is an important aspect.

Table 1: (Chemicals used and their function)

Chemicals/ Reagents	Function	Amount
Bamboo Sawdust		50g
Distilled Water	To washed the lignin from the acids and remove residual lignin	300 ml
Formic Acid	Extraction process	350 ml
Acetic acid	Extraction process	120ml
Peroxy Formic	Treatment	98ml
Peroxy Acetic	Treatment	42ml
Hydrogen Peroxide, H_2O_2	Treated and bleaching	8ml
Crude Oil		140ml
Brine		3ml

Du Nouy Ring Method

This method introduces a step where it uses a ring which is made out of platinum. This ring will be dipped into the solution which is below the interface and will be lifted up above the surface. The meniscus of the liquid will actually move upwards when the ring is being lifted. The meniscus of the liquid will eventually break at a certain point where it is separated from the ring and the force produced will be calculated.

Sessile Drop Test

This test is referred to as an observation microscopic test. By observation, the measurement can be made by having to take into account of the wetting angles on small core samples. This can be done by having to drop a liquid the type of liquid that needs to be measured on a smooth solid surface and the angle produced on the solid surface will be measured by having to measure the tangent to the drop profile at the drop edge.

Sand pack

This method is used to identify the total oil recover using different concentration. By adding sand in separating funnel , brine poured into the funnel to saturation the sand column only the exact amount of brine required to saturate the sand ,crude oil was poured into the funnel two funnel one for light crude oil and the amount of oil poured were taken as initial oil in place was poured into the funnel two funnel one for light crude oil and the amount of oil poured were taken as initial oil in place The Faucet was closed and distilled water was poured to simulate the secondary recovery. Finally adding Lignin solution with 2% and 5% concentrations with brine 0.3wt % was used to simulate the tertiary recovery with different concentration.

Results and Discussion

Efficiency of IFT Properties

Effect of Lignin Concentration on IFT

From the experiments conducted, we have found that there were various results that were able to be compared based on the IFT of the crude oil/brine system. the results have shown that the IFT of crude oil without the surfactant was measured at 24.27 mN/m on average as shown in table 2. The IFT that was measured at this value indicated that the oil may have a high value of IFT which can be lowered by adding a surfactant in the further process as shown in table 3. A declination can be seen as the surfactant was added to the system. The surfactant was varied from a concentration of 2000ppm to 6000ppm. This has indicated a sharp fall in IFT and by increasing the concentration of surfactant, decrement of IFT can be seen throughout the experiment as shown in figure 2.

Table 2: (Below shows the initial IFT of crude oil)

Number of Trials	IFT Pure Crude Oil (mN/m)
1st Trial	24.45
2nd Trial	24.09

Average	24.27

Table 3: (IFT Value For Crude Oil After Added With Lignin Surfactant)

Lignin Concentration (ppm)	Brine (ml) Constant	IFT (mN/m) 1st Trial	IFT (mN/m) 2nd Trial	Average
0	3	24.45	24.09	24.27
2000	3	17.58	17.25	17.415
4000	3	11.03	11.01	11.02
5000	3	10.62	10.53	10.575
6000	3	9.98	9.43	9.705

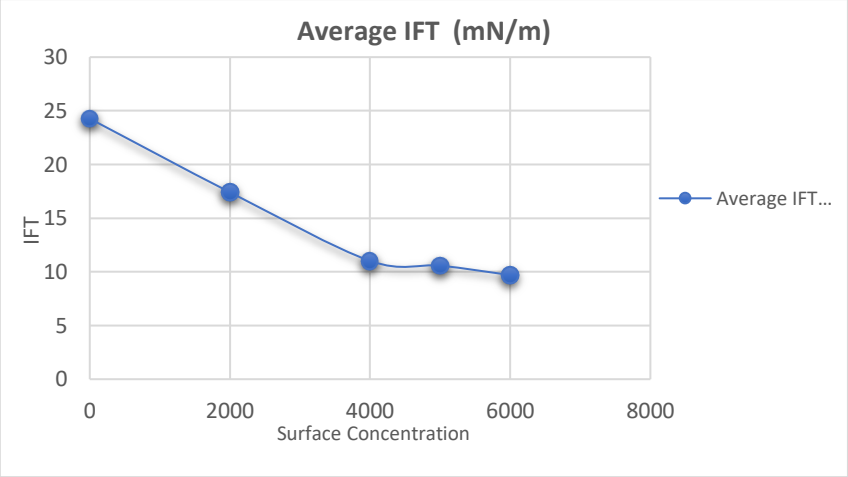

Figure 2-: (Average IFT Of Crude Oil vs Surfactant Concentration)

Critical Micelle Concentration (CMC)

From the data provided, we are able to compute the surfactant was added and the decrement of IFT can be measured. The drop reaches up to the point where the average IFT remains nearly constant which is 9.705 mN/m at 6000 ppm. The comparison of IFT can be compared between at 5000 ppm and 6000 ppm which is there is only a slight difference in the difference. This shows that the surfactant has reached its CMC at 5000 ppm whereby an increment of surfactant would not have any effect if it is being increased. By having to look at the low concentration we are able to study that low concentration of surfactant exists as the isolated molecule. By having to increase it up to the CMC point, Nanoparticles will be produced and this particle is formed spontaneously providing a sharp change in the properties of the surfactant. The CMC value is essential in the industry of petroleum because it indicates the economic data of the surfactant. From here, it can be concluded that higher concentration of surfactant does not indicate a greater effect of the decrement in IFT.

Difference of Effect on IFT by Lignin Surfactant

The IFT values on the different concentration of Lignin surfactant is shown in table 4 below. The IFT value initially decreases and reaches a minimum value, then increases up to the certain concentration of surfactant and finally attain a constant trend. At lower concentration range the

surfactant molecules preferably adsorb at the interface between oil and water from the aqueous surfactant solution and hence interfacial tension of the solution starts to decrease rapidly as shown in figure 3.

Table 4: (Percentage of IFT Reduction)

Lignin Concentration	CMC
Lignin 2000 ppm	28.24%
Lignin 4000 ppm	54.59%
Lignin 5000 ppm	56.42%
Lignin 6000 ppm	60.01%

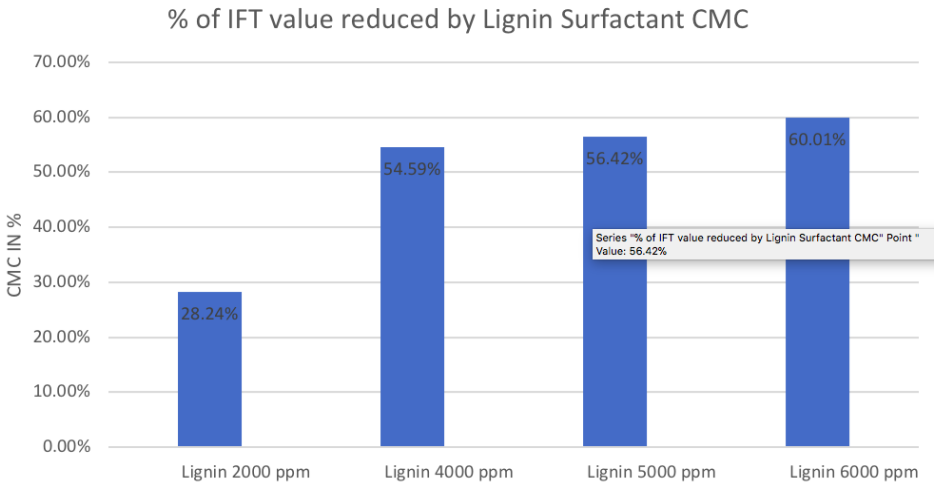

(Figure 3: Percentage of IFT Reduction)

This figure shows the comparison between the research by Kumar, S., & Mandal, A. (2016). By comparing the % of IFT value reduced by lignin surfactant.

Effect of Lignin on Wettability

Wettability test describes the behavior of crude oil and surfactants for actual contact angle. The contact angle was majored in different types of core samples, for crude oil there is different contact angle due to a different type of rock as shown in 5. Then add brine solution with 3 wt % with crude oil to make the wettability Then the crude oil with the addition of lignin whereby the difference can be seen compared to the wettability of crude oil. Added lignin with 2000 ppm and 5000 ppm make the wettability less as shown in table 6 and 7. It can be observed that lignin can be more effective on Carbonite sample, namely Moo3008 and Cp8 samples, whereby the wettability value yield is lowest among the four samples.

Figure 4 shows that the initial contact angle of crude oil and Brine 3 wt % do not have significant difference in contact angle reduction and remains as water-wet. The addition of 2000 ppm lignin surfactant into the crude oil wettability changes. Finally, the contact angle showed Adding 5000 ppm of lignin surfactant which further lowers the wettability to remain in the water-wet value. By adding the lignin resulted in a reduced of the contact angle, thus altering the weakly water-wet core sample to strongly water-wet. Changes of wettability from oil-wet to water-wet increases the oil recovery significantly.

Table

Core Sample	Core Type	Contact Angle (Average)	Contact Angle (Actual)
MOO308	Carbonate Stone	12.0255	167.9745
Cp8	Carbonate Stone	11.62	168.38
9	Sandstone	11.79	168.21
6-11	Sandstone	13.35	166.65

5:(Crude oil)

Table 6: (Lignin 2000 ppm +Crude oil + Brine 3wt%)

Core Sample	Core Type	Contact Angle (Average)	Contact Angle (Actual)
MOO308	Carbonate Stone	29.3621	150.6379
Cp8	Carbonate Stone	28.6522	151.3478
9	Sandstone	21.3659	158.6341
6-11	Sandstone	20.9789	159.0211

Core Sample	Core Type	Contact Angle (Average)	Contact Angle (Actual)
MOO308	Carbonate Stone	42.36	137.64
Cp8	Carbonate Stone	41.29	138.71
9	Sandstone	38.6743	141.3257
6-11	Sandstone	38.2174	141.7826

Table 7: (Lignin 5000 ppm + Crude oil +brine 3wt%)

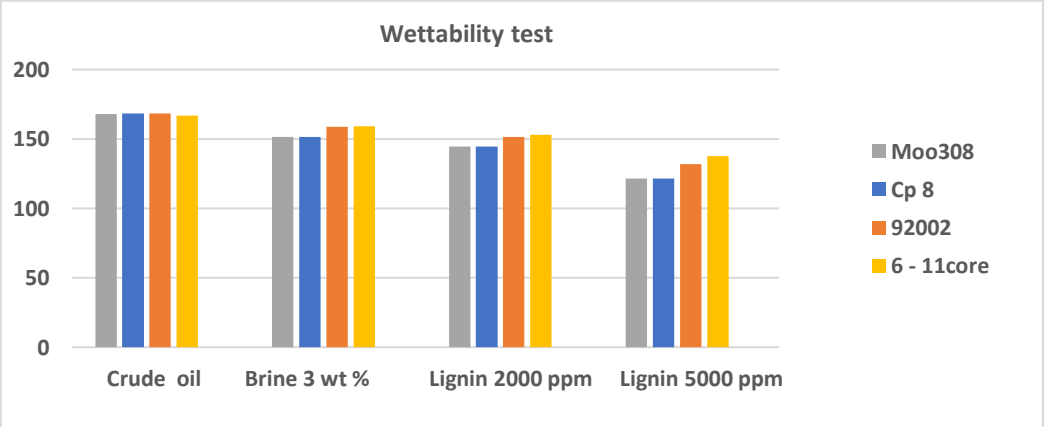

Figure 4: (Wettability Observation of Crude oil before and after Surfactant is Added)

Sandpack

This method is used to determine the effect of lignin in EOR and to investigate the total recovery.

Calculation involved

$$\text{Porosity } (\emptyset) = \frac{Pore\ volume}{Bulk\ volume} \times 100 \quad \text{Equation 3.1}$$

$$\text{Initial Oil Saturation Soil} = \frac{OOIP}{Vp} \times 100 \quad \text{Equation 3.2}$$

$$\text{Primary recovery (PR)} = \frac{PR\ IN\ ML}{OOIP} \times 100 \quad \text{Equation 3.3}$$

$$\text{Secondary recovery (SR)} = \frac{PR\ IN\ ML}{OOIP} \times 100 \quad \text{Equation 3.4}$$

$$\text{Tertiary recovery (TR)} = \frac{PR\ IN\ ML}{OOIP} \times 100 \quad \text{Equation 3.5}$$

$$\text{Total Recovery in (\%)} = \frac{\boldsymbol{Total\ Recovery}}{\boldsymbol{OOIP}} \quad \text{Equation 3.6}$$

After the calculation has done for sand pack using EOR calculations for primary, secondary and tertiary recovery. It results that at 2 wt.% of lignin will increase the tertiary recovery for 25%, but for lignin 5wt% increases the recovery of 33.3% as shown in figure 5 which can be good resultant for EOR methods.

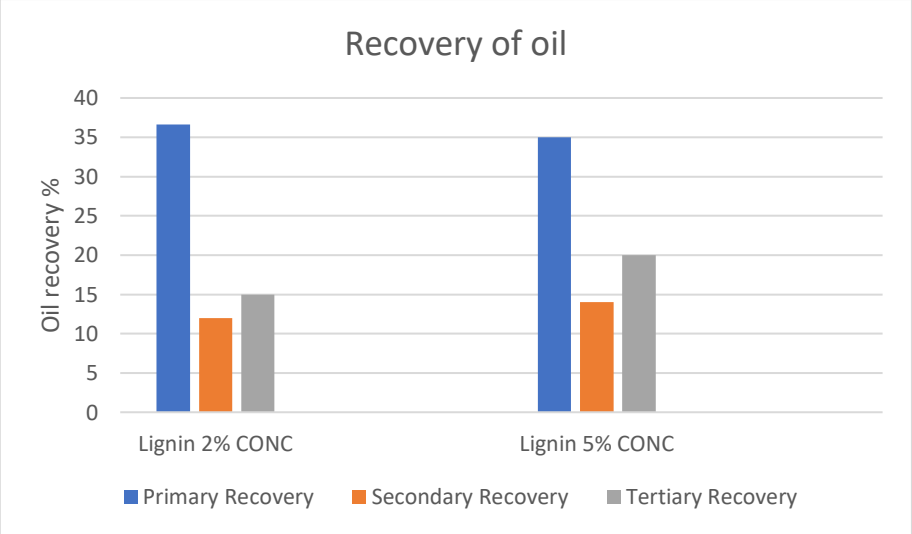

Figure 5 : (Differences results using EOR for sand pack on light Crude Oil)

Finally, the total recovery for 2wt % of lignin is 81.66 and for 5 wt.% of lignin is 91.66 as shown in Figure 6.

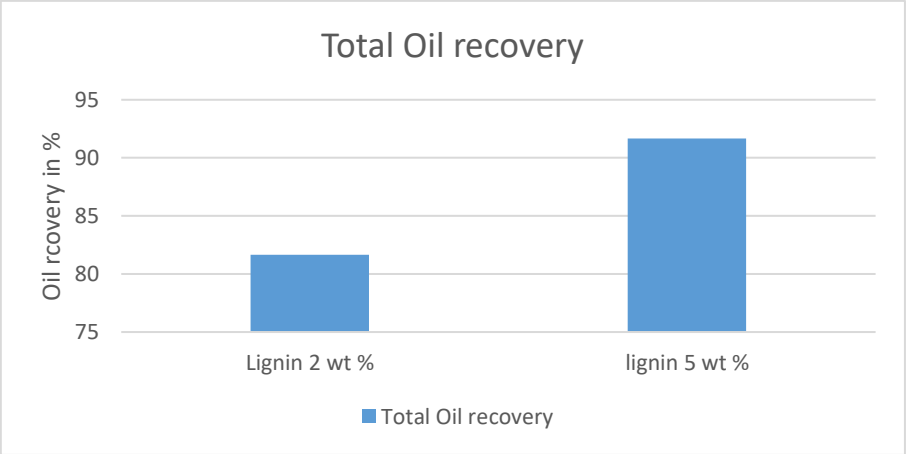

Figure 6: (Total Oil Recovery)

Conclusion

Sawdust has been widely used to make pallets and furniture after being discarded as a byproduct. By having to variate the usage of sawdust, this may help the industry to expand more by having more options to choose. In Malaysia, it has been proved that sawdust which comes from various sources comes in an abundant volume which may not be a limitation of having to use sawdust as a surfactant. Malaysia lies in the tropical which produces a lot of trees and this may help to produce more sawdust in the future. The wastage of sawdust can also be controlled by having this option. Sawdust which has been soaked and wet may not be able to be used to build furniture but the lignin in the sawdust can still be extracted. This will curb the pollution of having to discard sawdust which may decrease the percentage in air pollution. Sawdust can also be considered as an economically attractive product which can be measure through the abundancy of it. By having to study more on the sawdust, the EOR sector can be improved and EOR can be more economic feasible through the channel of having to use sawdust as a surfactant. Concluding to this research, it is known that the lignin extracted from the sawdust can be used as a surfactant through the research of having to test the wettability and also by having to alter the crude oil IFT when being mixed together.

According to the IFT measurement in this research, the extracted lignin from sawdust had lower the IFT value of crude oil which from 24.7 mN/m to 9.705 mN/m. The extracted lignin had reduced the 75.06% IFT value of crude oil successfully. Besides, the contact angle of crude had reduced for MOO308 Carbonate sample from 167.97 º to 137.64 º, Cp8 Carbonate sample from 168.38 º to 138.71 º , sample 9 Sandston 168.21 º to 141.32 º and sample 6-11 Sandstone from 166.65 º to 141.78 º by adding lignin surfactant.

For Salinity is resulted by 3 wt % of brine and the solubility of lignin in brine and water referred at the appendix. Finally, for the sand pack for EOR methods the tertiary recovery is 33.3%.

Recommendation

A comparison was done in between the synthetic surfactants and it was found that bio-surfactants are economical. The reason to this is because bio-surfactants can be produced at a very economical rate. Compared to bio-surfactant, synthetic surfactant will lead to the depletion of non-renewable resources which can be a disadvantage in having to produce a

surfactant. It has been proved that the production of synthetic surfactant may also cause pollution which can be a downside to the environment. In addition to this, the synthetic surfactant can be slightly biodegradable even if it decomposes after time which toxic will be released if the surfactants do decompose. Apart from this, bio-surfactants are actually consist of renewable resources. These days, authorities have become more firm and strict. This is because authorities want to curb the pollution problem which is worsening as day goes by. Stricter regulations have been made to monitor the activities done by the industries. Activities done by industries may affect the health of living organisms around the area and regulations regarding this issue has been made these days which in the future pollution can be decreased and this problem can be countered.

Acknowledgment

The authors wish to thank UCSI University for their continuous support on this research and providing some chemicals., Special thanks for Mrs Farhana Bt Abdul Barri for his continuous encouragement and supervision of this project.

References

Anderson, W. G. (1987). Wettability literature survey-part 6: the effects of wettability on waterflooding. *Journal of Petroleum Technology*, *39*(12), 1-605.

Buckley, J. S., & Liu, Y. (1998). Some mechanisms of crude oil/brine/solid interactions. *Journal of Petroleum Science and Engineering*, *20*(3), 155-160.

Cuiec, L., Bourbiaux, B., & Kalaydjian, F. (1994). Oil recovery by imbibition in low-permeability chalk. *SPE Formation Evaluation (Society of Petroleum Engineers);(United States)*, *9*(3).

Davies, R. M. (2012). Physical and mechanical properties of palm fruit, kernel and nut. *Journal of Agricultural Technology*, *8*(7), 2147-2156.

Demikhova, I. I., Likhanova, N. V., Perez, J. R. H., Falcon, D. A. L., Olivares-Xometl, O., Berthier, A. E. M., & Lijanova, I. V. (2016). Emulsion flooding for enhanced oil recovery: Filtration model and numerical simulation. *Journal of Petroleum Science and Engineering*, *143*, 235-244.

ElMofty, O. (2012). Surfactant enhanced oil recovery by wettability alteration in sandstone reservoirs.

Farad, S., Manan, M. A., Nsamba, H. K., Jaafar, W. M. K. B. W., Isa, K., & Joseph, W. (2016). Enhancing Oil Recovery Using Formulated Surfactants Extracted from Oil Palm and Local Coconut Coir Containing Lignosulfonate. *Technology*, *3*(2), 53-60.

Holmberg K, Jönsson B (2003) Surfactants and polymers in aqueous solution. John Wiley & Sons, England

Hognesen, E.J., Strand, S., and Austad, T. 2005. Waterflooding of Preferential Oil-Wet Carbonates: Oil Recovery Related to Reservoir Temperature and Brine Composition. Paper SPE 94166 presented at the SPE Europec/EAGE Annual Conference, Madrid, Spain, 13-16 June.

G. Hirasaki, D.L. Zhang, Surface chemistry of oil recovery from fractured, oil-wet, carbonate formation, SPE J. June (2003) 151–162.

Hirasaki, G.J., Zhang, D.L., 2004. Surface chemistry of oil recovery from fractured, oil-wet, carbonate formations. SPE J. 9 (2), 151–162

Schramm, L. L. (2000). *Surfactants: fundamentals and applications in the petroleum industry*. Cambridge University Press.

Seethepalli, A., Adibhatla, B., & Mohanty, K. K. (2004, January). Wettability alteration during surfactant flooding of carbonate reservoirs. In *SPE/DOE Symposium on Improved Oil Recovery*. Society of Petroleum Engineers.

Xie, X., Weiss, W. W., Tong, Z. J., & Morrow, N. R. (2005). Improved oil recovery from carbonate reservoirs by chemical stimulation. *SPE Journal*, *10*(03), 276-285.

Xu W, Ayirala SC, Rao DN (2005) Measurement of surfactant-induced interfacial interactions at reservoir conditions. SPE Journal SPE Paper 96021

Ye Z, Zhang F, Han L, Luo P, Yang J, Chen H (2008) The effect of temperature on the interfacial tension between crude oil and gemini surfactant solution. Colloids Surf, A Physicochem Eng Asp 322(1–3):138–141.

Zhang, D. L., Liu, S., Puerto, M., Miller, C. A., & Hirasaki, G. J. (2006). Wettability alteration and spontaneous imbibition in oil-wet carbonate formations. *Journal of Petroleum Science and Engineering*, *52*(1), 213-226.

Proceeding: 5th International Conference on Applied Sciences and Engineering (ICASEA, 2018)
(eISBN 978-967-15744-1-6)
Capthorne Hotel, Cameron Highlands, Malaysia

DEVELOPMENT OF HIGH TEMPERATURE HIGH PRESSURE (HTHP) WATER BASED DRILLING MUD USING SYNTHETIC POLYMERS, AND NANOPARTICLES.

Mansoor Ali Khan[1]
Pro. Dr. Hikmat Said Al-Salim[2]
Leila Niloofar Arsanjani[3]

[1] Chemical and Petroleum Engineering Department, UCSI University, Malaysia.
[2] Chemical and Petroleum Engineering Department, UCSI University, Malaysia.
[3] Head of R&D Department, Scomi Oiltools, Malaysia.

Abstract: *It is important to understand the aspects influencing water based mud (WBM) rheology in order to maintain a firm control over rheological properties of high temperature high pressure (HTHP) and high density water based mud. This paper focuses mainly on the rheological properties of water-based drilling fluid under high pressure and high temperature condition. This work focuses on the design, optimization and formulation of a HTHP water-based drilling fluids in accordance with the required specification such as rheological properties and fluid loss. To meet the aforementioned drilling fluid properties, the research was limitless to the use of clay, polymers, and nanoparticles. Polymers provide excellent rheological and fluid loss properties to water base muds but degrade at high temperature. The experimental method used was generally mixing of water base mud with certain formulation and then performing mud testing. The experimentation were conducted according to "Recommended Practice on Standard Field Procedure for Testing Drilling Fluid" API RP 13B and "Recommended Practice 13I Standard Field Procedure for Laboratory Testing Drilling Fluid" API 13I to meet the American Petroleum Institute (API) requirements and obtain trustworthy results. The main laboratory tests involved in this project are mud preparation, static rheology test, pH and HTHP static filter press. A bentonite clay and high temperature synthetic polymers have been successfully tested at 400 degree F with excellent rheological and filtration properties. The base mud formulation consists of the commercial chemicals provided by Scomi Oiltools, Malaysia. The base mud formulation has a stable rheology and excellent fluid loss properties at 400 F. A very thin and impermeable filter cake has been obtained with minimum fluid loss at a temperature of 400 F. Researchers have successfully used nanoparticles for providing excellent rheology, thermal stability and fluid loss control. Two nanoparticles namely, Carbon nanotubes (CNT) and Zinc Oxide were tested on the base WBM system to analyze their effects on HTHP rheology, fluid loss, and filter cake quality. A very positive results have been obtained using Carbon nanotubes (CNT). The use of CNT in WBM increased HTHP rheology by 14% and reduced fluid loss by 25%. Moreover, this research provide solutions to the problems related to HTHP WBM development like clay gelation, solid sagging, and low end rheology. The aforesaid problems have been fixed by using high temperature polymeric deflocculants, polymeric viscosifier, and bentonite extender respectively.*

***Keywords**: HTHP, Rheology, Fluid loss, Carbon nanotubes (CNT), Sag*

Introduction

High Temperature and Pressure (HTHP) condition are experienced in wells that have downhole temperatures greater than 300 oF and pressure of 10,000 Psi and higher. The most predominant problem that can affect drilling fluids in HTHP conditions, is the thermal degradation of the water based mud system, and inducing changes in its properties under HTHP conditions. Oil-based mud have the ability to resist thermal degradation and withstand severe downhole condition like HTHP. However oil based mud imposes a negative impact on the environment and it is not economically viable compare to the other type of mud systems such as WBM. Hence, drilling into formations with HTHP requires an eco-friendly WBM drilling fluid possessing stable rheological and enhanced fluid loss properties (M.I. Abduo et al. 2016).

The main function of bentonite in WBM is to elevate viscosity and reduce filtration loss to wellbore walls. Bentonite can be classified into either Ca-bentonite with low swelling capacity or Na-bentonite with high swelling capacity (Abu-Jdayil 2011). According to Shan Wenjun et al. (2014), the clay property will be greatly affected with increasing temperature due to hydration and coalescence of Bentonite clay particle in high temperature condition. Clay gelation process in WBM requires special attention at temperatures higher than 300 F. The mud loses its shear-thinning property especially under static aging condition and cause excessive gel strengths. To avoid excessive mud viscosities and gel strengths, bentonite concentration used should be minimum. Bentonite concentration should not be exceeded more than 3 lb/bbl when formulating HTHP WBM (Johann P. Plank 1992).

A successful HTHP well drilling requires an appropriate control on drilling mud rheology. As Johann P. Plank (1992) stated that “if concentration of Bentonite or clay materials exceeds acceptable levels and results in viscosity problems, polymeric deflocculants can be used as a last resort to control rheology.” In the past, high solids dispersed drilling fluid systems for HTHP drilling contained lignosulfonate and lignite for rheology and fluid loss control. The conventional lignite/lignosulfonate high- solid dispersed muds function at alkalinity (pH 9) and require high dosages of lignite/lignosulfonate at temperature above 360 F because of thermal degradation. Chrome lignite degradation by-product is CO2 which flocculates clay and Bentonite, causing high yield point and gel strength (Johann P. Plank 1992). The recent development of synthetic short chain polymeric deflocculants improved the temperature stability and low dosages compared to conventional lignite/lignosulfonates. They are temperature-stable above 400 F.

Nanotechnology and surfactant has contributed to novel developments in petroleum industry in the past few decades. The rheology at HTHP condition is affected by breaking bonds between mud particles at high temperature (Putri Yunita et al. 2015). Nano based drilling fluid greatly reduces frictional resistance between drill pipe and wellbore wall by forming a lubricating film at wall and pipe interface. Shale formation consists of reactive clays, which stick to the drill bit and centralizer, causing balling effect. Nano based mud could be a better choice in drilling operation in reactive shale because of it hydrophobic film forming characteristic (Ibrahim El Diasty, 2013). Due to the presence of large quantity of very minute particles with high surface area, thermal conductivity, high temperature stability, high mobility,

and thermal conductivity, effective interaction with internal and external surfaces of rock, nanoparticle-based drilling fluids are anticipated to play a key role in future and current high temperature and high pressure drilling operations (Amanullah et al, 2011). Multiwall Carbon Nanotube (MWCNT) has been successfully used by M.I. Abduo et al. (2015) to improve HTHP rheological stability and fluid loss.

Experimental Procedure

The methodology is divided into several steps, as shown in Figure 1. The specifications of HTHP drilling mud were set according to the field experience by drilling fluid engineers of Scomi Oiltools Sdn. Bhd. The two steps involved are before hot rolling (BHR) and after hot rolling (AHR). BHR consists of Bentonite (Drill-Gel) pre-hydration for 16 hours, mixing of fresh water base mud, rheology and pH test, and hot rolling. The tests involved after hot rolling (AHR) are same as BHR with an extra HTHP fluid loss test.

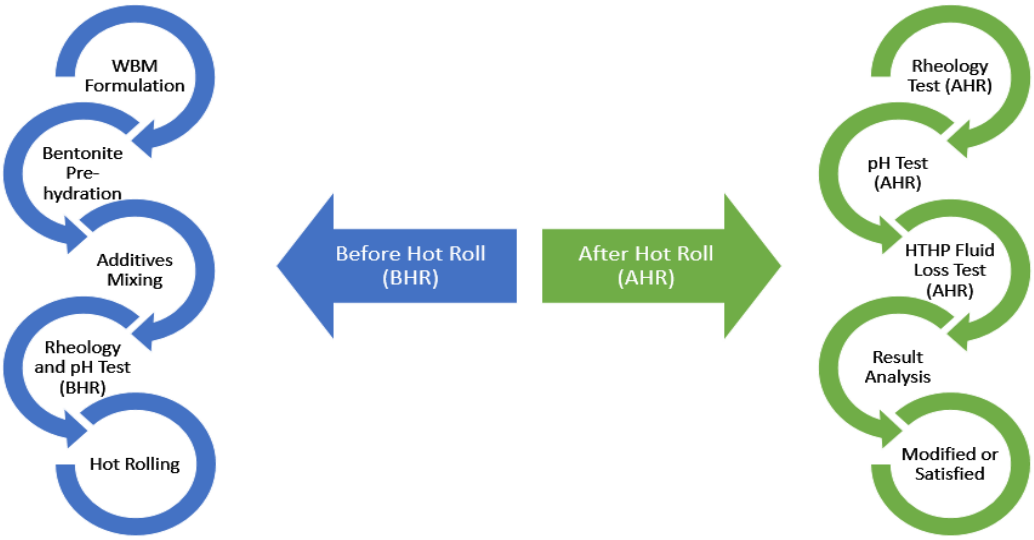

Figure 1: Experimental flow

Drill-Gel Pre-Hydration

Pre-hydrated Drill-Gel was prepared by adding 35 lb/bbl of Drill-Gel and 1 lb/bbl of caustic soda to 0.97 bbl of water. The mixture was stirred at high speed for 30 minutes using Hamilton beach mixer. It was then kept for 16 hours at room temperature for better hydration.

Additive Mixing

The order of chemicals mixed is shown in table 1. The way of adding chemicals and mixing time for each chemical is an important aspect in water base mud mixing. The polymers were added very slowly, and more mixing time was given to each polymer for better hydration. A relatively higher mixing time was also given to Drill-Bar and Drill-Gel.

Rheology Test

Rheology test represents the flow behaviour and hole cleaning efficiency of drilling mud. This test is used to record rheology parameters like yield point (YP), plastic viscosity (PV), and gel

strength using Fann viscometer-model 35SA. For HTHP mud the tests were done at 150 F according to API standards.

Calculation involved

$PV_{cps} = 600_{rpm} - 300_{rpm}$ $Equation\ 1$

$YP_{lb/100ft^2} = PV - 300_{rpm}$ $Equation\ 2$

pH Test

pH meter was used to find the pH of drilling fluid. pH plays an important role in water base mud and affects mud properties. Water-base drilling fluids are generally maintained in the 8 to 12 pH range for improved chemical solubility and performance, as well as for anti-corrosion of drilling and completion tools (Scomi).

Table 1: Chemicals used and their function

Additive	Function	Base (lb/bbl)	Base + CNT (lb/bbl)	Base+ZnO (lb/bbl)
Drill Water (bbl/bbl)	Base fluid	0.523	0.523	0.523
Caustic Soda	pH modifier	To pH 10	To pH 10	To pH 10
Soda Ash	control hardness	0.7	0.7	0.7
Hydro-Defoam HT	Foam remover	1	1	1
Hydro-Therm LV	HT Fluid Loss Polymer	6.2	6.2	6.2
Hydro-Therm R	HT Fluid Loss Polymer & Rheology modifier Polymer	1.8	1.8	1.8
Hydro-Zan	Rheology modifier	0.7	0.7	0.7
Sodium Chloride	Salinity	74.42	74.42	74.42
Hydro-Plast	HT fluid loss, shale stability	4	4	4
Hydro-Seal R	Bridging material, lubricity	4	4	4
Hydro-Sperse RS	HTHP Rheology stabilizer	2	2	2
Carbon nanotubes	Rheology & fluid loss improver	-	0.5	-
Zinc Oxide	Rheology improver and H_2S scavenger	-	-	0.5
Drill-Bar	Weighting agent	Up to 14 ppg	Up to 14 ppg	Up to 14 ppg
Drill-Gel	Viscosifier and Fluid loss control	8	8	8
Magnesium Oxide	pH buffer	1.5	1.5	1.5
Ox-Scav L	Polymer extender	1	1	1
Hydro-Buff HT	Polymer extender, HT rheology improver	1.5	1.5	1.5

Hot Rolling

Hot rolling is a process, which simulates a wellbore mud circulation in the laboratory using a roller oven and mud aging cell. The purpose of hot rolling is to check how the mud properties will change after a mud circulation at certain temperature. The mud samples were hot rolled at 380 F and 400 F for 16 hours under 200 Psi pressure.

HTHP Fluid Loss Test

High temperature and high-pressure filter press is used at high temperatures and high pressures to find the fluid loss. This test can be performed at original down-hole temperature giving realistic values of fluid loss. All the HTHP fluid loss tests were performed using Ofite HTHP filter press with threaded cells (500 mL) at temperature 380 to 400 F and 500 Psi differential pressure.

The paper represents an optimized formulation for HTHP dispersed water base mud. The base formulation is an enhanced system of polymers, clay, and dispersant with improved mud properties at elevated temperatures. The base is further improved by formulation with nanoparticles like Carbon Nanotube (CNT) and Zin Oxide. The normal field specifications that were established to describe the performance of the ideal fluid included a Plastic Viscosity (PV) of less than 50 cP, Yield Point (YP) in a range of 18 to 30 lb/100ft^2 and HTHP fluid-loss of less than 20 ml at 380-400 ^{o}F, and 500-psi differential pressure on hardened paper. The rheological properties were measured according to API standards using fann 35SA viscometer at 150 F (66 C).

Results & Discussion

Formulation of Base

The water base mud was initially formulated with Drill-Gel as viscosifier and without Hydro-Sperse RS. The rheological properties after hot rolling at 380 F for 16 hours increased to high and unacceptable range (above 30 lb/100ft2). The plastic viscosity (PV) and yield point (YP) were too high for practical application (PV above 50 cP). This increase in rheology is caused by high temperature clay gelation phenomena. Shan Wenjun et al. (2014) attributed this to the clay property which is greatly affected with increasing temperature due to hydration and coalescence of clay particles under high temperature condition.

The same formulation was then mixed with a polymeric deflocculant known as Hydro-Sperse RS. Hydro-Sperse RS stabilized the rheology by dispersing the clay at high temperature. The polymer uncoiled and attained a straight chain configuration when dissolved in water due to mutual repulsion of same charged groups along the chain. Hydro-Sperse RS efficiently improved the action by stimulating clay platelet disaggregation. Un-hydrated clay platelets are aggregated by edge to face and face to face electrostatic bonding as shown in Figure 2.

Figure 2: Clay platelet aggregation before hydration

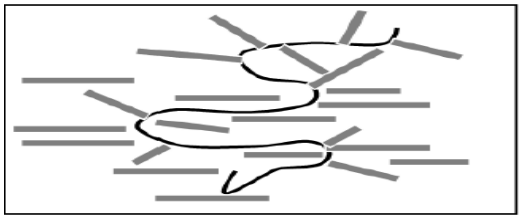

Figure 3: Short chain anionic polymers enhances disaggregation

When water contacts polymer becomes uncoil and adsorbs on clay where polymer's negative charge neutralize positive charge of clay. This causes platelet disaggregation because polymer overcomes the bond strength of the macrostructure as shown in Figure 3. It becomes more effective compared to untreated clay because a larger fraction of clay gets activated for hydration (Newman 1987). The Figure 4 below shows the rheology curves with and without Hydro-Sperse RS. Another analysis in this research is the contribution of Hydro-Sperse RS to HTHP fluid loss. The optimum concentration for the lowest fluid loss was deduced to be 2 lb/bbl as shown in Figure 5. This can be explained as Hydro-Sperse RS disperse clay particles causing the formation of a thin and impermeable filter cake which in turn reduces fluid loss.

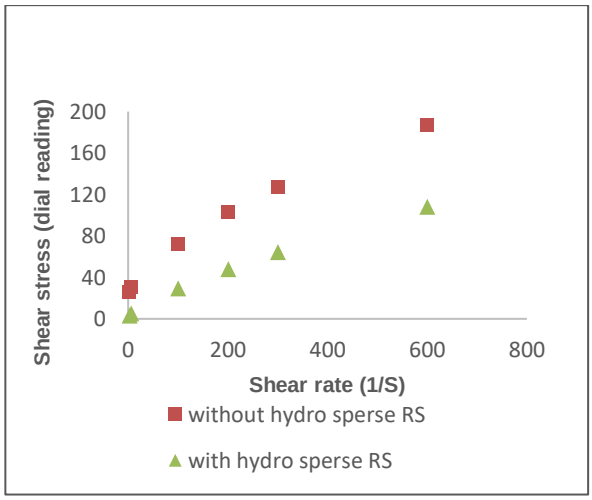

Figure 4: Effect of Hydro-Sperse RS on Rheology after hot rolling

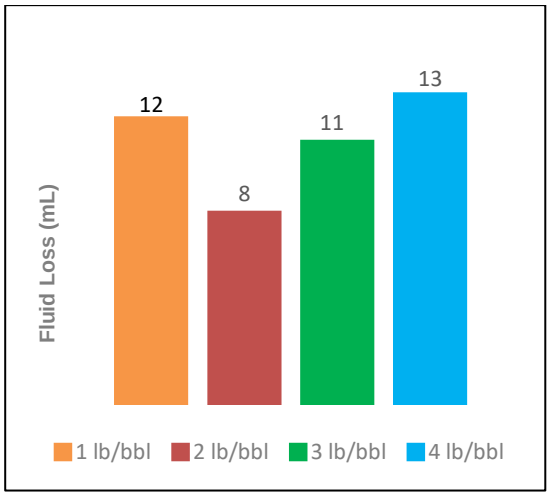

Figure 5: Effect of Hydro-Sperse RS on Fluid loss

Figure 6: Barite sagging due to low LSRV

The low end rheology or low shear rate viscosity (LSRV) refers to 3 and 6 rpm dial reading of

Fann viscometer. The low wellbore annular shear rate is best approximated by 6 rpm reading, equivalent to a shear rate of 10.2 sec^{-1}. The 6 rpm reading for drilling fluids is important for cleaning the hole and suspend the cuttings. LSRV values are the main inhibitive mechanism for barite sagging at dynamic condition. These properties should be maintained within the range for a particular set of wellbore condition (Scomi). The use of Hydro-Sperse RS stabilized the rheology (PV and YP) at high temperature but reduced the low end rheology (LSRV). The decrease in LSRV resulted in severe sagging of solids as shown in Figure 6. The LSRV was successfully elevated by using Hydro-Zan and Hydro-Buff HT. Hydro-Zan polymer is stable up to 250 F and degrades at temperature higher than 250 F. The synergy of hydro-zan and Hydro-Buff HT is explained as Hydro-Zan efficiently stabilized LSRV until a temperature of 250 F, while above that, Hydro-Buff HT is responsible for stabilization of LSRV and overall rheology because of its high temperature stability. This strategy efficiently eliminated solid sagging at high temperature. The overall testing results are shown in Table 2.

Table 2—Drilling fluid properties at 380-400 F

Drilling Fluid	Temperature (°F)	Plastic viscosity (cP)	Yield point (lb/100 ft²)	10 sec Gel (lb/100 ft²)	10 min Gel (lb/100 ft²)	HTHP Fluid loss (mL)	Cake thickness (1/32 inch)
Base	150 °F (BHR)	56	46	7	34	-	-
	150 °F (AHR 380 °F)	41	18	3	7	8	3
	150 °F (AHR 400 °F)	41	22	4	7	9	4
Base + CNT*	150 °F (BHR)	60	55	10	36	-	-
	150 °F (AHR 380 °F)	55	31	5	11	6	2
	150 °F (AHR 400 °F)	47	25	5	8	8	3
Base+ZnO	150 °F (BHR)	56	46	8	35	-	-
	150 °F (AHR 380 °F)	46	21	4	10	9	4
	150 °F (AHR 400 °F)	42	20	4	7	9	4

(*) Carbon Nanotubes

Rheological Properties

Rheology of drilling fluid dictates successful drilling as well as hole cleaning. At HTHP conditions, the conventional water base mud system loses its rheology and results in major drilling problems. High temperature weakens or breaks the bonds among the mud particles and cause a severe drop in rheology. For this reason, the results after hot rolling (AHR) will be closer to reality and more meaningful at these conditions. It can be seen from Figure 7 that rheology is higher for mud sample with nanoparticles. The concentration of both Carbon

nanotubes (CNT) and Zinc Oxide nanoparticle is 0.15% by weight. A small concentration of both nanoparticles improved the rheology of mud at 400 F. The rheology can be broadly explained in terms of PV, YP and gel strength as follows.

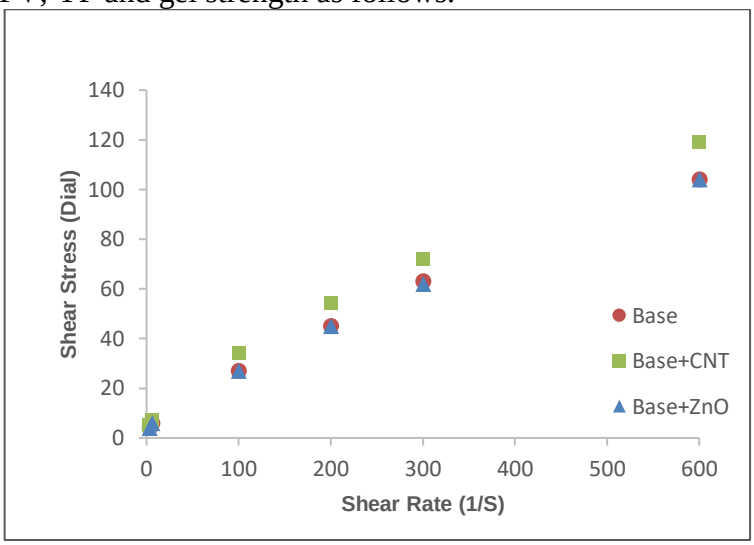

Figure 7: Rheology curve for all samples at 150F (AHR@400F)

Plastic Viscosity (PV)

Drilling fluids usually consist of dispersed solids in continuous phase of fluid. PV (Plastic viscosity) is caused by mechanical friction of solids which constitute to total flow resistance. From Figure 8, it can be seen that PV increases for both samples containing nanoparticles compared to base sample. Many factors like increasing percent volume of solids, constant percent volume of solids, and decreasing particles size in drilling fluid increases plastic viscosity. Small particles size has high surface to volume ratio, which causes increased frictional drag (Scomi). The PV is higher for Carbon nanotube fluid compared to ZnO because its particle size is very small compared to ZnO and hence has a high surface to volume ratio.

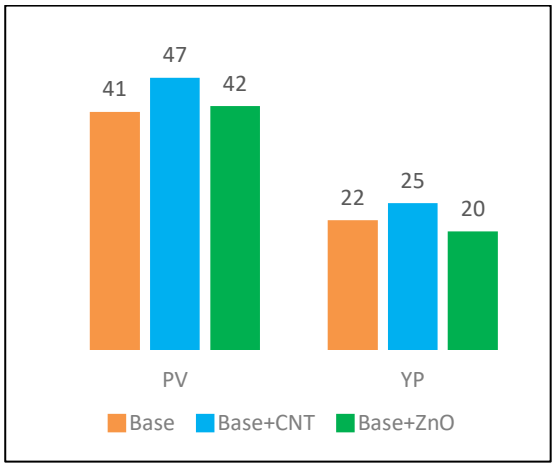

Figure 8: PV & YP after hot rolling at 400F

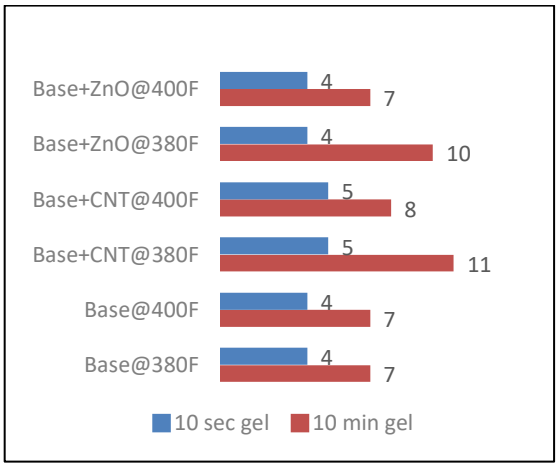

Figure 9: Gel strength

Yield Point (YP)

The electrochemical attractive forces in the mud particles cause flow resistance and is termed as yield point. The surface of dispersed particles in mud can have positive, negative, or neutral charge. These charges cause electrochemical attractive or repulsive forces under dynamic condition, giving rise or drop to yield point respectively (Scomi). From Figure 8, it can be seen that YP of base sample is thermally stable up to 400 ^{o}F. Table 2 shows the drop in YP for all the samples after hot rolling at 380 and 400 ^{o}F. The YP or rheology for all the samples are in a stable range after hot rolling. Adding Carbon nanotubes and Zinc Oxide nanoparticle further increased and stabilized the solid carrying capacity (YP). Carbon nanotubes efficiently increased and stabilized yield point of the base mud sample. This increase in YP is due to increasing quantity of solid particle and complex interactions among carbon nanoparticles and other additives. ZnO loses a proton in aqueous medium when pH is high and obtain a net negative surface charge (P.S. Bedi et al. 2015). This negative charge is responsible for interaction of ZnO with other charged particles and hence modify YP of the mud system. The most stable YP is given by carbon nanotubes compared to zinc oxide and base.

Gel Strength

Gel strength is the power of forces of attraction in drilling mud at static condition. Figure 9 shows that gel strength for all the samples are in a range of 4 to 11 lb/100ft^2. These gels are considered as low gels and hence are desired in mud engineering perspective. High strength of attractive force cause high gelation, and vice versa. Flocculation of solids in the mud causes excessive gelation which results in high mud pump pressure to break the gel after a shutdown period. These gels are neither progressive nor high flat gels as these are undesired in the drilling industry (Scomi).

HTHP Filtration Properties

The combination of synthetic fluid loss polymers, dispersant, and clay enhanced the fluid loss properties of the base mud sample up to 400 ^{o}F. The fluid loss can be seen in Figure 10. Dispersant and fluid loss polymers are negatively charged low molecular weight polymers of short chain length. These negatively charged polymer adsorbs on positively charged clay platelets causing neutralization of charges. This creates an overall negative charge and deflocculation occurs. The dispersion or deflocculation of clay particles result in the formation of a thin and impermeable filter cake. The formation of thin and impermeable filter cake resists excess fluid loss to wellbore formation. The synthetic fluid loss polymers used in this water base mud system also work as secondary viscosifier. The lower fluid loss can also be explained by the fact that a viscous base fluid of mud reduces fluid loss. This proves that the used polymers are stable up to or perhaps above 400 ^{o}F. The addition of Carbon nanotubes to the base further enhanced the fluid loss properties. Carbon nanotubes not only reduced fluid loss but also filter cake thickness at high temperature and high pressure. The filter cake is shown in Figure 11. Carbon nanotubes reduced the fluid loss by physically plugging the nano-sized pores of the filter cake (A.I. El-Diasty). This resulted in a thin impermeable filter cake with reduced fluid loss compared to other two samples. Zinc oxide did not show any improvement in fluid loss.

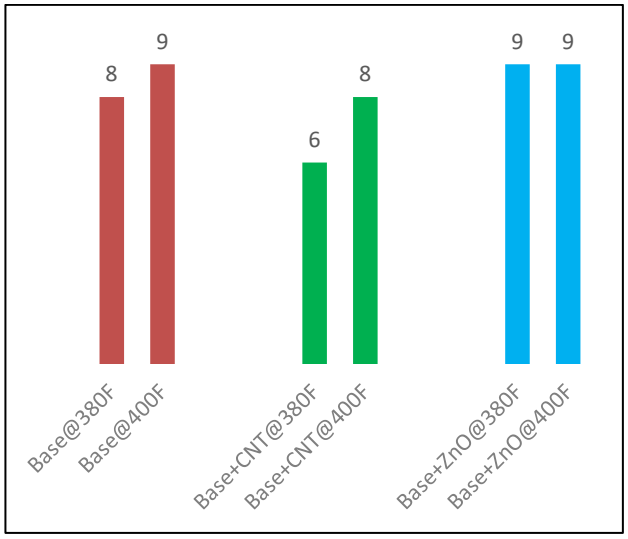

Figure 10: HTHP fluid loss in mL at 380-400 F

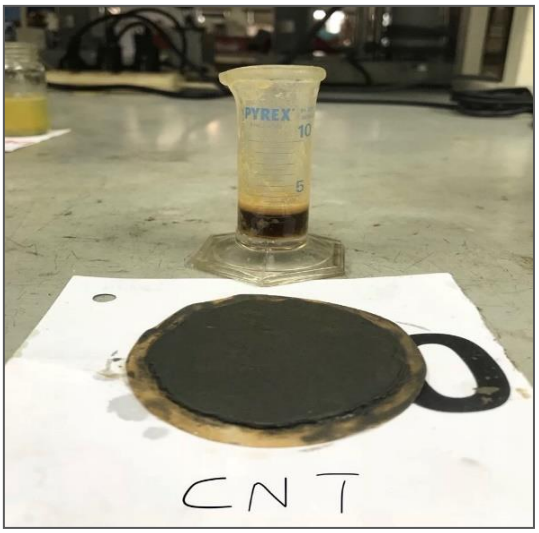

Figure 11: Filtrate and filter cake of base+CNT at 380F

Conclusion

In the current era, HTHP well drilling is a norm and needs a fluid with thermally stable rheology, fluid loss and other mud properties. This study shows that a conventional water base mud system can be optimized by using engineered synthetic polymers, dispersants, and clay to efficiently withstand a high temperature up to or above 400 ^{o}F. The base formulation itself has optimized rheological stability and excellent filtration properties at 400 ^{o}F. It is also concluded that Carbon nanotubes comparatively helped in thermal stability, rheological and filtration properties of water base mud at high temperature and high pressure. Zinc Oxide nanoparticles showed a small improvement in rheology with an exclusive benefit of being hydrogen sulphide scavenger.

Recommendation

The additives involved in the base formulation are Scomi Oiltools commercial chemicals with optimized rheology stability and superior filtration properties at ultra HTHP conditions. These novel chemicals and formulation can be readily applied to currently deep HTHP wells around the globe. This water base mud system can be made high performance inhibitive water base system like KCl/Polymer system, glycol or formate system for drilling reactive shale formations. It is also recommended to analyse acid or surfactant treated carbon nanotubes in water base mud.

Acknowledgment

The authors wish to thank UCSI University and SCOMI for their continuous support on this research and providing some chemicals. We would like to extend sincere thanks to Ms. Niloorfar Arsanjani for her continuous support. Special thanks for Prof. Dr. Hikmat Said Al Salim for his continuous encouragement and supervision of this project.

References

Abu-Jdayil, B. 2011. Rheology of Sodium and Calcium Bentonite-Water Dispersion: Effect of Electrolytes and Aging Time. *Int. J. Miner. Process*. 98 (3-4): 208-21.

Johann P. Plank 1992. Water Base Muds Using Synthetic Polymers Developed For High Temperature Drilling. *Oil and Gas Journal.*

S. Wenjun, T. Shixian, F.Fan, Y. Weimin and Z. Zhitao. Research on The Drilling Fluid Technology For High Temperature Over 240 ºC. *Procedia Engineering.* 73 (2014) 218 – 219.

Ahmed S. Mohammed 2016. Effect of Temperature on The Rheological Properties With Shear Stress Limit of Iron Oxide Nanoparticle Modified Bentonite Drilling Muds. *Egyptian Journal of Petroleum* (2017) 26, 791–802.

Annis, M. R. 1967. High Temperature Flow Properties of Water-Based Drilling fluids. *J. Pet. Technol.* 19 (08): 1074-1080. SPE-1698-PA.

Putri Yunita, Sonny Irawan, Dina Kania, UTP, UPM, "Evaluation of Non-ionic and anionic surfactant as additives for WBM" *American Journal of Chemistry* 2015 5(3A): 52-55.

Scomi Oiltools Engineering Manual, section 5, pg 17-23.

M.I. Abduo , A.S. Dahab, Hesham Abuseda, A.M. AbdulAziz, M.S. Elhossieny. Comparative Study of Using Water-Based Mud Containing Multiwall Carbon Nanotubes Versus Oil-Based Mud in HPHT Fields. *Egyptian Journal of Petroleum* (2016) 25, 459-464.

Newman, A.C.D. (ed.). Mineralogical Society Monograph No. 6 "Chemistry of Clays and Clay Minerals." John Wiley and Sons, New York, 1987.

P.S. Bedi, A. Kaur. An Overview on Uses of Zinc Oxide Nanoparticles. *World Journal of Pharmacy And Pharmaceutical Sciences* 2015 4(12): 1177-1196.

Md. Amanullah, M.K. AL-Arfaj and Z. Al-Adullatif; Preliminary Test Results of Nano-based Drilling Fluids for Oil and Gas, the SPE/IADC Drilling Conference and Exhibition held in Amsterdam, The Netherlands, 1-3 March 2011, SPE/IADC 139534.

A.I. El-Diasty, A.M.S.Ragab; Application of Nanotechnology in The Oil and Gas Industry: Latest Trend worldwide and Future Challenges in Egypt, SPE 164716, 2013.

Proceeding: 5th International Conference on Applied Sciences and Engineering (ICASEA, 2018)
(eISBN 978-967-15744-1-6)
Capthorne Hotel, Cameron Highlands, Malaysia

WATER TRANSPORT PROPERTIES OF BIO-NANOCOMPOSITES REINFORCED BY SUGAR PALM (*ARENGA PINNATA*) NANOFIBRILLATED CELLULOSE

R.A. Ilyas[1], S.M. Sapuan[12]
sapuan@upm.edu.my
M.R. Ishak[3]
E.S. Zainudin[2]
M.S.N. Atikah[4]

[1]Laboratory of Biocomposite Technology, Institute of Tropical Forestry and Forest Products, Universiti Putra Malaysia, 43400 UPM Serdang, Selangor, Tel.: +603-89471788; Fax: +603-86567122
[2]Department of Mechanical and Manufacturing Engineering, Universiti Putra Malaysia, 432400 UPM Serdang, Selangor, Malaysia
[3]Department of Aerospace Engineering, Universiti Putra Malaysia, 43400 UPM Serdang, Selangor, Malaysia
[4]Department of Chemical and Environmental Engineering, Universiti Putra Malaysia, 43400 UPM Serdang, Selangor, Malaysia

---

Abstract: *In present work, sugar palm nanofibrillated cellulose (SPNFCs) nanocomposites were casted and utilized as biodegradable reinforcement materials to improve the water barrier properties of the sugar palm starch (SPS)-based films. SPNFCs with three different sizes based on cycling time (5, 10 and 15 cycles denoted as SPS/SPNFCs-5C, SPS/SPNFCs-10C, and SPS/SPNFCs-15C) were incorporated into SPS plasticizers together with glycerol and sorbitol using solution casting method. Then, the SPS and SPS/SPNFCs bionanocomposites were submitted for water absorption and solubility test. Adding of 0.5 wt. % SPNFCs-15C loading had significantly improved water absorption and water solubility properties of the nanocomposite films by 18.84% and 39.38%, respectively, compared with the neat film. This was ascribed by the high compatibility between SPNFCs and SPS matrices, which was supported under the observation of the field emission scanning electron microscopy (FESEM).*

Keywords*: Sugar Palm; Nanofibrillated Cellulose, Nanocomposites; Water Absorption; Water Solubility*

Introduction

Growing environmental awareness along with strict environmental policies have forced plastic manufacturing industry to discover new materials that can substitute synthetic petroleum-based plastic. The utilization of products that were made by conventional petroleum-based polymer had created many potential problems due to their non-renewable sources and ultimate disposal (Ilyas Rushdana, Sapuan Salit, Lamin Sanyang, & Ridzwan Ishak, 2017a). Therefore, one of the alternatives is to substitute this conventional material with biodegradable biocomposites. This is due to their advantages, for instance, sustainable sources, environmentally friendly, more economical, light weight and simplified end-of-life disposal issues. Besides, biocomposite also have become substitute materials in some engineering applications. Briefly,

biocomposite can be defined as combination of two or more elements, where at least one of the elements come from natural resources, either plant, animals or microorganism (M L Sanyang, Ilyas, Sapuan, & Jumaidin, 2018). Concisely, biocomposites are comprised of reinforcement of natural fibre and matrix, either in the form of thermosetting or thermoplastic polymer. Whereas, bionanocomposite is a novel class of nanosized materials, in which they contain the constituent of biological origin and particles with at least one dimension in the range of 1–100 nm. The design of nanoscale structures could enhance the morphology, functional properties and stability of the polymer matrix used in the films and coating (Ilyas, Sapuan, Sanyang, & Ishak, 2016). Cellulose is the most abundant renewable polymer in the world as it is found in plant cell walls (i.e. flax, hemp, kenaf and ramie), and it can also be synthesized by some bacteria (i.e. gluconacetobacter, agrobacterium, pseudomonas, rhizobium, and sarcin) (Ilyas Rushdana, Sapuan Salit, Lamin Sanyang, & Ridzwan Ishak, 2017b). Besides, it has remarkable reinforcing properties due to its abundant hydroxyl group within large surface area. There are two types of nanoreinforcements that can be obtained from plant cellulose; nanofibrillated cellulose (NFC) and nanocrystalline cellulose (NCC). These nanocellulose can be obtained by synthesizing the cellulose chain using either mechanical or chemical or both combined treatment. The NFC have nanosized diameter (2-20 nm, depending on the origin), with several micrometer length. Each NFC is formed by aggregation of elementary fibrils, which are made of alternating crystalline and amorphous regions. The crystalline region, also known as nanocrystalline cellulose (NCC) can be isolated via strong acid hydrolysis. NCC has nanosized diameter ranging 8-20 nm, with length ranging from 100 nm up to 1-2 µm, resulting in high aspect ratio. Moreover, these nanofibre were reported to have high modulus (150 GPa) and high strength (10 GPa), in which they are very suitable for reinforcement purposes.

Recently, sugar palm fibre (SPF) has gained many attentions from many researchers due to its high proportion of cellulose which can be readily isolated from other component, such as hemicellulose and lignin. The cellulose was obtained from SPF by delignification and mercerization process (Ilyas, Sapuan, Ishak, & Zainudin, 2017). Ilyas et al., (2018) isolated nanocrystalline cellulose from SPF via hydrolysis treatment for the purpose of reinforcement with polymer matrix. Malainine (2005) studied the effect of nanofibrillated cellulose from *Opuntia ficus-indica* parenchyma cell reinforced on starch matric and had revealed that the reinforcement of NFC enhanced their mechanical and water barrier properties. However, no previous research works had been devoted to the development of sugar palm nanofibrillated cellulose (SPNFCs) reinforced thermoplastic starch matrix of which was derived from natural resources. In this study, biopolymer used for the matrix is extracted from sugar palm tree (sugar palm starch) and the nanofiller SPNFCs was also isolated from sugar palm fibre via taken from the same tree (*Arenga pinnata*). A truly environmental-friendly biocomposites are obtained from a single tree.

It is well acknowledged that biocomposites provide superb benefits to human mankind. Nevertheless, there are some problems associated with natural polymer matrices, which are associated with moisture absorption due to the abundance of hydroxyl groups in their structure. The moisture that was built-up in biocomposites can lead to physical degradation such as thickness swelling and dimensional changes, as well as lowering the mechanical properties of film. The thickness swelling can lead to reduction in the adhesion between the fibres and matrix. As a consequence, the moisture absorption initiates undesirable effect to the mechanical properties of biocomposites. Therefore, water absorption test is generally performed for quality control purposes of bionanocomposite materials. In the present study, nanocomposite materials

were prepared from sugar palm nanofibrillated cellulose obtained from sugar palm fibre and a sugar palm starch via solution casting method. The goal of this work is to study the effect of nanocellulose size on the water absorption properties and the water solubility behaviour of thermoplastic starch. Sugar palm starch was used as a matrix with water, sorbitol and glycerol as a plasticizer and with SPNFCs-5 cycles, SPNFCs-10 cycles, and SPNFCs-15 cycles, as reinforcements.

Experimental

Materials

Sugar palms fibre (SPF) and sugar palm starch (SPS) were extracted and collected from sugar palm trees at Jempol, Negeri Sembilan (Malaysia). Sodium hydroxide, sodium chlorite (80% purity), acetic acid, sorbitol and glycerol plasticizer were supplied by Sue Evergreen Sdn Bhd (Semenyih, Malaysia).

Preparation of SPNFCs

Sugar palm fibres (SPF) were collected from different part of sugar palm trees (sugar palm frond, trunks, ijuk and bunch), as it wrapped around the tree trunk from top to bottom. A knife was used to remove SPF from the tree. Then, a Fritsch pulverisette mill was used for grinding and screening to gain an even size of SPF particles, about an average of 2 mm. The cellulose preparation procedures were reported elsewhere (Sanyang et al., 2016). Briefly, the SPF were extracted using two main processes, known as delignification and mercerization. The initial and second processes were conducted in accordance with ASTM D1104-56 (1978) and ASTM D1103-60 (1977) for the removal of lignin and hemicellulose, respectively, resulted in production of sugar palm celluloses (SPC). SPNFCs were prepared via mechanical treatment. Sugar palm cellulose (SPC) was refined for 20,000 revolutions in a PFI-mill according to ISO 5264-2:2002. Then, the fibres were isolated by the process of high pressurized homogenization (HPH). Typically, 1.8 % fibre suspension in water was processed in a high pressurized homogenizer (GEA Niro Soavi, Panda NS1001L, Parma, Italy) at 500 bar. Samples were passed with various cycle of 5, 10 and 15 times through an intensifier pump. The nanofibre with different cycles of 5, 10 and 15 times were denoted as SPS/SPNFCs-5C, SPS/SPNFCs-10C, and SPS/SPNFCs-15C, respectively. Through this process, fibres were broken down from macro-sized structure to nano-sized structures, forming slurries of nanofibrillated cellulose. The NFCs suspensions were then collected and were freeze-dried at -110 ºC using ethylene gas and stored at cool place prior to sample analysis and nanocomposite films preparation.

Preparation Of The SPS/Spnfcs Nanocomposite Films

The fabrication of plasticizer sugar palm starch/ sugar palm nanofibrillated celluloses (SPS/SPNFCs) composite film was based on a solution casting methods. In order to obtain homogenous nanocomposite film, starch, sorbitol, glycerol, SPNFCs and distilled water were mixed and sonicated together (Muhammed Lamin Sanyang et al., 2016). Briefly, a solution of SPNFCs was prepared by mixing and sonicating it with 190 mL of distilled water with known concentration of SPNFCs (0.5 wt. % on the starch basis). The SPNFCs content was fixed at 0.5 wt. % based on the starch basis. Then, 10 g of SPS and plasticizer (30% on the starch basis) were mixed with the SPNFCs solution and stirred at 1000 rpm for 20 minutes at 85 ºC in a

disperser for the starch to be gelatinized. The ratio of plasticizer used was 1:1 with combination of sorbitol and glycerol ratio. Then, the film-forming suspension was left to cool down and was placed under vacuum to remove air bubbles inside the suspension prior to casting of the suspension by putting 45 g of the suspension into petri dishes sized of 15-cm diameter. The petri dishes containing the film-forming solution were placed in an oven at 40°C overnight. SPS films were prepared without SPNFCs served as the control (designed as SPS film), whereas the nanocomposite film with different cycles of 5, 10 and 15 times were denoted as SPS/SPNFCs-5C, SPS/SPNFCs-10C, and SPS/SPNFCs-15C, respectively. The resulting films were kept in the desiccator at room temperature for a week to ensure the equilibrium of the water content in the films prior any characterization tests.

Transmission Electron Microscopy (TEM)

The structure and diameter measurement of sugar palm nanofibrillated cellulose (SPNFCs) were determined by Hitachi H-7100 transmission electron microscopy (Hitachi, Tokyo, Japan). The images was obtained from high-resolution transmission electron microscopy (HRTEM). Prior to the testing by HRSEM, samples were placed on the surface of copper grid coated with a thin carbon film. After that, the samples were stained with uranyl acetate for 1 min and allowed to dry at room temperature. The purpose of the staining step was to get better visual and contrast image via TEM.

Field Emission Scanning Electron Microscopy (Fesem)

Surface characteristics of the SPS and SPS/SPNFCs films were determined by a FEI NOVA NanoSEM 230 machine (FEI, Brno-Černovice, Czech Republic) with an accelerating voltage of 3 kV in order to observe the degradation phenomenon after the biodegradability test. Before being tested by FESEM, samples were coated with gold to avoid charging using an argon plasma metallizer (sputter coater K575X) (Edwards Limited, Crawley, United Kingdom) (Sheltami et al., 2012).

Water Absorption

Water absorption analysis was carried out in accordance to ASTM D 570-98. Firstly, the samples were dried for 24 h at 50 °C and cooled in desiccator to gain even weight. Then, the films were weighed and soaked in distilled water at room temperature. After a particular soaking period, the films were taken out of the water and wiped with a cloth and weighed again. The differences between the initial and final masses of the films were calculate using Eq. (1) (Edhirej et al., 2017):

$$\text{Water absorption (\%)} = \frac{M_{final} - M_{initial}}{M_{initial}} \times 100 \quad (1)$$

Water Solubility

Three samples from each formulation of the nanocomposite films (30 mm × 10 mm) were dried in an vacuum oven 105 °C for 24 h, following the method of Shojaee et al. (2013). The samples were weighed to determine the initial dry matter of each film (W_i). Each sample was immersed in 50 mL of distilled water in a beaker that was sealed and periodically stirred under constant agitation at 23 ± 2 °C for 6 h. Finally, the insoluble portion of the film sample was removed,

oven dried at 105 ºC for 24 h and weighed to determine the weight of the solubilized dry matter (W_o). Water solubility of each film was determined by Eq. (2) .

$$\text{Solubility (\%)} = \left[\frac{W_i - W_o}{W_i}\right] \times 100 \quad (2)$$

Experimental Result and Discussion

Physical Properties of Sugar Palm Nanofibrillated cellulose (SPNFCs)

The physical properties of the sugar palm nanofibrillated cellulose (SPNFCs) from different cycle of High Pressurized Homogenizer (HPH) treatment were determined using Image J software, Origin 7.5 software and a Gaussian line shape to the peaks of the images collected from the TEM analysis.

Table 1: Physical Properties of SPNFCs-5C, SPNFCs-10C and SPNFCs-15C

Fibres	Diameter (nm)
Sugar Palm Cellulose (SPC)	11870
SPNFCs-5C	21.37 ± 6.91
SPNFCs-10C	11.54 ± 2.77
SPNFCs-15C	5.5 ± 0.99

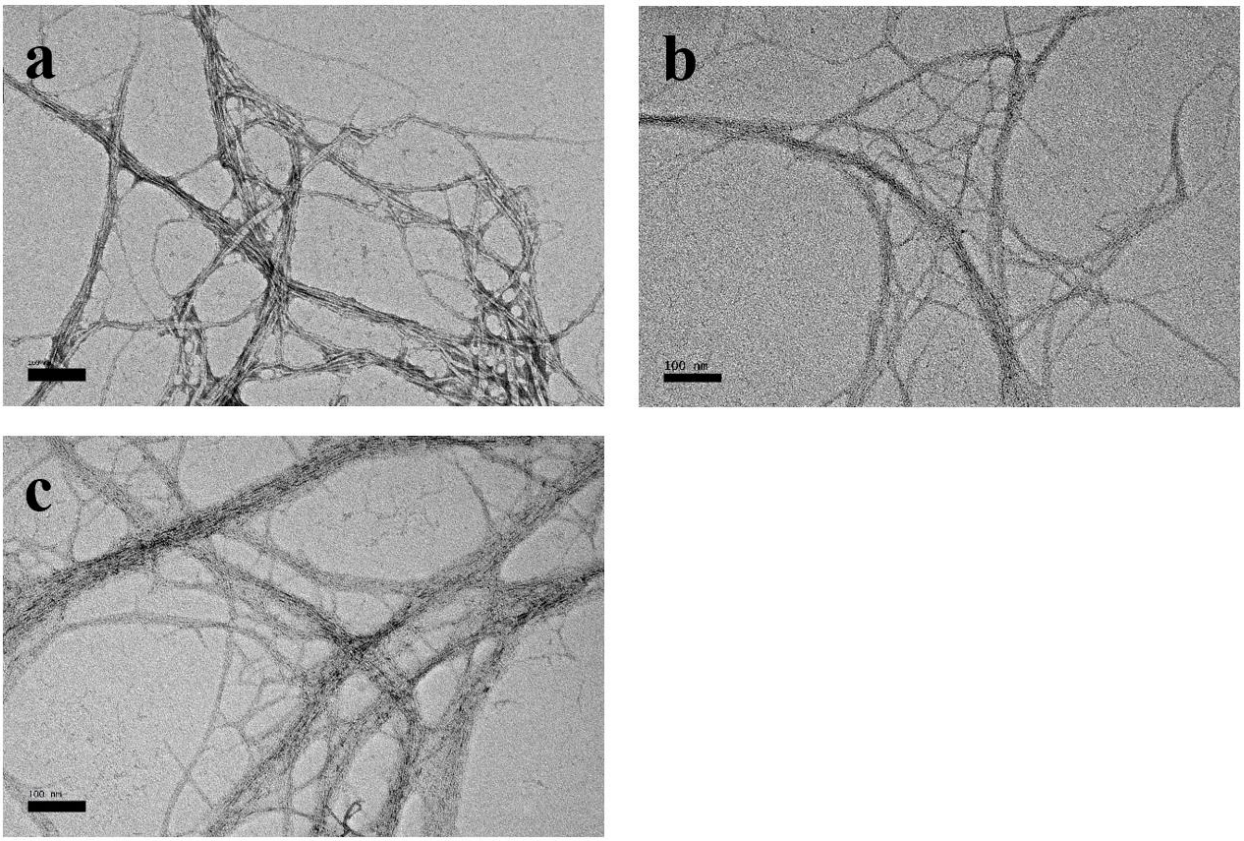

Figure 1: TEM micrographs of the (a) SPNFCs-5C, (b) SPNFCs-10C and (c) SPNFCs-15C.

Table 1 and Figure 1 show the physical properties of nanofibrillated cellulose and TEM micrograph, respectively. TEM micrograph of sugar palm nanofibrillated cellulose (SPNFCs) (Figure 1) revealed their nanometric dimensions. The diameter of the SPNFCs-5C, SPNFCs-10C and SPNFCs-15C were approximately 21.37 ± 6.91 nm, 11.54 ± 2.77 nm, and 5.5 ± 0.99 nm, respectively. The diameter analyzed for SPNFCs-15C were similar to the nano-structures that were isolated from other agro-waste sources such as such as banana (5 nm) (Zuluaga, Putaux, Restrepo, Mondragon, & Gañán, 2007), flax fibre (5 nm) (Bhatnagar, 2005), potato tuber cell (5 nm) (Alain et al., 2000), and wider than prickly pear fruit (2-5 nm)(Habibi et al., 2009). Besides that, SPNFCs-10C have similar diameter with cassava bagasse (2-11 nm) (Teixeira et al., 2009) and raw cotton linter (*Gossypium hirsutum*) (12 nm) (Morais et al., 2013). Whereas, the SPNFCs-5C have similar diameter with pineapple leaf (30 nm) (Balakrishnan et al., 2017), sugarcane bagasse (35 nm) (Mandal & Chakrabarty, 2011), wheat straw (30-70 nm) (Kaushik, Singh, & Verma, 2010), rutabaga (80 nm) (Bhatnagar, 2005). These resultant images revealed the use of high pressurized homogenization treatment on sugar palm fibres and certified that the aqueous suspensions contained sugar palm NFCs residing mostly of individual and some aggregates.

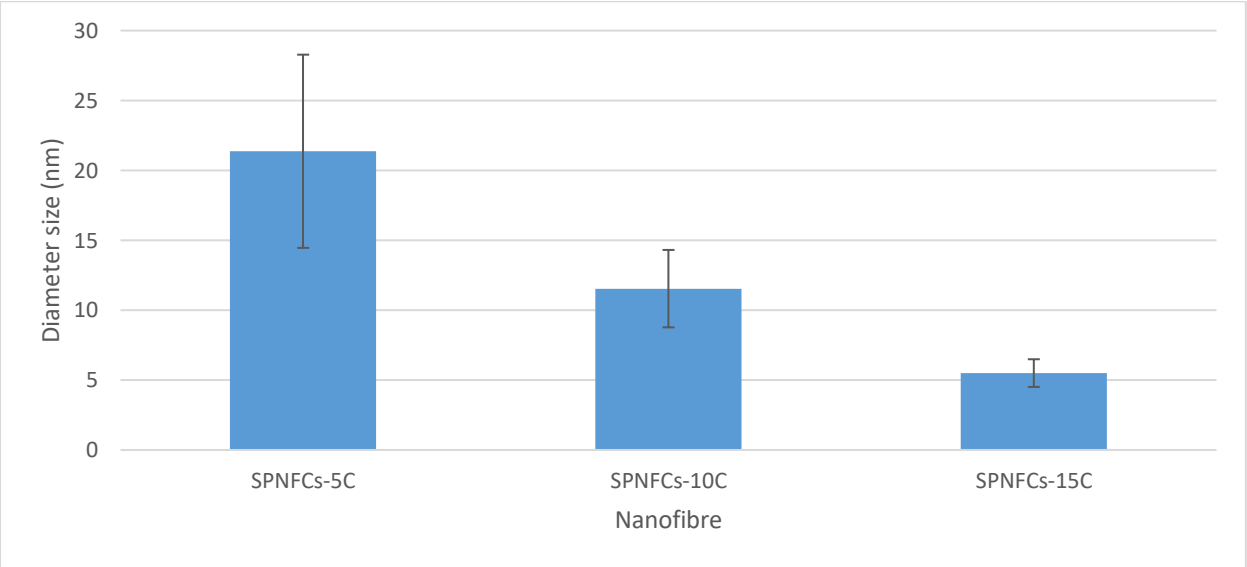

Figure 2: Length and diameter of SPNFCs-5C, SPNFCs-10C and SPNFCs-15C.

Figure 2 shows the diameter of SPNFCs-5C, SPNFCs-10C and SPNFCs-15C. The differences between the SPNFCs-5C, SPNFCs-10C and SPNFCs-15C were the reduction of diameter. Based on Table 1, the reduction of the SPNFCs-5C diameter from SPC was 99.82%. This was attributed by breaking the interfibrillar hydrogen bond between nanofibril via high pressurize homogenizer treatment on SPC. The process continued for SPNFCs-10C and SPNFCs-15C for 10 cycles and 15 cycles, indicated the changes in the size of the SPNFCs which was reduced by 46.00 % and 74.26 %, respectively compared to SPNFCs-5C. This was also caused by the longer reaction HPH cycling via mechanical treatment on the fibres, which loosening the interfibrillar hydrogen bonding within nanofibres. Besides, longer cycling time could reduce the structure (diameter) of SPNFCs. Thus, the longer the cycling times of HPH, the smaller the diameter of the nanofibres produced. Thus, in order to defibrillate the sugar palm nanofibrils, the interfibrillar hydrogen bond energy should be beaten separately rather than to cut them. The differences of the diameter obtained was depending notably on the homogenization pressure,

number of passes, sample pretreatment as well as on the fibres origin (Abdul Khalil, Bhat, & Yusra, 2012; Besbes, Rei, & Boufi, 2011).

Surface Morphology of Bionanocomposite Film

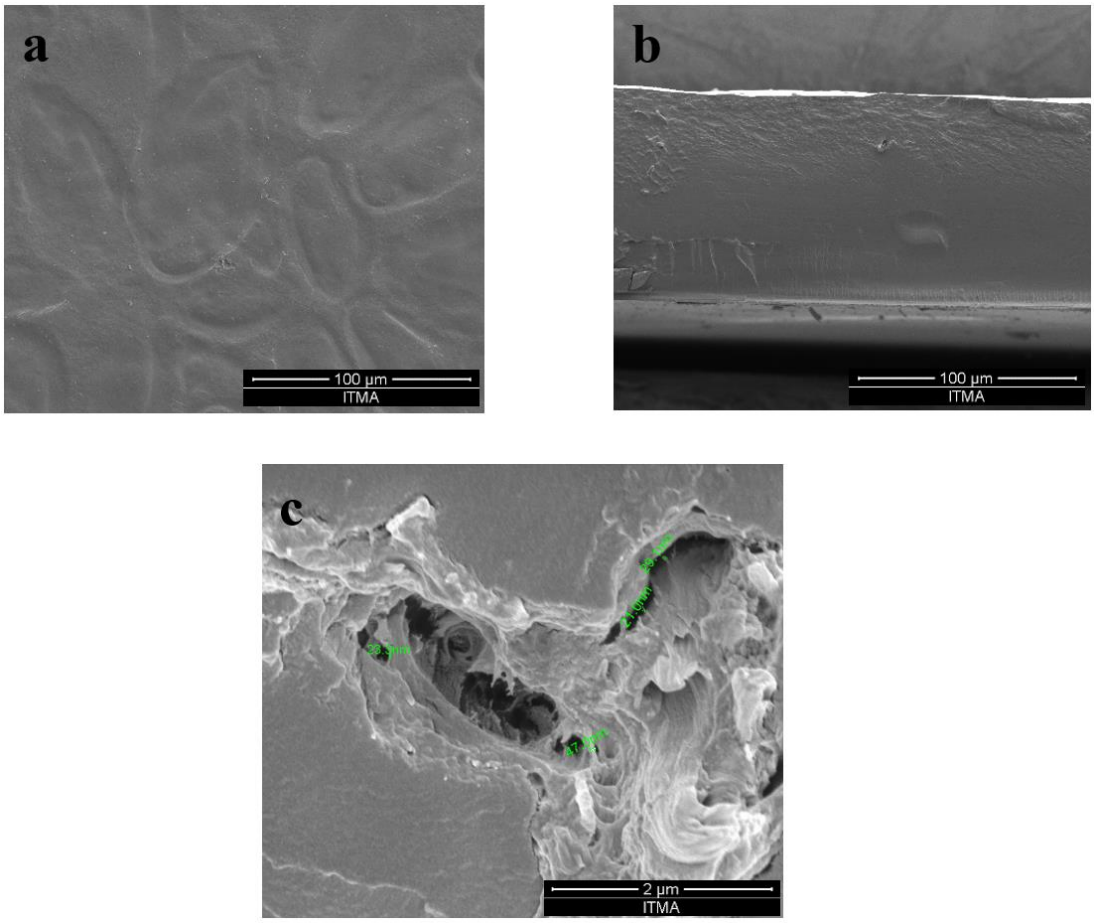

Figure 3: Surface morphology of SPF/SPNFCs bionanocomposite (a) surface, (b) cross-sectional (100 µm), and (c) cross-sectional (2 µm).

Figure 3 showed the surface morphology of SPS-based films reinforced SPNFCs by using FESEM. The Figure 3 (a) micrograph of the SPS/SPNFCs films showed a smooth and continuous surface with no trace of starch granular or cracks and agglomerations of SPNFCs. Besides that, high dispersion of SPNFCs (Figure 3(c)) is a good sign of strong interfacial adhesion between the two components of the SPS/SPNFCs nanocomposite film. These good distributions translate into high resistance of water barrier properties, which can be indicated

through the water absorption and water solubility test. Moreover, it has been stated by Bilbao-Sainz et al. (2011) that the functional properties of the composite was enhanced when the fibres well-dispersed into the polymeric matrix.

Water absorption

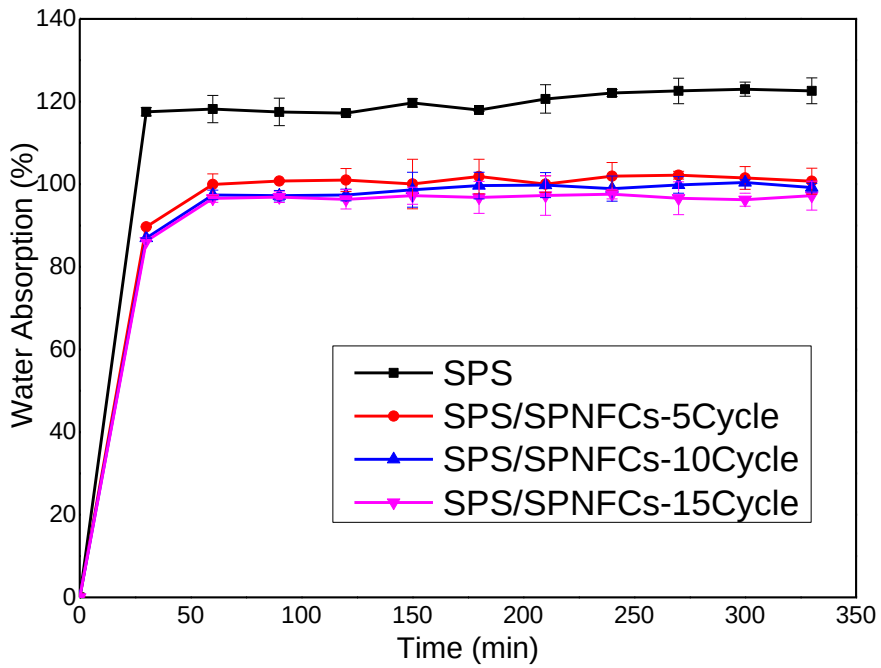

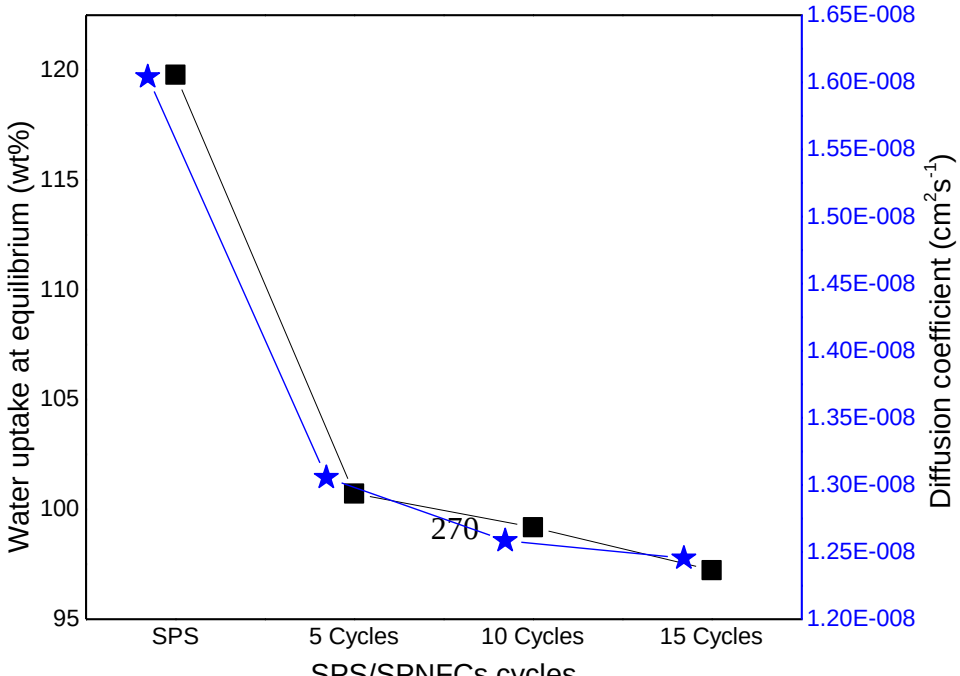

Figure 4: (a) Water absorption and (b) water uptake at equilibrium (■) and diffusion coefficient (★) of the SPS and SPS/SPNFCs nanocomposite film as function of SPNFCs content.

One of the most crucial study in biofilm is water absorption which indirectly attributed to the properties of water that would acts as a plasticizer in biofilm. Figure 4 revealed the percentage of water absorption of SPNFCs-5C, SPNFCs-10C and SPNFCs-15C nanocomposite films. In Figure 4(a), it can be seen that the neat SPS gave the highest percentage of water absorption, followed by SPS/SPNFCs-5C, SPS/SPNFCs-10C, and SPS/SPNFCs-15C, with value of 119.79%, 100.72%, 99.18% and 97.23%, respectively. This phenomenon showed that biofilm reinforced with SPNFCs has lower hydrophilicity. The water absorption of the neat SPS biofilm was higher than reinforced SPNFCs that was due to the presence of hydroxyl groups in film molecules. Film with higher concentration of starch matrix tend to absorb more water compared to biofilm that have low concentration of starch (Sahari, Salit, Zainudin, & Maleque, 2014). Moreover, as the diameter size of SPNFCs reduced via HPH cycling process, the percentage of the water absorption also decreased. Film with big particle size of SPNFCs exhibited greater tendency to absorb water, which possibly due to a lower response to stress (Edhirej, Sapuan, Jawaid, & Zahari, 2017a). In this work, water absorption tests revealed that stabilizing the mixtures with SPNFCs decreased the water absorption capacity. This was attributed to the strong adhesion between the SPNFCs and SPS in which they tend to form strong hydrogen bonding via the physical interlocking with non-polar matrices and the OH-groups of hydrophilic polymer matrices (Majeed et al., 2013; Minelli et al., 2010). The result of this experiment conducted are quite similar to those from previous work (Sahari et al., 2014).

Besides that, the weight gain because of water absorption of all bionanocomposite films were linearly increased with the increase of immersion time and became more constant after 1 h, following a Fickian diffusion process. Based on the Figure 4 (a) also, the water uptake-*t* curves show two well-separated zones, in which at shorter times, $t < 1$ h, the kinetic of absorption is very fast, however at extended times, $t > 1$ h, the kinetic of absorption is very slow and lead to a flat line, equivalent to the water uptake equilibrium. Generally, water absorption is influenced by fibre orientation, permeability, surface protection, exposed surface area, diffusivity, temperature, and fibre content (Vilay, Mariatti, Mat Taib, & Todo, 2008). However in this work, fibre content and temperature were kept constant, whereas the SPNFCs nanofibres orientation in the SPS biofilm was assumed to be identical due to the same processing parameters.

The water uptake at equilibrium of neat SPS biofilm and SPS/SPNFCs nanocomposite films as a function of SPNFCs cycling process was plotted in Fig. 4(b). From the Figure stated, it can be seen that neat SPS film absorbed about 119.79 wt. %. It can be simply explained that 1 g of starch could absorbed 2.198 g of water. The water uptake equilibrium decreased non-lineally with increment of SPNFCs nanofibres HPH cycle, and about 97.23 wt. % of water uptake was observed for the SPS/SPNFCs-15C nanocomposites film. Compared with neat SPS, the nanocomposite film showed a lowered swelling capacity. The kinetic study of the sorption in

polymers as a mean of resolving the diffusion coefficient has been widely used. The partial differential equation for mass transfer (diffusion) is expressed as (Vergnaud, 1991).

$$\frac{\partial C}{\partial t} = D(\frac{\partial^2 C}{\partial x^2})$$

Where, C is the concentration at time *t*, and distances *x*, and distance *x*, from the polymer surface. For an infinite slab with a constant *D* and at short times:

$$\frac{M_t - M_0}{M_\infty} = \frac{4}{L}\left[\frac{Dt}{\pi}\right]^{1/2}$$

Where, M_t and M_0 are the weight of the sample at time *t* and the initial weight of the sample, respectively. M_∞ is the equilibrium water sorption, and *L* is the thickness of the sample.

The ratio of the amount of water absorbed by the specimen at time *t*, $(M_t - M_0)/ M_\infty$, was plotted as a function of $t^{1/2}$, and the diffusion coefficient (D) was, therefore, calculated from the slope of the initial linear part of the resulting curves. As shown in Fig. 4(b), the neat SPS film showed the highest D value of about $1.586 \times 10^{-8} cm^{-10} s^{-1}$. The neat SPS was observed to have higher D value compared to nanocomposite films, in which this phenomena could be attributed to the hydrophilic behavior of SPS, in which chemical properties of starch itself is composed of multi-hydroxyl polymer with three hydroxyl groups per monomer (Ma, Yu, & Kennedy, 2005). Interestingly, with an increase of nanofillers cycle in the SPS biopolymer from 5 cycles to 15 cycles, the D value of the nanocomposites decreases from $1.586 \times 10^{-8}\ cm^{-10} s^{-1}$ to $1.442 \times 10^{-8}\ cm^{-10} s^{-1}$. This spectacle occurred due to the high surface area and abundant hydroxyl group of SPNFCs which indirectly caused strong adhesion between the nanofiller/ matrix adhesion (SPNFCs and SPS). As a result, the water becomes harder to penetrate and stored within the starch polymer matrix. Therefore, increase in the SPNFCs concentration, decreased the hydrophilic of SPS/SPNFCs nanocomposite films. Moreover, these strong hydrogen bonding interactions within the nanocomposite films tend to stabilize the starch matrix when it is exposed to highly moist atmosphere. High crystallization of SPNFCs concentration in the nanocomposite also might be attributed to the decrement of the diffusion coefficient and water uptake at equilibrium of the biofilms (Lu, Weng, & Cao, 2005). Therefore, the increase of HPH cycling of SPNFCs nanofiller, would decrease the SPNFCs diameter size, which indirectly resulted in low water uptake when reinforced with thermoplastic starch. This summarized that the biofilms reinforced SPNFCs are less water sensitive that neat SPS.

Besides that, the interface between glycerol plasticizer and starch matrix could promote moisture adsorption because of the dimensional changes in the area where the adhesion between interfaces (glycerol-starch) is poor, hence forming a path that speed up the water molecules accumulation. Interestingly, due to the chemical similarity between SPNFCs and SPS, structural and interface defects was reduced dramatically, hence forming a strong resistance for water molecules to pass through or stored in the film. It can be concluded that the nano-reinforcement process that arise within the structure of polymer matrix had influenced the permeation process that depends mainly on the formation of the tortuous path by SPNFCs and diffusion coefficient, whereas at high moisture contents still produces a barrier effect on the movement of water molecule (Slavutsky & Bertuzzi, 2014).

Film Solubility In Water

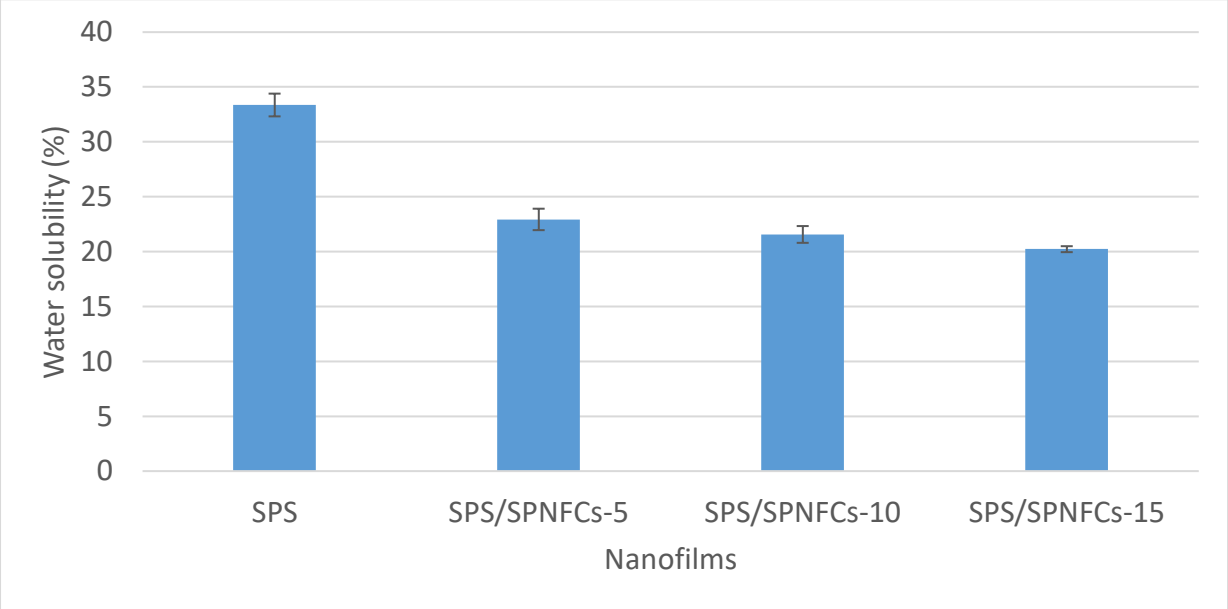

Figure 5: Water solubility of the SPS and SPS/SPNFCs nanocomposite films.

One of the main property of films for food packaging applications is film solubility. Several potential uses may require water insolubility to improve water resistance and product integrity for storage of food safety. The problems arouse in using starch as film packaging is the water resistance properties, explained by water solubility, in which the film has high water solubility. Thus, the reinforcement of SPNFCs within SPS matrix polymer is predicted to overcome this limitation. The film solubility of neat SPS and SPS/SPNFCs nanocomposite films are displayed in Figure 5. It can be seen that all biofilms did not remain intact once they are immersed in water.

The water solubility behavior depends on the diameter size of nanofiller, in which the more the HPH cycle, the smaller the SPNFCs diameter. The water solubility decreased with the diameter of SPNFCs. The addition of SPNFCs reduced the films solubility from 33.36 % to 20.22 %. The SPS/ SPNFCs-15C showed the lowest film solubility value of 20.22%, which proved that the films have good water stability. Besides, it was also an indication of strong interactions between nanofiller-SPNFC and SPS starch chains within the biofilm matrix. The terrific ability of SPNFCs in interacting with starch chains were attributed to the interaction of abundance of hydroxyl groups of SPNFCs and starch hydrogen bond. Hence, these interactions provide resistance and stability to SPS/SPNFCs films. Moreover, according to Tunc et al. (2007), these interfaces enhanced the cohesive properties of the biopolymer matrix and reduced the sensitivity of water due to water molecules were not able to break these strong bonds. Rhim and Ng (2007) in different report, reported that the water solubility resistance were improved when it was reinforced with nanofillers, in which this was attributed to the strong formation of hydrogen bond between hydroxyl groups of the biopolymer and nanofiller. These results were also supported by Abdollahi et al., (2013) in their research project on alginate nanocomposite films. It can be summarized that the reinforcement of SPNFCs improved the water resistance properties of the films which was a relevant characteristic for food packaging materials to improve shelf-life of food products.

Conclusion

Sugar palm fibre (*Arenga pinnata*) were successfully individualized via the method of delignification, mercerization and high pressurize homogenizer process under a shear action to produce nanofibrillated cellulose suspensions. Individualized nanofibrillated cellulose possessed 'spaghetti-like' form with high aspect ratio fibres almost 5-20 nm in diameter. Increasing HPH cycling process would decrease the SPNFCs diameter. The resulting suspension was utilized to process bionanocomposite with combination of both matric and natural fibres that are obtained from less utilized parts of sugar palm tree. It was observed that the water absorption effect on the SPS and SPS/SPNFCs bionanocomposite had brought a significant improvement when the size of the SPNFCs were reduced. Whereas, the water solubility test revealed that the SPS soluble faster as compared to SPS/SPNFCs bionanocomposites. Thus, this bionanocomposite shows improvement in water absorption and water solubility properties for packaging materials application.

Acknowledgement

The authors would like to thank Universiti Putra Malaysia for the financial support through the Graduate Research Fellowship (GRF) scholarship, Universiti Putra Malaysia Grant scheme Hi-COE (6369107) and FRGS/1/2017/TK05/UPM/01/1 (5540048). The authors are grateful to Dr. Muhammed Lamin Sanyang for guidance throughout the experiment. The authors also thank Dr. Rushdan Ibrahim for their advice and fruitful discussions.

References

Abdollahi, M., Alboofetileh, M., Rezaei, M., & Behrooz, R. (2013). Comparing physico-mechanical and thermal properties of alginate nanocomposite films reinforced with organic and/or inorganic nanofillers. *Food Hydrocolloids*, *32*(2), 416–424. https://doi.org/10.1016/j.foodhyd.2013.02.006

Abdul Khalil, H. P. S., Bhat, A. H., & Yusra, A. F. I. (2012). Green composites from sustainable cellulose nanofibrils: A review. *Carbohydrate Polymers*, *87*(2), 963–979. https://doi.org/10.1016/j.carbpol.2011.08.078

Alain, D., Danièle, D., & Michel, R. V. (2000). Cellulose microfibrils from potato tuber cells: Processing and characterization of starch-cellulose microfibril composites. *Journal of Applied Polymer Science*, *76*(14), 2080–2092. https://doi.org/10.1002/(SICI)1097-4628(20000628)76:143.0.CO;2-U

Balakrishnan, P., Sreekala, M. S., Kunaver, M., Huskić, M., & Thomas, S. (2017). Morphology, transport characteristics and viscoelastic polymer chain confinement in nanocomposites based on thermoplastic potato starch and cellulose nanofibers from pineapple leaf. *Carbohydrate Polymers*, *169*, 176–188. https://doi.org/10.1016/j.carbpol.2017.04.017

Besbes, I., Rei, M., & Boufi, S. (2011). Nanofibrillated cellulose from Alfa , Eucalyptus and Pine fibres : Preparation , characteristics and reinforcing potential. *Carbohydrate Polymers*, *86*(3), 1198–1206. https://doi.org/10.1016/j.carbpol.2011.06.015

Bhatnagar, A. (2005). Processing of Cellulose Nanofiber-reinforced Composites. *Journal of Reinforced Plastics and Composites*, *24*(12), 1259–1268. https://doi.org/10.1177/0731684405049864

Edhirej, A., Sapuan, S. M., Jawaid, M., & Zahari, N. I. (2017a). Effect of various plasticizers and concentration on the physical, thermal, mechanical, and structural properties of

cassava-starch-based films. *Starch/Staerke*, *69*(1–2), 1–11. https://doi.org/10.1002/star.201500366

Edhirej, A., Sapuan, S. M., Jawaid, M., & Zahari, N. I. (2017b). Preparation and characterization of cassava bagasse reinforced thermoplastic cassava starch. *Fibers and Polymers*, *18*(1), 162–171. https://doi.org/10.1007/s12221-017-6251-7

Habibi, Y., Mahrouz, M., & Vignon, M. R. (2009). Microfibrillated cellulose from the peel of prickly pear fruits. *Food Chemistry*, *115*(2), 423–429. https://doi.org/10.1016/j.foodchem.2008.12.034

Ilyas, R. A., Sapuan, S. M., & Ishak, M. R. (2018). Isolation and characterization of nanocrystalline cellulose from sugar palm fibres (Arenga Pinnata). *Carbohydrate Polymers*, *181*(November), 1038–1051. https://doi.org/10.1016/j.carbpol.2017.11.045

Ilyas, R. A., Sapuan, S. M., Ishak, M. R., & Zainudin, E. S. (2017). Effect of Delignification on the Physical, Thermal, Chemical, and Structural Properties of Sugar Palm Fibre. *BioResources*, *12*(4), 8734–8754. https://doi.org/10.15376/biores.12.4.8734-8754

Ilyas, R. A., Sapuan, S. M., Sanyang, M. L., & Ishak, M. R. (2016). Nanocrystalline cellulose reinforced starch-based nanocomposite: A review. In *5th Postgraduate Seminar on Natural Fiber Composites* (pp. 82–87). Serdang, Selangor: Universiti Putra Malaysia. Retrieved from https://www.researchgate.net/publication/315675302_Nanocrystalline_cellulose_reinforced_starch-based_nanocomposites_A_Review

Ilyas Rushdana, A., Sapuan Salit, M., Lamin Sanyang, M., & Ridzwan Ishak, M. (2017a). Nanocrystalline Cellulose As Reinforcement For Polymeric Matrix Nanocomposites And Its Potential Applications: A Review. *Current Analytical Chemistry*, *13*. https://doi.org/10.2174/1573411013666171003155624

Ilyas Rushdana, A., Sapuan Salit, M., Lamin Sanyang, M., & Ridzwan Ishak, M. (2017b). Nanocrystalline Cellulose As Reinforcement For Polymeric Matrix Nanocomposites And Its Potential Applications: A Review. *Current Analytical Chemistry*, *13*, 1–54. https://doi.org/10.2174/1573411013666171003155624

Kaushik, A., Singh, M., & Verma, G. (2010). Green nanocomposites based on thermoplastic starch and steam exploded cellulose nanofibrils from wheat straw. *Carbohydrate Polymers*, *82*(2), 337–345. https://doi.org/10.1016/j.carbpol.2010.04.063

Lu, Y., Weng, L., & Cao, X. (2005). Biocomposites of Plasticized Starch Reinforced with Cellulose Crystallites from Cottonseed Linter. *Macromolecular Bioscience*, *5*(11), 1101–1107. https://doi.org/10.1002/mabi.200500094

Ma, X., Yu, J., & Kennedy, J. F. (2005). Studies on the properties of natural fibers-reinforced thermoplastic starch composites. *Carbohydrate Polymers*, *62*(1), 19–24. https://doi.org/10.1016/j.carbpol.2005.07.015

Majeed, K., Jawaid, M., Hassan, A., Abu Bakar, A., Abdul Khalil, H. P. S., Salema, A. A., & Inuwa, I. (2013). Potential materials for food packaging from nanoclay/natural fibres filled hybrid composites. *Materials & Design*, *46*, 391–410. https://doi.org/10.1016/j.matdes.2012.10.044

Malainine, M. E., Mahrouz, M., & Dufresne, A. (2005). Thermoplastic nanocomposites based on cellulose microfibrils from Opuntia ficus-indica parenchyma cell. *Composites Science and Technology*, *65*(10), 1520–1526. https://doi.org/10.1016/j.compscitech.2005.01.003

Mandal, A., & Chakrabarty, D. (2011). Isolation of nanocellulose from waste sugarcane bagasse (SCB) and its characterization. *Carbohydrate Polymers*, *86*(3), 1291–1299. https://doi.org/10.1016/j.carbpol.2011.06.030

Minelli, M., Baschetti, M. G., Doghieri, F., Ankerfors, M., Lindström, T., Siró, I., & Plackett,

D. (2010). Investigation of mass transport properties of microfibrillated cellulose (MFC) films. *Journal of Membrane Science*, *358*(1–2), 67–75. https://doi.org/10.1016/j.memsci.2010.04.030

Morais, J. P. S., Rosa, M. D. F., de Souza Filho, M. de sá M., Nascimento, L. D., do Nascimento, D. M., & Cassales, A. R. (2013). Extraction and characterization of nanocellulose structures from raw cotton linter. *Carbohydrate Polymers*, *91*(1), 229–235. https://doi.org/10.1016/j.carbpol.2012.08.010

Rhim, J.-W., & Ng, P. K. W. (2007). Natural Biopolymer-Based Nanocomposite Films for Packaging Applications. *Critical Reviews in Food Science and Nutrition*, *47*(4), 411–433. https://doi.org/10.1080/10408390600846366

Sahari, J., Salit, M. S., Zainudin, E. S., & Maleque, M. A. (2014). Degradation Characteristics of SPF/SPS Biocomposites Fabrication of SPF/SPS biocomposites. *Fibres and Textiles in Eastern Europe*, *22*(5107), 96–98.

Sanyang, M. L., Ilyas, R. A., Sapuan, S. M., & Jumaidin, R. (2018). Sugar Palm Starch-Based Composites for Packaging Applications. In *Bionanocomposites for Packaging Applications* (pp. 125–147).

Sanyang, M. L., Sapuan, S. M., Jawaid, M., Ishak, M. R., & Sahari, J. (2016). Effect of sugar palm-derived cellulose reinforcement on the mechanical and water barrier properties of sugar palm starch biocomposite films. *BioResources*, *11*(2), 4134–4145. https://doi.org/10.15376/biores.11.2.4134-4145

Sheltami, R. M., Abdullah, I., Ahmad, I., Dufresne, A., & Kargarzadeh, H. (2012). Extraction of cellulose nanocrystals from mengkuang leaves (Pandanus tectorius). *Carbohydrate Polymers*, *88*(2), 772–779. https://doi.org/10.1016/j.carbpol.2012.01.062

Shojaee-Aliabadi, S., Hosseini, H., Mohammadifar, M. A., Mohammadi, A., Ghasemlou, M., Ojagh, S. M., … Khaksar, R. (2013). Characterization of antioxidant-antimicrobial κ-carrageenan films containing Satureja hortensis essential oil. *International Journal of Biological Macromolecules*, *52*, 116–124. https://doi.org/10.1016/j.ijbiomac.2012.08.026

Slavutsky, A. M., & Bertuzzi, M. A. (2014). Water barrier properties of starch films reinforced with cellulose nanocrystals obtained from sugarcane bagasse. *Carbohydrate Polymers*, *110*, 53–61. https://doi.org/10.1016/j.carbpol.2014.03.049

Teixeira, E. de M., Pasquini, D., Curvelo, A. A. S., Corradini, E., Belgacem, M. N., & Dufresne, A. (2009). Cassava bagasse cellulose nanofibrils reinforced thermoplastic cassava starch. *Carbohydrate Polymers*, *78*(3), 422–431. https://doi.org/10.1016/j.carbpol.2009.04.034

Tunc, S., Angellier, H., Cahyana, Y., Chalier, P., Gontard, N., & Gastaldi, E. (2007). Functional properties of wheat gluten/montmorillonite nanocomposite films processed by casting. *Journal of Membrane Science*, *289*(1–2), 159–168. https://doi.org/10.1016/j.memsci.2006.11.050

Vergnaud, J. M. (1991). Liquid transport processes in polymeric materials: modeling and industrial applications. *Prentice Hall*.

Vilay, V., Mariatti, M., Mat Taib, R., & Todo, M. (2008). Effect of fiber surface treatment and fiber loading on the properties of bagasse fiber-reinforced unsaturated polyester composites. *Composites Science and Technology*, *68*(3–4), 631–638. https://doi.org/10.1016/j.compscitech.2007.10.005

Zuluaga, R., Putaux, J. L., Restrepo, A., Mondragon, I., & Gañán, P. (2007). Cellulose microfibrils from banana farming residues: Isolation and characterization. *Cellulose*, *14*(6), 585–592. https://doi.org/10.1007/s10570-007-9118-z

Proceeding: 5th International Conference on Applied Sciences and Engineering (ICASEA, 2018)
(eISBN 978-967-15744-1-6)
Capthorne Hotel, Cameron Highlands, Malaysia

EVALUATION OF EFFECTIVENESS OF NANOPARTICLES AND GEMINI SURFACTANTS ON ENHANCED OIL RECOVERY (EOR) METHOD

Wang Chern Shen[1]

[1]Wang Chern Shen[1], UCSI University

***Abstract*:** *Surfactant flooding is one of the Enhanced Oil Recovery (EOR) methods where the surfactants are utilised in order to reduce the oil-water interfacial tension (IFT) and their ability of wettability alteration to change the reservoir rock from oil-wet to water-wet for better oil recovery. However, high concentration of surfactant required and the high cost of surfactants as compared to other EOR methods results in the limited usage of this method in EOR process. Therefore, the aim of this study is to find alternatives to revise the surfactant flooding for a more cost-effective yet high efficient EOR method. By reviewing the properties of nanoparticles and Gemini Surfactants, the effectiveness of the presence of Titanium Oxide nanoparticles and the mixture of both Titanium Oxide nanoparticles and Gemini Surfactants towards Enhanced Oil Recovery properties under atmospheric condition will be determined through experimental procedures. The physico-chemical properties of both Gemini Surfactant and Nanoparticles were studied through Interfacial Tension measurement, Contact Angle measurement and Core Flooding experiment by using Tensiometer, Contact Angle Analyser as well as sand pack column respectively. Four experimental set up were carried out which include the combination of Titanium Oxide nanoparticles and Gemini Surfactants acting as co-surfactant. The results of all the set up are compared and it showed that the mixture of both Titanium Oxide nanoparticles and Gemini Surfactant has relatively better capability in the interfacial tension reduction as well as the ability in altering the wettability from oil-wet to water-wet system for maximum oil recovery in a reservoir as proven in the core flooding experiment. Further studies can be aimed at different types, concentration of Gemini Surfactant and nanoparticles, crude oil samples with different densities, under varying condition such as salinity, temperature and pressure for better evaluation of the performance of Gemini Surfactant and nanoparticles to be applied in EOR process.*

***Keywords**: Gemini Surfactant . Titanium Oxide . nanoparticles . Enhanced Oil Recovery . Interfacial Tension . Wettability Alteration . Core Flooding*

Introduction

Surfactant flooding is one of the most prominent EOR methods applied in both onshore and offshore field to increase the amount of crude oil to be recovered from a specific oil field after the production rates of existing oil fields are in a constant decline. Surfactant flooding is done by injecting detergent-like surfactant down to the oil field as the surfactant is capable to aid in lowering down the interfacial tension of the crude oil and ease the process of oil recovery. The mechanism of surfactant flooding ranges from interfacial tension (IFT) reduction, wettability alteration, mobility control as well as emulsification. By lowering the oil/water interfacial

tension, the capillary pressure and the water will be able to displace the extra oil. However, there are several challenges for the application of surfactant flooding in EOR which ranges from low sweep efficiency, high cost required due to high concentration of surfactant needed as well as the potential formation damage (Sun *et al.* 2017).

Gemini Surfactant has been introduced to the world as a surfactant originates from the class of surfactant molecules which possess more than one hydrophilic head group and one hydrophobic tail. Due to its two or more hydrophilic head group and hydrophobic tail, Gemini Surfactant family has proven to have high surface activity as well as relatively low critical micelle concentration (CMC) values comparing with the conventional surfactants. CMC is the exact concentration of the surfactant at which the micelles are formed when the ability of surfactant in reducing the surface free energy reaches maximum and further increase in concentration of surfactant will have less significant effects.

Application of nanotechnology is undeniably one of the most noteworthy recent debates in oil and gas industry as well as other industries. The fact that nanoparticles is capable to decrease the interfacial tension between oil and water phases, spontaneously forming emulsion, altering the wettability of porous medium as well as modification of flow characters have earned nanotechnology a ticket to be considered in EOR process. As the nanoparticles are proven magically capable in various applications, the nanoparticles will be further investigate in order to study its synergy with other surfactants in order to more sophisticatedly strengthen the method of Enhanced Oil Recovery (Mohajeri *et al*. 2015). Surfactant flooding is claimed to be one of the most potential method of Enhanced Oil Recovery among other methods to be applied in depleted reservoirs after water flooding. However, the challenges faced by surfactant flooding is none other than the high cost of the method due to the enormous amount of surfactant required in order to improve the oil recovery. As both Gemini Surfactant and Nanoparticles are proven to be capable in terms of their physico-chemical properties to be applied in EOR methods, this paper will showcase their individual effectiveness in EOR as well as the synergistic relationship between Gemini Surfactant and nanoparticles when nanoparticles act as the co-surfactant of Gemini Surfactant applying to the EOR methods.

Literature review

Surfactant Flooding

In the present world, most of the oil fields are being developed and the crude oil is being extracted through water flooding method. However, it is common that residual oil will remain undeveloped or unproduced after the water flooding. Surfactant flooding has been rate as one of the potential tertiary oil recovery methods (EOR) in depleted reservoirs after water flooding which acts as secondary recovery. As one of the chemical flooding agent, surfactants are claimed to be an effective one due to its ability to effectively contribute in the reduction of the interfacial tension (IFT) between the oil and water interfaces, improving the sweep efficiency and displacement efficiency which leads to reduction in residual oil saturation (Jiravivitpanya *et al.* 2017).

Nanotechnology

The discovery of nanotechnology has been a miracle-like revolution to all of the industries not limited to oil and gas industries. Nanoparticles with particles size of 1-100 nm own distinctive properties due to their extreme small size as well as larger surface are per unit volume leading to being more reactive than other molecules. The major difference between conventional material and nanomaterial is the location of the atoms, where the atoms of conventional material located in the interior of the particles while the atoms of nanomaterial located on the surface of the particles, leading to high reactivity which yield materials with outstanding chemical, mechanical and other properties (Fakoya and Shah, 2017). According to Fakoya and Shah (2017), addition of nanoparticles into any fluid including surfactant-based fluids will yield nano-fluid which can be defined as dilute liquid suspensions of nanoparticles where one of their dimensions is smaller than 100 nm.

As the oil and gas industries are dealing with hardships ranging from wellbore instability, emulsion instability, high temperature high pressure (HTHP) applications, according to Singh and Ahmed (2010), nanotechnology has the potential to overcome these challenges and improve the productivity. Application of various metal oxide nanoparticles was proven to be able to perform well in stabilizing carbon dioxide foam at certain concentration which indicates their ability in solving stabilizing problems (Alomair *et al*. 2015). One of the metal oxide nanoparticles, Titanium Oxide, TiO_2 has proven its capability by improving the oil recovery by 31% in a water flooding tests from oil-wet Berea sandstone by altering the wettability of sandstone cores from oil-wet system to water-wet system (Negin *et al.* 2016).

Gemini Surfactant

In term of structure, conventional surfactant typically consists of single hydrophobic tail which connects to an ionic or polar head group. Gemini Surfactant is a newly generated surfactant which has a long hydrocarbon chain followed by an ionic group, a spacer, then second ionic group followed by a hydrocarbon tail as illustrated in Figure 1. Gemini Surfactants
are the surfactants which were named as dimeric surfactant due to their structure of having two hydrophobic tail and they are proven to provide greater surface activity. According to Nguele *et al.* (2015), when a surfactant consists of two identical hydrophobic chain which known as monomer (*m*) which linked together with a spacer (*s*), it will be categorised as dimeric surfactant (*m-s-m*). In this paper, Gemini Surfactant which is going to be investigated will be dimeric surfactant of quaternary ammonium bromide connected with a trimethylene spacer group with code *m-3-m*.

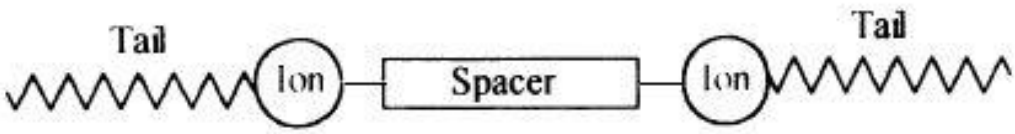

Figure 1: Schematic representation of a Gemini Surfactant

As stated, Gemini Surfactants are surfactants which are constructed by at least two hydrophobic chains and two polar/ionic head connected by wide ranges of spacer groups, hence these structures contribute to their unique properties in aqueous solution such as relatively low critical micellar concentration compared to the conventional surfactant as well as high surface. This is due to the fact that critical micelle concentration (CMC) is depending on both the chemical architecture of the surfactant as well as the spacer group between the monomers,

supporting by various former studies (Nguele *et al.* 2015). For Gemini Surfactant which possess at least two hydrophobic groups in a single molecule, they are relatively more solvent structure-disruptive as compared to the conventional surfactant. From previous findings of Nguele *et al.* (2015), it had been found that at low CMC of Gemini Surfactant *12-3-12* and *16-3-16*, static surface tension was lowered at a magnitude of 81% and 94% respectively. In EOR processes, the major drive mechanism for surfactant flooding for improving oil displacement from pore spaces as well as reservoir rock in the reservoir are the interfacial tension reduction as well as the ability of surfactant in wettability alteration. According to Gao and Sharma (2013), Gemini Surfactants have demonstrated ultra-low interfacial tension (ULIFT) towards the higher end of salinity with their high tolerance in salinity. In research, it has proven that Gemini Surfactants are able to achieve the minimum interfacial tension at an extremely low concentration (Kamal, 2016). A conventional surfactants require 0.2 to 2 wt% in order to achieve interfacial tension in the range of 10^{-3} mN/m whereas only 0.02 wt% of Gemini Surfactants are sufficient to achieve this low IFT values (Gao and Sharma, 2013). Apart from that, with the support of studies from Ye *et al* (2008), the fact that Gemini Surfactants are able to have marvellous synergy with both Gemini Surfactants as well as the conventional surfactants to effectively forming mixed micellar aggregates with a compact arrangement leading to enhancing the solubility of the surfactant makes Gemini Surfactant a good candidate for EOR application. Nevertheless, as Gemini Surfactant consists of more than a single hydrophilic head groups and hydrophobic tails, they are proven to be able to advance improving the wettability alteration through an investigation result which states that Anionic Gemini Surfactant has shown extensive effectiveness in wettability alteration due to its ionic nature. Hence, Gemini Surfactant is considerably applicable in EOR methods.

Methodology

Materials

The materials that were used in the experimental studies are 3wt% $NaCl$ synthetic brine solution, Dimeric Quaternary Ammonium Bromide with Trimethylene Space (*m-3-m*) Gemini Surfactant, TiO_2 nanoparticles powder, sandstones and carbonates core samples, light crude oil and sand. These materials are obtained through various available sources ranging from lecturers from UCSI University to Core Laboratory Malaysia.

Apparatus

The apparatus that will be used in the research are,

- CMS-300 (Automated Core Measurement System) for Routine Core Analysis
- Tensiometer for IFT and Surface Tension measurement using Du Nuoy Ring Method
- Phoenix 150 Contact Angle Analyser for contact angle measurement
- Core Flooding Setup (Vertical Sand Packing) for oil recovery efficiency measurement

Experimental

CMC of Gemini Surfactant Determination

The CMC value of Gemini Surfactant was determined by using conductivity test as well as phase behavior micro-emulsion test. For conductivity test, the graphical demonstration of the CMC measurement is depicted in Figure 2. For micro-emulsion phase behavior test, various concentration of Gemini Surfactant were dissolved in 3wt% brine solution with crude oil with

ratio of 1:1 and left for 24 hours for phase behavior investigation. The CMC value of Gemini Surfactant was determined based on the two tests.

Physico-Chemical Properties Analysis

All the analysis was analyzed based on the set up as illustrated in Table 2.

Table 2: Experimental Set up

Experiment Set Up	Content
(i)	Crude Oil + Brine Solution
(ii)	Crude Oil + Brine Solution + Titanium Oxide Nanoparticle (0.05 wt%)
(iii)	Crude Oil + Brine Solution + Gemini Surfactant (0.1wt%)
(iv)	Crude Oil + Brine Solution + Gemini Surfactant + Titanium Oxide Nanoparticles

Interfacial Tension Reduction (Tensiometer)

Four experimental setup were prepared as shown in Table 2. The aqueous surfactant solution was prepared in a beaker and the platinum ring was placed inside the beaker on Tensiometer. The interfacial tension and surface tension of the oil/surfactant interface and air/water phase was tested by Tensiometer. The IFT and surface tension recorded was generated and the procedure was repeated by replacing the other experimental setup.

Wettability Alteration (Contact Angle Measurement)

The core samples were prepared by soaking them in the brine solution before being used as the surface where the crude oil will be dropped on. Then, by using Phoenix Contact Angle Analyzer, determine the average contact angle between the oil droplet and the core sample surface. The result was generated and the observation was captured by the device. As the brine solution was the control, the procedure will be repeated by soaking the core samples in aqueous Gemini Surfactant, Titanium Oxide Nano-fluid and the mixture of both of them.

Core Flooding Experiment (Sand Packing)

By simulating a clean sandstone reservoir, 200 grams of fine sand was weighted, well mixed with 40mL of crude oil sample and transferred into a vertical core flood column with the outlet of column sealed with paraffin film to avoid flow. As a control set up, 80mL of 3wt% brine solution will be heated to 60℃ and transferred into the core flood column. The pressure was fixed at atmospheric pressure and the gravity force was used as the driving force for the oil recovery. The paraffin film was then removed to allow flow and the oil recovery factor was calculated based on the volume recovered from the core flooding experiment. The procedure was then repeated by replacing brine solution with the aqueous Gemini Surfactant and Titanium Oxide Nano-fluid. The experimental set up was illustrated in Figure 3.

Result and Discussion

CMC Determination of Gemini Surfactant

From the graph of Conductivity versus Gemini Surfactant Concentration as shown in Figure 4, it can be observed that the intersection point falls at the concentration when 82 mL of concentrated aqueous Gemini Surfactant was added into the deionized water for conductivity

test. This indicates that he optimum concentration (CMC) of the Gemini Surfactant sample (Dimeric Quaternary Ammonium Bromide with Trimethylene Spacer) falls around 0.1025wt%. The phase behavior test which involved aqueous Gemini Surfactant with varying concentration showed significant micro-emulsion. The middle-phase of the micro-emulsion for the 0.1wt% aqueous Gemini Surfactant set up shows the most significant result as compared to other concentration set up as shown in Figure 5. It indicates that at this concentration of Gemini Surfactant, the hydrophile-lipophile properties of the surfactant monolayer at the water/oil interface are balanced, bicontinuous-type micro-emulsions will be formed and at this condition, the solubilisation of water and oil is maximized at the minimum usage of surfactant amount (Solans and Garcia-Celma, 1997). Hence, it can be concluded that the CMC value of this Gemini Surfactant falls at 0.1wt% and Gemini Surfactant at this optimum concentration was used in the further analysis for their physico-chemical properties.

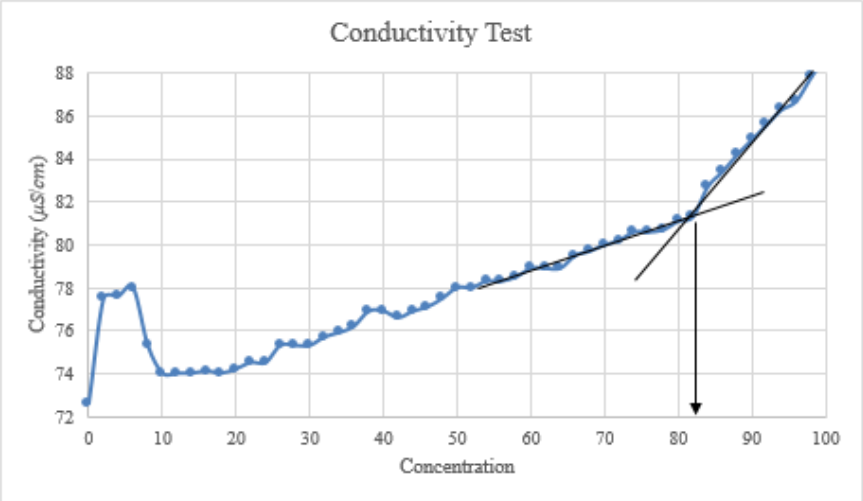

Figure 4: Graph of Conductivity versus Gemini Surfactant Concentration

Physico-Chemical Properties Analysis for EOR

Wettability Alteration (Contact Angle Measurement)

Figure 6 and Table 3 shows the comparison of contact angle measurement with light crude oil in both sandstones and carbonates core samples among the four setup which included untreated brine solution, 0.05wt% TiO_2 nanoparticles treated Nano-fluid, 0.1wt% Gemini Surfactant treated solution and combination of both Gemini Surfactant and Nano-fluid treated solution were tabulated. In sandstones core 6-118, a significant alteration of wettability from strongly oil-wet (157°) to water-wet (73°) can be observed by both TiO_2 nanoparticles and Gemini Surfactant as well as their combination. As stated in the literature review, the wetting heterogeneity does affect the oil recovery which made the capability of surfactant in altering wettability important in EOR. Although in other core samples, the alteration is not as great as 6-118 sandstones sample, the slight reduction in contact angle on carbonate core samples proved the wettability alteration capability of TiO_2 nanoparticles and Gemini Surfactant as well. The result can conclude that both of TiO_2 nanoparticles and Gemini Surfactant are more effective in altering the wettability of sandstones rock compared to carbonate rocks. In addition, the synergy of TiO_2 nanoparticles and Gemini Surfactant shows positive outcome as the combination of both surfactants reduced the contact angle the most, altering the wettability from oil-wet to water-wet and neutral-wet significantly in sandstones rock. As wettability

alteration is one of the primary parameters for EOR, the use of the combination of TiO_2 nanoparticles and Gemini Surfactant in optimal concentration which change wettability towards water-wet results in capillary force reduction and yield greater oil recovery is effective in improving EOR (Esfandyari Bayat *et al.* 2014).

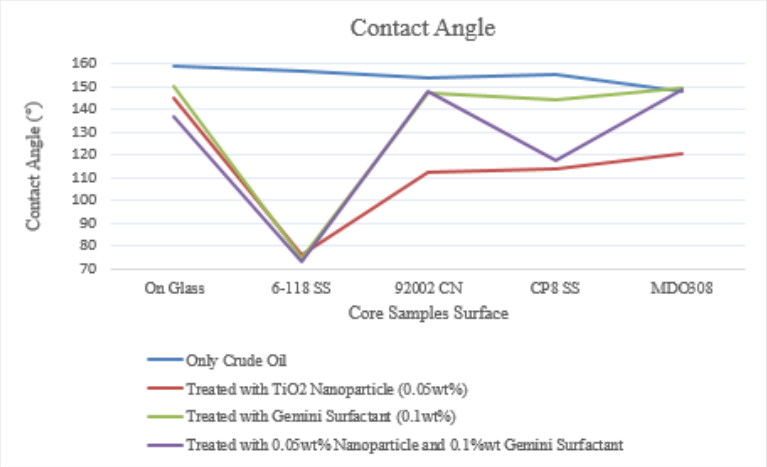

Figure 6: Comparison of the Contact Angle for all experimental setup

Interfacial Tension Reduction

The comparison of the surface tension reduction results from different set up are tabulated as shown in Figure 7. Based on assumptions, the interfacial tension between the oil/surfactant phase were able to achieve ultra-low IFT by both Gemini Surfactant only as well as the mixture of both aqueous Gemini Surfactant and TiO_2 Nano-fluid which falls in the range of 0.001 mN/m at low surfactant concentration. From Figure 7, It can be observed that both TiO_2 Nano-fluid and Gemini Surfactant are very effective in reducing the surface tension as well as the interfacial tension. From Figure 7, it can be proven that the synergy between Gemini Surfactant and TiO_2 nanoparticles are showing positive outcome as the surface tension reduction in the combination setup was the greatest reduction among other setup where Gemini Surfactant and Nano-fluid are used independently. Hence, it can be concluded that the mutualism relationship between Gemini Surfactant and TiO_2 nanoparticles at optimal concentration is acceptable and strongly effective to be used in EOR application as they are achieving the ultra-low IFT at low surfactant concentration.

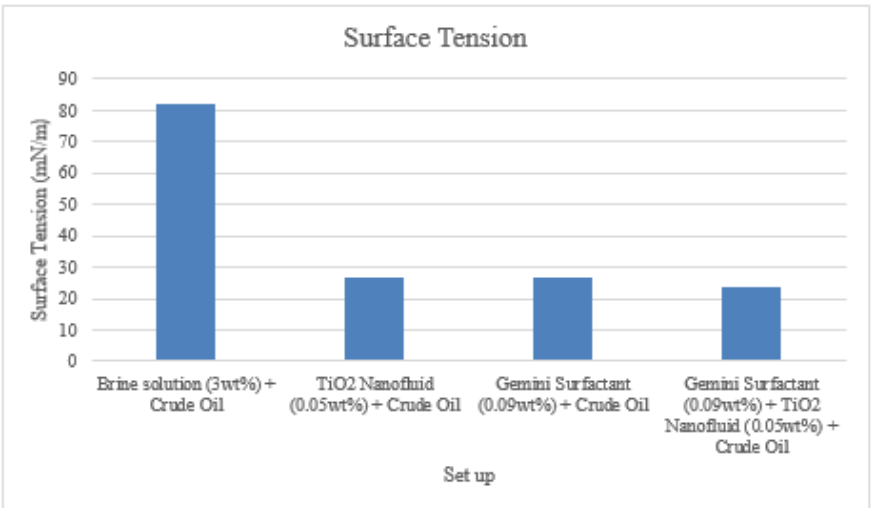

Figure 7: Summary of the IFT/Surface Tension reduction for all experimental setup

Core Flooding Experiment (Vertical Sand Pack)

The result from the core flooding experiment was tabulated in Figure 8. As shown, the oil recovery of both Gemini Surfactant and TiO_2 Nano-fluid as well as their combination surfactant mixture were compared with the recovery using brine solution only. From the analyses in the previous section, the combination of Gemini Surfactant and TiO_2 Nano-fluid stood out with relatively effective EOR properties, resulting in the highest net oil recovery of

48.25% at 60℃ with an increase of 4.25% as compared to the independent setup of Gemini Surfactant and TiO_2 Nano-fluid. It can be explained that the major influencing factor in the oil recovery was the wettability alteration of the sand to water-wet condition (Elmofty, 2012). It has been shown that with the combination of both IFT reduction and wettability alteration which plays vital role in mobilization of immobile oil as well as capillary force reduction, the setup which Gemini Surfactant and TiO_2 Nano-fluid act as co-surfactant achieved the highest oil recovery due to their excellent synergism.

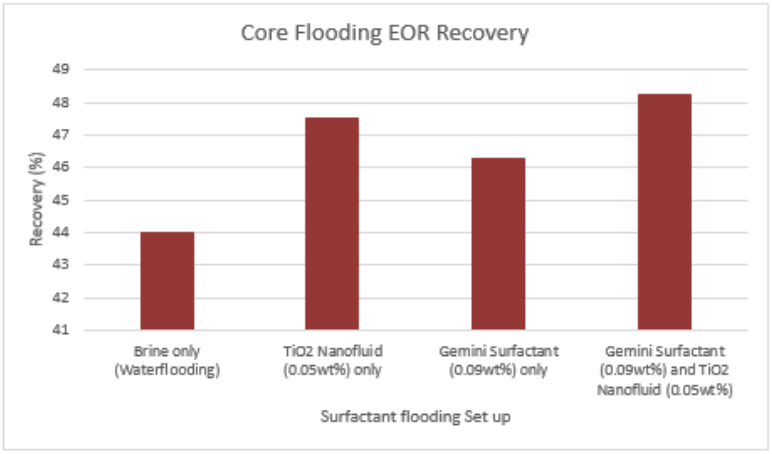

Figure 8: Summary of the Oil Recovery Efficiency of Experimental Setup

Conclusion

The following extensive conclusions can be gained owing to the outcomes from this research:

Both Gemini Surfactant and TiO_2 nanoparticles are effective in EOR method as they reduced interfacial tension to ultra-low IFT close to 0 mN/m and drastically reduce the surface tension by an average of 70% at low surfactant concentration.

The addition of Gemini Surfactant and TiO_2 Nano-fluid in brine solution (3 wt%) as the surfactant successfully altered the wettability of various core samples (sandstones and carbonate) from strongly oil-wet to water-wet or neutral-wet which favour the EOR application. The surfactants showed better results in sandstones as compared to carbonate samples, however, the reduction of contact angle on both core samples indicate the effectiveness of both Gemini Surfactant and TiO_2 Nano-fluid in wettability alteration.

The core flooding experiment results indicated that both Gemini Surfactant and TiO_2 Nano-fluid are effective in oil recovery by improving the recovery factor from 44% OOIP to 47.5%

and 46.25% respectively. The combination of Gemini Surfactant and TiO_2 Nano-fluid at their optimal concentration achieved the highest oil recovery at 48.25%, indicating the excellent synergy between the two surfactants.

As both Gemini Surfactant and TiO_2 nanoparticles showed marvellous synergistic interaction in terms of EOR properties, it can be concluded that the combination will be very effective surfactant with high tolerance of salinity (3wt% $NaCl$) at 60℃ to be utilized in surfactant flooding application in Enhanced Oil Recovery under atmospheric condition.

Recommendation

The existence of limitation cannot be denied in this research. Therefore, the following recommendations are suggested in order to polish this research with various advance methods and alternatives so the accuracy of the findings can be refined.

As the crude oil sample provided is light oil, various density of oil ranging from light to heavy crude oil is suggested to be used to apply on this research in order to simulate more variety of reservoir with different crude oil.

Due to the lack of sophisticated equipment, specific interfacial tension (IFT) Tensiometer is suggested to be utilised in order to determine the interfacial tension value instead of identifying the value based on assumption according to the graph generated for surface tension. Besides, proper set up of core flooding experiment is suggested to be used in order to achieve results with higher reliability.

Acknowledgement

The author would like to express his gratitude to the lecturers of UCSI University as well as the author's supervisor, Ms Farhana Binti Abdul Barri for her assistance and support in this research. I would also like to thank Professor Hikmat who provided guidance and advice in the progress of completing the research.

References

Alomair, O. A., Matar, K. M., & Alsaeed, Y. H. (2015). Experimental Study of Enhanced-Heavy- Oil Recovery in Berea Sandstone Cores by Use of Nanofluids Applications, *4007*(August 2014), 14–16.

Elmofty, O. (2012). Surfactant enhanced oil recovery by wettability alteration in sandstone reservoirs.

Esfandyari Bayat, A., Junin, R., Samsuri, A., Piroozian, A., & Hokmabadi, M. (2014). Impact of Metal Oxide Nanoparticles on Enhanced Oil Recovery from Limestone Media at Several Temperatures. *Energy & Fuels*, *28*(10), 6255–6266. https://doi.org/10.1021/ef5013616

Fakoya, M. F., & Shah, S. N. (2017). Emergence of nanotechnology in the oil and gas industry : Emphasis on the application of silica nanoparticles. *Petroleum*, 1–15. https://doi.org/10.1016/j.petlm.2017.03.001

Gao, B., & Sharma, M. M. (2013). A New Family of Anionic Surfactants for Enhanced-Oil-Recovery Applications, (October), 8–10.

Jiravivitpanya, J., Maneeintr, K., & Boonpramote, T. (2017). Experiment on Measurement of Interfacial Tension for Subsurface Conditions of Light Oil from Thailand, *18007*.

Kamal, M. S. (2016). A Review of Gemini Surfactants: Potential Application in Enhanced Oil Recovery. *Journal of Surfactants and Detergents*, *19*(2), 223–236. https://doi.org/10.1007/s11743-015-1776-5

Mohajeri, M., Hemmati, M., & Sadat, A. (2015). Journal of Petroleum Science and Engineering An experimental study on using a nanosurfactant in an EOR process of heavy oil in a fractured micromodel. *Journal of Petroleum Science and Engineering*, *126*, 162–173. https://doi.org/10.1016/j.petrol.2014.11.012

Negin, C., Ali, S., & Xie, Q. (2016). AC SC. *Petroleum*. https://doi.org/10.1016/j.petlm.2016.10.002

Nguele, R., Sasaki, K., Salim, H. S., & Sugai, Y. (2015). Physicochemical and microemulsion properties of dimeric quaternary ammonium salts with trimethylene spacer for enhanced oil recovery, 3487–3497. https://doi.org/10.1007/s00396-015-3701-x

Singh, S., & Ahmed, R. (2010). SPE 130413 Vital Role of Nanopolymers in Drilling and Stimulations Fluid Applications, (September), 19–22.

Solans, C., & García-Celma, M. J. (1997). Surfactants for microemulsions. *Current Opinion in Colloid and Interface Science*, *2*(5), 464–471. https://doi.org/10.1016/S1359-0294(97)80093-3

Sun, X., Zhang, Y., Chen, G., & Gai, Z. (2017). Application of Nanoparticles in Enhanced Oil Recovery : A Critical Review of Recent Progress. https://doi.org/10.3390/en10030345

Ye, Z., Zhang, F., Han, L., Luo, P., Yang, J., & Chen, H. (2008). Colloids and Surfaces A : Physicochemical and Engineering Aspects The effect of temperature on the interfacial tension between crude oil and gemini surfactant solution, *322*, 138–141. https://doi.org/10.1016/j.colsurfa.2008.02.043

Appendix

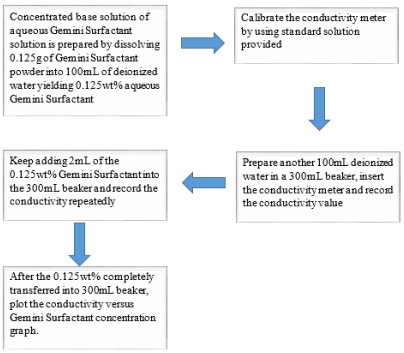

Figure 2: Procedure of Conductivity Test

Figure 3: Core Flooding Experimental Set Up

Figure 5: Micro-emulsion of 0.1wt% of Gemini Surfactant.

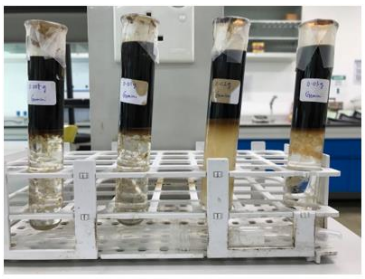

Figure 9: Phase Behaviour Micro-emulsion of Gemini Surfactant with Varying Concentration.

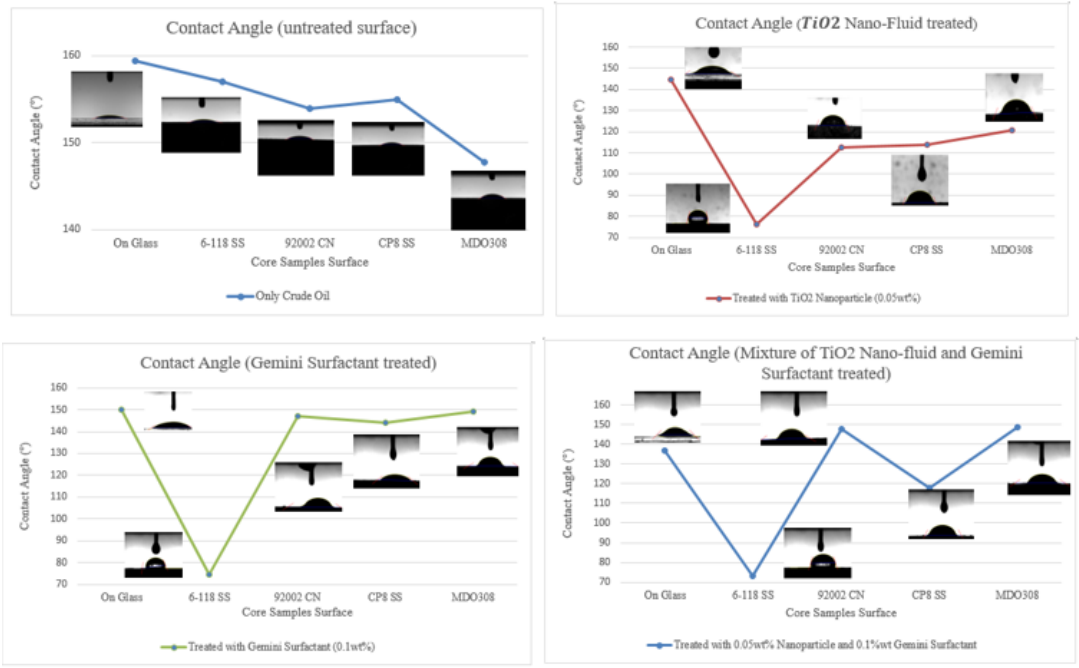

Figure 10: Contact Angle Measurement for all Experimental Setup

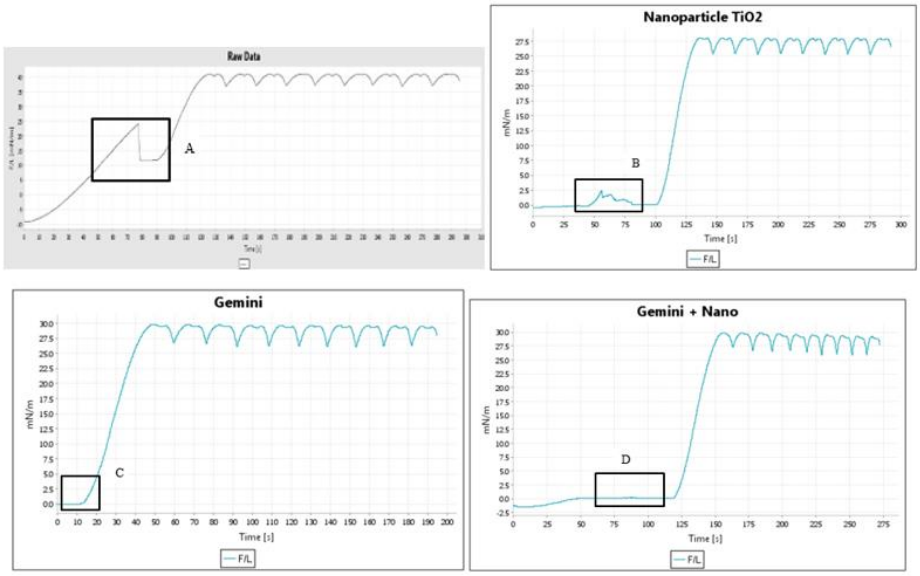

Figure 11: IFT and Surface Tension measurement for all Experimental Setup

Table 1: CMC values of representative conventional surfactant (1-4) and Gemini Surfactants

Surfactant	CMC/mM
1. $C_{12}H_{25}N^{+}(CH_3)_3\ Br^{-}$ (DOTAB)	16
2. $C_{12}H_{25}N^{+}(CH_3)_3\ Cl^{-}$ (DOTAC)	22
3. $C_{16}H_{33}N^{+}(CH_3)_3\ Br^{-}$ (CTAB)	1
4. $C_{12}H_{25}OSO_3^{-}Na^{+}$ (SDS)	8
5. $C_{12}H_{25}N^{+}(CH_3)_2\text{-}(CH_2)_n\text{-}N^{+}(CH_3)_2C_{12}H_{25}2Br^{-}$ (n = 3 – 8)	1
6. $C_{12}H_{25}N^{+}(CH_3)_2\text{-}(CH_2)_{16}\text{-}N^{+}(CH_3)_2C_{12}H_{25}2Br^{-}$	0.12
7. $C_{16}H_{33}N^{+}(CH_3)_2\text{-}(CH_2)_2\text{-}N^{+}(CH_3)_2C_{16}H_{33}2Br^{-}$	0.003
8. $C_{16}H_{33}N^{+}(CH_3)_2\text{-}(CH_2)_5\text{-}N^{+}(CH_3)_2C_{16}H_{33}2Br^{-}$	0.009
9. $C_{16}H_{33}N^{+}(CH_3)_2\text{-}(CH_2)_2\text{-}O\text{-}(CH_2)_2\text{-}N^{+}(CH_3)_2C_{16}H_{33}2Br^{-}$	0.004
10. $C_{16}H_{33}N^{+}(CH_3)_2\text{-}\ CH_2\text{-}(CH_2\text{-}O\text{-}CH_2)_3\text{-}CH_2\text{-}N^{+}(CH_3)_2C_{16}H_{33}2Br^{-}$	0.02
11. $C_{12}H_{25}N^{+}(CH_3)_2\text{-}CH_2\text{-}CH(OH)\text{-}CH_2\text{-}N^{+}(CH_3)_2C_{12}H_{25}2Br^{-}$	0.8
12. $C_{12}H_{25}N^{+}(CH_3)_2\text{-}CH_2\text{-}C_6H_4\text{-}CH_2\text{-}N^{+}(CH_3)_2C_{12}H_{25}2Br^{-}$	0.03
13. $C_{12}H_{25}OPO_2^{-}\text{-}O\text{-}(CH_2)_6\text{-}OPO_2^{-}OC_{12}H_{25}2Na^{+}$	0.4

Table 3: Result of Contact Angle Measurement and Wettability Alteration

	Core Sample	Without Surfactant	TiO_2 nanoparticles	Gemini Surfactant	Gemini Surfactant + TiO_2 nanoparticles
Sandstones	6-118 (SS)	157.04	76.20	74.46	73.27
Contact Angle (°)	CP8 (SS)	154.95	113.78	144.14	117.56
Approximate Wettability	6-118 (SS)	Strongly Oil-wet	Water-wet	Water-wet	Water-wet
	CP8 (SS)	Strongly Oil-wet	Neutral-wet	Oil-wet	Neutral-wet
Carbonate	92002 (CB)	153.87	112.41	146.89	147.69
Contact Angle (°)	MDO308 (CB)	147.73	120.52	149.09	148.43
Approximate Wettability	92002 (CB)	Strongly Oil-wet	Neutral-wet	Oil-wet	Oil-wet

	MDO308 (CB)	Oil-wet	Neutral-wet	Oil-wet	Oil-wet

Proceeding: 5th International Conference on Applied Sciences and Engineering (ICASEA, 2018)
(eISBN 978-967-15744-1-6)
Capthorne Hotel, Cameron Highlands, Malaysia

NANOCELLULOSE REINFORCED STARCH POLYMER COMPOSITES: A REVIEW OF PREPARATION, PROPERTIES AND APPLICATION

R.A. Ilyas[1]
S.M. Sapuan[12]
sapuan@upm.edu.my
M.R. Ishak[3]
E.S. Zainudin2
M.S.N. Atikah[4]

[1]Laboratory of Biocomposite Technology, Institute of Tropical Forestry and Forest Products, Universiti Putra Malaysia, 43400 UPM Serdang, Selangor, Malaysia 603-89471788; Fax: +603-86567122
[2]Department of Mechanical and Manufacturing Engineering, Universiti Putra Malaysia, 432400 UPM Serdang, Selangor, Malaysia
[3]Department of Aerospace Engineering, Universiti Putra Malaysia, 43400 UPM Serdang, Selangor, Malaysia
[4]Department of Chemical and Environmental Engineering, Universiti Putra Malaysia, 43400 UPM Serdang, Selangor, Malaysia

---

Abstract: *Nanocellulose from biomass have recently gained attention due to their renewability, biodegradability, high mechanical strength, as well as low density and high economic value. This paper provides an overview of recent progresses made in the area of nanocellulose reinforced plasticized starch. Following this, the article is divided into two sections; first part deals with characterization and processing of cellulose nanocomposites, and the second part elaborates new development in different area of application. The types of nanocellulose covered are those isolated from plants via acid hydrolysis chemical (nanocrystalline cellulose), mechanical treatment (nanofibrillated cellulose) and under culturing conditions (bacterial nanocellulose). Researches highlighted in this paper are interfacial properties of nanocellulose within the thermoplastic starch. The applications and new advances covered in this review are the use of nanocellulose to reinforce adhesive composite, to protect pharmaceutically active proteins from digestion, as microcapsules for small molecules and as biodegradable films for food packaging application.*

***Keywords**: Nanofibrillated cellulose; Nanocrystalline cellulose; Nanocellulose; Nanocomposite; Thermoplastic starch*

Introduction

Natural fibres

According to Food and Agricultural Organization (FAO), world production of all fibres in 2016 was estimated to have exceeded 100 million metric tons with natural fibres accounted for approximately 30% of the total of fibre production (Figure 1). Specifically, natural fibres production rose from 28 million metric tons to an estimated 30 million in 2016 from wide range of plants and animals. These fibres were utilized to form twines, fabrics, and ropes, which

previously played important roles in human societies since earlier civilization. Nowadays, natural fibres have played vital role in supporting the world's population and allowing communication to be done more easily with paper and packaging.

The term "natural fibres" is used to define various types of fibres that are naturally produced by animals, plants and minerals. Thus, it is important to clarify that in this article, 'natural fibres' are related to 'plant fibre'; also called 'cellulosic fibres', 'lignocellulosic fibres', or 'vegetable fibres'. Natural fibres are composed of three main components named lignin, hemicellulose and cellulose. Other minor components such as extractives, pectin and pigments can also be traces, however, in lower quantities. For this reason, natural fibres are also referred as lignocellulosic or cellulosic fibres. The cell structure and chemical compositions of natural fibres are quite complicated as different types of fibres have different cell structure and chemical compositions. Briefly, each fibre is basically made up of several parts or elements namely as composite, in which rigid micro-size cellulose are embedded in a soft matrix, mainly composed of hemicellulose and lignin.

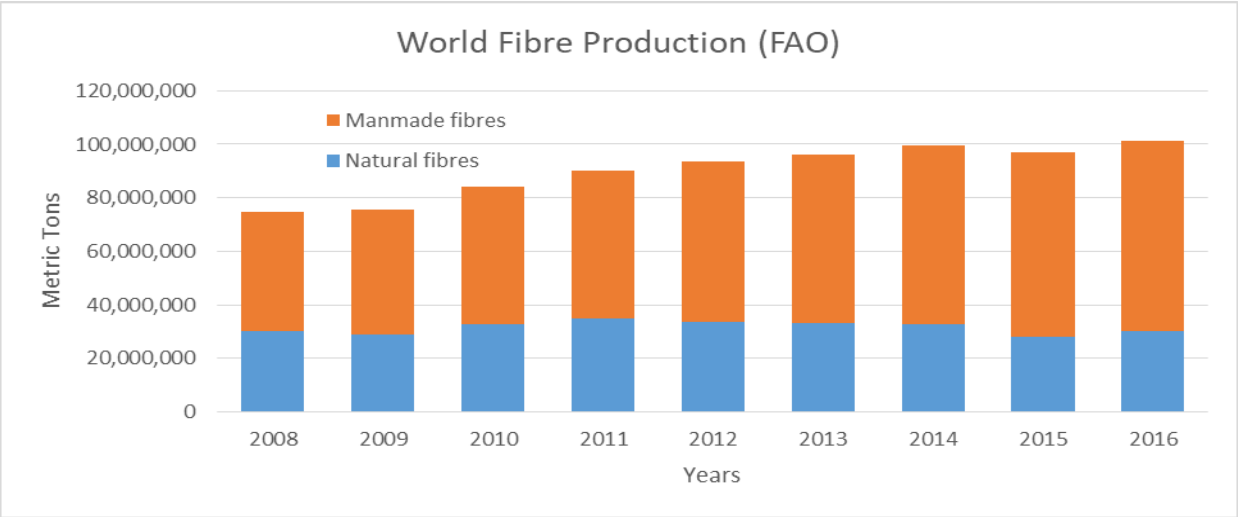

Figure 1: World fibre production developed from data provided by http://faostat3.fao.org/, FAO statistics

Cellulose

Cellulose are among the most abundant renewable biopolymers on earth, occurring in most natural fibres, especially plant-based materials, besides serving as the dominant reinforcing phase in plant structures. This structural materials are naturally organized as microfibrils linked together to form cellulose fibres. Besides that, some of the cellulose can be biosynthesized ranging from higher to lower plants, algae, tunicate and some bacteria and fungi. Cellulose composed of linear homopolysaccharides that made up of β-D-glucopyranose units linked together by β-1-4 linkages. Basic chemical structure of cellulose is displayed in Figure 2, where each monomer bears three hydroxyl groups. Basic structural component of cellulose is known as microfibrillated cellulose which is formed during biosynthesis. The aggregation of poly-β-(1-4)-D-glucosly chain would form into fibril, which is long thread-like bundle of molecules laterally stabilized by intermolecular hydrogen bond (Figure 3). Individual microfibrillated cellulose have diameter ranging from 2 to 20 nm, with specifically can be illustrated as a string of cellulose crystals linked along the microfibril axis by alternate amorphous regions.

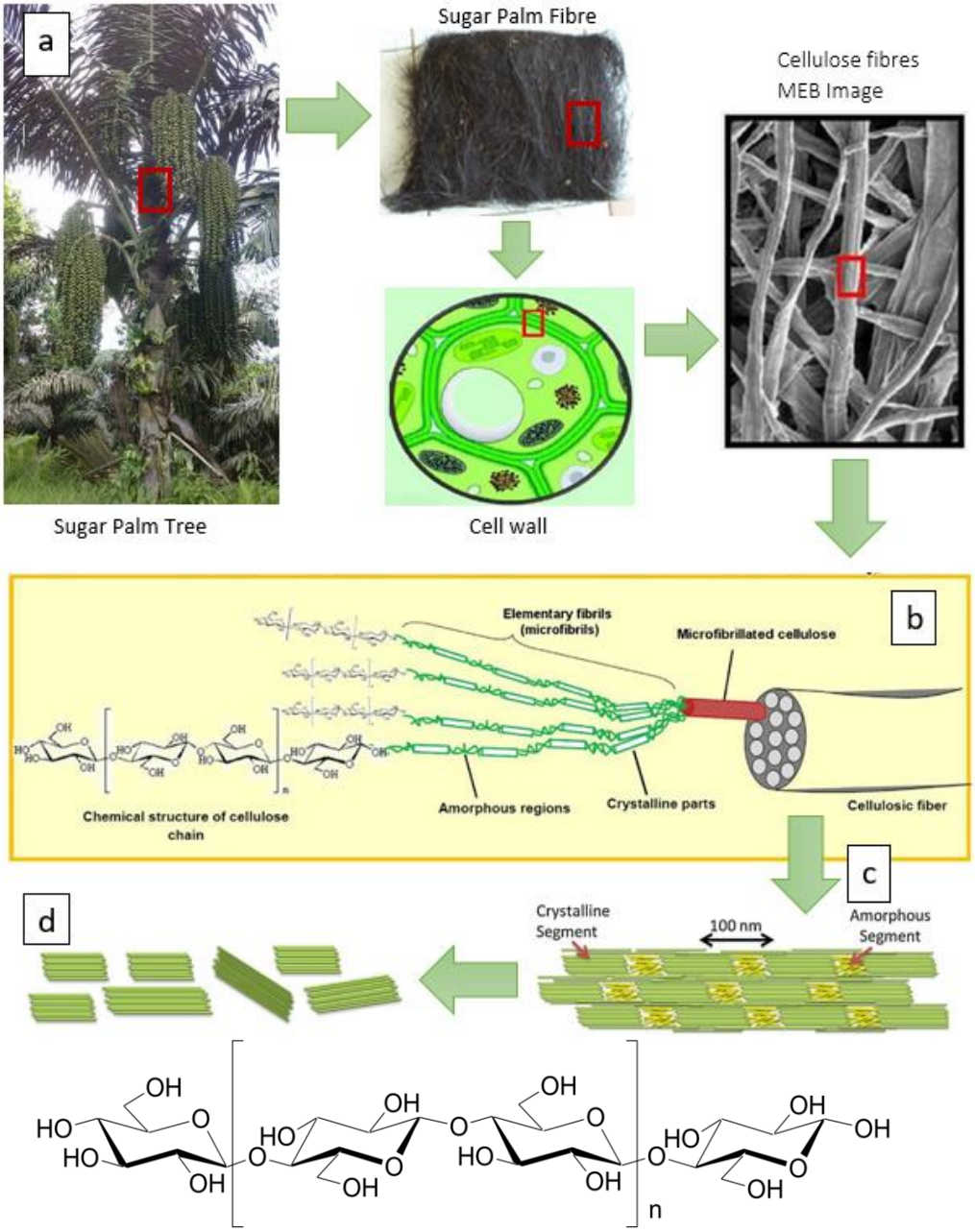

Figure 2: Basic chemical structure of cellulose

Figure 3: Fibre structures highlighting the origin of NCCs from (a) cellulosic plant sources, (b) cellulose fibres and (c) microfibrils bundles consisting amorphous regions and crystalline parts, (d) nanocrystalline cellulose (NCCs) (Ilyas, Sapuan, & Ishak, 2018).

Types of Nanocellulose

Generally, nanocellulose can be divided into three major types, which are nanofibrillated cellulose (NFCs), nanocrystalline cellulose (NCCs), and bacterial nanocellulose (BNCs) (Abitbol et al., 2016). Comparison between the three major nanocellulose is as illustrated in Table 1. These nanocellulose can be produced via bottom-up or top-down methods. NCCs and NFCs are usually obtained via the top- down approach such as enzymatic, chemical or physical methodologies for isolation and extraction from crops, higher plants and by-products of forestry and agriculture such as banana-stems, rice straws, pineapples, oil palm, rubber, lalang,

and sugar palm fibres. In contrast, bacterial nanocelluloses (BNCs) are produced by a particular family of bacteria (*Glueconoacetobackerxylinius*) and are cultivated in a culture medium as microfibrils through a bottom up approach (Klemm et al., 2011).

Table 1: Comparison between the different types of nanocellulose (Ilyas Rushdana, Sapuan Salit, Lamin Sanyang, & Ridzwan Ishak, 2017; Klemm et al., 2011)

	Nanocrystalline cellulose (NCCs)	Nanofibrillated cellulose (NFCs)	Bacterial nanocellulose (BNCs)
Images	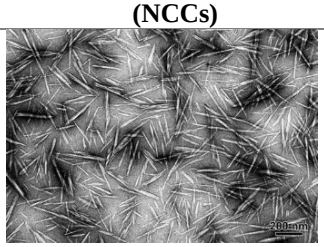 Transmission electron microscope (100nm) (Habibi et al., 2008)	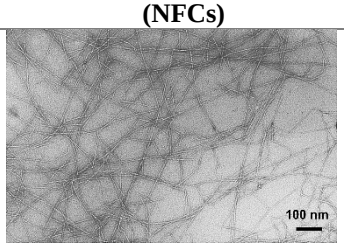 Transmission electron microscope (100nm) (Saito, T., Kimura, S., Nishiyama, Y., & Isogai, 2007)	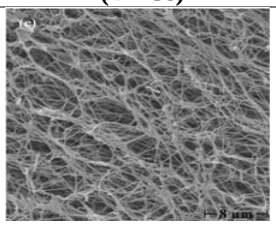 Scanning microscope (8µm) (Heßler & Klemm, 2009)
Synonyms	Crystallites, whiskers, nanowhiskers, cellulose nanocrystals, rod-like cellulose microcrytals	Microfibrillated cellulose, nanofibrils, microfibrils, cellulose, nanofibre	Biocellulose,bacterial cellulose, microbial cellulose,
Common source	Wood, cotton, hemp, flax, rice straw, wheat straw, ramie, avicel, mcc, tunicin, algae, bacterial cellulose, pea hull fibre, branch-bark of mulberry,black spruce and eucalyptus, tunicate, valonia, kraft wood, pine and spruce, palm oil, pineapple leaf fibre, grass, swede root, chardonnay grape skins, coconut fibre, softwood wood flour, kenaf fibre, rice husk, sabdariffa fibres, wood fibres, corncob	Pea hull, kenaf, hardwood and softwood pulp, cotton linter, cotton, cassava bagasse, sugarcane baggase, cotton, algae (valonia), tunicate cellulose, bacterial cellulose, tunicate cellulose, sugar beet pulp, wheat straw, date palm tree (rachis/ leaflets), coconut husk fibre, recycled pulp, acacia pulp, banana, capimdourado, mulberry, flax, hemp, *luffacylindrica*, mengkuang leaves, curaua,	Low molecular weight sugar, alcohols, several bacteria species such as gluconacetobacter, agrobacterium, pseudomonas, rhizobium, and sarcin.
Formation process	Chemical or enzymatic treatment prior to delamination of wood pulp by mechanical pressure, acid hydrolysis	Acid hydrolysis, Integration of mechanical shearing process via high pressure homogenization and enzymatic hydrolysis, TEMPO-mediated oxidation	Bacterial synthesis and cultivation in aqueous culture media present by glucose, oxygen and phosphate.
Average size	Diameter: 5-80 nm Length: 100-250 nm	Diameter: 5-70 nm Length: 100-250 nm (from plant); 100 nm to several micrometer (from cellulose of tunicates, algae, bacteria)	Diameter: 20-100 nm Length: 1.0-5.0 µm Different types of nanofibre networks
Tensile Strength	2-6 GPa	2-4 GPa	200-300 MPa
Young's modulus	50-143 GPa	15-150 GPa	15-35 Pa

Bionanocomposites

Definition of nanocomposites

The term "nano" is used to designate nanometer scale item which denote a factor of 10^{-9}, whereas nanotechnology is the understanding and control of matter at the nanoscale, at dimensions between approximately 1 and 100 nanometers. For polymer nanocomposite, it is defined as polymer that reinforced filler which the filler size has at least one dimension smaller than 100 nm. Due to its reinforcement with nanostructural properties of filler, nanocomposite is known as a new generation of nanostructured hybrid material. The bionanocomposite component can be made up of organic/organic, inorganic/inorganic and inorganic/organic sources (Esteves, Barros-Timmons, & Trindade, 2004). According to Siqueira et al., (Siqueira, Bras, & Dufresne, 2010a), bionanocomposite can be defined in two ways, in which the nanofiller material is made up from renewable nanoparticle (e.g., nanocrystalline cellulose (NCCs), nanofibrillated cellulose (NFCs) or bacterial nanocellulose (BNCs)) reinforce petroleum-derived polymers (epoxies, PP and PE), or nanofiller is made up of inorganic or synthetic nanofillers (e.g., nanoclay, ZnO2 nanoparticle and carbon nanorubes) reinforced biopolymers (e.g., starch, PLA and PHA).

Nanocellulose based Nanocomposite

Nanocellulose is well known for its low density, wide availability, renewable nature, biodegradability with an intrinsic properties such as abundant surface hydroxyl groups, large specific surface area, high aspect ratio, high crystallinity, high thermal resistance, and good mechanical and electrical conductive properties (Ilyas Rushdana et al., 2017). Thus, due to these advantages, nanocellulose is a highly potential candidate as nanofiller for reinforcement in composite materials. It has been reviewed by Ilyas et al. (Ilyas, Sapuan, Sanyang, & Ishak, 2016; Ilyas Rushdana et al., 2017), that reinforcing nanocellulose in polymeric matric can enhance the strength, stiffness, flame retardancy, toughness, and barrier properties of nanocomposite compared to neat polymer. Moreover, due to the large surface area of nanocellulose filler, the incorporation of small percentage of nanocellulose resulted in remarkable improvement of the nanocomposite properties. This phenomenon occurs due to the cellulose hydrogen bonding network within the polymer matrix which will be discussed later in section 3.3. Fibre matrix interfacial bonding.

Nanocomposite preparation

Preparation of nanocellulose based nanocomposite is considered as important work in this field as it displayed the effectiveness of reinforcement of high aspect ratio nanocellulose within polymer. Favier et al., (Favier, Chanzy, & Cavaille, 1995) had reported that uniform dispersion of nanofiller within polymer would resulted in high mechanical properties at very low nanofiller volume. One of the drawback that correlated to the use of nanocellulose to incorporate polymer nanocomposites is the difficultness to disperse in non-polar medium due to their polar surface. Alternately, in polar or aqueous medium, nanocellulose can disperse well. According to Dufresne (2014), there are two main methods that can be used to prepare nanocellulose nanocomposite films:

- Extrusion with freeze-dried cellulose nanofibre;
- Water or organic solvent evaporation by solvent casting.

The first way to gain nanocellulose reinforced polymer composites is a extrusion method (melting compounding technique) (Oksman, Mathew, Bondeson, & Kvien, 2006). Extrusion

technique is a recent method that was used to make such kind of nanocomposites, however, the focal issue is to work with nanocellulose in the dry state. Indeed, as soon as these nanocellulose are dried, strong hydrogen bonds establish and most of the time agglomerations are obtained, thus, limiting the reinforcement of nanocellulose with polymer matrix. On the other hand, it was reviewed that nanocomposites prepared by solution casting and evaporating a mixture of nanocellulose and thermoplastic starch (TPS) or latex presented higher mechanical properties than nanocomposites of the same mixture prepared by freeze-drying and continued by hot-pressing (Dufresne, Cavaillé, & Helbert, 1997; Helbert, Cavaillé, & Dufresne, 1996). The very large reinforcing effect reported for cast and evaporated materials was ascribed to the formation of a rigid nanocellulose/nanocellulose network, probably linked by hydrogen bonds. It was suggested that the formation of this network is more predominant in the evaporated films due to lower processing times.

The second method is the most commonly used which is summarized in Figure 4, and three systems can be distinguished depending on the polymer used as matrix, for example;

- water soluble polymers,
- polymer emulsions, and
- non-hydrosoluble polymers.

For non-hydrosoluble polymer, there are two techniques can be done in order to obtain non-agglomerate distribution of nanocellulose in the polymer:

- coating of the surface of the nanocellulose with surfactants having polar heads and long hydrophobic tails;
- grafting of hydrophobic chains at the surface of nanocellulose.

These procedures allow the preparation of polymer nanocomposites by mixing the nanoparticle suspensions in organic medium with a solution of polymer (Siqueira, Bras, & Dufresne, 2010b).

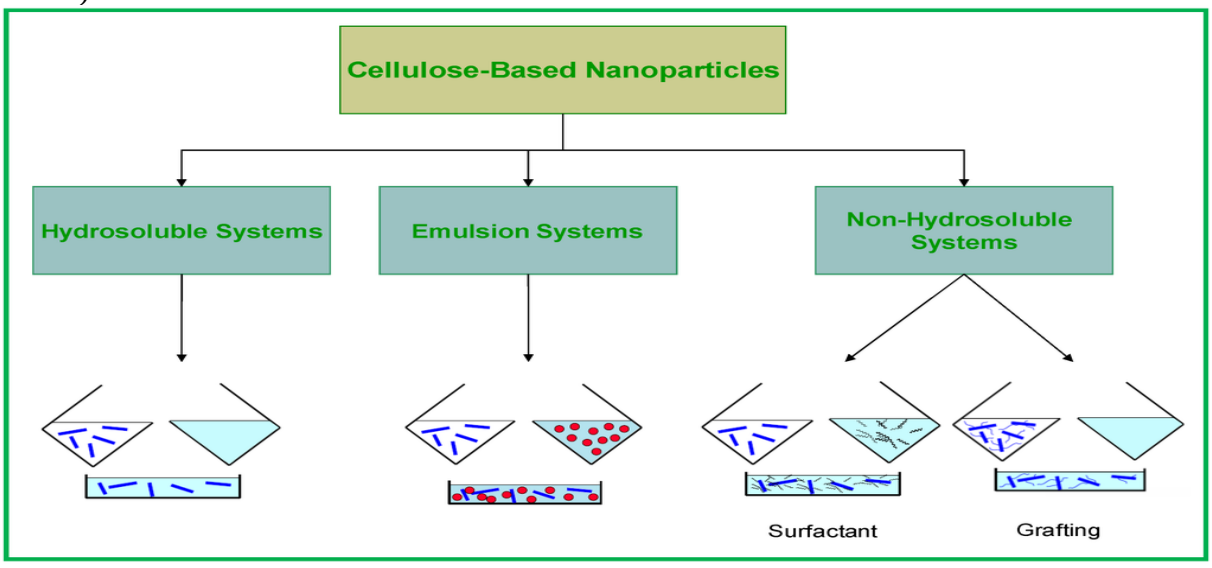

Figure 4: General scheme of strategies used for preparation of cellulose based nanocomposites by solvent casting.

Nanocellulose reinforced starch-based nanocomposite

Bioplastic can be simply defined as a material that are made up of 100% renewable material. One of the bioplastic that is widely used is starch. Starch, which is also a renewable material has gained huge attention among scientists to substitute conventional petroleum-based plastics, specifically for disposable applications. However, the usage of thermoplastic starch is greatly hindered by their intractable nature, poor water sensitivity, poor mechanical strength, and brittleness. Thus, one of the methods to overcome these problems is by reinforcing it with nanocellulose. Cellulose nanostructure have been most usually applied as reinforcing phases with polymer matrix due to their amazing properties when contacted with polymer matrix. By reinforcing nanocellulose and starch polymer, it has been proven to enhance starch mechanical strength and water barrier properties (Slavutsky & Bertuzzi, 2014).

Various source of nanocrystalline cellulose reinforced starch-based nanocomposite

Recently, due to high aspect ratio and mechanical strength of NCC, there is a consciousness of using NCC as loading-bearing in developing new and inexpensive biodegradable material. In this section, starch is used as a polymer in which solution casting method is mostly used in this reviewed data collected. Table 2 below summarized mechanical properties of some nanocrystalline cellulose reinforced starch-based nanocomposite. It can be summarized that different types of starches and NCC sources resulted in different mechanical properties.

The differences between current work and other works listed in Table 2 and Table 3 are the sources of fibres used in making of nanocrystalline cellulose (NCCs) and nanofibrillated cellulose (NFCs). Natural fibres from various plants is used to isolate NCCs, through the process of delignification, mercerization and hydrolysis. In experiment conducted by Ilyas et al. (Ilyas et al., 2018), delignification (using sodium chlorite, $NaClO_2$) and mercerization (using sodium hydroxide, NaOH) treatments is being used to remove the amorphous structure in fibres, such as lignin and hemicellulose, respectively, which also splits the fibres into smaller fibrils known as cellulose microfibrils. After that, the cellulose macrofibrils undergone hydrolysis process (1200 rpm, 45^{o}C, 60 wt. %, H_2SO_4) to remove the amorphous region within the cellulose (Ilyas et al., 2018). The concentration of sulphuric acid (H_2SO_4) was fixed and the time was varied for 30 min, 45 min and 60 min. The optimum results for NCCs gained from this experiment is chosen to reinforce sugar palm starch. However, for the NFCs, most of the researchers used high pressurized homogenizer (HPH) mechanical process to extract nanofibril from cellulose fibre. Usually, 500 bar pressure or higher was used with different cycle number of 5 cycle, 10 cycle and 15 cycle for the experiment. Similarly, the optimum resulted of NFCs gained from this experiment will be chosen to reinforce starch.

Table 2: Examples of starch based polymer, NCC nanocomposites and their mechanical properties.

Starch-based polymers	NCC Sources	Isolation Chemical / Time of NCC	Manufacturing technique	Tensile strength (MPa)	Young's modulus (MPa)	Ref.	Year
Maize starch	Tunicin	55 wt % H_2SO_4 / 20 mins	Solution-casting	0.24 – 20	51 – 315	(Anglès & Dufresne, 2000, 2001)	2000, 2001
Maize starch	Waxy maize starch	H_2SO_4 / 5 days	Solution-casting	1 – 15	11 – 320	(Angellier, Molina-Boisseau, Dole,	2004, 2006

						& Dufresne, 2006)(Angellier, Choisnard, Molina-Boisseau, Ozil, & Dufresne, 2004)	
Wheat starch	Cottonseed linter	64 wt % H2SO4 / 4 h	Solution-casting	2.5 – 7.8	36 – 301	(Lu, Weng, & Cao, 2005)	2005
Wheat starch	Ramie	64 wt % H2SO4 / 4 h	Solution-casting	2.8 – 6..9	56 – 480	(Lu, Weng, & Cao, 2006)	2006
Potato starch	MCC	64 wt % H_2SO_4 / 2 h	Solution-casting	13.7	460	(Kvien, Sugiyama, Votrubec, & Oksman, 2007)	2007
Pea starch	Hemp	64 wt % H_2SO_4 / 4 h	Solution-casting	3.9 – 11.5	31.9 – 823.9	(Xiaodong Cao, Chen, Chang, Stumborg, & Huneault, 2008)	2008
Pea starch	Flax	64 wt % H_2SO_4 / 4 h	Solution-casting	3.9 – 11.9	31.9 – 498.2	(X. Cao, Chen, Chang, Muir, & Falk, 2008)	2008
Maize starch	Tunicate	–	Solution-casting	42	208 – 838	(Mathew, Thielemans, & Dufresne, 2008)	2008
Pea starch	Bamboo	50 wt % H_2SO_4 / 48 h	Solution-casting	2.5 – 12	20.4 – 210.3	(D. Liu, Zhong, Chang, Li, & Wu, 2010)	2010
Wheat starch	Microcrystalline cellulose (MCC)	36.5 wt.% HCl	Solution-casting	3.15 – 10.98	–	(Chang, Jian, Zheng, Yu, & Ma, 2010)	2010
Potato starch	Potato peel waste	64 wt % H_2SO_4 / 90 mins	Solution-casting	–	460	(Chen, Lawton, Thompson, & Liu, 2012)	2012
Plasticized starch	Cotton cellulose powders	H_2SO_4	Solution-casting	–	–	(Yang, Tang, Wang, Kong, & Zhang, 2014)	2014
Maize starch	Sugarcane bagasse	64 wt % H_2SO_4/ 3 h	Solution-casting	17.4	520	(Slavutsky & Bertuzzi, 2014)	2014
Potato starch	Cotton linter	64 wt % H_2SO_4 / 1 h	Solution-casting	4.93	–	(Noshirvani, Ghanbarzadeh, Fasihi, & Almasi, 2016)	2016
Sugar Palm Starch	Sugar palm fibre	60 wt% H_2SO_4 / 45 min	Solution-casting	11.5	178	Current study	2017

Table 3: Examples of starch based polymer, NFC nanocomposites and their mechanical properties.

Starch-based polymers	NFC Sources	NFC Preparation	Manufacturing technique	Tensile strength (MPa)	Young's modulus (MPa)	Ref.	Year

Cassava starch	Cassava bagasse	Hydrolyzed in 6.5 M H_2SO_4 / 40 min	Solution-casting	4.8	84.3	(E. de M. Teixeira et al., 2009)	2009
Mango puree	Wheat	-	Solution-casting	8.76	322.05	(Azeredo et al., 2009)	2009
Maize starch	Wheat straw	High Pressurize Homogenizer/ 15 min	Solution-casting	6.75	220	(Kaushik, Singh, & Verma, 2010)	2010
Maize starch	Cotton cellulose	Hydrolyzed in 6.5M sulfuric acid/ 75 min	Solution-casting	0.35	3.12	(E. D. M. Teixeira et al., 2011)	2011
Potato starch	Softwood wood flour	Super masscolloider	Solution-casting	17.5	1317.0	(Hietala, Mathew, & Oksman, 2013)	2013
Potato starch	Rice straw	Ultrasonication	Solution-casting	5.01	160	(Nasri-Nasrabadi, Behzad, & Bagheri, 2014)	2014
Maize starch	Kenaf	Super masscolloider	Solution-casting	2.35	53.6	(Karimi, Tahir, Dufresne, Karimi, & Abdulkhani, 2014)	2014
Corn starch	Kenaf	Super masscolloider	Solution-casting	38.0	141.0	(Babaee, Jonoobi, Hamzeh, & Ashori, 2015)	2015
Corn starch	Bamboo fibre	-	Solution-casting	11.2	12.4	(Llanos & Tadini, 2017)	2017
Sugar Palm Starch	Sugar palm fibre	High Pressurize Homogenizer, 500 bar	Solution-casting	-	-	Current study	2017

Table 4: Sugar palm fiber reinforced sugar palm starch polymer composites

Filler	Polymer	Tensile strength	Author	Year
-	Sugar palm starch	2.42 Mpa	Sahari et al.(J Sahari, Sapuan, Zainudin, & Maleque, 2012)	
Sugar palm fibre (SPF)	Sugar palm starch	5.5 Mpa	Sahari et al. (Japar Sahari, Salit, Zainudin, & Maleque, 2014; J Sahari et al., 2012)	2012, 2014
Sugar palm cellulose (SPC)	Sugar palm starch	10.5 Mpa	Sanyang et al. (Sanyang, Sapuan, Jawaid, Ishak, & Sahari, 2016)	2016
Sugar palm nanocrystalline cellulose (SPNCCs)	Sugar palm starch	11.47 ± 0.25 Mpa	Current study	2017
Sugar palm nanofibrillated cellulose (SPNFCs)	Sugar palm starch	-	Current study	2017

Studies related to starch/NCC films are extensively reported (see Table 2 and 3) but to the best of our knowledge, there are no studies conducted on the isolation of nanocrystalline cellulose (NCCs) and nanofibrillated cellulose (NFCs) from sugar palm fibre as well as preparation of sugar palm nanocellulose reinforced sugar palm starch films. Thus, the aim of the current study

is to enhance the functional properties of SPS films by combining them with NCCs and NFCs nanofiller.

Fibre matrix interfacial bonding

Nanostructured fillers play an important role in biocomposite fabrication, since they bring various desired functionalities to the composites. NFC gels can be converted to films by dilution and dispersion in water and then either cast (Alain Dufresne, Cavaill, & Vignon, 1997; Saito, T., Kimura, S., Nishiyama, Y., & Isogai, 2007) or vacuum filtered (Henriksson & Berglund, 2007; Iwamoto, Abe, & Yano, 2008; S, 2015). When the water is removed from the NFC gel, a cellulose nanofiber network is formed with interfibrillar hydrogen bonding, resulted in formation of stiff and strong films. Henriksson et al. (Henriksson & Berglund, 2007) reported that the mechanical properties of NFC films were reduced when immersed in water but much of the structure was retained. The nanofibers in the film were not redispersible in water, which is due to the strong interaction between adjacent nanofibers after drying, most likely dominated by hydrogen bonding. Despite random in-plane NFC orientation, NFC films have interesting mechanical properties. As discussed by Berglund (Berglund, 2006), Young's modulus may approach 20 GPa and strength can reach 240 MPa. However, most literature indicates lower modulus and strength values. Besides improving mechanical properties of starch, addition of NFC to the matrix resulted in a decrease of both water uptake at equilibrium and the water diffusion coefficient. Mondragon et al. (Mondragón, Arroyo, & Romero-García, 2008) applied glyceryl monostearate (GMS) as surfactant in TPS-NFC nanocomposites prepared by solution casting. As expected, cellulose nanofibers derived from husks and corncobs increased the Young's modulus and tensile strength of TPS films due to the strong interactions between the starch matrix and the high aspect ratio nanofibres (Siró & Plackett, 2010). The properties of fiber-reinforced composites depend on many factors, including fiber size, fiber/matrix adhesion, volume fraction of fiber, fiber aspect ratio, fiber orientation, and stress/transfer efficiency through the interface (Samir, Alloin, Sanchez, & Dufresne, 2004). Fiber content in composites is a critical factor since fiber agglomeration through hydrogen bonding tends to occur at higher filler loadings. Beyond the optimum amount, further addition of fiber into these composite systems resulted in gradual decrement of mechanical properties of the materials. The diminished performance of the composites at higher amounts of fiber loading is possibly due to the lack of resin infusion and/or the presence of so many fiber ends in the materials, which could cause crack initiation and hence, potential composite failure beforehand. The cellulosic network is surrounded by a soft phase and the interactions between the filler and the matrix are strongly reduced (Soykeabkaew, Laosat, Ngaokla, Yodsuwan, & Tunkasiri, 2012).

Applications

There are many potential uses of starch composite, include their use as delivery vehicles that protect pharmaceutically active proteins from digestion (HP, AL, & PL, 2000), as microcapsules for small molecules (Korus, Tomasik, & Lii, 2003) and as biodegradable films for food packaging application (Weber, Haugaard, Festersen, & Bertelsen, 2002). Other applications of reinforcement of nanofibre with different polymer is list in Table 5:

Table 4: Application of reinforcement of nanofibre with different polymer

Polymer component	Manufacturing technique	Applications

Methylcellulose	Hydrogel by aqueous dispersion	Thermoreversible and tunable nanocellulose-based hydrogels (McKee et al., 2014)
Plasticized starch	Solution casting	Transparent materials (Nasseri & Mohammadi, 2014)
Starch	Blending (Yang et al., 2014), solution casting (Slavutsky & Bertuzzi, 2014)	Air permeable, resistant, surface-sized paper(Yang et al., 2014), food packaging (Slavutsky & Bertuzzi, 2014)
PVA	Solution casting	Stretchable photonic devices(Wang & Walther, 2015), Wound diagnosis/ biosensor scaffolds(Schyrr et al., 2014), conductive materials (Montes et al., 2015)
Plasticized PLA	Twin-screw extruder	Film blowing, packaging (Herrera, Salaberria, Mathew, & Oksman, 2016)
Maleic-anhydride grafted PLA	Electrospinning	Bone tissue engineering (Zhou et al., 2013)
Cellulose esterified with lauroyl chloride	Solution casting and thermorpressing	Interface melting (Timhadjelt, Serier, Belgacem, & Bras, 2015)
PC	Matster batch melt extrusion process	Optical devices (Mariano, El Kissi, & Dufresne, 2015)
PC based polyurethane blend	Solution casting	Smart actuators and sensors (Li et al., 2015)
Ethylene-co-vinyl acetate rubber	Solution mixing and vulcanization	Transparent, rubbery materials (Ma, Jiang, Hoch, Dong, & Chen, 2015)
PU	Solution casting	High temperature biomedical devices (J. C. Liu, Martin, Moon, & Youngblood, 2015)

Future directions

Bionanocomposites find great potential in many applications, remarkably in packaging, electronics and biomedical sectors. Currently, food packaging films with high barrier properties are being explored. The applications of bionanocomposites in various electronic systems are budding, and it is expected to be a vibrant area of research in future. Significant researches are in progress to extend the application of these nanocomposites for various consumer electronic systems, aiming at the reduction of global e-wastes. Polymer nanocomposites reinforced with carbon nanotubes showed improved electrical conductivity, and extend their application as EMI shielding materials. Bionanocomposites with HAp and layered double hydrox- ides (LDH) have been explored for various biomedical applications. Given these functionalities, nanofillers in bioplastics have excellent potential to revolutionize the utilization of nanocomposites and expand their use in high value applications (Reddy, Vivekanandhan, Misra, Bhatia, & Mohanty, 2013).

Conclusions

The present review paper showed the use of nanocellulose as reinforcements in polymer matrix focussing on starch biopolymer. This review also aimed to provide knowledge and data that have been collected through the experiment conducted by several researchers in this

nanocomposite area. It have been recorded that during 20 years, an increasing number of scientists in the area of cellulose nanocomposites have been developed. Besides that, the present contribution summarized some selected work done in the field of nanocellulose extracted from different sources and by different methods. There are significant influence of the source of nanocellulose on the mechanical properties of nanocomposite. However, it is also related to the preparation of nanocellulose itself and the nanocellulose concentration that being added into starch polymer. The well-dispersion of nanocellulose in a polymer matrix is challenging case. Besides that, it is worth stating that there are many safety concerns about this nanocellulose, as their size allows them to penetrate into cells and eventually remain in the body system. Thus, there is no consensus about categorizing nanomaterials as new materials.

Acknowledgement

The authors would like to thank Universiti Putra Malaysia for the financial support through the Graduate Research Fellowship (GRF) scholarship, Universiti Putra Malaysia Grant scheme Hi-COE (6369107) and FRGS/1/2017/TK05/UPM/01/1 (5540048). The authors are grateful to Dr. Muhammed Lamin Sanyang for guidance. The authors also thank Dr. Rushdan Ibrahim for their advice and fruitful discussions.

References

Abitbol, T., Rivkin, A., Cao, Y., Nevo, Y., Abraham, E., Ben-Shalom, T., … Shoseyov, O. (2016). Nanocellulose, a tiny fiber with huge applications. *Current Opinion in Biotechnology*, *39*(I), 76–88. https://doi.org/10.1016/j.copbio.2016.01.002

Angellier, H., Choisnard, L., Molina-Boisseau, S., Ozil, P., & Dufresne, A. (2004). Optimization of the Preparation of Aqueous Suspensions of Waxy Maize Starch Nanocrystals Using a Response Surface Methodology. *Biomacromolecules*, *5*(4), 1545–1551. https://doi.org/10.1021/bm049914u

Angellier, H., Molina-Boisseau, S., Dole, P., & Dufresne, A. (2006). Thermoplastic Starch−Waxy Maize Starch Nanocrystals Nanocomposites. *Biomacromolecules*, *7*(2), 531–539. https://doi.org/10.1021/bm050797s

Anglès, M. N., & Dufresne, A. (2000). Plasticized Starch/Tunicin Whiskers Nanocomposites. 1. Structural Analysis. *Macromolecules*, *33*(22), 8344–8353. https://doi.org/10.1021/ma0008701

Anglès, M. N., & Dufresne, A. (2001). Plasticized Starch/Tunicin Whiskers Nanocomposite Materials. 2. Mechanical Behavior. *Macromolecules*, *34*(9), 2921–2931. https://doi.org/10.1021/ma001555h

Azeredo, H. M. C., Mattoso, L. H. C., Wood, D., Williams, T. G., Avena-Bustillos, R. J., & McHugh, T. H. (2009). Nanocomposite edible films from mango puree reinforced with cellulose nanofibers. *Journal of Food Science*, *74*(5). https://doi.org/10.1111/j.1750-3841.2009.01186.x

Babaee, M., Jonoobi, M., Hamzeh, Y., & Ashori, A. (2015). Biodegradability and mechanical properties of reinforced starch nanocomposites using cellulose nanofibers. *Carbohydrate Polymers*, *132*(3), 1–8. https://doi.org/10.1016/j.carbpol.2015.06.043

Berglund, L. (2006). New concepts in natural fiber composites. In *In Proceedings of the 27th Ris¢ International Symposium on Materials Science: Polymer Composite Materials for Wind Power Turbines* (pp. 1–9).

Cao, X., Chen, Y., Chang, P. R., Muir, A. D., & Falk, G. (2008). Starch-based nanocomposites

reinforced with flax cellulose nanocrystals. *Express Polymer Letters*, *2*(7), 502–510. https://doi.org/10.3144/expresspolymlett.2008.60

Cao, X., Chen, Y., Chang, P. R., Stumborg, M., & Huneault, M. A. (2008). Green composites reinforced with hemp nanocrystals in plasticized starch. *Journal of Applied Polymer Science*, *109*(6), 3804–3810. https://doi.org/10.1002/app.28418

Chang, P. R., Jian, R., Zheng, P., Yu, J., & Ma, X. (2010). Preparation and properties of glycerol plasticized-starch (GPS)/cellulose nanoparticle (CN) composites. *Carbohydrate Polymers*, *79*(2), 301–305. https://doi.org/10.1016/j.carbpol.2009.08.007

Chen, D., Lawton, D., Thompson, M. R., & Liu, Q. (2012). Biocomposites reinforced with cellulose nanocrystals derived from potato peel waste. *Carbohydrate Polymers*, *90*(1), 709–716. https://doi.org/10.1016/j.carbpol.2012.06.002

Dufresne, A. (2014). *Polymer Nanocomposites from Biological Sources. In Encyclopedia of Nanoscience and Nanotechnology*. (H. S. Nalwa, Ed.) (2nd ed.). Valencia, CA, USA: American Scientific Publisher.

Dufresne, A., Cavaill, J.-Y., & Vignon, M. R. (1997). Mechanical behavior of sheets prepared from sugar beet cellulose microfibrils. *Journal of Applied Polymer Science*, *64*(6), 1185–1194. https://doi.org/10.1002/(SICI)1097-4628(19970509)64:6<1185::AID-APP19>3.0.CO;2-V

Dufresne, A., Cavaillé, J.-Y., & Helbert, W. (1997). Thermoplastic nanocomposites filled with wheat straw cellulose whiskers. Part II: Effect of processing and modeling. *Polymer Composites*, *18*(2), 198–210. https://doi.org/10.1002/pc.10274

Esteves, A. C. C., Barros-Timmons, A., & Trindade, T. (2004). Nanocompósitos de matriz polimérica: estratégias de síntese de materiais híbridos. *Química Nova*, *27*(5), 798–806. https://doi.org/10.1590/S0100-40422004000500020

Favier, V., Chanzy, H., & Cavaille, J. Y. (1995). Polymer Nanocomposites Reinforced by Cellulose Whiskers. *Macromolecules*, *28*(18), 6365–6367. https://doi.org/10.1021/ma00122a053

Habibi, Y., Goffin, A.-L., Schiltz, N., Duquesne, E., Dubois, P., & Dufresne, A. (2008). Bionanocomposites based on poly(ε-caprolactone)-grafted cellulose nanocrystals by ring-opening polymerization. *Journal of Materials Chemistry*, *18*(41), 5002. https://doi.org/10.1039/b809212e

Helbert, W., Cavaillé, J. Y., & Dufresne, A. (1996). Thermoplastic nanocomposites filled with wheat straw cellulose whiskers. Part I: Processing and mechanical behavior. *Polymer Composites*, *17*(4), 604–611. https://doi.org/10.1002/pc.10650

Henriksson, M., & Berglund, L. A. (2007). Structure and properties of cellulose nanocomposite films containing melamine formaldehyde. *Journal of Applied Polymer Science*, *106*(4), 2817–2824. https://doi.org/10.1002/app.26946

Herrera, N., Salaberria, A. M., Mathew, A. P., & Oksman, K. (2016). Plasticized polylactic acid nanocomposite films with cellulose and chitin nanocrystals prepared using extrusion and compression molding with two cooling rates: Effects on mechanical, thermal and optical properties. *Composites Part A: Applied Science and Manufacturing*, *83*, 89–97. https://doi.org/10.1016/j.compositesa.2015.05.024

Heßler, N., & Klemm, D. (2009). Alteration of bacterial nanocellulose structure by in situ modification using polyethylene glycol and carbohydrate additives. *Cellulose*, *16*(5), 899–910. https://doi.org/10.1007/s10570-009-9301-5

Hietala, M., Mathew, A. P., & Oksman, K. (2013). Bionanocomposites of thermoplastic starch and cellulose nanofibers manufactured using twin-screw extrusion. *European Polymer Journal*, *49*(4), 950–956. https://doi.org/10.1016/j.eurpolymj.2012.10.016

HP, G., AL, M., & PL, K. (2000). Starch encapsulation technology for producing recombinant proteins in plants. In *American Association of Cereal Chemists*. Kansas City.

Ilyas, R. A., Sapuan, S. M., & Ishak, M. R. (2018). Isolation and characterization of nanocrystalline cellulose from sugar palm fibres (Arenga Pinnata). *Carbohydrate Polymers*, *181*(November), 1038–1051. https://doi.org/10.1016/j.carbpol.2017.11.045

Ilyas, R. A., Sapuan, S. M., Sanyang, M. L., & Ishak, M. R. (2016). Nanocrystalline cellulose reinforced starch-based nanocomposite: A review. In *5th Postgraduate Seminar on Natural Fiber Composites* (pp. 82–87). Serdang, Selangor: Universiti Putra Malaysia. Retrieved from https://www.researchgate.net/publication/315675302_Nanocrystalline_cellulose_reinforced_starch-based_nanocomposites_A_Review

Ilyas Rushdana, A., Sapuan Salit, M., Lamin Sanyang, M., & Ridzwan Ishak, M. (2017). Nanocrystalline Cellulose As Reinforcement For Polymeric Matrix Nanocomposites And Its Potential Applications: A Review. *Current Analytical Chemistry*, *13*. https://doi.org/10.2174/1573411013666171003155624

Iwamoto, S., Abe, K., & Yano, H. (2008). The Effect of Hemicelluloses on Wood Pulp Nanofibrillation and Nanofiber Network Characteristics. *Biomacromolecules*, *9*(3), 1022–1026. https://doi.org/10.1021/bm701157n

Karimi, S., Tahir, P., Dufresne, A., Karimi, A., & Abdulkhani, A. (2014). A comparative study on characteristics of nanocellulose reinforced thermoplastic starch biofilms prepared with different techniques. *Nordic Pulp & Paper Research Journal*, *29*(1), 41–45.

Kaushik, A., Singh, M., & Verma, G. (2010). Green nanocomposites based on thermoplastic starch and steam exploded cellulose nanofibrils from wheat straw. *Carbohydrate Polymers*, *82*(2), 337–345. https://doi.org/10.1016/j.carbpol.2010.04.063

Klemm, D., Kramer, F., Moritz, S., Lindström, T., Ankerfors, M., Gray, D., & Dorris, A. (2011). Nanocelluloses: A new family of nature-based materials. *Angewandte Chemie - International Edition*, *50*(24), 5438–5466. https://doi.org/10.1002/anie.201001273

Korus, J., Tomasik, P., & Lii, C. Y. (2003). Microcapsules from starch granules. *Journal of Microencapsulation*, *20*(1), 47–56. https://doi.org/10.1080/02652040210162531

Kvien, I., Sugiyama, J., Votrubec, M., & Oksman, K. (2007). Characterization of starch based nanocomposites. *Journal of Materials Science*, *42*(19), 8163–8171. https://doi.org/10.1007/s10853-007-1699-2

Li, Y., Chen, H., Liu, D., Wang, W., Liu, Y., & Zhou, S. (2015). pH-Responsive Shape Memory Poly(ethylene glycol)–Poly(ε-caprolactone)-based Polyurethane/Cellulose Nanocrystals Nanocomposite. *ACS Applied Materials & Interfaces*, *7*(23), 12988–12999. https://doi.org/10.1021/acsami.5b02940

Liu, D., Zhong, T., Chang, P. R., Li, K., & Wu, Q. (2010). Starch composites reinforced by bamboo cellulosic crystals. *Bioresource Technology*, *101*(7), 2529–2536. https://doi.org/10.1016/j.biortech.2009.11.058

Liu, J. C., Martin, D. J., Moon, R. J., & Youngblood, J. P. (2015). Enhanced thermal stability of biomedical thermoplastic polyurethane with the addition of cellulose nanocrystals. *Journal of Applied Polymer Science*, *132*(22), 1–8. https://doi.org/10.1002/app.41970

Llanos, J. H. R., & Tadini, C. C. (2017). Preparation and characterization of bio-nanocomposite films based on cassava starch or chitosan, reinforced with montmorillonite or bamboo nanofibers. *International Journal of Biological Macromolecules*. https://doi.org/10.1016/j.ijbiomac.2017.09.001

Lu, Y., Weng, L., & Cao, X. (2005). Biocomposites of Plasticized Starch Reinforced with Cellulose Crystallites from Cottonseed Linter. *Macromolecular Bioscience*, *5*(11), 1101–

1107. https://doi.org/10.1002/mabi.200500094

Lu, Y., Weng, L., & Cao, X. (2006). Morphological, thermal and mechanical properties of ramie crystallites—reinforced plasticized starch biocomposites. *Carbohydrate Polymers*, *63*(2), 198–204. https://doi.org/10.1016/j.carbpol.2005.08.027

Ma, P., Jiang, L., Hoch, M., Dong, W., & Chen, M. (2015). Reinforcement of transparent ethylene-co-vinyl acetate rubber by nanocrystalline cellulose. *European Polymer Journal*, *66*, 47–56. https://doi.org/10.1016/j.eurpolymj.2015.01.037

Mariano, M., El Kissi, N., & Dufresne, A. (2015). Melt processing of cellulose nanocrystal reinforced polycarbonate from a masterbatch process. *European Polymer Journal*, *69*, 208–223. https://doi.org/10.1016/j.eurpolymj.2015.06.007

Mathew, A. P., Thielemans, W., & Dufresne, A. (2008). Mechanical properties of nanocomposites from sorbitol plasticized starch and tunicin whiskers. *Journal of Applied Polymer Science*, *109*(6), 4065–4074. https://doi.org/10.1002/app.28623

McKee, J. R., Hietala, S., Seitsonen, J., Laine, J., Kontturi, E., & Ikkala, O. (2014). Thermoresponsive Nanocellulose Hydrogels with Tunable Mechanical Properties. *ACS Macro Letters*, *3*(3), 266–270. https://doi.org/10.1021/mz400596g

Mondragón, M., Arroyo, K., & Romero-García, J. (2008). Biocomposites of thermoplastic starch with surfactant. *Carbohydrate Polymers*, *74*(2), 201–208. https://doi.org/10.1016/j.carbpol.2008.02.004

Montes, S., Carrasco, P. M., Ruiz, V., Cabañero, G., Grande, H. J., Labidi, J., & Odriozola, I. (2015). Synergistic reinforcement of poly(vinyl alcohol) nanocomposites with cellulose nanocrystal-stabilized graphene. *Composites Science and Technology*, *117*, 26–31. https://doi.org/10.1016/j.compscitech.2015.05.018

Nasri-Nasrabadi, B., Behzad, T., & Bagheri, R. (2014). Preparation and characterization of cellulose nanofiber reinforced thermoplastic starch composites. *Fibers and Polymers*, *15*(2), 347–354. https://doi.org/10.1007/s12221-014-0347-0

Nasseri, R., & Mohammadi, N. (2014). Starch-based nanocomposites: A comparative performance study of cellulose whiskers and starch nanoparticles. *Carbohydrate Polymers*, *106*(1), 432–439. https://doi.org/10.1016/j.carbpol.2014.01.029

Noshirvani, N., Ghanbarzadeh, B., Fasihi, H., & Almasi, H. (2016). Starch-PVA Nanocomposite Film Incorporated with Cellulose Nanocrystals and MMT: A Comparative Study. *International Journal of Food Engineering*, *12*(1), 37–48. https://doi.org/10.1515/ijfe-2015-0145

Oksman, K., Mathew, A. P., Bondeson, D., & Kvien, I. (2006). Manufacturing process of cellulose whiskers/polylactic acid nanocomposites. *Composites Science and Technology*, *66*(15), 2776–2784. https://doi.org/10.1016/j.compscitech.2006.03.002

Reddy, M. M., Vivekanandhan, S., Misra, M., Bhatia, S. K., & Mohanty, A. K. (2013). Biobased plastics and bionanocomposites: Current status and future opportunities. *Progress in Polymer Science*, *38*(10–11), 1653–1689. https://doi.org/10.1016/j.progpolymsci.2013.05.006

S, A. K. H. P. (2015). *Handbook of Polymer Nanocomposites. Processing, Performance and Application*. (J. K. Pandey, H. Takagi, A. N. Nakagaito, & H.-J. Kim, Eds.). Berlin, Heidelberg: Springer Berlin Heidelberg. https://doi.org/10.1007/978-3-642-45232-1

Sahari, J., Salit, M. S., Zainudin, E. S., & Maleque, M. A. (2014). Degradation Characteristics of SPF/SPS Biocomposites Fabrication of SPF/SPS biocomposites. *Fibres and Textiles in Eastern Europe*, *22*(5107), 96–98.

Sahari, J., Sapuan, S. M., Zainudin, E. S., & Maleque, M. A. (2012). Effect of Water Absorption on Mechanical Properties of Sugar Palm Fibre Reinforced Sugar Palm Starch

(spf / sps) Biocomposites. *Journal of Biobased Materials and Bioenergy*, *6*(November 2015), 1–5. https://doi.org/10.1166/jbmb.2012.1267

Saito, T., Kimura, S., Nishiyama, Y., & Isogai, A. (2007). Cellulose nanofibers prepared by TEMPO-mediated oxidation of native cellulose. *Biomacromolecules*, *8*(8), 2485–2491.

Samir, M. A. S. A., Alloin, F., Sanchez, J. Y., & Dufresne, A. (2004). Cross-linked nanocomposite polymer electrolytes reinforced with cellulose whiskers. *Macromolecules*, *37*(13), 4839–4844. https://doi.org/10.1021/ma049504y

Sanyang, M. L., Sapuan, S. M., Jawaid, M., Ishak, M. R., & Sahari, J. (2016). Effect of sugar palm-derived cellulose reinforcement on the mechanical and water barrier properties of sugar palm starch biocomposite films. *BioResources*, *11*(2), 4134–4145. https://doi.org/10.15376/biores.11.2.4134-4145

Schyrr, B., Pasche, S., Voirin, G., Weder, C., Simon, Y. C., & Foster, E. J. (2014). Biosensors Based on Porous Cellulose Nanocrystal–Poly(vinyl Alcohol) Scaffolds. *ACS Applied Materials & Interfaces*, *6*(15), 12674–12683. https://doi.org/10.1021/am502670u

Siqueira, G., Bras, J., & Dufresne, A. (2010a). Cellulosic Bionanocomposites: A Review of Preparation, Properties and Applications. *Polymers*, *2*(4), 728–765. https://doi.org/10.3390/polym2040728

Siqueira, G., Bras, J., & Dufresne, A. (2010b). Cellulosic Bionanocomposites: A Review of Preparation, Properties and Applications. *Polymers*, *2*(4), 728–765. https://doi.org/10.3390/polym2040728

Siró, I., & Plackett, D. (2010). Microfibrillated cellulose and new nanocomposite materials: A review. *Cellulose*, *17*(3), 459–494. https://doi.org/10.1007/s10570-010-9405-y

Slavutsky, A. M., & Bertuzzi, M. A. (2014). Water barrier properties of starch films reinforced with cellulose nanocrystals obtained from sugarcane bagasse. *Carbohydrate Polymers*, *110*, 53–61. https://doi.org/10.1016/j.carbpol.2014.03.049

Soykeabkaew, N., Laosat, N., Ngaokla, A., Yodsuwan, N., & Tunkasiri, T. (2012). Reinforcing potential of micro- and nano-sized fibers in the starch-based biocomposites. *Composites Science and Technology*, *72*(7), 845–852. https://doi.org/10.1016/j.compscitech.2012.02.015

Teixeira, E. D. M., Lotti, C., Corrêa, A. C., Teodoro, K. B. R., Marconcini, J. M., & Mattoso, L. H. C. (2011). Thermoplastic corn starch reinforced with cotton cellulose nanofibers. *Journal of Applied Polymer Science*, *120*(4), 2428–2433. https://doi.org/10.1002/app.33447

Teixeira, E. de M., Pasquini, D., Curvelo, A. A. S., Corradini, E., Belgacem, M. N., & Dufresne, A. (2009). Cassava bagasse cellulose nanofibrils reinforced thermoplastic cassava starch. *Carbohydrate Polymers*, *78*(3), 422–431. https://doi.org/10.1016/j.carbpol.2009.04.034

Timhadjelt, L., Serier, A., Belgacem, M. N., & Bras, J. (2015). Elaboration of cellulose based nanobiocomposite: Effect of cellulose nanocrystals surface treatment and interface "melting." *Industrial Crops and Products*, *72*, 7–15. https://doi.org/10.1016/j.indcrop.2015.02.040

Wang, B., & Walther, A. (2015). Self-Assembled, Iridescent, Crustacean-Mimetic Nanocomposites with Tailored Periodicity and Layered Cuticular Structure. *ACS Nano*, *9*(11), 10637–10646. https://doi.org/10.1021/acsnano.5b05074

Weber, C. J., Haugaard, V., Festersen, R., & Bertelsen, G. (2002). Production and applications of biobased packaging materials for the food industry. *Food Additives and Contaminants*, *19*(January 2013), 172–177. https://doi.org/10.1080/0265203011008748

Yang, S., Tang, Y., Wang, J., Kong, F., & Zhang, J. (2014). Surface Treatment of Cellulosic

Paper with Starch-Based Composites Reinforced with Nanocrystalline Cellulose. *Industrial & Engineering Chemistry Research*, *53*(36), 13980–13988. https://doi.org/10.1021/ie502125s

Zhou, C., Shi, Q., Guo, W., Terrell, L., Qureshi, A. T., Hayes, D. J., & Wu, Q. (2013). Electrospun Bio-Nanocomposite Scaffolds for Bone Tissue Engineering by Cellulose Nanocrystals Reinforcing Maleic Anhydride Grafted PLA. *ACS Applied Materials & Interfaces*, *5*(9), 3847–3854. https://doi.org/10.1021/am4005072

5TH INTERNATIONAL CONFERENCE ON APPLIED SCIENCES AND ENGINEERING APPLICATION (ICASEA 2018)

Organizing Committee:

Chairman	Assoc. Prof. Dr. Nor Azwadi Che Sidi	UTM
Co-Chairman	Dr Shamsul Jamel Elias	UiTM
Treasurer	Nurul Syazni Muhamad	GAE
Technical Committee	Zafira Zainuddin	GAE
	Nurul Nabila Kamarul Haslan	GAE
Technical Reviewer	Dr Faizah Che Ros	UTM
	Dr Nabilah Zaini	UTM
	Dr Wan Azani Mustafa	UniMAP
	Dr Khairunnisa Mohd Pa'ad	UTM
	Dr Shaza Eva Mohamad	MJIIT
	Dr Siti Rahmah Aid	MJIIT
	Dr Zainudin A. Rasid	MJIIT
	Dr Nor Ruwaida Jamian	MJIIT
	Dr Azura Hamzah	MJIIT
	Dr Aznah Nor Anuar	MJIIT
	Mohamad Shukri Zakaria	UTeM
	Radzi Abdul Rasih	UiTM
	Nurfatehah Wahyuny Che Jusoh	UTM
	Tey Wah Yen	UTM
Liaison Officer	Muhamad Firdaus Abdull Razab	GAE

Published by:
Global Academic Excellence (M) Sdn. Bhd.
(1257579-U)
KELANTAN

eISBN 978-967-15744-1-6